THE UNIVERSITY *of* EDINBURGH

Extreme precision and extreme complexity: source modelling and data analysis development for the laser interferometer space antenna

Alexander Iain Burke

Doctor of Philosophy
University of Edinburgh
August, 2021

Foreword by the author

I recall early on in my PhD having a look at Christopher Berry's thesis just to gain a marginally terrifying idea about what I would have to write by the end. In his acknowledgements he states "Completing a PhD is hard.". Well, Christopher, I fundamentally disagree with you. Completing a PhD is not hard. It is *brutal*. Though it has been, without a doubt, the best four years of my life.

My PhD experience began in Edinburgh when I naïvely knocked on Jonathan Gair's office door, waited ~ 15 seconds for the standard "come in", and told him I was interested in gravitational waves and black holes. I still remember our discussion as if it were yesterday, him sat with his feet up on the desk in his usual way, discussing the consequences of the first detection GW150914 and the science case for the LISA mission. Jonathan is brilliant at many things, but one thing in particular is that he asks the right questions. He sat and reeled off what felt like hundreds of projects whilst I sat, nodding away, wide-eyed, largely oblivious about what I was about to get myself into.

Eagerly I accepted the PhD position and I began my research in the statistics department at The University of Edinburgh, usually surrounded by mathematicians who were only interested in ring theory and non-commutative geometry. I could see them cringe whenever I truncated a Taylor series to the first term, or swapped the order of integration — not that I cared, provided the result made sense. A year and a half in, I met with Jonathan in Edinburgh to discuss some of my broken research where we had a very productive four-hour meeting, as usual. However, five minutes before he had to leave to deliver a tutorial, he dropped the bombshell that he was moving to the Albert Einstein Institute (AEI) in Germany in March 2019. Terrified that I would incur the wrath of my exceptionally patient and understanding partner, Joanne, we discussed and came to the agreement it would be the best thing for me. I packed up my stuff and headed off to Berlin and this is where the fun begins.

I arrived in Germany on July the 31st, 2019, bleary-eyed, scared but excited. My language skills were not particularly strong, though, the phrase "Ein döner kebap, doppelfleische, mit Käse, bitte" was actually all I needed. The AEI is one of the best places in the world for research in gravitational wave astronomy, full of exceptionally talented PhD students and post doctorates. I'm sure that even the manager of the cluster has more experience in solving parameter estimation problems than your typical expert student. Remarkably I was welcomed with open arms, even after I screwed up by missing a flight to a retreat at Ringberg by entering the wrong name onto the boarding card (Ollie $\neq$ Alexander). How embarrassing. Though, shortly after I began my stay at the AEI, my work, knowledge and progress accelerated at rate much greater than it would have done in Edinburgh. Whether this was because I was in the company of truly astounding scientists, or fueled by the kebabs and beer in Berlin, is still up for debate. My time at the AEI has been life changing and I can't thank Jonathan enough for giving me the opportunity to be part of such a brilliant group of gravitational wave astronomers.

It is late in the evening, two days before I submit this thesis, and I am sat in my supervisor's basement (my own choice entirely) looking back on my time in Scotland and Germany. I am proud of what I have achieved and it has been an honour to be part of the next generation gravitational wave astronomers.

Alexander (Ollie) Burke.

Acknowledgements

Aside from the details presented in section 4.2.3, this is the hardest part of the thesis to write. First and foremost, I would like to thank my supervisor, Jonathan Gair, for his exceptional guidance, patience, and crystal clear explanations over the past four years. As many people in the field know, Jonathan is gifted. Always, without a doubt, the smartest man in the room who will always dig you out of a tight spot when you really need it, which, for me, he did frequently. Being honest with the reader, I truly could not have asked for a better supervisor. I also wish to thank Joan Simón, unofficially my second supervisor, for his guidance and support with the work in this thesis. Joan is great fun to work with, beautifully meticulous with his calculations and *never* made me feel like I was asking him a silly question (of which there were many).

I'd like to thank my Edinburgh office mates: Graeme Auld, Fred Tomlinson and Ross Grassie for our many messy evenings in the Jazz Bar and finding essentially any excuse to head to the pub as a "research" trip. I am indebted to my fellow Tacos, Christine Simpson (Tesla, her dog, included) and Matthew Edwards for putting up with my terrible banter. Christine for proof-reading my terrible English and being such an excellent, caring friend and Matt for finding any excuse to discuss research in a bar, normally with the goal of drinking an inhuman volume of gin. Interesting to say, though, that this volume of gin formed the basis of the Bayesian section of chapter 5.

At the AEI, I have been exceptionally lucky to be in the presence of some of the best scientists I have ever had the pleasure of working with. I particularly want to thank Chris Kavanagh for being (without a doubt) the easiest and most straightforward co-author of my life and Michael Katz for his wizard-like programming skills, insight into data analysis and his emotional support in the final stages of this thesis. I honestly don't know what I would have done without you Mike. To all the PhD students at the AEI, you guys are legends and I have been blessed being in your company. A special mention is given to Andrea Antonelli (and his mother) for sending me delicious Italian food at various times throughout my time at the AEI. Roberto, thanks for not pointing the blame at me when the cluster at the AEI had a meltdown (Deyan, we know it was you, stop denying it). Finally, Lorenzo Speri, arguably the most brilliant and *sociable* human being I've ever met. Lorenzo is special and achieved what I could only have thought was impossible: a man that was able to corrupt me more than I corrupt others. I will deeply miss our heavy evenings in biergartens in Berlin discussing science. Thank you for being the best academic friend one could ask for.

Unfortunately it is impossible to list all my friends outside of academia, who have indirectly helped me over these past four years. To the Whatsapp group that shall not be named, thank you for all the laughs. Particular mention to my best friends, Louis Smith and Alex Quinn, for the excellent banter you have provided over the years. I couldn't forget Rachael Green and Catherine Smith for being the best diving buddies one could ever ask for. Rachael for putting up with my terrible underwater dancing (*cha-cha slide*) and Cat for getting me out of a sticky situation underwater (I owe you one for that) and the careful proofreading *this* work.

Joanne, you are such a warrior for the sheer hell you have put up with, and I can only describe you as the true MVP of the research contained in this thesis. Thank you for always being there for me, through thick and thin. Finally, and how could I forget, I wish to thank my loving family — Jim and Katherine, Rachel and Nathan Green and Jamie Burke for all the love and support you have given me over the past 28 years. I love you guys. Cheers.

Apologies

Now, in comparison to the acknowledgements section, this section is almost trivial to write. First of all, I'd like to apologise to my supervisor, Jonathan Gair, for putting up with me over the past four years, having to repeat yourself constantly, dealing with me in a hungover state, and me being a pest in general. Your patience is astounding and how you managed to cope with me as a student is still beyond me. I owe you a bottle of whisky for your efforts.

To my Edinburgh friends, I am sorry that I abandoned you. A special mention to Graeme when I accidentally deleted a chunk of your code when I tried to write you a pleasant message on your editor one evening. Also, how could I forget when I pulled the power socket making your five-day simulation worthless. To Matt Edwards, words cannot describe how apologetic I am for that messy evening in Poznań the week before you left for New Zealand. I seriously owe you one (well, technically speaking, you still owe me) for that evening. Thank you for being the recipient of my stream of unconsciousness.

To Andrea, I apologise for constantly finding ways to keep you from returning home at 8pm on a Saturday evening. Actually, I retract my apology, you need to get a grip and stay out longer, at least 10pm. Riccardo, I admit that I feel a little guilty about constantly berating you ~~for your choice to live in Golm for two years~~ for dodging fun nights out since you were playing Dungeons and Dragons. Lorenzo, I am sorry that I constantly ate your food, drank your beer and grappa, crashed on your couch, left your fridge open and never switched off your lights. I must have been the worst unofficial flatmate you could have asked for. Nils and Niko, I am sorry for nearly making you both throw up whenever you looked at my code and whenever I have discussed `python` "environments" with you. Perhaps one day I will upgrade to *two* environments. Luca, my AEI office mate, I am sorry for constantly distracting you and pressuring you into having a beer in the office, not that this was a difficult task. Stefano, I apologise on behalf of Scotland that a "pizza-crunch" is considered a national treasure. Finally, I'd like to apologise to Alessandra Buonnano for corrupting her division into spending two hour long lunch breaks practicing with diabolos. Honestly, it was like my own little school, I am still convinced that the extra creativity could only have enhanced the research of the division.

Joanne, I am so sorry for ditching you in Edinburgh and moving to Berlin half-way through my PhD. You put up with so much. With my exceptionally long work days, radio silence throughout writing my thesis, and my general rollercoaster ride of a PhD. From my usual rants, I'm pretty sure that you could give a lecture on the difficulty of computing Fisher matrices for EMRIs. You are amazing and you are going to do so well in life. Keep doing what you always do, and remember that none of my work would have been possible without your support.

To my family, I am sorry for being a nuisance over these past 28 years. I'm sorry, mum and dad, for being a nightmare at school asking the teacher time and time again (never giving up) *why* things happened, Rachel for our general competitiveness, though, I'm pretty certain that I wouldn't have got this far in academia if you hadn't presented your school grades to me in the fashion that you did. Finally, Jamie, for constantly winding you up and driving you to near breaking point. To be fair Jamie, I only did this because you are so well put together you need to be challenged every now and again. Take this as a compliment.

Finally, I apologise to my examiners John Peacock and Christopher Moore for being subjected to the endless torrent of calculations and statements that define my thesis. I appreciated the roasting, since I could walk away with full knowledge that I had fully earned my doctorate.

To the Very Rev Prof Alan Main TD, MA, BD, STM, PhD, DD,

my grandfather. A true inspiration. I love you.

Declaration

All original research contained in this thesis was formed through a collaborative effort. Chapters 1, 2 and 3 are *introductory* chapters where I repeat, though interpret in my own style, essential features of gravitational wave astronomy used in this work. Below I will highlight my personal contributions in each of the *research chapters* 4, 5, 6, 7 and 8.

- In chapter 4, I am the lead author who wrote the paper [1], argued the direction the paper should take, derived the main transition equations of motion in the paper and independently wrote the code to exemplify these transition equations of motion. Jonathan Gair and Joan Simon acted as advisors in this project. Jonathan Gair took the lead in section 4.2.3. Aside from this, the work is my own.

- I am also the lead author of the research presented in chapter 5. I wrote the paper [2] and developed all the code both verify and therefore claim how tightly one can constrain the spin parameter of near-extremal black holes. Joan Simon led the section 5.3, the analytical prescription of the Fisher matrix and I verified all his calculations both analytically and numerically. Jonathan Gair acted in an advisory role throughout the entire project. Matt Edwards provided advice on the Bayesian section of the paper.

- I am also the lead author on the EMRI systematics research presented in chapter 6. I have developed all the code used to generate the results within that chapter. Chris Kavanagh and Jonathan Gair acted as advisors. Chris Kavanage gave insight into the EMRI waveform model we use and acted as the bridge between the self force community and me. This research is complete and will be submitted by October.

- There is no lead author of the results presented in 7, since Andrea Antonelli (a fellow PhD student) and I put in equal contributions. I was the first to develop the code that generalised the CV formalism and was on hand to assist Andrea through his sections 7.3.1, 7.3.2 and 7.3.3. I took the main lead on 7.3.4, which were the first results generated for the paper, and independently lead 7.4. In addition, I was the only author that verified all of Jonathan Gair's calculations presented in section 7.1. Andrea and I both were the lead writers of the paper [3] and Jonathan acted in an advisory role.

- For the research presented in 8, I am the lead researcher. I derived all the formulas presented and wrote all the code to both verify the analytic results and present a case-study on the importance of understanding the effect data gaps have on parameter estimation. Jonathan acted as in an advisory role. This research is still in progress and will be finalised by the end of this year.

Using TexCount, there are $59,934 < 70,000$ words in this thesis. Finally, the use of "we", "our" and "the author" in the main text is purely stylistic.

(*Alexander Iain Burke*)

Abstract

Gravitational wave (GW) observations made with the LIGO and Virgo interferometers are transforming our understanding of the astrophysics of stellar origin compact objects (CO). The planned Laser Interferometer Space Antennae (LISA) will extend these observations to lower frequencies, thus higher mass systems and will have similar transformative potential. However, this potential can only be realised through the development of new waveform models and data analysis tools. This is the focus of this thesis.

The primary GW source discussed in this work are Extreme mass-ratio inspirals (EMRIs), the inspiral of a small CO of mass $1M_{\odot} - 100M_{\odot}$ into a super-massive black hole (SMBH) with mass $10^{(4-7)}M_{\odot}$. Through analytical and numerical means, we develop tools that model circular and equatorial adiabatic inspiral-transition-plunge trajectories and resultant EMRI waveforms, regardless of the central SMBH spin. From a Fisher matrix (FM) approach we show analytically and verify numerically that constraints on the spin parameter from LISA observations of near-extremal EMRIs surpass those of moderately spinning EMRIs by ~ 3 orders of magnitude. Using the Cutler-Vallisneri (CV) formalism that is based off the FM, we investigate accuracy requirements of low eccentricity Schwarzschild based EMRI waveforms. We determine what level of numerical precision the components of the gravitational-self-force must be computed in order to not significantly bias parameter estimates. The CV formalism is then extended to account for an arbitrary number of waveforms with modelling errors and an astrophysical foreground and detector noise. The formalism is illustrated with simplified, yet realistic, scenarios appropriate to third-generation ground-based and the space-based detectors. In the final piece of this work, we present the impact that data gaps have on parameter estimation in the context of LISA. Data gaps could potentially introduce correlations amongst noise components in the frequency domain. The likelihood, signal-to-noise ratio and FM are generalised to take these correlations into account. We conclude by presenting a case study, exemplifying the detrimental effect of mis-modelling the noise as a stationary process rather than the correct non-stationary process due to the presence of data gaps.

Notation and Conventions

In this work we will use the space-like metric signature $(-,+,+,+)$ and use conventions for the Riemann tensor $R^{\mu}_{\rho\nu\sigma}$ and Ricci tensor $R_{\mu\nu} = R^{\rho}_{\mu\rho\nu}$ given by Misner-Thorne-Wheeler [4]. Greek letters stand for space-time indices $\mu = \{0,1,2,3\}$ and Latin letters are used for spatial indices $i = \{1,2,3\}$. Derivatives with respect to coordinates use the short-hand $\partial_\mu = \partial/\partial x^\mu$.

We use geometrized units ($G = c = 1$) and Boyer-Lindquist coordinates (t, r, θ, ϕ) to denote the Kerr/Schwarzschild space-time. For extreme mass-ratio inspirals, we denote the *primary* to be the larger black hole with mass M and the *secondary* to be the compact object with mass μ with *mass-ratio* is given by $\eta = \mu/M \ll 1$. Any quantity carrying a tilde refers to a rescaled dimensionless quantity i.e. $\tilde{r} = r/M$, $\tilde{t} = t/M$, $\tilde{E} = E/\mu$ and $\tilde{L} = L/M\mu$, but we keep a as the dimensionless Kerr spin parameter with *no* tilde. This is with the exception in section 2.4 where we retain units to "simplify" the presentation. Dotted quantities (e.g. $\dot{\tilde{E}}$) denote coordinate time derivatives. The quantity $M_\odot$ denotes the mass of the sun. Orbit averaging, or time averaging procedures are denoted $\langle\cdot\rangle$. Unfortunately, chapter 7 is the exception to all of this: we assume η to be the symmetric mass ratio $\eta = (M_1 M_2)/(M_1 + M_2)^2$ for M_1 and M_2 individual component masses and retain factors of G and c.

Functional quantities given hats/tildes refer to the continuous/discrete time Fourier transform. Expressions $A \sim \mathcal{O}(B)$ or, for brevity, $A \sim B$ stress that both A and B scale in the same way. The exception to this is when probability distributions are involved e.g. $A \sim N(\mu, \sigma^2)$ implies A is normally distributed with mean μ and σ^2. Parameter spaces are denoted $\boldsymbol{\theta}$ with individual parameters $\theta^i \in \boldsymbol{\theta}$ and parameter derivatives $\partial_i = \partial/\partial\theta^i$. The ensemble average, or equivalently, time average of an (ergodic) process $X(t)$ is denoted by $\langle X(t)X^\star(t')\rangle$ and, in vector format, $\mathbb{E}[\boldsymbol{X}\boldsymbol{X}^\dagger]$ where $\boldsymbol{X} = \{X_i\}_{i=1}^N$ is *discretized*. The $a^\star(t)$ and $\boldsymbol{a}^\dagger$ correspond to complex conjugation and hermitian conjugate respectively.

Due to the variation in the projects in this thesis, standardizing notation has been *highly* non-trivial. The author deeply apologises for any source of confusion and takes *full responsibility* for notational blunders found throughout this work.

Contents

Acronyms

1PA First Order Post-Adiabatic. 38

2PA Second Order Post-Adiabatic. 39

AdS Anti-de Sitter. 27

BBH Binary Black Hole. 13

BH Black Hole. 12

BL Boyer-Lindquist. 26

CE Cosmic Explorer. 16

CFT Conformal Field Theory. 27

CO Compact Object. 19

CTFT Continuous Time Fourier transform. 51

CV Cutler-Vallisneri. 69

DTFT Discrete Time Fourier Transform. 51

EM Electromagnetic. 6

EMRI Extreme Mass-Ratio Inspiral. 19

ET Einstein Telescope. 16

FM Fisher Matrix. 64

GB Galactic Binary. 17

GRC General Relativistic Correction. 45

GSF Gravitational Self-Force. 36

GSU Gravitational Sensor Unit. 16

GW Gravitational Wave. 1

IFT Inverse Fourier Transform. 51

ISCO Inner-most Stable Circular Orbit. 32

LC Lindblom Criterion. 69

LG Lorenz Gauge. 4

LIGO Laser interferometric Gravitational-wave observatory. 12

LISA Laser Interferometer Space Antennae. 16

LPF LISA Pathfinder. 17

LSA Linear Signal Approximation. 65

MBHB Massive Black Hole Binary. 18

MCMC Markov-Chain Monte-Carlo. 74

MH Metropolis-Hastings. 75

NHEK Near-Horizon Extremal Kerr. 28

NIT Near-Identity Transformation. 154

NR Numerical Relativity. 25

NS Neutron Star. 12

ODE Ordinary Differential Equation. 115

OMS Optical Metrology Subsystem. 16

OT Ori-Thorne. 80

PDE Partial Differential Equation. 41

PINK-TACO Parameter Inference for Near-extremal Kerr Toolkit for Accessing Cosmological Observations. 222

PN Post-Newtonian. 25

PN-SF Post-Newtonian expansion of the Self-Force. 169

PSD Power Spectral Density. 54

RMS Root-Mean-Square. 47

SMBHB Super Massive Black Hole Binary. 17

SNR Signal-to-Noise ratio. 61

SVD Singular Value Decomposition. 209

SWSH Spin Weighted Spheroidal Harmonic. 42

TT Transverse-Traceless Gauge. 7

Chapter 1

Introduction

1.1 Gravitational waves

Almost six years have passed since the groundbreaking discovery of gravitational waves (GWs) on the 14th of September, 2015. Sourced by the acceleration of material bodies, GWs are propagating oscillating gravitational fields that travel at the speed of light. The detection of GWs was remarkable since, despite Albert Einstein predicting them as a byproduct from his general theory of relativity in 1916 [5, 6, 7], it took nearly one hundred years to directly prove their existence using experimental observations. The detection was an extraordinary feat, and will only be marked as one of the greatest scientific achievements of the century. To this day, modern day GW detectors are the most sensitive man-made instruments to have ever existed on Earth, and are able to measure minuscule displacements on the order of $\sim 10^{-21}$. Assuming the North Sea was fixed in volume, this is equivalent to dropping a pipette of water into the Sea and measuring the fractional change in the volume. In the following subsections, we describe the journey between the moment of their prediction to the groundbreaking detection, marking what could only be described as a new era for gravitational physics. No longer are we restricted to the Universe's secrets through telescopic observations made by eye, now we have the toolkit to listen to the deepest and darkest secrets of the *gravitational* universe.

1.1.1 Einstein's field equations

Einstein's general theory of relativity unified two fundamental concepts: space and time. Indeed, Einstein himself provided a new interpretation of gravity that it is not so much a force, as originally proposed by Isaac Newton, but more a warping of space *and* time (spacetime). At the cornerstone of general relativity lies Einstein's famous field equations, which govern how

spacetime reacts to the presence of matter/energy. Explicitly

$$R_{\mu\nu} - \frac{1}{2} g_{\mu\nu} \mathcal{R} = \frac{8\pi G}{c^4} T_{\mu\nu} \,, \tag{1.1}$$

where the left-hand side governs curvature with curvature tensors $R_{\mu\nu}$ the Ricci tensor, $\mathcal{R}$ the Ricci scalar and $g_{\mu\nu}$ the metric tensor. The right-hand side is the stress energy tensor, encapsulating the density and energy/momentum flux in spacetime. The Ricci tensor and scalar can be calculated by computing the Christoffel symbols (of the second kind) and Riemann curvature tensor

$$\Gamma^{\mu}{}_{\nu\rho} = \frac{1}{2} g^{\mu\sigma} (\partial_\rho g_{\sigma\nu} + \partial_\nu g_{\rho\sigma} - \partial_\sigma g_{\nu\rho}) \tag{1.2a}$$

$$R^{\rho}{}_{\sigma\mu\nu} = \partial_\mu \Gamma^{\rho}{}_{\nu\sigma} - \partial_\nu \Gamma^{\rho}{}_{\mu\sigma} + \Gamma^{\rho}{}_{\mu\lambda} \Gamma^{\lambda}{}_{\nu\sigma} - \Gamma^{\rho}{}_{\mu\lambda} \Gamma^{\lambda}{}_{\mu\sigma} \tag{1.2b}$$

$$R_{\mu\nu} = R^{\rho}{}_{\mu\rho\nu} \tag{1.2c}$$

$$\mathcal{R} = g^{\mu\nu} R_{\mu\nu} \,. \tag{1.2d}$$

In (1.1), the tensor objects on the left embody the curvature of spacetime, whereas the object on the right defines the matter/energy content. John Archibald Wheeler, the scientist who also coined the term "black hole", summarised this equation beautifully: "spacetime tells matter how to move, and matter tells spacetime how to curve". These field equations embody this idea by describing deformations in spacetime as a result of matter and energy being present.

Notice that left-hand side of (1.1) is in terms of curvature so has units 1/Area and the right-hand side $T_{\mu\nu}$ encodes stress, pressure and energy with units Force/Area. So to be dimensionally consistent, this implies that

$$F_G = \frac{c^4}{8\pi G} \approx 10^{42} \,\mathrm{kg\,m\,s^{-2}}, \tag{1.3}$$

where F_G could be regarded as a "geometric force". Thus, spacetime is incredibly rigid — requiring a massive quantity of energy to be distorted. In the next subsection, we use Einstein's field equations to derive how flat spacetime disturbances propagate through a vacuum spacetime.

1.1.2 Linearized gravity

We consider a weakly perturbed gravitational field and write the metric tensor as

$$g_{\mu\nu} = \eta_{\mu\nu} + h_{\mu\nu}, \qquad |h_{\mu\nu}| \ll 1 \,. \tag{1.4}$$

The flat part of spacetime is represented by the Minkowski metric $\eta_{\mu\nu} = \text{diag}(-1, 1, 1, 1)$ and $h_{\mu\nu}$ encodes information on the perturbations of the flat spacetime. From this point onwards, we shall neglect quadratic terms in h and assume the components are small, $|h_{\mu\nu}| \ll 1$.

We begin by substituting both equation (1.4) and the inverse $g^{\mu\nu} = \eta^{\mu\nu} - h^{\mu\nu}$ into (1.2a), to obtain

$$\Gamma^{\mu}{}_{\nu\rho} = \frac{1}{2}\eta^{\mu\sigma}(\partial_\nu h_{\sigma\rho} + \partial_\rho h_{\nu\sigma} - \partial_\sigma h_{\rho\nu})\,. \tag{1.5}$$

The Christoffel symbols Γ can now be used to find an expression for the Riemann tensor. Since we are working to leading order in $h_{\mu\nu}$, the last two terms of (1.2b) can be ignored simplifying calculations. Plugging (1.5) into (1.2c)-(1.2d) yield both the Ricci tensor and scalar respectively

$$R_{\mu\nu} = -\frac{1}{2}\Box h_{\mu\nu} + \frac{1}{2}\partial^\gamma\partial_\mu h_{\nu\gamma} + \frac{1}{2}\partial^\gamma\partial_\nu h_{\mu\gamma} - \frac{1}{2}\partial_\mu\partial_\nu h \tag{1.6}$$

$$\mathcal{R} = -\Box h + \partial^\mu\partial^\nu h_{\mu\nu}\,. \tag{1.7}$$

Here $h = \eta^{\mu\nu}h_{\mu\nu}$ and $\partial^2 = \partial^\mu\partial_\mu := \Box$ the d'Alembert operator. Substituting these curvature tensors into the field equations (1.1) gives

$$\Box h_{\mu\nu} - \partial^\gamma\partial_\mu h_{\nu\gamma} - \partial^\gamma\partial_\nu h_{\mu\gamma} + \partial_\mu\partial_\nu h + \eta_{\mu\nu}(\partial^\rho\partial^\gamma h_{\rho\gamma} - \Box h) = -\frac{16\pi G}{c^4}T_{\mu\nu}\,. \tag{1.8}$$

The above equation is far from convenient, and doesn't offer any striking results. However, one can make use of the substitution $\bar{h}_{\mu\nu} = h_{\mu\nu} - \frac{1}{2}\eta_{\mu\nu}h$ to simplify the equation above. A short calculation reveals $\bar{h} = \eta^{\mu\nu}\bar{h}_{\mu\nu} = -h$, implying that $h_{\mu\nu} = \bar{h}_{\mu\nu} - \frac{1}{2}\eta_{\mu\nu}\bar{h}$. Inserting this into equation (1.8) provides a few cancellations

$$\Box\bar{h}_{\mu\nu} - \partial^\gamma\partial_\mu\bar{h}_{\nu\gamma} - \partial^\gamma\partial_\nu\bar{h}_{\mu\gamma} + \eta_{\mu\nu}\partial^\gamma\partial^\kappa\bar{h}_{\gamma\kappa} = -\frac{16\pi G}{c^4}T_{\mu\nu}\,. \tag{1.9}$$

This equation, still, is not particularly pleasant. We can see that we have a wave-like term $\Box\bar{h}_{\mu\nu}$ but in the presence of three additional terms. These non-wavelike terms disappear provided $\partial^\rho\bar{h}_{\mu\rho} = 0$. In the next section we will introduce a *gauge* transformation and then fix particular coordinates on the manifold to ensure such a condition.

1.1.3 The Lorenz gauge

In this section, we propose to choose a coordinate transformation that not only preserves the nearly Lorentzian properties of (1.4), but also dramatically simplifies the resultant Einstein equations for a weakly perturbed flat spacetime. Consider an inertial frame S with coordinates

(t, x, y, z) and consider a linear transformation (via a Lorentz boost with velocity v) to another frame S' with coordinates (t', x', y', z'). In the S' coordinate frame, the metric tensor takes the form

$$g'_{\rho\sigma} = \Lambda^{\mu}{}_{\rho}\Lambda^{\nu}{}_{\sigma}g_{\mu\nu}. \tag{1.10}$$

Substituting (1.4) into (1.10), one can show that the metric tensor in the new coordinate frame S' is $g'_{\rho\sigma} = \eta_{\rho\sigma} + \Lambda^{\mu}{}_{\rho}\Lambda^{\nu}{}_{\sigma}h_{\mu\nu} = \eta_{\rho\sigma} + h'_{\rho\sigma}$. Hence when performing Lorentz transformations from one frame to the other, the new metric tensor $g'_{\rho\sigma}$ will still describe a weakly perturbed flat spacetime with metric perturbations $|h'_{\rho\sigma}| \ll 1$. Furthermore, the quantity $h_{\mu\nu}$ transforms like a tensor in special relativity (transforms like a tensor under Lorentz transformations).

Let us now introduce an infinitesimal coordinate transformation of the form $x^{\beta\prime} = x^{\beta} + \chi^{\beta}(x^{\alpha})$ with $|\chi^{\beta}| \ll 1$. We can understand how $h_{\mu\nu}$ transforms by computing the metric tensor $g'_{\rho\sigma}$ in the $x^{\beta\prime}$ coordinate basis

$$\begin{aligned} g'_{\rho\sigma} &= \frac{\partial x^{\mu}}{\partial x^{\rho\prime}}\frac{\partial x^{\nu}}{\partial x^{\sigma\prime}}g_{\mu\nu} \\ &= (\delta^{\mu}{}_{\rho}\delta^{\nu}{}_{\sigma} - \partial_{\rho}\chi^{\mu}\delta^{\nu}{}_{\sigma} - \partial_{\sigma}\chi^{\nu}\delta^{\mu}{}_{\rho})(\eta_{\mu\nu} + h_{\mu\nu}) \\ &= \eta_{\rho\sigma} + h_{\rho\sigma} - \partial_{\rho}\chi_{\sigma} - \partial_{\sigma}\chi_{\rho} \\ &= \eta_{\rho\sigma} + h'_{\rho\sigma}, \end{aligned}$$

where we have worked to leading order in both $h_{\mu\nu}$ and χ^{μ}. Notice that the final equation above has the same form of the metric tensor we derived applying a Lorentz transformation from one frame S to S'. Also, on the assumption that $|\partial_{\rho}\chi_{\beta}| \ll 1$ then the new coordinate system described by $g'_{\rho\sigma}$ still represents a weakly perturbed flat spacetime. What we learn here is that we are free to add an infinitesimal translation (χ^{β}) to the original coordinates x^{β} whilst maintaining the validity of the assumption that the spacetime is nearly flat. The idea then is to choose the coordinates χ^{β} suitably in order to simplify Einstein's equations as much as possible. Specifying χ^{β} is known as fixing the *gauge* and choosing

$$h'_{\rho\sigma} = h_{\rho\sigma} - \partial_{\rho}\chi_{\sigma} - \partial_{\sigma}\chi_{\rho} \tag{1.11}$$

is known as a *gauge transformation*, specifically the *Lorenz gauge* (LG). In the next section, we show that the components of χ^{β} can be suitably chosen in order to ensure that $\partial^{\rho}\bar{h}_{\mu\rho} = 0$, reducing (1.9) to a wave equation.

1.1.4 The wave equation

The previous section showed that by introducing $x^{\beta\prime} = x^\beta + \chi^\beta(x^\alpha)$ for $|\chi^\beta| \ll 1$, the transformed metric perturbations take the form

$$h^{(\mathrm{LG})}_{\mu\nu} = h_{\mu\nu} - \partial_\nu \chi_\mu - \partial_\mu \chi_\nu \,. \tag{1.12}$$

We can relate $\bar{h}^{(\mathrm{LG})}_{\mu\nu}$ to $\bar{h}_{\mu\nu}$ by computing

$$\begin{aligned}
\bar{h}^{(\mathrm{LG})}_{\mu\nu} &= h^{(\mathrm{LG})}_{\mu\nu} - \frac{1}{2}\eta_{\mu\nu} h^{(\mathrm{LG})} \\
&= h_{\mu\nu} - \partial_\nu \chi_\mu - \partial_\mu \chi_\nu - \frac{1}{2}\eta_{\mu\nu}\eta^{\rho\sigma}(h_{\rho\sigma} - \partial_\sigma \chi_\rho - \partial_\rho \chi_\sigma) \\
&= \bar{h}_{\mu\nu} - \partial_\nu \chi_\mu - \partial_\mu \chi_\nu + \eta_{\mu\nu}\partial^\rho \chi_\rho \,.
\end{aligned}$$

We can then calculate the quantity of interest $\partial^\nu \bar{h}^{(\mathrm{LG})}_{\mu\nu}$

$$\partial^\nu \bar{h}^{(\mathrm{LG})}_{\mu\nu} = \partial^\nu \bar{h}_{\mu\nu} - \Box \chi_\mu \,. \tag{1.13}$$

If we want this quantity to be zero, χ_μ must satisfy

$$\partial^\nu \bar{h}^{(\mathrm{LG})}_{\mu\nu} = 0 \iff \partial^\nu \bar{h}_{\mu\nu} = \Box \chi_\mu \,, \tag{1.14}$$

Where the right-most equality can be solved for χ_μ using standard methods for solving wave equations. Expressing the metric perturbation $h_{\mu\nu}$ in terms of $\bar{h}^{(LG)}_{\mu\nu}$ and χ_μ will mean the last three terms on the left-hand side of (1.8) will cancel, which gives

$$\Box \bar{h}^{(\mathrm{LG})}_{\mu\nu} = -\frac{16\pi G}{c^4} T_{\mu\nu} \,. \tag{1.15}$$

For notational convenience, we will drop the (LG) superscript and assume we use the Lorenz gauge unless specified otherwise. Suppose now we are in free space such that $T_{\mu\nu} = 0$. We can reinsert our units so that equation (1.15) reads

$$\left(-\frac{\partial}{\partial t^2} + c^2 \nabla^2\right) \bar{h}_{\mu\nu} = 0 \,. \tag{1.16}$$

The above equation is remarkable: equation (1.16) proves that in free space, at first order in the metric perturbation $\bar{h}_{\mu\nu}$, distortions in the fabric of spacetime travel as a wave at the speed of light, c, hence the term *gravitational wave*.

1.1.5 The stretch and squeeze of spacetime

Unlike electromagnetic (EM) waves, GWs interact very weakly with matter as discussed following (1.1), which is both a blessing and a curse for GW astronomy. Although difficult to detect, GWs can travel cosmic distances relatively undisturbed, which will allow us to probe regions inaccessible to EM observations using GW observations.

We will now discuss how GWs interact with matter. By choosing a suitable coordinate system, GWs both squeeze and stretch spacetime. One of the first scientists to provide a practical study of general relativity was Felix Pirani[1]. In 1950, Pirani published a paper that studied curvature tensors in general relativity from a practical point of view. In general relativity, the choice of coordinate system can simplify calculations at the expense of practicality. Described in [9], Pirani's goal was to show that "abstract" notions in general relativity could be described by physically observable quantities. In particular, he showed that GWs propagating through a medium would move particles (of that medium) back and forth, a fundamental concept what modern day GW detectors use to detect GWs. We summarise his work here.

Given equation (1.16), we can assume a simple plane wave solution

$$\bar{h}_{\mu\nu} = \mathrm{Re}\left(A_{\mu\nu}e^{ik_\alpha x^\alpha}\right) , \tag{1.17}$$

where $A_{\mu\nu}$ are the wave amplitudes and $k_\alpha x^\alpha$ is the wave number. Equation (1.17) has 16 components, though only 2 are independent. Since $\bar{h}_{\mu\nu} = \bar{h}_{\nu\mu}$ the 16 independent components reduce to 10. The gauge condition $\partial^\nu \bar{h}_{\mu\nu} = 0$ implies $k^\alpha A_{\alpha\nu} = 0$, four (linear) equations for each component of ν, which fixes four components of $A_{\mu\nu}$ reducing the number of independent components from 10 to 6. To remove the last four independent quantities, we first recall the gauge transformation $x^{\beta'} = x^\beta + \chi^\beta$ that resulted in equation (1.14). Consider a similar transformation of the form $x^{\beta'} = x^\beta + \kappa^\beta(x^\alpha)$ for $|\kappa^\beta| = |\chi^\beta + \gamma^\beta| \ll 1$. Under this transformation, we must have

$$\partial^\nu \bar{h}_{\mu\nu} = \Box\kappa_\mu \iff \Box\gamma_\mu = 0. \tag{1.18}$$

The components of χ^β and γ^β are chosen to ensure the Lorenz gauge condition (1.14) is satisfied. The equation for $\Box\gamma_\mu = 0$ yields four additional equations we can use to adjust the components of our gauge transformation $x^{\beta'} = x^\beta + \kappa^\beta$. We can choose γ^β such that $A_{\mu\nu}$ is traceless such that $A^\mu_\mu = 0$ and $A_{\mu t} = 0$. From (1.16), at first order in $\bar{h}^{\mathrm{TT}}_{\mu\nu}$, metric propagations travel at the speed of light (travel along null curves) so we must have the condition $k^\alpha k_\alpha = 0$. We

[1] Interestingly, Pirani had a strong dislike in the notion of black holes and hoped their concept would be eradicated in the scientific community. He then grew disappointed [8].

can orient our spatial coordinate axes so the wave propagates in the z direction by setting $k^\alpha = (\omega, 0, 0, \omega)$ and $k_\alpha = (-\omega, 0, 0, \omega)$. It then follows from the condition $k^\alpha A_{\alpha\mu} = 0$ that $A_{\mu z} = 0$. The choice of the components of γ^β fixes the gauge transformation that is usually called the *transverse-traceless* (TT) gauge. This implies that the 6 components have finally been reduced to 2 independent components $A_{xy} = A_{yx}$ and $A_{xx} = -A_{yy}$. The final equation reads

$$\bar{h}^{(\mathrm{TT})}_{\mu\nu} = \mathrm{Re}\left(A_{\mu\nu} e^{ik_\alpha x^\alpha}\right) . \tag{1.19}$$

In this coordinate system, the wave is travelling in the z direction (transverse) and is also traceless. Setting $x^3 = z = 0$, equation (1.17) reduces to

$$\bar{h}^{(\mathrm{TT})}_{\mu\nu} = A_{\mu\nu} \cos(\omega t) , \tag{1.20}$$

with $A_{xx} = -A_{yy}$ and $A_{xy} = A_{yx}$. From now on we will assume we are working in the (TT) gauge and drop the superscript.

We now give a brief discussion on the effect of a GW written in the TT gauge propagating through a ring of test particles in free fall, confined to their own local inertial frame. Consider a particle confined to the origin of a circle and a second particle located on the circumference. We assume both particles are at rest so their four velocity $U^\alpha = (1, 0, 0, 0)$. The location of the second particle is given in polar coordinates $\xi^\beta = (0, \epsilon\cos\theta, \epsilon\sin\theta, 0)$. We wish to now describe how the separation ξ^β is governed when a GW has passed through the $z-$direction. For a weak gravitational field, where the proper time can be approximated by coordinate time, we can use the geodesic deviation equation

$$\frac{\partial^2}{\partial t^2}\xi^\beta = R^\beta_{\mu\rho\sigma} U^\mu U^\rho \xi^\sigma ,$$

which can be expressed as

$$\begin{aligned} \frac{\partial^2}{\partial t^2}\xi^x &= R^x{}_{ttx}\epsilon\cos\theta + R^x{}_{tty}\epsilon\sin\theta \\ \frac{\partial^2}{\partial t^2}\xi^y &= R^y{}_{ttx}\epsilon\sin\theta + R^y{}_{tty}\epsilon\cos\theta . \end{aligned} \tag{1.21}$$

By substituting the (TT) gauged metric perturbations into (1.2b), one can calculate each of the Riemann curvature tensor components in (1.21) to obtain

$$\begin{aligned} \frac{\partial^2}{\partial t^2}\xi^x &= \frac{1}{2}\epsilon\cos\theta\frac{\partial^2}{\partial t^2}\bar{h}_{xx} + \frac{1}{2}\epsilon\sin\theta\frac{\partial^2}{\partial t^2}\bar{h}_{xy} \\ \frac{\partial^2}{\partial t^2}\xi^y &= \frac{1}{2}\epsilon\cos\theta\frac{\partial^2}{\partial t^2}\bar{h}_{xy} - \frac{1}{2}\epsilon\sin\theta\frac{\partial^2}{\partial t^2}\bar{h}_{xx} . \end{aligned} \tag{1.22}$$

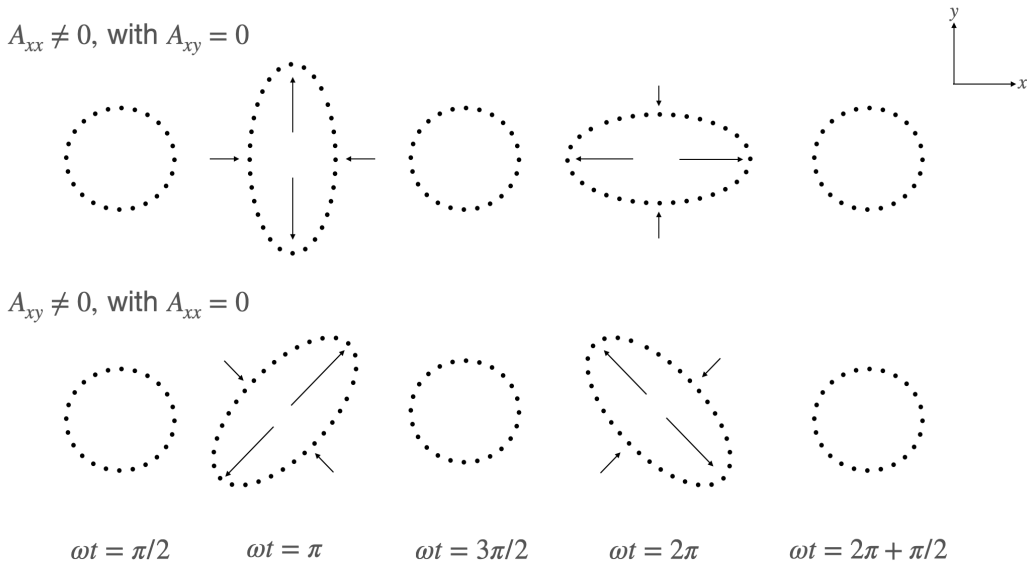

Figure 1.1: Effect of a GW passing through a ring of test particles in free fall in the z direction.

Substituting (1.20) into the above equation yields

$$\begin{aligned} \xi^x &= \epsilon \cos\theta + \frac{1}{2}\epsilon \cos\theta A^{TT}_{xx} \cos(\omega t) + \frac{1}{2}\epsilon \sin\theta A^{TT}_{xy} \cos(\omega t) \\ \xi^y &= \epsilon \sin\theta + \frac{1}{2}\epsilon \cos\theta A^{TT}_{xy} \cos(\omega t) - \frac{1}{2}\epsilon \sin\theta A^{TT}_{xx} \cos(\omega t)\,. \end{aligned} \tag{1.23}$$

We are now in a position to discuss the affect a propagating GW would have on a ring of test particles by varying $\theta \in [0, 2\pi]$. Let us first set $A_{xy} = 0$ and consider the solutions for ξ^x and ξ^y in equation (1.23). Making reference to the top row of figure 1.1, we see that the ring of particles are "squeezed" in x and "stretched" in y as ωt varies from 0 to 2π. The proper distances between the particles are changing in response to the GW passing through the z direction. To understand the bottom row, its more straightforward if we change coordinates using $x' = (x - y)/\sqrt{2}$ and $y' = (x + y)/\sqrt{2}$. All we are doing here is rotating our (x, y) coordinate system through an angle of $\pi/4$. In our new coordinate system, $x' = \epsilon \cos(\theta + \pi/4)$ and $y' = \epsilon \sin(\theta + \pi/4)$. Repeating a similar calculation leading to (1.23), we obtain

$$\begin{aligned} \xi^{x'} &= \epsilon \cos(\theta + \pi/4) + \frac{1}{2}\epsilon \sin(\theta + \pi/4) A^{TT}_{xy} \cos(\omega t) \\ \xi^{y'} &= \epsilon \sin(\theta + \pi/4) + \frac{1}{2}\epsilon \cos(\theta + \pi/4) A^{TT}_{xy} \cos(\omega t)\,, \end{aligned} \tag{1.24}$$

identical to (1.23) (for $A_{xy} = 0$) but rotated by $\pi/4$. The affect on the ring of particles is the same as the top row of figure 1.1 but at an angle of $\pi/4$.

For $A_{xx} \neq 0$ and $A_{xy} \neq 0$, the two solutions represent both the plus and cross polarisations respectively. In general we can write any metric perturbation travelling in the z direction $h_{\mu\nu}$

as a linear combination of it is two basis polarisations h_+ and $h_\times$ so that

$$\bar{h}^{(\mathrm{TT})}_{\mu\nu} = h_+ e^+_{\mu\nu} + h_\times e^\times_{\mu\nu} \,. \tag{1.25}$$

We denote the plus polarisation $e^+_{\mu\nu} = \delta_{\mu 1} - \delta_{\nu 2}$ and cross polarisation $e^\times_{\mu\nu} = \delta_{\mu 3} + \delta_{\nu 2}$ and real valued scalar functions h_+ and h_x are the the amplitude of the plus and cross polarised waves respectively. The key concept behind GW detection is to try to measure the effect of a GW on an object through its strain and try to measure that very same strain. This "stretching" and "squeezing" principle is fundamental for GW detectors to claim observation of a GW event. In the next section, we discuss GW detectors.

1.2 Gravitational wave detectors

1.2.1 Joseph Weber's detector

The issue of whether gravitational radiation could ever be detected was famously raised in the 1957 Chapel Hill Conference. This was the first in a series of general relativity meetings where many topics of relevance for contemporary research were addressed, from the "marriage" of GR with quantum mechanics advocated by Wheeler, to the proposal by Bryce DeWitt to solve Einstein's equations using "electronic" computers (which arguably marked the birth of numerical relativity). The most relevant topic (for this thesis) discussed at the 1957 conference was whether GWs could carry energy or not. From Pirani's work on how material particles in free fall react to gravitational radiation, Richard Feynmann provided a striking thought experiment: the "sticky bead argument" [10].

Consider a rigid rod with two strings of beads attached at opposite ends. A passing GW travelling orthogonal to the rod will make the ring of beads slide along the bar. As a consequence, due to friction, the movement of the beads on the bar will generate heat. The heat is sourced by kinetic energy transfer from the beads to the bar. Thus the GW has carried energy to the bar.

Feynmann's sticky bead argument convinced many scientists that GWs must carry energy. Joseph Weber, an engineer at the University of Maryland, became captivated in the various discussions on GWs. Inspired by Feynmann's thought experiment, Weber returned to Maryland to begin designing a detector with the goal of observing GWs [11]. Weber and his team built a detector in the form of a large metal cylinder that would act as an antenna: a passing GW would vibrate the cylinder and these mechanical vibrations would be converted into electrical

Figure 1.2: Joseph Weber, pictured at the University of Maryland with his resonant bar detector.

impulses by Piezoelectric sensors [12]. An image of his experiment is shown in figure (1.2). The sensitivity achieved by Weber's resonant bar detector was an impressive feat. However, with great sensitivity comes greater likelihood of making false claims of detection and Weber had to find a way to mitigate vibrations induced on the cylinder *not* caused through GWs.

To do so he built two instruments, one based in Maryland and the other in the Argonne National Laboratory in the state of Illinois. If a trigger was detected by both instruments, separated by the light travel time $\lesssim 3.1\,\mathrm{ms}$, then there was greater likelihood it was a GW observation. However, if a signal was detected in only one instrument then the recorded signal was likely to be spurious — perhaps due to local conditions such as thunderstorms or (minor) earthquakes. To reduce seismic noise arising from local vibrations from the Earth, Weber suspended the cylinders using steel wires. He argued that the dominant noise contribution was thermal noise, where the turbulent movement of particles in the cylinder would vary on the order of $\sim 10^{-16}$. Notice that this noise source is approximately five orders of magnitude larger than the amplitude of the GWs we are detecting today.

In 1959, Weber claimed that he recorded a simultaneous signal in *both* detectors and ruled out any other possibility that it could be anything but a transient GW [13]. This was a very exciting moment, spurring experimental physicists to build resonant bar detectors of their own in an attempt to verify his claims. Some of the detectors were more sensitive than Weber's original design that claimed the detection of GWs, but no GWs were detected. The scientific community, disheartened by the recent null detections, started to cast doubt about the existence of GWs. This was until the revolutionary discovery of a binary pulsar system by Joseph Hooten Taylor

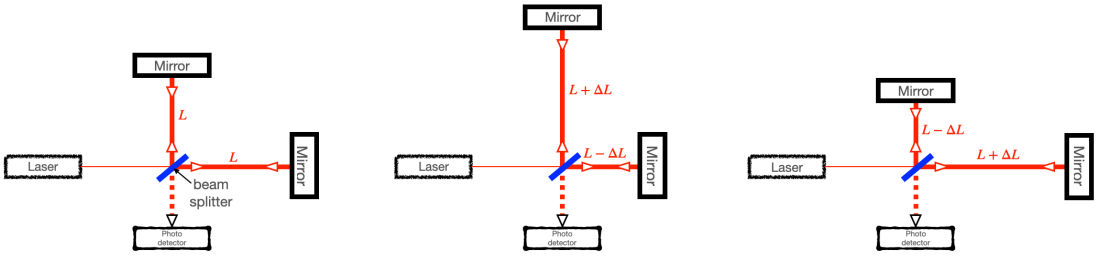

Figure 1.3: A cartoon depiction of a Michelson-Morley interferometer. In the first panel, the arms have equal length as no GW has passed through the z direction. The latter two panels show the deviations of the arm lengths due to the passage of a GW.

and Allan Russel Hulse in 1974 [14]. The orbital decay of this pulsar system agreed precisely with the equations of motion predicted by general relativity [15, 16, 17, 18]. More specifically, the decay of the orbit was due to energy loss via GW emission as predicted by general relativity. This was the first *indirect* detection of GWs and revitalised efforts to directly detect GWs.

1.2.2 Laser interferometry

Laser interferometry is an experimental technique where interference of light waves is used to measure differences in light travel time in order to extract useful information about the system. Figure 1.3 shows a schematic of the Michelson-Morley instrument [19]. A laser generates an incoming beam of light that is split into two separate optical paths using a beam splitter. The two split rays reflect off two mirrors and are recombined causing constructive or destructive interference. If the waves are perfectly in phase, they will constructively interfere and a signal can be observed at the photo-detector. On the other hand, if the split waves are perfectly out of phase then there will be a zero reading by the detector. Assuming that the length of the arms are calibrated so that the waves de-constructively interfere, then perturbations to the arm lengths will result in a non-zero reading. This is because it has taken longer for the light to travel down one arm than it has the other. Interferometry can be used to make exceptionally precise measurements of the difference in arm lengths.

In the 1970s, Rainer Weiss pushed forward the idea of using laser interferometry to detect gravitational radiation. Through Pirani's work it is understood that GWs alter the proper displacement between particles. However, GWs do not alter the speed of light, a fundamental constant in Einstein's theory of general relativity. As a GW propagates through the interferometer, the proper displacement between the beam splitter and mirrors will oscillate in response. They will be stretched and squeezed, altering the light travel time, leading to an interference pattern through constructive/destructive interference of the rays. This is shown in the middle and right-most panels of 1.3. To understand the fractional changes in the arm lengths, we

go back to the calculations present in subsection 1.1.5. Assuming, for simplicity, we are only sensitive to the plus polarisation of GWs. Equation (1.23) with $A_{xy} = 0$ tells us that the proper displacement along the x and y axes is $L(1 + h/2)$ and $L(1 - h/2)$ respectively for h the GW amplitude. The strain of either arm is

$$\frac{\Delta L}{L} = \frac{L(1 + h/2) - L}{L} = \frac{h}{2}\,. \tag{1.26}$$

A problem here is that GWs are miniscule. Even the Universe's most catastrophic events: collisions between black holes (BHs) or neutron stars (NSs), induce a strain measured on Earth that can be as small as a millionth the diameter of a proton, $h \sim 10^{-21}$. This places a *huge* demand on the sensitivity of GW detectors.

First of all, the interferometer arm lengths must be long in order to make the change in arm length measurable. Ronald Drever introduced the idea of "Fabry-Pérot cavities" [20, 21] in order to extend the length of the arms in order to avoid building a $\sim$ 500km interferometer. Drever suggested adding an extra mirror so that the light is bounced back and forth along each arm multiple times before recombining at the beam splitter. This emulated the effect of having larger interferometer arms. For a one kilometer interferometer, bouncing the light back and forth roughly five hundred times achieves the arm lengths we require to detect GWs. Aside from this, there are many noise sources a GW detector must overcome: quakes and vibrations of the Earth contribute to seismic and gravity gradient noise; the quantum nature of light inducing fluctuations in the electromagnetic field that contribute to shot noise; the individual photons that collide with the mirrors source radiation pressure noise; and the motion of particles in the mirrors cause fractional changes in the size of the mirrors leading to a thermal noise contribution. A comprehensive review of noise sources for laser interferometric GW detectors can be found in [22]. It should be clear to the reader the challenges that must be overcome with regard to GW detection. This problem required a world-wide collaboration.

In 1988, the Laser Interferometric Gravitational-wave Observatory (LIGO) project [23] was funded by the National Science Foundation. The project was originally led by Rainer Weiss, Kip Thorne and Ronald Drever. Due to (major) disagreements on instrumentation issues, Drever was replaced by Barry Barish — a high-energy physicist with experience leading large projects in physics. The idea was to build two 4km Michelson-Morley detectors, one in Hanford, Washington and the other in Livingston, Louisiana, where construction began in 1994 and finished three years later. Both of these detectors would be sensitive to GWs in the frequency band $f \in (10, 10^3)$ Hz. Images of the two detectors are shown in figure 1.4. Barish proposed to

Figure 1.4: On the left/right is the LIGO detector in Louisianna/Hanford

build an early GW detector the initial-LIGO (iLIGO) detector as a test of concept, for it to be replaced by advanced-LIGO (aLIGO) using more sophisticated technology. Although iLIGO would struggle to detect signals, the hope was that aLIGO would, indeed, be sensitive enough to observe GWs. The plan worked. LIGO detected the first GW event, a binary black hole (BBH) merger, on the 14th of September, 2015 [24]. Nearly one hundred years after Albert Einstein predicted their existence, GW science became a reality.

1.2.3 LIGO: A new window to the Universe

The first aLIGO observation, dubbed GW150914, of the transient GW signal from the collision of two stellar mass BHs [24] in September 2015 spectacularly opened the new field of GW astronomy.

The source of GW150914 was at a distance of $\sim 410\,\mathrm{Mpc}$, and composed of two stellar mass binary BHs with mass $\sim 36M_\odot$ and $\sim 29M_\odot$ that coalesced approximately 1300 million years ago to form a single remnant BH of mass $\sim 62M_\odot$. In total, three solar masses worth of energy were emitted in the form of gravitational radiation. In the final milliseconds before they coalesced, the peak luminosity of the waves was as high as $\sim 10^{49}\,\mathrm{W}$, greater than the combined light emitted by all the stars in the observable universe. Up to this point we only had the ability to *see* the universe through EM observations. We now have the tools to be able to *listen* to the universe through GW observations.

For their momentous efforts, Weiss, Barish and Thorne were awarded the Nobel Prize in Physics 2017 "for decisive contributions to the LIGO detector and the observation of gravitational waves". Furthermore, all scientists that were part of the LIGO scientific collaboration were awarded the "Special Breakthrough Prize in Fundamental Physics" for their unified efforts

to detect such a phenomena that Einstein originally thought was an impossibility. Not only was this the first direct detection of GWs, but also clear evidence that BHs exist — a concept that disturbed notable scientists for decades. The observed GWs immediately answered a number of questions, examples being whether general relativity can accurately describe the strong field dynamics of BHs or whether is it possible for BHs to merge within the Hubble time (age of the universe) and finally, do GWs exist? The GW observation GW150914 also posed new questions: why were the observed BH masses so large? why was their spin consistent with zero rotation? The first detection spawned a plethora of further papers that performed a more meticulous analysis on the source properties of GW150914 [25, 26, 27, 28, 29, 30, 31].

The second GW event, GW151226 [32], was the detection of a signal from another BBH with smaller component masses than GW150914. Before this detection there was a trigger of a detection: a potential candidate observation, named LVT151012. This trigger did not meet the rigorous standards for detection that both GW150914 and GW151226 passed and, for this reason, LVT151012 was deemed an event of low significance. With improved search pipelines, the confidence that LVT151012 was a GW event was increased until it was finally accepted as a true GW event — GW151012. At this point, the detectors were shut down and the sensitivity of the instruments were upgraded in preparation for the second observing run. Towards the end of the second observing run, the European led Virgo GW observatory joined in the hunt for GWs. With the presence of a third detector, the sky location of the source can be better constrained through triangulation.

By the end of the second observing run in August 2017, the LIGO/Virgo detectors had observed ten BBH mergers and a single binary NS inspiral [33]. The binary NS event, GW170817, was an exceptional event in GW astronomy [34]. Two NSs enclosed in a binary with component masses $\sim 0.86 M_{\odot}$ and $\sim 2.26 M_{\odot}$ emitted a GW signal in the LIGO band elapsing ~ 100 seconds until they coalesced. As this was a three detector observation, the sky location of the source was well constrained. This event also generated an EM counterpart: a gamma ray burst named GRB170817A, detected by the Fermi-GBM detector roughly 1.7 seconds after the binary coalesced. Similar to GW150914, these first "multi-messenger" observations provided a number of profound discoveries. The merger produced a kilonova, an exceptionally powerful and luminous explosion, resulting in the formation of heavier-than-iron "r-process" elements that are found throughout our Universe [35], but cannot be made through usual stellar supernovae. Through this GW observation, alone, it was possible to constrain "speed of gravity" and test the Shapiro time delay mechanism from the delay between merger part of the signal and the EM observation [36]. Finally, from the measurements from the distance with the GW

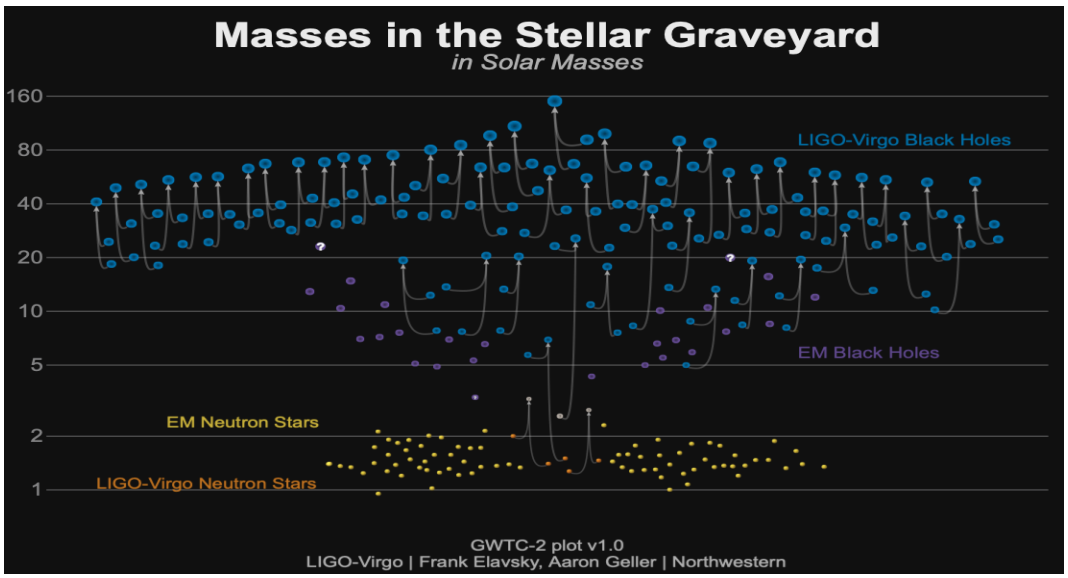

Figure 1.5: This image shows the number of EM and GW observations of isolated/binary BHs and NSs. (Blue) BBHs detected by LIGO and Virgo, (purple) isolated BHs through EM observations, (orange) binary NSs through LIGO/Virgo, (yellow) isolated Nss through EM observations. *Credit: Visualization: LIGO -Virgo / Frank Elavsky, Aaron Geller / Northwestern*

observation and the measurement of the redshift from the EM observation, an estimate of the Hubble constant [37, 38] was derived. From future observations of GWs with EM counterparts, problems such as the *Hubble tension*, conflicting estimates of the Hubble constant from EM measurements, could be solved [39, 40, 41]. This handful of observations from O2, including GW170817, has already had a profound impact on our understanding of the astrophysics of compact objects and ruled out a number of modified theories of gravity [42, 43, 44, 45, 46].

The first half of the third observing run [47] saw the number of detections increase to 39 candidate events where a handful were exceptional – an event requiring individual publication due to non-standard source properties. To name a few, the observation of GW190425, a GW event from yet another binary NS [48]. Then GW190814 [49], a BBH observation with very asymmetric component masses – an inspiral of a $\sim 2.6M_\odot$ compact object into a $\sim 23M_\odot$ black hole. This smaller component mass represent either the lightest BH *or* the heaviest NS observed to date. From this observation the *mass gap*, an alleged gap in the range of BH masses predicted by models of stellar evolution for black holes, could be probed [50, 51, 52]. Finally, they had GW190521, the merging of two BHs to form a $\sim 130M_\odot$ black hole remnant [53, 54]. A summary of known compact object binaries are shown in figure 1.5.

The current LIGO/Virgo detectors are optimally sensitive to GWs with frequencies between 10 Hz and 1000 Hz. At the upper end of the frequency range, sensitivity is limited by shot noise and at the lower end by seismic noise. Lower frequency sensitivity is important for detecting longer inspirals that can provide tighter constraints on astrophysical parameters, or heavier

mass binaries that may reside within the mass gap. High frequency sensitivity is important for resolving the merger stage of binary NSs with the goal of constraining the equation of state of these compact objects [55, 56, 57]. There are plans for third generation ground-based detectors — Einstein Telescope (ET) [58, 59, 60] and Cosmic Explorer (CE) [61, 62, 63], which would broaden the sensitivity band at both ends. The instrument ET will be built underground to reduce seismic noise and the mirrors cryogenically cooled to reduce the thermal noise. CE Explorer, on the other hand, will be built above ground but with 40km arm lengths to achieve greater sensitivity for lower frequency GWs. Unfortunately though, for a ground-based detector, the Earth will always be present making it impossible to shield gravity entirely.

The lower frequency band $f < 1\,\mathrm{Hz}$ will offer a rich taxonomy of GW sources. Black holes with much higher masses are expected to exist in the centers of most galaxies [64] and should be even stronger sources of GWs. Higher mass binaries emit lower frequencies, most of which are inaccessible to ground-based detectors. To access the lower frequency, we have to eliminate seismic noise. What is the best way to do this? The obvious answer — remove the Earth by putting a GW observatory into space.

1.3 The laser interferometer space antennae

The space-bourne GW observatory, the Laser Interferometer Space Antennae (LISA), is scheduled for launch in $\sim$ 2034 [65]. A mission led by ESA with NASA collaboration, the LISA detector will have the potential to observe signals sweeping through three decades of frequencies $f \in [0.1\,\mathrm{mHz}, 0.1\,\mathrm{Hz}]$. Before we discuss astrophysical sources for LISA, we will describe the key characteristics of the LISA mission.

1.3.1 The instrument design

The LISA mission utilizes ideas of laser interferometry as described in section 1.2.2. The instrument as a whole consists of a triangular configuration of three spacecraft. Each individual craft hosts two gold-plated $\sim 2.9\,\mathrm{kg}$ test masses in free fall following their own geodesic trajectory. An interferometer measures fractional changes in the displacement between the two test masses. An optical metrology subsystem (OMS) is used to measure the test masses position and a gravitational sensor unit (GSU) measures spurious accelerations with respect to the test masses local inertial frame. Perturbations to the craft from external (material) sources will be counteracted using micro-Newton thrusters, allowing for fine-tuning of the trajectory of each craft. Each craft is laser locked in phase to another craft forming 6 laser links in total, which act

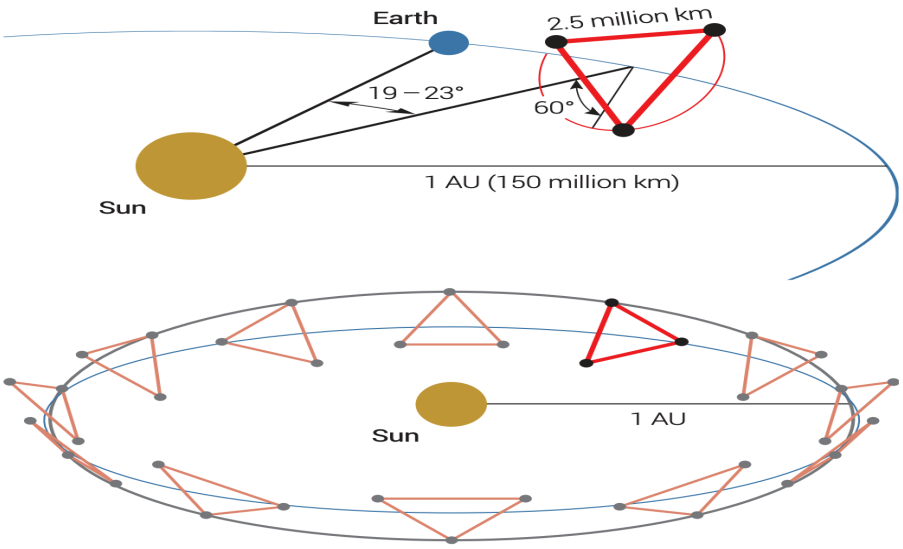

Figure 1.6: The orbit of the LISA instrument, taken from [65]

as two Michelson-Morely interferometers (in addition to the interferometers on board the craft). Unlike LIGO's design, LISA will not be static. The LISA spacecraft will trail the Earth, in a heliocentric orbit between $\sim$ 50-65 million kilometres from Earth and will orbit in a cartwheeling fashion [66] as depicted by figure 1.6. Due to the motion of the craft, the sky position of sources can be constrained to considerable accuracy. The total mission lifetime of LISA will be $\sim$ 6 years, with possible extension to ten years. The instrument has a very complicated configuration and, for this reason, it was necessary to provide a proof of technology. The LISA pathfinder (LPF) did precisely that.

The LPF was launched on the 3rd of December 2015, and it showed that the test masses could be released and controlled to maintain a relative acceleration noise of $5.2 \pm 0.1\,\mathrm{fm\,s^{-2}}/\sqrt{\mathrm{Hz}}$ for $f \in (0.7, 20)\,\mathrm{mHz}$ [67]. This was lower than the LPF requirement by a factor of five and within a factor ~ 1.25 of the requirement for the LISA mission. For frequencies $f \geq 60\,\mathrm{mHz}$, the test masses spurious accelerations were controlled by a factor ~ 2 better than the LPF requirement. In light of these results, and the huge scientific potential we will soon discuss, in June 2017 the LISA mission was accepted for launch in the 2030s. For a more comprehensive review on the instrumentation side of LISA, the author encourages the reader to see [68, 65].

1.3.2 Astrophysical sources for LISA

The LISA instrument will be able to detect signals ranging from *high mass* binaries at large cosmological distances, $z \sim 20$, to low mass galactic binaries (GBs) in our own galaxy. Sources for LISA include: the inspiral-merger-ringdown of supermassive black hole binaries (SMBHBs)

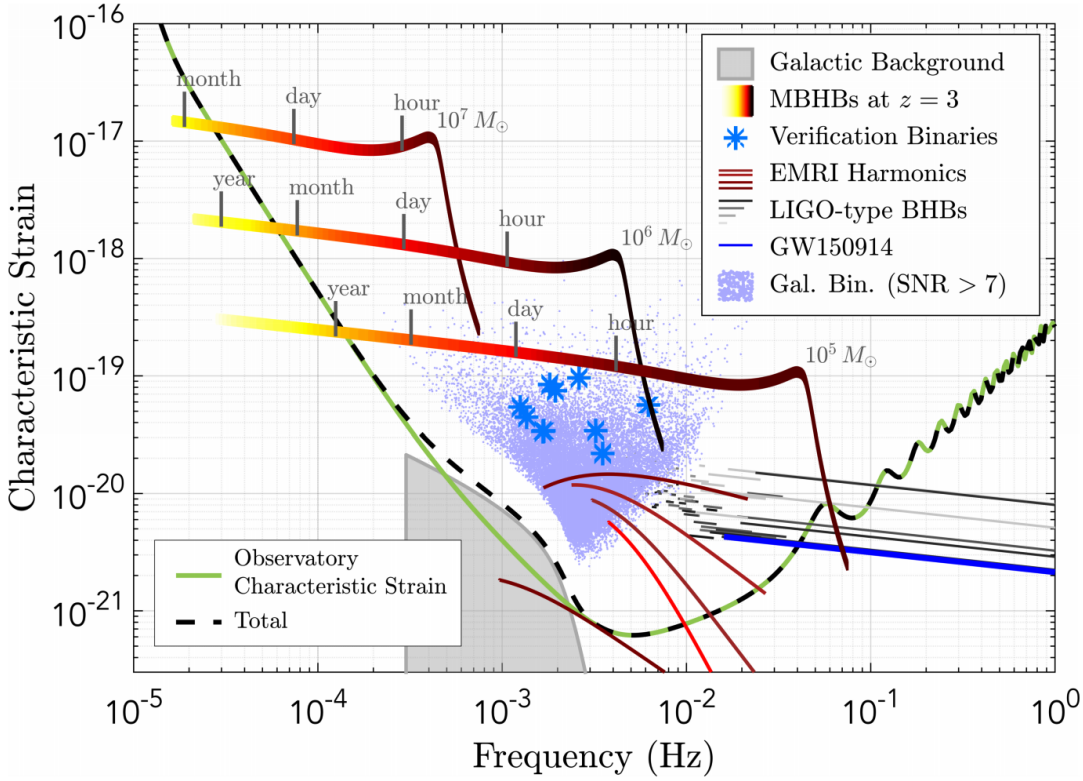

Figure 1.7: Taken from [65], we plot the spectrum of LISA GW sources against the LISA sensitivity curve. Sources above the LISA sensitivity curve are detectable.

with total mass $\sim 10^{4-7} M_\odot$; signals emanating from tens of thousands of galactic binaries harboured in our own milky way; and, the long inspiral phase of stellar compact objects $\sim 10 - 60 M_\odot$ into SMBHs of mass $10^{4-7} M_\odot$. This latter source is called extreme mass-ratio inspirals and they are the primary focus of this thesis in chapters 4, 5 and 6. If any of these systems were detected through GW observations, the scientific impact would be tremendous. A typical frequency domain representation of sources for LISA is given in figure 1.7. In the following subsections, we discuss a few of the sources that will be relevant for the research contained in this thesis.

1.3.2.1 Massive black holes

One of the prime sources of gravitational radiation for LISA are massive black hole binaries (MBHB) with masses $\sim 10^{4-7} M_\odot$ up to a redshift of $z \sim 20$ [69, 70, 71]. It is expected that LISA should observe between 10 and 100 MBH mergers per year [70]. LISA observations of MBHBs will allow us to probe potential formation channels of "light seed" or "heavy seed" black holes in the very early universe [72, 73, 74, 75]. Working in geometrized units, the amplitude of the waves scale in proportion to the total mass of the system so MBH signals

are much louder when compared to stellar origin binary black holes observed by ground-based observatories. This allows for tight measurements better than $\sim 1\%$ on the (redshifted) masses and spin magnitude of the primary/secondary BHs [70]. We also expect to measure the sky location to ~ 10 degrees and the luminosity distance to approximately 10%. Given that MBHs reside at the centres of most galaxies and are expected to accrete matter [76, 77, 78, 79, 80], a potential EM counterpart could be observed [81] and, along with the measurement of the luminosity distance, a constraint on the Hubble constant could be obtained. MBHs are also excellent laboratories for tests of general relativity [82, 83]. Examples include testing the no-hair theorem, or whether the two components of the binary are *exotic* compact objects such as boson stars or gravastars [84, 85].

1.3.2.2 Galactic binaries

Galactic binaries are binaries of white dwarfs, black holes or neutron stars in our own galaxy with orbital periods of the order of a few hours. Such systems are expected to be slowly evolving, quasi-monochromatic sources that are present across the full range of frequencies that LISA is sensitive to [86]. At low frequencies, the number of GBs will be enormous, on the order of tens of millions [87]. Some brighter signals can be resolved and subtracted from the data stream, but many will be unresolvable — forming an astrophysical foreground of noise for the instrument [88, 89]. By measuring the astrophysical parameters of the GBs, we will be able to learn about both the formation and evolution of these systems [90]. Of the resolvable GBs, there will be a handful of verification binaries [91, 92] that could play an important role in assessing the performance of the LISA mission. LISA is expected to observe some GBs undergoing mass transfer, offering clues on the number of mass-transferring systems in the galaxy. Finally, GBs can be used for tests of general relativity by placing constraints on massive-graviton theories [93] or on the time evolution of Newton's gravitational constant G [94, 95].

1.3.2.3 Extreme mass ratio inspirals

Extreme mass-ratio inspirals (EMRIs) are one of the most exciting possible sources of gravitational radiation for LISA [96, 97, 98]. An EMRI involves the slow inspiral of a stellar-origin compact object (CO) of mass $\mu \sim 10 M_\odot$ into a MBH in the centre of a galaxy. For a central BH with mass $M \sim 10^{(4-7)} M_\odot$, EMRIs emit GWs in the millihertz frequency band and so are prime sources for the LISA detector. EMRIs begin when, as a result of scattering processes in the stellar cluster surrounding the MBH, the CO becomes gravitationally bound to the primary [99]. The subsequent inspiral of the CO towards the horizon of the primary is

driven by the emission of GWs. The orbits are highly relativistic, expected to be both eccentric and inclined with observation times of six months, a year, or, perhaps, the entirety of the LISA mission lifetime. For these reasons, EMRIs pose a challenging problem for both source modellers [100, 101, 102, 103, 104, 105] and data analysts [106, 107].

A consequence of being within the deep field regime of the central hole's spacetime for long periods of time is that the dynamics of the smaller body is immensely sensitive to the central hole's characteristics. The information about the source is carried by the time evolution of the phase in a GW [108, 109]. The slow evolution of EMRIs means that many cycles can be observed during the inspiral, which, if detected, will provide constraints on the astrophysical parameters of the source with remarkable precision [110, 111, 71]. For example, work has indicated that LISA will be able to place constraints on the eccentricities, masses and spins to one part in 10^4 [112, 102, 101, 103]. EMRI observations make it possible to accurately map out the spacetime geometry of the central hole [113, 114, 115, 116], offering *precision* tests of general relativity where the nature of the central spacetime can be tested to unparalleled degree [117, 114, 116]. Through multiple observations of EMRIs, each with tight constraints on their astrophysical parameters, both mass and spin distributions of the population of sources could be obtained [97]. Finally, bright EMRIs can provide cosmological constraints even without observation of an optical counterpart. By comparing the locations of observed GW events with galaxy catalogs with known redshifts, constraints on the Hubble constant can be obtained with increasing certainty as the number of observations increase. It has been shown in [118] that the Hubble constant can be constrained to within $\sim 1\%$, provided ~ 20 EMRIs are observed at redshift $z < 0.5$ for LISA. For further details of cosmology with EMRIs, we refer the reader to [119]

Event rates indicate that we would expect to observe at worst one event to at best several thousand per year [120, 97]. The large uncertainty is due to the complexity of the physics of stellar clusters is still not well understood. Of the sources considered for LISA, EMRIs will be the primary research focus of this work. They will be discussed in more detail in chapter 2 to form the basis of the research presented in chapters 4, 5 and 6.

1.3.3 Complexity of LISA data

The LISA data stream will be subject to a number of complicating factors that are not present in current ground-based detectors. The hardware of the instrument could malfunction causing transient noise sources, called glitches, or cause irretrievable segments of data that we refer to as data gaps. Further, event rates discussed in each of the subsections 1.3.2.1, 1.3.2.2 and

1.3.2.3 imply that LISA will observe *multiple overlapping sources* in both time and frequency. We give a brief review of each of these unavoidable features below.

1.3.3.1 Overlapping sources

LISA will observe sources emitting GWs that are in band for months, years or even longer. For this reason, unlike current ground-based detectors, the LISA data stream could contain millions of overlapping GW signals. As discussed in (1.3.2.2), there will be millions of unresolvable GBs that will form a stochastic confusion foreground [121]. This foreground will be a potential source of bias in recovered parameters if the foreground is not incorporated into probabilistic models describing the data stream. MBHBs, in comparison to EMRIs, could be exceptionally bright sources at low redshifts $z \sim 1$. The use of imperfect waveform models to subtract these MBHBs will leave *residuals* in the data stream, some that could be of comparable strength to the weaker EMRI source. This highlights the need for accurate waveform models to both detect and perform parameter estimation on signals in the LISA data stream. Furthermore, if target signals are overlapping for significant lengths of time and frequency, sampling algorithms can become confused between sources due to inter-source correlations. Data analysis pipelines may have to consider the simultaneous signal extraction parameter estimation of all GW sources present in the data stream. This ambitious idea is called the *global-fit* and is still being explored [122, 123]. We discuss these points further in the research chapter 7.

1.3.3.2 Instrumental artefacts

Another point of concern are potential malfunctions in the LISA hardware that could cause either data gaps (long timescales) or glitches (short time-scales). An example of a system malfunction that caused a data gap was observed in the LPF data [67, 124]. An irretrievable loss of data over a period of ~ 6 days occurred due to a failure in discharging the test mass in the LISA spacecraft when the spacecraft was subjected to significant solar winds [125, 67, 126]. Collisions between the spacecraft with micro-meteors or dust particles could also perturb the spacecraft, forcing deviations in the test-masses geodesic orbit. These small perturbations will feature as short time-scale noise artefacts, picked up by the GSU or OMS. Minor electrical fluctuations in the hardware could also show bursts of noise, or even dust particles *within* the spacecraft can interfere with the internal interferometer. Instrumental artefacts such as these we have little control over and can only reduce them to the best of our ability. Other types of gaps, such as *scheduled gaps*, will occur when re-pointing the spacecraft antennae. Due to the orbital motion of LISA, if not adjusted, the antennae will gradually drift so they are no longer

pointing toward the Earth. The implication of this is that the data cannot be transmitted back. The antennae must be periodically re-oriented, which will produce excessive noise and render the data stream unusable. This action will happen either weekly, with re-orientation lasting 3.5 hours or fortnightly, with re-pointing lasting 7 hours [65, 124]. There is ongoing study in attempt to determine which type of re-pointing is optimal for LISA science and, in particular, how to treat these data gaps [124, 127, 128, 129, 130]. During this period, LISA will likely no longer record data, posing as a gap in the data stream. As shown in [124], scheduled gaps can have a significant impact on recovered parameters of massive black holes observed through LISA. The signal grows brighter as the merger is approached and the effect of a gap during the merger phase can drastically degrade the precision of parameter measurements [124]. For this reason, for some MBHBs a *protected period* might be triggered in which no re-pointing is due, to preserve data around merger. For other sources, such as EMRIs, we do not expect constraints on parameters to be hampered through data gaps. However, if these data gaps are mishandled, they can lead to severe problems in parameter estimation pipelines. It is critical to assess the impact on parameter estimation of data gaps. This will be the focus of the final research chapter 8.

1.4 The structure of this thesis

The goal of this introduction was to introduce GWs, a summary of recent ground-based detections and outlined plans for the future LISA mission. For the LISA mission, it should be clear to the reader that there will be significant complexity behind data analysis algorithms specific to the mHz GW spectrum. This is due to the sheer number of overlapping sources, instrumental noise artefacts, communication outages causing gaps and the modelling of GW sources involved. The only way we can solve such problems is with dedicated effort, which is the focus of this thesis. This thesis contributes to each of these challenges, but, before the research is discussed, it is essential to describe the framework of both EMRIs and the data analysis tools used. We give a brief discussion on all the chapters presented in this thesis below.

- The *introductory* chapter 2 gives a brief introduction to EMRIs from a waveform modelling perspective. In particular, we describe the Kerr geometry 2.1; rapidly rotating BHs 2.1.1; geodesic motion 2.2; modelling deviations from geodesic motion 2.3; the two-timescale approach 2.3.1; the adiabatic and post-adiabatic approximations 2.3.2; and, conclude the chapter with a discussion of the Teukolsky formalism 2.4.

- The *introductory* chapter 3 describes our signal processing algorithms 3.1; modelling the

data stream 3.2; characterising stationary noise 3.2.1 leading to an alternate derivation of the Whittle-likelihood 3.2.2; the notion of matched filtering and signal-to-noise ratio 3.2.3; parameter precision studies 3.3 using Fisher matrices 3.3.2; waveform systematics using the Lindblom-Criterion 3.4.1 and Cutler-Vallisneri 3.4.2 formalism; and, parameter estimation using Bayesian techniques 3.5. *All* details contained in chapters 2 and 3 are used in the *research* based chapters 4, 5, 6, 7 and 8 for which we now give a brief summary.

- The *research* chapter 4 uses the ideas presented in chapter 2, specifically sections 2.1.1, 2.2.2, 2.2.3, 2.3.2 and 2.4 to model the final stages of a small CO inspiralling on a circular equatorial orbit into a MBH for all (physical) spin parameters allowed by general relativity.

- The *research* chapter 5 uses the ideas from 2.2.3, 2.3.2 and 2.4 to argue using fully relativistic adiabatic EMRI waveforms that precision measurements on the rotation parameter of near-extremal BHs are expected to supersede those of moderately spinning holes. These results are based on a Fisher matrix approach 3.3.2 that are then verified using Bayesian techniques presented in section 3.5.

- The *research* chapter 6 presents a systematic study on EMRI waveforms. For eccentric orbits into a non-spinning black hole, we argue using the Cutler-Vallisneri formalism 3.4.2 how accurately components of gravitational self force have to be calculated in order not to recover significantly bias recovered parameters. The trajectory of the smaller body is modelled in the spirit of 2.3.1, and we use this model to investigate accuracy requirements on the adiabatic and post-adiabatic components 2.3.2.

- The *research* chapter 7 extends the Cutler-Vallisneri 3.4.2 formalism to compute waveform systematics for the case of multiple and overlapping signals and an unfitted foreground of sources. We illustrate the formalism using sources specific for space-based detectors (LISA) and ground-based detectors (ET). Using this generalised formalism, we discuss how such a formalism can be used to *correct* biases that occur in sequential parameter estimation of sources.

- The final *research* chapter 8 discusses the impact that data gaps have on parameter estimation studies, which relies heavily on ideas presented throughout chapter 3. In particular, data gaps introduce non-stationary behaviour in the noise model so the ideas from section 3.2 must be generalised. Quantities such as the likelihood, signal-to-noise ratio and Fisher matrix are then corrected to incorporate the non-stationary feature of the noise. We conclude using a simulation study that shows the effect of mis-modelling the noise as stationary when it is, in fact, non-stationary.

Chapter 2

Extreme Mass-Ratio Inspirals

There is no exact solution to the two-body problem in general relativity, instead the motion between two bodies in a curved spacetime is approached using approximate schemes. Numerical relativity (NR) solves the field equations in full generality, giving rise to the most accurate waveforms known to date [131, 132, 133]. However, due to the complexity of the field equations (1.1), such simulations are expensive and become computationally prohibitive as the mass ratio gets smaller and the number of cycles increases, making NR simulations of EMRIs challenging [134, 135]. Post-Newtonian (PN) expansions serve as analytical approximations to Einstein's field equations, where a small parameter (such as the ratio between velocity and the speed of light) is used as an expansion parameter. PN expansions are an excellent approximation to *weak-field* dynamics of orbiting compact objects but lose out on accuracy as the bodies become more strong field [136, 137]. In the case of EMRIs, both NR and PN are challenging to use since NR becomes too computationally expensive due to the number of orbits and PN approximations break down since the CO spends $\sim$ years within the strong field. For EMRIs, one can use the small mass ratio $\eta = \mu/M \ll 1$ as a perturbative variable in Einstein's field equations to describe the trajectory of the CO subject to the MBH's spacetime. We call this *black hole perturbation theory* and, for EMRIs, this is the leading approximate scheme used to generate *accurate* waveforms regardless of how strong or weak field the source is.

This chapter is organised as follows. The rotating BH (Kerr) geometry is discussed in 2.1 along with the geometry near the horizon of a rapidly rotating BH in section 2.1.1. A brief review of geodesic orbits is given in section 2.2 with particular attention given to circular and equatorial orbits, the main class of orbits used throughout this thesis. We outline the two-timescale approach, an essential ingredient to understanding the evolution EMRIs under the influence of GW emission, in section 2.3. The final section 2.4 is devoted to a short review of

black hole perturbation theory using the Teukolsky formalism.

2.1 The Kerr solution

The Kerr metric represents a 2-parameter family of solutions to the vacuum Einstein equations $R_{\mu\nu} = 0$. The metric describes the gravitational field of an uncharged, axisymmetric, stationary and rotating BH [138]. For a BH of mass M and angular momentum J, The Kerr line element assumes the form in (dimensionless) Boyer-Lindquist (BL) coordinates $(\tilde{t}, \tilde{r}, \theta, \phi)$ [139]

$$\begin{aligned} \mathrm{d}\tilde{s}^2 = &-\left(1 - \frac{2\tilde{r}}{\tilde{\Sigma}^2}\right)\mathrm{d}\tilde{t}^2 + \tilde{\Sigma}^2\left(\frac{1}{\tilde{\Delta}}\mathrm{d}\tilde{r}^2 + \mathrm{d}\theta^2\right) \\ &+ \left(\tilde{r}^2 + a^2 + \frac{2\tilde{r}a^2}{\tilde{\Sigma}^2}\sin^2\theta\right)\sin^2\theta\mathrm{d}\phi^2 - \frac{4a\tilde{r}\sin^2\theta}{\tilde{\Sigma}^2}\mathrm{d}\tilde{t}\mathrm{d}\phi\,, \end{aligned} \tag{2.1}$$

where $(\tilde{r}, \tilde{t}) = (r/M, t/M)$. Here $\tilde{\Delta} = \tilde{r}^2 - 2\tilde{r} + a^2$ and $\tilde{\Sigma}^2 = \tilde{r}^2 + a^2\cos^2\theta$. The *dimensionless* spin parameter a is defined by $a = J/M^2$. The metric becomes singular when $\tilde{r} = \tilde{r}_\pm = 1 \pm \sqrt{1 - a^2}$ or when both $r = 0$ and $\theta = \pi/2$.

Curvature in Einstein's theory of general relativity is invariant under coordinate transformations. By computing scalar quantities, such as the Ricci scalar $\mathcal{R}$ or Kretschmann scalar $R_{\mu\nu\rho\sigma}R^{\mu\nu\rho\sigma}$, it can be seen that both scalars diverge when $\tilde{\Sigma}^2 = 0$, meaning that, regardless of what coordinate system the Kerr metric (2.1) is expressed in, the singularity $\tilde{\Sigma}^2$ is a *curvature* singularity and cannot be removed through coordinate transformations. On the other hand, the singularity present at surfaces defined by $\tilde{\Delta} = 0$ can be avoided by changing to coordinates such as *Kerr-Schild* coordinates, originally proposed by Kerr [138]. This means that the singularity $\tilde{\Delta} = 0$ is a coordinate singularity, simply an artefact of the coordinate system proposed by Boyer and Lindquist.

The horizons of the BH are given by $\tilde{\Delta} = 0$ with solutions $\tilde{r} = \tilde{r}_\pm = 1 \pm \sqrt{1 - a^2}$. We call the $\tilde{r} = \tilde{r}_-$ horizon the *inner horizon* (also called a *Cauchy horizon*) and the outer horizon $\tilde{r} = \tilde{r}_+$ the *event horizon* of the Kerr BH. Once a material particle or photon passes the event horizon it has no choice but to plunge towards the Cauchy horizon of the BH $\tilde{r} = \tilde{r}_-$. However, once the photon or material particle enters the region $0 < \tilde{r} < \tilde{r}_-$, the trajectory becomes timelike and the particle is free to move around the region $0 < \tilde{r} < \tilde{r}_-$. The particle thus has freedom *not* to enter the ring like singularity at defined by the disk $\tilde{\Sigma} = 0$, that is when $\tilde{r} = 0$ and $\theta = \pi/2$. For further details on the causal structure of the Kerr spacetime, we refer the reader to classic textbooks on the subject [140, 141, 142, 143, 144].

In this work, we will restrict ourselves to the spacetime admitted with $\tilde{r} > \tilde{r}_+$ as that is

most relevant to our work. In the limit as $a \to 0$, the Schwarzschild solution is found [145]. The Kerr spacetime is asymptotically flat, since $\tilde{r} \to \infty$ admits the Minkowski metric spherical polar coordinates. In chapters 4 and 5, we analyse orbits of massive particles around rapidly rotating BHs so the next subsection gives a review of this interesting sub-class of Kerr BH spacetimes.

2.1.1 Rapidly rotating black holes

For the horizons $\tilde{r}_\pm$ to exist, we require $a \leq 1 \iff J \leq M^2$. One can then see that Einstein's theory of general relativity imposes a (physical) upper bound on the angular momentum of a BH. In more familiar units, the angular momentum must satisfy

$$J \leq \frac{GM^2}{c} \,.$$

For rotation parameters $a > 1$, the horizons no longer exist and the curvature singularity is exposed. This is a violation of Roger Penrose's cosmic censorship conjecture [146], so we shall disregard this case as it is unphysical. We call a Kerr BH an *extreme* Kerr BH if and only if $J = M^2$. More formally, in Planck units, an extreme BH is one that admits zero Hawking temperature

$$T_{\rm H} = \frac{1}{4\pi} \frac{\tilde{r}_+ - \tilde{r}_-}{\tilde{r}_+^2 + a^2} \,.$$

That is, a hole where the horizons in BL coordinates coincide. The existence of a double pole in the function $\tilde{\Delta}$ determining the BH horizons in this limit is responsible for an enhancement of symmetry in the near horizon geometry of the Kerr BH [147], a feature that remains true for *any* extremal BH in $D \geq 4$ dimensions [148].

As we will see, the enhancement of symmetry within the near-horizon geometry of near-extremal BHs leads to the *near-horizon* metric having a warped[1] $\mathrm{AdS}_2 \times S^2$ geometry, i.e. resembling a product between a two-dimensional Anti-de Sitter (AdS) space and the two-sphere. AdS spaces are often used in theories of quantum gravity, and have a correspondence with conformal field theories (CFT), the so called AdS/CFT correspondence. A similar correspondence was shown in [149], eluding to a potential Kerr/CFT correspondence [150]. For this reason, near-horizon geometries of extremal BHs provide an excellent laboratory for testing the quantum nature of BHs [151]. Furthermore, the enhancement of symmetry arising from the near-horizon regime provides greater analytic control over various observables: like the total energy carried away through GW emission [152].

[1] This "warped" spacetime actually refers to the geometry of an S^2 bundle over AdS_2. In other words, at every point in AdS_2 there exists an S^2 geometry.

Following [153], we can explore this geometry by a suitable change of coordinates. In the following discussion, it is more convenient to express the Kerr metric (2.1) in an alternative form

$$g = -e^{2\nu}\mathrm{d}\tilde{t}^2 + e^{2\psi}(\mathrm{d}\phi - \omega\mathrm{d}\tilde{t})^2 + \tilde{\Sigma}^2\left(\frac{\mathrm{d}\tilde{r}^2}{\tilde{\Delta}} + \mathrm{d}\theta^2\right),$$

with quantitites

$$e^{2\nu} = \frac{\tilde{\Delta}\tilde{\Sigma}^2}{(\tilde{r}^2+a^2)^2 - \tilde{\Delta}a^2\sin^2\theta}, \quad e^{2\psi} = \tilde{\Delta}\sin^2\theta e^{-2\nu}, \quad \omega = \frac{2\tilde{r}a}{\tilde{\Delta}\tilde{\Sigma}^2}e^{2\nu}.$$

In the following discussion, we consider maximally extremal holes where $a = 1$. To zoom into the throat (near-horizon) geometry of the hole, we use the following coordinate transformation

$$\tilde{r} = 1 + \lambda R, \quad \tilde{t} = T/\lambda, \quad \tilde{\phi} = \Phi + \frac{T}{2\lambda},$$

and examine the limit as $\lambda \to 0$. The following quantities have the following expansion for $\lambda \ll 1$

$$\begin{aligned}
e^{2\nu} &= -\frac{1}{4}R^2(1+\cos^2\theta)\lambda^2 + \mathcal{O}(\lambda^3), \\
e^{2\psi} &= \frac{2\sin^2\theta}{1+\cos^2\theta} + \mathcal{O}(\lambda), \\
\omega &= \frac{1}{2}\left(1 - R\lambda + \frac{R^2}{4\sin^2\theta}\lambda^2\right) + \mathcal{O}(\lambda^3), \\
d\phi - \omega d\tilde{t} &= \left(d\Phi + \frac{R}{2}dT\right) + \mathcal{O}(\lambda),
\end{aligned}$$

giving the *near-horizon extremal Kerr* (NHEK) metric

$$g = \left(\frac{1+\cos^2\theta}{2}\right)^2\left[-\frac{R^2}{2}\mathrm{d}T^2 + \frac{2}{R^2}\mathrm{d}R^2 + 2\mathrm{d}\theta^2\right] + \frac{4\sin^2\theta}{1+\cos^2\theta}\left(\mathrm{d}\Phi + \frac{R}{2}\mathrm{d}T\right)^2 + \mathcal{O}(\lambda). \quad (2.2)$$

The NHEK spacetime (2.2) admits more symmetries than the general Kerr spacetime in BL coordinates (2.1). First of all, since the metric components are independent of T and Φ, we can identify $\partial/\partial T$ and $\partial/\partial\Phi$ as Killing vectors of (2.2). There is a further dilation isometry $R \to cR$ and $T \to T/c$ for $c \in \mathbb{R}$. Finally, one of the most remarkable features of the NHEK spacetime is that it reduces to two dimensional AdS space (AdS_2), in Poincaré coordinates, when either $\theta = 0$ or $\theta = \pi$. Given that AdS_2 also exhibits a dilation isometry, this suggests that the general NHEK spacetime (2.2) could be thought of as an AdS_2 metric with extra

symmetry. From [153], we introduce a final coordinate change

$$R = (1+y^2)^{1/2}\cos\tau + y, \quad T = \frac{(1+y^2)^{1/2}\sin\tau}{R}, \quad \Phi = \psi + \log\left|\frac{\cos\tau + y\sin\tau}{1+(1+y^2)^{1/2}\sin\tau}\right|.$$

After considerable effort, the NHEK spacetime can be shown to take the form

$$g = \left(\frac{1+\cos^2\theta}{2}\right)^2\left[-(1+y^2)\mathrm{d}\tau^2 + \frac{\mathrm{d}y^2}{1+y^2} + \mathrm{d}\theta^2\right] + \frac{2\sin^2\theta}{1+\cos^2\theta}\left(\mathrm{d}\psi + y\mathrm{d}\tau\right)^2, \tag{2.3}$$

which is precisely a *warped version* of $\mathrm{AdS}_2 \times S^2$. It is not precisely $\mathrm{AdS}_2 \times S^2$ due to the theta dependance at the front, but remarkably close. Authors [154] refer to this as *near* $\mathrm{AdS}_2 \times S^2$. This warped spacetime contains all symmetries from AdS_2 with additional translational symmetries in ψ. Since AdS_2 has the $SO(2,1)$ isometry group that is isomorphic to $\mathbb{SL}(2,\mathbb{R})$, the group of 2×2 real matrices with unit determinant, we have that the NHEK spacetime has the isometry group $\mathbb{SL}(2,\mathbb{R})\times U(1)$. Notice that this is an *enhancement* from the usual symmetry of Kerr $\mathbb{R}\times U[1]$ corresponding to time translation and rotational symmetry.

The presence of the isometry group $\mathbb{SL}(2,\mathbb{R})\times U(1)$ provides greater kinematical control over orbits related to the NHEK spacetime. For this reason, an approximate analytical expression for the dissipation of energy due to GW emission can be obtained [155, 156]. This result is used in both chapters 4 and 5. We discuss this in more depth in subsection 2.4.2.

In our work we will not consider maximally extremal BHs, but *near-extremal* BHs with rotation parameter defined by $a = \sqrt{1-\epsilon}$ with $|\epsilon| \ll 1$. The near-horizon geometry of near-extremal BHs (near NHEK) possesses similar symmetries to the NHEK spacetime. *Locally*, the spacetime is a warped version of $\mathrm{AdS}_2 \times S^2$ with additional corrections due to the spin parameter ϵ and coupling limit λ [157, 158, 159].

From here on, we will no longer work within the NHEK spacetime 2.2 and instead consider the generic Kerr metric (2.1). We will focus on orbits of particles subject to a background Kerr spacetime that will begin the inspiral *far* from the horizon where (2.2) can no longer be used to describe such orbits. The next section gives a review of the Kerr geodesics, focusing on a particular class of orbits: circular and equatorial.

2.2 The geodesic equations

In the test particle limit, the orbit itself is purely geodesic and characterised by the background spacetime. According to Noether's theorem, all spacetime symmetries lead to conserved quantities [160]. For $p^\mu = \mu(\mathrm{d}x^\mu/\mathrm{d}\tau)$ the four-momentum of the particle, it is natural to let the

energy of the orbit $E = -p_t$ be associated with time translation and similarly the angular momenta $L = p_\phi$ be a consequence of axial symmetry. The third constant of motion is the secondary's rest mass $-\mu^2 = g_{\mu\nu}p^\mu p^\nu$ and the fourth and final constant of motion is the Carter constant[2] defined by [161]

$$Q = p_\theta^2 + \cos^2\theta(a^2(\mu^2 + E^2) + \csc^2\theta L^2)\,. \tag{2.4}$$

With four constants of motion and four degrees of freedom, the Kerr geodesics are then analytically tractable.

It can be shown that if $Q = 0$, then the particle is confined to the equatorial plane of the Kerr BH. The right-hand side of (2.4) is a positive quantity so $Q \geq 0$. The constant Q is minimised at the value $\theta = \pi/2$ and, if $\theta = \pi/2$, then $\dot{\theta} = 0 \Rightarrow p_\theta = 0$. We thus infer that the particle is constrained to the equatorial plane of the Kerr BH if and only if $Q = 0$. In our work, we will not consider general geodesics but instead an important class of them — geodesics that are confined to the equatorial plane. Restricting to the aforementioned class of orbits with $\theta = \pi/2$, one obtains

$$\left(\frac{\mathrm{d}\tilde{r}}{\mathrm{d}\tilde{\tau}}\right)^2 = \frac{[\tilde{E}(\tilde{r}^2+a^2) - a\tilde{L}]^2 - \Delta[(\tilde{L}-a\tilde{E})^2 + \tilde{r}^2]}{\tilde{r}^4} = G(\tilde{r},\tilde{E},\tilde{L},a)\,, \tag{2.5a}$$

$$\frac{\mathrm{d}\theta}{\mathrm{d}\tilde{\tau}} = 0\,, \tag{2.5b}$$

$$\frac{\mathrm{d}\phi}{\mathrm{d}\tilde{\tau}} = \frac{-\left(a\tilde{E}-\tilde{L}\right) + a(\tilde{E}[\tilde{r}^2+a^2] - a\tilde{L})/\tilde{r}}{\tilde{r}^2} = \Phi(\tilde{r},\tilde{E},\tilde{L},a)\,, \tag{2.5c}$$

$$\frac{\mathrm{d}\tilde{t}}{\mathrm{d}\tilde{\tau}} = \frac{-\Delta a(a\tilde{E}-\tilde{L}) + (\tilde{r}^2+a^2)(\tilde{E}[\tilde{r}^2+a^2] - a\tilde{L})}{\Delta\tilde{r}^2} = T(\tilde{r},\tilde{E},\tilde{L},a)\,, \tag{2.5d}$$

with dimensionless quantities $\tilde{r} = r/M, \tilde{\tau} = \tau/M, \tilde{E} = E/\mu$ and $\tilde{L} = L/\mu M$. Here $G(\tilde{r},\tilde{E},\tilde{L},a) = \tilde{E}^2 - V_{\text{eff}}(\tilde{r},\tilde{E},\tilde{L},a)$ with effective potential

$$V_{\text{eff}}(\tilde{r},\tilde{E},\tilde{L}) = 1 - \frac{a^2(\tilde{E}^2-1) - \tilde{L}^2}{\tilde{r}^2} - \frac{2(a\tilde{E}-\tilde{L})^2}{\tilde{r}^3} - \frac{2}{\tilde{r}}\,. \tag{2.6}$$

The effective potential can be used to characterise stability of the orbit given constants of motion $\tilde{E}$ and $\tilde{L}$. Here $\tilde{\tau}$ is the (dimensionless) proper time experienced by the particle.

[2] Using the Hamilton-Jacobi theory, this miraculous constant was found by Carter when he realised that the r and θ motions of the Kerr spacetime are separable.

2.2.1 Circular and equatorial orbits

In this section we derive conditions and relations that are valid for both *stable* and *circular* orbits. For a geodesic orbit to be circular at $\tilde{r} = \tilde{r}_0$, we require $\mathrm{d}\tilde{r}/\mathrm{d}\tilde{\tau} = 0$ implying that $G(\tilde{r}, \tilde{E}, \tilde{L}, a) = 0$ from the radial geodesic equation (2.5a). Similarly, we require that $\mathrm{d}^2\tilde{r}/\mathrm{d}\tilde{\tau}^2 = 0$ giving the relation $\partial G/\partial\tilde{r} = 0$. Solving the two equations

$$G(\tilde{r}, \tilde{E}, \tilde{L}) = \frac{\partial G(\tilde{r}, \tilde{E}, \tilde{L})}{\partial \tilde{r}} = 0 \tag{2.7}$$

for both $\tilde{E}(\tilde{r}, a)$ and $\tilde{L}(\tilde{r}, a)$, one obtains closed form expressions for the geodesic *energy* and azimuthal *angular momentum* valid for particle of mass μ on a prograde circular and equatorial orbit around the Kerr BH of mass M with spin parameter a

$$\tilde{E}(\tilde{r}, a) = \frac{1 - 2/\tilde{r} + a/\tilde{r}^{3/2}}{\sqrt{1 - 3/\tilde{r} + 2a/\tilde{r}^{3/2}}}\,, \tag{2.8a}$$

$$\tilde{L}(\tilde{r}, a) = \tilde{r}^{1/2}\frac{1 - 2a/\tilde{r}^{3/2} + a^2/\tilde{r}^2}{\sqrt{1 - 3/\tilde{r} + 2a/\tilde{r}^{3/2}}}\,. \tag{2.8b}$$

Substituting equations (2.8a) and (2.8b) into the geodesic equations (2.5c) and (2.5d), one obtains evolution equations for $(t(\tilde{r}, \tilde{\tau}), \phi(\tilde{r}, \tilde{\tau}))$

$$\frac{\mathrm{d}\phi}{\mathrm{d}\tilde{\tau}} = \frac{1}{\tilde{r}^{3/2}\sqrt{1 - 3/\tilde{r} + 2a/\tilde{r}^{3/2}}}\,, \tag{2.9a}$$

$$\frac{\mathrm{d}\tilde{t}}{\mathrm{d}\tilde{\tau}} = \frac{1 + a/\tilde{r}^{3/2}}{\sqrt{1 - 3/\tilde{r} + 2a/\tilde{r}^{3/2}}}\,, \tag{2.9b}$$

the ratio of which yields the angular frequency of the particle as observed by an observer at infinity

$$\tilde{\Omega} = \mathrm{d}\phi/\mathrm{d}\tilde{t} = (\tilde{r}^{3/2} + a)^{-1}\,. \tag{2.10}$$

We remark here that circular orbits do not exist for all values of the radial coordinate $\tilde{r}$. Indeed, circular orbits will exist provided the denominator of (2.8a) is non-negative

$$1 - 3/\tilde{r} + 2a/\tilde{r}^{3/2} \geq 0\,. \tag{2.11}$$

Writing $x = \sqrt{\tilde{r}}$, the limiting case of the above equation yields the solution

$$x = \left(\sqrt{a^2 - 1} - a\right)^{-1/3} + \left(\sqrt{a^2 - 1} - a\right)^{1/3}\,, \tag{2.12}$$

which, after substituting $-a = \cos(y)$ for $y \in [\pi/2, 3\pi/2]$ into the above equation, one obtains the radial coordinate for the *light ring*

$$\tilde{r}_{\rm LR} = 2 + 2\cos\left(\frac{2}{3}\cos^{-1}(-a)\right) . \tag{2.13}$$

Equation (2.13) saturates the bound (2.11) implying such an orbit has infinite energy per unit rest mass. This is precisely the minimum BL radial coordinate that admits circular orbits for photons.

An analogous radial coordinate to the light ring exists for material particles on circular and equatorial orbits around Kerr BHs. Differentiating (2.5a) with respect to proper time and introducing $\tilde{r} = \tilde{r}_0 + \delta$, one obtains for $|\delta| \ll 1$

$$\ddot{\delta} - \frac{1}{2}\frac{\partial^2 G}{\partial \tilde{r}^2}\bigg|_{\tilde{r}_0} \delta = 0 . \tag{2.14}$$

In order for $\tilde{r}$ to not exhibit exponential growth as proper time increases, we must have the condition $\partial^2 G/\partial \tilde{r}^2 \leq 0$. Hence for material particles on both stable and circular orbits, we have the three conditions

$$G = \frac{\partial G}{\partial \tilde{r}} = 0 , \quad \frac{\partial^2 G}{\partial \tilde{r}^2} \leq 0 . \tag{2.15}$$

Solving equations (2.15), the conditions for a material particle to remain on a *stable* circular orbit are

$$1 - \tilde{E}^2 \geq \frac{2}{3\tilde{r}} , \tag{2.16}$$

$$\tilde{r}^2 - 6\tilde{r} + 8a\tilde{r}^{1/2} - 3a^2 \geq 0 . \tag{2.17}$$

Saturation of the last inequality, characterising marginal stability, means we can solve for the corresponding coordinate as a function of the spin parameter. This is called the *inner-most stable circular orbit* (ISCO) [162]

$$\begin{aligned} \tilde{r}_{\rm isco} &= 3 + Z_2 - [(3 - Z_1)(3 + Z_1 + 2Z_2)]^{1/2} , \\ Z_1 &= 1 + (1 - a^2)^{1/3}[(1 + a)^{1/3} + (1 - a)^{1/3}] , \\ Z_2 &= (3a^2 + Z_1^2)^{1/2} . \end{aligned} \tag{2.18}$$

The radial coordinate $\tilde{r}_{\rm isco}$ is the minimum radial coordinate that admits stable and circular orbits. All orbits for $\tilde{r} < \tilde{r}_{\rm isco}$ are unstable where in this case the particle has no choice but to

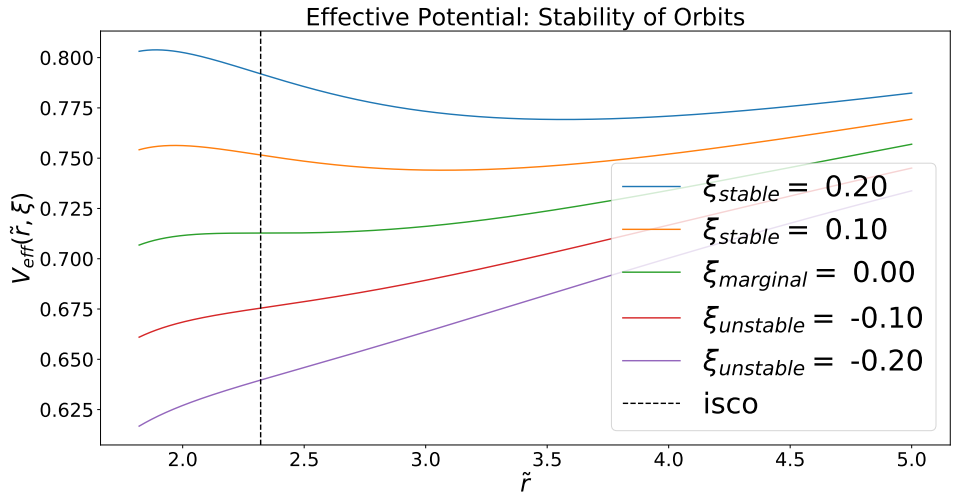

Figure 2.1: Here we plot $V_{\text{eff}}(\tilde{r}, \tilde{E}, \tilde{L}, a)$ as a function of $\tilde{E}(\xi)$ and $\tilde{L}(\xi)$ with rotation parameter $a = 0.9$ fixed. The blue and orange curves with $\xi > 0$ admit both stable and circular orbits where there exists a minimum to the potential $V_{\text{eff}}(\tilde{r})$. The green curve shows the marginally stable orbit for $\xi = 0$, with the point of inflection located at $\tilde{r}_{\text{isco}}$. Finally, the red and lilac curves yield unstable orbits with $\xi < 0$.

plunge towards the horizon of the BH. In order to get a more intuitive feel for these results, we can explain them using the *effective potential* V_{eff}, first introduced in equation (2.5a).

2.2.2 The radial potential

Consider the radial geodesic equation

$$\left(\frac{\mathrm{d}\tilde{r}}{\mathrm{d}\tilde{\tau}}\right)^2 = G(\tilde{r}, \tilde{E}, \tilde{L}) = \tilde{E}^2 - V_{\text{eff}} = \tilde{E}^2 - 1 + \frac{a^2(\tilde{E}^2 - 1) - \tilde{L}^2}{\tilde{r}^2} + \frac{2(a\tilde{E} - \tilde{L})^2}{\tilde{r}^3} + \frac{2}{\tilde{r}}\,. \tag{2.19}$$

It is important to note here that the particle is on a *geodesic* in the Kerr spacetime. For now, since there is no energy dissipation of the orbit due to GW emission, we treat E and L as constants of motion.

The effective potential is best understood within the vicinity of the ISCO. Following [163] and details considered in chapter 4 (cf. equation (4.14)), we consider $\tilde{E}(\xi) = \tilde{E}_{\text{isco}} + \tilde{\Omega}_{\text{isco}}\xi$ and $\tilde{L} = \tilde{L}_{\text{isco}} + \xi$. The parameter ξ here measures the deviation of the constants of motion $\tilde{E}$ and $\tilde{L}$ from their ISCO values. Substituting these expressions into $V(\tilde{r}, \tilde{E}, \tilde{L}, a)$, we can plot the effective potential as a function of ξ in figure 2.1.

In this figure, when $\xi > 0$ the particle lies at the minimum of the potential and thus the orbit is stable and circular. When $\xi = 0$, there exists a point of inflection on the radial potential at the radial coordinate $\tilde{r} = \tilde{r}_{\text{isco}}$. The radial coordinate $\tilde{r}_{\text{isco}}$ marks the point where the orbit

transitions from being stable to unstable. Finally, for $\xi < 0$, the orbit ceases to be stable and for this choice of ξ, the body has no choice but to plunge towards the horizon of the Kerr BH. In chapter 4, we will discuss this transition behaviour in more depth. In particular, we will focus on a particular case when the primary is near maximally spinning. In the next subsection, we give a brief review of circular and equatorial orbits of particles into near-extreme Kerr BHs.

2.2.3 Near-extremal circular orbits

We consider particle geodesics that are both circular and equatorial around a primary BH of mass M and spin $a \to 1$. We define the parameter $\epsilon = \sqrt{1-a^2}$ with $|\epsilon| \ll 1$. The location of the horizons of the BH take a simple form $\tilde{r}_\pm = 1 \pm \epsilon$. Substituting $a = \sqrt{1-\epsilon^2}$ into (2.18) and expanding for $\epsilon \to 0$, one obtains

$$\tilde{r}_{\rm isco} = 1 + 2^{1/3}\epsilon^{2/3} + \mathcal{O}(\epsilon^{4/3})\,. \tag{2.20}$$

Similarly, one can obtain a perturbative expansion of the energy, azimuthal angular momentum and angular frequency at the ISCO in terms of ϵ

$$\tilde{E}_{\rm isco} = \frac{1}{\sqrt{3}}\left(1 + 2^{1/3}\epsilon^{2/3} + \mathcal{O}(\epsilon^{4/3})\right)\,, \tag{2.21a}$$

$$\tilde{L}_{\rm isco} = \frac{2}{\sqrt{3}}\left(1 + 2^{1/3}\epsilon^{2/3} + \mathcal{O}(\epsilon^{4/3})\right)\,, \tag{2.21b}$$

$$\tilde{\Omega}_{\rm isco} = \frac{1}{2}\left(1 - \frac{3}{2^{5/3}}\epsilon^{2/3} + \mathcal{O}(\epsilon^{4/3})\right)\,. \tag{2.21c}$$

Notice that $|\tilde{r}_+ - \tilde{r}_{\rm isco}| = \mathcal{O}(\epsilon^{2/3})$ for prograde orbits. It can be shown that for retrograde orbits that $\tilde{r}_{\rm isco} = 9 - (45/32)\epsilon^2$ and thus $|\tilde{r}_+ - \tilde{r}_{\rm ISCO}| = \mathcal{O}(1)$. Thus, it is only prograde orbits that can fully probe the near-horizon geometry of a near-extremal BH. Since we are primarily interested in the near-horizon regime of near-extremal BHs, we will only consider prograde orbits for the remainder of this discussion. Similarly, we can expand $d\tilde{t}/d\tilde{\tau}$ at $\tilde{r}_{\rm isco}$ for circular orbits in the near-extremal case. We find that

$$\frac{{\rm d}\tilde{t}}{{\rm d}\tilde{\tau}} = \frac{2\cdot 2^{2/3}}{\sqrt{3}}\epsilon^{-2/3} - \frac{\sqrt{3}}{2} + \mathcal{O}(\epsilon^{2/3})\,, \tag{2.22}$$

which shows a divergence as $\epsilon \to 0$. The divergence in equation (2.22) occurs due to our choice of coordinate system and mimics the effect of particle freezing (near) the horizon as observed from infinity. The expansions above will be essential in chapter 4.

One can see that as $\epsilon \to 0$, we have that $\tilde{r}_{\rm isco} \to \tilde{r}_+ \to 1$. Thus the horizon and the ISCO

coincide in BL coordinates for extremal holes. This is, again, simply an artefact of the choice of coordinate system. The proper separation between the horizon and the ISCO is *finite* and *non-zero*. To see this, consider when $\theta = \pi/2$, ϕ and t are constant and consider the proper separation $\Delta\tilde{\ell}$

$$\Delta\tilde{\ell} = \int_{\tilde{r}_+}^{\tilde{r}_{\rm isco}} \frac{\tilde{r}}{\sqrt{\tilde{r}^2 - 2\tilde{r} + a^2}} \mathrm{d}\tilde{r} = \left[\sqrt{\tilde{\Delta}} + \log\left(\frac{\tilde{r} - 1 + \sqrt{\tilde{\Delta}}}{\sqrt{1 - a^2}} \right) \right]_{\tilde{r}_+}^{\tilde{r}_{\rm isco}}$$
$$= \frac{4}{3}\log(2) - \frac{1}{3}\log\epsilon, \quad |\epsilon| \ll 1\,. \tag{2.23}$$

What we learn from (2.23) is that the horizon and ISCO location of the BH are *distinct* and scale in proportion to $\Delta\tilde{\ell} \sim -\frac{1}{3}\log\epsilon$. The length of the throat of the BH defined as the proper displacement between the outer horizon and ISCO grows in length as $\epsilon \to 0$. For more details, we refer the reader to [164].

2.3 Deviations from geodesic motion

So far in this discussion, we have focused on geodesic orbits, for which the azimuthal angular momentum, $\tilde{L}$, and energy, $\tilde{E}$, are *constant*. For realistic, astrophysical orbits, the "constants" of motion will cease to be constant and now become time evolving quantities. Indeed, at every instance of time throughout the inspiral, the particles geodesic lies tangent to the trajectory where each equatorial geodesic is characterised by two integrals of motion $\tilde{E}$ and $\tilde{L}$. The acceleration of the two bodies sources GWs, envoking time dependence on the constants of motion $\tilde{E} := \tilde{E}(t)$, $\tilde{L} := \tilde{L}(t)$ due to GW emission. We call this back reaction, or *radiation-reaction*: the reaction and thus change to the orbital dynamics of the smaller body as a consequence of gravitational radiation being emitted. For bound geodesics, this time evolution in the constants of motion drives the smaller body closer to the one-way membrane of the central hole — the event horizon.

Radiation reaction in general relativity draws similar analogies to radiation reaction in EM, whereby the acceleration of a charged particle due to the presence of an EM field leads to the production of additional EM fields that subsequently interact with the particle and affect its motion [165, 166]. As discussed in section 17 of [167], linearized solutions to the EM field equations admit unstable solutions that are unphysical. Linearized radiation reaction in general relativity does not appear to show the same instabilities, although unphysical gauge modes are excited in numerical simulations which creates complications for numerical relativity solutions of the field equations. In general relativity, the techniques used to model the "self-interaction"

of the secondary with its personal world-line are exceptionally sophisticated. This field of study is called the *gravitational self-force* (GSF), and will be the focus of discussion in the next two sections.

For EMRI orbits, there exist two timescales: the orbital time-scale and inspiral time-scale that are well separated in proper/coordinate time. A result of this is that the motion can be well described using the two-timescale approach, which forms the basis of the research in chapter 6. We discuss the two time-scale approach in more detail in the next section.

2.3.1 The two-timescale approach

In this subsection, we review the two-timescale procedure used to build *general* orbital trajectories of small compact objects in the vicinity of a more massive BH. Intuitively, the orbit can be described as a forced geodesic

$$\frac{\mathrm{d}^2 x^\mu}{\mathrm{d}\tilde{\tau}^2} + \Gamma^\mu_{\rho\sigma}\frac{\mathrm{d}x^\rho}{\mathrm{d}\tilde{\tau}}\frac{\mathrm{d}x^\sigma}{\mathrm{d}\tilde{\tau}} = 0 + \eta a^{\mu(1)} + \eta^2 a^{\mu(2)} + \mathcal{O}(\eta^3)\,, \tag{2.24}$$

where $a^{\mu(1)}$ and $a^{\mu(2)}$ are forcing functions. These forcing functions arise due to the presence of the smaller body, though could be influenced by additional environmental effects such as multiple body interactions or accretion disks of the primary BH [168, 169]. We neglect such effects throughout this work. Generalising the work by Mino [170], Hinderer and Flanagan [171] showed that the forced geodesic equation above can be represented in a different form using the action-angle formalism

$$\begin{aligned}\frac{\mathrm{d}q^\alpha}{\mathrm{d}\tilde{\tau}} &= \omega_\alpha(\tilde{\boldsymbol{J}}) + \eta g^{(1)}_\alpha(q_\theta, q_{\tilde{r}}, \tilde{\boldsymbol{J}}) + \eta^2 g^{(2)}_\alpha(q_\theta, q_{\tilde{r}}, \tilde{\boldsymbol{J}}) + \mathcal{O}(\eta^2)\,,\\ \frac{\mathrm{d}\tilde{J}_i}{\mathrm{d}\tilde{\tau}} &= \eta G^{(1)}_i(q_\theta, q_{\tilde{r}}, \tilde{\boldsymbol{J}}) + \eta^2 G^{(2)}_i(q_\theta, q_{\tilde{r}}, \tilde{\boldsymbol{J}}) + \mathcal{O}(\eta^3)\,.\end{aligned} \tag{2.25}$$

Here q^α are 2π periodic angle variables associated with BL coordinates that describe the position of the small body on the orbit, and $\tilde{J}_i$ action variables representing constants of motion that are conserved along a geodesic. Each of $g^{(n)}_\alpha(q_{\tilde{r}}, q_\theta)$ and $G^{(n)}_i(q_{\tilde{r}}, q_\theta)$ are forcing functions corresponding to powers of the mass ratio η. They are independent of $q_{\tilde{t}}$ and q_ϕ since the Kerr BH is stationary and axisymmetric, so independent of coordinates $\tilde{t}$ and ϕ. These forcing functions are responsible for the deviations from geodesic motion due to GW emission. For $\eta = 0$, the motion is geodesic with $\tilde{J}_i$ constant and angular variables evolving at a rate corresponding to their associated fundamental frequencies ω_α. Expressions for these fundamental frequencies can be obtained using the Hamilton-Jacobi theory and are expressed explicitly in [172], equations (24-26). We do not give the explicit forms of $g^{(n)}_\alpha$ and $G^{(n)}_i$ as they are not needed for the

following discussion.

Each of the forcing terms $g_\alpha^{(n)}$ and $G_i^{(n)}$ can be separated into an averaged part $\langle\cdot\rangle$ and oscillatory part $\delta(\cdot)$. We can write

$$\begin{aligned} g_\alpha^{(n)}(q_{\tilde{r}}, q_\theta, \tilde{\boldsymbol{J}}) &= \langle g_\alpha^{(n)}(\tilde{\boldsymbol{J}})\rangle + \delta g_\alpha^{(n)}(q_{\tilde{r}}, q_\theta, \tilde{\boldsymbol{J}}), \quad \text{for } |\delta g_\alpha^{(n)}(q_{\tilde{r}}, q_\theta, \tilde{\boldsymbol{J}})| \ll \langle g_\alpha^{(n)}(\tilde{\boldsymbol{J}})\rangle\,, \\ G_i^{(n)}(q_{\tilde{r}}, q_\theta, \tilde{\boldsymbol{J}}) &= \langle G_i^{(n)}(\tilde{\boldsymbol{J}})\rangle + \delta G_i^{(n)}(q_{\tilde{r}}, q_\theta, \tilde{\boldsymbol{J}}), \quad \text{for } |\delta G_i^{(n)}(q_{\tilde{r}}, q_\theta, \tilde{\boldsymbol{J}})| \ll \langle G_i^{(n)}(\tilde{\boldsymbol{J}})\rangle\,, \end{aligned} \tag{2.26}$$

with averaged parts denoted by integrating out the dependence on the angular variables

$$\begin{aligned} \langle g_\alpha^{(n)}(\tilde{\boldsymbol{J}})\rangle &= \left(\frac{1}{2\pi}\right)^2 \int_0^{2\pi} \mathrm{d}q_{\tilde{r}} \int_0^{2\pi} \mathrm{d}q_\theta\, g_\alpha^{(n)}(q_\theta, q_{\tilde{r}}, \tilde{\boldsymbol{J}})\,, \\ \langle G_i^{(n)}(\tilde{\boldsymbol{J}})\rangle &= \left(\frac{1}{2\pi}\right)^2 \int_0^{2\pi} \mathrm{d}q_{\tilde{r}} \int_0^{2\pi} \mathrm{d}q_\theta\, G_i^{(n)}(q_\theta, q_{\tilde{r}}, \tilde{\boldsymbol{J}})\,. \end{aligned} \tag{2.27}$$

The coupled equations (2.25) can be written in terms of these new variables. We have that

$$\begin{aligned} \frac{\mathrm{d}q^\alpha}{\mathrm{d}\tilde{\tau}} &= \omega_\alpha(\tilde{\boldsymbol{J}}) + \eta\langle g_\alpha^{(1)}(\tilde{\boldsymbol{J}})\rangle + \eta\delta g_\alpha^{(1)}(q_\theta, q_{\tilde{r}}, \tilde{\boldsymbol{J}}) + \eta^2\langle g_\alpha^{(2)}(\tilde{\boldsymbol{J}})\rangle + \ldots \\ \frac{\mathrm{d}\tilde{J}_i}{\mathrm{d}\tilde{\tau}} &= \eta\langle G_i^{(1)}(\tilde{\boldsymbol{J}})\rangle + \eta\delta G_i^{(1)}(q_\theta, q_{\tilde{r}}, \tilde{\boldsymbol{J}}) + \eta^2\langle G_i^{(2)}(\tilde{\boldsymbol{J}})\rangle + \ldots\,. \end{aligned} \tag{2.28}$$

For now we stop to inspect the individual parts of equation (2.28). The leading order evolution of the constants of motion is the *orbit-averaged* component of $G_i^{(n)}(\tilde{\boldsymbol{J}})$, the largest contributing factor to how the Kerr constants change over time. The averaged forcing term $G_i^{(n)}(\tilde{\boldsymbol{J}})$ is nearly constant and varies over the inspiral time-scale $\tilde{t}_{\rm insp} \sim \mathcal{O}(1/\eta)$. The oscillatory terms $\delta g_\alpha^{(n)}$ and $\delta G_i^{(n)}$ vary rapidly around zero on the orbital timescale $\tilde{t}_{\rm orb} \sim O(1)$. Since the inspiral time-scale is much larger than the orbital time-scale, the oscillations nearly average away before $\tilde{\boldsymbol{J}}$ changes appreciably. The averaged forcing term $\langle g_\alpha^{(n)}(\tilde{\boldsymbol{J}})\rangle$ is interesting because it corresponds to a *shift* in the orbital frequencies

$$\omega_\alpha^{(\rm shift)}(\tilde{\boldsymbol{J}}) = \omega_\alpha(\tilde{\boldsymbol{J}}) + \eta\langle g_\alpha^{(1)}(\tilde{\boldsymbol{J}})\rangle\,. \tag{2.29}$$

This feature is not secular and does not vary on the radiation reaction time-scale. A consequence of the shift to the fundamental frequencies is that various positional elements of the orbit change by an amount comparable to $\sim \eta$. An example for circular equatorial orbits is the position of the ISCO in BL coordinates [173]. We will derive the corresponding shift in the radial ISCO coordinate for near-extreme BHs in section 4.2.1, in chapter 4.

2.3.2 Adiabatic and post-adiabatic approximation

The equations (2.28) are an expansion in the small parameter η. Truncating the series at any power of the mass ratio will introduce errors when modelling the trajectory, and thus the waveform, in turn leading to errors in parameter estimation.

By averaging equation (2.26) over q_r and q_θ, the oscillatory terms vanish. Neglecting the second-order forcing functions, and the non-dissipative piece $\langle g_\alpha^{(1)} \rangle$, we find the *adiabatic approximation*[3]

$$\begin{aligned} \frac{\mathrm{d}q^\alpha}{\mathrm{d}\tilde{\tau}} &\approx \omega_\alpha(\tilde{\boldsymbol{J}})\,, \\ \frac{\mathrm{d}\tilde{J}_i}{\mathrm{d}\tilde{\tau}} &\approx \eta \langle G_i^{(1)}(\tilde{\boldsymbol{J}}) \rangle\,. \end{aligned} \tag{2.30}$$

Here the angular variables evolve with respect to their (geodesic) fundamental frequencies on short time-scales, whereas the constants of motion $\tilde{J}_i$ evolve on the radiation-reaction time-scale. The approximation is reasonable up until the moment the inspiral time-scale is comparable to the orbital time-scale, that is, in the vicinity of the last stable orbit. In both chapters 4 and 5, we will use the adiabatic approximation.

At the next to leading order in equation (2.30), we have the *first-order post-adiabatic* (1PA) approximation

$$\begin{aligned} \frac{\mathrm{d}q^\alpha}{\mathrm{d}\tilde{\tau}} &\approx \omega_\alpha(\tilde{\boldsymbol{J}}) + \eta \langle g_\alpha^{(1)}(\tilde{\boldsymbol{J}}) \rangle\,, \\ \frac{\mathrm{d}\tilde{J}_i}{\mathrm{d}\tilde{\tau}} &\approx \eta \langle G_i^{(1)}(\tilde{\boldsymbol{J}}) \rangle + \eta \delta G_i^{(1)}(q_\theta, q_{\tilde{r}}, \tilde{\boldsymbol{J}}) + \eta^2 \langle G_i^{(2)}(\tilde{\boldsymbol{J}}) \rangle\,. \end{aligned} \tag{2.31}$$

At order η, the two-timescale equations (2.31) now include extra effects coming from the averaged quantity $\langle g_\alpha^{(1)}(\tilde{\boldsymbol{J}}) \rangle$ and the oscillatory $\delta G_i^{(1)}(q_\theta, q_{\tilde{r}}, \tilde{\boldsymbol{J}})$ quantity. Finally, we have the second order dissipative term $\langle G_i^{(2)}(\tilde{\boldsymbol{J}}) \rangle$, which is the current goal of GSF calculations. In chapter 6, we will investigate the 1PA approximation but neglect contributions from the second order dissipative piece.

Sticking to nomenclature found in the GW literature, the piece $\langle g_\alpha^{(1)}(\tilde{\boldsymbol{J}}) \rangle$ arises from the first order in η *conservative* effect of self interactions from the particle. Similarly, the part $\delta G_i^{(1)}(q_\theta, q_{\tilde{r}}, \tilde{\boldsymbol{J}})$ is the first order *oscillatory* and $\langle G_i^{(2)}(\tilde{\boldsymbol{J}}) \rangle$ the second-order orbit-averaged *dissipative* component of the GSF. The first order in η orbit-averaged component $\langle G_i^{(1)}(\tilde{\boldsymbol{J}}) \rangle$, is known to an excellent degree of precision for generic orbits in Kerr [104, 174]. For a handful of

[3] We comment that the following equation (2.30) excludes the effects of *resonances* in EMRI orbits. Resonances occur when the fundamental frequencies become commensurate, a rational multiple of one another, so the averaging process breaks down. As we only focus on equatorial geodesics, resonances will never feature in our trajectories. We will discuss this point in more detail later in section 2.3.3.

generic orbits, the first order conservative and dissipative components are known and can be calculated to high accuracy [175]. However, the past decade has seen focus on calculating the second order dissipative component of the GSF [176, 177, 178, 179]. Recently the gravitational binding energy and fluxes, were calculated at second order in the GSF for circular Schwarzschild orbits [180, 181]. For generic orbits around a Kerr BH, we do not yet have access to the second order orbit-averaged fluxes.

As black hole perturbation theory relies on expanding equations of motion in η, one has to be careful with truncation errors, which in turn affect the trajectory of the massive particle. An important question is what order of η is required so that waveforms are accurate enough for parameter estimation. An intuitive understanding can be obtained by understanding the influence the adiabatic and post-adiabatic components have on the orbital phase, which is the focus of the next subsection.

2.3.3 The orbital phase

As discussed later in section 3.4 and chapter 6, it is essential that our modelled waveforms closely match the true EMRI signal in the data stream. To enforce such a situation, we need both the amplitude to match the signal and, most importantly, the phase. At leading order, the phase evolution is governed by the forcing functions $\langle G_i^{(n)}(\tilde{\boldsymbol{J}})\rangle$, where each $\tilde{\boldsymbol{J}}$ are functionals of the most interesting astrophysical parameters (masses, spins, presence of eccentricity etc.). Over the radiation reaction time-scale, the usual rule of thumb is that we require tracking of the phase to $\lesssim 1$ radian. More concretely, as shown in [171], one can expand the orbital phase in powers of the mass ratio

$$\phi = \frac{1}{\eta}\phi_{\rm A}(t) + \phi_{\rm 1PA}(t) + \eta\phi_{\rm 2PA}(t) + \mathcal{O}(\eta^2)\,, \tag{2.32}$$

where $\phi_{\rm A}$ is the leading adiabatic evolution in the phase, $\phi_{\rm 1PA}$ the 1PA component to the phase (and so on). The leading order adiabatic piece contributes the most to the phase evolution, approximately η^{-1} cycles. The adiabatic piece of equation (2.32) is governed by the fluxes, the orbit-averaged dissipative components of the GSF. The form of the 1PA piece, $\phi_{\rm 1PA}$, comes from the first-order conservative and oscillatory part of the GSF, and the second-order orbit-averaged components of the GSF. Collectively, the adiabatic and 1PA pieces contribute roughly ~ 1 cycle over the radiation reaction time-scale. The *second-order post-adiabatic* (2PA) component to the phase $\phi_{\rm 2PA}$ contributes $\sim \eta$ cycles and is, therefore, deemed insignificant for parameter estimation purposes. Through a comparison between NR and black hole perturbation theory,

work has shown that $\phi_{\rm A}(t)$ and $\phi_{\rm 1PA}(t)$ are both order one for circular orbits into massive Schwarzschild BHs [182]. Assuming both $\phi_{\rm A}$ and $\phi_{\rm 1PA}$ are both order one for generic Kerr[4], in order to track the signal to within 1 cycle over the time of observation, it is essential that we have the full results from the 1PA components to the GSF.

In chapter 6, we will investigate to what numerical accuracy the 1PA components of the GSF must be known to ensure $\lesssim 0.1$ radians when tracking the orbital phase. We stick to a more stringent requirement than tracking the orbital phase to within $\lesssim 1$ radians, with the idea of being conservative with our results. Due to the waveform model we have access to, we will consider low eccentricity orbits in a Schwarzschild spacetime. Our study is an essential first step in EMRI systematics and we will explore these ideas in chapter 6.

We make a very important remark that we are ignoring the effect of *resonances* in the expansion 2.32. Resonances occur when the radial and polar fundamental frequencies become commensurate: a rational multiple of one another [171, 183]. On such a resonance, the averaging process leading to (2.30) produces extra terms, that do not average out, and so must be taken into account. We can understand this further by writing, for example, $G_i^{(n)}(\tilde{\boldsymbol{J}}, q_{\tilde{r}}, q_\theta)$ as a Fourier series while taking the average over the phase variables q_r and q_θ

$$\langle G_i^{(n)}(\tilde{\boldsymbol{J}}, q_{\tilde{r}}, q_\theta)\rangle = (G_i^{(n)}(\tilde{\boldsymbol{J}}))_{0,0} + \sum_{\mathrm{k}\neq 0,\mathrm{l}\neq 0} (G_i^{(n)}(\tilde{\boldsymbol{J}}))_{\mathrm{k,l}} \langle e^{i(\mathrm{k}q_{\tilde{r}}+\mathrm{l}q_\theta)\tilde{t}}\rangle \,. \tag{2.33}$$

The averaging procedure ensures that $\langle \exp(i(kq_{\tilde{r}}+lq_\theta))\rangle \approx 0$, only if the ratio $q_{\tilde{r}}/q_\theta \neq -l/k \in \mathbb{Q}$, i.e., a rational multiple of one another. If $l/k \in \mathbb{Q}$ occurs, extra contributions to (2.33) must be taken into account.

Thankfully, because our orbits are equatorial, there is no polar fundamental frequency and so the radial and polar frequencies cannot become commensurate. For this reason, we ignore the effect of resonances in this work. For general orbits, however, resonances are a very important feature that must be included in our models [184, 185, 186]. If resonances are taken into account, there is an extra contribution of order $\mathcal{O}(\eta^{1/2})$ to the evolution equations (2.28) and phase (2.32) that could, in theory, advance the number of cycles by ~ 100 for an inspiral with mass ratio $\eta = 10^{-5}$. As a consequence, if one does not include resonances in our EMRI waveforms, the number of detectable EMRI signals we can detect reduce [187], or drastically bias our recovered parameters as shown in [188].

In the next section, we will discuss BH perturbation theory at adiabatic order with the goal

[4]The statement that $\phi_{\rm A}$ and $\phi_{\rm 1PA}$ are both order one is a huge assumption due to the sheer complexity of the Kerr spacetime. If this is not the case, then further orders than the 1PA components of the GSF may be required. This will remain unknown until the second order components are well understood *or* the work from [182] is extended to generic Kerr orbits.

of deriving fully relativistic adiabatic waveforms.

2.4 The Teukolsky formalism

So far in this chapter we have discussed *orbits* of point particles around rotating BHs. As the orbits evolve, energy is carried from the system via GWs that then travel off towards infinity *and* down the throat of the hole. In this section, we will focus on the properties of the GWs generated by these orbits. The purpose of this section is to give a brief summary of the formalism used to compute these propagating waves and, in particular, describe Teukolsky's prescription for the gravitational waveform at infinity [189].

Note: In the following section, to simplify the presentation we will retain dimensions in the coordinates, so $[r] = M$, $[t] = M$, $[E] = \mu$, $[L] = M\mu$ and define $[a] = M$. We will revert to rescaled variables at the end of this section.

Outgoing and ingoing gravitational radiation is purely described through the two Weyl scalars ψ_4 and ψ_0 respectively. These scalars are defined by contracting of the Weyl tensor [190] with the ingoing and outgoing Kinnersley null tetrad

$$\psi_0 = C_{\alpha\beta\gamma\delta} l^\alpha m^\beta l^\gamma m^\delta \quad \text{(ingoing radiation)}\,, \tag{2.34}$$

$$\psi_4 = C_{\alpha\beta\gamma\delta} n^\alpha m^{\star\beta} n^\gamma m^{\star\delta} \quad \text{(outgoing radiation)}\,, \tag{2.35}$$

for null vectors $l^\alpha, m^\alpha, n^\alpha$ defined in [191]. Using the Newman-Penrose formalism [192], Teukolsky was able to show that perturbations to the Einstein field equations for $\psi = \{\psi_0, \psi_4\}$ are described by

$$\begin{aligned}\left[\frac{(r^2+a^2)^2}{\Delta} - a^2\sin^2\theta\right]\frac{\partial^2\psi}{\partial t^2} + \frac{4Mar}{\Delta}\frac{\partial^2\psi}{\partial t\partial\phi} + \left[\frac{a^2}{\Delta} - \csc^2\theta\right]\frac{\partial^2\psi}{\partial\phi^2} - \Delta^2\frac{\partial}{\partial r}\left(\frac{1}{\Delta}\frac{\partial\psi}{\partial r}\right) \\ - \csc\theta\frac{\partial}{\partial\theta}\left(\sin\theta\frac{\partial\psi}{\partial\theta}\right) + 4\left[\frac{a(r-M)}{\Delta} + \frac{i\cos\theta}{\sin^2\theta}\right]\frac{\partial\psi}{\partial\phi} + 4\left[\frac{M(r^2-a^2)}{\Delta} - r - ia\cos\theta\right]\frac{\partial\psi}{\partial t} \\ + (4\cot^2\theta + 2)\psi = 4\pi\Sigma T\,,\end{aligned} \tag{2.36}$$

for T the source term. The above equation is a linear partial differential equation (PDE) and known as the Teukolsky equation. For the scalar defining outgoing radiation, ψ_4, Teukolsky showed that equation (2.36) could be separated by considering an ansatz of the form

$$\psi_4 = \frac{1}{(r - ia\cos\theta)^4}\int_{-\infty}^{\infty}\sum_{lm} R_{lm\omega}(r)\,{}_{-2}S^{a\omega}_{lm}(\theta,\phi)e^{-i\omega t}\mathrm{d}\omega\,. \tag{2.37}$$

Plugging equation (2.37) into (2.36) yields differential equations for $R_{lm\omega}(r)$ and ${}_{-2}S^{a\omega}_{lm}(\theta,\phi) = {}_{-2}\,S^{a\omega}_{lm}(\theta)\exp(im\phi)$. First we have the angular Teukolsky equation

$$\frac{1}{\sin\theta}\frac{\mathrm{d}}{\mathrm{d}\theta}\left(\sin\theta\frac{\mathrm{d}\,{}_{-2}S^{a\omega}_{lm}}{\mathrm{d}\theta}\right)+\left[(a\omega)^2\cos^2\theta+4a\omega\cos\theta-\left(\frac{m^2-4m\cos\theta+4}{\sin^2\theta}\right)+\mathcal{E}_{lm}\right]{}_{-2}S^{a\omega}_{lm}=0\,, \tag{2.38}$$

with separation constant $\mathcal{E}_{lm}$. Solutions to this equation are *spin-weighted spheroidal harmonics* (SWSH), ${}_{-2}S^{a\omega}_{lm}(\theta)$, which reduce to spin-weighted spherical harmonics in the Schwarzschild limit $a \to 0$. For further details on spin-weighted spheroidal harmonics, the reader is referred to [193, 194, 195]. The separated radial equation for $R_{lm\omega}(r)$ is expressed by

$$\Delta^2\frac{\mathrm{d}}{\mathrm{d}r}\left(\frac{1}{\Delta}\frac{\mathrm{d}R_{lm\omega}}{\mathrm{d}r}\right)-V(r)R_{lm\omega}(r)=\mathcal{T}_{lm\omega}(r)\,, \tag{2.39}$$

with source term $\mathcal{T}_{lm\omega}$ and radial potential

$$V(r)=-\frac{K^2+4i(r-1)K}{\Delta}+8i\omega r+\lambda\,, \tag{2.40}$$

$$K^2=(r^2+a^2)\omega-ma,\quad \lambda=\mathcal{E}_{lm}-2am\omega+a^2\omega^2-2\,. \tag{2.41}$$

2.4.1 The Teukolsky waveform

By analysing asymptotic solutions $r \to \infty$ and $r \to r_+$ to the radial Teukolsky equation (2.39), it can be shown that ψ_4 takes the form [196, 194, 197]

$$\psi_4=\frac{1}{r}\sum_{lm}Z^{\infty}_{lm}(r)\;{}_{-2}S^{a\omega_m}_{lm}(\theta,\phi)e^{-i\omega_m(t-r^\star)},\quad r\to\infty\,. \tag{2.42}$$

Here $Z^{\infty}_{lm}(r)$ are the Teukolsky coefficients to the (outgoing) radial solution $R_{lm\omega}(r)$ and the frequencies ω have been decomposed into harmonics $\omega = m\Omega$ with Ω defined in (2.10). Finally $r^\star$ is the tortoise coordinate defined by

$$r^\star=r+\frac{2Mr_+}{r_+-r_-}\log\frac{r-r_+}{2M}-\frac{2Mr_-}{r_+-r_-}\log\frac{r-r_-}{2M}\,. \tag{2.43}$$

The curvature scalar ψ_4, in asymptotically flat spacetime, is related to the polarisations of the GW in the TT gauge through [198]

$$\psi_4=\frac{1}{2}(\ddot{h}_+-i\ddot{h}_x),\quad r\to\infty\,. \tag{2.44}$$

We obtain the result

$$h_+ - ih_\times = \frac{2}{r}\sum_{lm}\frac{1}{\omega_m^2}Z^\infty_{lm}\ {}_{-2}S^{a\omega_m}_{lm}(\theta,\phi)e^{-i\omega_m t}, \quad r\to\infty\,, \tag{2.45}$$

where we have relabelled $t - r^\star \to t$. The former is known as retarded time.

2.4.2 Energy/Angular momentum carried through GW emission

The amount of energy carried by GWs per unit area in the TT gauge (see section 1.1.5) is given by [199]

$$\begin{aligned}\left\langle \frac{\mathrm{d}E_{\rm GW}}{\mathrm{d}t\mathrm{d}A}\right\rangle &= \frac{1}{32\pi}\langle \dot{h}_{ij}\dot{h}^{ij}\rangle \\ &= \frac{1}{16\pi}\left\langle \left(\frac{\partial h_+}{\partial t}\right)^2 + \left(\frac{\partial h_\times}{\partial t}\right)^2\right\rangle,\end{aligned} \tag{2.46}$$

where in the second equality we used the fact that $h_{xx} = -h_{yy} = h_+$ and $h_{xy} = h_{yx} = h_\times$. Similarly, the angular momentum carried [200] in Cartesian coordinates is expressed as

$$\begin{aligned}\left\langle \frac{\mathrm{d}L^i_{\rm GW}}{\mathrm{d}t\mathrm{d}A}\right\rangle &= \frac{1}{32\pi}\langle -\epsilon^{ikl}\dot{h}_{ab}x_k\partial_l h^{ab} + 2\epsilon^{ikl}\dot{h}^a{}_l h_{ak}\rangle \\ &= -\frac{im}{16\pi}\left\langle \left(\frac{\partial h_+}{\partial t}\right)h_+ + \left(\frac{\partial h_\times}{\partial t}\right)h_\times\right\rangle, \quad \text{in the } z \text{ direction}\,.\end{aligned} \tag{2.47}$$

The second equality arises using symmetries of the Levi-civita tensor ϵ^{ikl} and the result

$$x\frac{\partial}{\partial y} - y\frac{\partial}{\partial x} = \frac{\partial}{\partial\phi} \tag{2.48}$$

for polar coordinates. We also used the fact that $\partial_\phi S(\theta,\phi) = imS(\theta,\phi)$.

We can compute the energy flux as a function of ω_m and the Teukolsky coefficients Z^∞_{ml}. We first use the identity

$$\left\langle \left(\frac{\partial h_+}{\partial t} - i\frac{\partial h_\times}{\partial t}\right)\left(\frac{\partial h_+}{\partial t} - i\frac{\partial h_\times}{\partial t}\right)^\star\right\rangle = \left\langle \left(\frac{\partial h_+}{\partial t}\right)^2 + \left(\frac{\partial h_\times}{\partial t}\right)^2\right\rangle,$$

that simplifies the evaluation of (2.46). Substitution of (2.45) into equation (2.46) gives

$$\left\langle \frac{\mathrm{d}E_{\rm GW}}{\mathrm{d}t\mathrm{d}A}\right\rangle = \frac{4}{\pi r^2}\sum_{lm}\sum_{pk}\frac{1}{\omega_m\omega_p}Z^\infty_{lm}(Z^\infty_{pk})^\star\ {}_{-2}S^{a\omega_m}_{lm}(\theta,\phi)({}_{-2}S^{a\omega_p})^\star_{pk}(\theta,\phi)e^{-it(\omega_m-\omega_p)}. \tag{2.49}$$

From here we can use equation (2.32) in [193]. Equation (2.32) states that SWSHs satisfy

orthogonality conditions

$$\int {}_{-2}S_{lm}^{a\omega_m}(\theta,\phi)({}_{-2}S^{a\omega_p})^{\star}_{pk}(\theta,\phi)\mathrm{d}A = r^2\delta_{lp}\delta_{mk}\,,$$

giving the orbit-averaged radiative flux at infinity

$$\left\langle \frac{\mathrm{d}E_{\mathrm{GW}}}{\mathrm{d}t} \right\rangle^{\infty} = \sum_{lm} \frac{|Z^{\infty}_{ml}|^2}{4\pi\omega_m^2}\,. \tag{2.50}$$

The angular momentum carried by the waves can be similarly calculated using

$$\left\langle \left(\frac{\partial h_+}{\partial t} - i\frac{\partial h_\times}{\partial t}\right)(h_+ - ih_\times)^{\star} \right\rangle = \left\langle \left(\frac{\partial h_+}{\partial t}\right)h_+ + \left(\frac{\partial h_\times}{\partial t}\right)h_\times \right\rangle - i\left\langle \left(\frac{\partial h_+}{\partial t}\right)h_\times + \left(\frac{\partial h_\times}{\partial t}\right)h_+ \right\rangle.$$

As the two polarisations are orthogonal, the orbit averaging process eliminates the last term leaving only the first term — the same form as (2.47). A similar calculation gives

$$\left\langle \left(\frac{\partial h_+}{\partial t} - i\frac{\partial h_\times}{\partial t}\right)(h_+ - ih_\times)^{\star} \right\rangle = 4i\sum_{ml}\frac{|Z^{\infty}_{ml}|^2}{\omega^3_{ml}}\,, \tag{2.51}$$

and we deduce the flux of angular momentum carried to infinity by the waves is

$$\left\langle \frac{\mathrm{d}L_{\mathrm{GW}}}{\mathrm{d}t} \right\rangle^{\infty} = \sum_{lm} \frac{m|Z^{\infty}_{ml}|^2}{4\pi\omega_m^3}\,. \tag{2.52}$$

To summarise, equations (2.50) and (2.52) are the first order in the mass ratio orbit-averaged dissipative components to the GSF — the fluxes.

To calculate the total flux we must also compute the rate of energy/angular momentum escaping down the throat of the black hole. This calculation is more involved so we do not present it here. As described in [196], the idea of the calculation is to first transform between the Kinnersley null tetrad to the Hawking-Hartle tetrad [201], an orthonormal frame that is well-behaved at the horizon of the BH. The energy and angular momentum flux at the horizon $r \to r_+$ is given by

$$\left\langle \frac{\mathrm{d}E_{\mathrm{GW}}}{\mathrm{d}t} \right\rangle^{H} = \sum_{lm} \alpha_{lm}\frac{|Z^{\infty}_{ml}|^2}{4\pi\omega_m^2}\,, \tag{2.53}$$

$$\left\langle \frac{\mathrm{d}L_{\mathrm{GW}}}{\mathrm{d}t} \right\rangle^{H} = \sum_{lm} \alpha_{lm}\frac{m|Z^{\infty}_{ml}|^2}{4\pi\omega_m^3}\,, \tag{2.54}$$

Here α_{lm} is a coefficient given by equation (4.17) in [194]. The *total* (orbit-averaged) energy

and angular momentum flux is given by

$$\left\langle \frac{\mathrm{d}E_{\rm GW}}{\mathrm{d}t} \right\rangle = \left\langle \frac{\mathrm{d}E_{\rm GW}}{\mathrm{d}t} \right\rangle^{\infty} + \left\langle \frac{\mathrm{d}E_{\rm GW}}{\mathrm{d}t} \right\rangle^{H}, \tag{2.55a}$$

$$\left\langle \frac{\mathrm{d}L_{\rm GW}}{\mathrm{d}t} \right\rangle = \left\langle \frac{\mathrm{d}L_{\rm GW}}{\mathrm{d}t} \right\rangle^{\infty} + \left\langle \frac{\mathrm{d}L_{\rm GW}}{\mathrm{d}t} \right\rangle^{H}. \tag{2.55b}$$

The orbit-averaged fluxes obey *balance laws*

$$\left\langle \frac{\mathrm{d}E}{\mathrm{d}t} \right\rangle = -\left\langle \frac{\mathrm{d}E_{\rm GW}}{\mathrm{d}t} \right\rangle, \tag{2.56a}$$

$$\left\langle \frac{\mathrm{d}L}{\mathrm{d}t} \right\rangle = -\left\langle \frac{\mathrm{d}L_{\rm GW}}{\mathrm{d}t} \right\rangle, \tag{2.56b}$$

where $\langle \mathrm{d}E/\mathrm{d}t \rangle$ is the orbit-averaged rate of change of energy of the system. In the adiabatic approximation (2.30), the orbit-averaged piece $\langle G_i(q_\theta, q_r) \rangle$ is given by either $\langle \mathrm{d}E_{\rm GW}/\mathrm{d}t \rangle$, or $\langle \mathrm{d}L_{\rm GW}/\mathrm{d}t \rangle$, depending on whether we seek $J = \{E, L\}$ evolution of the orbit. From knowledge of the right-hand sides of (2.56a) - (2.56b) for a given geodesic, one can move to a new geodesic with new parameters $E + \langle \mathrm{d}E/\mathrm{d}t \rangle \delta t$ and $L + \langle \mathrm{d}L/\mathrm{d}t \rangle \delta t$.

There is a simple law that relates the flux of angular momentum and energy. Considering $m/\omega_m = \Omega^{-1}$, we obtain a relationship between $\mathrm{d}E/\mathrm{d}t$ and $\mathrm{d}L/\mathrm{d}t$ valid for *circular* and *equatorial* orbits [202, 203]

$$\left\langle \frac{\mathrm{d}E}{\mathrm{d}t} \right\rangle = \Omega \left\langle \frac{\mathrm{d}L}{\mathrm{d}t} \right\rangle. \tag{2.57}$$

Equation (2.57) motivates why the behaviour of $E(r, a)$ near the ISCO can be approximated as $E - E_{\rm isco} = \Omega_{\rm isco}(L - L_{\rm isco})$, as we did in subsection 2.2.2 earlier in this chapter.

The fluxes $\langle \dot{E}^{\infty}_{\rm GW} \rangle$ and $\langle \dot{E}^{H}_{\rm GW} \rangle$ denote the (dimensionless and orbit-averaged) dissipative fluxes of gravitational radiation emitted towards infinity and towards the horizon respectively. From here on, we shall drop the angular brackets $\langle \dot{E} \rangle \to \dot{E}$, to avoid cumbersome notation. The components of the fluxes $\dot{E}$ are obtained by numerical solution of the Teukolsky equation sourced by a point particle. There exists an open source code in the BH Perturbation Toolkit (BHPT) [204] to do this for circular and equatorial orbits — specifically the Teukolsky package. In this thesis, we will parametrize the leading order in the mass ratio dissipative energy flux using the Finn and Thorne *dimensionless* parametrization [109]

$$\dot{\tilde{E}}_{\rm GW} = -\dot{\tilde{E}} = \frac{32}{5} \eta \tilde{\Omega}^{10/3} \dot{\mathcal{E}}(r, a). \tag{2.58}$$

Here $\dot{\mathcal{E}}$ is the dimensionless general relativistic correction (GRC) to the leading order PN expression for the total energy flux in harmonic m with the property that $\dot{\mathcal{E}} \to 1$ as $r \to \infty$.

a	$\dot{\tilde{E}}^{\rm Exact}_{\rm GW}/\eta$	$\dot{\tilde{E}}^{\rm NHEK}_{\rm GW}/\eta$	$\lvert\dot{\tilde{E}}^{\rm Exact}_{\rm GW} - \dot{\tilde{E}}^{\rm NHEK}_{\rm GW}\rvert/\eta$
$1-10^{-5}$	0.0264197	0.0261523	0.0002674
$1-10^{-6}$	0.0129344	0.0125200	0.0004143
$1-10^{-7}$	0.0061516	0.0059484	0.0002031
$1-10^{-8}$	0.0028875	0.0028082	0.0000793
$1-10^{-9}$	0.0013472	0.0013193	0.0000280
$1-10^{-10}$	0.0006273	0.0006176	0.0000097
$1-10^{-11}$	0.0002915	0.0002883	0.0000031
$1-10^{-12}$	0.0001354	0.0001344	0.0000009

Table 2.1: Comparing the NHEK flux (2.59) with exact flux data $\dot{\tilde{E}}^{\rm Exact}_{\rm GW}$ found in the BHPT. We fix the radial coordinate at $\tilde{r} = r_{\rm isco}$ and change the spin parameter a.

Values of $\dot{\mathcal{E}}$ are tabulated in Table II of [109] and further discussed in appendix B.2.

For near-extremal BHs, the energy flux of gravitational radiation admits a remarkably simple *analytic* form. As seen in 2.1.1, there is an enhancement of symmetry in the near horizon geometry of extreme Kerr. This extra symmetry provides an additional tool to compute the fluxes dE/dt analytically [205, 206, 207, 208, 209, 210, 211, 212, 213]. For circular equatorial orbits near the horizon of a near-extremal BH, the total energy flux has an approximation of the form [152]

$$\dot{\tilde{E}}^{\rm NHEK}_{\rm GW} = \eta(\tilde{C}_H + \tilde{C}_\infty)(\tilde{r} - \tilde{r}_+)/\tilde{r}_+, \quad \frac{\tilde{r} - \tilde{r}_+}{\tilde{r}_+} \ll 1\,. \tag{2.59}$$

The quantities C_H and C_∞ are constants provided analytically in equations (76) and (77) of [152], which describe the emission towards the horizon and infinity respectively. Numerically evaluating them using codes found in the BHPTand summing the contribution of the first $|m| \leq l = 30$ modes gives $C_H \approx 0.987$ and $C_\infty \approx -0.133$. Equation (2.59) is useful when working within the near-horizon geometry of the rapidly rotating hole, but it breaks down far from the horizon and extra terms are required to compute reliable fluxes. For various spin parameters, we compare (2.59) and exact results for the flux computed through the BHPT at the ISCO in table 2.1. As expected, (2.59) becomes more accurate as $a \to 1$.

At the ISCO, the total energy flux $\dot{\tilde{E}}^{\rm NHEK}_{\rm GW}$ scales with $\epsilon \ll 1$ through

$$\dot{\tilde{E}}^{\rm NHEK}_{\rm GW}\Big|_{\rm isco} = \eta(\tilde{C}_H + \tilde{C}_\infty)2^{1/3}\epsilon^{2/3} + \mathcal{O}(\epsilon)\,. \tag{2.60}$$

We will use (2.59) and the corresponding scaling law (2.60) in chapters 4 and 5. An issue with (2.59) is that it is only valid for near-horizon and near-extremal BHs. In both these chapters, we need to construct radial trajectories that begin *far* from the horizon where the analytical result (2.59) is no longer valid.

In the next subsection, we will describe an approximation to the Teukolsky based waveform

model (2.45) that we will use in chapters 4 and 5.

2.4.3 Sky-averaged Teukolsky waveform

The SWSHs have to be computed numerically by solving the angular Teukolsky equation (2.38). This can be avoided by approximating the waveform model (2.45) by a *root-mean-square* (RMS) amplitude, obtained through averaging over both the sky and the period of the waves. We follow the prescription in [109].

Recall the expression for the energy flux per unit area (2.46)

$$\left\langle \frac{\mathrm{d}E_{\mathrm{GW}}}{\mathrm{d}t\mathrm{d}A} \right\rangle = \frac{1}{16\pi} \left\langle \left(\frac{\partial h_+}{\partial t} \right)^2 + \left(\frac{\partial h_\times}{\partial t} \right)^2 \right\rangle . \tag{2.61}$$

By defining $h^2_{o,m} = \langle h^2_{+,m} + h^2_{\times,m} \rangle$ as the sky-averaged RMS waveform at harmonic m, we can use the expression above to derive an approximate form of the Teukolsky based waveform model (2.45). From (2.45), we understand that $\dot{h}^2_{o,m} \sim \omega^2_m \langle h_{o,m} \rangle^2$ and one can integrate (2.61) over the 2-sphere, which introduces a factor of $4\pi r^2$. We deduce that

$$\begin{aligned} h_{\mathrm{o},m} &= \frac{2\sqrt{\dot{E}^{\infty}_{m,\mathrm{GW}}}}{m\Omega r} \\ &= \frac{2\sqrt{\eta \dot{\tilde{E}}^{\infty}_{m,\mathrm{GW}}}}{m\tilde{\Omega}\tilde{r}} , \end{aligned} \tag{2.62}$$

with $\omega_m = m\Omega$ and we have rescaled variables so that $\dot{E} = \eta \dot{\tilde{E}}$, $\tilde{\Omega} = M\Omega$ and $\tilde{r} = r/M$. In equation (2.62) we have written the energy flux for the waves at harmonic m as

$$\dot{E}^{\infty}_{\mathrm{GW}} = \sum_{m=1}^{\infty} \dot{E}^{\infty}_{m,\mathrm{GW}}, \quad \text{with } \dot{E}^{\infty}_{m,\mathrm{GW}} = \sum_{l=-m}^{l=m} \frac{|Z^{\infty}_{lm}|^2}{4\pi\omega^2_m} , \tag{2.63}$$

We can use equation (2.62) to approximate harmonic m as a sinusoid with an arbitrary initial phase ϕ_0

$$h_{\mathrm{o}} \approx \sum_{m=1}^{\infty} \frac{2\sqrt{\eta \dot{\tilde{E}}^{\infty}_{m,\mathrm{GW}}}}{m\tilde{\Omega}\tilde{r}} \sin(2\pi \tilde{f}_m \tilde{t} + \phi_0) , \tag{2.64}$$

with frequency of the GWs at each harmonic m

$$2\pi \tilde{f}_m = m\tilde{\Omega} . \tag{2.65}$$

The energy flux at radial infinity per harmonic m can be written [109]

$$\dot{\tilde{E}}^{\infty}_{m,\mathrm{GW}} = \mathcal{A}_m \eta \tilde{\Omega}^{2+2m/3} \dot{\mathcal{E}}^{\infty}_m , \tag{2.66}$$

where

$$\mathcal{A}_m = \frac{2(m+1)(m+2)(2m)!m^{2m-1}}{(m-1)[2^m m!(2m+1)!!]^2},$$

and $(2m+1)!! = (2m+1)(2m-1)\ldots 3\cdot 1$. Here $\dot{\mathcal{E}}^{\infty}_m$ serves the same function as $\dot{\mathcal{E}}$ in equation (2.58). We remark here that (2.64) is a rough estimate of the Teukolsky based waveform (2.45), exhibiting a rough order of magnitude estimate for the amplitude but the correct phase evolution. The phase evolution is encoded through $\tilde{\Omega}(\tilde{r}, a)$ that depends on the radial trajectory $\tilde{r}(\tilde{t})$, which is common to both waveform models (2.64) and (2.45).

Knowledge of the fluxes at infinity $\dot{\tilde{E}}^{\infty}_{m,\mathrm{GW}}$ makes computation of (2.62) easier than the Teukolsky waveform (2.45), simply because we do not need to calculate the SWSH where no closed form analytical formula exists. `Mathematica` packages within the BHPT enable computation of $\dot{\tilde{E}}^{\infty}_{m,\mathrm{GW}}$ and ${}_{-2}S^{am\tilde{\Omega}}_{lm}(\theta,\phi)$. The approximate sky-averaged waveform model (2.64) will be used in chapter 4 and 5. In the next section, we will give a brief summary of all the results described in this chapter that will be used in the research chapters later in this thesis.

2.5 Concepts used throughout this work

Chapter 2 has brought forth the main concepts behind EMRIs that will be used in this work. The enhancement of symmetry of the Kerr spacetime when the spin parameter $a \to 1$ is key in finding an approximation for the total energy flux due to GW emission (2.59). Equation (2.59), alongside the ideas introduced in sections 2.2, 2.2.2 and 2.2.3, will be essential in chapter 4, which describes the transition from inspiral to plunge of a CO into a massive rotating BH. In chapter 5 we discuss how tightly one can constrain the spin parameter of near-extremal BHs. From the geodesic energy relation (2.8a) and (2.58), we derive an evolution equation for the radial trajectory in BL coordinates. The spin dependence in this radial trajectory is what ultimately drives the excellent measurement of the rotation parameter. We use both adiabatic (see equation (2.30)) waveforms based on the Teukolsky results in equation (2.45) and the sky-averaged approximation (2.64) to model the waveforms emitted by this source. In chapter 6, we use a waveform model specific for a particle in low eccentricity orbit around a Schwarzschild BH. We use a waveform model developed by van de Meent *et al* [214], based on the ideas in section 2.3.2 that exploits the *near-identity-transformation* first introduced in [215, 216]. We use this waveform model to test the level of precision required when calculating the adiabatic and 1PA components, excluding the second order dissipative field of the GSF, in order to recover parameters with minimal bias.

Chapter 3

Gravitational Wave Data Analysis

So far in our discussion, we have focused on the construction of EMRI gravitational waveforms given the source parameters. Such a task is formidable, requiring approximate methods to solve the two-body problem in general relativity —— a difficult and computationally very expensive task. Source modellers focus on building GW signals given source parameters. Here, we discuss the *inverse* problem: how do we perform inference on the source parameters given an observation of a GW signal? This chapter is organised as follows: in section 3.1, we discuss computational techniques that represent continuous time sinusoids as discrete time sinusoids, suitable for numerical calculations; section 3.2 covers properties of stationary Gaussian noise with the goal of deriving the Whittle-likelihood, the usual likelihood in GW astronomy; section 3.3 reviews the Fisher matrix and its use as a tool for estimating constraints on astrophysical parameters given a waveform model; the tools used for systematic studies of inaccurate waveforms are reviewed in section 3.4; and, finally, we briefly review Bayesian parameter estimation in section 3.5.

3.1 Signal processing

Errors induced through insufficient sampling of discrete time sinusoids can potentially lead to errors in data analysis pipelines. The conversion from a continuous in time sinusoid to a discretised sinusoid is subtle and has to be handled carefully. In this section, we outline notation and sinusoidal sampling algorithms.

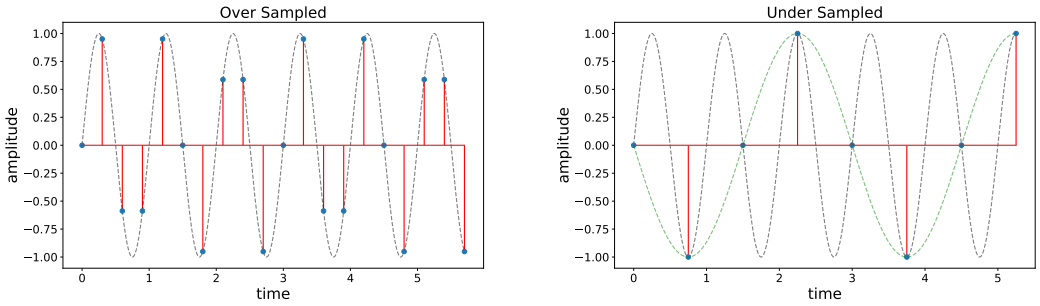

Figure 3.1: Here we sample a sinusoid of unit frequency $h(t) = \sin(2\pi t)$. The left plot oversamples using $\Delta t = 0.3$ whereas the right plot under-samples using $\Delta t = 0.75$. The red stem plots are the discrete samples, black dashed line the true continuous signal and the green dashed line the *aliased* signal given through under-sampling.

3.1.1 Sampling of discrete time sinusoids: time domain

Suppose a continuous signal is observed over a time segment $t \in [t_0, t_{\text{obs}}]$. Digitally, we can express this as $t_n = t_0 + n\Delta t$ for constant $\Delta t = t_{n+1} - t_n$ the *sampling interval*. Here $n \in [0, N-1]$ is the *time index* with $t_{\text{obs}} = t_0 + N\Delta t$. A continuous time sinusoid $h(t)$ can then be represented digitally through

$$h(t) \approx \{h[t_n]\}_{n=0}^{N-1} = \{h[t_0 + n\Delta t]\}_{n=0}^{N-1} . \tag{3.1}$$

We now assume that the initial measured time $t_0 = 0$ without loss of generality. The sampling interval Δt is related to the *sampling rate* F_s through $F_s = 1/\Delta t$. The smaller the sampling interval Δt, the larger the sampling rate F_s. We provide an example of under-sampling and over-sampling sinusoids in figure 3.1. We see from figure 3.1 that the choice of sampling rate is fundamental when representing continuous sinusoids in a digitised form.

The optimal sampling rate is provided by *Shannon's sampling theorem* [217]. The minimum sampling rate required in order to *resolve* the frequencies of the signal is twice the highest frequency of the signal. That is, we must have $F_s \geq 2f_{\max} \iff \Delta t = 1/2f_{\max}$. The maximum resolvable frequency of the signal is sometimes denoted f_{nyq}, the *Nyquist frequency*.

Insufficient sampling rates can lead to *aliasing* — high frequency content of the signal cannot be resolved and the reconstructed signal exhibits a lower frequency signal, as illustrated in 3.1. Aliasing will be discussed in more detail in the next subsection.

3.1.2 Sampling of discrete time sinusoids: frequency domain

The time domain representation of a sinusoid is one way of analysing and describing features of the signal. Given that GWs are simply a superposition of sinusoids with multiple (evolving)

frequencies, some may view it as more natural to analyse these signals in the frequency domain. The *Fourier transform* is a complex-valued function defined by

$$\mathcal{F}[h(t)] = \hat{h}(f) = \int_{-\infty}^{\infty} h(t) e^{-2\pi i t f} \mathrm{d}t \,. \tag{3.2}$$

Similarly, given a function in the frequency domain $\hat{h}(f)$, the corresponding time domain representation is given by the *inverse Fourier transform* (IFT)

$$\mathcal{F}^{-1}[\hat{h}(f)] = h(t) = \int_{-\infty}^{\infty} \hat{h}(f) e^{2\pi i t f} \mathrm{d}f \,. \tag{3.3}$$

Equation (3.2) is a continuous representation of the time domain signal in the frequency domain. Although useful for theoretical calculations, equation (3.2) must be discretised for numerical calculations. Let $h(t)$ be sampled at discrete time points $\{t_n = n\Delta t\}_{n=0}^{N-1}$ such that $h(t) \approx \{h[n\Delta t]\}_{n=0}^{N-1}$. Discretising (3.2) gives

$$\hat{h}(f_i) \approx \Delta t \cdot \tilde{h}(f_i) \,, \tag{3.4}$$

$$\tilde{h}(f_i) = \sum_{n=0}^{N-1} h[n\Delta t] \exp(-2\pi i f_i n \Delta t) \,. \tag{3.5}$$

Where each Fourier frequency $f_n = \{-\lfloor (N-1)/2 \rfloor \Delta f, \ldots, 0, \ldots, \lfloor (N-1)/2 \rfloor \Delta f\}$ with *frequency sampling interval* $\Delta f = 1/N\Delta t = 1/t_{\mathrm{obs}}$. Equation (3.5) is the dimensionless *discrete time Fourier transform* (DTFT) $\tilde{h}(f_i)$ and equation (3.4) is the discretised *continuous time fourier transform* (CTFT) $\hat{h}(f_i)$. As a final remark, tilded quantities refer to the DTFT, whereas hatted quantities denote the CTFT.

In chapters 5, 6 and 8, we zero-pad each time domain signal, so its length is equal to an integer power of two. In doing so, we can exploit the *fast Fourier transform* that numerically computes the DTFT in $\mathcal{O}(N \log_2 N)$ operations, rather than $\mathcal{O}(N^2)$ operations [218]. We will not do this in chapter 3 since the computational cost of the following simulations are small.

Results from computing the DTFT of a sinusoid $h(t) \approx h[t_n] = h[n\Delta t] = \sin(2\pi n \Delta t)$ with sampling intervals $\Delta t = 0.75$ and $\Delta t = 0.3$ are shown in figure 3.2. We see in the left panel of figure 3.2 that we can resolve the true frequencies of the signal $f = \pm 1\,\mathrm{Hz}$. However, in the right panel, we cannot resolve the frequencies since we are not sampling at a high enough rate. The frequencies are *aliased* so that they lie in the range $(-f_{\mathrm{nyq}}, f_{\mathrm{nyq}})$. Aliasing can be problematic for GW detectors since they are not uniformly sensitive over their frequency range, so, care must be taken when choosing the sampling rate when sampling sinusoids.

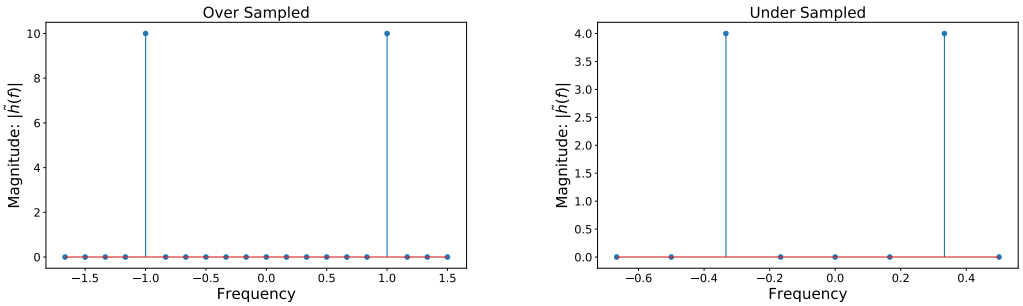

Figure 3.2: Here we compute the DTFT of a sinusoid of unit frequency $h(t) = \sin(2\pi t)$ when under and over sampled. The left plot oversamples using $\Delta t = 0.3$ whereas the right plot undersamples using $\Delta t = 0.75$. We are able to resolve the true frequencies on the left plot but the right plot we cannot resolve the true frequencies.

3.1.3 Spectral leakage

The DTFT assumes the function is periodic over the time interval. When this is not the case a phenomena called spectral leakage occurs. For example, consider the example above $h(t) = \sin(2\pi t)$, which has a period $\tau = 1$ second. If $N\Delta t/\tau$ is not an integer, then the signal will truncate either *before* or *after* it has completed a full cycle. This means that the periodic extension of the signal under scrutiny will exhibit discontinuities. The presence of these discontinuities is what is responsible for extra spectral contributions to Fourier components at the resolvable frequencies — a feature commonly referred to as *spectral leakage*.

All hope is not lost: the problem can be mitigated (though, never completely removed) using windowing functions that *smoothly* taper the signal to zero at the end points to try and enforce smoothness in the signals periodic extension. We now consider $H(t) = w(t)h(t)$ where $w(t)$ is a window function of choice. The CTFT of the windowed signal is given by $\mathcal{F}[H(t)] = (\hat{w} \star \hat{h})(f)$ for $\star$ denoting the convolution between $\hat{w}$ and $\hat{h}$. Thus the spectrum's shape of windowed signal is influenced by the spectrum of the window $\hat{w}(f)$.

The choice of window function is important, but largely situational. Indeed, in the case of wanting to resolve multiple frequencies of sinusoids with similar amplitudes, then the rectangular window is a good choice. However, when wanting to resolve two frequencies that are close together where one signal amplitude dominates over the other, then leakage can potentially obscure the lesser frequency so a Hann window may suffice. In our work we will use the *Tukey*

window defined by

$$w(t) = \begin{cases} \frac{1}{2}\left\{1 + \cos\left[\frac{2\pi}{\alpha t_{\rm obs}}\left(t - \frac{\alpha t_{\rm obs}}{2}\right)\right]\right\} & 0 \leq t \leq \frac{\alpha t_{\rm obs}}{2}\,, \\ 1 & \frac{\alpha t_{\rm obs}}{2} < t \leq 1 - \frac{\alpha t_{\rm obs}}{2}\,, \\ \frac{1}{2}\left\{1 + \cos\left[\frac{2\pi}{\alpha t_{\rm obs}}\left(t - t_{\rm obs} + \frac{\alpha t_{\rm obs}}{2}\right)\right]\right\} & t_{\rm obs} - \frac{\alpha t_{\rm obs}}{2} < t \leq t_{\rm obs}\,. \end{cases} \tag{3.6}$$

Where the choice of $\alpha \in [0, 1]$, determines the lobe lengths and can be tuned to balance high frequency resolution and leakage effects. For $\alpha = 0$ the Tukey window is a rectangular window and when $\alpha = 1$ a Hann window. We refer the reader to [219, 220] for further discussions on spectral leakage.

In chapters 4, 5, 6, 7 and 8 we rely on all the details discussed in section 3.1. Armed with signal processing tools, we are now in a position to discuss noise properties and the likelihood that is used throughout GW astronomy. This is the focus of the next section.

3.2 Modelling the data stream

The output data stream of a GW detector is assumed to be a superposition of noise $n(t)$ and a GW signal $h(t; \boldsymbol{\theta}_{\rm tr})$ with source parameters $\boldsymbol{\theta}_{\rm tr}$

$$d(t) = h(t; \boldsymbol{\theta}_{\rm tr}) + n(t)\,. \tag{3.7}$$

The data stream (3.7) contains two key quantities that determine successful extraction and parameter estimation of sources in GW astronomy. The first is a deterministic GW signal, for which *accurate* and *efficient* model templates are used to cross-correlate with the data $d(t)$, in order to pick up observational features of the true signal. The second is probabilistic detector noise: a culmination of instrumental and environmental fluctuations that perturb the GW detector. We stress here that the model templates and properties of the noise are of *equal* importance for parameter estimation.

In chapter 2 we gave a brief discussion of how to build *model* EMRI templates to use when searching for the (hopefully present) GW signal in the data stream $d(t)$. In the following subsections, we instead focus on the statistical properties of the noise, $n(t)$, which determines the probabilistic models that are used in inference schemes. We usually make a simplifying assumption that the noise properties are (weakly) stationary and Gaussian with zero mean. As we will see, in the next section, this assumption greatly reduces the complexity of parameter estimation.

3.2.1 The power spectral density

We call a time series $n(t)$ a stochastic process if all realisations $n(t_1), \ldots, n(t_N)$ belong to a family of probability distributions. One can further assume that the stochastic process is *weakly* stationary provided $n(t)$ has finite mean and variance that do *not* depend on time. We define the auto-correlation function $C_n(t, t')$ of the random process at two time points t and t' by

$$C_n(t, t') = \mathbb{E}[n(t)n^\star(t')] - \mathbb{E}[n(t)]\mathbb{E}[n^\star(t')]\,. \tag{3.8}$$

Here the expectation $\mathbb{E}$ is taken over the data generating process, i.e., the process that determines the statistical features of the noise, and the $n^\star(t)$ is the complex conjugate of the process $n(t)$. The assumption $n(t)$ is stationary implies that the auto-correlation function C_n only depends on the lag $\tau = t - t'$. For $n(t)$ with zero mean we have

$$C_n(t, t') = C_n(t - t', 0) := C(\tau)\,. \tag{3.9}$$

We are interested in the mean power of the noise $n(t)$ over a time interval $[-T/2, T/2]$, defined by

$$P_n = \lim_{T\to\infty} \frac{1}{T} \int_{-T/2}^{T/2} |n(t)|^2 \mathrm{d}t\,. \tag{3.10}$$

To simplify calculations, we can work in the Fourier domain. Consider $n_T(t) = n(t)\mathcal{I}[|t| < T/2]$ for $\mathcal{I}$ the indicator function — equal to one within the range considered and zero otherwise. Using Parseval's theorem it is possible to show

$$\begin{aligned} P_n = \lim_{T\to\infty} \frac{1}{T} \int_{-T/2}^{T/2} |n(t)|^2 \mathrm{d}t = \lim_{T\to\infty} \frac{1}{T} \int_{-\infty}^{\infty} |\hat{n}_T(f)|^2 \mathrm{d}f &= \int_{-\infty}^{\infty} \lim_{T\to\infty} \frac{1}{T} |\hat{n}_T(f)|^2 \mathrm{d}f \\ &= \int_{-\infty}^{\infty} S_n^{(2)}(f) \mathrm{d}f\,. \end{aligned}$$

For $S_n^{(2)}(f)$ the two-sided *power spectral density* (PSD), valid over *both* positive and negative frequencies

$$S_n^{(2)}(f) = \lim_{T\to\infty} \frac{1}{T} |\hat{n}_T(f)|^2, \quad f \in (-\infty, \infty)\,. \tag{3.11}$$

The PSD represents the power of the noise across the frequency spectrum. For circumstances involving real signals $n(t)$, we have the symmetry $\hat{n}(-f) = \hat{n}^\star(f)$. In this situation, it is more

sensible to define the *one-sided* PSD for $f \in [0, \infty)$

$$S_n^{(1)}(f) = \lim_{T\to\infty} \frac{2}{T}|\hat{n}_T(f)|^2\,, \tag{3.12}$$

where $S^{(2)}(f) = \frac{1}{2}S^{(1)}(f)$. For a real process $n(t)$ the PSD is an even function of frequency $S_n(-f) = S_n(f)$ and is non-negative. The two-sided PSD should be used when describing the power of a *complex* stochastic process over the entire frequency spectrum.

We will now show that the Fourier transform of the auto-correlation function $C_n(\tau)$ is given by the noise PSD. The auto-correlation function is defined by

$$C_n(\tau) = \lim_{T\to\infty} \frac{1}{T}\int_{-T/2}^{T/2} n(t)n^\star(t+\tau)\mathrm{d}t\,. \tag{3.13}$$

We can write (3.13) in a more convenient form using the IFT (3.3)

$$\lim_{T\to\infty} \frac{1}{T}\int_{-T/2}^{T/2} n(t)n^\star(t+\tau)\mathrm{d}t = \lim_{T\to\infty} \frac{1}{T}\int_{-T/2}^{T/2} |n(f)|^2 e^{-2\pi i f\tau}\mathrm{d}f\,, \tag{3.14}$$

where we used the integral representation of the Dirac delta function to simplify the above expression

$$\delta(f-f') = \int_{-\infty}^{\infty} e^{2\pi i t(f-f')}\mathrm{d}t\,. \tag{3.15}$$

Taking Fourier transforms of either side of (3.13) gives the following result

$$\begin{aligned}
\mathcal{F}[C_n(\tau)](f) &= \int_{-\infty}^{\infty}\left[\lim_{T\to\infty}\frac{1}{T}\int_{-T/2}^{T/2} n(t)n^\star(t+\tau)\mathrm{d}t.\right] e^{2\pi i f\tau}\mathrm{d}\tau \\
&= \lim_{T\to\infty}\frac{1}{T}\int_{-\infty}^{\infty}\int_{-\infty}^{\infty} |n_T(f')|^2 e^{2\pi i\tau(f-f')}\mathrm{d}\tau\mathrm{d}f' \\
&= \lim_{T\to\infty}\frac{1}{T}|\hat{n}_T(f)|^2\,.
\end{aligned}$$

From (3.11), the Fourier transform of the auto-correlation function is given by [221, 222]

$$S_n^{(2)}(f) = \int_{-\infty}^{\infty} C_n(\tau)e^{-2\pi i f\tau}\mathrm{d}\tau = \hat{C}_n(f)\,. \tag{3.16}$$

In GW astronomy, the noise in the time domain is *never* complex, so we will only consider the one-sided PSD defined by

$$\int_{-\infty}^{\infty} C_n(\tau)e^{-2\pi i f\tau}\mathrm{d}\tau = \hat{C}_n(f) = \frac{1}{2}S_n(f)\,. \tag{3.17}$$

where we now drop the (1) subscript from $S_n^{(1)}(f)$ and only consider the one-sided PSD of the

noise, unless specified otherwise.

3.2.2 The Whittle-likelihood

To perform inference on data we require a likelihood with covariance matrix that is consistent with the data generating process. A time domain likelihood is far less convenient than a frequency domain likelihood because the noise-covariance matrix in the time domain is dense, due to correlations between noise components across the observation time. In the Fourier domain, the complex normal distribution describing realisations of $\hat{n}(f)$ is [223]

$$p(n) = \frac{1}{\pi^n \sqrt{\det(\Sigma)\det(P)}} \exp\left\{ -\frac{1}{2} \begin{pmatrix} \hat{n}^\star(f) & \hat{n}(f) \end{pmatrix}^T \begin{pmatrix} \Sigma & R \\ R^\star & \Sigma^\star \end{pmatrix}^{-1} \begin{pmatrix} \hat{n}(f) \\ \hat{n}^\star(f) \end{pmatrix} \right\}, \tag{3.18}$$

with covariance $\Sigma = \langle \hat{n}(f)\hat{n}^\star(f')\rangle$, relation matrix $R = \langle \hat{n}(f)\hat{n}(f')\rangle$ and $P = \Sigma^\star - R^\dagger \Sigma^{-1} R$. Here $R^\dagger$ is the Hermitian transpose and $\Sigma^\star$ is the complex conjugate of the matrix. In the details following, we derive expressions for Σ and R.

For real *ergodic* stationary processes, the averaging over time in (3.13) is equivalent to an ensemble average [224]

$$C_n(\tau) = \langle n(t)n(t+\tau)\rangle \,. \tag{3.19}$$

Ergodicity in the context of time-series states that the statistical properties of the process can be deduced from a single, but long duration realisation. Using equations (3.17) and (3.2), the ensemble average between the noise at two different frequencies f and f' is related to the one-sided PSD through

$$\begin{aligned} \langle \hat{n}(f)\hat{n}^\star(f')\rangle &= \int_{-\infty}^{\infty}\int_{-\infty}^{\infty} e^{2\pi i(ft - f't')} \langle n(t)n(t')\rangle \mathrm{d}t\mathrm{d}t' \\ &= \int_{-\infty}^{\infty} e^{2\pi i t'(f-f')}\mathrm{d}t' \int_{-\infty}^{\infty} C(\tau) e^{-2\pi i f'\tau}\mathrm{d}\tau \\ &= \frac{1}{2}\delta(f-f')S_n(f')\,, \end{aligned} \tag{3.20}$$

From this expression, we deduce that for all $f \in (0, \infty)$

$$\langle \hat{n}(f)\hat{n}^\star(f')\rangle = \frac{1}{2}\delta(f-f')S_n(f') \tag{3.21}$$

$$\langle \hat{n}(f)\hat{n}(f')\rangle = 0\,. \tag{3.22}$$

Notice that (3.21) implies that frequency components among stationary noise are uncorrelated.

Both equations (3.21) and (3.22) determine the form of the distribution (3.18). As our calculations are numerical, we must discretise both (3.21) and (3.22) to determine the discrete analogue of (3.18).

We begin by writing $\delta(f - f')$

$$\begin{aligned}\delta(f - f') = \delta(f_k - f_p) &= \lim_{T\to\infty} \int_{-T}^{T} e^{2\pi i(f_k - f_p)t} \mathrm{d}t \\ &\approx \Delta t \sum_{m=-M}^{M-1} e^{2\pi i(f_k - f_p)t_m} \,.\end{aligned}$$

For M large, $f_i = i/N\Delta t$ and $t_m = m\Delta t$ for $m \in [-M, \ldots, 0, \ldots M-1]$ with $N = 2M$ time bins. Substituting in the above, we can evaluate the geometric series

$$\begin{aligned}\delta(f_k - f_p) &= \Delta t \sum_{m=-M}^{M-1} \left[e^{2\pi i\left(\frac{k-p}{M}\right)}\right]^m \\ &\approx \Delta t \frac{e^{-2\pi i(k-p)} - e^{2\pi i(k-p)}}{1 - e^{2\pi i\left(\frac{k-p}{M}\right)}}. \\ &= 2M\Delta t \delta_{kp} \,.\end{aligned}$$

The third equality is obtained using l'Hôspital's rule in the limit $(k - p) \to 0$. Given there are $N = 2M$ discrete time bins, we reach the desired conclusion

$$\delta(f_i - f_j) \approx N\Delta t \delta_{ij}, \quad t_{\text{obs}} \to \infty \,. \tag{3.23}$$

Using equation (3.23), we can compute the *discrete* covariance and relation matrix of the complex noise process $\tilde{n}(f)$ is,

$$\Sigma_{ij} = \langle \tilde{n}(f_i)\tilde{n}^\star(f_j)\rangle = \delta_{ij}\frac{NS_n(f_i)}{2\Delta t} \,, \tag{3.24}$$

$$R_{ij} = 0 \,. \tag{3.25}$$

Over the positive frequencies, we can write $\hat{n}(f)$ as a complex frequency series $\hat{n}(f) \approx \{\hat{\boldsymbol{n}}(f_i)\}_{i=0}^{\lfloor N/2+1\rfloor}$, then, from equation (3.18), we deduce that

$$p(n) = \frac{1}{\pi^n \det\Sigma} \exp\left[-\tilde{\boldsymbol{n}}^\dagger \Sigma^{-1} \tilde{\boldsymbol{n}}\right] \,. \tag{3.26}$$

Given that $n(t) = d(t) - h(t;\boldsymbol{\theta})$, we can now write down the Whittle-likelihood for a known

form of the PSD[1] [225]

$$p(d|\boldsymbol{\theta}) \propto \exp\left[-2\Delta t \sum_{i=0}^{\lfloor N/2+1 \rfloor} \frac{|\tilde{d}(f_i) - \tilde{h}(f_i;\boldsymbol{\theta})|^2}{N S_n(f_i)}\right] . \tag{3.27}$$

We can write (3.27) in a more compact form. We first define the usual noise-weighted inner product used throughout GW astronomy

$$(h|g) = \int_{-\infty}^{\infty} \frac{\hat{h}(f)\hat{g}^\star(f) + \hat{h}^\star(f)\hat{g}(f)}{S_n(f)} \mathrm{d}f \tag{3.28}$$

$$= 2\int_{0}^{\infty} \frac{\hat{h}(f)\hat{g}^\star(f) + \hat{h}^\star(f)\hat{g}(f)}{S_n(f)} \mathrm{d}f \,, \tag{3.29}$$

where, in the second equality, we have used the fact that $h(t)$ and $g(t)$ are both real signals and $S_n(-f) = S_n(f)$. Decomposing h and g into real and imaginary parts, equation (3.29) can be written as

$$(h|g) = 4\mathrm{Re}\int_0^\infty \frac{\hat{h}(f)\hat{g}^\star(f)}{S_n(f)}\mathrm{d}f \approx 4\Delta t \ \mathrm{Re} \sum_{i=0}^{\lfloor N/2+1 \rfloor} \frac{h(f_i)g^\star(f_i)}{S_n(f_i)} \,. \tag{3.30}$$

Finally, we can compare (3.30) with the likelihood (3.27) to obtain

$$\log p(d|\boldsymbol{\theta}) \propto -\frac{1}{2}(d-h|d-h) \,, \tag{3.31}$$

the usual log-likelihood seen throughout the GW literature

Simulating stationary frequency domain noise realisations using (3.21) and (3.22) is straightforward by making the split $\hat{n}(f) = \hat{n}_1(f) + i\hat{n}_2(f)$ to obtain

$$\langle \hat{n}_1(f)\hat{n}_1(f')\rangle = \langle \hat{n}_2(f))\hat{n}_2(f')\rangle = \frac{1}{4}\delta(f-f')S_n(f) \tag{3.32}$$

$$\langle \hat{n}_1(f')\hat{n}_2(f)\rangle = \langle \hat{n}_1(f)\hat{n}_2(f')\rangle = 0. \tag{3.33}$$

Equation (3.32) shows that the size of fluctuations in the real and imaginary components of the noise are the same. From (3.23), the expressions above can be discretised

$$\mathrm{Var}(\tilde{n}_1(f_i)) = \mathrm{Var}(\tilde{n}_2(f_i)) = \frac{N S_n(f_i)}{4\Delta t} \tag{3.34}$$

$$\mathrm{Cov}(\tilde{n}_1(f_i), \tilde{n}_2(f_j)) = 0 \,. \tag{3.35}$$

Hence for a known PSD, the real and imaginary parts of the (discrete and dimensionless) noise

[1] If the form of the PSD was unknown, then one would have to take into account the extra piece from the denominator $\log\det\Sigma \propto \sum_i \log S_n(f_i)$. This is the standard procedure if the stationary noise is unknown and the PSD has to be estimated. In this work, the form of the PSD is always known so will be treated as a constant and ignored in (3.27).

$\tilde{n}(f)$ can be separately drawn from a zero-mean normal distribution and then combined to form $\tilde{n}(f)$.

In this thesis, we will make use of the analytical approximation to the LISA sensitivity curve [226]

$$S_n(f) = \frac{10}{3L^2}\left(P_{\rm OMS}(f) + \frac{4P_{\rm acc}}{(2\pi f)^4}\right)\left(1 + \frac{6}{10}\left(\frac{f}{f_\star}\right)^2\right) + S_{\rm c}(f)\,. \tag{3.36}$$

Here $P_{\rm OMS}$ is the PSD of the single-link OMS describing the power of the combined noise in the craft's interferometer. The quantity $P_{\rm acc}$ is the PSD of the test mass acceleration noise, a combination of noise sources contributing the spurious accelerations of the test-masses. These were discussed earlier in section 1.3.1. Finally, L is the LISA arm lengths and $f_\star \approx 19.09$mHz. Analytical approximations to $P_{\rm OMS}$ and $P_{\rm acc}$ are given by

$$P_{\rm OMS} = (1.5\cdot 10^{-11}{\rm m})^2\left(1 + \left(\frac{2{\rm mHz}}{f}\right)^4\right){\rm Hz}^{-1} \tag{3.37}$$

$$P_{\rm acc} = (3\cdot 10^{-15}{\rm ms}^{-2})^2\left(1 + \left(\frac{0.4{\rm mHz}}{f}\right)^2\right)\left(1 + \left(\frac{f}{8{\rm mHz}}\right)^4\right){\rm Hz}^{-1}\,. \tag{3.38}$$

The last piece to equation (3.36) is $S_c(f)$, the power of the *unresolved* sources at individual frequencies. A fit to the confusion source $S_c(f)$ is given in [226]

$$S_c(f) = Af^{-7/3}e^{-f^\alpha + \beta f\sin(\kappa f)}[1+\tanh(\gamma(f_k - f))]\,{\rm Hz}^{-1}\,, \tag{3.39}$$

with parameters $(A, \alpha, \beta, \kappa, \gamma, f_k)$ that depend on mission life-time given in table 1 of [87]. In our analysis, unless stated otherwise, we will assume a single year observation of our sources with PSD parameters $(\alpha, \beta, \kappa, \gamma, f_k) = (0.133, 243, 482, 917, 0.00258\,{\rm Hz})$ and take the length of the arms to be $L = 2.5\times 10^9\,{\rm m}$. We will use the PSD above in the research chapters 5, 6, 7 and 8. We will also discuss the reasoning behind including $S_c(f)$ in equation (3.36) in appendix C.

The LISA sensitivity curve (3.36) is plotted in figure 3.3 for different choices of $S_c(f)$ conditional on the maturity of the mission. As the lifetime of the mission increases, the magnitude of $S_c(f)$ reduces as we can resolve a larger number of galactic binaries and subtract them from the data stream. As $S_c(f)$ reduces in magnitude, we have greater sensitivity to sources over the frequency band, implying tighter constraints on parameters and giving a better chance of identifying weaker GW signals in the data stream. The sensitivity of the instrument is characterised by the PSD, with optimal sensitivity given by a small neighbourhood around $f \approx 3$mHz.

3.2.3 Matched-filtering

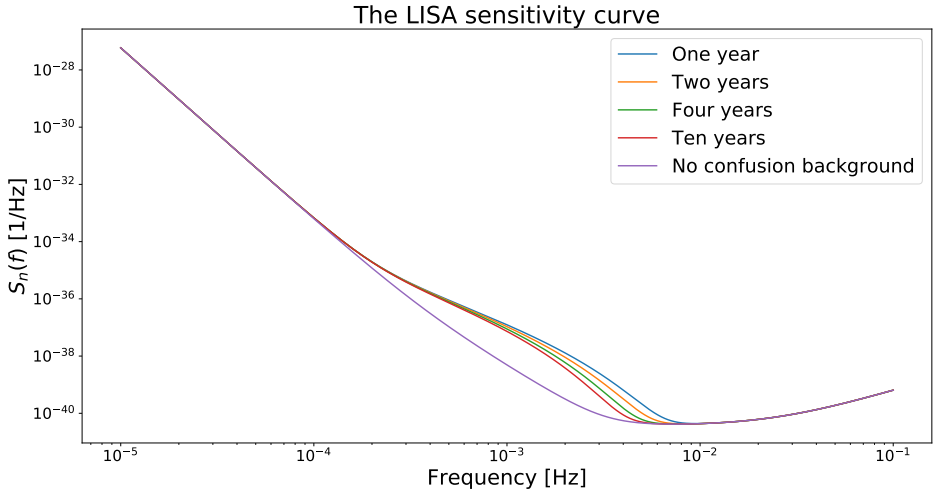

Figure 3.3: A plot of the sensitivity curve (3.36), as a function of frequency with different confusion noise backgrounds given by $S_c(f)$ in equation (3.39). The magenta curve is equation (3.36) with $S_c(f) = 0$, i.e., there is no background confusion noise.

3.2.3.1 Signal Detection

Matched-filtering is a technique where known templates are correlated against the data stream in attempt to detect the presence of the template in the data [227, 228]. When matched-filter searches are performed, the data stream is usually *whitened* when searching for potential GW signals. The act of whitening can be thought of as a linear transformation, which takes random variables with known covariance matrix to new random variables with covariance matrix equal to the identity matrix. For example, consider noise realisations $\hat{n}(f)$ that have an associated noise covariance matrix given by equation (3.24). By making the transformation $\hat{n}_{\rm w}(f) = (N\Delta t S_n(f)/4)^{-1/2}\hat{n}(f)$ it's easy to show that the whitened noise covariance matrix is equal to twice the identity matrix $\langle \hat{n}_{\rm w}(f_i), \hat{n}_{\rm w}(f_j)^\star \rangle = 2\delta_{ij}$. Since $\langle \hat{n}(f) \rangle = 0$, the real and imaginary parts of the whitened frequency domain noise $\hat{n}_{\rm w}(f)$ follow a standard normal distribution. The power of the real and imaginary components of the whitened noise over the sampled frequencies is normalised, allowing for any excess power at individual frequencies to be more obvious (an example would be a noise transient caused by a glitch in the detector). Similarly, if the full data stream was whitened, then excess power (caused by present GW signals) at individual frequencies would be more obvious. From a detection perspective, this technique can be successful when dealing with loud GW events, an example being GW150914 where the signal could be spotted by eye in the whitened data stream. Analogously, the act of whitening would be useful for signal detection of MBHBs for LISA, but, for quiet signals such as EMRIs, there is no such silver bullet.

The successful detection of EMRIs within the LISA data stream is an exceptionally difficult and arguably unsolved problem. In the author's opinion, performing a fully optimal matched-filtering search over the full data stream of LISA will be near impossible. For a year-long signal emitting frequencies close to 3 mHz, the number of cycles observed are $\sim$ 1 year $\times$ 3 mHz $\sim 10^5$ cycles. For a D dimensional parameter space, this would mean we would require $\sim 10^{5D}$ templates to perform such a search. Assuming that one has marginalised over the extrinsic parameters, generic orbits in the Kerr spacetime can have as many as $D = 9$ intrinsic parameters[2]. Hence, for such an orbit, we would require roughly $\sim 10^{45}$ templates to perform a fully optimal matched filter search for the EMRI throughout a year long stretch of data. It is clear that performing a fully optimal matched-filtering search for EMRI signals is computationally infeasible [120], and more sophisticated techniques are required for signal detection of EMRI signals. Techniques, such as time-frequency methods [229, 230] or human-intensive Monte-Carlo searches [231], have proven successful when detecting *isolated* EMRI signals buried in stationary Gaussian noise. However, there has been no attempt to generalise these methods when multiple overlapping EMRI signals are present in the data stream.

In light of the above, *none* of the work present in this thesis concerns signal detection from a LISA point of view. Since we do not focus on signal detection, we do not whiten data streams under investigation simply because there is little point whitening when performing inference on parameters. We will usually inject a *known* waveform model with *known* parameters into stationary Gaussian noise (with chapter 8 the exception) and then investigate parameter estimation/precision having assumed the detection phase has been successful using a fully optimal matched-filtering search. In the next section we discuss the notion of the Signal-to-Noise Ratio (SNR), a quantity arising from matched-filter statistics we will use throughout the research based chapters.

3.2.3.2 Signal-to-noise ratio

The SNR characterises the brightness of a signal in comparison to the background noise. The optimal filter is the matched filter that maximises the SNR in the presence of noise from a stochastic process. In the following discussion, we will derive the *Wiener optimal filter* that achieves the maximal SNR for a fully optimal matched-filtering search of the data stream.

For continuous functions $a(t)$ and $b(t)$, we define their cross correlation as

$$(a * b)(t) = \int_{-\infty}^{\infty} a^{\star}(t+\tau) b(\tau) \mathrm{d}\tau \,, \tag{3.40}$$

[2]Such as the primary mass; secondary mass; spin parameters of both primary and secondary; initial eccentricity; initial radius and the three orbital phases specifying the smaller COs initial position on the orbit

with t the lag. The ratio between the cross correlation of some filter function $K(t)$ and the signal strength $h(t)$ with the filtered RMS amplitude of the correlated noise

$$\text{SNR} = \left(\frac{S}{N}\right)(t) = \frac{\left|\int_{-\infty}^{\infty} K^\star(t+t')h(t')\mathrm{d}t'\right|}{\sqrt{\left\langle\left|\int_{-\infty}^{\infty} K^\star(t+t')n(t')\mathrm{d}t'\right|^2\right\rangle}}\,. \tag{3.41}$$

The goal here is to identify the function K that maximises the SNR (3.41) at a particular lag-time t.

The problem can be simplified by working in the frequency domain. Using the IFT (3.3), it can be shown that

$$\begin{aligned}\int_{-\infty}^{\infty} K^\star(t+t')h(t')\mathrm{d}t' &= \int_{-\infty}^{\infty}\int_{-\infty}^{\infty}\int_{-\infty}^{\infty} \hat{K}^\star(f)\hat{h}(f')e^{2\pi i t'(f'-f)}e^{-2\pi i f t}\mathrm{d}f\mathrm{d}f'\mathrm{d}t' \\ &= \int_{-\infty}^{\infty} \hat{K}^\star(f)\hat{h}(f)e^{-2\pi i f t}\mathrm{d}f\,,\end{aligned} \tag{3.42}$$

where we used (3.15) and the resulting delta function to evaluate the second integral. Similarly, one can show that the denominator (3.41) can be simplified

$$\begin{aligned}\left\langle\left|\int_{-\infty}^{\infty} K(t+t')n(t')\mathrm{d}t'\right|^2\right\rangle &= \int_{-\infty}^{\infty}\int_{-\infty}^{\infty} \hat{K}^\star(f)\hat{K}(f')\langle\hat{n}(f)\hat{n}^\star(f')\rangle e^{2\pi i t(f-f')}\mathrm{d}f\mathrm{d}f' \\ &= \frac{1}{2}\int_{-\infty}^{\infty} |\hat{K}(f)|^2 S_n(f)\mathrm{d}f\,,\end{aligned} \tag{3.43}$$

where we have used the condition (3.20) in the second equality. At zero lag, the SNR is thus given by

$$\left(\frac{S}{N}\right)(0) = \sqrt{2}\frac{\left|\int_{-\infty}^{\infty} \hat{K}^\star(f)\hat{h}(f)\mathrm{d}f\right|}{\sqrt{\int_{-\infty}^{\infty} |\hat{K}(f)|^2 S_n(f)\mathrm{d}f}}\,. \tag{3.44}$$

We now seek to find the filter $\hat{K}(f)$ that maximises the above expression. One can rewrite the numerator using the Cauchy-Schwarz inequality

$$\begin{aligned}\left|\int_{-\infty}^{\infty} \hat{K}(f)\hat{h}(f)\mathrm{d}f\right| &= \left|\int_{-\infty}^{\infty} (\hat{K}^\star(f)\sqrt{S_n(f)})\left(\frac{\hat{h}(f)}{\sqrt{S_n(f)}}\right)\mathrm{d}f\right| \\ &\leq \sqrt{\int_{-\infty}^{\infty} |\hat{K}(f)|^2 S_n(f)\mathrm{d}f \int_{-\infty}^{\infty} \frac{|\hat{h}(f')|^2}{S_n(f')}\mathrm{d}f'}\,,\end{aligned}$$

giving a bound to equation (3.44)

$$\left(\frac{S}{N}\right)(0) = \sqrt{2}\frac{\left|\int_{-\infty}^{\infty} \hat{K}^\star(f)\hat{h}(f)\mathrm{d}f\right|}{\sqrt{\int_{-\infty}^{\infty} |\hat{K}(f)|^2 S_n(f)\mathrm{d}f}} \leq \sqrt{2\int_{-\infty}^{\infty} \frac{|\hat{h}(f)|^2}{S_n(f)}\mathrm{d}f}\,. \tag{3.45}$$

For the choice of Kernel $\hat{K}(f) \propto \hat{h}(f)/S_n(f)$ we see that the above bound is saturated. With

the optimal filter $\hat{K}(f) \propto \hat{h}(f)/S_n(f)$, the optimal matched-filtering SNR is given by

$$\left(\frac{S}{N}\right)(0) = \sqrt{2\int_{-\infty}^{\infty} \frac{|\hat{h}(f)|^2}{S_n(f)} \mathrm{d}f}\,. \tag{3.46}$$

In the notation of (3.29), the SNR takes the form

$$\left(\frac{S}{N}\right)^2 = \rho^2 = (h|h) = 4\int_0^{\infty} \frac{|\hat{h}(f)|^2}{S_n(f)} \mathrm{d}f \tag{3.47}$$

$$\approx 4\Delta t \sum_{i=0}^{\lfloor N/2+1 \rfloor} \frac{|\tilde{h}(f_i)|^2}{N S_n(f_i)}\,, \tag{3.48}$$

where equation (3.48) will be used to calculate SNRs throughout this thesis.

With the likelihood (3.31) and optimal matched-filtering SNR (3.47) in hand, we are now in the position to discuss inference on parameters of sources of interest. In the next subsection, we discuss the tools we will use for parameter precision studies in this thesis.

3.3 Parameter precision

3.3.1 The Fisher matrix

A local approximation to the log-likelihood at the parameter value that maximises the likelihood, formally the best fit parameters $\boldsymbol{\theta}_{\rm bf}$, is given by

$$\log p(d|\boldsymbol{\theta}) \propto -\frac{1}{2}\boldsymbol{\Theta}^T[-\nabla\nabla^T \log p(d|\boldsymbol{\theta})]_{\boldsymbol{\theta}=\boldsymbol{\theta}_{\rm bf}}\boldsymbol{\Theta}\,, \quad \text{(matrix form)} \tag{3.49}$$

$$= -\frac{1}{2}(\theta^i - \theta^i_{\rm bf})\left[-\frac{\partial^2 \log p(d|\boldsymbol{\theta})}{\partial\theta^i \partial\theta^j}\right]_{\boldsymbol{\theta}=\boldsymbol{\theta}_{\rm bf}} (\theta^j - \theta^j_{\rm bf})\,, \quad \text{(component form)}. \tag{3.50}$$

In the above equation, $\nabla = [\partial/\partial\theta^1, \ldots, \partial/\partial\theta^D]^T \in \mathbb{R}^{D\times 1}$ is a D dimensional vector of partial derivatives with respect to parameters and $\boldsymbol{\Theta}^i = (\theta^i - \theta^i_{\rm bf})$ represent (small) deviations from the best fit parameters. Let $H_{ij} = -\partial_i\partial_j \log p(d|\boldsymbol{\theta})$ denote the components of the *Hessian matrix* of the log-likelihood function. Formally, the Hessian matrix H in this context is also called the *observed information matrix* [232]. Notice that the form of (3.49) is similar to a multivariate Gaussian distribution with parameter covariance matrix, C, given by the inverse of the Hessian matrix

$$C = H^{-1} = [-\nabla\nabla^T \log p(d|\boldsymbol{\theta})]^{-1}_{\boldsymbol{\theta}=\boldsymbol{\theta}_{\rm bf}}\,. \tag{3.51}$$

By computing the expectation of the Hessian of the log-likelihood and finding the inverse, we can calculate an estimate of the parameter covariance matrix. We make this more concrete

below.

The expectation of the observed information matrix is given by

$$\mathbb{E}\left[-\frac{\partial^2 \log p(d|\boldsymbol{\theta})}{\partial\theta^i\partial\theta^j}\right] = \mathbb{E}\left[\frac{\partial \log p(d|\boldsymbol{\theta})}{\partial\theta^i}\frac{\partial \log p(d|\boldsymbol{\theta})}{\partial\theta^j}\right] - \mathbb{E}\left[\frac{1}{p(d|\boldsymbol{\theta})}\frac{\partial^2 p(d|\boldsymbol{\theta})}{\partial\theta^i\partial\theta^j}\right] \tag{3.52}$$

$$= \mathbb{E}\left[\frac{\partial \log p(d|\boldsymbol{\theta})}{\partial\theta^i}\frac{\partial \log p(d|\boldsymbol{\theta})}{\partial\theta^j}\right] - \frac{\partial^2}{\partial\theta^i\partial\theta^j}\int p(D|\boldsymbol{\theta})\mathrm{d}D \tag{3.53}$$

$$= \mathbb{E}\left[\frac{\partial \log p(d|\boldsymbol{\theta})}{\partial\theta^i}\frac{\partial \log p(d|\boldsymbol{\theta})}{\partial\theta^j}\right] . \tag{3.54}$$

Where we have assumed regularity conditions[3] in order to reach equation (3.53) and the fact that $\int p(D|\boldsymbol{\theta})\mathrm{d}D = 1$ to reach equation (3.54). Notice that equation (3.54) is the definition of the *Fisher matrix* (FM)

$$\Gamma_{ij} = \mathbb{E}\left[\frac{\partial \log p(d|\boldsymbol{\theta})}{\partial\theta^i}\frac{\partial \log p(d|\boldsymbol{\theta})}{\partial\theta^j}\right] , \tag{3.55}$$

a statistical quantity that represents the amount of information the data stream (formally a random variable), d, carries about an unknown parameter, θ^i, from an underlying distribution that models the data stream. Directly comparing equations (3.50) and (3.54) we see that the FM can be interpreted as the curvature of the log-likelihood near the best fit parameters. Making reference to equation (3.50), a high Fisher information indicates that the maximum is "sharp" with nearby parameter values yielding significantly different values of log-likelihood. Conversely, a low Fisher information suggests that the log-likelihood is "blunt" with nearby parameter values having similar log-likelihood. The FM is thus intimately related to *measurement precision* on sought parameters. Assuming that $\boldsymbol{\theta}_{\rm bf}$ are unbiased estimators of the true parameters $\boldsymbol{\theta}_{\rm tr}$ such that $\mathbb{E}[\theta^i_{\rm bf}] = \theta^i_{\rm tr}$, then it can be shown that the covariance on these estimators obey the Cramér-Rao bound [233, 234]

$$\mathrm{Cov}(\theta^i_{\rm bf}, \theta^j_{\rm bf}) \geq (\Gamma^{-1})^{ij} . \tag{3.56}$$

In section 3.3.2, we will discuss how we use the Cramér-Rao bound throughout this thesis. In particular, we will derive a convenient expression for the FM in terms of inner products of waveform derivatives.

3.3.2 Quantifying precision

Precision measurements on parameters can be obtained by understanding the curvature of the log-likelihood (3.31) in the vicinity of the peak. In this section, we will derive the form of the Fisher matrix (3.55) that will be used throughout this thesis.

[3] Specifically, we require that: $\partial_i p(d|\boldsymbol{\theta})$ exists almost everywhere; we also must be able to interchange partial derivatives and integrals with respect to θ^i; and, finally that the support of $p(d|\boldsymbol{\theta})$ is independent of parameters $\boldsymbol{\theta}$.

Consider a small perturbation around the true parameters $\boldsymbol{\theta} = \boldsymbol{\theta}_{\rm tr} + \Delta\boldsymbol{\theta}$. In the details that follow, we will use the *linear signal approximation* (LSA)

$$h(t;\boldsymbol{\theta}) = h(t;\boldsymbol{\theta}_{\rm tr}) + \partial_i h(t;\boldsymbol{\theta}_{\rm tr})\Delta\theta^i + \mathcal{O}\left([\Delta\theta^i]^2\right) , \tag{3.57}$$

which is valid close to the true parameters $\Delta\theta^i \ll 1$ and $\partial^2_{ij}h(t;\boldsymbol{\theta}_{\rm tr})\Delta\theta^j \ll \partial_i h(t;\boldsymbol{\theta}_{\rm tr})$. Substituting (3.57) into the log-likelihood function (3.31) yields

$$\begin{aligned} l(d|\boldsymbol{\theta}) &\propto -\frac{1}{2}(n(t) - \partial_i h\Delta\theta^i | n(t) - \partial_i h\Delta\theta^i) \\ &= -\frac{1}{2}[(n|n) - 2(n|\partial_i h) - \Gamma_{ij}\Delta\theta^i\Delta\theta^j] \\ &= -\frac{1}{2}(\Delta\theta^i - (\Gamma^{-1})^{ik}(\partial_k h|n))\Gamma_{ij}(\Delta\theta^j - (\Gamma^{-1})^{jl}(\partial_l h|n)) \\ &\qquad - \frac{1}{2}(n|n) - (\partial_i h|n)(\Gamma^{-1})^{ij}(\partial_j h|n) \qquad (3.58a) \\ &\approx -\frac{1}{2}(\Delta\theta^i - (\Gamma^{-1})^{ik}(\partial_k h|n))\Gamma_{ij}(\Delta\theta^j - (\Gamma^{-1})^{jl}(\partial_l h|n)) , \qquad (3.58b) \end{aligned}$$

with

$$\Gamma_{ij} = \left(\frac{\partial h}{\partial\theta^i}\middle|\frac{\partial h}{\partial\theta^j}\right) . \tag{3.59}$$

Since the signal amplitude scales with the SNR, $h \sim \rho$, we have that $\Gamma \sim \rho^2$ implying that $\Gamma^{-1} \sim 1/\rho^2$. The latter term in (3.58a) is $\mathcal{O}(1)$ whereas the first term is $\mathcal{O}(\rho)$, so the last two terms can be neglected for high SNRs. We deduce that, in the limit of high SNR, the likelihood can be approximated by a Gaussian, centered at $\Delta\theta^i = (\Gamma^{-1})^{ij}(\partial_j h|n)$ with covariance matrix given by Γ^{-1}.

Using the form of the Whittle-likelihood (3.31), one can compute a closed form expression for the expectation of the observed information matrix in terms of waveform derivatives

$$\begin{aligned} \mathbb{E}\left[-\frac{\partial^2}{\partial\theta^i\partial\theta^j}\log p(d|\boldsymbol{\theta})\right] &= -\left\langle\left(\frac{\partial^2 h}{\partial\theta^i\partial\theta^j}\middle|n\right)\right\rangle + \left\langle\left(\frac{\partial h}{\partial\theta^i}\middle|\frac{\partial h}{\partial\theta^j}\right)\right\rangle \qquad (3.60) \\ &= \left(\frac{\partial h}{\partial\theta^i}\middle|\frac{\partial h}{\partial\theta^j}\right) = \Gamma_{ij}, \qquad (3.61) \end{aligned}$$

where we have used the fact that the noise is a mean zero random variable. Notice further that

$$\mathbb{E}\left[\frac{\partial\log p(d|\boldsymbol{\theta})}{\partial\theta^i}\frac{\partial\log p(d|\boldsymbol{\theta})}{\partial\theta^j}\right] = \left\langle\left(\frac{\partial h}{\partial\theta^i}\middle|n\right)\left(\frac{\partial h}{\partial\theta^j}\middle|n\right)\right\rangle = \left(\frac{\partial h}{\partial\theta^i}\middle|\frac{\partial h}{\partial\theta^j}\right) = \Gamma_{ij} , \tag{3.62}$$

where we have used the fact that $\langle(a|n)(b|n)\rangle = (a|b)$. Notice that equation (3.62) is the definition of the FM (see (3.55)), the inverse of which yields the *Cramér-Rao lower bound* on the variance of unbiased estimators of parameters as discussed following equation (3.56). By

computing the matrix Γ, one is then able to make statements on how sensitive the likelihood is to perturbations around the true parameters. The FM is commonly used throughout GW astronomy to give measure on the amount of information $h(t;\boldsymbol{\theta})$ contains about a parameter set $\theta^i \in \boldsymbol{\theta}$ and, for the remainder of this thesis, we will identify Γ_{ij} as the FM.

From equation (3.58b), calculating the inverse FM provides a guide on the width of the likelihood giving the best possible constraint on estimated parameters. We note also that the maximum likelihood estimator for the parameter deviations is $\widehat{\Delta\theta^i} = (\Gamma^{-1})^{ij}(\partial_j h|n)$. This is a zero mean random variable with covariance matrix

$$\begin{aligned}\mathrm{Cov}[\widehat{\Delta\theta^i}, \widehat{\Delta\theta^j}] &= \mathbb{E}\left[(\Gamma^{-1})^{ij}(\partial_j h|n)(\Gamma^{-1})^{jk}(\partial_k h|n)\right] \\ &= (\Gamma^{-1})^{ik}(\Gamma^{-1})^{jp}\langle(\partial_k h|n)(\partial_p h|n)\rangle \\ &= (\Gamma^{-1})^{ij}\,, \end{aligned} \tag{3.63}$$

where we have used the general result that $(\Gamma^{-1})^{ik}\Gamma_{kj} = \delta^i{}_j$. The quantity $\widehat{\Delta\theta^i}$ is the noise induced statistical fluctuation from the true parameters. Strictly speaking, it is *not* a source of potential bias in parameters as it is accounted for in the width of the peak of the likelihood. The single noise realisation *shifts* the likelihood from the true parameters $\boldsymbol{\theta}_{\rm tr}$ to the recovered parameters $\boldsymbol{\theta}_{\rm bf}$, recovered through parameter estimation schemes. In fact, the $i^{\rm th}$ recovered parameter $\theta^i_{\rm bf}$, shifted from the $i^{\rm th}$ true parameter, should be consistent with $\theta^i_{\rm bf} = \theta^i_{\rm tr} + (\Gamma^{-1})^{ij}(\partial_j h|n)$ for large SNR. What we learn here is that over many noise realisations, the averaged noise induced fluctuation from the peak is consistent with the width of the likelihood governed by the inverse of the FM in the limit of high SNR.

From (3.63), precision measurements on source parameters taking into account parameter correlations are given by the square root of the diagonal elements of the inverse FM

$$\Delta\theta^i = \sqrt{(\Gamma^{-1})^{ii}}\,, \quad \text{no sum over } i\,. \tag{3.64}$$

Equation (3.64) will be used to quantify precision measurements on parameters in chapters 5, 6, 7 and 8.

The gravitational waveforms used throughout this thesis do not have closed form expressions for their derivatives with respect to waveform parameters. In order to calculate (3.59), we numerically differentiate each waveform using a finite order difference methods. For the research contained in chapters 5, 6 and 7, we use a fifth order stencil method [235]

$$f'(x) \approx \frac{-f(x+2\delta x) + 8f(x+\delta x) - 8f(x-\delta x) + f(x-2\delta x)}{12\delta x}\,, \tag{3.65}$$

for $\delta x \ll 1$. A Taylor expansion shows that the error scales in proportion δx^4.

Choosing the correct δx is challenging. Too small a value of δx then the derivatives will be contaminated with rounding errors. Too large a value of δx, then more terms are required in the expansion of $f(x)$. For all derivatives computed in this work, we have meticulously checked *many* step sizes to ensure convergence to the true waveform derivative. We found the fifth order method (3.65) was the ideal balance between time-consuming waveform evaluations and being accurate enough to describe the numerical derivative. In the next subsection, we discuss potential pitfalls of the FM.

3.3.3 Instability of the Fisher matrix

It is well known [236, 237, 238, 229, 239, 240] that a FM analysis, when not handled carefully, can incorrectly estimate precision measurements, leading to false conclusions. One first has to be sure that the regime of SNR is high enough so that the LSA (3.57) applies when truncating the perturbed waveform at first order. Numerical derivatives using equation (3.65) also exhibit convergence problems and are very problematic if the waveforms are not smooth. Finally, one has to invert the FM and, if the FM is ill conditioned (as often the case for GW signals), it could lead to errors in the elements of Γ^{-1}. This has the potential to draw incorrect conclusions about the source being analysed.

In the case of EMRIs, the main source we will consider, the computation of the FM is affected by numerical instabilities. A small perturbation of the system's (intrinsic) parameters lead to a large overall change in the waves phase evolution. A result of this is that EMRI observations offer tight constraints on the astrophysical parameters. Since waveforms are sensitive to small perturbations of the source parameters, the numerical derivatives $\partial_{\boldsymbol{\theta}} h(t;\boldsymbol{\theta})$ are large and so the elements of the FM can be enormous. However, not all parameter derivatives are large. The differences between the size of the elements in the FM for different parameters leads to significantly varying eigenvalues that, in turn, define the condition number of the FM. The alarmingly high condition numbers of these FMs, defined by the ratio of the maximum and minimum eigenvalues, can be countered by employing arbitrary precision arithmetic to calculate the inverse [241]. If possible, analytical derivatives of the parameters should be calculated in order to reduce round-off errors when computing approximate numerical derivatives. If this cannot be done, one must carefully choose perturbing values in (3.65) to reduce the accumulation of numerical error that could lead to contaminated results in the matrix inversion. The gold standard technique to verify FMs is the use of general Bayesian techniques that will be discussed in 3.5. In all cases where a FM is computed in this work, the results are verified using Bayesian

methods.

3.4 Systematic errors

Waveform models are not perfect. It would be both naïve and simply wrong to assume that signals within our template banks could match the true signal within the data stream *perfectly*. Unless the two body problem in general relativity is solved exactly, there will always be an associated numerical error in our waveform models. There are two causes for concern when using inaccurate waveforms to extract signals from the data stream; failure to claim detection, and, biases in recovered parameters. The first is not too much of a concern since our waveform models should be accurate enough for detection in the next ~ 15 years. The latter is more of an issue, recovered parameters that are significantly biased can lead to false inference of the source under scrutiny. Section 3.4 outlines the algorithm we used to *predict* parameter biases when using inaccurate waveforms.

3.4.1 Lindblom criterion

Here we review a criterion that dictates whether two waveform models are *distinguishable*. Recall that the form of a typical data stream

$$d(t) = h_e(t; \boldsymbol{\theta}_{\rm tr}) + n(t)\,, \tag{3.66}$$

where $h_e(t; \boldsymbol{\theta}_{\rm tr})$ is the *true* (exact) signal emitted from the source. This true waveform has true parameters $\boldsymbol{\theta}_{\rm tr}$ that we wish to infer. However, in a realistic scenario, we do not have access to the true waveform model. We can only generate *approximate* (model) templates to h_e, which we denote $h_m(t; \boldsymbol{\theta})$ such that $|h_e(\boldsymbol{\theta}_{\rm tr}) - h_m(\boldsymbol{\theta}_{\rm tr})| \ll 1$.

A basic systematic study on families of waveform templates can be performed by calculating waveform overlaps/mismatches. The overlap and mismatch function measure the similarity of two template waveforms $h_1 := h(t; \boldsymbol{\theta}_1)$ and $h_2 := h(t; \boldsymbol{\theta}_2)$

$$\mathcal{O}(h_1, h_2) = \frac{(h_1|h_2)}{\sqrt{(h_1|h_1)(h_2|h_2)}}\,, \tag{3.67}$$

$$\mathcal{M}(h_1, h_2) = 1 - \mathcal{O}(h_1, h_2)\,. \tag{3.68}$$

If $\mathcal{O}(h_1, h_2) = 1$, then the shape of the two waveforms matches perfectly. Waveforms with $\mathcal{O}(h_1, h_2) = 0$ are orthogonal, being as much in phase as out of phase over the observation. The

overlap does not show how biased parameters would be if inaccurate waveforms were used in parameter estimation schemes. The *Lindblom Criterion* (LC) [242, 243, 244] offers a simple, yet conservative solution to this purpose.

Defining $\delta h = h_{\rm e} - h_{\rm m}$, we say two models $h_{\rm e}$ and $h_{\rm m}$ are indistinguishable if and only if

$$(\delta h|\delta h) < 1\,, \tag{3.69}$$

with noise-weighted inner product $(\cdot|\cdot)$ defined in equation (3.29). Equation (3.69) can be motivated as follows. Consider $h = h_{\rm m} + \lambda(h_{\rm e} - h_{\rm m})$ with $\lambda \in [0, 1]$. If the uncertainty $\Delta\lambda < 1$, then we can tell the difference between $h_{\rm e}$ and $h_{\rm m}$. We can estimate how well this quantity can be measured from the FM by $\Gamma_{\lambda\lambda} = (\partial_\lambda h|\partial_\lambda h) = (\delta h|\delta h)$. We deduce that we can put a constraint on λ at the level

$$\Delta\lambda^2 = (\Gamma^{-1})_{\lambda\lambda} = \frac{1}{(\delta h|\delta h)}\,. \tag{3.70}$$

So, if $(\delta h|\delta h) < 1$ then $\Delta\lambda^2 > 1$ and the models are *indistinguishable* since λ cannot be measured accurately — this is Lindblom's indistinguishability criterion.

The advantage of the LC is that the calculation of $(\delta h|\delta h)$ is straightforward. It is not subject to numerical errors from waveform derivatives or inverses of matrices and so on. As only a single inner product (3.29) has to be calculated, statements on model uncertainties can be made with little computational effort. A major disadvantage of the LC is that it is very conservative [245]. Inaccurate waveform models used for parameter estimation could recover parameters with negligible bias, but fail the LC with $(\delta h|\delta h) \gg 1$. We will show examples of this in chapter 6.

3.4.2 The Cutler-Vallisneri formalism

In 1997, Flanagan and Hughes [243] derived an expression that predicts biases on recovered parameters when unfaithful waveform models to the true signal are used for parameter estimation schemes. Such an expression was seen again in Miller (2006) [244] but then popularised in Cutler and Vallisneri's paper [246]. In chapter 6, we use this criterion to estimate how precisely the post-adiabatic components to the self force must be calculated in order not to bias our parameters. This is further explored in chapter 7 where we generalise Cutler and Vallisneri's work to predict biases on parameters arising from modelling errors when fitting for *multiple* sources in the data stream whilst in the presence of an astrophysical foreground. Now, we present the foundations of the Cutler-Valisnerri (CV) formalism.

The relevant log-likelihood when considering waveform modelling errors is

$$\log p(d|\boldsymbol{\theta}) = -\frac{1}{2}(d(t) - h_m(t;\boldsymbol{\theta})|d(t) - h_m(t;\boldsymbol{\theta}))\,, \tag{3.71}$$

with $d(t) = h_e(t;\boldsymbol{\theta}_{\rm tr}) + n(t)$. We will now investigate the repercussions of using inaccurate waveform models such that $h_e(t;\boldsymbol{\theta}_{\rm tr}) \neq h_m(t;\boldsymbol{\theta}_{\rm tr})$.

The best-fit parameters are found by maximising the log-likelihood (3.71), and this is achieved by solving

$$(\partial_i h_m(t;\boldsymbol{\theta})|d - h_m(t;\boldsymbol{\theta}))|_{\boldsymbol{\theta}=\boldsymbol{\theta}_{\rm bf}} = 0\,. \tag{3.72}$$

Consider a perturbation around the true parameters $\boldsymbol{\theta}_{\rm bf} = \Delta\boldsymbol{\theta} + \boldsymbol{\theta}_{\rm tr}$. Using the LSA (3.57), a first order expansion in $\Delta\theta^i$ gives $h_m(t;\boldsymbol{\theta}_{tr}) - h_m(t;\boldsymbol{\theta}_{\rm bf}) \approx -\partial_i h_m(t;\boldsymbol{\theta}_{\rm bf})\Delta\theta^i$. Dropping the t in the notation, we can write

$$\begin{aligned} d - h_m(\boldsymbol{\theta}_{\rm bf}) &= n(t) + h_e(\boldsymbol{\theta}_{\rm tr}) - h_m(\boldsymbol{\theta}_{\rm tr}) + h_m(\boldsymbol{\theta}_{\rm tr}) - h_m(\boldsymbol{\theta}_{\rm bf}) \\ &\approx n(t) + \delta h(\boldsymbol{\theta}_{\rm tr}) - \partial_i h_m(\boldsymbol{\theta}_{\rm bf})\Delta\theta^i\,, \end{aligned} \tag{3.73}$$

where we have defined *residuals* $\delta h(\boldsymbol{\theta}) = h_e(\boldsymbol{\theta}) - h_m(\boldsymbol{\theta})$. Substituting into (3.72), we obtain

$$\begin{aligned} (\partial_i h_m(\boldsymbol{\theta}_{\rm bf})|s - h_m(\boldsymbol{\theta}_{\rm bf})) \approx (\partial_i h_m(\boldsymbol{\theta}_{\rm bf})|n) + (\partial_i h_m(\boldsymbol{\theta}_{\rm bf})|\delta h(\boldsymbol{\theta}_{\rm tr})) - \Delta\theta^j \Gamma_{ij}(\boldsymbol{\theta}_{\rm bf}) = 0\,, \\ \iff \Delta\theta^i = (\Gamma^{-1})^{ij}(\boldsymbol{\theta}_{\rm bf})\left[(\partial_j h_m(\boldsymbol{\theta}_{\rm bf})|n) + (\partial_j h_m(\boldsymbol{\theta}_{\rm bf})|\delta h(\boldsymbol{\theta}_{\rm tr}))\right]\,, \end{aligned} \tag{3.74}$$

where $\Gamma_{ij}(\boldsymbol{\theta}_{\rm bf}) = (\partial_i h_m(\boldsymbol{\theta}_{\rm bf})|\partial_j h_m(\boldsymbol{\theta}_{\rm bf}))$. Equation (3.74) yields, to first order in $\Delta\theta^i$, the shift to the peak of the likelihood due to the noise realisation and waveform modelling errors, which are encoded through δh. We remark here that all quantities, aside from the residuals, are evaluated at the best-fit parameters $\boldsymbol{\theta}_{\rm bf}$. For exploratory systematic studies it makes more sense to compute (3.74) using the *true* source parameters without having to calculate $\boldsymbol{\theta}_{\rm bf}$ using parameter estimation schemes. Hence, unless stated otherwise, we will evaluate (3.74) at $\boldsymbol{\theta}_{\rm tr}$ rather than the best-fit parameters. This approximation is justified only if the true parameters are in the vicinity of the best-fit parameters i.e., for high SNR.

In the following, we denote

$$\Delta\theta^i_{\rm noise} := (\Gamma^{-1})^{ij}(\boldsymbol{\theta}_{\rm tr})(\partial_j h_m|n)|_{\boldsymbol{\theta}=\boldsymbol{\theta}_{\rm tr}}\,, \tag{3.75}$$

$$\Delta\theta^i_{\rm syst} := (\Gamma^{-1})^{ij}(\boldsymbol{\theta}_{\rm tr})(\partial_j h_m|\delta h)|_{\boldsymbol{\theta}=\boldsymbol{\theta}_{\rm tr}}\,, \tag{3.76}$$

as the two contributions sourcing the shift in the peak of the likelihood — the former due to noise realisations, the latter due to waveform modelling errors. We remark that the statistical error $\Delta\theta^i_{\rm stat} \sim \rho^{-1}$, whereas the systematic error $\Delta\boldsymbol{\theta}^i_{\rm syst} \sim \rho^0$, which implies that systematic biases become more prominent the brighter the signal is.

The expression (3.74) for systematic errors appeared first in [243], see their equation (6.11). One can use the systematic error to set a criterion that must be passed for a certain waveform model h_m to be suitable for parameter estimation. Noise induced statistical fluctuations cannot be controlled but are accounted for in the width of the likelihood. This was shown in equation (3.63). Biases arising from waveform modelling errors can in principle be avoided by improving our waveform models. An example being including the 1PA components of the GSF rather than using the adiabatic approximation. Systematic biases can be ignored when they are smaller than statistical errors, i.e. the width of the likelihood. We thus deem a waveform model suitable for parameter estimation provided

$$\mathcal{R}_{\theta^i} = \frac{\Delta\theta^i_{\rm sys}}{\Delta\theta^i_{\rm stat}} < 1\,, \tag{3.77}$$

where $\Delta\theta^i_{\rm stat} = \sqrt{(\Gamma^{-1})^{ii}}$ with no summation convention applied. Similarly, if $\mathcal{R}_{\theta^i} > 1$ we would argue that the waveform model is unsuitable for parameter estimation. These ideas will be explored in more depth in chapters 6 and 7.

The FM as a tool in GW astronomy is used frequently. However, due to considerations present in subsection 3.3.3, the FM can be problematic. As it is only an approximation to the width of the likelihood in the case of high SNR, more general methods are required to test the validity of the FM. In the next section, we discuss Bayesian statistics ending with an outline of our parameter estimation algorithms.

3.5 Parameter estimation

3.5.1 The Bayesian paradigm

The FM is a tool originally appearing in classical frequentist statistics that can be used to predict the performance of a Bayesian statistic. Under frequentist statistics, statements are based on hypothetical repetitions of an experiment. The FM is computed from an ensemble average over infinitely many realisations of the noise process (see (3.62)). In the Bayesian paradigm, by contrast, we attempt to draw the best conclusions from an observation of a *single* data stream. Given that GW observations are unrepeatable, Bayesian statistics are well suited

to GW astronomy.

In contrast to frequentist statistics, we no longer assume that the parameters have a fixed value but are random variables with an (unknown) underlying probability distribution. We denote this distribution $p(\boldsymbol{\theta}|d)$, our distributional beliefs on the parameters $\boldsymbol{\theta}$ given the observed data stream. One can argue that this may be a more natural way of performing inference than repeating an experiment multiple times. However, in order to do so, one must specify a prior distribution $p(\boldsymbol{\theta})$ that represents our initial beliefs about the distribution $\boldsymbol{\theta}$ prior to observing the data stream. The prior distribution is the controversial element behind Bayesian statistics[4]. Then, having observed a data stream using a likelihood function $p(d|\theta)$, the prior is *updated* to form the posterior distribution.

In the author's opinion, human beings are inherently Bayesian. Consider the following example: the author is sat in his flat and looks out his window and spots a shop selling kebabs. He then entertains the thought of leaving his flat and buying a kebab but is left with the conundrum: will the kebab be good, or dreadful. Based on *prior* experience in Edinburgh, having had ~ 70 kebabs of which ~ 10 were good over a seven-year experience, the kebab is likely to be diabolical, so the author will not leave his flat this time. In Edinburgh, his posterior is updated through every horrible kebab to influence his further decisions. However, now the author is in Germany, Berlin in particular, and has experienced ~ 68 kebabs of which ~ 62 were outstanding over the period of two years[5]. His prior beliefs reflect this additional information (his location), and thus he leaves his flat and gets his kebab. The kebab was excellent, and his posterior has been updated to take this into account.

The point we wish to drive home is that experiments are not and should not be abstract concepts. We will always have prior knowledge about the process being investigated before obtaining any data. Take, for example, inference on the spin parameter of a central BH from an EMRI observation: we enforce the physical constraint of $a \in [0, 1]$ since we do not expect to observe naked singularities as this is a violation of the cosmic censorship conjecture. In such a scenario, we would specify a prior distribution on the spin parameter with zero support for $a \notin [0, 1]$. Examples include a uniform distribution $a \sim U[0, 1]$ or perhaps a beta distribution $a \sim \text{Beta}(\alpha, \beta)$ for shape parameters α, β.

In the next section, we outline the mathematical framework of Bayesian statistics and describe how we can simulate posterior distributions $p(\boldsymbol{\theta}|d)$ using Markov-Chain Monte-Carlo

[4]Scientists opposed to Bayesian statistics are quick to point out that potential inference drawn on parameters should not depend on the choice of prior distribution. Although this is true, assuming that the experiment is data driven then this should never be the case. The same data set can also be investigated using multiple priors to make sure the same conclusions are drawn. This is the concept of a prior sensitivity analysis.

[5]Well, 15 months factoring in a particular world event.

techniques.

3.5.2 Bayes' theorem

At the heart of Bayesian statistics lies Bayes' theorem

$$p(\boldsymbol{\theta}|d) = \frac{p(d|\boldsymbol{\theta})p(\boldsymbol{\theta})}{p(d)}\,. \tag{3.78}$$

Here, $p(d|\boldsymbol{\theta})$ is the likelihood, a probability density function of the observed data stream, d, conditioned on parameters, $\boldsymbol{\theta}$. The denominator $p(d) = \int p(d|\boldsymbol{\theta})p(\boldsymbol{\theta})d\boldsymbol{\theta}$ is the marginal likelihood, which is independent of parameters $\boldsymbol{\theta}$. The prior probability density function $p(\boldsymbol{\theta})$ reflects our *a-priori* beliefs on the parameters *before* the data stream has been observed. Finally, the posterior probability $p(\boldsymbol{\theta}|d)$ reflects our *a-posteriori* beliefs on the parameters $\boldsymbol{\theta}$ *after* the data stream has been observed.

The marginal likelihood $p(d)$ does not depend on the model parameters and can be treated as an overall normalising constant, writing the posterior as

$$p(\boldsymbol{\theta}|d) \propto p(d|\boldsymbol{\theta})p(\boldsymbol{\theta})\,. \tag{3.79}$$

Usually the form of the posterior $p(\boldsymbol{\theta}|d)$ is not known in a closed form, meaning that we rely on numerical sampling algorithms to obtain samples $\boldsymbol{\theta} \sim p(\boldsymbol{\theta}|d)$. Those drawn samples are called *posterior samples* and can be used to elicit inference about the parameters of the system having observed the data stream.

3.5.2.1 Monte-Carlo integration

Monte-Carlo integration is a technique used to approximate integrals using samples from a probability distribution. Various summary statistics such as the sample mean, or variance, can be calculated with ease from such samples. Let $\boldsymbol{\theta} = \{\theta^1, \theta^2, \ldots, \theta^N\}$ be N samples from a probability density function $p(\boldsymbol{\theta})$ and let $q(\boldsymbol{\theta})$ be a function of parameters $\boldsymbol{\theta}$. The Monte-Carlo estimate of $\mathbb{E}_{p(\boldsymbol{\theta})}[q(\boldsymbol{\theta})]$ is given by

$$\mathbb{E}_{p(\boldsymbol{\theta})}[q(\boldsymbol{\theta})] = \int_{\theta\in\boldsymbol{\theta}} q(\boldsymbol{\theta})p(\boldsymbol{\theta})\mathrm{d}\boldsymbol{\theta} \approx \frac{1}{N}\sum_{i=1}^{N} q(\theta^i)\,. \tag{3.80}$$

For given samples $\boldsymbol{\theta} \sim p(\boldsymbol{\theta}|d)$ from the posterior, one could calculate the sample mean and variance, respectively

$$\mathbb{E}_{p(\boldsymbol{\theta}|d)}[\boldsymbol{\theta}] = \int_{\theta\in\Theta} \boldsymbol{\theta} p(\boldsymbol{\theta}|d) \mathrm{d}\boldsymbol{\theta} \approx \frac{1}{N}\sum_{i=1}^{N} \theta^i \,, \tag{3.81}$$

$$\mathrm{Var}_{p(\boldsymbol{\theta}|d)}[\boldsymbol{\theta}] = \mathbb{E}_{p(\boldsymbol{\theta}|d)}[\boldsymbol{\theta}^2] - \left(\mathbb{E}_{p(\boldsymbol{\theta}|d)}[\boldsymbol{\theta}]\right)^2 \approx \frac{1}{N}\left[\sum_{i=1}^{N}(\theta^i)^2 - \frac{1}{N}\left(\sum_{i=1}^{N}\theta^i\right)^2\right] . \tag{3.82}$$

We remark here that the variance of the samples using (3.82) can be directly compared with the Fisher estimate of the variance (3.63), a useful check of the validity of the FM.

To obtain summary statistics describing the parameters, one has to obtain samples from the posterior distribution $p(\boldsymbol{\theta}|d)$. We outline a procedure for how to do this in the next subsection.

3.5.2.2 Direct sampling techniques

Techniques that can be used to generate samples $\boldsymbol{\theta} \sim p(\boldsymbol{\theta}|d)$ fall under two categories: *direct* sampling or *stochastic* sampling. Direct sampling algorithms draw samples directly from the target probability distribution. Stochastic methods use Markov chain Monte Carlo methods to generate a sequence of samples that are drawn from the target distribution.

Two examples of direct sampling are the method of inversion and rejection sampling. For the method of inversion, given a known form F of the cumulative distribution function of a random variable X, one can generate samples from the target density function by drawing $u \sim U[0,1]$ and evaluating $x = F^{-1}(u)$. We will use this technique in chapter 7. Rejection sampling is another sampling technique where the target distribution is enveloped by an easy-to-sample density function with similar properties to the target distribution. Samples are drawn from the enveloping density, and we reject those samples that lie within the boundary between the target density function and the surrounding density. Further information on these sampling techniques can be found in [247, 248, 249]

Both techniques can be quite efficient in low numbers of dimensions. For the method of inversion we require knowledge of the inverse function F^{-1}, which is problematic if it is not known analytically, or is expensive to estimate numerically. For rejection sampling, we require a density that envelopes and closely matches the features of the target distribution, which can be challenging in higher dimensions. As the number of parameters increase, both of these sampling algorithms can become very inefficient or impossible to implement. In higher dimensions, it is more common to use stochastic sampling techniques from the posterior distribution. Such techniques are called Markov-chain Monte-Carlo (MCMC) techniques, which will be described

over the next few sections.

3.5.2.3 Markov-chains

A Markov-chain is a stochastic sequence of random variables $\theta^0, \theta^1, \ldots, \theta^N$ with the property that θ^{n+1} only depends on the immediate *previous* variable θ^n and not earlier values $\theta^{n-1}, \ldots, \theta^0$. The dynamics of the chain are fully specified using a transition kernel, $\mathcal{K}(\theta^{n+1}|\theta^n)$, a conditional probability distribution for θ^{n+1} given θ^n. The transition kernel uniquely specifies the chain and, in particular, the probabilities associated in moving from one state of the chain to another. We assume that the Markov-chain is *irreducible*, so there is non-zero probability that one can move from one state to any other distinct state. We also assume that the Markov-chain is *ergodic* so that *all* states of the system can be reached in finitely many moves. Finally, we require that the distribution $p(\boldsymbol{\theta})$ satisfies the detailed balance equations

$$p(\boldsymbol{\theta})\mathcal{K}(\boldsymbol{\phi}|\boldsymbol{\theta}) = p(\boldsymbol{\phi})\mathcal{K}(\boldsymbol{\theta}|\boldsymbol{\phi}), \quad \forall \boldsymbol{\phi}, \boldsymbol{\theta}\,. \tag{3.83}$$

Equation (3.83) states that the probability of moving from state $\boldsymbol{\phi}$ to $\boldsymbol{\theta}$ is the same as moving from state $\boldsymbol{\theta}$ to $\boldsymbol{\phi}$. Provided equation (3.83) is satisfied, then the Markov-chain will converge to the stationary distribution $p(\boldsymbol{\theta})$, equivalent to the target posterior distribution $p(\boldsymbol{\theta}|d)$. For more mathematical details on the theory of Markov Chains, we refer the reader to [247, 250]. In the next subsection, we will describe the main MCMC technique we use throughout this thesis: the random-walk Metropolis-Hastings (MH) algorithm [251, 252].

3.5.3 Markov-chain Monte-Carlo

In the MH algorithm, a proposal distribution $q(\boldsymbol{\phi}|\boldsymbol{\theta})$ is specified to propose a new point $\boldsymbol{\phi}$ given the current parameter values $\boldsymbol{\theta}$. The algorithm is as follows

1. Choose an initial parameter set of parameter values $\boldsymbol{\theta}^0$.

2. For $i = 1, \ldots N$:

3. Draw a new point $\boldsymbol{\phi} \sim q(\boldsymbol{\phi}|\boldsymbol{\theta}^{i-1})$ from a proposal distribution q.

   (a) Calculate the acceptance ratio

$$\alpha = \min\left(1, \frac{p(\boldsymbol{\phi}|d)q(\boldsymbol{\theta}^{i-1})}{p(\boldsymbol{\theta}^{i-1}|d)q(\boldsymbol{\phi})}\right). \tag{3.84}$$

(b) Draw a value $u \sim U[0,1]$ and accept $\boldsymbol{\phi}$ if $u < \alpha$ and set $\boldsymbol{\theta}^i = \boldsymbol{\phi}$. Otherwise, reject it and set $\boldsymbol{\theta}^i = \boldsymbol{\theta}^{i-1}$.

(c) Return to step 2. Repeat until N iterations have been performed.

The constructed Markov chain from the MCMC algorithm above will *asymptotically* converge to its stationary distribution — the posterior distribution of the constructed chains. Usually we don't have knowledge about where in parameter space the true values lie so we start the algorithm at an arbitrary point. It may take time for the Markov chain to lose memory of the starting point and converge to the posterior distribution. The *earlier* samples are discarded as "burn-in" to ensure that the samples used are indicative of the posterior distribution. We would then discard B iterations as "burn-in" and have $N - B$ (dependent) samples from the posterior distribution. The remaining samples can be used to calculate Monte-Carlo estimates of the parameters of interest.

Convergence of the chains can be tested using trace plots. A trace plot is a plot of the parameter value in the chain as a function of iteration number. The early samples will show a trend as the chain moves towards parameter values with high posterior support. Once the chain begins to oscillate back and forth around a parameter value, we know that the algorithm is sampling properly.

trace plots are a quick method to check whether the chain has converged to the target distribution. In our work, we always know the injected waveforms true parameters and can test that the chain fluctuates around these parameters as one should expect. However, although the chain may have converged to the stationary distribution, there can be *mixing* problems where candidate values are either accepted too much or too little. As discussed in [253], the optimal acceptance rate for a single parameter is $\sim 44\%$ and for multiple parameters $\sim 23\%$. The acceptance rate can be controlled by tuning the parameters of the proposal distribution, such as the proposal variance. The choice of proposal distribution is key when it comes to the efficiency of the algorithm, which can be understood by making reference to figure (3.4).

As one can see, the efficiency of the algorithm depends strongly on the choice of proposal distribution q. The MH algorithm should converge for *any* choice of proposal distribution, but proposals that more closely match the shape of the posterior should lead to more rapid convergence. In our work we will use a normal proposal distribution and, as we expect that the shape of the posterior distribution should be approximated by the FM, we will usually set the covariance matrix of the normal proposal distribution to be equal to the inverse FM evaluated at the known injection parameters. In this thesis, there are no times we actively search for unknown signals in the data stream. Instead, we use MCMC as a tool to verify that the FM,

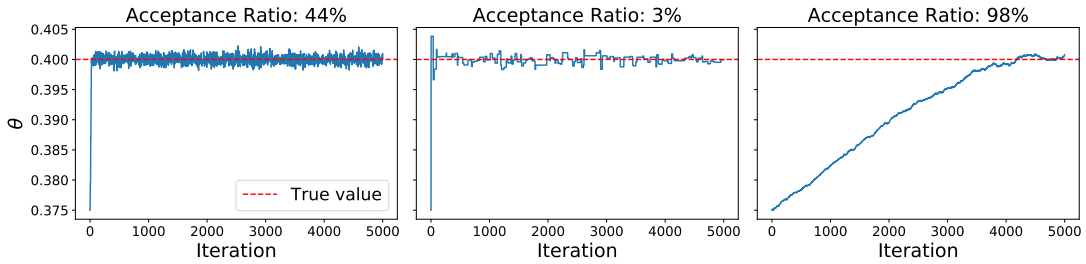

Figure 3.4: Here we show example trace plots when using a normal proposal distribution $q = N(\theta|\sigma_0^2)$ for different choices of proposal variance σ_0^2 in the MH algorithm. In the left plot we have tuned σ_0^2 to ensure a 44% acceptance rate, which means that this choice of σ_0^2 suitably reflects the posterior variance. In the middle plot we have chosen a very large value σ_0^2 that enforces too much movement of the chain, so samples are rejected frequently. The right most plot we have chosen a very small σ_0^2, which means it will take a long time for the chain to move around parameter space. These latter two choices of σ_0^2 yield inefficient sampling of the posterior.

a local approximation to the shape of the likelihood, is giving reliable precision estimates of the parameters. In the following section, we briefly summarise the topics we discussed in this chapter and describe how each topic will be used in research chapters of this thesis.

3.6 Concepts used throughout this work

Chapter 3 has introduced the main tools of data analysis that will be used in the research based chapters 5, 6, 7 and 8. The ideas from section 3.1 will be common to all these chapters and heavily utilised. The FM, introduced in 3.3.2 is the most used tool in this work: in chapter 5 we use it to show that the spin parameter of EMRIs where the primary is rapidly rotating can be constrained to *extraordinary* precision; in chapter 6 we use it to argue how accurately the 1PA components of the GSF must be computed in order to not significantly bias parameters; in chapter 7 we generalise the Cutler-Vallisneri formalism introduced in subsection 3.4.2 that relies on computing the FM; and, in chapter 8 we generalise the FM to account for non-stationary noise. In chapter 8 we discuss inference on source parameters when the waveform is buried in *non-stationary* Gaussian noise. The Whittle-likelihood (3.31) is no longer valid, and must be modified by incorporating a noise covariance matrix accounting for non-stationary features of the noise. In chapter 8, the details in section 3.2.2 will be essential. Finally, for reasons discussed in 3.3.3, whenever a FM has been used we test its validity using Bayesian parameter estimation that was described in section 3.5.

In the next chapter we describe a model for the final stage of the radial trajectory of a CO in orbit around a SMBH.

Chapter 4

Transition from Inspiral to Plunge: A complete near-extremal trajectory and associated waveform

4.1 Introduction

In this thesis, we study the full inspiral-transition-plunge trajectory of a CO into a MBH, *for any* spin of the primary BH. A concrete understanding of the transition dynamics is important, since, close to the ISCO where the transition occurs, the inspiral time-scale becomes comparable to the orbital time-scale. As the two time-scale analysis presented in 2.3.1 relies on these two time-scales being well separated in time, various approximations such as the adiabatic approximation (2.30) breaks down. So, in order to build complete radial trajectories encapsulating inspiral-transition-plunge, it is critical to understand the orbital dynamics of the CO close to ISCO.

Inspiral trajectories of COs on circular and equatorial orbits can be obtained by taking a coordinate time derivative of (2.8a)

$$\frac{d\tilde{r}}{d\tilde{t}} = \frac{\dot{\tilde{E}}}{\partial_{\tilde{r}}\tilde{E}} = -\frac{\dot{\tilde{E}}_{\rm GW}}{\partial_{\tilde{r}}\tilde{E}}\,. \tag{4.1}$$

The second equality uses the flux balance law: (2.56a) $\dot{\tilde{E}} = -\dot{\tilde{E}}_{\rm GW}$. Given that $\dot{\tilde{E}}_{\rm GW} \sim \eta$, the radial evolution evolves adiabatically. Given a relationship for the first-order (orbit-averaged)

dissipative flux above, adiabatic inspirals can be numerically calculated with ease. However, as the ISCO is approached the quantity $\partial_{\tilde{r}}\tilde{E} \to 0$ giving a (nonphysical) divergence in the radial velocity $\dot{\tilde{r}}$. This divergence marks a break-down in the adiabatic approximation, so alternative radial evolution equations are required to model the transition from the inspiral trajectory (4.1) to a plunging geodesic.

The transition to plunge was originally discussed by Ori-Thorne (OT) [254] for moderate values of the spin in the limit of small mass ratios. A similar but independent analysis conducted by Buonanno and Damour in [255] solved the problem for Schwarzschild BHs with arbitrary (reduced) mass ratio. The OT approach was to expand the radial geodesic equation (2.19) near the ISCO in order to derive an equation that could glue the inspiral dynamics to a plunging geodesic. Their resulting transition equation of motion depends on the mass ratio η, which is a small parameter. The technical reason why high spins require a separate discussion is because of the existence of a second independent small parameter $\epsilon = \sqrt{1-a^2} \ll 1$, previously discussed in section 2.2.3, that competes with the mass ratio $\eta = \mu/M \ll 1$. Since the dynamical equations describing the transition depend on the spin, the near extremal limit, i.e. $\epsilon \to 0$, modifies the original procedure discussed by OT. The transition to plunge for near-extremal EMRIs was previously considered in [256] and our work clarifies and extends those results in a number of ways. We point out the physical interpretation of the mathematical procedure used in [256], identify a missing term in transition equations of motion in the near-extremal regime and incorporate recent analytic results for the near-extremal energy flux (2.59) for the first time.

Chapter 4 is organised as follows. In section 4.2 we set up the master transition equation of motion in general and, in subsection 4.2.3, we estimate corrections due to eccentricity and non-geodesic past-history of the orbital evolution. The transition equations of motion in the *three* different scaling regimes $\eta \ll \epsilon$, $\eta \sim \epsilon$ and $\eta \gg \epsilon$ are described in subsections 4.2.4, 4.2.5 and 4.2.6 respectively. The numerical scheme to integrate our transition equations of motion for the $\epsilon \sim \eta$ regime is presented in section 4.3.1. We describe how to generate a near-extremal EMRI gravitational waveform encapsulating inspiral and plunge in subsections 4.3.2 and 4.3.3. We finish with a summary of our main results in section 4.4.

4.2 The transition equation of motion

Our discussion is organised as follows. First, we analyse in section 4.2.1 the effects arising from the radial GSF in the vicinity of the ISCO on the dynamics of this small body, justifying the

starting point in OT. Second, assuming the dissipative fluxes of energy and angular momentum for quasi-circular and equatorial orbits are still related as in circular orbits (see equation (2.57)) [202, 203]

$$\dot{\tilde{E}} = \tilde{\Omega}(\tilde{r})\dot{\tilde{L}}\,, \tag{4.2}$$

we derive in section 4.2.2 the transition equation for arbitrary BH spins *without* the OT assumption that both energy $\tilde{E}$ and angular momenta $\tilde{L}$ evolve *linearly* in proper time $\tilde{\tau}$. Third, given the quasi-circular nature of our assumed orbits, we argue in section 4.2.3 there can be corrections to (4.2) of the form

$$\dot{\tilde{E}} - \tilde{\Omega}(\tilde{r})\dot{\tilde{L}} \sim \eta\dot{\tilde{r}} + \eta e^2\,, \tag{4.3}$$

whose scaling behaviour on the trajectory of the small body is determined. Finally, in sections 4.2.4-4.2.6, we discuss in detail the existence of three different scaling regimes in our transition equation, depending on the BH spin, paying special attention to the near-extremal ones. We show the corrections due to (4.3) are subleading in all the regimes.

4.2.1 The self-force

Subsection 4.2.1 shows both that quasi-circular and equatorial orbits have vanishing dissipative effects and the conservative piece of the radial GSF can be neglected close to the ISCO. Consider the radial geodesic equation, equation (2.5a). Differentiating it with respect to proper time, one obtains

$$\frac{d^2\tilde{r}}{d\tilde{\tau}^2} - \frac{1}{2}\frac{\partial G}{\partial \tilde{r}} = \frac{1}{2}\left(\frac{d\tilde{E}}{d\tilde{\tau}}\frac{\partial G}{\partial \tilde{E}} + \frac{d\tilde{L}}{d\tilde{\tau}}\frac{\partial G}{\partial \tilde{L}}\right)\left(\frac{d\tilde{r}}{d\tilde{\tau}}\right)^{-1}\,. \tag{4.4}$$

It is shown in Appendix A.3 that equation (4.4) is equivalent to

$$\frac{d^2\tilde{r}}{d\tilde{\tau}^2} + \Gamma^{\tilde{r}}_{\rho\sigma}\frac{d\tilde{x}^\rho}{d\tilde{\tau}}\frac{d\tilde{x}^\sigma}{d\tilde{\tau}} = \eta\tilde{f}^{\tilde{r}}_{\rm diss}\,, \tag{4.5}$$

where we have pulled the η dependence out of the fluxes $d\tilde{E}/d\tilde{\tau}$ and $d\tilde{L}/d\tilde{\tau}$. Hence, the terms on the left-hand side of equation (4.4) correspond to the usual ones for geodesic motion, whereas the one on the right-hand side can be understood as the perturbing force $\tilde{f}^{\tilde{r}}_{\rm diss}$ exerted on the particle driving energy $\left(d\tilde{E}/d\tilde{\tau}\right)$ and angular momentum $\left(d\tilde{L}/d\tilde{\tau}\right)$ loss due to GW emission.

Mino showed [257] that the forcing term for general geodesic motion can be split into a dissipative and a conservative piece at first order in the mass ratio η

$$\tilde{f}^{\tilde{r}} = \left(\tilde{f}^{\tilde{r}}_{(1){\rm diss}} + \tilde{f}^{\tilde{r}}_{(1){\rm cons}}\right) + \mathcal{O}(\eta^2)\,. \tag{4.6}$$

For circular orbits, as considered by OT, the dissipative fluxes of energy and angular momentum are related by

$$\dot{\tilde{E}} = \tilde{\Omega}(\tilde{r})\dot{\tilde{L}}\,, \tag{4.7}$$

where it can be shown that the dissipative part of the radial GSF $\tilde{f}^{\tilde{r}}_{(1)\text{diss}}$ vanishes (see equation (4.42)), giving

$$\frac{d^2\tilde{r}}{d\tilde{\tau}^2} - \frac{1}{2}\frac{\partial G}{\partial \tilde{r}} = \eta \tilde{f}^{\tilde{r}}_{(1)\text{cons}} + \mathcal{O}(\eta^2)\,, \tag{4.8}$$

which is precisely equation (3.10) of OT in [254]. In the above equation, we neglect effects coming from the second order in the mass ratio dissipative component to the GSF. The quantity $\eta\tilde{f}^{\tilde{r}}_{(1)\text{cons}}$ is non-dissipative, implying it can be absorbed into the effective potential (2.1), which will then pose η corrections in positional elements in the orbit such as $\tilde{r}_{\text{isco}}, \tilde{E}_{\text{isco}}$ and $\tilde{L}_{\text{isco}}$. We now check whether it is justified neglecting these η contributions, particularly in the near-extremal limit.

We begin by studying the angular frequency $\tilde{\Omega}$. Recall from (2.29) that the conservative component of the GSF will cause a shift in geodesic frequencies, say $\tilde{\Omega}^{\text{shifted}}_{\text{isco}}$ with respect to the usual Kerr angular frequency $\tilde{\Omega}_{\text{isco}}$. From [258, 259], this shift is given by

$$(1+\eta)\tilde{\Omega}^{\text{shifted}}_{\text{isco}} = \tilde{\Omega}_{\text{isco}}(1 + \eta C_{\tilde{\Omega}}(a)) + \mathcal{O}(\eta^2)\,, \tag{4.9}$$

with the quantity $C_{\tilde{\Omega}}(a)$ discussed in depth and independently (numerically) calculated in both [173, 259]. According to [259], $C_{\tilde{\Omega}}(a) \in (1.24, 1.39)$. Hence, $C_{\tilde{\Omega}}(a) \sim \mathcal{O}(1)$ for all spins, and since $\tilde{\Omega}_{\text{isco}} \sim \mathcal{O}(1)$, it follows that for $\eta \ll 1$

$$|\tilde{\Omega}^{\text{shifted}}_{\text{isco}} - \tilde{\Omega}_{\text{isco}}| \approx \eta(C_{\tilde{\Omega}}(a) - 1)\tilde{\Omega}_{\text{isco}} \sim \eta\,. \tag{4.10}$$

It is further shown in [259] that $C_{\tilde{\Omega}}(a)$ oscillates[1] around the limiting value of $1 + 1/2\sqrt{3}$ as $a \to 1$.

Using equation (2.21c) in the high spin limit and $\eta \ll 1$, equation (4.9) becomes

$$|\tilde{\Omega}^{\text{shifted}}_{\text{isco}} - \tilde{\Omega}_{\text{isco}}| = \frac{\eta}{4\sqrt{3}} + \mathcal{O}(\eta^2) + \mathcal{O}(\eta\epsilon^{2/3})\,, \tag{4.11}$$

which implies that the change in the angular frequency at the ISCO due to conservative GSF effects is an $\mathcal{O}(\eta)$ quantity.

[1] $C_{\tilde{\Omega}}(a)$ is shown to actually oscillate around this limiting value as $a \to 1$. This phenomenon is non-trivial and still not well understood today. See [259] for more details.

Since $\tilde{\Omega}_{\rm isco}^{\rm shifted}$ is related to the shifted BL radial coordinate at the ISCO by

$$\tilde{r}_{\rm isco}^{\rm shifted} = \left(\frac{1}{\tilde{\Omega}_{\rm isco}^{\rm shifted}} - a\right)^{2/3} , \tag{4.12}$$

it follows, using equation (4.11), that the shifted ISCO location assumes the form

$$|\tilde{r}_{\rm isco}^{\rm shifted} - \tilde{r}_{\rm isco}| = \frac{2\eta}{3\sqrt{3}} + \mathcal{O}(\eta\epsilon^{2/3}) , \tag{4.13}$$

implying that the shifted ISCO radial coordinate is proportional to η with subleading corrections $\mathcal{O}(\eta\epsilon^{2/3})$.

It will be shown in this chapter that there are three different transition regimes depending on the ratio of ϵ and η. The "radial thickness" of the transition in each regime scales according to:

- For $\eta \ll \epsilon \Rightarrow \tilde{r} - \tilde{r}_{\rm isco} \sim \eta^{2/5} > \eta$
- For $\eta \sim \epsilon \Rightarrow \tilde{r} - \tilde{r}_{\rm isco} \sim (\eta/\epsilon)^{2/5}\epsilon^{2/3} \sim \eta^{2/3} > \eta$
- For $\eta \gg \epsilon \Rightarrow \tilde{r} - \tilde{r}_{\rm isco} \sim \eta^{2/3} > \eta$.

Thus, the effect of the conservative piece of the GSF is subleading in all regimes. That is, the radial size of the transition regime is *larger* and the shifted ISCO coordinate is contained within the transition radius. Accordingly, like in the original OT analysis, we shall ignore these effects.

4.2.2 Transition equation — generalities

To discuss the evolution of the orbit, we pursue the following strategy: we assume the corrections in (4.3) are subleading, and once the scaling behaviour of the different dynamical regimes are identified, we double-check the consistency of our original assumption.

To evolve the orbit, OT used the circular flux relationship (4.7) and additionally assumed that the energy, $\tilde{E}$, and angular momentum, $\tilde{L}$, evolve *linearly* in proper time, $\tilde{\tau}$, throughout the transition regime

$$\begin{aligned} \tilde{E} - \tilde{E}_{\rm isco} &= \tilde{\Omega}_{\rm isco}\frac{d\tilde{L}_{\rm isco}}{d\tilde{\tau}}(\tilde{\tau} - \tilde{\tau}_{\rm isco}) , \\ \tilde{L} - \tilde{L}_{\rm isco} &= \frac{d\tilde{L}_{\rm isco}}{d\tilde{\tau}}(\tilde{\tau} - \tilde{\tau}_{\rm isco}). \end{aligned} \tag{4.14}$$

In our analysis of the transition, we will *not* assume a strict equality in equation (4.14). Instead, we will keep track of the evolution of $\tilde{\Omega}_{\rm isco}^{-1}(\tilde{E} - \tilde{E}_{\rm isco}) - (\tilde{L} - \tilde{L}_{\rm isco})$, as also considered in [256].

OT proposed to analyse the transition to the plunging geodesic by expanding (4.4) around the ISCO trajectory $(\tilde{r}_{\rm isco}, \tilde{E}_{\rm isco}, \tilde{L}_{\rm isco})$, since the latter provides the natural starting point for the plunging trajectory for equatorial and circular orbits as discussed in section 2.2.2. It is physically natural to introduce the new variables δE, δL and R

$$\begin{aligned} \delta E &= \tilde{\Omega}_{\rm isco}^{-1}(\tilde{E} - \tilde{E}_{\rm isco}) \\ \delta L &= \tilde{L} - \tilde{L}_{\rm isco} \\ R &= \tilde{r} - \tilde{r}_{\rm isco} \end{aligned} \tag{4.15}$$

to study the inspiral evolution of the small body perturbatively around the primary. The presence of $\tilde{\Omega}_{\rm isco}$ is for technical convenience.

Instead of expanding (4.4), we find it more convenient to expand the radial geodesic equation (2.5a). We stress that our conclusions do not depend on this choice. The latter is given by

$$\begin{aligned} \left(\frac{d\tilde{r}}{d\tilde{\tau}}\right)^2 = G(\tilde{r}_{\rm isco}, \tilde{E}_{\rm isco}, \tilde{L}_{\rm isco}) + \sum_{i=1}^{\infty} \frac{1}{i!} \frac{\partial^i G}{\partial \tilde{r}^i}\bigg|_{\rm isco} (\tilde{r} - \tilde{r}_{\rm isco})^i \\ + \sum_{i=0}^{\infty} \frac{1}{i!} \left(\frac{\partial^{i+1} G}{\partial \tilde{r}^i \partial \tilde{E}}\bigg|_{\rm isco} (\tilde{E} - \tilde{E}_{\rm isco}) + \frac{\partial^{i+1} G}{\partial \tilde{r}^i \partial \tilde{L}}\bigg|_{\rm isco} (\tilde{L} - \tilde{L}_{\rm isco}) \right) (\tilde{r} - \tilde{r}_{\rm isco})^i \\ + \frac{1}{2} \sum_{i=0}^{\infty} \frac{1}{i!} \left(\frac{\partial^{i+2} G}{\partial \tilde{r}^i \partial \tilde{E}^2}\bigg|_{\rm isco} (\tilde{E} - \tilde{E}_{\rm isco})^2 + 2 \frac{\partial^{i+2} G}{\partial \tilde{r}^i \partial \tilde{L} \partial \tilde{E}}\bigg|_{\rm isco} (\tilde{E} - \tilde{E}_{\rm isco})(\tilde{L} - \tilde{L}_{\rm isco}) \right. \\ \left. + \frac{\partial^{i+2} G}{\partial \tilde{r}^i \partial \tilde{L}^2}\bigg|_{\rm isco} (\tilde{L} - \tilde{L}_{\rm isco})^2 \right) (\tilde{r} - \tilde{r}_{\rm isco})^i \,. \end{aligned} \tag{4.16}$$

Since $G(\tilde{r}, \tilde{E}, \tilde{L})$ is quadratic in $\tilde{E}$ and $\tilde{L}$, we have ignored the partial derivatives

$$\frac{\partial^n G}{\partial \tilde{E}^n} = \frac{\partial^n G}{\partial \tilde{L}^{n-k} \partial \tilde{E}^k} = \frac{\partial^n G}{\partial \tilde{E}^{n-k} \partial \tilde{L}^k} = \frac{\partial^n G}{\partial \tilde{L}^n} = 0 \quad \text{for } n \geq 3 \text{ and } k < n. \tag{4.17}$$

Plugging the variables (4.15), using the definition of the coefficients (A.8) and the results in (A.9)-(A.11), one can rewrite the general transition equation as

$$\left(\frac{dR}{d\tilde{\tau}}\right)^2 = \sum_{n=3}^{\infty} \frac{1}{n!} A_n \, R^n + \delta L \sum_{n=1}^{\infty} \frac{1}{n!} B_n \, R^n + \frac{\delta L^2}{2} \sum_{n=0}^{\infty} \frac{1}{n!} C_n R^n + \Gamma_{\odot} \,, \tag{4.18}$$

where $\Gamma_{\odot}$ is defined by

$$\begin{aligned} \Gamma_{\odot} = \frac{1}{2} \sum_{n=0}^{\infty} \frac{1}{n!} \tilde{\Omega}_{\rm isco} (\delta E - \delta L) \left(2 \frac{\partial^{n+1} G}{\partial \tilde{r}^n \partial \tilde{E}}\bigg|_{\rm isco} + 2 \left(\frac{\partial^{n+2} G}{\partial \tilde{r}^n \partial \tilde{E} \partial \tilde{L}}\bigg|_{\rm isco} + \tilde{\Omega}_{\rm isco} \frac{\partial^{n+2} G}{\partial \tilde{r}^n \partial \tilde{E}^2}\bigg|_{\rm isco} \right) \delta L \right. \\ \left. + \tilde{\Omega}_{\rm isco} \frac{\partial^{n+2} G}{\partial \tilde{r}^n \partial \tilde{E}^2}\bigg|_{\rm isco} (\delta E - \delta L) \right) R^n \,. \end{aligned} \tag{4.19}$$

Notice that $\Gamma_\odot \propto \delta E - \delta L$ at leading order in R. Hence, it encodes the deviations from the OT approximation (4.14).

The time evolution of $\delta E - \delta L$ near $\tilde{r}_{\rm isco}$ is controlled by the fluxes and the angular frequency. Throughout a quasi-circular inspiral far from ISCO, the CO inspirals on a sequence of circular geodesics defined by the constants of motion $\tilde{E}(\tilde{r}_{\rm circ}) = \tilde{E}_{\rm circ}$ and $\tilde{L}(\tilde{r}_{\rm circ}) = \tilde{L}_{\rm circ}$, as given in equation (2.8a) and equation (2.8b) respectively. The evolution of the constants of motion is linked through equation (4.7) above, which simply states that circular geodesics evolve into circular geodesics. For circular evolutions we therefore see that

$$\begin{aligned} \frac{d}{d\tilde{\tau}}(\delta E - \delta L) &= \tilde{\Omega}_{\rm isco}^{-1} \frac{d\tilde{E}}{d\tilde{\tau}} - \frac{d\tilde{L}}{d\tilde{\tau}} \\ &= (\tilde{\Omega}_{\rm isco}^{-1} \tilde{\Omega}(\tilde{r}) - 1) \frac{d\tilde{L}}{d\tilde{\tau}} \\ &\approx -\frac{\partial \log \tilde{\Omega}}{\partial \tilde{r}}\bigg|_{\rm isco} \eta \kappa R \\ \implies (\delta E - \delta L) &\sim \eta R \tilde{\tau} \,, \end{aligned} \tag{4.20}$$

where we expanded $\tilde{\Omega}(r)$ to first order in R and approximated $d\tilde{L}/d\tilde{\tau} \approx (d\tilde{L}/d\tau)_{\rm isco} = -\eta\kappa$ for κ constant defined by

$$\kappa = \left(\tilde{\Omega}^{-1} \frac{d\tilde{t}}{d\tilde{\tau}} \frac{d\tilde{E}_{GW}}{d\tilde{t}} \right)_{\rm isco} \sim \mathcal{O}(1) \quad \text{for } a \in [0,1]. \tag{4.21}$$

Thus we deduce that $\delta E - \delta L \sim \eta R \tilde{\tau}$ for circular inspirals close to $\tilde{r}_{\rm isco}$. We shall see that these corrections are indeed subleading in the regime considered by OT [254]. However, they will not be negligible for near-extremal BHs.

4.2.3 Corrections arising from deviations from adiabatic nearly-circular inspiral

Given our assumption that the orbit is nearly circular when it reaches the transition regime, one expects corrections to the relation (4.7) between the fluxes of energy and angular momentum satisfied for an exactly equatorial circular adiabatic inspiral. We discuss below two possible physical effects giving rise to such corrections: *eccentricity* and the *non-geodesic past-history of the orbital evolution*, both of which give rise to the corrections (4.3).

Eccentricity can lead to corrections to the transition equation that we will discuss further below, but eccentricity corrections to the fluxes tend to be suppressed during the transition regime. This is because the transition, for an arbitrary eccentric inspiral, corresponds to the orbit passing over the maximum of the effective potential given by equation (2.5a). This was

discussed in figure 2.1. The radial velocity throughout the transition regime is therefore always small, while the angular frequency remains $\mathcal{O}(1)$. Hence the orbit looks very much like a circular orbit, even if it is technically eccentric or even plunging. For nearly-circular transitions, the orbit is passing over a point of inflection of the effective potential and corrections to this approximately-circular assumption are even smaller.

Corrections from *non-geodesic past-history* enter because the GSF acting on the small object at a particular time is generated by the intersection of the particle world line with gravitational perturbations generated by the orbital motion in the immediate past [260]. The GSF acting on the orbit when it is at a particular radius will therefore have corrections that depend on how far, in radius, the orbit has moved over the relevant past-history. The latter is determined by the dominant, azimuthal, timescale, and is an $\mathcal{O}(1)$ quantity, when expressed in coordinate time[2]. The orbital radius therefore changes by an amount of $\mathcal{O}(\dot{\tilde{r}})$ over the relevant past-history. This is the scaling of the fractional change in the fluxes, and since $\dot{\tilde{E}} \sim \mathcal{O}(\eta\epsilon^{\frac{2}{3}})$ from (2.60) for near-extremal orbits, the non-geodesic past-history corrections to the coordinate-time fluxes thus scale like $\eta\epsilon^{2/3}\dot{\tilde{r}}$. In the regime $\eta \ll \dot{\tilde{r}}$, considered by OT, and discussed in Section 4.2.4, ϵ can be considered $\mathcal{O}(1)$ and so the scaling of this correction is $\eta\dot{\tilde{r}}$. This is the first type of correction in equation (4.3). In the adiabatic inspiral phase, these corrections are $\mathcal{O}(\eta^2)$ and form part of the 1PA component of the GSF. However, in the transition phase these corrections can be larger.

We have argued above that eccentricity corrections to the fluxes should be suppressed in the transition regime. We now make this more concrete. Eccentricity corrections to the fluxes enter as fractional corrections of $\mathcal{O}(e^2)$, since corrections to the orbit at linear order in eccentricity are oscillatory and average to zero over a complete orbit [203]. The corrections to the coordinate time fluxes thus scale like $\eta\epsilon^{\frac{2}{3}}e^2$ (which is ηe^2 in the OT regime discussed in Section 4.2.4). This is the second type of correction in equation (4.3). If these corrections are to be small relative to the non-geodesic past-history corrections, we need $e^2 < \dot{\tilde{r}}$. In the transition zone we will see that the proper time scales like $R^{-1/2}$, where $R = \tilde{r} - \tilde{r}_{\rm isco}$ is the radial distance from the ISCO, regardless of the spin of the primary. For non near-extremal BHs, i.e., those with $\eta \ll \epsilon$, proper time and coordinate timescale in the same way and the scaling of $\dot{\tilde{r}}$ is therefore the same as that of $R^{3/2}$. The constraint we obtain on eccentricity is therefore $e < R^{3/4}$. However, there is also a geometric constraint, which is that the variation in the orbital radius due to eccentricity should be small compared to the variation due to radiation reaction through the

[2]If we are more conservative, we could assume that the timescale for radial oscillations is the appropriate averaging timescale. This is not $\mathcal{O}(1)$, but $\mathcal{O}(T)$, the scaling of the time coordinate in the transition zone. Although this condition is more restrictive we will see below that even this condition does not change the conclusion that past-history corrections can be ignored in the transition zone.

transition zone. The latter is the scaling of R, while the former is a quantity of $\mathcal{O}(e)$, so we deduce an additional constraint $e < R < R^{3/4}$, the latter inequality following from the fact that R is a small quantity throughout the transition. We deduce that the geometrical constraint is stronger than the flux-correction constraint in the regime $\eta \ll \epsilon$. Using (2.22) in the near-extremal regime, $\eta \lesssim \epsilon$, $d\tilde{t}/d\tilde{\tau} \sim \epsilon^{-2/3}$ and so the constraint on the eccentricity changes to $e < \epsilon^{1/3} R^{3/4}$ if these corrections are to be subleading. This is then more stringent than the geometric constraint. However, in this regime we will see below that eccentricity cannot grow until deep inside the transition zone, so even the more stringent constraint is easily satisfied.

Eccentricity during the transition can arise either from the presence of residual eccentricity prior to the start of the transition zone, or due to the excitation of eccentricity during the transition. The latter manifests itself as additional terms in the transition equation, the existence of which we will check for carefully in our analysis. To understand the former, we need to analyse the growth of eccentricity during the adiabatic inspiral. We will assume that at the beginning of the inspiral the orbit is nearly circular. It was shown in [203] that, for small eccentricity, the evolution of eccentricity under radiation reaction takes the form $\dot{e} = f(\tilde{r}_0)e$, where $\tilde{r}_0$ is the mean orbital radius and e is an eccentricity defined such that the orbital apoapsis is at $\tilde{r} = \tilde{r}_0(1+e)$. For large $\tilde{r}_0$, $f(\tilde{r}_0) < 0$ and so the eccentricity decreases. In this regime any small eccentricity that is excited by small perturbations arising due to inspiral evolution or other effects is dampened and does not grow. However, for all spins $a < 1$, as the innermost stable circular orbit (or analogous separatrix) is approached, the sign of $f(\tilde{r}_0)$ changes and is greater than zero in the vicinity of the ISCO. This means that orbits near to the separatrix are unstable to eccentricity growth. We would therefore expect any eccentricity that is excited to begin to grow.

Denoting $\tilde{v}^2 = 1/\tilde{r}_0$, Kennefick [203] showed that the evolution of the orbital parameters,

for small eccentricity, was governed by equations of the form

$$\frac{\dot{\tilde{r}}_0}{\tilde{r}_0} = -\frac{2(1-3\tilde{v}^2+2a\tilde{v}^3)^{3/2}}{\tilde{v}^2(1-6\tilde{v}^2+8a\tilde{v}^3-3a^2\tilde{v}^4)}\dot{\tilde{E}}_0 \tag{4.22}$$

$$\frac{\dot{e}}{e} = \frac{1}{e^2}\left(\dot{\tilde{E}}_0 - \Omega(\tilde{v})\dot{\tilde{L}}_0\right) - j(\tilde{v})\left[\Gamma - h(\tilde{v})\dot{\tilde{E}}_0)\right] \tag{4.23}$$

where

$$\begin{aligned}
j(\tilde{v}) &= \frac{(1+a\tilde{v}^3)(1-2\tilde{v}^2+a^2\tilde{v}^4)(1-3\tilde{v}^2+2a\tilde{v}^3)^{1/2}}{\tilde{v}^2(1-6\tilde{v}^2+8a\tilde{v}^3-3a^2\tilde{v}^4)} \\
h(\tilde{v}) &= \frac{\mathcal{H}(\tilde{v})(1+a\tilde{v}^3)^{-1}(1-2\tilde{v}^2+a^2\tilde{v}^4)^{-2}}{2(1-6\tilde{v}^2+8a\tilde{v}^3-3a^2\tilde{v}^4)} \\
\mathcal{H}(\tilde{v}) &= 1-12\tilde{v}^2+66\tilde{v}^4-108\tilde{v}^6+a\tilde{v}^3+8a^2\tilde{v}^4 \\
&\quad -72a\tilde{v}^5-20a^2\tilde{v}^6+204a\tilde{v}^7+38a^3\tilde{v}^7-42a^2\tilde{v}^8 \\
&\quad -9a^4\tilde{v}^8-144a^3\tilde{v}^9+116a^4\tilde{v}^{10}-27a^5\tilde{v}^{11}.
\end{aligned}$$

Both Γ and $\dot{\tilde{E}}_0$ are components of the GSF, which can be evaluated by solving the Teukolsky equation. The quantity Γ is in fact a linear combination of quantities that are time derivatives and so the above equation takes the same form for any choice of time coordinate with respect to which to evaluate the fluxes. Kennefick's analysis used coordinate time and so we make the same choice in the following discussion. An explicit expression for Γ is given in [203] and the quantity $\dot{\tilde{E}}_0$ is the energy flux given in (2.58). Numerical calculations show that these are finite quantities of $\mathcal{O}(1)$ throughout parameter space. The first term in the eccentricity evolution equation vanishes for evolution driven by gravitational radiation reaction, while the quantity $h(\tilde{v})$ is singular at the ISCO. Therefore, close to ISCO the eccentricity evolution takes the form

$$\begin{aligned}
&\frac{\dot{e}}{e} \approx j(\tilde{v})h(\tilde{v})\dot{\tilde{E}}_0 \\
\Rightarrow \quad & r_0\frac{\mathrm{d}\ln e}{\mathrm{d}r_0} \approx -\frac{\tilde{v}^2(1-6\tilde{v}^2+8a\tilde{v}^3-3a^2\tilde{v}^4)j(\tilde{v})h(\tilde{v})}{2(1-3\tilde{v}^2+2a\tilde{v}^3)^{3/2}}.
\end{aligned} \tag{4.24}$$

Notice that the expression is entirely geodesic and independent of the energy flux $\dot{\tilde{E}}_0$. For non-extremal spin, both $j(\tilde{v})$ and $h(\tilde{v})$ have simple poles at $\tilde{r} = \tilde{r}_{\rm isco}$ and there is a simple zero in the term $(1-6\tilde{v}^2+8a\tilde{v}^3-3a^2\tilde{v}^4)$ in the numerator. Therefore as ISCO is approached the eccentricity evolves as

$$\frac{\mathrm{d}\ln e}{\mathrm{d}R} \approx -\frac{k(a)}{R} \quad \Rightarrow \quad e = e_0\left(\frac{R_0}{R}\right)^{k(a)} \tag{4.25}$$

with $R = \tilde{r} - \tilde{r}_{\rm isco}$ as before, and e_0 denotes the eccentricity when $R = R_0$ and $\tilde{r}_0 \gg \tilde{r}_{\rm isco}$. The

exponent $k(a)$ is given by $k(a) = \mathcal{H}(\tilde{v}_{\rm isco})/\mathcal{D}(\tilde{v}_{\rm isco})$

$$\mathcal{D}(\tilde{v}) = 2\tilde{v}^2(1 - 2\tilde{v}^2 + a\tilde{v}^4)(12\tilde{v} - 24a\tilde{v}^2 + 12a^2\tilde{v}^3)(1 - 3\tilde{v}^2 + 2a\tilde{v}^3) \tag{4.26}$$

and $\tilde{v}^2_{\rm isco} = 1/\tilde{r}_{\rm isco}$. We find that $k(a) = 1/4$ for all $a < 1$. The behaviour for near-extremal BHs is slightly different, which we will discuss further below.

For extremal BHs the various factors in the expression for $\mathrm{d}\ln e/\mathrm{d}\tilde{r}_0$ have repeated roots at the ISCO. To understand the behaviour for near-extremal BHs we therefore need to do an expansion in both R and ϵ. This takes the form

$$\frac{\mathrm{d}\ln e}{\mathrm{d}R} = \frac{a_0\epsilon^4 + a_1\epsilon^4 R + \sum_{i=2}^{5} a_i \epsilon^{\frac{2(6-i)}{3}} R^i + a_6 R^6 + \cdots}{\sum_{i=1}^{6} b_i \epsilon^{\frac{2(7-i)}{3}} R^i + b_7 R^7 + \cdots} \tag{4.27}$$

The terms omitted from both the numerator and denominator above are $\mathcal{O}(1)$ in ϵ. The ratio $a_0/b_1 = -1/4$, agreeing with the result for $k(a)$ found above. However, for $\epsilon \ll R$, the behaviour is not dominated by this term, but by the terms from a_6 in the numerator and from b_7 in the denominator. The leading order behaviour in this regime is therefore

$$\frac{\mathrm{d}\ln e}{\mathrm{d}R} = \frac{a_6}{b_7}\frac{1}{R}. \tag{4.28}$$

This is also exponential, but we find the ratio $a_6/b_7 = 3/2$, i.e., it is greater than zero and therefore the eccentricity *decreases* exponentially until we reach the regime $R \sim \epsilon$. This is the statement that the critical curve, where the sign of the eccentricity evolution changes, is in the near-horizon region, which is consistent with results in [261]. We conclude that for near-extremal BHs, eccentricity can only grow once the inspiraling object is already very close to the ISCO, which is typically already inside the transition zone.

To complete this discussion we need to determine the scaling of the initial eccentricity e_0. If the orbit is truly circular then the eccentricity remains zero, so there must be some mechanism to excite an initial eccentricity which can then grow. Eccentricity can be excited by other physical processes, such as the presence of perturbing material, e.g., dust, or gravitational interactions with third bodies. Those processes are important, but in the pure-vacuum case eccentricity could still in principle be excited by the evolution under radiation reaction. We argued earlier that corrections to the fluxes far from the horizon scale like $\eta\dot{\tilde{r}}$ which is η^2 during the adiabatic inspiral. These corrections mean that the first term in equation (4.23) is no longer exactly zero. Setting that term to η^2 we find an evolution equation of the form $\mathrm{d}e^2/\mathrm{d}\tilde{t} \sim \eta^2$. After a few orbits the eccentricity is then $\mathcal{O}(\eta)$. This eccentricity induced by second order corrections to

the evolution is damped by the process described above, until we reach the critical curve where it grows, eventually exponentially near the ISCO. This suggests appropriate initial conditions are $e_0 \sim \eta$ and $R_0 \sim \mathcal{O}(1)$.[3] We note that this mechanism could also excite eccentricity during the transition zone itself, but this would be of order $e^2 \sim \eta \dot{\tilde{r}} \epsilon^{\frac{2}{3}}$ and hence no larger than the non-geodesic past-history corrections described above. If eccentricity grew coherently throughout the transition zone, the eccentricity induced by this process would be no larger than $e^2 \sim \eta \dot{\tilde{r}} \epsilon^{\frac{2}{3}} T$, where T is the coordinate time elapsed through the transition zone, which is typically smaller than the eccentricity grown during adiabatic inspiral prior to the start of the transition zone.

In summarise, we expect corrections to the evolution equations that arise from higher-order terms in the flux to scale like $\eta \epsilon^{\frac{2}{3}} \dot{\tilde{r}}$ (which is $\eta \dot{\tilde{r}}$ in the OT regime discussed in Section 4.2.4), and we expect residual eccentricity in the transition zone to be no more than $e \sim \eta R^{-k(a)}$. In the non-near extreme case, these eccentricity corrections will be important when $e > R$, which implies $R < \eta^{1/(1+k(a))}$. In the near-extreme case, the corrections only become important when $R \sim \epsilon$, so we simply need to check that this is well inside the transition zone. In the analysis that follows we will evaluate the scaling of these terms and show that they are sub-dominant for inspirals into near-extremal BHs.

4.2.4 Ori and Thorne regime

Consider non-extremal BHs, i.e. rotating BHs where the extremality parameter ϵ is not close to zero so that $\eta \ll \epsilon$. In this regime of spins and according to the discussion below (A.13)-(A.18), all the coefficients controlling the general transition equation (4.18) and (4.19) are $\mathcal{O}(1)$. This is the regime originally discussed in [254].

Omitting coefficients of order one, the dominant contributions to the transition equation are

$$\left(\frac{dR}{d\tilde{\tau}}\right)^2 \sim R^3 + R\,\delta L + \Gamma_\odot, \quad \Gamma_\odot \sim \delta E - \delta L\,, \tag{4.29}$$

where we also omitted any further terms from (4.18) and (4.19) since they are subleading. Looking for a scaling solution $R \sim \eta^p$ and $\tilde{\tau} - \tilde{\tau}_{\rm isco} \sim \eta^q$, it follows, using equation (4.14) that

[3] A natural continuation of this argument would be to say that the second-order GSF induced corrections continue to drive eccentricity growth, over the whole of the inspiral, lasting a coordinate time $\sim \eta^{-1}$, leading to a final eccentricity of $\mathcal{O}(\eta^{1/2})$, which can be larger than the eccentricity grown through the mechanism discussed here. However, this assumes that the eccentricity grows coherently and monotonically. In practice, once the eccentricity is $\mathcal{O}(\eta)$, the radial motion due to eccentricity becomes larger than the amount the radius evolves over the relevant past-history that determines the GSF and so the argument that the latter is the dominant contribution to corrections no longer applies. Knowledge of the second-order GSF would be required to fully explore the further evolution of the eccentricity and this is not currently available. However, we expect that the growth of initial eccentricities of $\mathcal{O}(\eta)$ through the instability mechanism will be the dominant contributor to the residual eccentricity in the transition zone.

$\delta L \sim \eta^{1+q}$. Requiring all dominant terms to have the same scaling fixes $p = 2/5$ and $q = -1/5$, so that

$$R = \eta^{2/5}\mathcal{R}\,, \quad \tilde{\tau} - \tilde{\tau}_{\rm isco} = \eta^{-1/5}\mathcal{T}\,, \quad \delta L = \eta^{4/5}\delta\mathcal{L}\,. \tag{4.30}$$

Notice the overall scaling of the transition equation is $(d\tilde{r}/d\tilde{\tau})^2 \sim \eta^{6/5}$. The remaining question is whether the dominant term in $\Gamma_\odot \sim \delta E - \delta L$ is subleading or not. From (4.20), it follows $\delta E - \delta L \sim \eta^{6/5}$ in this regime, suggesting the change of variables

$$\Gamma_\odot = \eta^{6/5}\mathcal{Y}\,. \tag{4.31}$$

We can then write the schematic transition equation as

$$\left(\frac{d\mathcal{R}}{d\mathcal{T}}\right)^2 \sim \mathcal{R}^3 + \mathcal{R}\delta\mathcal{L} + \mathcal{Y}\,. \tag{4.32}$$

Terms in Eqs. (4.18) and (4.19) that have been dropped can be seen to scale like the above terms multiplied by additional powers of $\mathcal{R}$ or $\delta\mathcal{L}$. Since both $\mathcal{R}$ and $\delta\mathcal{L}$ are small quantities in the transition zone, these terms are sub-leading and we can ignore them.

The above scaling analysis proves the dominant terms in (4.18) in the regime $\eta \ll \epsilon$ are captured by

$$\left(\frac{dR}{d\tilde{\tau}}\right)^2 \simeq -\frac{2}{3}\alpha R^3 + 2\beta\,\delta L\,R + \Gamma_\odot + \dots \tag{4.33}$$

where we neglected all subleading corrections, kept the same original notation as in OT [254] for the coefficients

$$\alpha = -\frac{1}{4}\frac{\partial^3 G}{\partial\tilde{r}^3}\bigg|_{\rm isco} \tag{4.34}$$

$$\beta = \frac{1}{2}\left(\frac{\partial^2 G}{\partial\tilde{r}\partial\tilde{E}}\tilde{\Omega} + \frac{\partial^2 G}{\partial\tilde{r}\partial\tilde{L}}\right)_{\rm isco} \tag{4.35}$$

and the dominant contribution to (4.19) reduces to

$$\Gamma_\odot \simeq \tilde{\Omega}_{\rm isco}(\delta E - \delta L)\frac{\partial G}{\partial\tilde{E}}\bigg|_{\rm isco} + \dots\,, \tag{4.36}$$

Keeping all coefficients of order one, the natural scaled variables to introduce are

$$\begin{aligned} R &= \eta^{2/5}\alpha^{-3/5}(\beta\kappa)^{2/5}X \\ \tilde{\tau} - \tilde{\tau}_{\rm isco} &= \eta^{-1/5}(\alpha\beta\kappa)^{-1/5}T \\ \delta E - \delta L &= \eta^{6/5}Y \\ \delta L &= -\eta^{4/5}(\alpha\beta)^{-1/5}\kappa^{4/5}T \end{aligned} \tag{4.37}$$

where

$$\kappa = \left(\tilde{\Omega}^{-1}\frac{d\tilde{t}}{d\tilde{\tau}}\frac{d\tilde{E}_{\rm GW}}{d\tilde{t}}\right)_{\rm isco} . \tag{4.38}$$

Plugging this into (4.33), one obtains

$$\left(\frac{dX}{dT}\right)^2 = -\frac{2}{3}X^3 - 2XT + C_0\left(\tilde{\Omega}\frac{\partial G}{\partial E}\right)_{\rm isco} Y + \mathcal{O}(\eta^{2/5})$$

where we defined $C_0 = \alpha^{4/5}(\kappa\beta)^{-6/5}$. From now on, we ignore the subleading corrections.

The analogue of the acceleration equation (4.4) reduces to

$$\frac{d^2X}{dT^2} = -X^2 - T - \frac{1}{2(dX/dT)}\left(2X - C_0\left[\tilde{\Omega}\frac{\partial G}{\partial \tilde{E}}\right]_{\rm isco}\frac{dY}{dT}\right). \tag{4.39}$$

This depends on the time evolution of the circularity deviation parameter, Y, whose dominant contribution is derived in (4.20). Inserting the re-scaled variables (4.37) into equation (4.20)

$$\frac{dY}{dT} = -\frac{\partial \log\tilde{\Omega}}{\partial\tilde{r}}\bigg|_{\rm isco}(\beta C_0)^{-1}X\,, \tag{4.40}$$

leads to a transition equation

$$\frac{d^2X}{dT^2} = -X^2 - T - \frac{1}{2(dX/dT)}\left(2X + \beta^{-1}\left[\frac{\partial\tilde{\Omega}}{\partial\tilde{r}}\frac{\partial G}{\partial\tilde{E}}\right]_{\rm isco}X\right). \tag{4.41}$$

We now show that the term in parenthesis must vanish for circular orbits. A direct calculation using (2.5a),(2.8a), (2.8b) and (2.10) shows that equatorial circular orbits satisfy

$$\frac{\partial G}{\partial\tilde{E}}(\tilde{r})\,\tilde{\Omega}(\tilde{r}) + \frac{\partial G}{\partial\tilde{L}}(\tilde{r}) = 0\,, \tag{4.42}$$

where the equality holds for any circular orbit labelled by $(\tilde{r}, \tilde{E}, \tilde{L})$. Differentiating (4.42) with

respect to $\tilde{r}$, we can derive further equalities satisfied for any such orbits. The ones below

$$\frac{\partial\tilde{\Omega}}{\partial\tilde{r}}\frac{\partial G}{\partial\tilde{E}} = -\left(\frac{\partial^2 G}{\partial\tilde{r}\partial\tilde{E}}\,\tilde{\Omega} + \frac{\partial^2 G}{\partial\tilde{r}\partial\tilde{L}}\right) \tag{4.43}$$

$$\frac{\partial\tilde{\Omega}}{\partial\tilde{r}}\frac{\partial G}{\partial\tilde{E}} = -2\beta \tag{4.44}$$

for β given in equation (4.35), and so the last term vanishes in (4.41). This was inevitable, since this term is precisely the term that arises from the dissipative part of $f^{\tilde{r}}$ from equation (4.6), as identified earlier. The leading order evolution of Y is driven by maintaining the circularity of the orbit and so with this condition we expect the radial GSF corrections to be subleading.

The resulting transition equation of motion in the regime of low spins $\eta \ll \epsilon$ is

$$\frac{\mathrm{d}^2 X}{\mathrm{d}T^2} = -X^2 - T \tag{4.45}$$

and Y is evolved through the ODE (4.40). We note that the transition equation does not depend on Y in this regime. Corrections to this equation arising from evolution of Y enter at an order $\eta^{2/5}$ higher than leading and so are subdominant. As discussed earlier the evolution of Y is related to deviations from the linear-in-proper-time evolution of energy and angular momentum and so the fact that these corrections do not enter the transition equation for $\eta \ll \epsilon$ demonstrate that the linear evolution assumed by OT is appropriate in this regime.

Let us check the self-consistency of the transition equation (4.45) by verifying that all neglected corrections to it are indeed smaller when evaluated on the scaling regime (4.37). First, as discussed in section 4.2.1, the corrections to the orbit due to the conservative piece in the GSF are order $\mathcal{O}(\eta)$, see (4.13). This is indeed smaller than the "radial thickness" $R \sim \eta^{2/5}$ in (4.37). Second, corrections due to $\eta\dot{\tilde{r}}$, appearing in (4.3), are $\mathcal{O}(\eta^{8/5})$. Hence, these corrections are $\mathcal{O}(\eta^{3/5})$ smaller than the dominant δL and δE scaling in (4.37) [4]

Finally, corrections arising from eccentricity are subleading provided $e < R = \tilde{r} - \tilde{r}_{\rm isco}$, as discussed in Section 4.2.3. In the non-extremal case we therefore need $e < \eta^{\frac{2}{5}}$, due to (4.25). This yields the constraint

$$\eta^{1-2k/5} < \eta^{2/5} \quad \Rightarrow \quad 3 - 2k > 0 \quad \Rightarrow \quad k < \frac{3}{2}.$$

We saw previously that $k = 1/4 < 3/2$ for all spins $a < 1$, which satisfies this bound. We

[4] Using the more conservative assumption that the averaging timescale is determined by the period of radial oscillations, which scales with $T \sim \eta^{-\frac{1}{5}}$, the corrections are still suppressed by a factor of $\eta^{\frac{2}{5}}$. Third, corrections to $d\Gamma_{\odot}/d\tilde{\tau}$ arising from non-geodesic past history corrections to the fluxes scale like $\eta^{8/5}$ and those arising from additional terms in the expansion of the azimuthal frequency as a function of radius scale as $\eta^{9/5}$, which are both subdominant to the leading $\eta^{7/5}$ scaling, albeit only by a factor of $\eta^{1/5}$.

deduce that eccentricity corrections are subdominant in the non-near-extremal regime.

4.2.5 General transition equation of motion — near-extremal

Let us consider rapidly rotating BHs with spin parametrized by $a = \sqrt{1-\epsilon^2}$ for $\epsilon \ll 1$. The discussion below equations (A.13)-(A.18) allows us to identify the a priori dominant contributions to the transition equation (4.18) as

$$\begin{aligned} \left(\frac{dR}{d\tilde{\tau}}\right)^2 &\sim R^3 + R\,\delta L\,\epsilon^{2/3} + R^2\delta L + \delta L^2\,\epsilon^{4/3} + \Gamma_\odot \\ \Gamma_\odot &\sim (\delta E - \delta L)\left(\epsilon^{2/3} + R + \delta L\,\epsilon^{2/3}\right) . \end{aligned} \tag{4.46}$$

Since the functional dependence of the above equation does not depend on η, we learn the η scaling should be the same as before if we keep the R^3 and $R\,\delta L$ terms. Hence, we are left to determine any possible ϵ scaling. Proceeding as before, we look for scalings of the form $R \sim \eta^{2/5}\epsilon^p$ and $\tilde{\tau} - \tilde{\tau}_{\rm isco} \sim \eta^{-1/5}\epsilon^q$. We learn from equation (4.14) that $\delta L \sim \eta^{4/5}\epsilon^q$. Requiring these dominant terms to scale in the same way determines $p = 4/15$ and $q = -2/15$, so that

$$\begin{aligned} R &= \eta^{2/5}\epsilon^{4/15}\mathcal{R}\,, \quad \tilde{\tau} - \tilde{\tau}_{\rm isco} = \eta^{-1/5}\epsilon^{-2/15}\mathcal{T}\,, \\ \delta L &= \eta^{4/5}\epsilon^{-2/15}\delta\mathcal{L}\,. \end{aligned} \tag{4.47}$$

Hence, if $\eta \sim \epsilon$, the term $R^2\delta L$ scales like the velocity squared $(d\tilde{r}/d\tilde{\tau})^2 \sim \eta^{6/5}\epsilon^{4/5} \sim \epsilon^2$ and must be kept in the transition equation, whereas the term $\delta L^2\epsilon^{4/3}$ is $\mathcal{O}(\epsilon^{2/3})$ smaller and, consequently, subdominant.

The only remaining question is whether $\Gamma_\odot$ is relevant in this regime or not. Using (4.20) and the scalings (4.47), we infer $(\delta E - \delta L) \sim \eta^{6/5}\epsilon^{2/15}$. Since in the regime $\eta \sim \epsilon$, $R \sim \delta L \sim \epsilon^{2/3}$ we conclude $\Gamma_\odot \sim \eta^{6/5}\epsilon^{4/5} \sim (d\tilde{r}/d\tilde{\tau})^2$ and must be kept in the transition equation. Introducing the finite variable $\mathcal{Y}$

$$\Gamma_\odot = \eta^{6/5}\epsilon^{4/5}\mathcal{Y}\,, \tag{4.48}$$

the general transition equation in the $\eta \sim \epsilon$ regime reduces to

$$\left(\frac{d\mathcal{R}}{d\mathcal{T}}\right)^2 \sim \mathcal{R}^3 + \mathcal{R}\delta\mathcal{L} + \mathcal{R}^2\delta\mathcal{L} + \mathcal{Y}\,. \tag{4.49}$$

Notice the radial velocity throughout the transition regime scales like $d\tilde{r}/d\tilde{\tau} \sim \eta^{3/5}\epsilon^{2/5} \sim \eta$ in the regime $\epsilon \sim \eta$. This is as in the adiabatic regime, but smaller than in the OT regime where $d\tilde{r}/d\tilde{\tau} \sim \eta^{3/5}$.

As a self-consistency check, we can write the radial geodesic equation using the change of

variables (4.47) and (4.48)

$$\left(\frac{d\mathcal{R}}{d\mathcal{T}}\right)^2 \sim \sum_{i=3}^{\infty} \eta^{2(i-3)/5}\epsilon^{4(i-3)/15}\mathcal{R}^i + \delta\mathcal{L}\mathcal{R} + \sum_{m=2}^{\infty}\left(\frac{\eta}{\epsilon}\right)^{2(m-1)/5}\epsilon^{2(m-2)/3}\mathcal{R}^m\delta\mathcal{L} + \eta^{2/5}\epsilon^{4/15}\delta\mathcal{L}^2 + \sum_{n=1}^{\infty}\left(\frac{\eta}{\epsilon}\right)^{2(n+1)/5}\epsilon^{2(5n-1)/15}\delta\mathcal{L}^2\mathcal{R}^n + \mathcal{Y}. \quad (4.50)$$

It is apparent that the dominant terms are the $i = 3$ and $m = 2$ terms, all others being subleading.

The above scaling analysis proves the dominant terms in (4.18) in the regime $\eta \sim \epsilon$ are captured by

$$\left(\frac{dR}{d\tilde{\tau}}\right)^2 \simeq -\frac{2}{3}\alpha R^3 + 2\beta\,\delta L\,R + \gamma\,\delta L\,R^2 + \Gamma_\odot + \dots \quad (4.51)$$

where α and β are defined as in (4.34)-(4.35) and γ

$$\gamma = \left(\frac{\partial^3 G}{\partial\tilde{r}^2\partial\tilde{E}}\tilde{\Omega} + \frac{\partial^3 G}{\partial\tilde{r}^2\partial\tilde{L}}\right)_{\rm isco}, \quad (4.52)$$

As shown in (A.1), they are approximated by

$$\alpha \to 1\,, \quad \beta \to 2^{-2/3}\sqrt{3}\epsilon^{2/3} \equiv \hat{\beta}\,\epsilon^{2/3}\,, \quad \gamma \to \sqrt{3}\,, \quad (4.53)$$

for $\epsilon \to 0$. Furthermore, the dominant contributions to $\Gamma_\odot$ are

$$\Gamma_\odot = \tilde{\Omega}_{\rm isco}(\delta E - \delta L)\left(\frac{\partial G}{\partial\tilde{E}}\bigg|_{\rm isco} + \frac{\partial^2 G}{\partial\tilde{r}\partial\tilde{E}}\bigg|_{\rm isco} R + \dots\right). \quad (4.54)$$

Keeping all coefficients of order one, the natural scaled variables to introduce are

$$\begin{aligned} R &= \eta^{2/5}\epsilon^{4/15}\alpha^{-3/5}(\hat{\beta}\kappa)^{2/5}X\,, \\ \tilde{\tau} - \tilde{\tau}_{\rm isco} &= \eta^{-1/5}\epsilon^{-2/15}(\alpha\hat{\beta}\kappa)^{-1/5}T\,, \\ \delta E - \delta L &= \eta^{6/5}\epsilon^{2/15}Y \\ \delta L &= -\eta^{4/5}\epsilon^{-2/15}(\alpha\hat{\beta})^{-1/5}\kappa^{4/5}T\,. \end{aligned} \quad (4.55)$$

Since $\eta \sim \epsilon$, it follows that $R \sim \epsilon^{2/3}$. Hence, the near ISCO expansion corresponds to the near horizon geometry of the primary BH since, in BL coordinates, $|\tilde{r}_{\rm isco} - \tilde{r}_+| \sim \epsilon^{2/3}$. As a result, we will be able to use the (leading order and analytic) expression for the energy flux due to

gravitational radiation in (2.59). For $\epsilon \to 0$, κ in equation (4.38) takes the form

$$\kappa = \left(\tilde{\Omega}^{-1}\frac{d\tilde{t}}{d\tilde{\tau}}\frac{d\tilde{E}}{d\tilde{t}}\right)_{\rm isco} \to \frac{8}{\sqrt{3}}(\tilde{C}_H + \tilde{C}_\infty). \tag{4.56}$$

Notice $\kappa \sim \mathcal{O}(1)$ since $\tilde{C}_H + \tilde{C}_\infty \sim \mathcal{O}(1)$.

Ignoring subleading terms, the general transition equation (4.51) reduces to

$$\left(\frac{dX}{dT}\right)^2 = -\frac{2}{3}X^3 - 2XT - \frac{1}{2}(\eta/\epsilon)^{2/5}C_1 T X^2 + \tilde{\Gamma}_\odot \tag{4.57}$$

with

$$C_1 = \gamma(\alpha\hat{\beta}\kappa)^{-3/5}\kappa \tag{4.58}$$

$$\tilde{\Gamma}_\odot = \epsilon^{-4/5}\eta^{-6/5}\alpha^{4/5}(\hat{\beta}\kappa)^{-6/5}\Gamma_\odot. \tag{4.59}$$

Notice the appearance of the new term proportional to TX^2, compared to the OT regime, is due to the regime $\eta \sim \epsilon$.

Taking a further T derivative, we find the analogue of the acceleration equation (4.4) in this regime

$$\frac{d^2X}{dT^2} = -X^2 - T - \frac{1}{2}(\eta/\epsilon)^{2/5}C_1 XT + \frac{1}{2(dX/dT)}\left(-2X - \frac{1}{2}(\eta/\epsilon)^{2/5}C_1X^2 + \frac{d\tilde{\Gamma}_\odot}{dT}\right). \tag{4.60}$$

The time evolution of $\Gamma_\odot$ in (4.54) has two contributions : one proportional to dY/dT, which can be computed to second order in X^2 using (4.20) and a second one proportional to $Y(dX/dT)$. Altogether yields

$$\begin{aligned}\frac{d\tilde{\Gamma}_\odot}{dT} = &-(\hat{\beta}\epsilon^{2/3})^{-1}\frac{\partial\tilde{\Omega}}{\partial\tilde{r}}\frac{\partial G}{\partial\tilde{E}}X - (\eta/\epsilon)^{2/5}(\alpha\hat{\beta}\kappa)^{-3/5}\kappa\left(\frac{\partial\tilde{\Omega}}{\partial\tilde{r}}\frac{\partial^2 G}{\partial\tilde{r}\partial\tilde{E}} + \frac{1}{2}\frac{\partial^2 G}{\partial\tilde{r}^2}\frac{\partial\tilde{\Omega}}{\partial\tilde{r}}\right)_{\rm isco}X^2 \\ &+ (\eta/\epsilon)^{2/5}\alpha^{1/5}(\hat{\beta}\kappa)^{-4/5}\left(\tilde{\Omega}\frac{\partial^2 G}{\partial\tilde{r}\partial\tilde{E}}\right)_{\rm isco}Y\frac{dX}{dT}.\end{aligned} \tag{4.61}$$

We can simplify this equation further. Consider taking a time derivative of (4.44)

$$\frac{\partial\tilde{\Omega}}{\partial\tilde{r}}\frac{\partial^2 G}{\partial\tilde{r}\partial\tilde{E}} + \frac{1}{2}\frac{\partial^2\tilde{\Omega}}{\partial\tilde{r}^2}\frac{\partial G}{\partial\tilde{E}} = -\frac{1}{2}\left(\frac{\partial^3 G}{\partial\tilde{r}^2\partial\tilde{E}}\tilde{\Omega} + \frac{\partial^3 G}{\partial\tilde{r}^2\partial\tilde{L}}\right) \tag{4.62}$$

$$= -\frac{1}{2}\gamma. \tag{4.63}$$

Now, equation (4.61) can be written in a remarkably simple form

$$\frac{d\tilde{\Gamma}_{\odot}}{dT} = 2X + \frac{1}{2}(\eta/\epsilon)^{2/5} C_1 X^2 + (\eta/\epsilon)^{2/5} \alpha^{1/5} (\hat{\beta}\kappa)^{-4/5} \left(\tilde{\Omega} \frac{\partial^2 G}{\partial \tilde{r} \partial \tilde{E}} \right)_{\rm isco} Y \frac{dX}{dT}. \tag{4.64}$$

We see from this equation that the first two terms in the parenthesis of equation (4.60) cancel, this leaves only one non-trivial contribution to the acceleration equation

$$\frac{d^2X}{dT^2} = -X^2 - T - (\eta/\epsilon)^{2/5} (C_1 XT - C_2 Y)\,, \tag{4.65}$$

with constant defined by

$$C_2 = \frac{1}{2} \alpha^{1/5} (\hat{\beta}\kappa)^{-4/5} \left(\tilde{\Omega} \frac{\partial^2 G}{\partial \tilde{r} \partial \tilde{E}} \right)_{\rm isco}. \tag{4.66}$$

and evolution equation for Y such that

$$\frac{dY}{dT} = -\Lambda \left. \frac{\partial \log \tilde{\Omega}}{\partial \tilde{r}} \right|_{\rm isco} X, \text{ with } \Lambda = \alpha^{-4/5} \kappa^{6/5} \hat{\beta}^{1/5}. \tag{4.67}$$

In our treatment of the OT regime (non near-extremal spins), the terms in equation (4.65) were neglected since they scaled with $\eta^{2/5}$ and were subdominant. In the near-extremal case, one can clearly see that the XT and Y term are comparable to the (rescaled) radial acceleration provided $\eta \sim \epsilon$. As such, they *must* be included in the analysis. Our final transition equation of motion differs from equation (43) in [256], which correctly included the Y term but missed the cross term XT, which is the same order as the terms being retained. Our analysis improves on [256] in two additional ways. Firstly, Y was introduced in [256] as a mathematical construct to ensure conservation of the four-velocity norm. The evolution equation for Y was derived by forcing the equation of motion obtained from differentiation of the kinetic energy equation, equation (2.5a), to agree with that obtained by expansion of the left-hand-side of the acceleration equation, equation (4.4). This is equivalent to setting the radial GSF term to zero, which is equivalent to imposing the circular-to-circular condition. This physical interpretation of the procedure was not made clear in [256], nor the interpretation of Y as representing departures from the linear-in-proper-time evolution. Secondly, the scaling of the flux given in equation (2.59), given by (2.60) was not known at that time and this was left as an unspecified power of ϵ. Now that we know this scaling we can do a more complete analysis of the near-extremal regime.

The quantities above can be computed in the near-extremal limit, $\epsilon \to 0$,

$$\begin{aligned}\Lambda &= 2^{52/15}(\tilde{C}_H + \tilde{C}_\infty)^{6/5}/\sqrt{3} + \mathcal{O}(\epsilon^{2/3}) \\ C_1 &= 2^{8/5}(\tilde{C}_H + \tilde{C}_\infty)^{2/5} + \mathcal{O}(\epsilon^{2/3}) \\ C_2 &= 2^{-13/15}\cdot 3^{-1/2}(\tilde{C}_H + \tilde{C}_\infty)^{-4/5} + \mathcal{O}(\epsilon^{2/3}).\end{aligned} \tag{4.68}$$

Equations (4.65) and (4.67) are a coupled set of ODEs which will link the adiabatic inspiral to a plunging geodesic.

As in the previous section we now consider the size of corrections to the transition equation. Corrections to the circular flux-balance law in the geodesic part of the transition equation scale like $\eta\,\dot{\tilde{r}}\,\epsilon^{\frac{2}{3}}$ according to (4.3). These are $\mathcal{O}(\epsilon)$ smaller than the terms kept in this regime[5]. Similarly, corrections to the linear-in-proper-time angular momentum evolution enter through corrections to δE and δL and scale like $d\tilde{r}/d\tilde{\tau}$ times terms that are being retained. These are therefore subdominant since $d\tilde{r}/d\tilde{\tau} \sim \eta^{3/5}\epsilon^{2/5} \ll 1$. These corrections also contribute additional terms through corrections to the radial GSF part of the transition equation. These are of order $\eta\cdot\partial G/\partial\tilde{E}$ and $\eta\cdot\partial G/\partial\tilde{L}$, which scale like $\eta\epsilon^{2/3}$ and so are a factor of $(\eta/\epsilon)^{1/5}\epsilon^{1/3}$ smaller than the leading order terms in the transition equation and are therefore sub-dominant.

Eccentricity corrections enter like fractional e^2 corrections to the fluxes, and are only more important than the corrections described above if $e > R \sim \eta^{2/5}$ or $e^2 > \dot{\tilde{r}}$. In the near-extremal regime $\dot{\tilde{r}} \sim \epsilon^{2/3}\,\mathrm{d}r/\mathrm{d}\tau \sim \eta^{5/3}$ and so eccentricity corrections become important when $e > \eta^{5/6}$. However, as shown in Section 4.2.3, for near-extremal inspirals eccentricity can only grow once $\tilde{r} - \tilde{r}_{\rm isco} \sim \mathcal{O}(\epsilon)$. In the transition zone $\tilde{r} - \tilde{r}_{\rm isco} \sim (\eta/\epsilon)^{2/5}\epsilon^{2/3} \gg \epsilon$ and so eccentricity has not started to grow when the transition zone is reached. Residual eccentricity from the adiabatic inspiral would be $\mathcal{O}(\eta)$ and eccentricity excited during the transition would be $\mathcal{O}(\eta^{4/5}\epsilon^{8/15})$ (or $\mathcal{O}(\eta^{7/10}\epsilon^{7/15})$ if it was coherently excited throughout the transition). These are smaller than the threshold $\eta^{5/6}$ at which the eccentricity corrections become more important than the non-geodesic past history corrections, which we have already shown to be sub-leading.

4.2.6 General transition equation - very near-extremal

The final regime concerns very rapidly rotating BHs, where $\epsilon \ll \eta$. Using the results in appendix A.1, one can identify the a priori dominant contributions to the transition equation

[5] Using the conservative assumption about the averaging timescale, these corrections are sub-leading by a factor of $\eta^{\frac{2}{3}}$.

(4.18) and (4.19) to be (ignoring coefficients of $\mathcal{O}(1)$)

$$\begin{aligned}\left(\frac{dR}{d\tilde{\tau}}\right)^2 &\sim R^3 + R\,\delta L\,\epsilon^{2/3} + R^2\delta L + \delta L^2\,\epsilon^{4/3} + \Gamma_\odot \\ \Gamma_\odot &\sim (\delta E - \delta L)\left(\epsilon^{2/3} + R + \epsilon^{2/3}\delta L\right)\,.\end{aligned} \tag{4.69}$$

It is natural to expect that terms involving some explicit factors of ϵ should be sub-leading in this regime. Assuming a scaling solution of the form $R \sim \eta^\alpha$ and $\tilde{\tau} - \tilde{\tau}_{\rm isco} \sim \eta^\beta$, we learn using (4.14) that $\delta L \sim \eta^{\beta+1}$. Imposing the dominant terms R^3 and $R^2\delta L$ scale like $(dR/d\tilde{\tau})^2$ yields the scaling solutions $\alpha = 2/3$ and $\beta = -1/3$, so that

$$R = \eta^{2/3}\mathcal{R}\,, \quad \tilde{\tau} = \eta^{-1/3}\mathcal{T}\,, \quad \delta L = \eta^{2/3}\delta\mathcal{L}\,. \tag{4.70}$$

As a consistency check, notice the terms $\epsilon^{2/3}R\delta L \sim \eta^2(\epsilon/\eta)^{2/3}$ and $\epsilon^{4/3}\delta L^2 \sim \eta^{8/3}(\epsilon/\eta)^{4/3}$ are sub-dominant compared to the leading scaling $(d\tilde{r}/d\tilde{\tau})^2 \sim \eta^2$.

The remaining question is whether $\Gamma_\odot$ is negligible in this regime or not. Using the scalings (4.70) together with (4.20), we infer that $\delta E - \delta L \sim \eta^{4/3}$. It follows $\Gamma_\odot \sim \eta^2$ from the term linear in R in the second equation in (4.69). Introducing the finite variable $\mathcal{Y}$

$$\Gamma_\odot = \eta^2\mathcal{Y}, \tag{4.71}$$

leads to the transition equation of motion

$$\left(\frac{d\mathcal{R}}{d\mathcal{T}}\right)^2 \sim \mathcal{R}^3 + \mathcal{R}^2\delta\mathcal{L} + \mathcal{Y}\,. \tag{4.72}$$

Notice the radial velocity throughout the transition regime scales as $d\tilde{r}/d\tilde{\tau} \sim \eta$, as it were throughout the adiabatic inspiral regime and in the near-extremal case [see sec.(4.2.5)]. Thus the radial motion is fastest throughout the transition regime when the primary is of moderate spin: $\eta \ll \epsilon$.

As a consistency check, we can substitute the scalings (4.70) and (4.71) into the general

transition equation (4.18)

$$\left(\frac{d\mathcal{R}}{d\mathcal{T}}\right)^2 \sim \sum_{i=3}^{\infty} \eta^{2(i-3)/3}\mathcal{R}^i + (\epsilon/\eta)^{2/3}\delta\mathcal{L}\mathcal{R} + \sum_{m=2}^{\infty} \eta^{2(m-2)/3}\mathcal{R}^m\delta\mathcal{L} + \epsilon^{2/3}(\epsilon/\eta)^{2/3}\delta\mathcal{L}^2 + \epsilon^{4/3}\delta\mathcal{L}^2\mathcal{R} + \sum_{n=2}^{\infty} \eta^{2(n-1)/3}\delta\mathcal{L}^2\mathcal{R}^n + \mathcal{Y}. \quad (4.73)$$

Clearly the dominant terms occur when both $i = 3$ and $m = 2$ with the rest being subleading.

The above scaling analysis proves the dominant terms in (4.18) in the regime $\epsilon \ll \eta$ are captured by

$$\left(\frac{dR}{d\tilde{\tau}}\right)^2 \simeq -\frac{2}{3}\alpha R^3 + \frac{1}{2}\gamma\,\delta L\,R^2 + \Gamma_\odot + \dots \quad (4.74)$$

where α and γ are given in equation (4.53) with

$$\Gamma_\odot \simeq \tilde{\Omega}_{\rm isco}(\delta E - \delta L)\left.\frac{\partial^2 G}{\partial\tilde{r}\partial\tilde{E}}\right|_{\rm isco} R + \dots . \quad (4.75)$$

Keeping all coefficients of order one, the natural rescaled variables in this regime are

$$\begin{aligned} R &= \eta^{2/3}\alpha^{-3/5}\kappa^{2/5}X \\ \tilde{\tau} - \tilde{\tau}_{\rm isco} &= \eta^{-1/3}(\alpha\kappa)^{-1/5}T \\ \delta E - \delta L &= \eta^{4/3}Y \\ \delta L &= -\eta^{2/3}\alpha^{-1/5}\kappa^{4/5}T. \end{aligned} \quad (4.76)$$

In these variables, the radial velocity equation (4.74) can be expressed as

$$\left(\frac{dX}{dT}\right)^2 = -\frac{2}{3}X^3 - \frac{1}{2}K_1X^2T + \tilde{\Gamma}_\odot \quad (4.77)$$

with

$$\begin{aligned} K_1 &= \gamma\alpha^{-3/5}\kappa^{2/5}\,, \\ \tilde{\Gamma}_\odot &= \eta^{-2}\alpha^{4/5}\kappa^{-6/5}\Gamma_\odot\,, \end{aligned} \quad (4.78)$$

and κ as in (4.38).

Taking a further derivative with respect to T yields the acceleration equation

$$\frac{d^2X}{dT^2} = -X^2 - K_1XT + \frac{1}{2(dX/dT)}\left(\frac{d\tilde{\Gamma}_\odot}{dT} - \frac{1}{2}K_1X^2\right). \quad (4.79)$$

Using (4.20) together with (4.76), one finds that

$$\frac{d\tilde{\Gamma}_{\odot}}{dT} = \alpha^{1/5}\kappa^{-4/5}\tilde{\Omega}_{\rm isco}\frac{\partial^2 G}{\partial\tilde{r}\partial\tilde{E}}\bigg|_{\rm isco}\frac{dX}{dT}Y + \frac{1}{2}\alpha^{-3/5}\kappa^{2/5}\left(\frac{\partial\tilde{\Omega}}{\partial\tilde{r}}\frac{\partial^2 G}{\partial\tilde{r}\partial\tilde{E}} + \frac{1}{2}\frac{\partial^2 G}{\partial\tilde{r}^2}\frac{\partial\tilde{\Omega}}{\partial\tilde{r}}\right)_{\rm isco} X^2\,. \quad (4.80)$$

Plugging this back in (4.79) and using equation (4.63), the K_1X^2 term cancels and one is left with

$$\frac{d^2X}{dT^2} = -X^2 - K_1XT + K_2Y \quad (4.81)$$

together with the evolution equation for $Y(T)$ given by

$$\frac{dY}{dT} = -\alpha^{-4/5}\kappa^{6/5}\frac{\partial\log\tilde{\Omega}}{\partial\tilde{r}}\bigg|_{\rm isco} X\,. \quad (4.82)$$

where

$$K_2 = \frac{1}{2}\alpha^{1/5}\kappa^{-4/5}\tilde{\Omega}_{\rm isco}\frac{\partial^2 G}{\partial\tilde{r}\partial\tilde{E}}\bigg|_{\rm isco}\,.$$

In the limit $\epsilon \to 0$, the constants K_1 and K_2 approach the values

$$K_1 \to 2^{6/5}3^{3/10}(\tilde{C}_H + \tilde{C}_\infty)^{2/5}$$
$$K_2 \to 2^{-7/5}3^{-1/10}(\tilde{C}_H + \tilde{C}_\infty)^{-4/5}.$$

As argued in previous sections, corrections to the circular flux-balance law contribute terms to the transition equation which scale like $d\tilde{r}/d\tilde{\tau} \sim \mathcal{O}(\eta)$ times terms that are being retained and like $\eta\epsilon^{2/3}$. Corrections to the linear-in-time angular momentum evolution enter with the same scaling as the former. The retained terms in the transition equation scale like $\eta^{4/3}$ in the very near extremal regime and so these corrections are both sub-leading. Eccentricity corrections enter like fractional e^2 corrections to the fluxes, but, as in the near-extremal case, eccentricity cannot grow until the transition zone has already been reached, and so these corrections are no larger than $\mathcal{O}(\eta^{5/3}\,\epsilon^{2/3})$ and are also sub-leading.

We conclude this subsection by noting that the transition equation of motion (4.81) is perfectly well behaved in the limit $\epsilon \to 0$ and can therefore be used to compute an inspiral into a maximally spinning BH with $a = 1$. In this case, the horizon coincides with the ISCO in BL coordinates. However, the proper distance is $\Delta\tilde{\ell} \sim \frac{1}{3}\ln\epsilon$ (see Fig.2 in [164] together with explanations in [164, 262] and more recently in appendix A of [263] and explicitly calculated in equation (2.23)). Hence, we terminate the integration of the ODE (4.81) at $\tilde{r} = \tilde{r}_+$, since our numerics are specific to BL coordinates. The presence of the horizon manifests itself in the transformation from proper time to coordinate time, which will be discussed, for non-extremal

inspirals, in the next sub-section.

4.3 Results

4.3.1 Numerical integration

We now seek to compute a full worldline $\tilde{r}(\tilde{\tau})$ for $\infty > \tilde{r} \geq \tilde{r}_+$. Out of the three regimes just discussed, we restrict ourselves to the $\epsilon \sim \eta$ one. This is because the $\eta \ll \epsilon$ regime has already been considered in the literature [254, 256, 264, 265] and the $\epsilon \ll \eta$ regime has been argued to be inaccessible throughout the transition regime in [266]. The latter conclusion follows from the observation that the waves emanating from the secondary produce a *spin down* effect on the primary leading to a maximum attainable spin with $\epsilon \sim \eta$. For $\epsilon \sim \eta$, we try to find the solution to

$$\frac{d^2X}{dT^2} = -X^2 - T - (\eta/\epsilon)^{2/5}(C_1 XT - C_2 Y), \text{ with } \frac{dY}{dT} = -\frac{3}{4}\Lambda X\,, \tag{4.83}$$

which deviates off the past adiabatic inspiral and evolves into a geodesic plunge. The constants in equation (4.83) are given by equation (4.68). We can derive an equation for an adiabatic inspiral in proper time by using the quasi-circular approximation. Using our far-horizon expression for the energy flux defined by equation (2.59) with both equations (2.9b) and (2.8a), one derives

$$\frac{d\tilde{r}}{d\tilde{\tau}} = -\eta\frac{64}{5}\tilde{\Omega}^{7/3}\frac{(2a - 3\tilde{r}^{1/2} + \tilde{r}^{3/2})\tilde{r}}{\tilde{r}^2 - 6\tilde{r} + 8a\tilde{r}^{1/2} - 3a^2}\dot{\mathcal{E}}(\tilde{r}). \tag{4.84}$$

This equation diverges at the ISCO marking the breakdown of the quasi-circular approximation. We shall use equation (4.83) to smoothly transition from the adiabatic inspiral equation (4.84) into a geodesic plunge to the horizon. We used a cubic spline to interpolate values for the relativistic correction $\dot{\mathcal{E}}(\tilde{r})$ using exact flux data found in the BHPT. We then numerically integrate equation (4.84) by stepping forwards in proper time until $\tilde{L}(\tilde{\tau}) - \tilde{L}_{\rm isco} \sim \eta^{4/5}\epsilon^{-2/15}$. When this criterion is met we can be sure that our model for the flux (2.59) throughout the transition regime is correct to leading order. Once this is satisfied, we stop integrating our adiabatic inspiral solution and begin integrating our transition equation of motion (4.83).

Since we do not terminate our adiabatic inspiral solution at the ISCO, we do not know the precise proper time where the particle crosses the ISCO. As such, the variable T is not a good choice of variable to integrate on the right-hand side of (4.83). Instead, we substitute T for δL

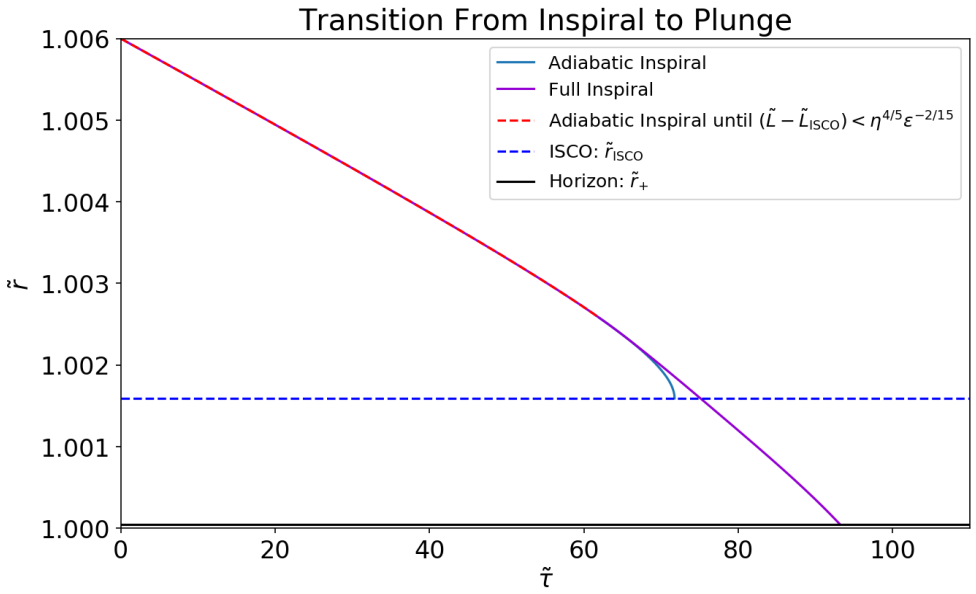

Figure 4.1: In both plots we consider mass ratio $\eta = 10^{-5}$ and spin $a = 1-10^{-9}$. The transition regime begins at $\tilde{r}_{\rm init} \approx 1.0026$ at $\tilde{\tau}_{\rm init} \approx 62.00$. The particle plunges into the horizon $\tilde{r}_+$ in proper time $\tilde{\tau}_+ \approx 93.19$.

from equation (4.55) into our transition equation of motion, giving *three* coupled ODEs

$$\begin{aligned}
\frac{d^2X}{dT^2} &= -X^2 + B_0\delta L + (\eta/\epsilon)^{2/5}(C_1 B_0 \delta L + C_2 Y) \\
\frac{dY}{dT} &= -\frac{3}{4}\Lambda X \\
\frac{d\delta L}{dT} &= B_0^{-1}, \quad B_0 = -\eta^{-4/5}\epsilon^{2/15}(\alpha\hat{\beta})^{1/5}\kappa^{-4/5}.
\end{aligned} \tag{4.85}$$

We use initial conditions determined by the end of the adiabatic inspiral equation (4.84) at some time $\tilde{\tau}_{\rm init}$.

$$\begin{aligned}
X(T_{\rm init}) &= \eta^{-2/5}\epsilon^{-4/15}\alpha^{-3/5}(\hat{\beta}\kappa)^{-2/5}(\tilde{r}_{\rm init} - \tilde{r}_{\rm isco}) \\
\left.\frac{dX}{dT}\right|_{T_{\rm init}} &= \eta^{-3/5}\epsilon^{-2/5}\alpha^{2/5}(\hat{\beta}\kappa)^{-3/5}\left.\frac{d\tilde{r}}{d\tilde{\tau}}\right|_{\tilde{\tau}_{\rm init}} \\
Y(T_{\rm init}) &= \eta^{-6/5}\epsilon^{-2/15}(\tilde{\Omega}_{\rm isco}^{-1}\delta E_{\rm init} - \delta L_{\rm init}) \\
\delta L(T_{\rm init}) &= \tilde{L}_{\rm circ}(\tilde{r}_{\rm init}) - \tilde{L}_{\rm isco}.
\end{aligned} \tag{4.86}$$

Where $\tilde{L}_{\rm circ}(\tilde{r}_{\rm init})$ corresponding to the circular angular momenta(2.8b) evaluated at the end of the inspiral, $\tilde{r}_{\rm init}$. Using this prescription, we are able to integrate the coupled ODEs equation (4.85) with initial conditions (4.86) to obtain Fig.(4.1). The transition solution smoothly deviates away from the adiabatic inspiral (blue curve), passes through the ISCO and reaches the horizon where the solution terminates. The plot on the right shows the full worldline in proper time $\tilde{r}(\tilde{\tau})$ where the inspiral starts at $\tilde{r} = 1.006$ and terminates at the horizon. This method ensures that $\tilde{r}(\tilde{\tau})$ is both continuous and once differentiable everywhere.

Also, by our choice of integrating (4.85) using the variable δL, we ensure continuity but *not* differentiability in $\tilde{L}$ throughout the full inspiral. We note here that Apte and Hughes in [264] also found discontinuities in their evolution of both $\tilde{L}$ and $\tilde{E}$ and added corrections to ensure both (first order) differentiability and continuity at $\tilde{\tau}_{\rm init}$. We consider a correction of the form

$$\tilde{L}(\tilde{\tau}) = \Delta\tilde{L}_{\rm cor} + \tilde{L}_{\rm isco} + \frac{d\tilde{L}_{\rm isco}}{d\tilde{\tau}}(\tilde{\tau} - \tilde{\tau}_{\rm isco}). \tag{4.87}$$

Recall that $\tilde{L}(\tilde{\tau}) - \tilde{L}_{\rm isco} = \delta L \sim \eta^{4/5}\epsilon^{-2/15} = (\eta/\epsilon)^{4/5}\epsilon^{2/3}$. This extra correction $\Delta\tilde{l}_{\rm cor}$ can be thought of as the next order in the taylor expansion of (4.87), excluding proper time evolution, such that $\Delta\tilde{L}_{\rm cor} \sim (d^2\tilde{L}/d\tilde{\tau}^2)_{\rm isco} \sim \eta^{6/5}\epsilon^{2/15} = (\eta/\epsilon)^{6/5}\epsilon^{4/3} \ll \delta L$. For $\eta \sim \epsilon$, we have that $\Delta\tilde{L}_{\rm cor} \sim \epsilon^{4/3} \ll \delta L \sim \epsilon^{2/3}$. This implies that adding a correction of the form $\Delta\tilde{L}_{\rm cor}$ *will* retain the spirit of the transition equations of motion. In other words, addition of $\Delta\tilde{L}_{\rm cor}$ is a subleading effect and no evolution equations have to be modified.

To calculate the evolution in $\tilde{E}$, one computes $\tilde{E}_{\rm circ}$ given by equation (2.8a) during the adiabatic inspiral regime. Using $\dot{\tilde{E}} = \tilde{\Omega}\dot{\tilde{L}}$, one integrates

$$\tilde{E} = \Delta\tilde{E}_{\rm cor} + \tilde{E}_{\rm isco} + \int_{\tilde{\tau}_{\rm isco}}^{\tilde{\tau}_+} \tilde{\Omega}(\tilde{r}) \left(\frac{d\tilde{L}}{d\tilde{\tau}}\right)_{\rm isco} d\tilde{\tau}. \tag{4.88}$$

The correction to $\Delta\tilde{E}_{\rm cor} \sim (\eta/\epsilon)^{6/5}\epsilon^{4/3}$ is chosen to ensure continuity with the end of the inspiral energy given by equation (2.8b). This is argued in a similar fashion as $\Delta\tilde{L}_{\rm cor}$.

Notice that the energy flux obeys $\dot{\tilde{E}} = \tilde{\Omega}(\tilde{r})\dot{\tilde{L}}_{\rm isco}$ and is thus *not* constant. This ensures that we are still granted a full cancellation of the dissipative part of the forcing term $\tilde{f}^{\tilde{r}}$ in equation (4.6). This will yield a continuous evolution $\tilde{E}$ at the matching point with a discontinuous first derivative. At this point we will have a full trajectory $\tilde{r}(\tilde{\tau})$ with (continuous) integrals of motion in proper time $\tilde{E}(\tilde{\tau})$ and $\tilde{L}(\tilde{\tau})$. In each of [254, 264, 265], the authors compute three separate worldlines in proper time; Adiabatic inspiral, transition, geodesic plunge. Apte *et al* in [264], provide an algorithm in which they freeze $\tilde{E}$ and $\tilde{L}$ when the extra terms in equation (4.45) exceed the leading order terms X^2 and T by $\sim 5\%$. As one would expect, as one ventures farther from the ISCO, the Taylor expansion used to derive these transition equations of motion will break down. As such, it is very natural for each of the aforementioned authors to compute a geodesic plunge to complete their worldlines in proper time $\tilde{r}(\tilde{\tau})$. For moderate spins (non near-extremal), $|\tilde{r}_+ - \tilde{r}_{\rm isco}| \sim \mathcal{O}(1) \nsim \eta^{2/5}$. For near-extreme BHs the ISCO is close to the horizon in BL coordinates $|\tilde{r}_{\rm isco} - \tilde{r}_+| \sim \epsilon^{2/3}$. The scaling of the near-extremal transition zone is also $\epsilon^{2/3}$ and so the horizon is reached while the object is still in the transition zone in BL coordinates. We therefore do not expect to need to add a geodesic plunge to compute full

near-extremal inspirals. To verify this we numerically calculate the extra terms in (4.85), which are

$$\begin{aligned} C_3 X^3, \text{ where } C_3 &= \frac{1}{12}\left(\frac{\eta}{\epsilon}\right)^{2/5} \epsilon^{2/3} \frac{\partial^4 G}{\partial \tilde{r}^4}\bigg|_{\text{isco}} \alpha^{-8/5} (\hat{\beta}\kappa)^{2/5} \\ C_4 XY, \text{ where } C_4 &= \frac{1}{2}\left(\frac{\eta}{\epsilon}\right)^{4/5} \epsilon^{2/3} \left(\tilde{\Omega}\frac{\partial^3 G}{\partial \tilde{r}^2 \partial \tilde{E}}\right)_{\text{isco}} (\alpha\hat{\beta}\kappa)^{-2/5}. \end{aligned} \tag{4.89}$$

We compare the solution to (4.85) when these terms are omitted or included in Figure 4.2. The difference is at most 1% even the horizon $\tilde{r}_+$. We conclude that we can use the solution from (4.85) *throughout* the plunging regime, for $\tilde{r}(\tilde{\tau}) \in [\tilde{r}_+, \tilde{r}_{\text{isco}}]$. It would be useful in the future to compare our results with the analytic geodesic plunges found in [213].

4.3.2 Radial trajectory in Boyer-Lindquist coordinates

In section 4.3.1, we computed the full worldline encapsulating inspiral, transition and plunge parametrised as $\tilde{r}(\tilde{\tau})$. We now intend to do the same but in coordinate time so that our worldline is in BL coordinates $(\tilde{t}, \tilde{r}(\tilde{t}), \theta = \pi/2, \phi(\tilde{t}))$.

For the quasi-circular inspiral solution, we integrate the circular relation relating coordinate time to proper time via equation (2.9b)

$$\tilde{t} = \int_0^{\tilde{\tau}_{\text{init}}} \frac{1 + a/\tilde{r}^{3/2}}{\sqrt{1 - 3/\tilde{r} + 2a/\tilde{r}^{3/2}}} d\tilde{\tau} \tag{4.90}$$

where $\tilde{r}(\tilde{\tau})$ is the worldline constructed by integrating equation (4.84) up to some suitable point to begin the transition solution, in our case, $\tilde{r}(\tilde{\tau}_{\text{init}}) = \tilde{r}_{\text{init}}$. To compute the trajectory in coordinate time $\tilde{r}(\tilde{t})$ throughout the transition regime, we must integrate

$$\tilde{t} = \tilde{t}(\tilde{\tau}_{\text{init}}) + \int_{\tilde{\tau}_{\text{init}}}^{\tilde{\tau}_+} T(\tilde{r}, \tilde{E}, \tilde{L}, a) d\tilde{\tau}, \tag{4.91}$$

where $T(\tilde{r}, \tilde{E}, \tilde{L}, a)$ is given by equation (2.5d). Throughout the transition regime, we use the model for both $\tilde{L}(\tilde{\tau})$ and $\tilde{E}(\tilde{\tau})$ given by equation (4.87) and equation (4.88). This will yield the $\tilde{r}(\tilde{t})$ throughout the transition regime. Combining these results yield a full trajectory from radial infinity to the horizon in coordinate time $\tilde{r}(\tilde{t})$.

To calculate the angular frequency $d\phi/d\tilde{t} = \tilde{\Omega}$ in coordinate time we substitute $\tilde{r}(\tilde{t})$ found previously into equation (2.10). This now gives $\tilde{\Omega}(\tilde{t})$ valid throughout the adiabatic inspiral regime. Using our solutions for $\tilde{E}(\tilde{\tau})$ and $\tilde{L}(\tilde{\tau})$ defined through equation (4.87) and equation (4.88) and $\tilde{r}(\tilde{t})$ throughout the transition regime, we calculate

$$\tilde{\Omega} = \frac{d\phi}{d\tilde{\tau}}\left(\frac{d\tilde{t}}{d\tilde{\tau}}\right)^{-1} = \frac{2a\tilde{E}\tilde{r} - a^2\tilde{L} + \tilde{\Delta}\tilde{L}}{\tilde{E}(\tilde{r}^2 + a^2)^2 - 2a\tilde{L}\tilde{r} - \tilde{\Delta}a^2\tilde{E}}. \tag{4.92}$$

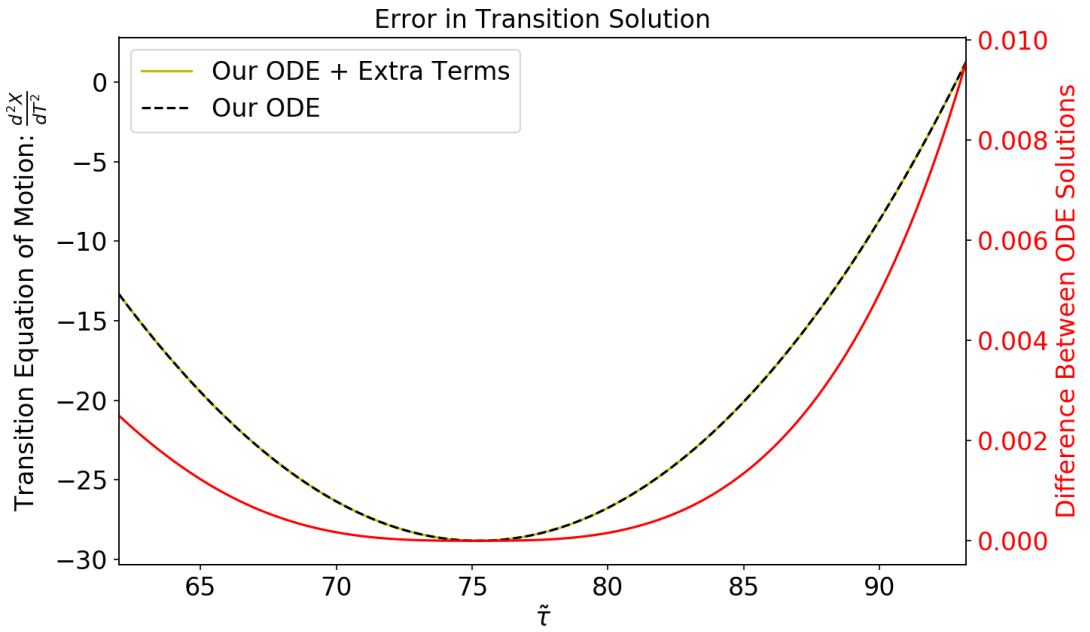

Figure 4.2: Solution to (4.85) (black dashed line) and difference in solution when including the higher-order corrections given in equation (4.89) (red solid line). The numerical difference is small throughout the transition regime reaching a maximum at plunge of $\sim 1\%$.

Where $\tilde{\Delta} = \tilde{r}^2 - 2\tilde{r} + a^2$ where we used both (2.5c) and (2.5d). The algorithm presented in section 4.3.2 will provide a trajectory in coordinate time $\tilde{r}(\tilde{t})$, which will be used for our waveform generation. An example is shown in figure 4.3, and we stress here that $\tilde{r}(\tilde{t})$ is continuous and (once) differentiable.

4.3.3 Near-extremal waveform

By combining the results from the previous sections, we are now armed to build a near-extremal waveform encapsulating the transition from inspiral to plunge. To do so, we follow the details presented in chapter 2 in section 2.4.3. For simplicity, we neglect the SWSH and consider the simplified waveform model (2.64). We outline our algorithm below.

Recall the sky-averaged RMS gravitational waveform at radial infinity

$$h_{\rm o} = \frac{2\sqrt{\eta \dot{\tilde{E}}^{\infty}_{m,\rm GW}}}{m\tilde{\Omega}D} \sin(2\pi \tilde{f}_m t + \phi_0)\,, \tag{4.93}$$

with $f_m = m\tilde{\Omega}/2\pi$ the GW frequency per harmonic m and $\dot{E}^{\infty}_{m,\rm GW}$ the outgoing energy flux at harmonic m. These were discussed in section 2.4.3. For a spin parameter $a = 1 - 10^{-9}$, we use an open source `Teukolsky` solver in the BHPT to construct a cubic spline for each outgoing flux $\dot{\tilde{E}}^{\infty}_{m,\rm GW}$ for $m = \{1, \ldots, 20\}$. The Teukolsky coefficients in equation (2.45) are defined such that $\tilde{Z}^{\infty}_{lm} \to 0$ as $\tilde{r} \to \tilde{r}_+$ [194]. This implies that $\dot{\tilde{E}}^{\infty}_{m,\rm GW} \to 0$ as $\tilde{r} \to \tilde{r}_+$, giving us reason to

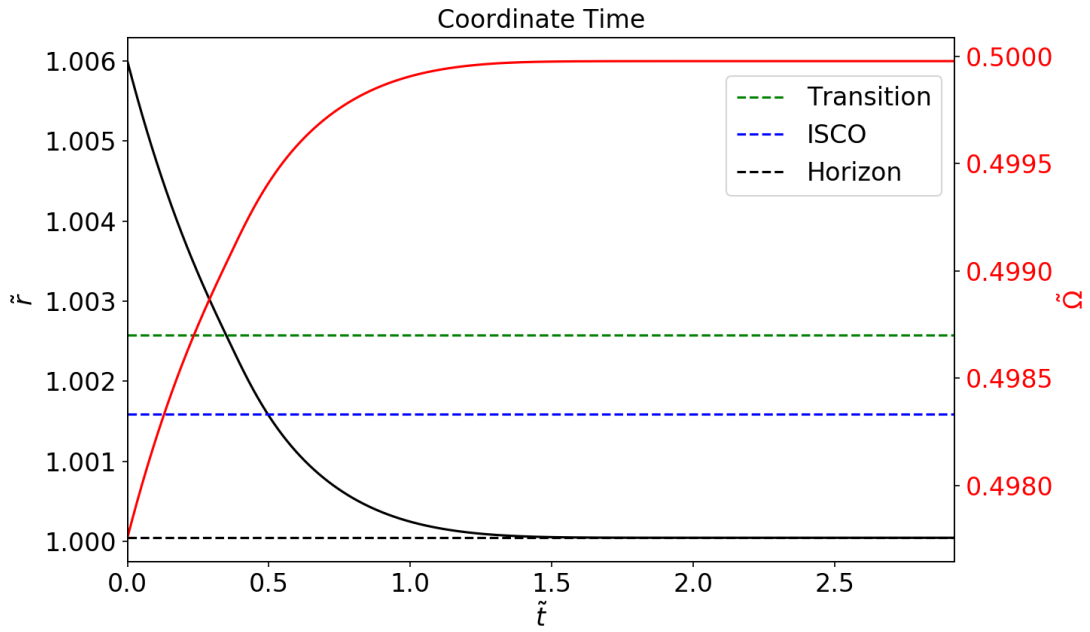

Figure 4.3: The red curve shows the angular frequency $\tilde{\Omega}$ and the black curve shows the trajectory in coordinate time $\tilde{r}(\tilde{t})$. Notice the smooth evolution of both $\tilde{r}(\tilde{t})$ and $\tilde{\Omega}$ during the start of the transition (green dashed curve). This smooth evolution continues through the ISCO (blue dashed curve) and evolves towards the horizon (black dashed curve).

smoothly extrapolate each of the outgoing fluxes per harmonic m to zero once the ISCO has been reached — a similar approach to that found in [267].

In order, the radial trajectory $\tilde{r}(\tilde{\tau})$ is constructed in proper time using (4.84), (4.85) with initial conditions $\tilde{r}_{\rm init} = 3$ and transition equation initial conditions (4.86). No plunging geodesic is attached since the transition equations of motion are valid all the way to the horizon. The proper time evolution in $\tilde{r}(\tilde{\tau})$ is then converted into coordinate time using (4.90) and (4.91) respectively. Outside the transition regime we calculate $\tilde{\Omega}(\tilde{t}) = (\tilde{r}(\tilde{t})^{3/2} + a)^{-1}$ and during the transition (4.92). All quantities we have calculated are all continuous once differentiable since we have incorporated the modified $\tilde{L}(\tau)$ and $\tilde{E}(\tau)$ from (4.87) and (4.88). Using this result, we plot an RMS sky-averaged near-extremal waveform containing inspiral and transition/plunge in figure 4.4.

We notice that the waveform in Figure 4.4 exhibits the usual dampening before the ISCO is reached as seen by Gralla *et al* in [211]. A close-up of the waveform at the point the transition is made is shown in the bottom panel of figure 4.4. We remark that both the amplitude and phase evolution of the signal quantitatively matches the adiabatic Teukolsky based waveform present in [211], figure 3. The exponential dampening feature shown in figure 4.4 is a unique feature to near-extreme EMRIs as a GW source. The dampening feature arises due to the energy flux at infinity $\dot{E}_{\infty,m} \to 0$ as $\tilde{r} \to \tilde{r}_{\rm isco}$. As the smaller body inspirals, more gravitational radiation

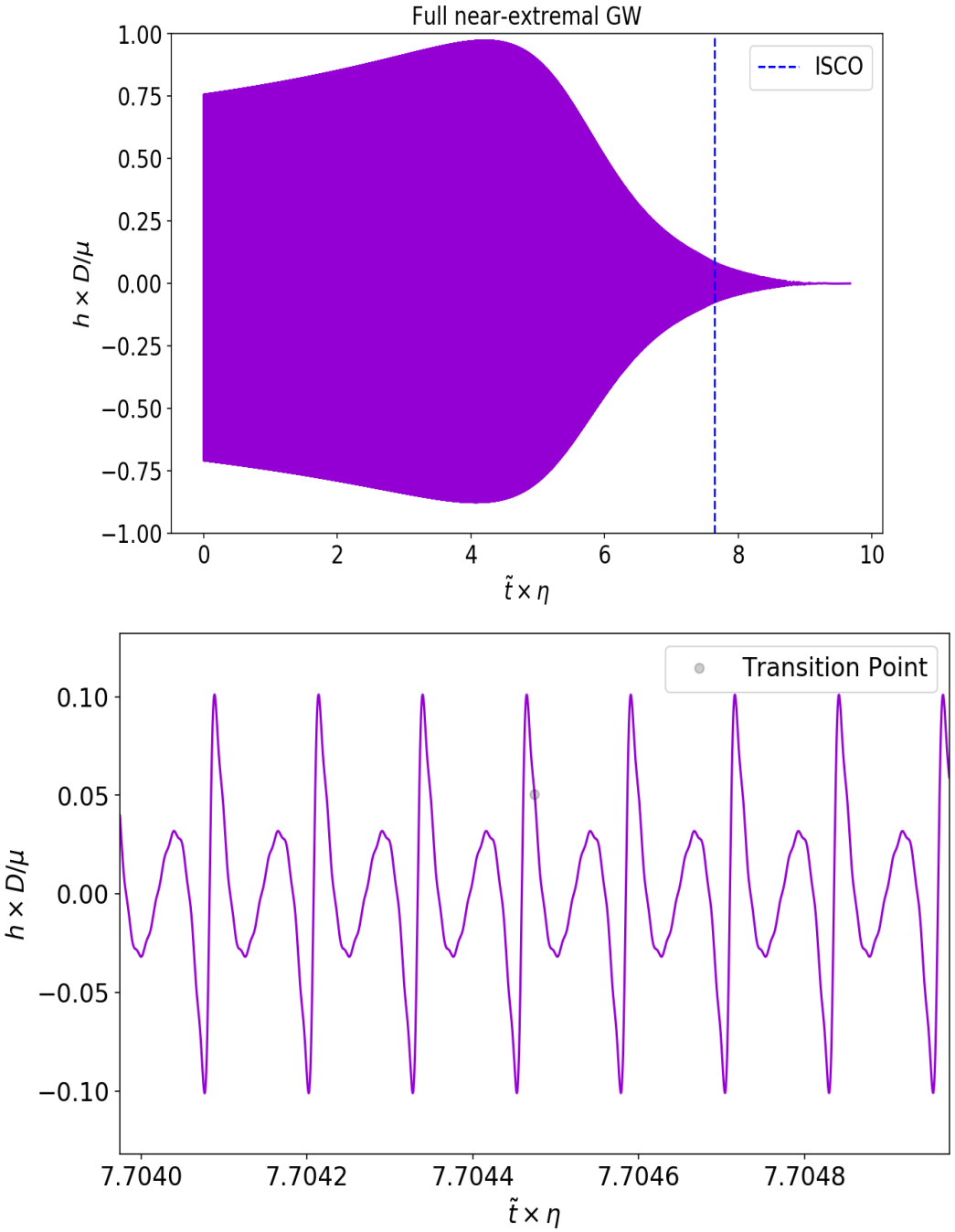

Figure 4.4: (Top Plot) Here we plot the RMS gravitational waveform for both inspiral, transition and plunge using the first twenty harmonics. Notice the smooth evolution of $h(\tilde{t})$. We terminate evolution of the waveform close to the plunge $\tilde{r} = \tilde{r}_+ + \delta$ for suitably chosen $0 < \delta \ll 1$, otherwise the waveform will continue to decay for infinite coordinate time. This is obvious since the (point-like) particle as observed from infinity will never reach the horizon. In this example, we considered $a = 1 - 10^{-9}$ and $\eta = 10^{-5}$ so that we are in the $\epsilon \sim \eta$ regime. (Bottom Plot) We plot a zoomed in version of the top plot to show the reader the smooth evolution of our adiabatic inspiral waves into the transition waves. The faded black dot indicates the moment the transition solution is turned on.

is sent down the throat and so the amplitude of the waves are suppressed. We will discuss this in more detail in chapter 5

4.4 Conclusion

This chapter has presented a solution to the problem of the transition from inspiral to plunge, *for any* primary spin, for CO on a circular and equatorial orbit around a MBH. This work has extended the treatment of Ori & Thorne [254] which was the first analysis of this problem but did not apply to systems with near-extremal spins. This work also extended the analysis of [256] which did consider near extremal spins, by providing a better physical interpretation of the procedure, identifying a missing term in the analysis and updating the treatment to use recent calculations of the near-extremal energy flux. We have also carefully identified the scaling of the various higher order terms arising from effects such as eccentricity and non-geodesic past-history to carefully demonstrate that these are all sub-dominant. Previous treatments have assumed that the quasi-circular assumption holds throughout the inspiral, but without rigorous justification. We have demonstrated that initial eccentricities excited during the adiabatic inspiral regime grow by the time the transition regime is reached, but are still sufficiently small to be sub-dominant. We have shown that corrections to the flux balance law (4.7) arising from eccentricity and from the non-geodesic past-history of the orbital evolution are also sub-dominant, if only marginally, but there are non-trivial deviations from the linear-in-proper-time evolution of energy and angular momentum in (4.14) that was assumed in OT. These deviations are encoded in the evolution of the parameter $\tilde{\Gamma}_{\odot}$ through the transition regime.

Based on these arguments, we have derived a transition equation for each of the three scaling regimes: $\eta \ll \epsilon$, $\eta \sim \epsilon$ and $\eta \gg \epsilon$ and described a numerical scheme to generate a full inspiral trajectory in coordinate time, from radial infinity to the horizon. For near-extremal BHs, we found that there was no need to attach a geodesic plunge onto the transition solution as the inspiraling object reaches the horizon while still within the transition regime. Finally, we used these inspiral trajectories to construct a near-extremal waveform exhibiting the transition and plunging dynamics using results from the BHPT [204].

The OT procedure is straightforward, but with surprisingly rich phenomenology. Through semi-analytic means, one is able to derive an equation which describes the dynamics within the vicinity of the ISCO. However, *in practice*, the OT theory has several shortcomings. The point at which the transition solution is taken to start has a significant influence on the time it takes the particle to reach the horizon and so the OT procedure does *not* define a unique worldline

given a particular set of parameters for the source. This is clearly not physical behaviour. We argued in section 4.3.1 that if the switch from the adiabatic inspiral to the transition equation is made when the constraint $\delta L \sim \eta^{4/5}\epsilon^{-2/15}$ is satisfied, the solution will be almost unique. This was verified numerically and we found it leads to plunge times consistent within $\pm 0.5M$. This very same problem was found in [264] but they saw no effect in their waveform analysis. For the $\eta \ll \epsilon$ case, there is a further degree of freedom as to when to attach the geodesic plunge. To do so, one must "freeze" the integrals of motion $\tilde{E}, \tilde{L}$ at the end of the transition regime and integrate the Kerr geodesic equations forward in coordinate time. Attaching the geodesic plunge is discussed, at length, in [264] but does not have a unique solution. Care must be taken as to when the transition solution and the geodesic plunge is attached or comparatively different radial trajectories will be produced. Fortunately for the $\epsilon \sim \eta$ case, there is no need to attach a geodesic plunge as shown earlier in section 4.3.1.

Another issue with the OT method is that it can lead to discontinuities in the constants of motion $\tilde{E}(\tau)$ and $\tilde{L}(\tau)$ if the OT equations are integrated backwards from the ISCO rather than forwards from the point of the switch from the adiabatic inspiral to transition regime. Discontinuities in the constants of motion lead to discontinuities in the coordinate time trajectories and in the waveforms which must be avoided if these waveforms are to give physically reasonable results in parameter estimation studies. Our solution, which was to integrate forward not backwards, yields continuous, but not first order differentiable, trajectories. The procedure described in [264] provides both. For parameter estimation studies we only require continuity of $\tilde{E}$ and $\tilde{L}$ and first order differentiability of $\tilde{r}(\tilde{t})$ and so our procedure should be sufficient, although this should be examined more carefully.

There are natural extensions of this work. First of all, our waveforms are missing the quasi-normal mode ringdown contribution. Hence, it would be very interesting to generate a *full* waveform taking these into account, together with the plunging dynamics discussed here. Details on how to construct the waveform including this effect were discussed in [268]. It would also be of interest to extend the current analysis to inspirals that are not circular and equatorial. The extension of OT was first performed in [265] who attempted to solve the problem for generic orbits; both eccentric and inclined orbits. Sundararajan's treatment was corrected by [264] in the case of arbitrary inclination. Hence, no one, as of yet, has considered the transition from inspiral to plunge in the case of eccentric orbits *and* inclined orbits. These orbits are expected for EMRIs formed through standard astrophysical channels [111]. The extension to eccentric orbits will require more careful modelling of the GSF and the use of the (eccentricity-dependent) separatrix in place of the ISCO among other complications. A model

of the transition for inspirals on *generic* orbits into BHs *arbitrary* spin will be invaluable for the analysis of future LISA EMRI observations and is an important future topic of study. Finally, the waveforms constructed in this chapter can be used to carry out a parameter estimation study to understand how well the parameters of near-extremal EMRIs can be measured with observations by LISA. Of particular interest is how well the spin can be determined, since the identification of an object that definitely has spin above the Thorne limit would be of profound significance. This topic is explored in chapter 5 where we show that near-extremal waveforms offer unparalleled precision measurements on the spin parameter.

Chapter 5

Constraining the spin parameters of near-extremal black holes using LISA

5.1 Introduction

Super massive black holes with a large spin parameter are abundant throughout our universe. Observations indicate that MBHs reside in the centres of most galaxies, where these BHs are known to accrete matter and hence are predicted to have very high spins [80, 269, 109, 270, 271, 272]. The dimensionless Kerr spin parameter of a Kerr BH, cannot exceed 1, since the resulting spacetime contains a naked singularity no longer encased within a well defined horizon. Thorne [273] showed that a moderately spinning BH cannot be spun up by thin-disc accretion above a spin of $a \approx 0.998$. However, in principle primordial BHs could be formed with spins exceeding that value [274]. As discussed in section 2.1.1, near-extremal BHs with spins close to the limit of $a = 1$ have interesting properties, and we focus our attention on these here.

This past decade, researchers [205, 211, 152, 212, 209, 206, 207, 208, 209, 210, 213] have explored the rich properties of near-extremal EMRIs. The characteristics of the gravitational waves emitted from these systems are unique, exhibiting an exponential dampening phase close to ISCO (see figure 4.4), which would prove a smoking gun for the existence of these near-extremal systems (see [211]). In this chapter, we show qualitatively that the inspiraling dynamics of the CO into a near-extremal MBH is very different from that into a moderately spinning BH, and these differences are reflected in the emitted GWs. As such, in order to detect and

correctly perform parameter estimation on these near-extremal sources, it is essential to update our family of waveform models to include them. We will argue throughout this work that, if observed, near-extreme BHs offer *significantly* greater precision measurements on the Kerr spin parameter than moderately spinning systems. In particular, LISA will have the capability to successfully conclude whether the central object in an EMRI system is truly a near-extremal BH. Thus, if near-extremal BHs exist, LISA observations of EMRIs may be one of the best ways to find them.

In this chapter we will consider only EMRIs on circular and equatorial orbits around near-extremal primary BHs. This choice is made primarily for computational convenience, but there are also astrophysical scenarios that produce such systems. As discussed in [275], COs can form within accretion disks around MBHs. When these objects fall into the central BH, the resultant EMRI will be circular and equatorial. Super-Eddington accretion can provide a means to spin up a BH past the Thorne limit [276], and so it is not unreasonable to expect that this EMRI formation channel would be more important for near-extremal systems. The standard EMRI formation channel, involving capture of a CO via scattering interactions, tends to form EMRIs with moderate initial eccentricities. However, this eccentricity decreases during the inspiral due to the emission of gravitational radiation [277]. This decrease in eccentricity continues until the orbit reaches a critical radius at which is starts to increase again [278, 197]. The critical radius moves closer to the last stable orbit as the spin parameter increases and for near-extremal systems is located within the regime where transition from inspiral to plunge occurs [255, 163]. We showed in chapter 4 that the increase in eccentricity is a subdominant effect throughout the transition regime. As the spin increases, we therefore expect that for an object captured at a fixed radius, the amount of eccentricity dissipated before the critical radius increases, and the eccentricity gained after the critical radius decreases. Therefore, even in the standard capture picture it is reasonable to assume the eccentricity is small at the end of the inspiral. We will show in this paper that very precise measurements of spin for near-extremal systems are possible, but this precision comes from observation of features [211] in the final phase of the inspiral, which is where the near-circular assumption is most likely to be valid.

This chapter is organised as follows. In section 5.2, we set notation and discuss the trajectory of a CO on a circular and equatorial orbit around a near-extremal Kerr BH. In section 5.3, we show that the spin dependence of kinematical quantities appearing in the radial evolution rather than radiation-reactive effects dominate the spin precision measurements for near-extremal EMRI systems. Our Teukolsky based waveform generation schemes are outlined in section 5.4. We discuss prospects for detection in section 5.5, arguing that LISA is more sensitive to heavier

mass systems $M \sim 10^7 M_\odot$ than lighter systems $M \sim 10^6 M_\odot$. Our FM results are presented in section 5.6. Here we show that we can constrain the spin parameter $\Delta a \sim 10^{-10}$, even when correlations amongst other parameters are taken into account. Finally, in section 5.7, we perform a Bayesian analysis to verify our FM results, before finishing with conclusions and outlooks in section 5.8.

5.2 Orbital motion

We consider the inspiral of a secondary test particle of mass μ on a circular, equatorial orbit around a primary SMBH with mass M and Kerr spin parameter $a \lesssim 1$ where the mass ratio is assumed small $\eta = \mu/M \ll 1$. The secondary is on a prograde orbit aligned with the rotation of the primary BH with $a > 0$ and dimensionful angular momentum $L > 0$.

The orbit of the secondary into the primary MBH will be circular and equatorial. The energy and angular frequency of a particle on this orbit are defined by equations (2.8a) and (2.10). As the main aim of this chapter is to constrain the spin parameter of these near-extremal BHs, we do *not* incorporate the transition from inspiral to plunge. We plan to tackle that problem in a future research project.

As discussed in chapter 4, equation (4.1), the radial evolution of the secondary in coordinate time is can be modelled through

$$\frac{d\tilde{r}}{d\tilde{t}} = -\frac{\dot{\tilde{E}}_{\rm GW}}{\partial_{\tilde{r}}\tilde{E}} \,. \tag{5.1}$$

Here $\dot{\tilde{E}}_{\rm GW}$ is the orbit-averaged first order dissipative flux defined in equation (2.55a) with relation to total energy dissipation of the orbit through (2.56a). The ordinary differential equation (ODE) (5.1) is easily numerically integrated given an expression for the energy flux $\dot{\tilde{E}}_{\rm GW}$, such as (2.58).

The inspirals are evolved from some initial coordinate radius and evolved to a coordinate radius $\tilde{r}_{\rm cut} \gtrsim 1 + \alpha^{-3/5}(\hat{\beta}\kappa)^{2/5}\epsilon^{4/15}\eta^{2/5}$ with α, γ and κ defined in (4.34), (4.52) and (4.38) respectively, and $\beta = \hat{\beta}\epsilon^{2/3}$ defined in (4.35). In order to avoid potential artifacts arising from the quasi-circular approximation breaking down. We will always consider $\eta \lesssim \epsilon$ so this choice is conservative. We motivated this truncation for the radial coordinate in the details contained in the previous chapter 4, specifically equation (4.55).

All the numerical work presented in this chapter, which is found in section 5.5 onwards, will use the exact fluxes obtained from BHPT. However, to understand our numerical results, we develop a set of new analytic tools in sections 5.3.1 and 5.3.3. These will partially make use of

a	$\dot{\tilde{E}}_{\rm Exact}/\eta$	$\dot{\tilde{E}}^{+}_{\rm NHEK}/\eta$	$\dot{\tilde{E}}_{\rm NHEK}/\eta$	$\lvert\dot{\tilde{E}}^{+}_{\rm NHEK}-\dot{\tilde{E}}_{\rm Exact}\rvert/\eta$	$\lvert\dot{\tilde{E}}_{\rm NHEK}-\dot{\tilde{E}}_{\rm Exact}\rvert/\eta$
$1-10^{-5}$	0.0264197	0.0261523	0.0300885	0.0002674	0.0036688
$1-10^{-6}$	0.0129344	0.0125200	0.0137455	0.0004143	0.0008111
$1-10^{-7}$	0.0061516	0.0059484	0.006333	0.0002031	0.0001814
$1-10^{-8}$	0.0028875	0.0028082	0.0029294	0.0000793	0.0000419
$1-10^{-9}$	0.0013472	0.0013193	0.0013575	0.0000280	0.0000103
$1-10^{-10}$	0.0006273	0.0006176	0.0006296	0.0000097	0.0000023
$1-10^{-11}$	0.0002915	0.0002883	0.0002922	0.0000031	0.0000007
$1-10^{-12}$	0.0001354	0.0001344	0.0001356	0.0000009	0.0000002

Table 5.1: NHEK fluxes at the ISCO computed using the approximations Eq. (2.59) (denoted $\dot{\tilde{E}}^{+}_{\rm NHEK}$) and Eq. (5.2) (denoted $\dot{\tilde{E}}_{\rm NHEK}$), and computed exactly using BHPT (denoted $\dot{\tilde{E}}_{\rm Exact}$ and based on the first thirty m and l modes).

the leading contribution to (2.59)

$$\dot{\tilde{E}}^{\rm NHEK}_{GW} \approx \eta(\tilde{C}_H + \tilde{C}_\infty)x \ , \quad x = \tilde{r} - 1 \ll 1. \tag{5.2}$$

This differs from (2.59) by $\mathcal{O}(\epsilon)$ contributions since $\tilde{r}-1$ measures the BL radial distance to the extremal horizon and *not* the radial distance to the near-extremal horizon $\tilde{r}_+$. The approximation (5.2) can be derived from first principles by solving the Teukolsky equation in the NHEK region. Our numerical analysis based on the BHPT, suggests the spin dependence of certain observables, to be discussed in section 5.3.2, is better captured by (5.2). Table 5.1 compares the flux at $\tilde{r}_{\rm isco}$ computed using BHPT to that obtained from the near-extremal approximations of Eq.(2.59) and Eq.(5.2). This table corroborates that (5.2) is a good approximation to the total energy flux, particularly in the limit as $a \to 1$, where it outperforms the full expression, (2.59).

5.2.1 Waveform models

In this work, we shall consider two different waveform models. For the analytic discussion in section 5.3, we will use the sky-averaged waveform model presented in section 2.4.3. Whereas the numerical results in sections 5.6 and 5.7, we use the Teukolsky based waveform described in section 2.4.1. To remind the reader, the sky-averaged RMS gravitational waveform at infinity (2.62)

$$h(\tilde{t};\boldsymbol{\theta}) \approx \sum_{m=2}^{\infty} h_{{\rm o},m} \sin(2\pi \tilde{f}_m \tilde{t} + \phi_0) \, . \tag{5.3}$$

For simplicity, we ignore the $m = 1$ contribution since, as argued in [109], this is subleading to the $m \geq 2$ contributions. The phase depends on the initial phase ϕ_0 and the frequencies of

the waves are given at each harmonic in m (2.65)

$$\tilde{f}_m = \frac{m}{2\pi}\tilde{\Omega}\,. \tag{5.4}$$

The relation between the RMS amplitude and the outgoing radiation flux in harmonic m is

$$h_{o,m} = \frac{2\sqrt{\eta \dot{\tilde{E}}^{\infty}_{m,\mathrm{GW}}}}{m\tilde{\Omega}\tilde{D}}\,, \tag{5.5}$$

where $\tilde{D} = D/M$ is the distance to the source from earth. Using Eq.(2.66), we can rewrite $h_{o,m}$ as

$$h_{o,m} = \sqrt{\frac{8(m+1)(m+2)(2m)!m^{2m-1}}{(m-1)[2^m m!(2m+1)!!]^2}\dot{\mathcal{E}}^{\infty}_{m}}\frac{\eta}{\tilde{D}}\tilde{\Omega}^{m/3} \tag{5.6}$$

for $m \geq 2$. We note that the effect of the averaging is that this waveform model does not represent the waveform measured by any physical observer. However, it captures the main physical features of the waveform which encode information about the source parameters.

For the numerical study, we will use the Teukolsky based waveform model (2.45)[1]

$$h_+ - ih_\times = \frac{1}{\tilde{D}}\sum_{l=2}^{\infty}\sum_{m=-l}^{l}\frac{1}{m^2\tilde{\Omega}^2}\,\tilde{G}_{ml}e^{-i(m\tilde{\Omega}\tilde{t})}\,, \tag{5.7}$$

where

$$\tilde{G}_{ml} = {}_{-2}S^{am\tilde{\Omega}}_{ml}(\theta)\exp(i\phi)\tilde{Z}^{\infty}_{ml}(\tilde{r},a)\,, \tag{5.8}$$

depends on the radial Teukolsky coefficient at infinity $Z^{\infty}_{ml}(\tilde{r},a)$, and the viewing angle (θ,ϕ). The latter dependence is through the SWSH ${}_{-2}S^{am\tilde{\Omega}}_{ml}(\theta,\phi) = {}_{-2}S^{am\tilde{\Omega}}_{ml}(\theta)\exp(i\phi)$ defined as solutions to (2.38). We note here that we treat the large r quantity in (2.45) as the distance to the source D.

This work will consider two viewing angles: face on $(\theta,\phi) = (0,0)$ and edge on $(\theta,\phi) = (\pi/2,0)$. Using the identities [194]

$${}_{-2}S^{a(-m)\tilde{\Omega}}_{(-m)l}(\pi/2,0) = (-1)^l({}_{-2}S^{am\tilde{\Omega}}_{ml}(\pi/2,0))^\star \tag{5.9}$$

$$\tilde{Z}^{\infty}_{(-m)l} = (-1)^l(\tilde{Z}^{\infty}_{ml})^\star, \tag{5.10}$$

[1]The waveform model (5.7) was taken directly from [194], which is why there is a factor of two missing when compared to (2.45). The author believes this is a typo in [194] rather than a typo in (2.45). This will not affect our results since our conclusions are drawn from analysing the evolution of the signal as it evolves in frequency, rather than amplitude. One could simply rescale the distance $\tilde{D} \mapsto \tilde{D}/2$ in (5.7) to achieve the same results presented in this chapter.

where barred quantities are complex conjugates, we can write equation (5.7) as

$$\begin{aligned} h_+ - ih_\times &= \sum_{l=2}^{\infty}\left[\sum_{m=-l}^{-1} {}_{-2}S_{ml}^{am\tilde{\Omega}}(\pi/2,0)\tilde{Z}_{ml}^{\infty}e^{i(m\tilde{\Omega}\tilde{t})} + \sum_{m=1}^{l} {}_{-2}S_{ml}^{am\tilde{\Omega}}(\pi/2,0)\tilde{Z}_{ml}^{\infty}e^{i(m\tilde{\Omega}\tilde{t})}\right] \\ &= \sum_{l=2}^{\infty}\left(\sum_{m=1}^{\infty}[\ {}_{-2}S_{ml}^{am\tilde{\Omega}}(\pi/2,0)\tilde{Z}_{ml}^{\infty}e^{i(m\tilde{\Omega}\tilde{t})}]^{\star} + {}_{-2}S_{ml}^{am\tilde{\Omega}}(\pi/2,0)\tilde{Z}_{ml}^{\infty}e^{i(m\tilde{\Omega}\tilde{t})}\right) \\ &= 2\mathrm{Re}\left(\sum_{l=2}^{\infty}\sum_{m=1}^{\infty} {}_{-2}S_{ml}^{am\tilde{\Omega}}(\pi/2,0)\tilde{Z}_{ml}^{\infty}e^{i(m\tilde{\Omega}\tilde{t})}\right). \end{aligned}$$

Extracting the η dependence from $\tilde{Z}_{ml}^{\infty}$ and collecting real and imaginary parts reveals

$$h_+ = \frac{2\eta}{\tilde{D}}\left(\sum_{m=1}^{\infty}\frac{1}{m^2\tilde{\Omega}^2}\exp(-i[\phi_0 + m\tilde{\Omega}\tilde{t}])\sum_{l=m}^{\infty}\tilde{G}_{ml}\right), \tag{5.11}$$

for the edge-on case. Notice here that there is no cross polarisation component and have also tacked on an arbitrary initial phase. For the face-on case, we write

$$h_+ - ih_\times \approx \frac{\eta}{4\tilde{\Omega}^2\tilde{D}}G_{22}\exp(-i[\phi_0 + 2\tilde{\Omega}\tilde{t}]). \tag{5.12}$$

Note we have neglected higher order l modes with $m = 2$ fixed in equation (5.12) since the Teukolsky amplitudes $\tilde{Z}_{l2}^{\infty}$ for $l > 2$ are negligible in comparison to the dominant quadrupolar $l = m = 2$ mode. Figure 1. in [152] further justifies our claim that higher order m modes when $l = 2$ can be ignored for face-on sources. Furthermore, the only spheroidal harmonics that are non-vanishing at $\theta = 0$ are those with $m = +2$ [194, 279].

To generate the Teukolsky waveforms, the SWSH are calculated using the SpinWeightedSpheroidalHarmonics `mathematica` package in the BHPT, whereas the Teukolsky amplitudes $\tilde{Z}_{ml}^{\infty}$ are calculated using the Teukolsky package from the same toolkit.

For the remainder of this study, we will only consider the plus polarised signal $h(t;\boldsymbol{\theta}) \equiv h_+(t;\boldsymbol{\theta})$ for the face-on and edge-on observations. We will not study how well one can constrain the viewing angles (θ, ϕ) since their inclusion will affect the amplitude of the signal, rather than the evolution of the phase. Given the nature of our orbits, our parameter space will only be six dimensional $\boldsymbol{\theta} = \{\tilde{r}_0, a, \mu, M, \phi_0, \tilde{D}\}$, where $\tilde{r}_0$ stands for the initial size of the circular orbit. We stress these waveform models do not include the LISA response functions, which affect the amplitude evolution of the signal and induce modulations, due to Doppler shifting, through the motion of the LISA spacecraft [280, 281]. Since these response functions do not depend on the *intrinsic* parameters of the system that we are most interested in, we omit these here and, consequently, they will also be omitted in our analytic discussion based on this waveform

model.

We finish this waveform discussion with a comment regarding the relation between the two models considered in this work. The (dimensionful) Teukolsky amplitudes are related to the energy flux for each (l, m) mode by

$$\dot{E}^{\infty}_{lm,\mathrm{GW}} = \frac{|Z^{\infty}_{lm}|^2}{4\pi m^2 \Omega^2}. \tag{5.13}$$

As seen in chapter 2 subsection 2.4.3, averaging over the sky and the period of the waves the Teukolsky waveform (5.7) reduces to (5.3). Our numerical results indicate that the spin precision measurements are driven by the radial trajectory given by (5.1), which is common to both (5.3) and (5.7), while not being largely influenced by the spin dependence on the waveform amplitude. Given this fact and since it is analytically much easier to analyse the waveform model (5.3), this is the one being discussed in the analytics section 5.3 to explain the increase in the spin precision measurement for near-extremal primaries.

5.3 Analytic estimates of spin precision

Before discussing numerical results on the measurement precisions for the parameters $\boldsymbol{\theta}$ of near-extremal EMRIs, we would like to develop some analytic tools that will allow us to understand the precisions we find numerically. In particular the fact that spin measurements for near-extremal primaries are noticeably *tighter* than those obtained for more moderately rotating primaries.

Our analysis will be centred on using the FM formalism introduced in section 3.3.2. Throughout this section, we will use the waveform model (5.3) for analytical convenience. We will focus on the spin-spin component of the FM (3.59)

$$\Gamma_{aa} = 4 \int_0^{\infty} df \frac{|\partial \hat{h}(f, r(a), t; \boldsymbol{\theta})/\partial a|^2}{S_n(f)} \tag{5.14}$$

in the following analytic discussion. Our numerical and statistical analysis will be more general and employ the Teukolsky based model (5.7). In future work, we will extend this analytic considerations to multiple parameter study.

If all other parameters were known perfectly, the estimated precision on the spin parameter would be

$$\Delta a \approx 1/\sqrt{\Gamma_{aa}}. \tag{5.15}$$

Thus, to compare precisions between near-extremal (denoted *ext*) and moderately rotating

(denoted *mod*) primaries one is led to study the ratio

$$\frac{\Gamma^{\rm ext}_{aa}}{\Gamma^{\rm mod}_{aa}}\,. \tag{5.16}$$

Consider the sky-averaged RMS GW amplitude (5.3)

$$h(t) = \sum_m h_m(t) \approx \sum_m \frac{2\sqrt{\eta \dot{\tilde{E}}^{\infty}_{m,\rm GW}}}{m\tilde{\Omega}\tilde{D}}\,\sin(m\tilde{\Omega}\tilde{t})\,, \tag{5.17}$$

where we have chosen the initial phase $\phi_0 = 0$ for simplicity. The FM depends on the PSD of the detector. In the numerical calculations presented later we will use the full frequency dependent PSD, but to derive our analytic results we will approximate $S_n(f) \approx S_n(f_\circ)$, a constant. The rationale for this is that EMRIs evolve quite slowly and so the total change in the PSD over the range of frequencies present in the signal is small. Between 1 mHz and 100 mHz, the (square root of the) LISA PSD changes by just one order of magnitude, which is much smaller than the three orders of magnitude improvement in spin measurement precision that we find numerically. Additionally, the difference in the ISCO frequencies across all combinations of mass and spin considered in our numerical analysis is less than a factor of 2.5. PSD variations can not therefore explain the numerical results, and so we can ignore these in deriving the analytic results which do explain the numerics. Under this approximation, one can envoke *Parseval's theorem*

$$\Gamma_{aa} \approx \frac{4}{S_n(f_\circ)}\int_0^\infty dt\,(\partial_a h(t))^2\,. \tag{5.18}$$

We additionally assume that the choice of $f_\circ$ does not depend on the spin, and therefore the ratio (5.16) is independent of $S_n(f_\circ)$. Again, this approximation could introduce at most an order of magnitude uncertainty, and most likely much less than that. Once the FM is written in the form (5.18), we can use the semi-analytic waveform model (5.17) to evaluate it. In appendix B.1, we argue the dominant contribution can be approximated by

$$\begin{aligned}
\Gamma_{aa} &\approx \frac{8M}{\tilde{D}^2\,S_n(f_\circ)}\sum_m \Gamma_{aa,m}\\
\Gamma_{aa,m} &\approx \int_{\tilde{t}_0}^{\tilde{t}_{\rm cut}} d\tilde{t}\,\dot{\tilde{E}}^{\infty}_{m,\rm GW}\,(\tilde{\Omega}\tilde{t})^2\,\left(1+\frac{3}{2}\sqrt{\tilde{r}}\,\partial_a\tilde{r}\right)^2\,.
\end{aligned} \tag{5.19}$$

Here $\tilde{t}_0$ is the coordinate time at which the observation starts and $\tilde{t}_{\rm cut}$ is the coordinate time at the end of the observation. For the results in this paper, we analyse ~ 1 year long signals and fix $\tilde{t}_{\rm cut}$ independently of spin, such that all inspirals terminate before $\tilde{r}_{\rm isco}$ is reached.

As seen in (5.19), a proper understanding of the precision in the spin measurement requires

quantifying the spin dependence of the inspiral trajectory of the secondary, i.e. $\partial_a \tilde{r}$.

5.3.1 Spin dependence on the radial evolution

Our primary goal here is to understand the spin dependence on the radial trajectory of the secondary ($\partial_a \tilde{r}$) for any spin parameter a of the primary. The trajectory of the secondary is the integral of the inspiral equation

$$\partial_{\tilde{r}} \tilde{E}(\tilde{r}, a) \frac{d\tilde{r}}{d\tilde{t}} = -\dot{\tilde{E}}_{\rm GW}(\tilde{r}, a)\,. \tag{5.20}$$

This follows from energy conservation (2.56a), where $\tilde{E}(\tilde{r}, a)$ is the energy of a circular orbit (2.8a) and $\dot{\tilde{E}}_{\rm GW}(\tilde{r}, a)$ is the energy rate carried away by GWs (2.58). While $\tilde{E}(\tilde{r}, a)$ is *kinematic*, that is, derived through geodesic properties, $\dot{\tilde{E}}_{\rm GW}$ is *dynamic*, that is, it is a radiation reactive term determined by solving Teukolsky's equation for a point particle source. The former is under analytic control, whereas the latter typically requires numerical treatment.

The quantity $\partial_a \tilde{r}$ captures the change in the secondary's trajectory when the spin parameter a of the primary varies, keeping the remaining primary and secondary parameters fixed, including $\tilde{t}$. More explicitly, the integral $\tilde{r}(\tilde{r}_0, a)$ of (5.20) depends on the initial condition $\tilde{r}(\tilde{t}_0) = \tilde{r}_0$ and it depends on the spin parameter a both through $(\partial_{\tilde{r}} \tilde{E})$ and $(\dot{\tilde{E}}_{\rm GW})$ information, but *not* through $\tilde{t}$, which is simply labelling the points in the trajectory. We will comment on the possible spin dependence on the initial condition $\tilde{r}_0$ below.

One possible way to compute $\partial_a \tilde{r}$ is to integrate (5.20) and to take the spin derivative explicitly afterwards. A second, equivalent, way is to observe $\tilde{r}$ is a monotonic function of $\tilde{t}$ at fixed spin and initial radius $\tilde{r}_0$. Hence, it can be used as the integration coordinate to study $\partial_a \tilde{r}(\tilde{r})$. To do this, notice that the total spin derivative of the kinematic and dynamic functions in (5.20), at fixed $\tilde{r}_0$ and $\tilde{t}$, is

$$\begin{aligned} \frac{\partial}{\partial a} \partial_{\tilde{r}} \tilde{E}(\tilde{r}(a), a)\bigg|_{\tilde{r}_0, \tilde{t}} &= (\partial^2_{\tilde{r}} \tilde{E})\, \partial_a \tilde{r} + \partial^2_{a\tilde{r}} \tilde{E}\,, \\ \frac{\partial \dot{\tilde{E}}_{\rm GW}}{\partial a}\bigg|_{\tilde{r}_0, \tilde{t}} &= \left(\partial_{\tilde{r}} \dot{\tilde{E}}_{\rm GW}\right) \partial_a \tilde{r} + \partial_a P_{\rm GW}\,. \end{aligned} \tag{5.21}$$

To ease our notation, all spin partial derivatives in the right hand side, and in the forthcoming discussion, should be understood as computed at fixed $\tilde{r}_0$ and $\tilde{t}$. Defining $u = \partial_a \tilde{r}$ (to ease notation) and computing the total spin derivative of equation (5.20), we obtain

$$\left[u \partial^2_{\tilde{r}} \tilde{E} + \partial^2_{a\tilde{r}} \tilde{E} + \partial_{\tilde{r}} \tilde{E} \frac{du}{d\tilde{r}}\right] \frac{d\tilde{r}}{d\tilde{t}} = -\frac{d\dot{\tilde{E}}_{\rm GW}}{da}\,. \tag{5.22}$$

Plugging in the radial velocity using (5.20) one obtains

$$\frac{du}{d\tilde{r}} + \left(\frac{\partial^2_{\tilde{r}} \tilde{E}}{\partial_{\tilde{r}} \tilde{E}} - \frac{\partial_{\tilde{r}} \dot{\tilde{E}}_{\rm GW}}{\dot{\tilde{E}}_{\rm GW}} \right) u = - \frac{\partial^2_{a\tilde{r}} \tilde{E}}{\partial_{\tilde{r}} \tilde{E}} + \frac{\partial_a \dot{\tilde{E}}_{\rm GW}}{\dot{\tilde{E}}_{\rm GW}}. \tag{5.23}$$

Equation (5.23) is a first order *linear* ODE, valid for *any* spin and for *any* location of the secondary, whose solution describes the desired spin dependence in the radial trajectory $\partial_a \tilde{r}(\tilde{r})$.

The general solution to (5.23) is a sum of the homogeneous solution u_h and a particular solution u_p. The solution will depend on an initial condition $u(\tilde{r}_0)$. The initial condition of the radial trajectory is[2]

$$\tilde{r}(\tilde{r}_0, a, t = 0) = \tilde{r}_0 \qquad \Rightarrow \qquad \left. \frac{\partial \tilde{r}}{\partial a} \right|_{r_0, t=0} = 0, \tag{5.24}$$

from which we deduce $u(t = 0) = 0$.

The homogeneous version of equation (5.23) is equivalent to

$$\frac{du_h}{u_h} + d \log \left(\frac{\partial_{\tilde{r}} \tilde{E}}{\dot{\tilde{E}}_{\rm GW}} \right) = 0 \Rightarrow u_h = k_0 \frac{\dot{\tilde{E}}_{\rm GW}}{\partial_{\tilde{r}} \tilde{E}} \tag{5.25}$$

where k_0 is an arbitrary integration constant. We follow a standard approach and look for a particular solution of the form $u_p = k(\tilde{r}, a) u_h$. Plugging this into (5.23) gives

$$k(\tilde{r}, a) = \int \frac{\partial_{\tilde{r}} \tilde{E}}{\dot{\tilde{E}}_{\rm GW}} \left(- \frac{\partial^2_{a\tilde{r}} \tilde{E}}{\partial_{\tilde{r}} \tilde{E}} + \frac{\partial_a \dot{\tilde{E}}_{\rm GW}}{\dot{\tilde{E}}_{\rm GW}} \right) d\tilde{r} \tag{5.26}$$

$$= - \int \frac{\partial_{\tilde{r}} \tilde{E}}{\dot{\tilde{E}}_{\rm GW}} \partial_a \log \left(\frac{\partial_{\tilde{r}} \tilde{E}}{\dot{\tilde{E}}_{\rm GW}} \right) d\tilde{r}. \tag{5.27}$$

Combining our results, we obtain

$$\partial_a \tilde{r} = \frac{\dot{\tilde{E}}_{\rm GW}}{\partial_{\tilde{r}} \tilde{E}} \left(k_0 - \int \frac{\partial_{\tilde{r}} \tilde{E}}{\dot{\tilde{E}}_{\rm GW}} \partial_a \log \left(\frac{\partial_{\tilde{r}} \tilde{E}}{\dot{\tilde{E}}_{\rm GW}} \right) d\tilde{r} \right). \tag{5.28}$$

The above equation is valid for *any* spin, for *any* location of the secondary and for *any* flux $\dot{\tilde{E}}_{\rm GW}$. The analytic result (5.28) will allow us to determine what the dominant source of the spin dependence is in different regions of the trajectory.

In figure 5.1 we show the near perfect agreement between the solution to (5.28) and our numerical calculation of $\partial_a \tilde{r}$ using finite difference method

$$\partial_a \tilde{r} \approx \frac{\tilde{r}(a + \delta, \tilde{t}, \dot{\tilde{\mathcal{E}}}(a + \delta)) - \tilde{r}(a - \delta, \tilde{t}, \dot{\tilde{\mathcal{E}}}(a - \delta))}{2\delta}. \tag{5.29}$$

[2]The initial condition $u(\tilde{r}_0)$ can play an important role when gluing a numerical calculation for $\partial_a \tilde{r}$ with an analytic one in some specific piece of the trajectory where the information determining the solution to (5.23) is under analytic control. We will be more explicit about this when we discuss $\partial_a \tilde{r}$ in the region close to ISCO.

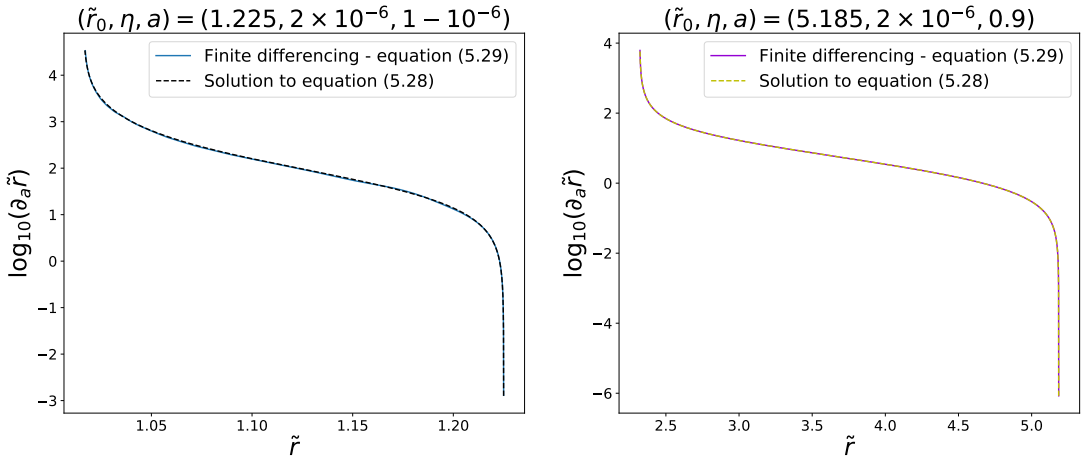

Figure 5.1: The dashed curves (black dashed and yellow dashed) on each figure is the solution to (5.28) with $k_0 = 0$ corresponding to $\partial_a \tilde{r}(\tilde{r_0}) = 0$. In both plots, the solid colours (blue and violet) are $\partial_a \tilde{r}$ calculated using a fifth order stencil method. In each plot, the intrinsic parameters given in the titles.

the method used to calculate year-long trajectories used for our FM results in later sections, for both moderately and rapidly rotating primaries.

Following [109], we express the energy flux as a relativistic correction factor, $\dot{\mathcal{E}}$, times the leading order Newtonian flux

$$\dot{\tilde{E}}_{\rm GW} = \frac{32}{5} \eta \tilde{\Omega}^{10/3} \dot{\mathcal{E}} \,. \tag{5.30}$$

Plugging this into Eq. (5.28) gives

$$\partial_a \tilde{r} = \frac{\tilde{\Omega}^{10/3} \dot{\mathcal{E}}}{\partial_{\tilde{r}} \tilde{E}} \left(k_0 - \int \frac{\partial_{\tilde{r}} \tilde{E}}{\tilde{\Omega}^{10/3} \dot{\mathcal{E}}} \left(\frac{\partial^2_{a\tilde{r}} \tilde{E}}{\partial_{\tilde{r}} \tilde{E}} - \frac{\partial_a \dot{\mathcal{E}}}{\dot{\mathcal{E}}} + \frac{10}{3} \tilde{\Omega} \right) d\tilde{r} \right) , \tag{5.31}$$

Analysing the integrand in (5.31), we see that the first and third terms are *kinematic*, i.e., driven by geodesic physics, whereas the second is *dynamical*, i.e., driven by the energy flux. Comparison between these terms at different stages of the inspiral, as a function of the spin, can help us to determine what the driving source of spin dependence is in each case. In the next subsection, we investigate the contribution of both the geodesic and radiation reactive terms to $\partial_a \tilde{r}$.

5.3.2 Comparison of radial evolution for moderate and near-extremal black holes

Despite the universality of (5.28) or (5.31), the dependence on the energy flux makes it not feasible to analytically integrate $\partial_a \tilde{r}$ along the entire secondary trajectory. However, we can integrate (5.28) in *specific* regions of the secondary trajectory.

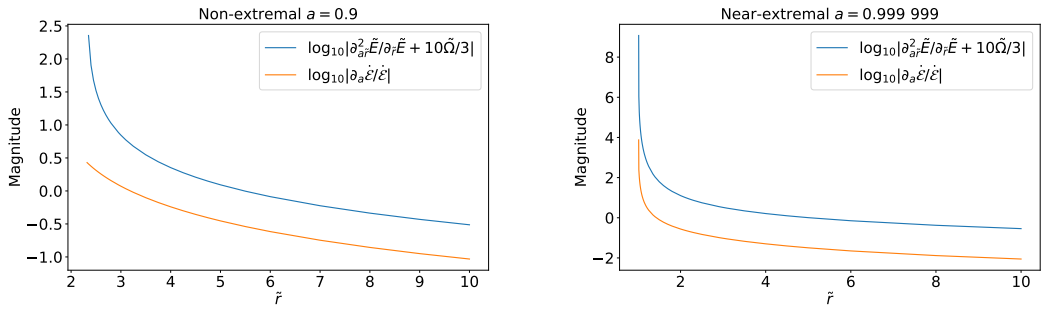

Figure 5.2: The top plot compares the kinematic and radiation reaction quantities given in the integrand of (5.31) for a spin of $a = 0.999999$. The bottom plot is the same but for a spin parameter of $a = 0.9$. Notice that in these two cases the kinematical quantities *dominate* over the relativistic correction terms.

It is possible to prove that $d\partial_a\tilde{r}/d\tilde{r} < 0$ and hence that $\partial_a\tilde{r}$ grows monotonically over the inspiral. It is therefore natural to study the behaviour of $\partial_a\tilde{r}$ close to ISCO, where its contribution to the FM (5.19) will be maximal. We first compare the kinematic and dynamical contributions to (5.31). Using results from the BHPT, we have numerically calculated the spin derivative of $\dot{\mathcal{E}}$ for two primaries with spin parameters $a = 0.9$ and $a = 1 - 10^{-6}$. These are compared with the kinematic sources in the integrand of equation (5.31) in figure 5.2. These figures show that

$$\left|\frac{\partial^2_{a\tilde{r}}\tilde{E}}{\partial_{\tilde{r}}\tilde{E}} + \frac{10}{3}\tilde{\Omega}\right| \gg \left|\frac{\partial_a\dot{\mathcal{E}}}{\dot{\mathcal{E}}}\right|, \tag{5.32}$$

for both spin parameters. This suggests it is the kinematic sources in (5.31) that drive the spin dependence of the secondary trajectory, particularly close to ISCO. Although we have only verified it for two choices of spin parameter, we will assume this approximation holds for *any* spin parameter $a \geq 0.9$.

We first consider moderately spinning BHs close to ISCO. Dropping the dynamical contribution to the integrand of (5.31), we can compare the two remaining terms. The angular velocity piece is bounded and order one, but $\partial_{\tilde{r}}\tilde{E}$ tends to zero at ISCO, which means that $\partial^2_{a\tilde{r}}\tilde{E}/\partial_{\tilde{r}}\tilde{E}$ dominates close to ISCO, allowing us to use the approximation

$$\frac{\partial_{\tilde{r}}\tilde{E}}{\tilde{\Omega}^{10/3}\dot{\mathcal{E}}}\left(\frac{\partial^2_{a\tilde{r}}\tilde{E}}{\partial_{\tilde{r}}\tilde{E}} - \frac{\partial_a\dot{\mathcal{E}}}{\dot{\mathcal{E}}} + \frac{10}{3}\tilde{\Omega}\right) \approx \frac{\partial^2_{a\tilde{r}}\tilde{E}}{\tilde{\Omega}^{10/3}\dot{\mathcal{E}}}\,. \tag{5.33}$$

Since, for moderate spins, the variation of $\tilde{\Omega}$ and $\dot{\mathcal{E}}$ with radius close to ISCO is negligible compared to the variation in $\partial^2_{a\tilde{r}}\tilde{E}$, we will approximate them by their values at $\tilde{r}_{\rm isco}$. This allows us to integrate (5.28) to give the spin dependence of the radial trajectory for moderately

spinning BHs

$$\partial_a \tilde{r} \approx \frac{1}{\partial_{\tilde{r}} \tilde{E}} \left(k_{\rm mod} \tilde{\Omega}_{\rm isco}^{10/3} \dot{\tilde{\mathcal{E}}}_0(a, \tilde{r}_{\rm isco}) - \partial_a \tilde{E} \right) , \tag{5.34}$$

where $k_{\rm mod}$ is an arbitrary constant. Since

$$\partial_{\tilde{r}} \tilde{E} = \frac{\tilde{r}^2 - 3a^2 + 8a\sqrt{\tilde{r}} - 6\tilde{r}}{2\tilde{r}^{7/4} \left(\tilde{r}^{3/2} - 3\sqrt{\tilde{r}} + 2a \right)^{3/2}} , \tag{5.35}$$

it follows from (A.5) such that $\partial_{\tilde{r}} \tilde{E}(\tilde{r}_{\rm isco}) = 0$. For moderately rotating primaries and near ISCO, we can expand $\tilde{E} \approx \tilde{E}(\tilde{r}_{\rm isco}) + \frac{1}{2} \partial_{\tilde{r}}^2 \tilde{E}(\tilde{r}_{\rm isco}) \, (\tilde{r} - \tilde{r}_{\rm isco})^2$ leading to

$$\begin{aligned} \partial_a \tilde{E} &\approx \partial_a \tilde{E}(\tilde{r}_{\rm isco}) + \partial_{\tilde{r}}^2 \tilde{E}(\tilde{r}_{\rm isco}) \, (\tilde{r} - \tilde{r}_{\rm isco})(-\partial_a \tilde{r}_{\rm isco}) \\ \partial_{\tilde{r}} \tilde{E} &\approx \partial_{\tilde{r}}^2 \tilde{E}(\tilde{r}_{\rm isco}) \, (\tilde{r} - \tilde{r}_{\rm isco}) \end{aligned} \tag{5.36}$$

Using these expansions in Eq. (5.34) we deduce $\partial_a \tilde{r} = \tilde{k}_{\rm mod}/(\tilde{r} - \tilde{r}_{\rm isco}) + \partial_a \tilde{r}_{\rm isco}$, where $\tilde{k}_{\rm mod} = k_{\rm mod} \tilde{\Omega}_{\rm isco}^{10/3} \dot{\tilde{\mathcal{E}}}_0(a, \tilde{r}_{\rm isco}) / \partial_{\tilde{r}}^2 \tilde{E}(\tilde{r}_{\rm isco})$. Assuming that $\tilde{r}_0$ is sufficiently close to $\tilde{r}_{\rm isco}$ that this approximation holds throughout the range $[\tilde{r}_{\rm isco}, \tilde{r}_0]$, we can use the boundary condition (5.24) to determine $\tilde{k}_{\rm mod} = \partial_a \tilde{r}_{\rm isco} (\tilde{r}_{\rm isco} - \tilde{r}_0)$ and hence

$$\partial_a \tilde{r} \approx (-\partial_a \tilde{r}_{\rm isco}) \, \frac{\tilde{r}_0 - \tilde{r}}{\tilde{r} - \tilde{r}_{\rm isco}} . \tag{5.37}$$

We now repeat this analysis for near-extremal primaries. Near ISCO, the energy flux can be approximated by the NHEK flux ($x \equiv \tilde{r} - 1 \ll 1$)

$$\dot{\tilde{E}}_{\rm GW} \approx \eta (\tilde{C}_\infty + \tilde{C}_H) x \, . \tag{5.38}$$

Using this approximation, there is no explicit spin dependence and so the $\partial_a \dot{\tilde{E}}_{\rm GW}$ term in Eq. (5.26) vanishes. Expanding (5.35) for $x = \tilde{r} - 1 \ll 1$ and $\epsilon \ll 1$, the denominator involves

$$\tilde{r}^{3/2} - 3\sqrt{\tilde{r}} + 2a = \frac{3}{4} x^2 - \epsilon^2 - \frac{1}{4} x^3 + \frac{9}{64} x^4 + \mathcal{O}(x^5, x\epsilon^2, \epsilon^4),$$

while the numerator has the expansion

$$\tilde{r}^2 - 3a^2 + 8a\sqrt{\tilde{r}} - 6\tilde{r} = \frac{1}{2} x^3 - \epsilon^2 - \frac{5}{32} x^4 + \mathcal{O}(x^5, x\epsilon^2, \epsilon^4) \, .$$

We conclude

$$\partial_{\tilde{r}} \tilde{E} \approx \frac{2}{3\sqrt{3}} \left(1 - \frac{11}{8} x - \frac{x_{\rm isco}^3}{x^3} \right) + \mathcal{O}(x^2, \epsilon^2/x^2). \tag{5.39}$$

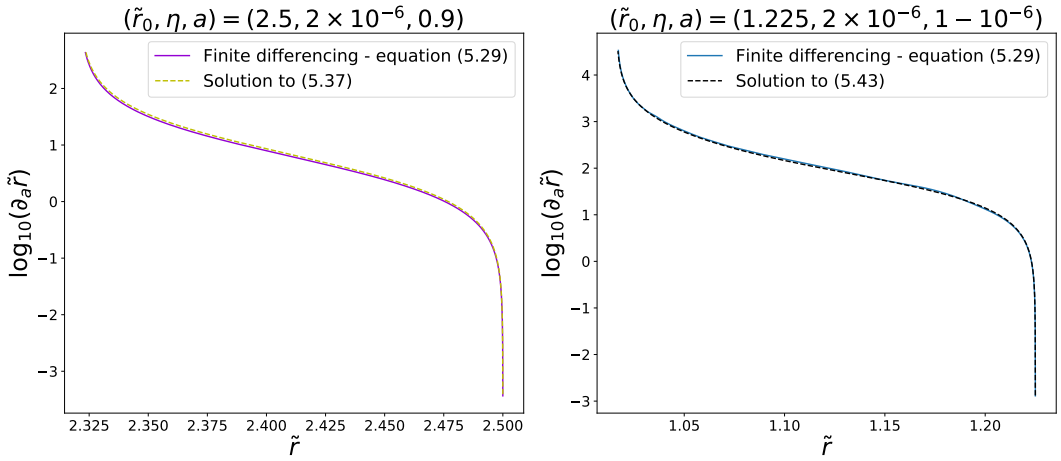

Figure 5.3: The yellow dashed and black dashed curves are solutions to (5.37) and (5.43). The purple and blue curves are the true solutions to $\partial_a \tilde{r}$ obtained numerically without near-ISCO simplifications. We see both approximations capture the leading order behaviour of the spin derivative of the radial trajectory very well.

Using this approximation in Eq. (5.26) we find

$$k(\tilde{r}, a) \approx -\int \frac{\partial^2_{a\tilde{r}} \tilde{E}}{\dot{\tilde{E}}_{\rm GW}} \, \mathrm{d}\tilde{r} \tag{5.40}$$

$$\approx \frac{2x^2_{\rm isco}}{\eta(\tilde{C}_\infty + \tilde{C}_H)\sqrt{3}} \frac{\partial x_{\rm isco}}{\partial a} \int x^{-4} \mathrm{d}x \tag{5.41}$$

$$\approx \frac{8}{9\sqrt{3}\eta(\tilde{C}_\infty + \tilde{C}_H)} \frac{1}{x^3} \tag{5.42}$$

where we have used $x_{\rm isco} \approx 2^{1/3}\epsilon^{2/3}$ and $\dot{\tilde{E}}_{\rm GW}$ defined in (5.38). This is valid for $x \ll 1$ and includes the corrections due to $x \sim x_{\rm isco}$. Assuming $\tilde{r}_0$ is close to ISCO, so that the initial condition (5.24) holds, we conclude that the spin dependence in the near-ISCO region of a near-extremal BH is

$$\partial_a \tilde{r} \approx \frac{8}{9\sqrt{3}\, x^2 \partial_{\tilde{r}} \tilde{E}} \left(1 - \frac{x^3}{x_0^3}\right) . \tag{5.43}$$

Figure 5.3 compares (5.37) and (5.43) to the full $\partial_a \tilde{r}$ computed numerically without using the near-ISCO approximations. We see that the approximations are very accurate in the region close to the ISCO where they are valid.

Before continuing, we will comment further on the choice of flux (5.2) instead of (2.59). The latter has an *explicit* dependence on $\tilde{r}_+ = 1 + \epsilon$. Consequently, it carries an additional spin dependence. In particular, $\partial_a \tilde{r}_+ = -a/\epsilon$. Thus, for near-extremal primaries this spin dependence can induce extra diverging sources for $\partial_a \tilde{r}$ with a very specific sign. We can easily compute their effects by integrating the ODE with such an energy flux source. The result one finds does *not* agree with the numerical evaluation of $\partial_a \tilde{r}$ generated from the BHPT, which

computes the exact flux[3]. We conclude that (5.2) appears to capture the spin dependence of our observable (the amplitude of the GW) more accurately than (2.59). This is in fact the reason we chose to work with (5.2).

Let us close this discussion with a brief comparison between the analytic results for moderate and near-extremal spins. We write $\tilde{r} - \tilde{r}_{\rm isco} \sim \delta > \eta^{2/5}$, the latter inequality ensuring that we avoid entering the transition region [282, 283]. By writing $x = \tilde{r} - 1 = \delta + x_{\rm isco}$, we can expand Eq. (5.39) for $\delta \ll x_{\rm isco}$ such that for near-extremal BHs

$$\partial_{\tilde{r}} \tilde{E} \approx \frac{2}{3\sqrt{3}} \left(3\frac{\delta}{x_{\rm isco}} - \frac{11}{8}\delta - \frac{11}{8} x_{\rm isco} + \cdots \right).$$

The first term is dominant unless $\delta \lesssim x_{\rm isco}^2 \sim \epsilon^{4/3}$. The constraint $\delta > \eta^{2/5}$ ensures this is only violated if $\epsilon > \eta^{3/10}$. This will be satisfied for all the cases that we consider in this paper, but we emphasise this is not a physical constraint. When this constraint is violated, additional terms become important in the expansion which we have ignored, and these ensure that $\partial_{\tilde{r}} \tilde{E} \to 0$ at $\tilde{r}_{\rm isco}$. We conclude the scaling of $\partial_{\tilde{r}} \tilde{E}$ is $\delta/\epsilon^{2/3}$ for near-extremal BHs, compared to δ for moderate spins.

It follows using (5.37) and (5.43) that

$$\partial_a \tilde{r} \propto \begin{cases} \frac{1}{\delta}, & \text{moderate spins} \\ \frac{\epsilon^{2/3}}{\delta(\delta+\epsilon^{2/3})^2}, & \text{near-extremal spins} \end{cases}. \tag{5.44}$$

The spin dependence on the radial trajectory for near-extremal primaries is *larger* than for moderately rotating ones.

5.3.3 Precision of spin measurement

In the previous section we showed the effect that the spin parameter has on the radial trajectory. This was achieved by studying the *general* linear ODE for $\partial_a \tilde{r}$, Eq. (5.28). By arguing that the kinematic terms dominate the behaviour of $\partial_a \tilde{r}$, for *both* the near-extreme and moderately spinning BHs, analytic solutions were found near the ISCO. We were able to conclude that $\partial_a \tilde{r}$ grows much more rapidly close to the ISCO for near-extreme BHs than for moderately spinning BHs. We also emphasise that Eq. (5.32) shows that corrections to $\partial_a \tilde{r}$ of the form $\partial_a \dot{\mathcal{E}}$ are *subdominant*. We now explore the consequences of these results for the precision of spin measurements, computed using the FM formalism.

[3]In particular, it is no longer the case that $\partial_a \tilde{r}$ is monotonically increasing all along the inspiral trajectory, whereas the BHPT data is monotonically increasing, a feature our ODE with flux (5.2) reproduces.

Inspection of (5.19) suggests there are two main effects: the dependence on $\tilde{t}^2$ and the dependence on $(\partial_a \tilde{r})^2$. First, the fact that $\tilde{t} \sim \mathcal{O}(\eta^{-1})$ follows from integrating (5.20), and therefore the contribution to the FM due to $\tilde{t}^2$ is large and scales like η^{-2}. Second, $\partial_a \tilde{r}$ is monotonically increasing as the secondary spirals inwards. Thus, its maximal contribution comes from the region close to ISCO, which supports results in [97]. Eq. (5.44) shows this contribution is largest in the last stages *before* entering into the transition regime. As changes in $\tilde{\Omega}$ close to ISCO are negligible, the factor $(\tilde{\Omega}\tilde{t})^2$ is, approximately, the square of the number of cycles, a proxy widely used in the literature in discussions of the precision of measurements. Our estimate (5.19) confirms this intuition and shows the spin precision will be further increased by large values of the radial spin derivative, $\partial_a \tilde{r}$.

5.3.4 Comparison of spin measurement precision for moderate and near-extremal black holes

The FM estimate (5.19) depends on the spin derivative of the radial evolution, on the duration of the inspiral and on the energy flux. Eq. (5.44) shows that, at a fixed distance to the corresponding ISCO, $\partial_a \tilde{r}$ is larger for a near-extremal primary than for a moderately rotating primary. As a consequence of time dilation near the BH horizon, $\dot{E} \to 0$ near the ISCO for near-extremal primaries, but remains finite for moderately rotating ones. This means that the energy flux for near-extremal inspirals is much smaller than that for moderate spins, but the duration of the inspiral is longer. However, we can write (5.19) as an integral over the BL radial coordinate $\tilde{r}$. In that case, the integrand is proportional to

$$\Gamma_{aa,m} = \int_{\tilde{r}_{\rm cut}}^{\tilde{r}_0} d\tilde{r} \frac{\dot{\tilde{E}}^{\infty}_{m,\rm GW}}{\dot{\tilde{E}}_{\rm GW}} (\tilde{t}\,\tilde{\Omega})^2 \, (\partial_{\tilde{r}} \tilde{E}) \left(1 + \frac{3}{2}\sqrt{r}\partial_a \tilde{r}\right)^2 \tag{5.45}$$

close to the relevant ISCO. While the energy fluxes are much smaller for near-extremal inspirals, the ratio of energy fluxes appearing above is an order one quantity for all spin parameters. The expression above is therefore a product of factors that have been argued to be either of comparable magnitude or much smaller for moderately rotating primaries. We therefore expect the precision of spin measurements to be much higher for near-extremal EMRIs.

A quantitative comparison between the near-extremal and the moderately spinning sources requires a precise calculation of the ratio (5.16) computed along the entire respective trajectories. In general, this is a hard analytic task since both energy fluxes $\dot{\tilde{E}}_{\rm GW}$ and $\dot{\tilde{E}}^{\infty}_{m}$ must be handled through numerical means and long observations of inspirals (starting in the weak field) require calculations performed in the frequency domain where $S_n(f)$ shows non-trivial (non-

constant) behaviour. This would be no more straightforward than direct numerical computation of the FM and so we do not pursue it here.

For any sources whose trajectory lies entirely in the near-ISCO region, these analytic approximations allow us to compute the ratio (5.16) reliably. This can be exploited to obtain an analytic approximation to the FM for such sources and this calculation will be pursued elsewhere. Additionally, earlier arguments tell us that it is the near-ISCO regime that dominates the spin precision and so these expressions are sufficient to understand the increase in spin precision seen for near-extremal inspirals.

5.3.4.1 Near-extremal source

From (5.43), it follows

$$\partial_a \tilde{r} \approx \frac{4}{3x_0^3}\,\frac{x}{x^3 - x_{\rm isco}^3}\,(x_0^3 - x^3)\,. \tag{5.46}$$

Since $\sqrt{\tilde{r}}\partial_a \tilde{r}$ grows fast and the rate of change of $\tilde{r}$ and $\tilde{\Omega}$ is small, near-ISCO, we can approximate (5.19) by

$$\Gamma_{aa} \approx 18 \frac{\mu}{(\eta\tilde{D})^2\, S_n(f_\circ)}\, \tilde{r}_{\rm ext}\, \tilde{\Omega}_{\rm ext}^2 \sum_m \int_0^{\tilde{t}_{\rm cut}} d(\eta\tilde{t})\, \frac{d\tilde{E}^{\infty}_{m,\rm GW}}{\eta d\tilde{t}}\, (\eta\tilde{t})^2\, (\partial_a \tilde{r})^2. \tag{5.47}$$

Here, $\tilde{t}_{\rm cut}$ is the time at the end of the integration, where $x = x_{\rm cut}$. Our approximations break down when the transition regime breaks down, so we can assume $x_{\rm cut} \sim \eta^{2/5} + \epsilon^{2/3}$, which is a small quantity. Using $d\tilde{E}^{\infty}_m/d\tilde{t} = \eta \tilde{C}_{\infty m}\, x$ and assuming $x_0 \geq x \gg x_{\rm isco}$, the trajectory can be approximated by $x(\tilde{t}) \approx x_0\, e^{-y}$ with $y = \alpha\, \eta\tilde{t} \equiv \frac{3\sqrt{3}}{2}\,(\tilde{C}_{\rm H} + \tilde{C}_\infty)\,\eta\tilde{t}$. This form of the trajectory is explicitly shown in the calculation leading up to equation (16) in [211]. Using these results, the FM reduces to

$$\Gamma^{\rm ext}_{aa} \approx \frac{64\mu}{(\eta\tilde{D})^2\, S_n(f_\circ)}\, \frac{\tilde{r}_{\rm ext}\, \tilde{\Omega}_{\rm ext}^2}{(3x_0\alpha)^3} \cdot G(y_{\rm cut}) \left(\sum_m \tilde{C}_{\infty m}\right)\,, \tag{5.48}$$

with $e^{y_{\rm cut}} = x_0/x_{\rm cut}$ and

$$G(y_{\rm cut}) = -9y_{\rm cut}^3 + (9y_{\rm cut}^2 + 2)\,\sinh 3y_{\rm cut} - 6y_{\rm cut}\,\cosh 3y_{\rm cut} \approx \frac{x_0^3}{2x_{\rm cut}^3}\left[\left(3\log\frac{x_0}{x_{\rm cut}} - 1\right)^2 + 1\right]\,,$$

where in the last step we used $x_0 \gg x_{\rm cut}$.

5.3.4.2 Moderately spinning source

Using the radial evolution (5.20), we can expand this near the ISCO. From equation (5.36) and (5.30), we obtain

$$(\tilde{r}-\tilde{r}_{\rm isco})^2-(\tilde{r}_0-\tilde{r}_{\rm isco})^2\approx-\frac{64}{5}\eta\,\tilde{\Omega}_{\rm isco}^{10/3}\,\frac{\dot{\mathcal{E}}_0(a)}{\partial_{\tilde{r}}^2\tilde{E}(\tilde{r}_{\rm isco})}\,\tilde{t}\,, \tag{5.49}$$

Notice that computing the spin derivative of the above equation reduces to (5.37), as expected. From this result, we can approximate the FM for moderate spins similar to our procedure before for near-extremal spins

$$\Gamma_{aa}^{\rm mod}\approx 18\left(\frac{5\partial_{\tilde{r}}^2\tilde{E}(\tilde{r}_{\rm isco})}{64\dot{\mathcal{E}}_0}\right)^3\frac{\mu}{(\eta\tilde{D})^2\,S_n(f_\circ)}\,\frac{\tilde{r}_{\rm isco}\,(\partial_a\tilde{r}_{\rm isco})^2}{\tilde{\Omega}_{\rm isco}^8}\quad(\tilde{r}_0-\tilde{r}_{\rm isco})^6\,F(\delta)\left(\sum_m\left.\frac{d\tilde{E}^\infty_{m,\rm GW}}{\eta\,d\tilde{t}}\right|_{\rm isco}\right), \tag{5.50}$$

where $\delta\equiv\frac{\tilde{r}_{\rm cut}-\tilde{r}_{\rm isco}}{\tilde{r}_0-\tilde{r}_{\rm isco}}<1$ and

$$F(\delta)=-2\log\delta-4(1-\delta)-(1-\delta^2)+\frac{8}{3}(1-\delta^3)-\frac{1}{2}(1-\delta^4)-\frac{4}{5}(1-\delta^5)+\frac{1}{3}(1-\delta^6)\,. \tag{5.51}$$

5.3.4.3 Ratio of Fisher matrices

Within these approximations, the ratio (5.16) now reduces to

$$\begin{aligned}\frac{\Gamma_{aa}^{\rm ext}}{\Gamma_{aa}^{\rm mod}}&\approx\frac{256}{9}\left(\frac{64}{45\sqrt{3}\,\partial_{\tilde{r}}^2\tilde{E}(\tilde{r}_{\rm isco})}\right)^3\frac{\tilde{r}_{\rm ext}\tilde{\Omega}_{\rm ext}^2}{\tilde{r}_{\rm isco}\tilde{\Omega}_{\rm isco}^2\,(\partial_a\tilde{r}_{\rm isco})^2}\,\frac{G(y_{\rm cut})}{x_0^3\,(\tilde{r}_0-\tilde{r}_{\rm isco})^6\,F(\delta)}\,\mathcal{T}\,,\\ \mathcal{T}&=\frac{\sum_m\tilde{C}_{\infty m}}{(\tilde{C}_{\rm H}+\tilde{C}_\infty)^3}\,\frac{(\tilde{\Omega}_{\rm isco}^{10}\,\dot{\mathcal{E}}_0^3)}{\sum_m\left.\frac{d\tilde{E}^\infty_{m,\rm GW}}{\eta\,d\tilde{t}}\right|_{\rm isco}}\end{aligned} \tag{5.52}$$

The most relevant feature for our current discussion is the quotient dependence

$$\frac{G(y_{\rm cut})}{x_0^3\,(\tilde{r}_0-\tilde{r}_{\rm isco})^6\,F(\delta)}\approx\frac{1}{x_{\rm cut}^3\,(\tilde{r}_0-\tilde{r}_{\rm isco})^6F(\delta)} \tag{5.53}$$

The first two denominator factors increase the ratio, since $x_{\rm cut}\ll 1$ and $\tilde{r}_0-\tilde{r}_{\rm isco}<1$. The last could in principle be large, due to the logarithmic term. However, δ and $x_{\rm cut}$ have similar scalings and therefore $x_{\rm cut}F(\delta)\ll 1$. We deduce that the spin component of the FM is *much larger* for near-extremal inspirals than for moderate spins. This is confirmed by the numerical results that will be reported in subsequent sections.

We finish by noting that the FMs increase in magnitude as the trajectory is cut off closer to $\tilde{r}_{\rm isco}$. In the case of moderate spin, we already noted the logarithmic dependence of $F(\delta)$ as

$\delta \to 0$. This has previously been observed in the literature, see for example Fig.(11) in [97]. For near-extremal EMRIs, if $x_{\rm cut} \sim x_{\rm isco} \sim \epsilon^{2/3}$, then for fixed x_0 and as $\epsilon \to 0$ the spin FM scales as $\Gamma_{aa} \sim (\log(\epsilon)/\epsilon)^2$. We deduce that observing the latter stages of inspiral is important for precise parameter measurement, for any primary spin.

In summary, we have derived an analytic approximation, valid close to ISCO, for the spin component of the FM. This indicates that this component is much larger for near-extremal spins and therefore we expect much more precise measurements of the spin parameter in that case. The approximation depends sensitively on certain quantities, such as the cut-off radius, $x_{\rm cut}$, that are somewhat arbitrary. However, for any choice the near-extremal precision is a few orders of magnitude better. This provides support for the numerical results that we will obtain in Sec.(5.6), which show a similar trend.

5.4 Waveform generation

In this section we provide more details on how we construct the waveform model used to compute the FM in the next section. The waveform model was previously given in Eq. (5.3) and Eq. (5.7). Here, we describe how the various terms entering these equations are evaluated.

5.4.1 Energy flux

Both waveform models (5.3) and (5.7) depend on the radial trajectory $\tilde{r}(\tilde{t}, a, \eta, \dot{\mathcal{E}})$. The amplitude evolution using the Teukolsky formalism depends on the spheroidal harmonics ${}_{-2}S_{ml}^{am\tilde{\Omega}}(\theta, \phi)$ and Teukolsky amplitudes at infinity $\tilde{Z}^{\infty}_{ml}(\tilde{r}, a)$. The energy flux at infinity $\dot{\tilde{E}}^{\infty}_{ml,\rm GW}(\tilde{r}, a)$ is related to the Teukolsky amplitudes $\tilde{Z}^{\infty}_{ml}$ through equation (5.13). Thus, to accurately generate the waveforms (5.3) and (5.7) far from the horizon where near-extremal simplifications can not be made, the various radiation reactive terms $\tilde{Z}^{\infty}_{ml}, \dot{\tilde{E}}_{\rm GW}(\dot{\mathcal{E}}), \dot{\tilde{E}}^{\infty}_{m,\rm GW}(\dot{\mathcal{E}}^{\infty}_{m})$ have to be handled numerically. This section outlines our numerical routines to do so.

We use the BHPT to calculate the first order dissipative radial fluxes $\dot{\tilde{E}}_{\rm GW}$ for $a = 1 - \{10^{-i}\}_{i=3}^{i=9}$ from which $\dot{\mathcal{E}}$ in Eq. (5.30) can be computed. We used the `Teukolsky` mathematica script in the toolkit and tuned the numerical precision to ~ 240 decimal digits to avoid numerical instabilities when computing $\dot{\tilde{E}}_{\rm GW}$ in the near-horizon regime for rapidly rotating holes. For moderately spinning holes $a \lesssim 0.999$, we computed the Teukolsky amplitudes with ~ 80 decimal digits of precision.

Each coefficient appearing in Eq. (5.6) is itself a sum over l modes, $\dot{\tilde{E}}^{\infty}_{m,\rm GW} = \sum_{|l|=m}^{\infty} \dot{\tilde{E}}^{\infty}_{ml,\rm GW}$. Both the sum over l and the sum over m in Eq. (5.6) can be truncated without appreciable

loss of accuracy. As discussed in [213], near-extremal EMRIs require a significant number of harmonics to be included to obtain an accurate representation of the GW signal. To illustrate for a high spin of $a = 1 - 10^{-9}$, we used the BHPT to compute $\dot{\tilde{E}}^{\infty}_{ml,\mathrm{GW}}$ for harmonics $|m| \leq l \in \{1, \ldots, 20\}$. Figure 5.4 illustrates the convergence as the number of harmonics is increased.

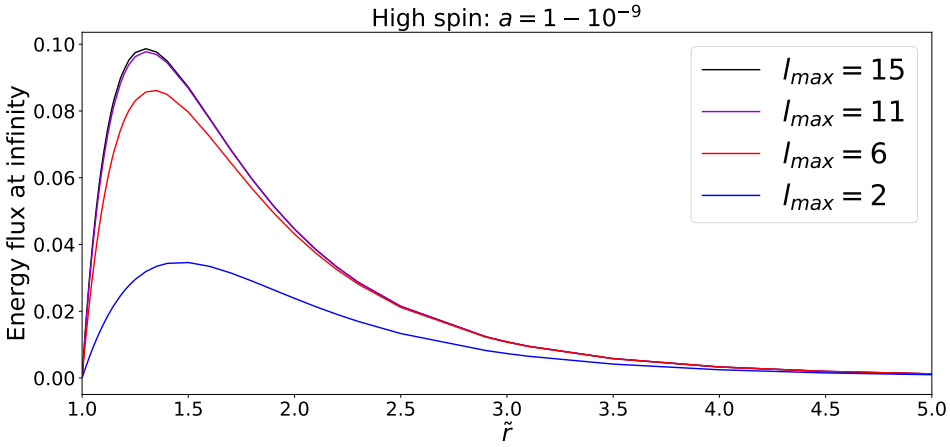

Figure 5.4: Comparison of the total energy flux at infinity (black curve) including different harmonic $\dot{\tilde{E}}^{\infty}_{lm,\mathrm{GW}}$ contributions. Note that at $\tilde{r} \approx 1.3$, the $l = 2$ harmonic energy flux $\dot{\tilde{E}}^{\infty}_{2}$ contributes $\sim 32\%$ of the total energy flux, whereas including the first $l_{\mathrm{max}} = 11$ harmonics (violet curve) contributes more than $\sim 98\%$.

Based on these results, we include harmonics with $l \leq l_{\mathrm{max}} = 20$ to calculate the total energy flux $\dot{\tilde{E}}_{\mathrm{GW}}$

$$\dot{\tilde{E}}_{\mathrm{GW}} = \sum_{|l|=2}^{l_{\mathrm{max}}} \sum_{|m|\leq l} (\dot{\tilde{E}}^{\infty}_{ml} + \dot{\tilde{E}}^{H}_{ml}), \tag{5.54}$$

using the Teukolsky package in the BHPT. In the same numerical routine, we compute $\dot{\tilde{E}}^{\infty}_{m,\mathrm{GW}} = \sum_{|l|=m}^{l_{\mathrm{max}}} \dot{\tilde{E}}^{\infty}_{ml,\mathrm{GW}}$ using $l_{\mathrm{max}} = 20$ for $m \leq 20$. These formulas are rearranged to obtain $\dot{\mathcal{E}}$ and $\dot{\mathcal{E}}^{\infty}_{m}$ using (5.30) and (2.66).

Finally for our Teukolsky based waveforms used in numerics section 5.6, we use the BHPT to extract the Teukolsky amplitudes $Z^{\infty}_{ml}(\tilde{r}, a)$ and build an interpolant over r for each harmonic $m = \{1, \ldots, l_{\mathrm{max}} = 20\}$

$$G_m(\tilde{r}, a) = \sum_{l=m}^{\infty} {}_{-2}S^{am\tilde{\Omega}}_{ml}(\theta) \exp(i\phi) \tilde{Z}^{\infty}_{ml}(\tilde{r}, a) \tag{5.55}$$

for each viewing angle $(\theta, \phi) = (\pi/2, 0)$ and $(\theta, \phi) = (0, 0)$. To summarise, we use (5.55) in (5.7) to compute FMs numerically in section 5.6. To aid our analytic study, we use the computed $\dot{\tilde{E}}^{\infty}_{m,\mathrm{GW}}$ in the waveform model (5.3) when evaluating the ratio (5.52).

5.4.2 Radial trajectory & waveform

The radial trajectory can be constructed by numerically integrating the ODE (5.1) using an interpolant for $\dot{\mathcal{E}}(\tilde{r})$ and suitable initial conditions. As before, we use the spin independent initial condition $\tilde{r}(\tilde{t}_0 = 0) = \tilde{r}_0$. Fig.(5.5) shows some example radial trajectories for various spin parameters, computed using flux data from the BHPT. In the high spin regime, the exponential decay of the radial coordinate is prominent as discussed in [211, 284]. Throughout our

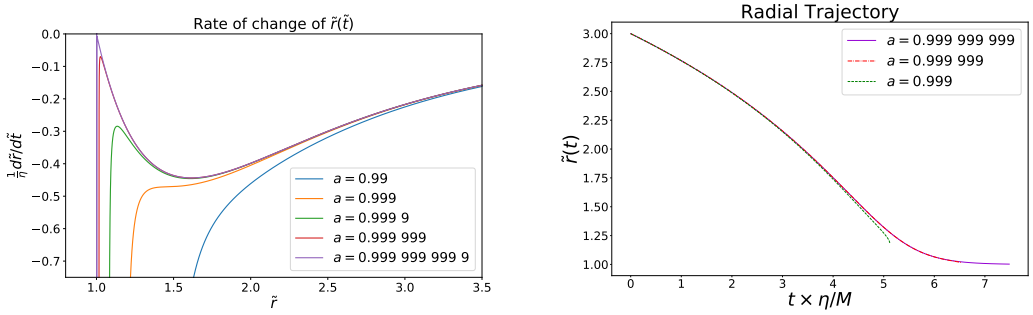

Figure 5.5: The top panel shows how $d\tilde{r}/d\tilde{t}$ varies with $\tilde{r}$. The higher the spin parameter, the more time the secondary spends in the throat before plunge. The lower panel shows the corresponding inspiral trajectory. The exponential decay in the radial coordinate is clearly shown when the primary is near maximal spin, as seen in [211].

simulations, the observation ends after a fixed amount of time, chosen such that this is before the transition to plunge for all parameter values used to compute the FM. This is important to avoid introducing artifacts from the termination of the waveform, given that the transition to plunge is not properly included in this waveform model. It is clear from Figure (5.5) that larger the spin parameter, the longer the secondary spends in the dampening regime. See equation (22) of [211] for further details.

The spin dependence of the radial evolution can be calculated by integrating (5.1) and then taking numerical derivatives. We consider two reference cases, both with component masses $\mu = 10M_\odot$ and $M = 2 \times 10^6 M_\odot$, but with different spin parameters $a = 0.9$ and $a = 1 - 10^{-6}$. We compute one year long trajectories, with $\tilde{r}(0) = 5.08$ in the first case and $\tilde{r}(0) = 4.315$ in the second. The spin derivative of the radial evolution can be calculated by perturbing the spin and using the symmetric difference formula for $\delta \ll 1$

$$\frac{\partial \tilde{r}}{\partial a} \approx \frac{\tilde{r}(a+\delta, \tilde{t}, \dot{\tilde{\mathcal{E}}}(a+\delta)) - \tilde{r}(a-\delta, \tilde{t}, \dot{\tilde{\mathcal{E}}}(a-\delta))}{2\delta}. \tag{5.56}$$

Figure 5.6 plots the quantity $|\partial_a \tilde{r}|^2$ appearing in the FM estimation (5.19). By inspection, it is clear that $|\partial_a \tilde{r}|^2$ is largest when the spin parameter is close to unity and when the radius is close to $\tilde{r}_{\rm isco}$, matching our analytical conclusions using approximations (5.43) and (5.34).

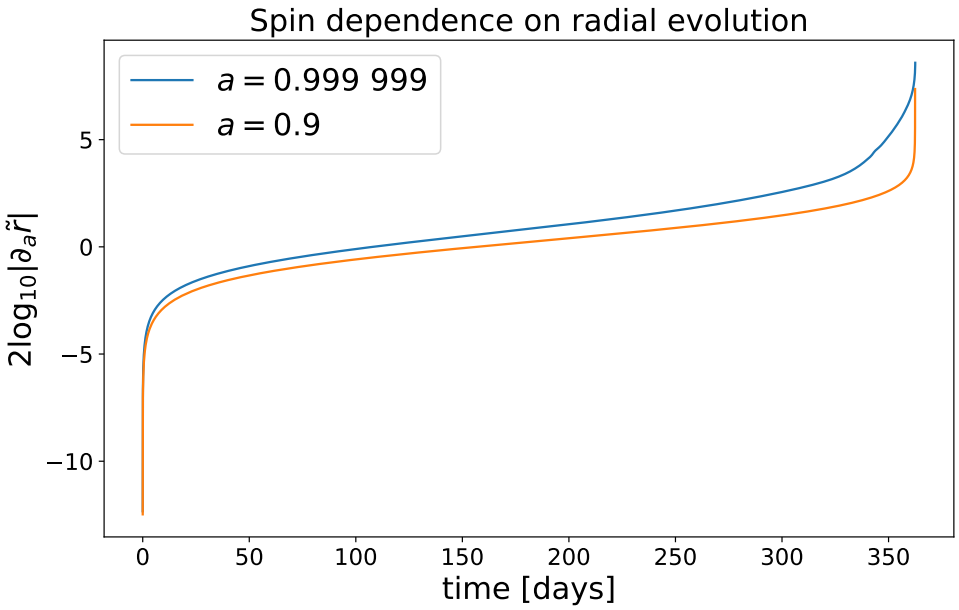

Figure 5.6: The blue curve is $\partial_a \tilde{r}$ for $a = 0.999999$. The orange curve is $\partial_a \tilde{r}$ for $a = 0.9$. Notice that the spin dependence on r grows rapidly in the near-ISCO region of the rapidly rotating hole.

Using the semi-analytic model (5.3) we now evaluate the estimate (5.52), for the same two systems, but different r_0 to ensure that the assumptions made in deriving Eq. (5.52) still hold ($\tilde{r}_0 = 2.85$ for $a = 0.9$ and $\tilde{r}_0 = 1.2$ for $a = 1 - 10^{-6}$). We choose termination points $\tilde{r}_{\rm cut} = \tilde{r}_{\rm isco} + \lambda$ with $\lambda \sim \{\lambda_{\rm ext} = 10^{-4}, \lambda_{\rm mod} = 10^{-2}\}$, just outside the transition region. Finally, the expression $\sum C_{\infty,m}$ was calculated using the high_spin_fluxes.nb mathematica notebook in the BHPT, including harmonics up to $m = 20$. We find the ratio to be

$$\frac{\Gamma^{\rm ext}_{aa}}{\Gamma^{\rm mod}_{aa}} \sim 500, \tag{5.57}$$

giving a rough estimate that the spin precision increases by at least two orders of magnitude for these two sources.

This verifies claims made in section 5.3.3. When correlations with other parameters and the shape of the PSD are ignored, we predict a precision on the spin parameter roughly *two* orders of magnitude higher than for moderately spinning BHs.

To generate gravitational waveforms for the numerical study we use the Teukolsky waveform model (5.7), discussed in chapter 2 in subsection 2.4.1. The waveform depends on parameters $\boldsymbol{\theta} = \{a, \tilde{r}_0, \mu, M, \phi_0, \tilde{D}\}$. We will consider two classes of near-extremal source, differentiated by the magnitude of their component masses and mass ratio. The first "heavier" source has

parameters

$$\boldsymbol{\theta}_{\rm heavy} = \{\tilde{r}(t_0 = 0) = 1.225, a = 1 - 10^{-6}, \mu = 20M_\odot, \\ M = 10^7 M_\odot, \phi_0 = \pi, \\ D = \{D_{\rm edge} = 1.8, D_{\rm face} = 3\}{\rm Gpc}\} \quad (5.58)$$

and the second "lighter" source has

$$\boldsymbol{\theta}_{\rm light} = \{\tilde{r}(t_0 = 0) = 4.3, a = 1 - 10^{-6}, \mu = 10M_\odot, \\ M = 2 \times 10^6 M_\odot, \phi_0 = \pi, \\ D = \{D_{\rm edge} = 1, D_{\rm face} = 4\}{\rm Gpc}\}, \quad (5.59)$$

where $D_{\rm edge}$ and $D_{\rm face}$ refer to the distance if each source is viewed edge-on/face-on respectively. The distances are fine tuned[4] so that we achieve a signal to noise ratio of $\rho \sim 20$. This is discussed later in section 5.5. The lighter source is sampled with sampling interval $\Delta t_s \approx 4$ seconds and the heavier one with $\Delta t_s \approx 25$ seconds. We note here that $\Delta t_s = M\Delta\tilde{t}$ where $\Delta\tilde{t}$ is the dimensionless sampling interval used to integrate (5.1). The sampling interval is chosen from Shannon's sampling theorem such that $\Delta t_s < 1/(2f_{\rm max})$, where

$$f^{\rm edge}_{\rm max} = \frac{20}{2\pi}\frac{\tilde{\Omega}_{\rm isco}}{M}, \quad f^{\rm face}_{\rm max} = \frac{2}{2\pi}\frac{\tilde{\Omega}_{\rm isco}}{M} \quad (5.60)$$

are the highest frequencies present in the waveform for the edge-on and face-on cases respectively. To illustrate, near-extremal waveforms with parameters $\boldsymbol{\theta}_{\rm light}$ for both edge-on and face-on viewing angles are plotted in Fig.(5.7). Notice from this figure that we see the characteristic dampening feature unique to near-extremal EMRIs as a source, first observed in [211]. We also saw this in figure 4.4 at the end of chapter 4.

The lighter source is interesting because it exhibits both an "inspiral" regime and n exponentially decaying regime that we will refer to as "dampening". The heavier source is interesting because the dampening regime lasts more than one year and so the signal is in the dampening region for the entire duration of the observation. In the next section, we discuss detectability of these two types of sources by LISA.

[4]Strictly speaking, distance here is not a physical parameter since our waveform model does not include the LISA response to the strains h_+ and $h_\times$.

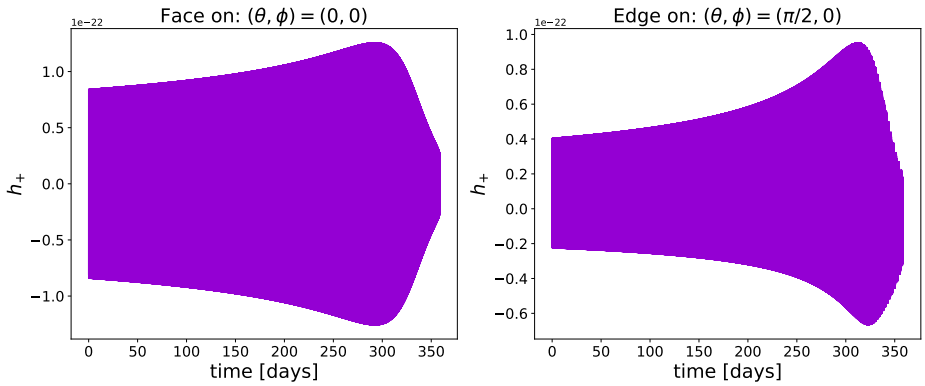

Figure 5.7: A near-extremal waveform with parameters $\boldsymbol{\theta}_{\text{light}}$ viewed face-on (left) and edge-on (right). The dampening region lasts ~ 55 days. The edge-on case is asymmetric due to the large number of $l = 20$ modes and shows prominent relativistic beaming near the ISCO as observed in figure 3.b) of [211].

5.5 Detectability

The LISA PSD reaches a minimum around 3mHz, and is fairly flat within the band from 1 to 100mHz. Using equation (5.4), an edge-on near-extremal inspiral with primary mass of $\sim 10^7 M_\odot$ dominant harmonic will have a frequency of ~ 3.2mHz at plunge, while the $m = 20$ harmonic has frequency of 64 mHz. Such heavy sources are thus ideal systems for observing the near-ISCO dynamics. For the lighter mass considered, $2 \times 10^6 M_\odot$, the near-ISCO dynamics are at frequencies a factor of 5 higher, where the LISA PSD starts to rise. While the near-ISCO radiation will still be observable for these systems, its relative contribution to the signal will be relatively reduced. We therefore expect to obtain more precise spin measurements for the heavier of the two reference systems.

To remind the reader, the discrete analogue of the optimal matched filtering SNR is defined by Eq. (3.47)

$$\rho^2 \approx \frac{4\Delta t_s}{N} \sum_{i=0}^{\lfloor N/2+1 \rfloor} \frac{|\tilde{h}(f_i)|^2}{S_n(f_i)}. \tag{5.61}$$

Here N is the length of the time series, Δt_s is the sampling interval (in seconds) and $f_i = i/N\Delta t_s$ are the Fourier frequencies (in Hertz). To avoid problems with spectral leakage, prior to computing the Fourier transform, we smoothly taper the end points of our signals using the Tukey window defined by (3.6). As discussed in chapter 3, subsection 3.1.3, this is essential in order to reduce spectral artefacts through conversion from the time domain into the frequency domain.

For the heavier source, we use $\alpha = 0.25$ to reduce leakage effects significantly and frequency resolution is not a problem since the frequencies of the signal are contained within the LISA

frequency band (for all harmonics). For the lighter source, we use $\alpha = 0.05$ to reduce edge effects while retaining the ability to *resolve* the frequencies where the signal is dampened. We found that calculated SNRs and parameter measurement precisions are insensitive to the choice of α in the heavier system. The lighter system is more sensitive: for larger α, more of the dampening regime is lost, with a corresponding impact on the measurement precisions. We believe that $\alpha = 0.05$ is large enough to reduce leakage but small enough to resolve as much of the dampening regime as possible.

After tapering, we zero pad our waveforms to an integer power of two in length, in order to facilitate rapid evaluation of the DTFT using the fast Fourier transform using (3.5). Computing the SNR in this way gives $\rho \sim 20$ for the light and heavy sources respectively when viewed both edge-on and face-on under the configuration of parameters $\boldsymbol{\theta}_{\text{light}}$ and $\boldsymbol{\theta}_{\text{heavy}}$.

In all cases we marginally exceed the threshold of $\rho \approx 20$ which is typically assumed to be required for EMRI detection in the literature [97, 102].

As mentioned above, the lighter source exhibits two regimes of interest - the initial gradually chirping phase, where the waveform resembles those for moderately spinning primaries, and then the exponentially damped phase while the secondary is in the near-horizon regime. It is natural to ask what proportion of the SNR, and later what proportion of the spin measurement precision, is contributed by each regime. For both edge-on and face-on systems, we separate the two parts of the waveform using Tukey windows and compute the SNR contributed by each part to find

$$\rho^2_{\text{face-on}} \sim \begin{cases} 83\% & \text{Outside dampening region} \\ 17\% & \text{Dampening region.} \end{cases} \tag{5.62}$$

$$\rho^2_{\text{edge-on}} \sim \begin{cases} 96\% & \text{Outside dampening region} \\ 4\% & \text{Dampening region.} \end{cases} \tag{5.63}$$

For the face-on source, there is just a single dominant harmonic, and the frequency of this harmonic is such that it lies in the most sensitive part of the LISA frequency range. This helps to enhance the relative SNR contributed by the dampening region. The edge-on source, by contrast, has multiple contributing harmonics, which are spread over a range of frequencies, and the proportional contribution of the dampening region to the overall SNR is therefore diminished.

For a non-evolving signal the SNR accumulates like $\sqrt{T_{\text{obs}}}$, where T_{obs} is the total observation time. The pre-dampening regime lasts 308 days, and so from duration alone we would expect

a fraction $\sqrt{308/365} \approx 93\%$ of SNR to be accumulated there. The difference to what we find above is explained by differences in amplitudes of the individual harmonic(s). The heavier system is within the dampening regime throughout the last year of inspiral and so all of the SNR of $\rho \sim 20$ is accumulated there. This may seem counter-intuitive given the exponential decay of the signal during the dampening regime. However, the exponential decay rate is relatively slow, a large number of harmonics contribute to the SNR and the emission is all within the most sensitive range of the LISA detector. This is clear from looking at the time-frequency spectrogram of the heavier signal shown in Fig.(5.8). What we learn from this figure is that there are a significant number of harmonics that have comparable power to the dominant $m = 2$ harmonic. We see also that the angular frequency at each harmonic, and thus f_m, shows little rate of change for $M \sim 10^7$ and $\eta \sim 10^{-6}$. This is consistent with [213, 211], where it was shown that a large number of m harmonics is required to produce an accurate representation of the GW signal for a near-extremal EMRI, particularly for near edge-on viewing angles. For moderately spinning BHs $a \sim 0.9$ there are not as many dominant harmonics, so those waveforms are cheaper to evaluate.

We are now ready to move on to compute FM estimates of parameter measurement precisions. This will be the focus of the next section.

5.6 Constraints on the spin parameter

We now compute the FM (3.59) numerically without making the simplifying assumptions used in sections 5.3.2 and 5.3.3. We will use one simplification, which is to *ignore* the spin dependence in $\dot{\mathcal{E}}$, $Z^{\infty}_{lm}(\tilde{r}, a)$ and ${}_{-2}S^{am\tilde{\Omega}}_{lm}(\theta, \phi)$ and fix these at the values computed for $a = 1 - 10^{-9}$ using the BHPT. We argued in Eq. (5.32) that the spin dependence of the flux correction is a sub-dominant contribution in the near-ISCO regime, and this is further justified in Appendix B.2 (see Fig. B.2 in particular). While $\partial_a \dot{\mathcal{E}}$ does grow as the ISCO is approached, it remains sub-dominant to the spin dependence of the kinematic terms. This approximation is likely conservative in the sense that we are removing information about the spin from the waveform model and so the true measurement precision is most likely higher. Nonetheless, we expect this to be a small effect, and have verified that relaxing this assumption does not significantly change the result for the heavier reference source (see Figure 5.9). We note that we make this assumption only for computational convenience. Waveform models used for parameter estimation on actual LISA data should use the most complete results available to ensure maximum sensitivity and minimal parameter biases.

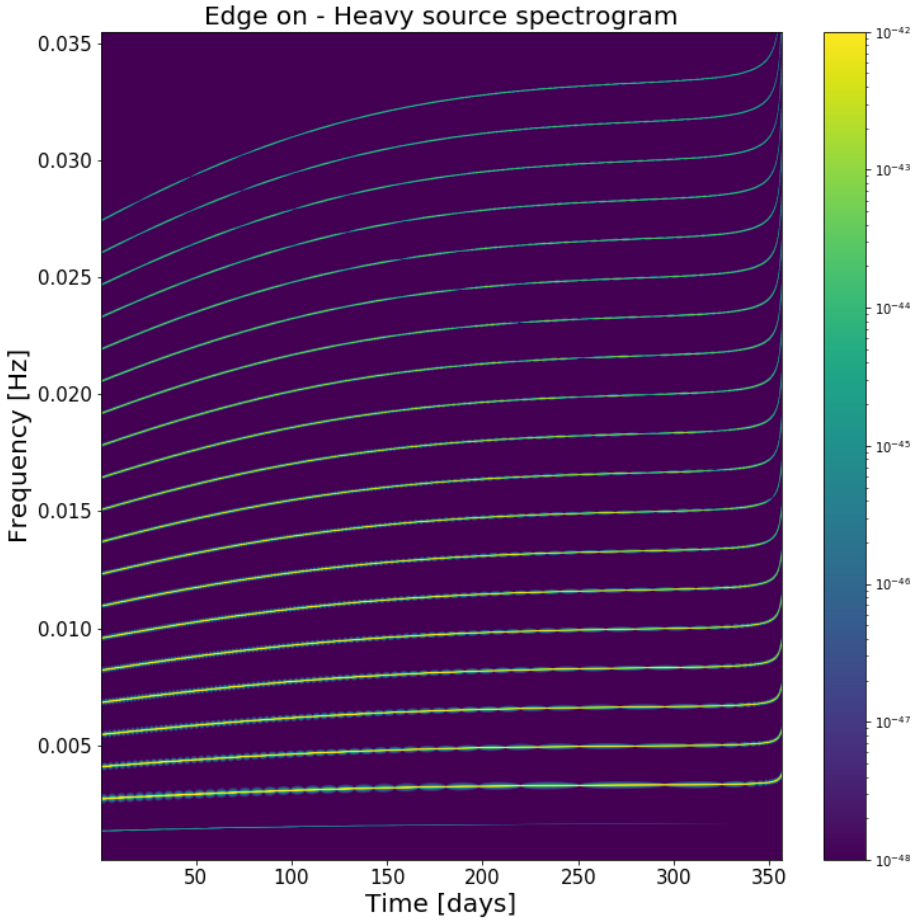

Figure 5.8: Here we plot the spectrogram of $h(\boldsymbol{\theta}_{\text{heavy}}; t)$ viewed edge on. We see 20 tracks in the time-frequency plane corresponding to the $m \in \{1, \ldots, 20\}$ harmonics. The colorbar shows that the $m = 2$ harmonic (second lowest track in frequency) is dominant, but that there are several other harmonics which contribute significantly to the radiated power

.

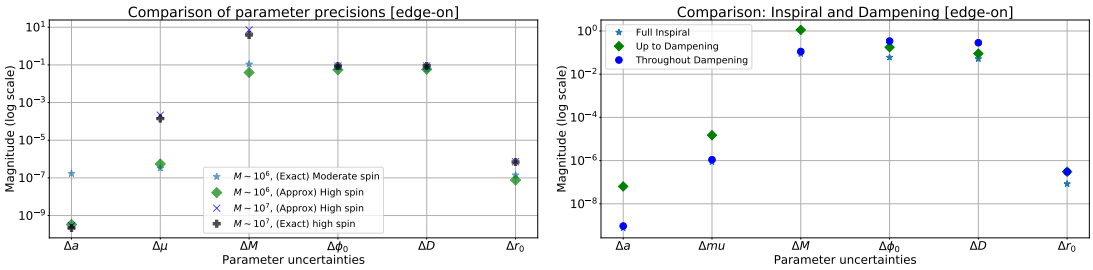

Figure 5.9: (Left plot) Parameter measurement precision, as estimated using the FM formalism, for the three reference sources, with parameters $\boldsymbol{\theta}_{\rm light}$ (green diamonds), $\boldsymbol{\theta}_{\rm heavy}$ (purple crosses) and $\boldsymbol{\theta}_{\rm mod}$ (blue asterisks). The black diamonds show the precisions obtained when including the spin-dependence of the relativistic corrections, $\dot{\mathcal{E}}$ in the waveform model for the heavy source. (Right plot) Parameter measurement precisions for the source with parameters $\boldsymbol{\theta}_{\rm light}$, computed using the full waveform (blue asterix), only the inspiral phase (blue dot) and only the dampening phase (green diamond).

To compute the waveform derivatives required to evaluate (3.59), we use the fifth order stencil method

$$\frac{\partial f}{\partial x} \approx \frac{-f_2 + 8f_1 - 8f_{-1} + f_{-2}}{12\delta x}, \tag{5.64}$$

for $\delta x \ll 1$ and $f_i = f(x + i\delta x)$. To avoid numerical instability of $\partial_a h$ for the near-extremal spin values of $a \leq 1 - 10^{-9}$, we ensure that $\delta x < 1 - a$ so the perturbed waveform does not have spin exceeding $a = 1$. We further assume that $\partial_a \tilde{t}_{\rm end}$ is zero so there is *no* spin dependence on the total observation time.

In addition to the sources with parameters $\boldsymbol{\theta}_{\rm heavy}$ and $\boldsymbol{\theta}_{\rm light}$, we now consider a third source with parameters

$$\boldsymbol{\theta}_{\rm mod} = \{\tilde{r}(t_0 = 0) = 5.01, a = 0.9, \mu = 10 M_\odot, \tag{5.65}$$

$$M = 2 \cdot 10^6 M_\odot, \phi_0 = \pi, D_{\rm edge} = 1{\rm Gpc}\}, \tag{5.66}$$

with SNR ~ 20.

FM estimates of parameter measurement precisions for all three sources viewed edge-on are shown in Figure 5.9. We do not present the results for a face-on observation as they are near-equivalent to the measurements presented in figure 5.9 for equivalent SNR.

We see from this figure that we should be able to constrain the spin parameter of near-extremal EMRI source with rotation parameter $a = 1 - 10^{-6}$ to a precision as high as $\Delta a \sim 10^{-10}$, even when accounting for correlations amongst the waveform parameters. This is true for both the lighter and the heavier sources viewed edge-on and face-on, with a constraint a factor of a few better for the heavier source. The right panel of the figure compares the contribution to the measurement precision for the lighter source from the two different phases of the signal. We

see that the high spin precision comes almost entirely from the observation of the dampening regime and this phase of the signal contributes much more information than we would expect based on its contribution to the total SNR[5].

The spin measurement precision for the near-extremal systems is three orders of magnitude better than for the system with moderate spin, while all other parameter measurements are comparable.

Comparing to the exact FM result with spin dependence included in all the various terms, we see that the two precisions are almost *identical*: the exact result offers precisions that are marginally better in comparison to our approximate result (removing spin dependence from the corrections). This figure thus justifies ignoring the spin dependence of $\dot{\mathcal{E}}$, since relaxing that assumption makes almost no difference to the results. This numerically confirms our belief that the spin dependence in the corrections to the fluxes are *subdominant* in the analysis leading to (5.19). In the same plot 5.9, we also compare results of near-extremal BHs to moderately spinning holes. A direct comparison shows an increase in the spin precision by ~ 3 orders of magnitude, which agrees with the intuition given by the earlier analytic analysis, Eq. (5.57).

To our knowledge, these are the first circular and equatorial parameter precision studies for EMRIs that have employed Teukolsky-based *adiabatic* waveforms, rather than approximate waveform models (or "kludges"), which have been used for many studies [102, 103, 101]. Comparing our results for the moderately spinning system to these previous studies, we find that our results are very comparable, but a factor of a few *tighter*. This could be because we are including only a subset of parameters and ignoring the details of the LISA response, or because we have a more complete treatment of relativistic effects. A more in depth study addressing both of these limitations would be needed to understand the origin of the differences. However, the agreement between our results and previous studies are sufficiently close, and considerably less than the difference we find between the moderate and near-extremal spin cases, to give us confidence that our results are not being unduly influenced by these simplifications.

In Figure (5.10) we show how the parameter estimation precision for the source with parameters $\boldsymbol{\theta}_{\rm light}$ changes as we vary the spin parameter, while keeping all other parameters unchanged. We present results for both face-on and edge-on viewing angles. This shows that while the measurement precision for most of the parameters is largely independent of spin in the near-extremal regime, the spin precision steadily increases as $a \to 1$. We note that even at a spin of $1-10^{-9}$, the measurement precision satisfies the constraint $\Delta a < |1-a|$ and therefore a LISA EMRI observation would be able to resolve that the system was not maximally extremal,

[5] In (5.19), the growth of $\partial_a \tilde{r}$ exceeds the growth of $S_n(f) \sim$ const in the dampening regime. This sources the high precision measurement.

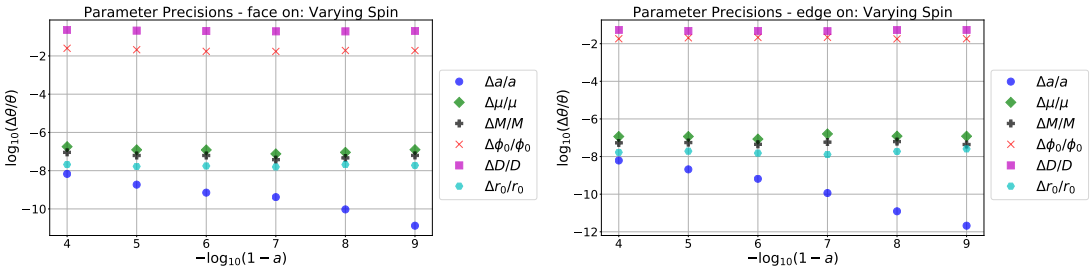

Figure 5.10: We keep $\boldsymbol{\theta}_{\text{light}} \backslash \{a\}$ fixed and vary $a = 1 - 10^{-i}$ for $i \in \{4, \ldots, 9\}$ while computing estimates on the precision of the measured parameters using the FM. Results are shown for sources viewed face-on (left) and edge-on (right).

i.e., that $a < 1$. Focusing on spin parameters $a > 1 - 10^{-9}$ would require use of arbitrary precision programmes and we relegate that for future work.

Due to large condition numbers, inverting FMs for EMRI sources is a highly non-trivial task. In appendix B.3, we provide multiple diagnostic tests of our FM algorithm and verify that, in the single parameter case, the spin parameter precision is a suitable representation of the 1σ width of the Gaussian likelihood as shown in figure B.4. These single parameter tests of the FM are useful tests to verify that a single parameter algorithm yields sensible results. However, real instabilities of the numerical procedure are prominent the moment the inverse of the FM is performed when correlations are present. Hence, it is both necessary and sufficient to verify our FM calculations using an *independent* procedure. The next section is dedicated to performing a parameter estimation study on both near-extremal EMRIs with parameters $\boldsymbol{\theta}_{\text{light}}$ and $\boldsymbol{\theta}_{\text{heavy}}$.

5.7 Verifying constraint measurements: MCMC

The FM is a local approximation to the likelihood, valid in the limit of sufficiently high SNR. We can verify that this local approximation is correctly representing the parameter measurement uncertainties by numerically evaluating the likelihood using MCMC. To reduce the computational cost of these simulations we use a face-on viewing profile and thus only consider the $m = 2$ harmonic. We have shown in figure (5.10) that parameter precision measurements are not largely dependent on the choice of viewing angle for the lighter source. We have further verified this claim for the heavier source.

We follow the Metropolis-Hastings algorithm presented in chapter 3, subsection 3.5. Noise realisations are generated using (3.34) and we use the Whittle likelihood defined in (3.31). We construct two separate data streams, each with Gaussian stationary noise and one of two signals $h(\{\boldsymbol{\theta}_{\text{heavy}}, \boldsymbol{\theta}_{\text{light}}\}; t)$ for the waveform model (5.7) for face-on viewing only. As before,

we construct waveforms ignoring the spin dependence in $\dot{\mathcal{E}}$, the Teukolsky amplitudes $\tilde{Z}^{\infty}_{lm}$ and the spheroidal harmonics ${}_{-2}S^{am\tilde{\Omega}}_{lm}(\theta,\phi)$. We evaluate these for a fixed spin parameter of $a = 1 - 10^{-9}$.

We remind the reader the main drive for the tight constraints on the spin parameter is due to the spin dependence induced through the kinematic terms present in (5.7), as discussed in section 5.6, and not its dynamical terms, justifying our approximation.

In accordance with Bayes' theorem, we set priors on the parameter set $\boldsymbol{\theta} = (\tilde{r}_0, a, \mu, M, \phi_0, D)$ corresponding to either the light or heavy source, distinguished by the masses and distances.

The priors on a, ϕ_0 and D for both sources were

$$\begin{aligned} a &\sim 1 - U[10^{-4}, 10^{-8}] \\ \phi_0 &\sim U[0, 2\pi] \\ D &\sim U[1, 8]\text{Gpc}. \end{aligned}$$

The priors on μ, M and $\tilde{r}_0$ were chosen differently for the heavy and light source as

$$\begin{aligned} \mu_{\text{heavy}} &\sim U[18, 22] M_\odot \\ \mu_{\text{light}} &\sim U[8, 12] M_\odot \\ M_{\text{heavy}} &\sim U[0.9, 1.1] \times 10^7 M_\odot \\ M_{\text{light}} &\sim U[1.9, 2.1] \times 10^6 M_\odot. \\ \tilde{r}_0^{\text{heavy}} &\sim U[1.2, 1.3] \\ \tilde{r}_0^{\text{light}} &\sim U[4.2, 4.4] \end{aligned}$$

The prior on a ensures that we do not move outside the range in which our approximations are valid, $a \gtrsim 0.9999$. The tight priors on the individual component masses helped to improve the computational efficiency of our algorithm. However, there was no evidence of the MCMC chains reaching the edges of the priors in our simulations, so we are confident these restrictions are not influencing the results.

The purpose of this section is to show that our FM predictions are a good guide for the parameter precision on the parameters. The MCMC algorithm should work with *any* proposal distribution, just some increase sampling efficiency more than others. Since we believe the parameters are highly correlated, we chose to use a proposal distribution that took these correlations into account. Hence, to aid sampling of the algorithm, we chose the variance-covariance matrix of the proposal distribution to be the inverse of the FM evaluated at the true param-

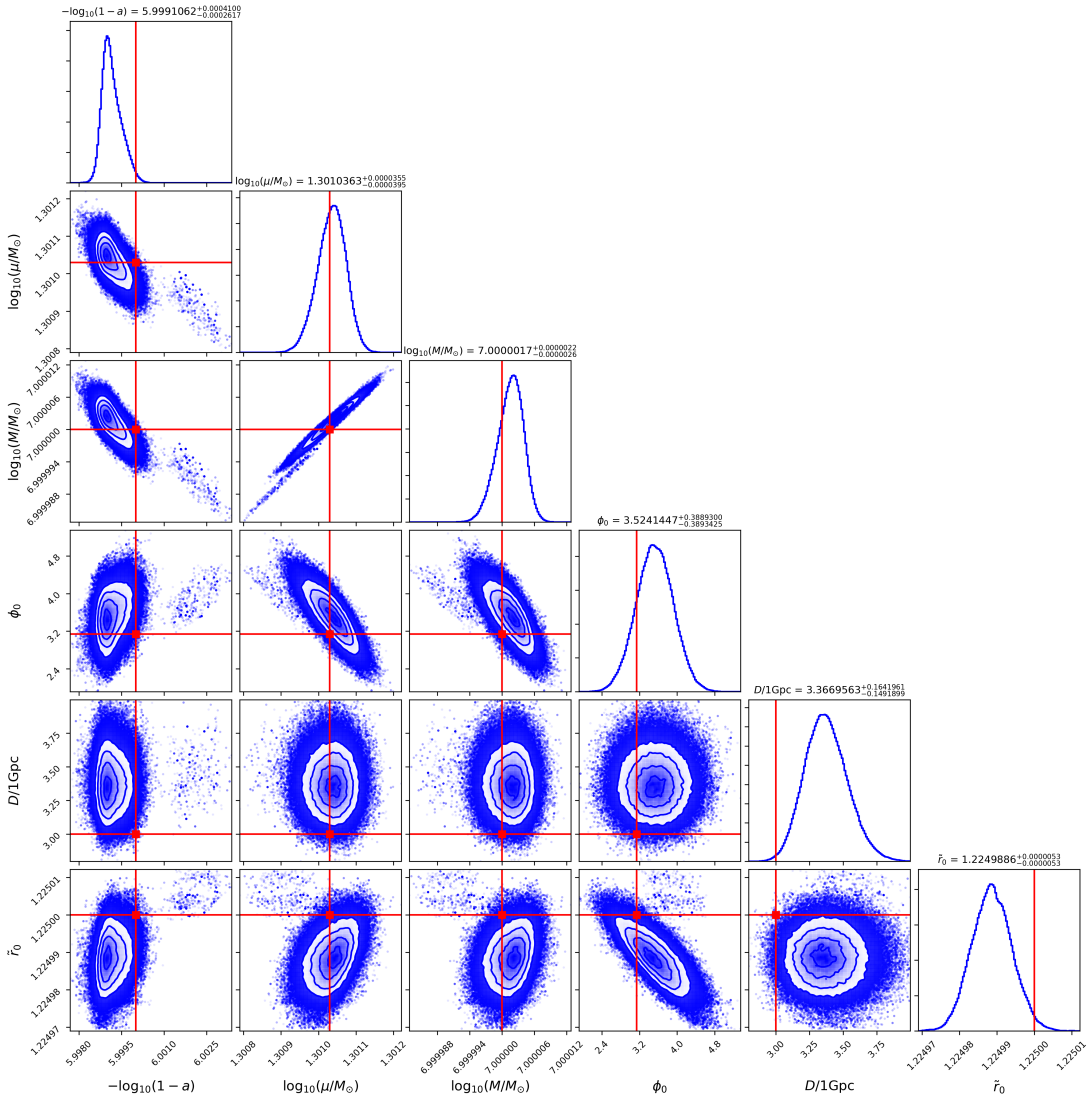

Figure 5.11: The diagonal plots represent the marginalised posterior distributions on the parameters $\boldsymbol{\theta}_{\mathrm{heavy}}$. The plots below the diagonal are the joint two-dimensional posterior distributions. The red lines indicate the true values of the injected signal.

eters of the signal. Under our choice of proposal distribution, if the sampler turned out to be inefficient then the FM would be a poor choice of proposal distribution. Hence we feel like there is no loss of generality when using the inverse FM as the proposal distribution.

Evaluating the likelihood for EMRI waveforms is an expensive procedure. In order to obtain a sufficient number of samples from the posterior, we used high performance computing facilities and ran 20 unique chains for $N = 40,000$ iterations. All chains analysed the same input data set, but with different initial random seeds. This ensures that the dynamics of the chains are different but the noise realisations are the same for each MCMC procedure. We run the algorithm presented in subsection 3.5 to obtain marginal posterior distributions and two-dimensional contour plots for the two sources. These are shown in figures (5.11) and (5.12).

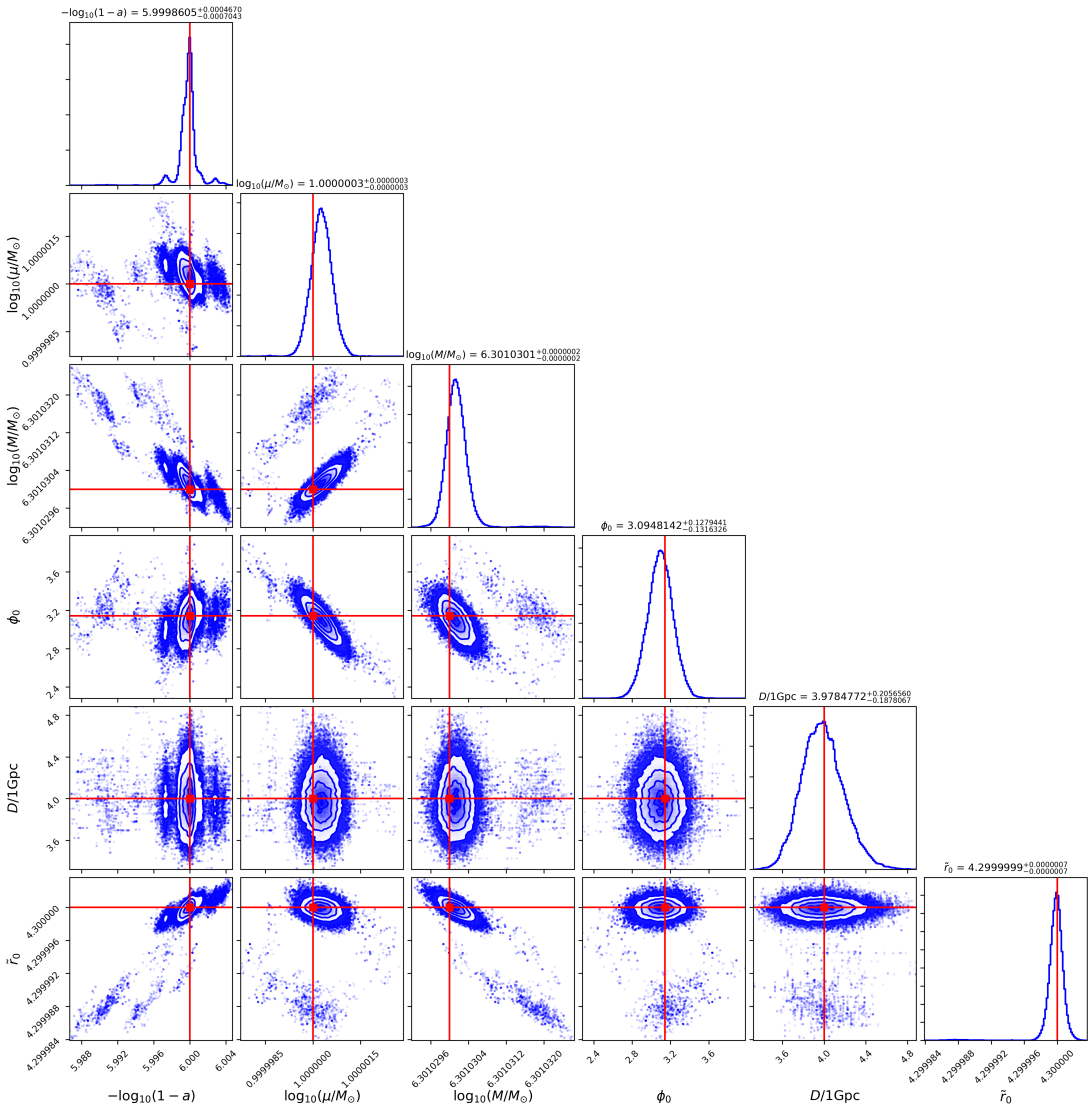

Figure 5.12: As Figure 5.11, but now for the source with parameters $\boldsymbol{\theta}_{\mathrm{light}}$.

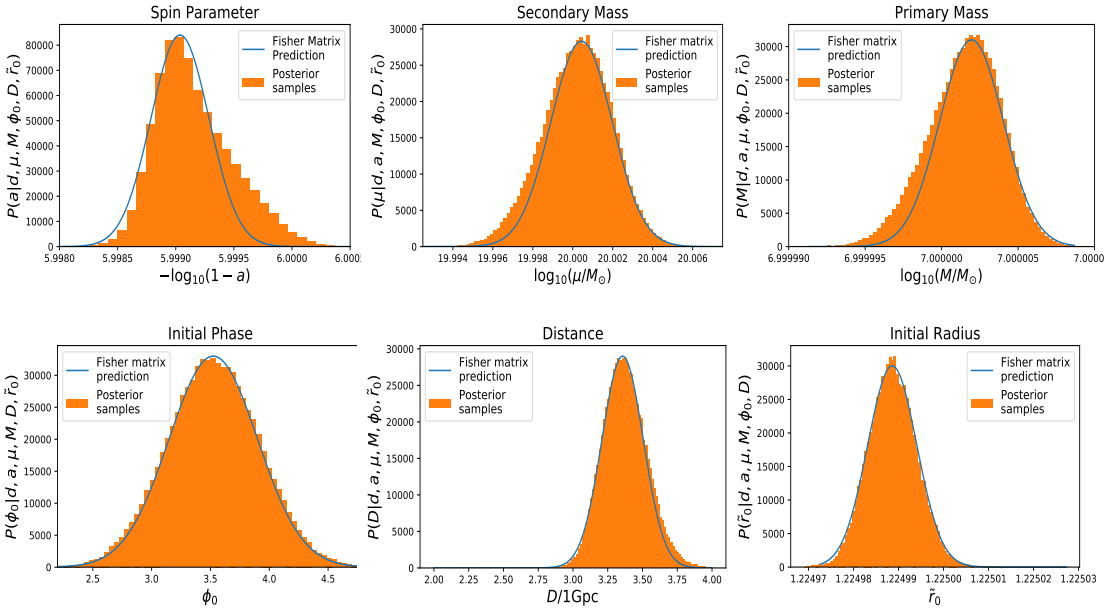

Figure 5.13: For the source with parameters $\boldsymbol{\theta}_{\rm heavy}$,we compare the one-dimensional marginalised posterior distributions (orange histograms) to a Gaussian distribution (blue solid line), centred at the posterior mean, and with standard deviation set to the prediction of the FM.

These plots confirm the high precisions of parameter measurements that were seen with the FM. The relative uncertainties $\Delta\theta/\theta$ are similar for the two sources, although we can measure the spin parameter more precisely for the heavier source. For the most part the posteriors are unimodal, apart from the spin posterior of the lighter source. We have verified that the secondary modes are real features of the likelihood, and correspond to the waveform phase shifting by one cycle within the late dampening regime. We also note that shifts in the peak of the posterior away from the true value are larger for the heavier source than for the lighter source. This appears to be due to the particular noise realisation. For other noise realisations the noise-induced statistical fluctuation from the true parameters for the heavier source are smaller. For noise-free data sets, we find posterior distributions peaked at the true parameters, as expected.

The primary reason for doing the MCMC simulations was to verify the FM results found earlier. In figures 5.13 and 5.14, we plot the marginalised posteriors on the parameters $\{\boldsymbol{\theta}_{\rm light}, \boldsymbol{\theta}_{\rm heavy}\}$ alongside a Gaussian distribution with variance given by the FM and centred at the mean value of the posterior distributions $p(\boldsymbol{\theta}|d)$.

These results nicely confirm the accuracy of the FM results for these sources. In each case, the 1σ precision predicted by the FM is slightly smaller than the width of the numerically computed posterior. This is to be expected as the FM also provides the *Cramer-Rao lower*

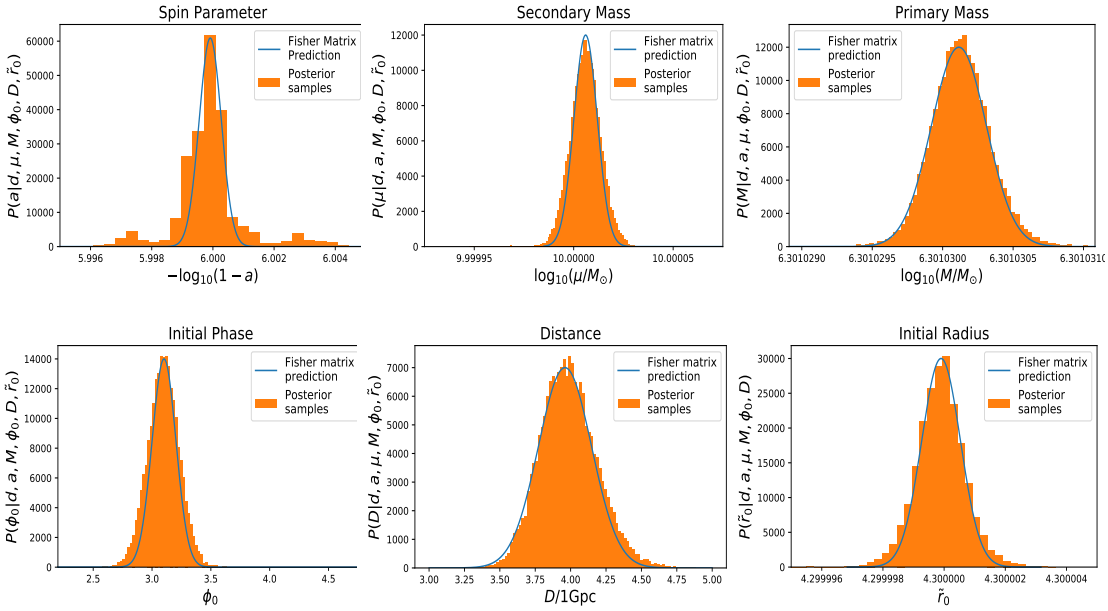

Figure 5.14: As Figure 5.13, but now for the lighter source with parameters $\boldsymbol{\theta}_{\text{light}}$.

bound on parameter uncertainties. However, the difference is very small. We are thus confident that all of our FM predictions are accurate, including the exploration of parameter space shown in Figure 5.10. We conclude that even at the near-threshold SNR of this source, $\rho \sim 20$, the FM can be used to confidently estimate the precision of parameters for near-extremal sources.

5.8 Conclusion

This chapter has shown that we expect tighter spin constraints on the Kerr spin parameter for EMRIs when the primary is rapidly rotating rather than moderately rotating. We argued that the spin precision is sourced through the rapid growth of the spin dependence on the radial trajectory throughout the near-ISCO regime. It was shown that radiation-reaction effects are subdominant to geodesic motion, which is what ultimately drives the excellent constraint on the spin parameter.

This details present in this chapter has tried to answer the question of how well LISA can constrain the spin parameter of an EMRI source, conditioned on the primary rapidly rotating. In the earlier sections of this paper, we were able to derive a *general* linear ODE whose solution describes the spin dependence on the radial trajectory. Using this ODE, we were able to argue that this spin dependence is much more significant for near-extremal primaries rather than moderately spinning primaries $a \sim 0.9$. It was also shown that the spin dependence on the radial evolution is dominated more by geodesics, rather than the radiation reactive terms. Using reasonable assumptions, analytic Fisher scalars were derived for both rapidly

rotating and moderately spinning BHs. It was then shown, explicitly, that the precision on spin parameters for near-extreme BHs should exceed that of moderately spinning ones by a few orders of magnitude. The exceptional precision is governed by the growth of the spin dependence of the trajectory near the ISCO. Given that the kinematical terms dominate the precision, we were able to build a near-extremal waveform model by removing the spin dependence in corrections to the radial fluxes. This meant we could build an interpolant, valid for quasi-circular and equatorial inspirals, into rapidly spinning BHs with $a \gtrsim 0.999$. Using this approximation, we were able to build a waveform model valid for near-extremal spins that could be used for parameter precision studies.

Our analysis showed that the LISA optimum masses for parameter estimation and precision studies are heavier mass systems $M \approx 10^7 M_\odot$. For heavier sources, the emitted frequencies will lie within the minimum of the LISA PSD during the dampening regime; when the signal provides most accurate information about the source. Analysing different parts of the signal, we were able to conclude that the end part of the signal will be "loud" in the data stream for spins approaching near-extremality $a \to 1$. For lighter mass sources $M \sim 10^6 M_\odot$, the accumulated SNR of the dampened part of the signal is weak. Fully numerical FM analysis revealed that we can constrain the spin parameter of a near-extremal EMRI ~ 3 orders of magnitude higher than moderately spinning BHs $a \sim 0.9$. For very near-extremal primaries $a \sim 1 - 10^{-9}$, one is able to constrain the spin parameter with precision $\Delta a \sim 10^{-12}$. This is, as far as we know, the tightest constraint on astrophysical parameter found in the literature. In the final section, with the view of verifying our FM calculations, we performed a parameter estimation study on these near-extremal sources. We showed that the signal parameters are able to be extracted with precision comparable to our FM estimates.

To conclude, we can safely say that the spin parameter of near-extremal EMRIs can be measured with *excellent* precision. We are also confident that the increase in precision is governed by the spin dependence on the radial trajectory. If the dampened part of the signal is not observed (where $\partial_a \tilde{r} \gg 1$), then we cannot make such precise statements on the spin of the primary BH.

There are a few extensions to this work. The first would be to include the results of the transition from inspiral to plunge from chapter 4 to our analysis here. We suspect that, although the SNR accumulation would be weak, the extra contribution from $\partial_a \tilde{r}$ could only *improve* the precision measurement. Another obvious extension would be to introduce more parameters in the parameter space, such as eccentricity and inclination. In this case, we are unsure whether the kinematic terms would dominate over the flux corrections. As such, we would require a more

complex and general waveform model. As seen in [211], eccentric trajectories of secondaries in the vicinity of near-extremal BHs exhibit *inverse* zoom-whirl behaviour. That is, the "zoom" part of the inspiral (near aperiastron) outputs larger amplitude radiation than the "whirl" phase. Perhaps this extra information, unique to near-extreme EMRIs, could provide even tighter constraints on the spin parameter a. It would be interesting to see whether the larger number of parameters will aid or hinder parameter precision/estimation studies. In recent work [285, 286, 287], adiabatic Teukolsky based waveforms have been constructed for a *spinning* particle on a circular and equatorial orbit around a MBH. A detailed analysis on whether the secondaries spin was performed with the conclusion that the secondaries spin parameter *cannot* be measured, confirming results from [288, 289]. Including this feature in our waveform model, it would be interesting to see by how much the primaries spin parameter constraint would *degrade* due to degeneracies between the secondary and primaries spin parameters. Another exciting area to investigate would be potential tests of general relativity. Due to the precision on both Δa and ΔM, near-extremal EMRIs would provide stringent tests of GR theories. One of which being the no-hair theorem which states that the Kerr BH can be uniquely parametrized in terms of two charges; mass and spin. We believe that it should be possible to measure the multipolar moments more accurately when the primary is near-extremal than if it were only moderately spinning. A paper exploring potential tests of general relativity using the near-extremal Kerr spacetime would be useful for the literature.

Finally, one other interesting direction to explore would be the effect of systematic errors (through innacurate waveform modelling) in our EMRI parameter estimation studies. Discussed in chapter 3, subsection 3.4, one could use the Cutler and Vallisneri formalism [246] to investigate how accurately we must model near-extremal EMRI waveforms. Indeed, given the tight constraints on the spin parameter, there is a chance our parameter recoveries could be dominated by systematic errors, rather than statistical errors induced through detector noise realisations. Given that we have shown precisions on the spin parameter on the order $\Delta a \sim 10^{-10}$, it would be of utmost importance to have immensely accurate waveform models in order to keep the systematic error to a minimum. In the next chapter, we investigate how accurately one must calculate the various pieces of the gravitational self force to perform parameter estimation. Rather than a near-extremal first order adiabatic waveform, we investigate a Schwarzschild space-time with a point particle on a low eccentricity orbit.

Chapter 6

Accuracy requirements in the gravitational self-force

6.1 Introduction

To perform successful extraction and parameter estimation of EMRIs, it is essential that our gravitational waveform templates are both *efficient* and *accurate*. Parameter estimation algorithms require waveforms to be generated efficiently over the entire (14 dimensional) parameter space, and accurate waveforms ensure that biases in our recovered parameters, due to modelling errors, are small enough to be ignored. It is thought, though not proven, that waveform models built from only the adiabatic self-force are sufficient for detection purposes, and such waveform models can already be produced efficiently for fully generic orbits around a Kerr BH [103, 102, 101]. Based on the criterion that we must track the orbital phase difference to within 0.1 radians, we will require waveforms with 1PA information [171, 290, 291, 292, 180].

The statement of needing 1PA waveforms for parameter estimation arises from the two-timescale analysis [171] by considering the criterion that the orbital phase of the secondary must be tracked within 0.1 radians. We discussed this in section 2.3.3, following (2.32). Perturbation calculations readily show that adiabatic inspirals are accurate to order 1 radian, whereas 1PA inspirals would have an error of the order of the small mass-ratio [293]. Such perturbative calculations assume "perfect" adiabatic and 1PA knowledge respectively. Self-force driven eccentric inspirals around a Schwarzschild BH have explicitly demonstrated that a phase error of 0.1 radians can be maintained by ensuring a relative numerical error in the 1PA self-force of 10^{-3} [292]. While these statements tell us intuitively that the waveform accuracy is sufficient to expect reasonable parameter estimation, they provide no insight into expected biases

on extracted parameters. Likewise, it is somewhat meaningless to continue to bound relative error on the 1PA self-force without understanding its effect on parameter estimation. Since the 1PA components of the GSF will be enormously expensive to compute over the entire Kerr parameter space, it is of clear importance to quantify where in the parameter space we should spend our time and effort calculating it, and how precisely.

In this work, we aim to refine the "0.1 radian in orbital phase" criterion used previously to quantify self-force accuracy requirements and argue for the more concrete and modernised statistical test — the CV formalism described in section 3.4.2. We will use this formalism to predict biases on recovered parameters when inaccurately computed 1PA information is incorporated into template waveforms used for parameter estimation. Using the CV formula, we wish to explore accuracy requirements on the GSF for EMRIs without relying on simple mismatch calculations. In this work we will use the self-force inspiral model of van de Meent and Warburton [214], made open source in the BHPT, to compute orbital evolutions and generate EMRI waveforms. This model cleanly splits the effects of the first order self-force on an inspiral into its adiabatic term, determined entirely from the orbit-averaged first order self-force, and its sub-leading 1PA term, determined from conservative and dissipative-oscillatory first order force. We comment here that results for the second order dissipative fluxes and the spin of the CO are 1PA effects but are unavailable for such orbits. We will neglect them here but, once they are available, they can be easily incorporated into this type of systematics study.

This chapter is organised as follows: In section 6.2, we give a brief review of the self-force approach, the near-identity transformation model that we use to compute self-force inspirals and our method for studying errors in the 1PA self-force. In section 6.3 we describe waveform generation and qualitatively discuss the use of adiabatic waveforms in detection pipelines. In section 6.4 we use the CV formula investigate the impact of errors in the 1PA terms on parameter estimation. We explore various models for the form of the error, including constant errors on the 1PA pieces, truncation errors on post-adiabtatic pieces through PN series, accuracy of 1PA components when one nears the separatrix before plunge and the relevance of the 2PA self-force.

6.2 Schwarzschild geodesics and the gravitational self-force

In (dimensionless) BL coordinates $(\tilde{t}, \tilde{r}, \theta, \phi)$, the metric for a Schwarzschild spacetime can be obtained in the limit that the rotation parameter $a \to 0$ in (2.1)

$$d\tilde{s}^2 = -\left(1 - \frac{2}{\tilde{r}}\right) d\tilde{t}^2 + -\left(1 - \frac{2}{\tilde{r}}\right)^{-1} d\tilde{r}^2 + \tilde{r}^2(d\theta^2 + \sin^2\theta d\phi^2) \tag{6.1}$$

with $\tilde{r} > \tilde{r}_+$ with $\tilde{r}_+ = 2$ the event horizon.

In a Schwarzschild spacetime, the motion of a test particle moving on an eccentric bound geodesic can be parameterised by two constants of motion, specifying a particular orbit, and one 'phase' variable, specifying the body's position on the orbit. As our constants, we use $(\tilde{p}, \tilde{e})$, the semi-latus rectum and eccentricity defined via

$$\tilde{p} = \frac{2\tilde{r}_{\rm min}\tilde{r}_{\rm max}}{(\tilde{r}_{\rm min} + \tilde{r}_{\rm max})} \tag{6.2}$$

$$\tilde{e} = \frac{\tilde{r}_{\rm max} - \tilde{r}_{\rm min}}{\tilde{r}_{\rm max} + \tilde{r}_{\rm min}} \tag{6.3}$$

where $\tilde{r}_{\rm min} = p/(1+e)$ and $\tilde{r}_{\rm max} = p/(1-e)$ are the radial locations of the periapse and apoapse of the orbit, the closest and farthest approach of the test body to the central BH respectively. For our phase variable, we use the relativistic anomaly ξ (following the notation of [214]) introduced by Darwin [294, 295]. In this parameterisation the BL radial coordinate of the motion is

$$\tilde{r} = \frac{\tilde{p}}{1 + \tilde{e}\cos\xi} \ . \tag{6.4}$$

As discussed in section 2.3, radiation reaction will cause a gradual change in the "constants" $\tilde{p}$ and $\tilde{e}$. We can parametrize the geodesic constants $(\tilde{p}, \tilde{e}) = (\tilde{p}(\chi), \tilde{e}(\chi))$ and phase $\xi = \xi(\chi)$ to be functions of some time parameter χ, which, following [214], we choose to coincide with ξ as $\eta \to 0$. Using the two-timescale approximation (2.25) and neglecting the dissipative component of the second order GSF, the dynamics are given by equations of the form [296]

$$\frac{d\tilde{p}}{d\chi} = \eta \mathcal{F}_{\tilde{p}}(\tilde{p}, \tilde{e}, \xi), \tag{6.5}$$

$$\frac{d\tilde{e}}{d\chi} = \eta \mathcal{F}_{\tilde{e}}(\tilde{p}, \tilde{e}, \xi), \tag{6.6}$$

$$\frac{d\xi}{d\chi} = 1 + \eta f_{\xi}(\tilde{p}, \tilde{e}, \xi). \tag{6.7}$$

In addition to these variables, for computing waveforms one will need the coordinate values $\tilde{t}, \phi$, which are given by

$$\frac{d\tilde{t}}{d\chi} = \omega_t(\tilde{p}, \tilde{e}, \xi), \tag{6.8}$$

$$\frac{d\phi}{d\chi} = \omega_\phi(\tilde{p}, \tilde{e}, \xi). \tag{6.9}$$

With ω_t and ω_ϕ expressions for the geodesic fundamental frequencies. In the above equations, all self-force information is contained in the functions $\mathcal{F}_{\tilde{p}}(\tilde{p}, \tilde{e}, \xi)$, $\mathcal{F}_{\tilde{e}}(\tilde{p}, \tilde{e}, \xi)$ and $f_\xi(\tilde{p}, \tilde{e}, \xi)$. We

also note that each of these functions are 2π periodic in ξ. By making a similar split as we did in equation (2.26), we can decompose the forcing functions into an *orbit averaged* piece that does not depend on ξ and an oscillatory piece that will depend on ξ. The difficulty in directly integrating Eqs. (6.5)-(6.9) is the presence of the phase variable ξ, which from Eq. (6.7) is a rapidly evolving quantity. With ξ present, one is required to integrate (6.5)-(6.9) over a small steps in χ, which can be computationally prohibitive. Instead, one can exploit that the dependence on ξ is periodic and, by a particular change of variables, one can *remove* the dependency of ξ on the right-hand side of the above equations. These new equations will not depend on ξ giving rise to rapid evolution of the orbital parameters. In the next section, we will discuss the *Near-Identity-Transformation* (NIT) that makes this possible.

6.2.1 Near-identity transformations

6.2.1.1 An example toy model

In this section (or chapter), we will *not* derive the full NIT'ed equations of motion for the Schwarzschild space-time. Such a derivation is found in [214], so we will not present it here. Instead, we will consider a simple example to provide intuition on the method. Consider example equations of motion of the form

$$\frac{d\tilde{p}}{d\chi} = \eta \mathcal{F}^{(1)}(\tilde{p}, \xi) + \mathcal{O}(\eta^2) \tag{6.10a}$$

$$\frac{d\xi}{d\chi} = 1 + \eta f_{\xi}^{(1)}(\tilde{p}, \xi) + \mathcal{O}(\eta^2), \tag{6.10b}$$

a simplified form of (6.5)-(6.9) neglecting evolution of the eccentricity, coordinate time and the azimuthal ϕ evolution for simplicity. We will also only work to *first-order* in the mass ratio η, since generalizing to η^2 is algebraically tedious with little more to learn than the following discussion offers. The goal here is to choose a change of variables for $\tilde{p}$ and ξ such that the ξ dependence on the right-hand side of the above equations are removed. Consider the following change of variables

$$\hat{p} = \tilde{p} + \eta Y(\tilde{p}, \xi) + \mathcal{O}(\eta^2) \tag{6.11a}$$

$$\hat{\xi} = \xi + \eta X(\tilde{p}, \xi) + \mathcal{O}(\eta^2) \tag{6.11b}$$

with corresponding inverses

$$\tilde{p} = \hat{p} - \eta Y(\hat{p}, \hat{\xi}) + \mathcal{O}(\eta^2) \tag{6.12a}$$

$$\xi = \hat{\xi} - \eta X(\hat{p}, \hat{\xi}) + \mathcal{O}(\eta^2), \tag{6.12b}$$

with X and Y functions to be determined. Taking a χ derivative of (6.11a)-(6.11b), substituting in (6.10a) and (6.10b) and using the inverse transformation above, one can write

$$\frac{d\hat{p}}{d\chi} = \eta \hat{\mathcal{F}}^{(1)}_{\tilde{p}}(\hat{p}, \hat{\xi}) + \mathcal{O}(\eta^2) \tag{6.13a}$$

$$\frac{d\hat{\xi}}{d\chi} = 1 + \eta \hat{f}^{(1)}_{\xi}(\hat{p}, \hat{\xi}) + \mathcal{O}(\eta^2). \tag{6.13b}$$

Where new hatted forcing functions depend only on the original forcing functions $\mathcal{F}^{(1)}$ and $f^{(1)}$ and various derivatives of X and Y with respect to hatted quantities. Explicitly,

$$\hat{\mathcal{F}}^{(1)} = \langle \mathcal{F}^{(1)}_{\tilde{p}}(\tilde{p}) \rangle + \delta \mathcal{F}^{(1)}_{\tilde{p}}(\tilde{p}, \xi) + \frac{\partial Y}{\partial \hat{\xi}} \tag{6.14}$$

$$\hat{f}^{(1)} = \langle f^{(1)}_{\xi}(\tilde{p}) \rangle + \delta f^{(1)}_{\xi}(\tilde{p}, \xi) + \frac{\partial X}{\partial \hat{\xi}}. \tag{6.15}$$

We have split the forcing functions into an averaged (over ξ) component $\langle \cdot \rangle$ and oscillatory component $\delta \cdot$. To proceed, we know that the oscillatory pieces and both X and Y depend on ξ that is 2π periodic. Writing $Y(\hat{p}, \hat{\xi})$ and $X(\hat{p}, \hat{\xi})$ as a Fourier decomposition, we can write all oscillatory terms in the equation above as

$$\hat{\mathcal{F}}^{(1)} = \langle \mathcal{F}^{(1)}_{\tilde{p}}(\tilde{p}) \rangle + \delta \mathcal{F}^{(1)}_{\tilde{p}}(\tilde{p}, \xi) + \frac{\partial Y}{\partial \hat{\xi}} = \langle \mathcal{F}^{(1)}_{\tilde{p}}(\tilde{p}) \rangle + \sum_{\mathrm{n} \neq 0} \left(\delta \mathcal{F}^{(1)}_{\tilde{p},n} + i\mathrm{n} Y^{(1)}_{\mathrm{n}} \right) e^{i\mathrm{n}\xi} \tag{6.16}$$

$$\hat{f}^{(1)} = \langle f^{(1)}_{\xi}(\tilde{p}) + \delta f^{(1)}_{\xi}(\tilde{p}, \xi) \rangle + \frac{\partial X}{\partial \hat{\xi}} = \langle f^{(1)}_{\xi}(\tilde{p}) \rangle + \sum_{\mathrm{n} \neq 0} \left(\delta f^{(1)}_{\xi,n} + i\mathrm{n} X^{(1)}_{\mathrm{n}} \right) e^{i\mathrm{n}\xi}, \tag{6.17}$$

Where, by the choice of $Y^{(1)}_{\mathrm{n}} = i\delta \mathcal{F}^{(1)}_{\tilde{p},\mathrm{n}}/\mathrm{n}$ and $X^{(1)}_{\mathrm{n}} = i\delta f^{(1)}_{\xi,\mathrm{n}}/\mathrm{n}$, we *eliminate* the oscillatory terms in (6.13a)-(6.13b). The only surviving term is the orbit averaged piece, which can be rapidly computed as it is independent of the rapidly evolving phase variable ξ. As a final step, we substitute both $\hat{p}(\chi)$ and $\hat{\xi}(\chi)$ into the inverse transformation (6.12a) and (6.12b) to obtain the trajectory in terms of the original variables $\tilde{p}$ and ξ.

6.2.2 Averaged evolution for Schwarzschild space-times

From [214], the transformed equations of motion in a Schwarzschild space-time, with new (dimensionless) variables given hats, are

$$\frac{d\hat{p}}{d\chi} = \eta\hat{\mathcal{F}}^{(1)}_{\hat{p}}(\hat{p},\hat{e}) + \eta^2\hat{\mathcal{F}}^{(2)}_{\hat{p}}(\hat{p},\hat{e}) + \mathcal{O}(\eta^3), \tag{6.18}$$

$$\frac{d\hat{e}}{d\chi} = \eta\hat{\mathcal{F}}^{(1)}_{\hat{e}}(\hat{p},\hat{e}) + \eta^2\hat{\mathcal{F}}^{(2)}_{\hat{e}}(\hat{p},\hat{e}) + \mathcal{O}(\eta^3), \tag{6.19}$$

$$\frac{d\hat{\xi}}{d\chi} = 1 + \eta\hat{f}^{(1)}_{\xi}(\hat{p},\hat{e}) + \mathcal{O}(\eta^3), \tag{6.20}$$

$$\frac{d\hat{t}}{d\chi} = \hat{\omega}_{\tilde{t}}(\hat{p},\hat{e}) + \eta\hat{f}^{(1)}_{\tilde{t}}(\hat{p},\hat{e}) + \mathcal{O}(\eta^2), \tag{6.21}$$

$$\frac{d\hat{\phi}}{d\chi} = \hat{\omega}_{\phi}(\hat{p},\hat{e}) + \eta\hat{f}^{(1)}_{\phi}(\hat{p},\hat{e}) + \mathcal{O}(\eta^2). \tag{6.22}$$

Where the explicit form of the fundamental frequencies and averaged forcing functions can be found in appendix A and B of [214]. Applying an inverse transformation to the averaged orbital parameters, we can recover the world-line $(\tilde{p}(\chi), \tilde{e}(\chi), \xi(\chi), \tilde{t}(\chi), \phi(\chi))$ and plug these in to an approximate waveform expression such as the quadrupole formula.

Without explicitly giving the form of the averaged forcing functions, we can make a number of remarks:

1. The functions $\hat{\mathcal{F}}^{(1)}_{\hat{p}}(\hat{p},\hat{e})$ and $\hat{\mathcal{F}}^{(1)}_{e}(\hat{p},\hat{e})$ depend on the orbit averaged dissipative first order self-force. If we were to include only these terms, this approximation coincides with the *adiabatic* approximation.

2. The method of NITs have introduced functions at $\mathcal{O}(\eta^2)$ in Eqs. (6.18)-(6.19), and at $\mathcal{O}(\eta)$ in Eqs. (6.21)-(6.22). These functions include the effects of the conservative first order self-force, and the oscillatory pieces of the dissipative first order self-force. They amount to *part* of the 1PA self-force. Once the second order dissipative self-force is known it could be easily implemented into the NIT model as an η^3 contribution.

3. The complete 1PA self-force, encapsulated in $\hat{\mathcal{F}}^{(2)}_{\hat{p}}(\hat{p},\hat{e})$, $\hat{\mathcal{F}}^{(2)}_{\hat{e}}(\hat{p},\hat{e})$, $\hat{f}^{(1)}_{\hat{t}}(\hat{p},\hat{e})$ and $\hat{f}^{(1)}_{\hat{\phi}}(\hat{p},\hat{e})$, will also include contributions from the second order self-force and effects due to the spin of the secondary. When this 1PA information is known, these terms can be included in the equations of motion above quite easily.

The purpose of this chapter is to determine what precision one must calculate the adiabatic and 1PA terms in (6.18)-(6.22). To do so, we can introduce an arbitrary error function[1] $f(J) =$

[1] This error function is not to be confused with the non-averaged forcing terms in equation (6.7)

$f(\tilde{p}, e)$ whose purpose is to simulate *numerical error* when calculating the forcing functions. We can modify the averaged forcing functions by considering

$$\hat{\mathcal{F}}_i^{(N)} \mapsto (1 + f(J))\hat{\mathcal{F}}_i^{(N)}, \quad i \in \{\tilde{p}, \tilde{e}\}, \text{ and } N \in \{1, 2\} \tag{6.23a}$$

$$\hat{f}_j^{(1)} \mapsto (1 + f(J))\hat{f}_j^{(1)}, \quad j \in \{\chi, \tilde{t}, \phi\} \ . \tag{6.23b}$$

Using the above approach, we can simulate numerical error on the adiabatic components ($N = 1$) or 1PA components ($N = 2$). For ($N = 2$) and setting $F(J) = -1$ we recover the adiabatic approximation.

Equation (6.23) will be used throughout this chapter. In section 6.4, we will provide a number of potential sources of error on the adiabatic and 1PA components. We will also highlight a rough estimate of what size the 2PA components must be to have a considerable effect on parameter estimation. Specifically, in section 6.4.1, we will try to understand how accurately the adiabatic components of the GSF must be computed by estimating biases on parameters using the CV algorithm, complemented by Bayesian techniques. We will do this using inaccurate model templates with adiabatic information, $N = 1$ in (6.23), with a flat error $F(J) = \delta_0$ for $|\delta_0| \ll 1$ across all components. We perform a similar study in 6.4.2, but instead estimate what numerical error in the 1PA components (through $\hat{\mathcal{F}}_i^{(2)}$ and $f_j^{(1)}$) can be afforded to keep biases at a minimum. In 6.4.3, we will introduce an extra term in (6.23) whose purpose is to approximate the effects of the 2PA components where we can then assess when these higher order corrections are important when performing inference. Finally, in light of hybrid post-Newtonian self-force expansions, we will let $f(\tilde{p}(\chi), \tilde{e}(\chi))$ evolve to replicate potential truncation errors of these hybrid expansions.

In the next section, we briefly discuss our waveform generation scheme and give a brief comparison between adiabatic and 1PA waveforms.

6.3 Adiabatic and 1PA waveforms

6.3.1 Waveform generation; parameter space and precision

We will use the `NIT` code presented in the BHPT that computes inspirals and associated snapshot waveforms for a test particle on an eccentric orbit around a massive Schwarzschild BH. We will neglect the effect of the LISA response function on the waveform for similar reasons discussed in chapter 5. To investigate eccentric Schwarzschild orbits, we use the parameter space $\boldsymbol{\theta} = (\tilde{p}_0, \tilde{e}_0, \xi_0, \eta, M)$ with (assumed perfectly known) distance tuned to achieve suitable

SNRs for this systematics study. Here ξ_0 is an initial orbital phase parameter corresponding to the initial condition $\xi(\chi_0) = \xi_0$ in (6.20). The correlations between distance and the other parameters are weak, justifying the approximation that the distance is a known parameter. We have tested this here and shown in chapter 5 that these correlations are small, although we were considering a different class of orbits we do not expect the results to change since D affects the amplitude and not the phasing. The `NIT` code will rapidly generate inspirals for $\tilde{e} \in (0, 0.2)$ and $\tilde{p} \in (6 + 2\tilde{e}, 12)$, where the trajectory is terminated close to the separatrix $\tilde{p}_s(e) = 6 + 2\tilde{e}$. By integrating Eqs.(6.18 — 6.22), evolution equations of $(\tilde{p}, \tilde{e}, \xi, \tilde{t}, \phi)$ as a function of χ are obtained. These orbital parameters are then plugged into the quadrupole formula to produce a waveform in the time domain. The details of the waveform generation can be found in [103, 297].

To determine the phase difference between two waveforms, h_1 and h_2 say, we build an interpolant for $\phi_1(\tilde{t})$ and $\phi_2(\tilde{t})$ respectively. Here ϕ_1 and ϕ_2 each determine the evolution of the orbital azimuthal phase of the CO. Marking $\tilde{t}_{\rm end}$ as the final coordinate time before the waveforms are terminated, the difference

$$\Delta\phi = \phi_1(\tilde{t}_{\rm end}) - \phi_2(\tilde{t}_{\rm end}) \tag{6.24}$$

is found and the final phase difference read off. By construction, $\tilde{t}_{\rm end}$ is the same for both waveforms, even if they plunge at different times.

Similar to chapter 5, to compute the FM (3.59) we use a fifth order central finite difference method defined by (3.65) with uniform grid spacing to evaluate numerical derivatives. Instead of η, we choose to include the secondary mass $\mu = \eta M$ as a parameter in the FM calculation for the sake of computational convenience. To invert Γ, we use the python package `mpmath` [241] in order to make use of arbitrary precision arithmetic in `python` and compute the inverse using `mpmath`'s internal functions.

For a year-long waveform with parameters $\boldsymbol{\theta} = (\tilde{p}_0, \tilde{e}_0, \xi_0, \mu, M) = (10, 0.1, 1, 10M_\odot, 10^6 M_\odot)$ accumulating SNR $\sim$ 20, we find Fisher constraints on the order of $\Delta\tilde{p}_0 \sim 10^{-5}, \Delta\tilde{e}_0 \sim 10^{-4}, \Delta\xi_0 \sim 10^{-1}, \Delta\mu/M_\odot \sim 10^{-3}, \Delta M/M_\odot \sim 26$. In this calculation we assumed there were no errors on the 1PA terms and have obtained similar constraints in [110]. With error $f(\tilde{p}, \tilde{e}) = 0$ and the same choice of parameters, the Fisher estimates above were checked using an MH MCMC algorithm. Selecting suitable uniform priors on the parameters and running the MH algorithm presented in section 3.5.3, we obtain the results in figure 6.1. We find that the FM agrees very well with the 1σ posterior width. From this simulation we believe that

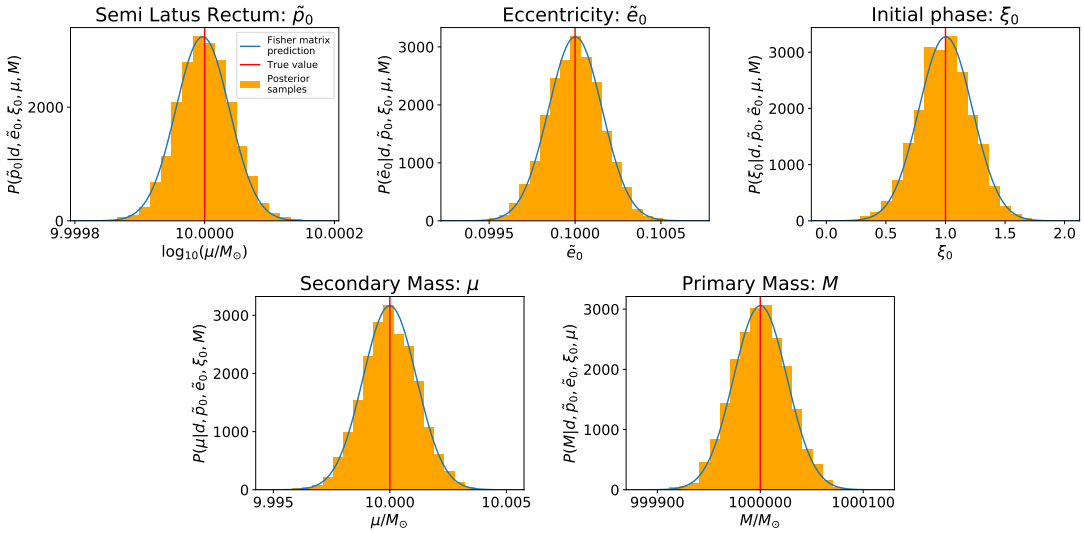

Figure 6.1: We compare the one-dimensional marginalised posterior distributions (orange histograms) to a Gaussian distribution (blue solid line), centred at the posterior mean, and with standard deviation set to the prediction of the FM.

the FM is not subject to numerical instabilities and provides a suitable guide to how well the parameters can be constrained — even at lower SNRs $\rho \sim 20$.

In the next section, we do a comparative study of both adiabatic waveforms with $F(J) = -1$ and error induced 1PA waveforms by choosing $F(J) \neq 0$ respectively in equations (6.23).

6.3.2 Detection and parameter estimation

We consider year-long signals with universal parameters ($\tilde{p}_0 = 10, \tilde{e}_0 = 0.1, \xi_0 = 0, M = 10^6 M_\odot$) and consider $\eta \in \{10^{-4}, 10^{-5}, 10^{-6}\}$ where the distance is chosen so that the SNR~ 28. A signal with full 1PA information for $f(J) = 0$ is generated denoted h_e. Four waveforms, h_m, with errors $f(J) \in \{-1, 1, 0.1, 0.01\}$ are then generated, the first being a purely adiabatic waveform (no 1PA information) and the last three waveforms including errors on the 1PA pieces of the GSF. We now provide a comparison between the waveforms below.

To aid our discussion, we define the *observed* SNR

$$\rho_d = (d|h)/\sqrt{h|h}\,, \tag{6.25}$$

and plot overlaps (3.67) and observed SNRs (6.25) in figure (6.2). In figure 6.2, it can be seen that the overlap between the purely adiabatic waveform (with $f(J) = -1$) and true 1PA waveform h_e decays as the observation time increases. As expected, the overlaps degrade with greater severity as η is increased and $f(J)$ deviates from zero. Including the 1PA components correct to two decimal digits results in high overlaps between the true 1PA waveform and

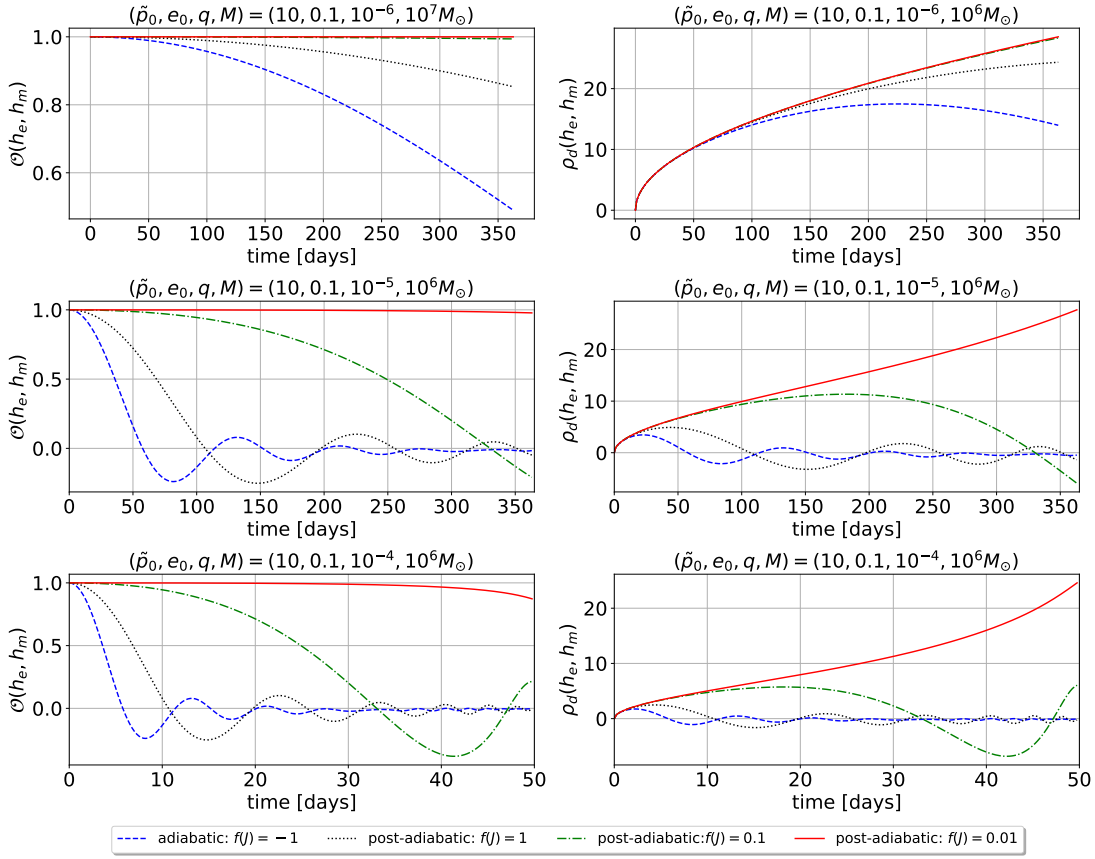

Figure 6.2: In all plots, the blue dashed line, grey dotted line, green dashed dotted line and red solid line correspond to overlaps (3.67) (left column) or SNRs (6.25) (right column) of a signal with $f(J) = 0$, h_e, and another signal h_m, with $f(J) = \{-1, 1, 0.1, 0.01\}$ respectively. The source parameters are given in the title of the plots

approximate model. Since the overlap between adiabatic waveforms and true 1PA waveforms are so small over the entire inspiral timescale, adiabatic waveforms cannot be used for parameter estimation purposes. However, including approximate 1PA components of the GSF in the orbital trajectories (that govern the phasing of the waveform), we see a significant impact on the overall overlap.

We see similar behavior in the observed SNR ρ_d shown by the rightmost column of 6.2. Provided the template starts to match some proposed signal in the data stream, then the observed SNR will accumulate. As discussed in both [102, 110], the detection threshold for EMRIs in stationary Gaussian noise is $\rho_{\rm det} \sim 20$. What we find for adiabatic waveform templates is that the SNR accumulates for the first 2, 14 and 200 days corresponding to mass ratios $\eta = 10^{-4}, 10^{-5}$ and 10^{-6} and reduces afterwards. When 1 digit of accuracy, $F(J) = 0.1$, is allowed in the 1PA forcing terms, we find that the accumulation of SNR and overlaps are significantly greater than when there is no 1PA information $F(J) = -1$. This hints that if cheap methods could be used to compute the 1PA components of the self-force accurate to one decimal digit, then it could

significantly improve our detection pipelines. To plot the results in figure 6.2, we have chosen an initial value of the parameters and calculated both the overlaps and SNR. One could, perhaps, make small perturbations to the parameters once the SNR begins to decrease over a period of time in an attempt to continue the growth in observed SNR. The goal here, then, would be to accumulate enough SNR to claim that there does exist an EMRI signal buried within the data stream.

Due to scheduled gaps[2] and other limitations of the space-craft, (as discussed in section 1.3.3.2 and 3.2.3), it will be impossible to search over a full data stream for the EMRI signal. Detection pipelines will have to take these features into account, and it may be sufficient to use adiabatic waveforms throughout the search phase with minor perturbations to the parameters to continue increasing ρ_d over each data segment. In the future publication of this work we will perform a more in depth analysis of this by searching for a waveform with full 1PA information using both an adiabatic waveform model and a waveform with 1PA information correct to one decimal digit. In the future sections, we will assess how accurately one must compute both the adiabatic and post-adiabatic components of the GSF.

6.4 Accuracy requirements

6.4.1 Adiabatic order: fluxes

In order to build both accurate and efficient models, we can not compute the GSF at the same time. Instead, adiabatic and 1PA GSF results will be tabulated across parameter space and interpolated. This allows `NIT` model can generate rapid waveforms whilst including GSF information. Hence, a prior stage to waveform generation is to compute relevant GSF information and build an interpolant for cheap evaluation.

However, computing the GSF is expensive and becomes more expensive as the level of precision is increased. It is for this reason that waveform modellers ask what accuracy the GSF must be known to over the parameter space. In this section, we explore how accurately the first-order orbit averaged dissipative components (the fluxes) must be calculated in order to eliminate the potential for significant biases in parameters.

In this analysis, we will assume *perfect* knowledge of the 1PA terms and place a flat error on the adiabatic components of the form $\hat{\mathcal{F}}^{(1)} \mapsto (1+\delta_0)\hat{\mathcal{F}}(1)$ for $|\delta_0| \ll 1$. Consider a waveform h_e generated with parameters $\boldsymbol{\theta} = (\tilde{p}_0, \tilde{e}_0, \xi_0, \mu, M) = (10, 0.1, 1, 10M_\odot, 10^6 M_\odot)$ with distance chosen so $\rho \sim 100$. In this section, we will carry out a systematics study through tracking the

[2]We remind the reader that scheduled data gaps, due to antennae repointing, could occur every 14 days elapsing 7 hours or 7 days last 3.5 hours.

δ_0	$\mathcal{O}(h_e, h_m)$	$(\delta h\|\delta h)$	$\Delta\phi$
10^{-4}	0.2163	14467	3.717
5.6234×10^{-5}	-0.0766	19874	2.090
3.1623×10^{-5}	0.3377	12225	1.175
1.7783×10^{-5}	0.7413	4774.3	0.6610
10^{-5}	0.9126	1613.5	0.3710
5.6234×10^{-6}	0.9718	521.07	0.2090

Table 6.1: We tabulate overlaps (second column), the LC (third column) and orbital phase difference (fourth column) when h_e is generated with an error on the fluxes within δ_0 (first column).

orbital phase, computing overlaps, the Lindblom criterion, the CV formalism where the latter we verify using MCMC. To remind the reader, the Lindblom criterion (introduced in section 3.4.1, equation (3.69)) states that two waveform models h_e and h_m are *indistinguishable* if

$$(\delta h|\delta h) < 1, \tag{6.26}$$

for $\delta h = h_e - h_m$ and inner product given in (3.30). In table 6.1, we tabulate overlaps, the LC and orbital phase difference between h_e and h_m when the fluxes used to generate h_m are correct to one part in $1/\delta_0$.

An immediate take home from here is that we require *accurate* knowledge of the fluxes when using EMRI waveforms for parameter estimation. This is clear from the overlaps and when tracking the orbital phase. The LC (introduced in section 3.4.1, equation (3.69)) in every case fails, though, this is expected since it is a very conservative criterion.

In figure 6.3, we plot results from an MCMC simulation where the true signal's fluxes have an error of $\sim 7 \times 10^{-6}$ on the fluxes. In such a scenario, we find that $\mathcal{O}(h_m, h_e) \sim 0.95$ with a discrepancy in the orbital phase $\Delta\phi \sim 0.26$. We find from these simulations that the CV formula predicts the bias well and that the FM is a suitable approximation to the width of the posterior. We have attempted MCMC simulations with $\delta_0 \gtrsim 10^{-5}$, but the biases on parameters are not accounted for by the CV formalism. This is due to the LSA breaking down as we venture farther from the true parameters.

In order not to break the LSA (3.57), we will only consider overlaps $\mathcal{O}(h_e, h_m) \gtrsim 0.95$. We generate approximate models for $\delta_0 = \{10^{-i}\}$ for $i \in \{7, 4, 2\} \times 10^{-6}$ and use the CV formalism to compute (3.77). The results are shown in figure 6.4. The results in figure 6.4 show that we must calculate the fluxes to a precision of 1 part in $\sim 5 \times 10^6$. This result is conservative in the sense that we would not expect to find such bright EMRIs with $\rho \sim 100$. Hence, the author believes that calculating the fluxes correct to ~ 6 decimal digits is sufficient for parameter

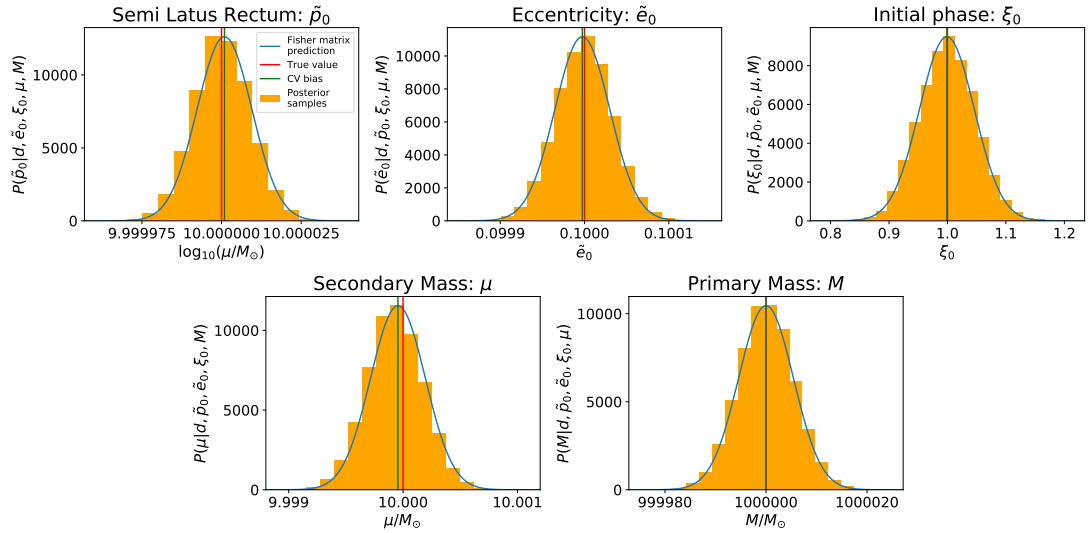

Figure 6.3: (Red lines) are the true parameter. (Orange histograms) are Posterior samples. (Green line) the predicted bias using the CV formalism and (blue curve) a Gaussian centered on the CV predicted bias with variance given by the FM prediction. Here we have incorporated an error of $\delta_0 \sim 7 \times 10^{-6}$ into the true waveform model.

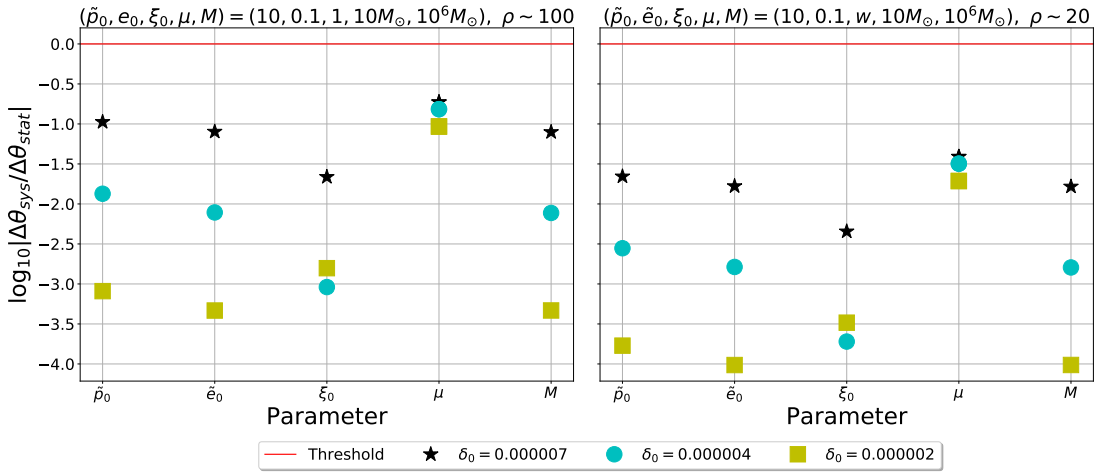

Figure 6.4: (red line) Indicates the threshold where biases exceed the width of the likelihood. All (coloured) data points on both plots is the ratio between the systematic error and inverse of the FM.

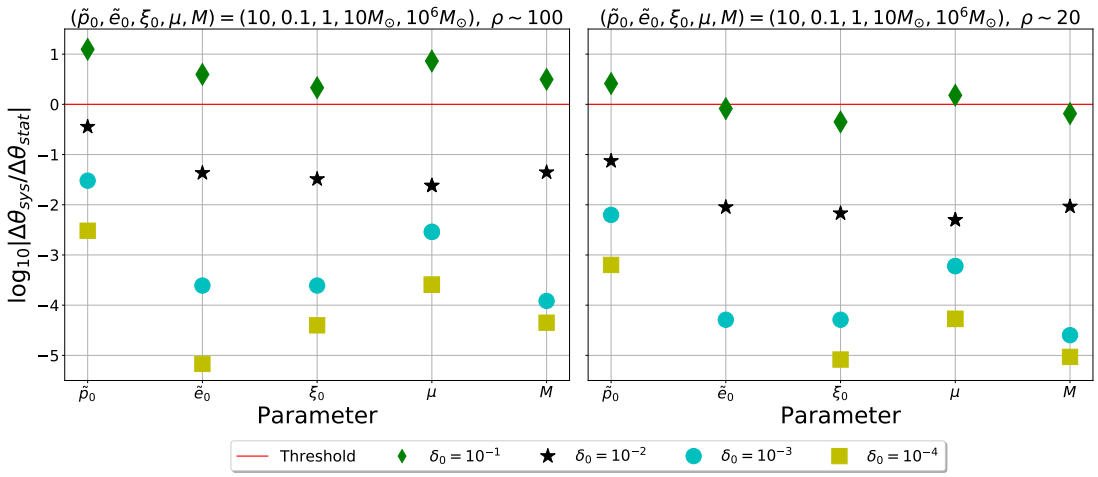

Figure 6.5: (red line) Indicates the threshold where biases exceed the width of the likelihood. All data points on both plots is the ratio between the systematic error and inverse of the FM. (green diamond) utilises 1PA information correct to one decimal digit. (black star) correct to 2 decimal digits. (turquoise circle) three decimal digits. (red diamond) four decimal digits. (black filled cross) five decimal digits.

estimation purposes. In the next section, we apply a similar treatment to understand the accuracy requirements of the 1PA components of the GSF.

6.4.2 Flat errors in post adiabatic components

6.4.2.1 Year long inspirals

We consider constant errors $f(J) = \delta_0 = \{10^{-i}\}_{i=1}^{i=4}$ and will compute both mismatches $\mathcal{M}$ and the CV criterion given by (3.77). We first consider a source with parameters $(\tilde{p}_0, \tilde{e}_0, \xi_0, \eta, M) = (10, 0.1, 1, 10^{-5}, 10^6 M_\odot)$. A comparison of the FM predictions on measurement precisions, and systematic biases are shown in Fig.(6.5) for signal-to-noise ratios $\rho \sim 100$ and $\rho \sim 20$.

In the left panel of Fig.6.5, we see that the predicted biases for $(\tilde{p}_0, \tilde{e}_0, \xi_0, \mu, M)$ are negligible and well contained within the 1σ likelihood only if $\delta_0 \lesssim 0.01$. This means that in order to mitigate the level of bias in parameters, one should compute the 1PA components of the GSF correct to *two decimal digits*. The systematic errors shown in the right panel of 6.5 with $\rho \sim 20$ are less pronounced, but nontrivial biases on parameters would be expected if we were to compute the 1PA information correct to one decimal digit. For this reason we believe it is sufficient to calculate the 1PA information correct to two decimal digits for all SNRs. We have checked the claim that $\delta_0 \sim 10^{-2}$ is suitable for parameter estimation using MCMC and the results are plotted in 6.6

We remark that a constant error of $\delta_0 = 10^{-2}$ yields a phase error $\Delta\phi \sim 0.163 \gtrsim 0.1$ radians and the corresponding overlap $\mathcal{O}(h_e, h_m) \approx 0.97$. Although, not by much, we have saturated

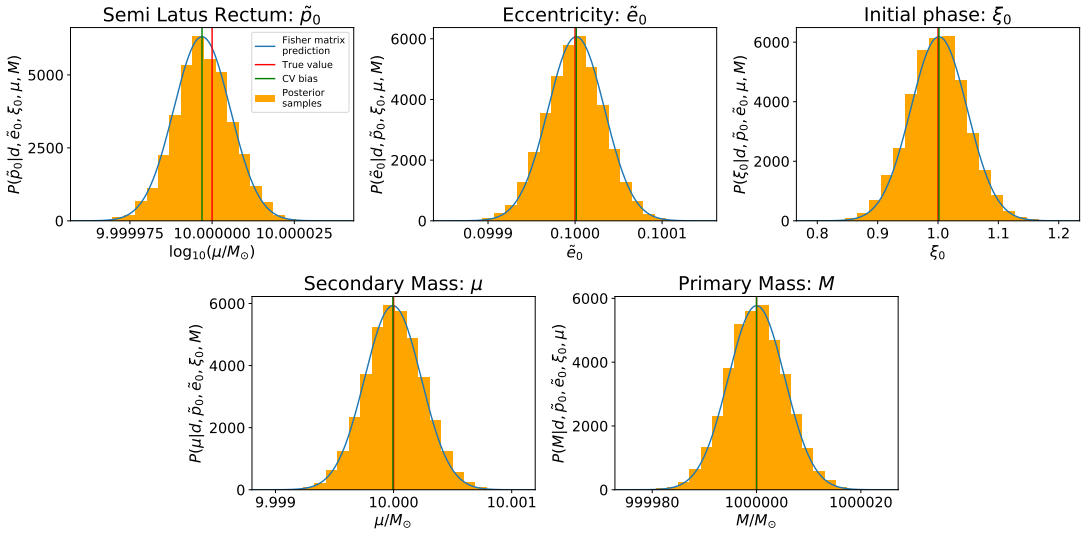

Figure 6.6: The red solid vertical lines indicate the true parameters, the blue curve a Gaussian distribution centred on the posterior distribution with variance equal to the FM prediction. The orange histograms are the resultant posteriors.

the original bound presented by [291, 290, 292] and still can recover parameters with negligible biases. Using the LC for a choice of $\delta_0 = 10^{-3}$, we found $(\delta h|\delta h) = 5 > 1$ implying that errors $\delta_0 \gtrsim 10^{-3}$ are insufficient for parameter estimation. This result is clearly too conservative as we have shown flat errors of the form $\delta_0 \sim 10^{-2}$ are sufficient for parameter estimation purposes.

Recall that systematic biases on parameters are independent of the SNR. Since the level of precision on parameters scales inversely with the SNR, systematic errors are more troublesome for brighter sources. In saying this, (significant) biases on the semilatus rectum are not a concern. Locating the parameters $(\tilde{e}_0, \mu, M)$ to suitable accuracy are more important for scoping out LISA science — such as population inference and the study of formation channels. Ignoring the resulting bias on $\tilde{p}_0$, we believe that knowledge of the 1PA information of the GSF to two decimal places is sufficient for this class of orbits up to $\rho \sim 1000$.

6.4.2.2 Shorter inspirals

We can perform a similar study but with shorter waveforms ~ 36.5 days. Consider a source with parameters $(\tilde{p}_0, \tilde{e}_0, \xi_0, \eta, M) = (7.5, 0.1, 1, 10^{-5}, 10^6 M_\odot)$. For this source, we fix $\rho \sim 100$ to mimic a (somewhat optimistic) bright and strong field source. The final $\tilde{p}_{t_{cut}} = 6.684$, approximately $\sim 0.4M$ away from the separatrix. We compute (3.77) and show our results in figure 6.7. The results of figure 6.7 lead us to believe that the 1PA terms should be computed to an error of $\delta_0 \sim 0.1$, i.e. *one decimal digit*, in order to mitigate biases in parameter estimates. We conclude that parameter estimation could be performed with trivial biases, assuming a flat error on the 1PA terms of $\delta_0 \lesssim 10^{-1}$ when considering this class of orbit. In other words,

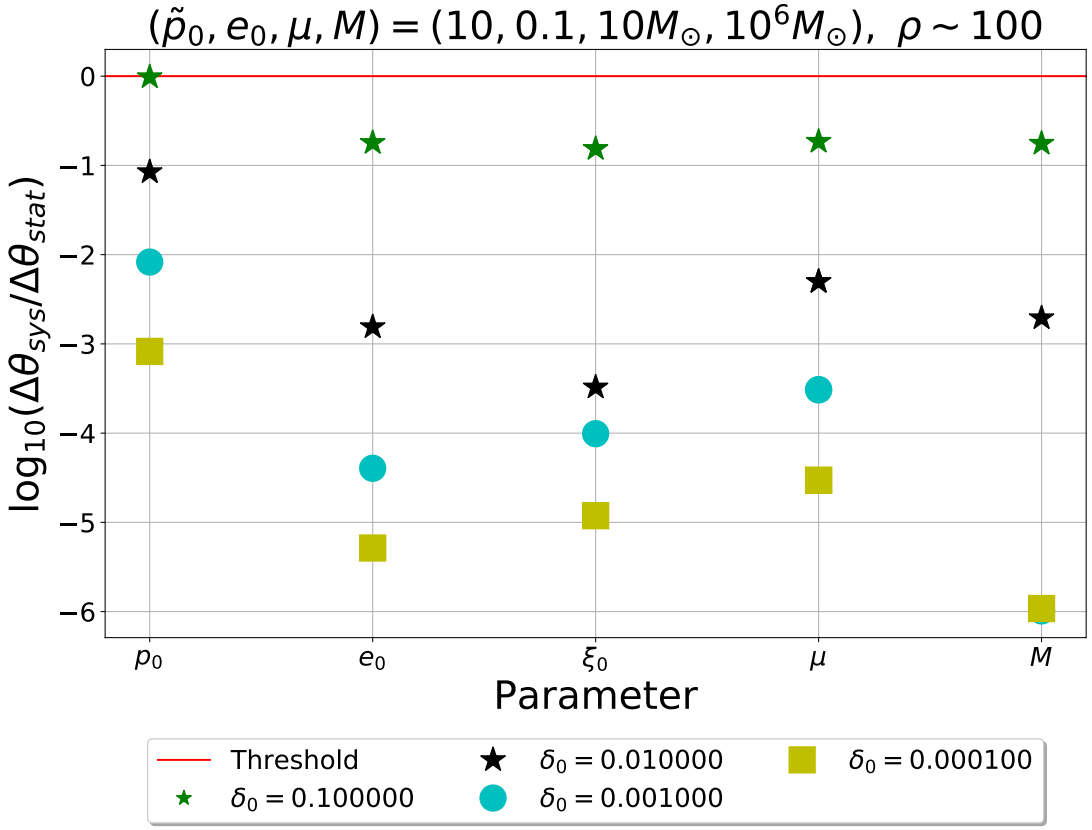

Figure 6.7: Same plots as above but for a 36.5 day long waveform. An error of $\delta_0 < 10^{-2}$ is conservative when calculating the CSF. For the important parameters $(\tilde{e}, \mu, M)$ we could calculate $\delta_0 \lesssim 0.1$ and still perform useful inference on these parameters.

we would only require the 1PA components of the GSF to be known to *one decimal digit* to perform successful parameter estimation on short data segments.

Ignoring resonances, recall that the orbital phase in terms of the adiabatic and 1PA pieces has an expansion of the form (2.32)

$$\phi = \frac{1}{\eta}\phi_{\rm A}(t) + \phi_{\rm 1PA}(t) + \eta\phi_{\rm 2PA}(t) + \mathcal{O}(\eta^2). \tag{6.27}$$

Where $\phi_{\rm A}, \phi_{\rm 1PA}$ and $\phi_{\rm 2PA}$ are the individual contributions to the phase due to the adiabatic, first 1PA and 2PA components of the GSF. Using the CV algorithm, we can test when contributions from the 2PA terms start to significantly alter the phasing of the template waveforms. This will be explored in the next section.

6.4.3 When will 2PA dominate over 1PA information?

In equations (6.18) - (6.22), we have included the forcing functions up to 1PA with only the second order dissipative GSF not included. This piece is not yet available for eccentric Schwarzschild orbits and is expected to be of similar magnitude to both the first order CSF and dissipative/oscillatory pieces [182].

We will now investigate the potential for 2-PA terms (3rd order in the self-force) to influence a typical inspiral. In this section, will assume that the 1PA term is known *perfectly* unless stated otherwise. It is known, though not proved, that we require knowledge of the 1-PA self-force information to ensure that $\Delta\phi \lesssim 0.1$ radians. This is based on the assumption that the 2-PA terms (and higher) are negligible.

Since 2PA information is unknown, we will approximate it using $1PA$ components but suppressed by the mass ratio and semilatus rectum. In other words, we consider errors of the form

$$\hat{\mathcal{F}}_i^{(2)} \mapsto (1 + \eta\delta_0/\tilde{p})\hat{\mathcal{F}}_i^{(2)}, \quad i \in \{\tilde{p}, \tilde{e}\} \tag{6.28a}$$

$$\hat{f}_j^{(1)} \mapsto (1 + \eta\delta_0/p)\hat{f}_j^{(1)}, \quad j \in \{\chi, \tilde{t}, \phi\}\ , \tag{6.28b}$$

for $\delta_0 \in \mathbb{R}$. From classical PN theory one finds higher-order-in-mass-ratio terms appear at successively higher PN orders, motivating the introduction of the factor of $1/p$ in (6.28). Using this choice of error, we investigate what values of δ_0 make the 2-PA terms start to have a non-trivial effect on phasing of the waveform.

We generate approximate signals h_m with parameters $(\tilde{p}_0 = 10, \tilde{e}_0 = \{0.01, 0.1, 0.19\}, \xi_0 =$

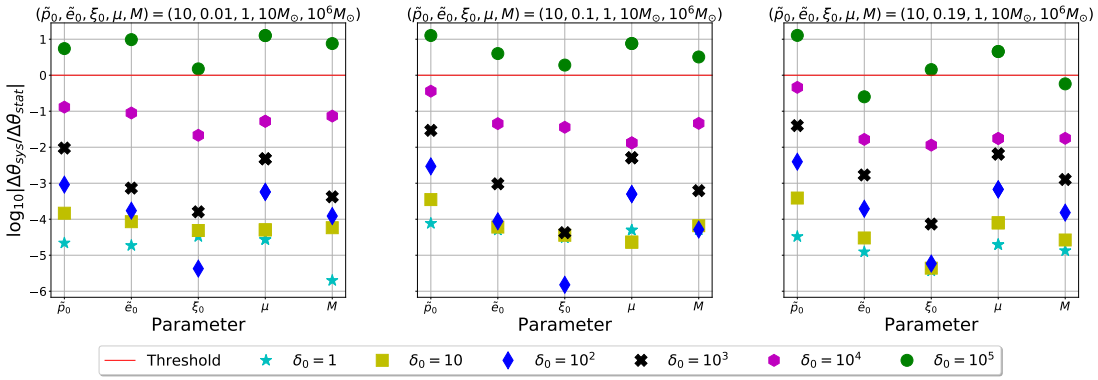

Figure 6.8: In all three plots we compute (3.77) for a system with parameters given in the titles of the plots. The red horizontal line indicates the threshold: for $\mathcal{R}_{\boldsymbol{\theta}} > 1$, we expect biases in our parameter estimates

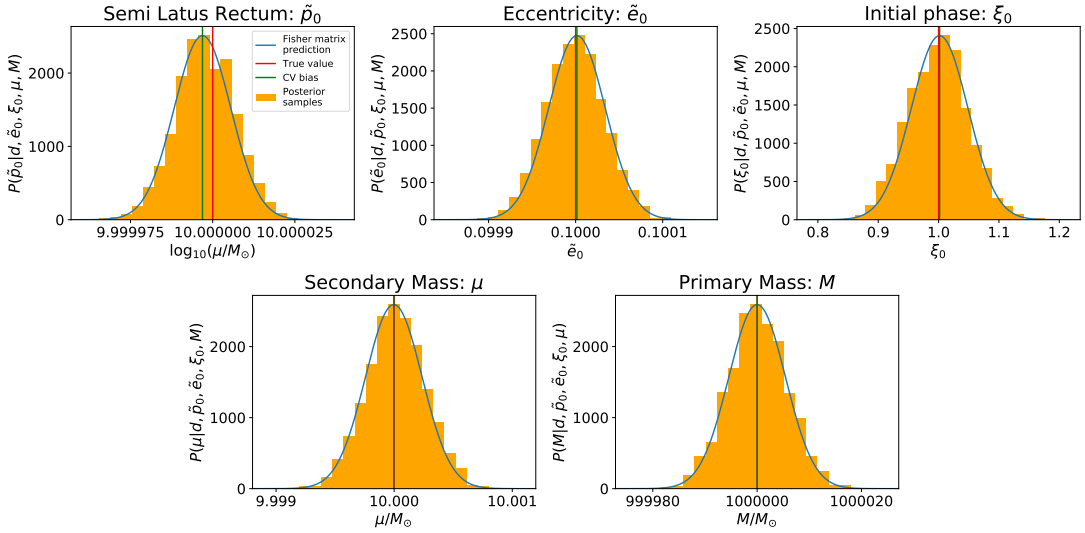

Figure 6.9: Orange histogram are posterior samples, blue curve is an overlapping Gaussian centred on the CV bias with width given by the inverse of the Fisher matrix. Here we perform PE on a signal h_e using 2PA information (6.28) with δ_0 using model templates h_m with $\delta_0 \equiv 0$.

$1, \eta = 10^{-5}, M = 10^6 M_\odot$) and $\delta_0 = 0$ so there is no 2PA information present in the waveform. Each waveform is normalized so that $\rho \sim 100$. We then generate h_e with $\delta_0 \in \{10^i\}_{i=1}^5$ and compute (3.77). The results are plotted shown in figure 6.8. For this configuration of parameters, we learn that for $\delta_0 \lesssim 10^4 = 1/(10\eta)$ we would not recover any significant biases on the parameters $p_0, \tilde{e}_0, \xi_0, \mu$ and M. We remark here that the LC (3.69), introduced in section 3.4.1 is violated for coefficients $\delta_0 > 10^3$. Again, the LC overestimates the choice of δ_0 where the 2PA components start to have a noticeable influence on the waveform (in terms of parameter recovery). We thus conclude that provided the coefficient $\delta_0 \lesssim 10^4$, then 1PA self-force components are sufficient for parameter estimation purposes. For the limiting value, $\delta_0 = 10^4$, we check this claim using MCMC with results shown in figure 6.9.

We have performed the same analysis but holding parameters $(\tilde{p}_0, \xi_0, e_0, M)$ constant but varying $\eta \in \{10^{-4}, 10^{-5}, 10^{-6}\}$. We see that for $\rho \sim 100$ that systematic biases on $(\tilde{e}_0, \tilde{\mu}, M)$ exceed the statistical error once $\delta_0 \sim 1/10q$ as we saw previously. As the results are near analogous, we do not present them here.

This study is obviously incomplete for multiple reasons. The first being the nature of our orbits (limited to $\tilde{p} \in (6+2\tilde{e}, 12)$ and $\tilde{e} \in (0, 0.2)$), the second that we are using a Schwarzschild spacetime than a more astrophysically relevant Kerr space-time and the third we do not have access to the second order dissipative self-force. We believe that it is valuable that this study is repeated for more generic orbits in the Kerr spacetime and when the 1-PA term in (6.18) - (6.22) is known.

6.4.4 Post-Newtonian errors

We now wish to include an error function that will mimic the type of errors one makes when using a post-Newtonian expansion of the self-force (PN-SF), of the type detailed in e.g. [298]. For eccentric orbits, PN-SF expansions are expressed as a large-p expansion that further relies on a small eccentricity expansion. This leads to expressions for the GSF of the form

$$F^{\alpha} = \frac{1}{\tilde{p}^{k_\alpha}} \left(\sum_{i=0}^{i_{\max}} \left[\sum_{j=0}^{j_{\max}} a_{ij}^{\alpha}(\chi) \tilde{e}^j + \mathcal{O}(\tilde{e}^{j_{\max}+1}) \right] \tilde{p}^{-i} + \mathcal{O}(\tilde{p}^{-i_{\max}-1}) \right), \tag{6.29}$$

where the $k_\alpha \in \mathbb{Z}^+$ give the leading order behaviour in $\tilde{p}$, and the $a_{ij}^{\alpha}(\chi)$ are periodic functions of χ. The coefficient a_{i0}^{α} has no explicit dependence on χ, as expected from the circular limit with $\tilde{e} = 0$.

PN-SF expansions provide analytical means for comparing with other methods such as classical PN theory, post-Minkowski expansions and effective one body approaches. They also immediately fill a large portion of the EMRI parameter space, albeit with a loss of accuracy in the strong field. Numerical results need to be computed for a range of $\{\tilde{p}, \tilde{e}, \chi\}$ and interpolated. PN-SF can serve as an effective basis for such interpolation which naturally includes physical information, and they can be cheap to evaluate as they are analytical. From this discussion, we can see why PN-SF expansions are useful and could provide an efficient basis when supplying GSF information used to generate accurate EMRI waveforms. However, with all methods involving expansions, there is an associated truncation error. Our goal in this section will be to provide a rough estimate on the required PN order (value of $i_{\max}$) to achieve accuracy in the 1PA terms. This is a difficult task because the PN expansion is an asymptotic expansion that is very poorly convergent in the strong field. This manifests as a fast numerical growth in the

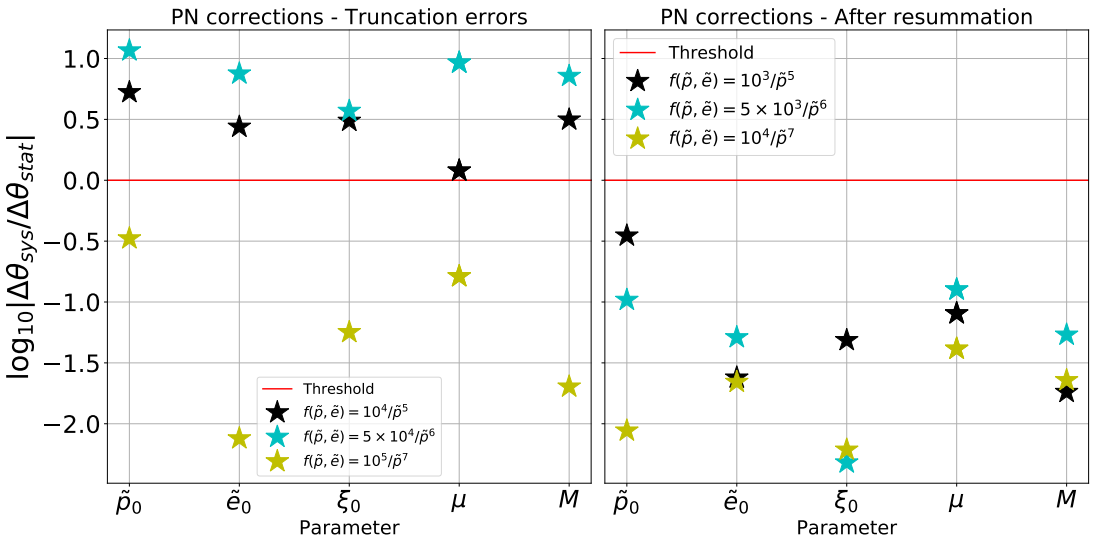

Figure 6.10: Here we plot on the logarithmic scale the ratio between systematic errors and statistical ones when including truncation errors above. Above the red line in both plots we would expect biases on the parameters which would exceed the width of the likelihood given by $\Delta\theta_{\text{stat}}$. On the left plot, the black stars, blue diamonds and yellow filled crosses correspond to error functions $f(\tilde{p},\tilde{e}) = \{10^4/\tilde{p}^5, 5\cdot10^4/\tilde{p}^6, 10^5/\tilde{p}^7\}$ and $f(\tilde{p},e) = \{10^3/\tilde{p}^5, 5\cdot10^3/\tilde{p}^6, 10^4/\tilde{p}^7\}$ on the right.

a^{α}_{ij} with increasing i. Hence, the error made for a given truncation is highly sensitive to the magnitude of the unknown coefficients with $i > i_{\text{max}}$.

The literature currently lacks explicit expressions for the 1PA GSF as a PN expansion. We assume that the forcing functions $\hat{F}^{(2)}$ and $\hat{f}^{(1)}$ are approximated using PN-SF expansions with truncation errors given by suitable choices of $f(\tilde{p},\tilde{e})$ defined in (6.23) on the 1PA terms ($N = 2$). The aim will then be to understand how a loss of accuracy in the strong field affects parameter estimation in a quantitative way. When PN-SF expressions do eventually become available, this work will provide a basis for a more thorough study. For our estimates we will use the following forcing functions, modelling a range of truncation errors (through i_{max}) and a range of coefficient growths (through a_{ij}):

1. $f(\tilde{p},\tilde{e}) = \delta_0/\tilde{p}^5, \quad \delta_0 = \{10^4, 10^3\},$

2. $f(\tilde{p},\tilde{e}) = \delta_1/\tilde{p}^6, \quad \delta_1 = \{5\times10^4, 5\times10^3\},$

3. $f(\tilde{p},\tilde{e}) = \delta_2/\tilde{p}^7, \quad \delta_2 = \{10^5, 10^4\}.$

These choices of δ_i for $i \in \{1,2\}$ are motivated by the magnitude of the coefficients in (6.29) coming from PN theory. All waveforms generated in this section have $\rho \sim 100$. Using the error function $f(\tilde{p},\tilde{e})$ defined in (6.23) on the 1PA terms ($N = 2$), we can modify the averaged forcing functions using (6.23a) and (6.23b) to find the results in figure 6.10.

In the left panel of figure 6.10, the only truncation error is $f(\tilde{p},\tilde{e}) \sim 10^5/\tilde{p}^7$, i.e., seventh PN order, that does not lead to significant biases on all parameters. Applying the same study where the coefficients (through δ_0) are reduced by an order of magnitude we find the results plotted in the right panel of 6.10. In this situation, the parameters are no longer subject to significant biases for all choices of truncation errors. We remark here that the LC (3.69) has failed, $(\delta h|\delta h) > 1$, in all cases considered here. In this scenario, we would argue that using PN-SF expansions to approximate the GF up to a truncation error of $f(\tilde{p},\tilde{e}) = 10^5/\tilde{p}^7$ would be suitable for parameter estimation. If we had the ability to re-sum the PN-SF expansions then we could consider truncating at lower powers of $p^{-i_{\max}}$, making the PN-SF expansions cheaper to evaluate.

6.5 Summarising conclusions and future work

In this work we have demonstrated the utility of the CV formalism to evaluate accuracy requirements for EMRI waveform modelling. In particular, we have investigated both the adiabatic and 1PA components of the self-force for both parameter estimation and detection of EMRI signals. We find that it provides a suitable test of accuracy requirements for EMRIs and provides significantly more insight on the level of bias in parameters than the standard criterion that the relative waveform phase error is bound to be $\Delta\phi \lesssim 0.1$ radians. Based on the results presented in this chapter, the author believes that the criterion $\Delta\phi \lesssim 0.1$ is actually rather conservative, but an excellent target for waveform modellers.

In section 6.3, we gave a review of the use of adiabatic waveforms for detection purposes and discussed why they could be used for detection pipelines for typical mass ratios $\eta \sim 10^{-5}$. In this discussion, we commented on how the limitations of the instrument (scheduled gaps) will affect our detection algorithms. The impact that data gaps would have on detection of EMRIs is something the author is unaware the EMRI community have considered. We believe that adiabatic waveforms could be used for detection purposes but not for parameter estimation due to severe dephasing over the inspiral time-scale. In section 6.4, we first addressed the question of how accurately one must compute the adiabatic components of the self-force from the viewpoint of parameter estimation using the CV formalism. For an eccentric Schwarzschild based orbit, we argued that one must compute the fluxes with roughly *six decimal digits* of precision for a year long inspiral with $\rho \sim 100$. This is much less than the 8 decimal digits stated in [292], although their class of orbits contained higher eccentricities $e \sim 0.5$. Similarly, we investigated the 1PA components and for the same class of orbits we argued that the 1PA terms must be calculated to

two decimal digits of precision. For the same parameters but shorter duration, ~ 1 month, the requirement of precision on the 1PA terms becomes smaller ~ 1 decimal digit of precision. This implies that we can afford greater inaccuracies when analysing signals with initial semilatus rectum close to the separatrix. In 6.4.3, we used the CV formula to gain intuition on what size the components of the 2PA components must be to begin affecting parameter estimation if they are not included. We concluded that provided the coefficient of the 2PA term is $\lesssim 1/10\eta$, i.e., comparable to the 1PA terms then neglecting the 2PA terms will not adversely affect parameter estimation schemes. Finally, we discussed various truncation errors in section 6.4.4 assuming that hybrid PN self-force expansions are used to cheaply generate the 1PA components.

The work contained here is the first systematic study of its kind for EMRIs, paying special attention to the impact on parameter estimation if inaccurately computed 1-PA terms are used to describe the orbital trajectories. Our work has simply scratched the surface of waveform systematic within the EMRI community. In particular, we have shown use of a statistical formalism that can test waveform accuracy though we have been limited to a small region in parameter space. An obvious first extension would be to apply the CV formula to a more extensive parameter space in Schwarzschild before eventually including more generic orbits around a Kerr BH. A model exploiting the NIT is being developed for equatorial eccentric orbits into a Kerr BH and should be ready for use by the end of this year.

In our analysis, we have separated the orbit averaged adiabatic piece in the first order in the mass ratio and the (available) 1PA pieces (first order conservative and dissipative-oscillatory piece). Our model applied a uniform error function onto all components of the self-force. It would be interesting to apply the above analysis to each component *individually* to map out which individual GSF piece we must compute to which accuracy. Finally, we would like to apply a more in depth treatment in 6.2 by *searching* for a 1-PA signal only using adiabatic waveforms when there are scheduled gaps in the data stream. No such detection algorithm exists and would be a valuable addition to the literature.

In the next chapter, we generalise the CV formalism to account for multiple waveform errors and confusion noise.

Chapter 7

Noisy neighbours: quantifying bias due to overlapping gravitational wave signals

In this chapter, we generalise the Cutler-Vallisneri formalism introduced in 3.4.2 to take into account waveform-modelling errors, an unmodelled (and unfitted) astrophysical background and detector noise. We derive generic metrics to assess the inference biases on source parameter characterisations. We describe how to apply this approach to several cases of relevance: i) parameter estimation in the presence of "confusion noise" from unfitted signals in the data; ii) parameter estimation for two overlapping signals with approximately coincident coalescence times; iii) parameter estimation for a population of sources using inaccurate waveform models; and iv) the case in which both confusion noise and mismodelling errors contribute to the final biases. Finally, we will show how these results can be used to mitigate biases in a sequential-fitting pipeline for LISA, without the need for expensive simultaneous fitting of identified sources.

The chapter is organised as follows: Sec. (7.1) contains the description of the Fisher formalism herein developed; Sec. (7.2) contains a brief review of our choices of waveform models; Sec. (7.3) discusses the illustrations of the formalism described above; Sec (7.4) describes the local-fit strategy; and Sec. (7.5) summarises our findings and describes some possible future avenues of investigation.

7.1 Generalisations of the CV formalism

We now generalise the formalism represented by Eqs. (3.75) and (3.76) to two new cases, the first being the presence of *confusion noise* from signals that have not been fitted for in parameter estimation, and the second being the inclusion of multiple signals in the data stream that are incorrectly modelled with approximate waveforms.

7.1.1 Source confusion bias

The likelihood (3.31) only assumes that the noise $n(t)$ is both stationary and Gaussian (with zero mean). The noise $n(t)$ is usually assumed to be detector related and modelled through the PSD via (3.21). However, in third-generation or space-based detectors there may be additional astrophysical contributions to the data stream from unresolved foregrounds of other GW signals [299, 300, 88, 301, 302, 303, 304, 305]. Confusion noise is normally assumed to be a stochastic, Gaussian and isotropic component of the data stream. For confusion noise created by merging sources, the Poisson distribution of merger times breaks the Gaussian approximation at higher frequencies where the background consists of a small number of sources. This is sometimes referred to as the "popcorn noise" regime [306]. For the case of white dwarf binaries in LISA, the sources do not merge in the detector band and so the popcorn noise regime does not apply, and the Gaussian approximation is generally valid. For our purposes, we represent the confusion noise as an additional superposition of GW sources and assume that the parameters of the signals in the superposition are drawn randomly from some astrophysical population. The total number of events should be represented by a random draw from a Poisson distribution with some rate, but for the purposes of this discussion we assume that this number is large but fixed. This will be discussed further in section 7.3.1.

The confusion noise $\Delta H_{\rm conf}$ can be represented as part of the signal component of the data stream (3.66),

$$d(t) = h_e(t;\boldsymbol{\theta}_{\rm tr}) + n(t) + \Delta H_{\rm conf}(t;\boldsymbol{\theta}^{(i)})\,. \tag{7.1}$$

To understand when such confusion foregrounds can lead to biases, one may consider it to be a (deterministic) superposition of N signals,

$$\Delta H_{\rm conf}(t;\boldsymbol{\theta}^{(i)}) = \sum_{i=1}^{N} h_e^{(i)}(t;\boldsymbol{\theta}^{(i)})\,. \tag{7.2}$$

The difference between the data stream and the model template is now

$$d - h_m = n + \Delta H_{\rm conf} + \delta h(\boldsymbol{\theta}_{\rm tr}) + h_m(\boldsymbol{\theta}_{\rm tr}) - h_m(\boldsymbol{\theta}_{\rm bf})\,, \tag{7.3}$$

from which we deduce the extra contribution to the biases (3.75) and (3.76) that originates from the source confusion term is

$$\Delta\theta^i_{\rm conf} = (\Gamma^{-1})^{ij}(\partial_j h_m|\Delta H_{\rm conf}). \tag{7.4}$$

By analogy with (3.77), source confusion from unfitted signals can be said to bias parameter estimates when its size exceeds the 1σ deviations arising from instrumental noise fluctuations, which is true if $\mathcal{R}(\Delta\theta_{\rm conf}) > 1$. To summarise, when inferring the parameters of a single source, the total error is given by the sum of statistical error from noise fluctuations and the biases from source confusion and waveform errors through

$$\Delta\theta^i = \Delta\theta^i_{\rm noise} + \Delta\theta^i_{\rm sys} + \Delta\theta^i_{\rm conf}, \tag{7.5}$$

with the above terms from left to right given by Eqs.(3.75,3.76,7.4) respectively.

In general, the confusion noise contribution to (7.5) depends on the particular sources from the unresolved population that are present in the data and so it is a random quantity. The correct way to handle this is to marginalise the likelihood of the corrected data stream, $d(t) - \Delta H_{\rm conf}(t;\boldsymbol{\theta}^{(i)})$, over the distribution of possible confusion backgrounds, $p(\Delta H_{\rm conf})$. This is a computationally expensive procedure and it is therefore difficult to obtain insights in that way. An alternative avenue to understanding when confusion is important is to use the formalism described here, working with the bias induced by the confusion noise, $\Delta\theta^i_{\rm conf}$, which is also a random quantity. We can characterise it at the order of the linear signal approximation through its mean and variance. Since the total confusion noise contribution is a superposition of contributions from N independent sources, the mean and variance of the total contribution is N times the mean and variance of the contribution from a single source, $h_e(\boldsymbol{\theta}_{\rm conf})$, which are

$$\mu^i_{\rm conf} = \int (\Gamma^{-1})^{ij}(\partial_j h_m|h_e(\boldsymbol{\theta}_{\rm conf}))\, p_{\rm pop}(\boldsymbol{\theta}_{\rm conf})\, {\rm d}\boldsymbol{\theta}_{\rm conf}\,, \tag{7.6}$$

$$\Sigma^{ij}_{\rm conf} = \int (\Gamma^{-1})^{ik}(\partial_k h_m|h_e(\boldsymbol{\theta}_{\rm conf}))(\Gamma^{-1})^{jl}(\partial_l h_m|h_e(\boldsymbol{\theta}_{\rm conf}))\, p_{\rm pop}(\boldsymbol{\theta}_{\rm conf})\, {\rm d}\boldsymbol{\theta}_{\rm conf} - \mu^i_{\rm conf}\mu^j_{\rm conf}. \tag{7.7}$$

Here, $p_{\rm pop}(\boldsymbol{\theta}_{\rm conf})$ is the probability density function of the population of confusion sources. We

would normally expect the mean to be close to zero, since for some sources in the population the bias would be positive and others negative and so it averages to zero (though this is not guaranteed to be the case). Regardless, the variance does not vanish, driving the total error to grow like a random walk as the total number of sources contributing to the confusion background increases.

For large N, we can find a scaling relationship for the total bias using the central limit theorem

$$\frac{\sqrt{N}}{(N\Sigma_{\rm conf})^{1/2}}(\Delta\theta_{\rm conf} - N\mu_{\rm conf}) \to \mathcal{N}(0,1) \tag{7.8}$$

$$\implies \Delta\theta^i - N\mu^i_{\rm conf} \approx \sqrt{N}(\Sigma^{ii}_{\rm conf})^{1/2}\, X, \tag{7.9}$$

where X is a standard Normal random variable. This behaviour will be investigated further in Sec.(7.3.1).

In appendix C, we give a treatment of the confusion noise under the assumption $\Delta H_{\rm conf}$ is a stationary time-series. In this prescription, making reference to Eq.(C.7), the power of the confusion noise is folded into the PSD to form a combined noise PSD $S_n(f) \mapsto S_n(f) + S_{\rm conf}(f)$. In realistic scenarios, due to the relative orientation of the galactic center with respect to the detector plane, the confusion noise will exhibit time-dependent amplitude modulations — a non-stationary effect. In this work we will not treat $\Delta H_{\rm conf}$ as a stationary time series and instead include it as an arbitrary superposition of sinusoids present in the data stream. We will treat both $n(t)$ and $\Delta H(t)$ as independent sources of noise and do not combine them into a single noise component $N(t)$.

7.1.2 Biases due to waveform modelling errors

We now generalise Equations (7.1) and (7.5) to the case of inference on multiple sources within the data stream. Similar ideas can be found in [88] for the case of massive black holes and galactic binaries in LISA. Here, we extend the discussion in [88] to include a prescription for the effect of waveform errors and confusion noise, generalising their results to multiple source types with an arbitrary number of sources. We suppose there are J different types of source in the data. We suppose that there are N_j sources of type j in the data stream, indexed by i, which each depend on a set of m_j parameters, denoted by $\boldsymbol{\theta}^{(j)}_i$, which determine the corresponding

gravitational waveform, $h^j(t;\boldsymbol{\theta}_i^{(j)})$. The complete data stream can be written as

$$\begin{aligned} d(t) &= h(t;\boldsymbol{\Theta}) + n(t) + \Delta H_{\rm conf} \\ &= \sum_{j=1}^{J}\sum_{i=1}^{N_j} h_e^{(j)}(t;\boldsymbol{\theta}_i^{(j)}) + n(t) + \Delta H_{\rm conf}. \end{aligned} \tag{7.10}$$

Here we have introduced a composite vector of parameters, $\boldsymbol{\Theta} = \{\boldsymbol{\theta}_i^{(j)}\}_{i=1,\ldots,N_j}^{j=1,\ldots,J}$, such that $\Theta_{N_{<j}+(i-1)m_j+k} = (\boldsymbol{\theta}_i^{(j)})_k$, where $N_{<j} = \sum_{l=1}^{j-1} N_l m_l$. For any given parameter in $\boldsymbol{\Theta}$, there is exactly one waveform in the above sum that depends on that parameter. Thus the derivatives of the signal reduce to derivatives of the specific waveform template. The combined FM has a block structure, with the on-diagonal blocks being the FMs for the individual sources, and the off-diagonal blocks being formed from overlaps of waveform derivatives of one source with waveform derivatives of another source. Through calculating the FM on parameters $\boldsymbol{\Theta}$, one is able to estimate the expected precision of measurements on individual parameters, taking into account *all* parameter correlations. This is (an estimate for) the precision that would be achieved in a simultaneous coherent fit to all sources in the data.

Without loss of generality, we illustrate this considering two classes of sources, with one source in the first class ($j = 1$, $N_1 = 1$) and an arbitrary number N_2 of sources in the second ($j = 2$). This split is only made for ease of exposition, and is quite arbitrary as the sources could always be relabelled so that the first source is the source of interest. We want to estimate the impact of confusion due to the presence of the population of (fitted) sources of type 2, on the precision of parameter estimation for source 1. We define the following quantities

$$\Gamma^{(1)}_{jk} = \left(\partial_j h^{(1)}(\boldsymbol{\theta}^{(1)}) \middle| \partial_k h^{(1)}(\boldsymbol{\theta}^{(1)})\right) \tag{7.11}$$

$$\left(\Gamma^{(2)}_i\right)_{jk} = \left(\partial_j h^{(2)}(\boldsymbol{\theta}_i^{(2)}) \middle| \partial_k h^{(2)}(\boldsymbol{\theta}_i^{(2)})\right) \tag{7.12}$$

$$\left(\Gamma^{\rm mix}_i\right)_{jk} = \left(\partial_j h^{(1)}(\boldsymbol{\theta}^{(1)}) \middle| \partial_k h^{(2)}(\boldsymbol{\theta}_i^{(2)})\right). \tag{7.13}$$

Here $\Gamma^{(1)}$ is the FM for the source of type 1, $\Gamma^{(2)}_i$ is the FM for the i'th source of type 2 ($i = 1, \ldots, N_2$) and $\Gamma^{\rm mix}_i$ is the mixed FM for the source of type 1 and the i'th source of type 2. In what follows, we find it useful to combine the FM contributions of the entire population of sources in a more compact form. One can write Eqs.(7.11-7.13) as

$$\left(\Gamma^{(2)}\right)_{m_2(i-1)+j,m_2(l-1)+k} = \left(\partial_j h^{(2)}(\boldsymbol{\theta}_i^{(2)}) \middle| \partial_k h^{(2)}(\boldsymbol{\theta}_l^{(2)})\right) \tag{7.14}$$

$$\Gamma^{\rm mix}_{j,m_2(i-1)+k} = (\partial_j h^{(1)}(\boldsymbol{\theta}^{(1)}) | \partial_k h^{(2)}(\boldsymbol{\theta}_i^{(2)})). \tag{7.15}$$

The FM for the full analysis and its inverse are therefore

$$\Gamma = \begin{pmatrix} \Gamma^{(1)} & \Gamma^{\rm mix} \\ (\Gamma^{\rm mix})^T & \Gamma^{(2)} \end{pmatrix}; \quad \Gamma^{-1} = \begin{pmatrix} \Gamma^{-1}_{11} & \Gamma^{-1}_{12} \\ (\Gamma^{-1}_{12})^T & \Gamma^{-1}_{22} \end{pmatrix} \tag{7.16}$$

with the components of the inverse[1]

$$\Gamma^{-1}_{11} = \left(\Gamma^{(1)} - \Gamma^{\rm mix}(\Gamma^{(2)})^{-1}(\Gamma^{\rm mix})^T\right)^{-1}, \tag{7.17}$$

$$\Gamma^{-1}_{22} = \left(\Gamma^{(2)} - (\Gamma^{\rm mix})^T(\Gamma^{(1)})^{-1}\Gamma^{\rm mix}\right)^{-1}, \tag{7.18}$$

$$\Gamma^{-1}_{12} = -\Gamma^{-1}_{11}\,\Gamma^{\rm mix}(\Gamma^{(2)})^{-1}. \tag{7.19}$$

The components Γ^{-1}_{11} encode the measurement precisions for source 1. If the degree of correlation between the source types is small, i.e., $|\Gamma^{\rm mix}| \ll 1$, we can approximate this as

$$\Gamma^{-1}_{11} \approx (\Gamma^{(1)})^{-1} + (\Gamma^{(1)})^{-1}\Gamma^{\rm mix}(\Gamma^{(2)})^{-1}(\Gamma^{\rm mix})^T(\Gamma^{(1)})^{-1}. \tag{7.20}$$

The first term is the measurement precision when there are no sources in the data, while the second represents the degradation in the precision due to confusion with the other sources. We can understand the form of the second term as follows. If the other sources were ignored when fitting for source 1, the parameter bias would be given by Eq. (3.76)

$$\Delta\theta^{(1),i}_{\rm sys} = (\Gamma^{(1)})^{-1}_{ij}(\partial_j h^{(1)}_m|\boldsymbol{h}^{(2)}) \tag{7.21}$$

where we are combining all of the sources of type 2 into the single term $\boldsymbol{h}^{(2)}$. This bias is dominated by the contribution from the true waveform. When we simultaneously fit for the sources of type 2, we imperfectly remove these signals, leaving a residual in the data of the form $\partial_j \boldsymbol{h}^{(2)}\Delta\theta^j_2$, where again we are combining the parameters of all of the sources of type 2 into a single parameter vector, $\boldsymbol{\theta}_2$. The parameter error, $\Delta\boldsymbol{\theta}_2$, is a random variable with covariance matrix $\langle\Delta\theta^j_2\Delta\theta^k_2\rangle = (\Gamma^{(2)})^{-1}_{jk}$. The bias on source 1 parameters can be approximated by $\Delta\theta^{(1),i}_{\rm sys} \approx (\Gamma^{(1)})^{-1}_{ik}(\partial_k h^{(1)}|\partial_l \boldsymbol{h}^{(2)}\Delta\theta^l_2)$. The covariance of the induced systematic error in the

[1] We note also that

$$\Gamma^{-1}_{11} = (\Gamma^{(1)})^{-1} + (\Gamma^{(1)})^{-1}\Gamma^{\rm mix}\Gamma^{-1}_{22}\,(\Gamma^{\rm mix})^T(\Gamma^{(1)})^{-1}$$
$$\Gamma^{-1}_{22} = (\Gamma^{(2)})^{-1} + (\Gamma^{(2)})^{-1}\Gamma^{\rm mix}\Gamma^{-1}_{11}\,(\Gamma^{\rm mix})^T(\Gamma^{(2)})^{-1}$$

which can sometimes be cheaper to compute than Eq. (7.18).

parameters of source 1 is then

$$\begin{aligned}\langle \Delta\theta^{(1),i}_{\rm sys} \Delta\theta^{(1),j}_{\rm sys}\rangle &= (\Gamma^{(1)})^{-1}_{ik}(\partial_k h^{(1)}|\partial_l \boldsymbol{h}^{(2)})\langle \Delta\theta^l_2 \Delta\theta^m_2\rangle(\partial_n h^{(1)}|\partial_m \boldsymbol{h}^{(2)})(\Gamma^{(1)})^{-1}_{nj} \\ &= \left[(\Gamma^{(1)})^{-1}\Gamma^{\rm mix}(\Gamma^{(2)})^{-1}(\Gamma^{\rm mix})^T(\Gamma^{(1)})^{-1}\right]_{ij},\end{aligned}$$

which is the second term from Eq. (7.20). There is nothing that can be done to mitigate uncertainties of this type, which arise from an over-abundance of sources in the data. However, as described above, additional uncertainties can arise from their inaccurate modelling. Previous studies have focused on biases from inaccurate modelling of the target source, but it is also important to ask if the inaccurate modelling of a large number of other sources can leave a sufficient residual in the data to cause problems.

To estimate this, we define $\delta h^{(1)} = h^{(1)}_e - h^{(1)}_m$ as the difference between the exact h_e and template h_m waveforms for the source of type 1, and similarly $\delta h^{(2)}_i = h^{(2)}_e(\boldsymbol{\theta}^{(2)}_i) - h^{(2)}_m(\boldsymbol{\theta}^{(2)}_i)$ for the i'th source of type 2. We also define $\delta h = \delta h^{(1)} + \sum_{i=1}^{N_2} \delta h^{(2)}_i$ as the combination of all waveform residuals. Let us define the bias vector $\boldsymbol{b}$

$$\boldsymbol{b} = (b^{(1)}_1, \ldots, b^{(1)}_{m_1}, (b^{(2)}_1)_1, \ldots, (b^{(2)}_1)_{m_2}, \ldots, (b^{(2)}_{N_2})_1, \ldots, (b^{(2)}_{N_2})_{m_2})^T, \tag{7.22}$$

such that $\boldsymbol{b} = [\boldsymbol{b}^{(1)}, \boldsymbol{b}^{(2)}] \in \mathbb{R}^{(m_1+N_2m_2)\times 1}$ with individual components given by

$$b^{(1)}_j = (\partial_j h^{(1)}(\boldsymbol{\theta}^{(1)})|\delta h), \quad (b^{(2)}_i)_j = (\partial_j h^{(2)}(\boldsymbol{\theta}^{(2)}_i)|\delta h).$$

Note that the bias defined here is only the contribution from modelling errors. The full shift in the peak of the likelihood may be found from a similar expression, with $n(t)$ and $\Delta H_{\rm conf}$ added to δh in the inner products. The quantity $b^{(1)}_j$ for $j = 1, \ldots, m_1$ are the components $\boldsymbol{b}$ for the first source of type 1. The quantity $(b^{(2)}_i)_j$ are the jth components of $\boldsymbol{b}$ with respect to the ith source of type 2. The vector $\boldsymbol{b}$ can be written more concisely as

$$b_j = b^{(1)}_j \quad \text{for } j = 1, \ldots, m_1, \tag{7.23}$$

$$b_{m_1+m_2(i-1)+j} = (b^{(2)}_i)_j \text{ for } i = 1, \ldots, N_2; j = 1, \ldots, m_2\,. \tag{7.24}$$

The biases computed from Eq. (3.76) are given by $\Delta\boldsymbol{\Theta} = \Gamma^{-1}\boldsymbol{b}$ and are thus

$$\Delta\boldsymbol{\Theta} := \begin{pmatrix} \Delta\boldsymbol{\theta}^{(1)} \\ \\ \Delta\boldsymbol{\theta}^{(2)} \end{pmatrix} = \Gamma^{-1} \begin{pmatrix} \boldsymbol{b}^{(1)} \\ \\ \boldsymbol{b}^{(2)} \end{pmatrix}, \tag{7.25}$$

Using Eqs.(7.14-7.16) and Eqs.(7.23,7.24), the bias in the source parameters of the signal of type 1 is

$$\Delta\theta_i^{(1)} = (\Gamma_{11}^{-1})^{ij} b_j + (\Gamma_{12}^{-1})^{im} b_{m_1+m}\,, \tag{7.26}$$

with components of (Γ_{11}^{-1}) and (Γ_{12}^{-1}) defined in Eqs.(7.17,7.19). Using the approximation that led to Eq. (7.20), that the elements of $\Gamma^{\rm mix}(\Gamma^{(2)})^{-1}(\Gamma^{\rm mix})^T$ are much smaller than those of $\Gamma^{(1)}$, we can approximate Eq. (7.26) as

$$\Delta\theta_i^{(1)} \approx [(\Gamma^{(1)})^{-1}]^{ij} b_j - [(\Gamma^{(1)})^{-1}]^{ij} (\Gamma^{\rm mix})_{jl} [(\Gamma^{(2)})^{-1}]^{lm} b_{m_1+m}\,. \tag{7.27}$$

We see that there are two contributions to the parameter bias on the single source of type 1: the standard CV bias (3.76) arising from mismodelling of that source; and an extra correction due to mismodelling of overlapping sources. If the sources from each source type are orthogonal, $\Gamma^{\rm mix} \to 0$ and the presence of other sources does not contribute a parameter bias. In testing the formalism below, we drop the source type indices for simplicity. The waveform and shift in the peak of the likelihood will be denoted

$$\begin{aligned} h(t;\boldsymbol{\Theta}) &= \sum_{i=1}^{N} h_e(t;\boldsymbol{\theta}_i) \quad \text{for } \boldsymbol{\Theta} = \{\boldsymbol{\theta}_1,\ldots,\boldsymbol{\theta}_N\}\,, \\ \Delta\Theta^i &= (\Gamma^{-1})^{ij} \left(\frac{\partial h}{\partial \Theta^j} \middle| n(t) + \delta h + \Delta H_{\rm conf} \right) \\ &= \Delta\Theta^i_{\rm noise} + \Delta\Theta^i_{\rm sys} + \Delta\Theta^i_{\rm conf}\,, \end{aligned} \tag{7.28}$$

with total theoretical error δh and FM denoted

$$\Gamma_{ij} = \left(\frac{\partial h}{\partial \Theta^i} \middle| \frac{\partial h}{\partial \Theta^j} \right), \quad \delta h = \sum_{i=1}^{N} (h_e^{(1)}(t;\boldsymbol{\theta}_i^{(1)}) - h_m^{(1)}(t;\boldsymbol{\theta}_i^{(1)})).$$

The Γ appearing in (7.28) is the joint FM $\Gamma \in \mathbb{R}^{(N\times m)\times(N\times m)}$, with m the dimension of each parameter space $\boldsymbol{\theta}_1,\ldots,\boldsymbol{\theta}_N$. Equation (7.28) is separated into a noise induced error, $\Delta\Theta^i_{\rm noise}$, and biases split into a confusion noise contribution, $\Delta\Theta^i_{\rm conf}$, and a contribution from theoretical errors, $\Delta\Theta^i_{\rm sys}$. Biases are then significant whenever $\mathcal{R}(\Delta\Theta^i_{\rm conf} + \Delta\Theta^i_{\rm sys}) > 1$.

7.2 Modelling signals and noise

To illustrate formalism described in section 7.1, we will consider a number of simplified scenarios. For all of these illustrations, we will model the signals using the `TaylorF2` waveform model

$$\hat{h}(f) = \mathcal{A}\left(\frac{\pi G M f}{c^3}\right)^{-7/6} e^{-i\psi(f)}\,, \tag{7.29}$$

$$\mathcal{A} = -\sqrt{\frac{5}{24}}\frac{c}{D_{\rm eff}\pi^{2/3}}\left(\frac{G\mathcal{M}_c}{c^3}\right)^{5/6}\,. \tag{7.30}$$

Here, $M_c := M\eta^{3/5}$ is the chirp mass, $\eta = M_1 M_2/(M_1+M_2)^2$ the *symmetric mass ratio*[2] and $D_{\rm eff}$ the effective distance. Note that we ignore the effect of the detector response function, which only affects the SNR of the binary and not its frequency evolution. For this reason $D_{\rm eff}$ should be treated effectively as an overall scaling factor, and not as a physical distance parameter. We retain only the leading-order amplitude $\mathcal{A}$ [307] in the waveform. The phase is PN-expanded in the velocity $v := (\pi M G f/c^3)^{1/3}$ and reads

$$\psi(f) = 2\pi f t_c - \phi_c + \frac{3v^{-5}}{128\eta}\left(1 + \sum_{n=2}^{n=7} v^n \psi_{\frac{n}{2}\rm PN}\right)\,, \tag{7.31}$$

with coefficients up to 3.5PN as given in Sec.IIIB of [308]. The constant portion of the phase depends on the time and phase at coalescence, t_c and ϕ_c. We have only included spin-orbit interactions in the 1.5PN phase through the spin parameter β, defined in [309]. We remark that β satisfies the inequality $|\beta| \lesssim 9.4$. We take the above `TaylorF2` model to be the exact waveform $\hat{h}_e(f;\boldsymbol{\theta})$. In these examples, for simplicity we will treat the phase, ϕ_c, time of coalescence, t_c, and distance, $D_{\rm eff}$, as perfectly-known parameters. The purpose of these examples is to illustrate the formalism of Sec.(7.1) and so this is not a serious restriction.

Finally, to represent modelling inaccuracies, we represent the approximate waveform by modifying the smallest contribution in the 3.5PN phase contribution

$$\psi^{(\epsilon)}_{\rm 3.5PN} := \pi\left(\frac{77096675}{254016} + \frac{378515}{1512}\eta - (1-\epsilon)\frac{74045}{756}\eta^2\right)\,, \tag{7.32}$$

(for $\epsilon \in [0,1]$). The true PN waveform has $\epsilon = 0$ and we will take a (fixed) value of $\epsilon \neq 0$ to represent the approximate model. Finally, we model confusion noise as a superposition of `TaylorF2` models, unless otherwise specified (see Sec. 4.3).

We generate detector noise in both ET and LISA using Eq. (3.34) and the we use the analytical fit to the LISA PSD (3.36) PSDs found in [226] (LISA) and [310] (ET).

[2] Under no circumstances should this be confused with the mass ratio $\eta = \mu/M$ used in earlier EMRI based chapters.

We now outline our algorithm to sample the signals modelled through equation (7.29) . We begin by choosing a starting frequency f_0 and final frequency determined by the last stable orbit in a Schwarzschild spacetime $f_{\rm max} = c^3/6\sqrt{6}\pi GM$. The calculated time to merger is then predicted through the 3.5PN chirp time (see Eq.(3.5a) of [307]). Invoking Shannon's sampling theorem [217], the spacing between time points Δt is chosen to be $\Delta t = 1/(2f_{\rm max})$. For multiple signals, we choose the minimum sampling interval common to all waveforms for given mass parameters. In doing so, we find the length of the signal $N_t = \lfloor t_{obs}/\Delta t \rfloor$ in the time domain. Combining all these elements, one is able to construct a list of sampling frequencies $f = [0, \Delta f, 2\Delta f, \ldots, \lfloor (N_t - 1)/2 \rfloor \Delta f]$ for $\Delta f = 1/N_t \Delta t$. Given the discrete Fourier frequencies, it is then possible to construct waveforms using (7.29).

We calculate the FMs as done in chapters 5 and 6. That is, we compute numerical derivatives of waveforms using (3.65) and evaluate equation (3.59) using frequency domain waveforms. In light of verifying our results, we use the Metropolis-Hastings algorithm presented in 3.5.

7.3 Results

In this section, we present four illustrations for the formalism described in Sec. 7.1. The first one concerns confusion and detector noise only. The second concerns the overlap of two signals with coincident coalescence. The third concerns theoretical errors from incorrectly removed waveforms only. The fourth considers all of the above combined.

7.3.1 Biases from detector and confusion noise

In this exploration, we consider a single reference signal in the LISA band and a confusion noise $\Delta H_{\rm conf}$ of binaries that follow a realistic mass distribution. Our aim is to understand how much the combined effects of the confusion signals affect recovery of the parameters of the reference signal, and whether we can predict the biases using the formalism described above. The data stream we consider is

$$\hat{d}(f) = \hat{h}_e(f; \boldsymbol{\theta}_{\rm tr}) + \Delta H_{\rm conf}(f; \boldsymbol{\theta}) + \hat{n}(f). \tag{7.33}$$

We recover the reference signal perfectly by modelling it with the exact waveform $\hat{h}_e(f; \boldsymbol{\theta}_{\rm tr})$ of (7.29) in both the FM and the MCMC sampling algorithms. We therefore expect no biases from modelling errors. We use the following configuration of true (injected) parameters,

$$\boldsymbol{\theta}_{\rm tr} = \{\log \mathcal{M}_c = 83.34, \eta = 0.210, \beta = 5.00\}\,, \tag{7.34}$$

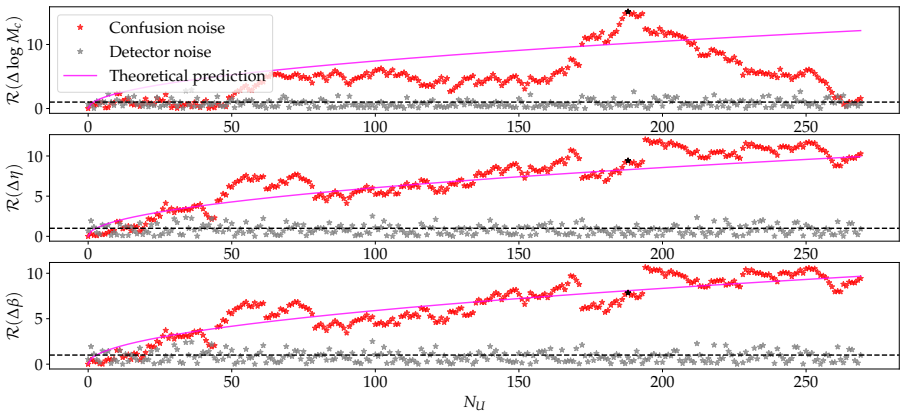

Figure 7.1: *Accumulation of bias from population of overlapping signals.* In red, the accumulation of bias on the parameters of the reference signal from massive black hole binaries that have not been resolved. In gray, the statistical errors arising from instrumental noise fluctuations. The noise is independently generated for each data set and so we expect the $\mathcal{R}$ values to follow a $N(0,1)$ distribution, which is consistent with what is seen in the figure. In purple, the theoretical prediction, which follows a $\sqrt{N}$ behaviour according to Eq.(7.9). In black, the data point with the largest bias in $\mathcal{M}_c$, for which the results were verified using an MCMC simulation, giving the posterior shown in Figure 7.2. We note that these panels are not independent, as they represent one-dimensional marginals of a three dimensional distribution that has large correlations.

which correspond to a spinning binary of total mass $M = 2\times10^6 M_\odot$. We complete the full set of parameters by choosing an effective distance $D_{\rm eff} = 1$Gpc and phase at coalescence $\phi_c = 0$, with time at coalescence given by the chirp time. We begin observing the binary at $f_0 = 0.25\,$mHz and stop at $f_{\rm max} = 2.2\,$mHz, corresponding to the ISCO frequency in a Schwarzschild spacetime for the chosen total mass. That is, we observe the binary until it chirps ~ 4.4 days after we have started observing it. These choices lead to an SNR of $\rho \sim 4200$ for this signal, for which we expect the Fisher formalism to be an excellent approximation.

To construct $\Delta H_{\rm conf}(f;\boldsymbol{\theta})$, we first build a mock catalogue of $N = 800$ sources, which are sampled from uniform distributions

$$\begin{aligned}\beta &\sim U[0.001, 9.4]\\ \eta &\sim U[0.001, 0.25]\\ \phi_c &\sim U[0, 2\pi]\end{aligned} \tag{7.35}$$

and t_c given by the individual chirp times. We distribute sources uniformly in volume by sampling distances $D^3_{\rm eff} \sim U[1, 125]$ Gpc. We let the total masses of the binaries in this catalog

follow a standard probability density function for massive black holes [311, 312, 313],

$$\frac{dN}{dM} = p(M|M_{\rm max}, M_{\rm min}) = \frac{\alpha\, M^{\alpha-1}}{M_{\rm max}^{\alpha} - M_{\rm min}^{\alpha}}, \tag{7.36}$$

for $P(M|M_{\rm max}, M_{\rm min})$ the density function with (total) masses ranging between $M_{\rm min} = 10^4 M_\odot < M < 10^7 M_\odot = M_{\rm max}$ and $\alpha = 0.03$ is the fit in Ref. [312] to the inactive massive black holes of [314]. We can sample from this distribution using direct sampling, which was briefly discussed in section 3.1.1 [248, 247]. Consider the cumulative distribution function

$$\begin{aligned} F(M) = \mathbb{P}(M_{\rm min} \leq M) &= \int_{M_{\rm min}}^{M} dM' \frac{\alpha\,(M')^{\alpha-1}}{M_{\rm max}^{\alpha} - M_{\rm min}^{\alpha}}, \\ &= \frac{(M)^{\alpha} - (M_{\rm min})^{\alpha}}{M_{\rm max}^{\alpha} - M_{\rm min}^{\alpha}}\,. \end{aligned}$$

Setting $F(M) = u$ and inverting the cumulative density function $F(M)$, one obtains

$$\log M = \alpha^{-1} \log\left[(M_{\rm max}^{\alpha} - M_{\rm min}^{\alpha})\, u + M_{\rm min}^{\alpha}\right]. \tag{7.37}$$

To sample from the density function $P(M|M_{\rm min}, M_{\rm max})$ we draw samples from $u \sim U[0,1]$ to obtain a realisation of the total mass M.

For each element of the catalogue, we compute the waveform of the binary using the exact model h_e. For those mass draws for which the frequency array of the binary is longer than that of the reference signal, we cut the former to be of the same length as the latter. Otherwise, we stop the evolution of the binary at its ISCO to avoid introducing an artificial portion of the waveform into the analysis. If the waveform has an observed SNR $\rho_{\rm obs} = \rho + N(0,1)$ [315], where $N(0,1)$ is a standard normal distribution, such that $\rho_{\rm obs} < \rho_{\rm threshold} = 15$ then we consider the binary as "missed", retain the waveform and add it to $\Delta H_{\rm conf}$ in a cumulative fashion. In our example, for $N = 800$ events in the mock catalogue, $N_{\rm U} = \mathcal{O}(270)$ have SNRs below the threshold and are thus unresolved. The final SNR of $\Delta H_{\rm conf}$ is ∼170 in this case.

Once $\Delta H_{\rm conf}$ is obtained and the data stream (7.33) is thus fully specified, we predict the biases from confusion noise $\Delta\boldsymbol{\theta}_{\rm conf}$ [namely, using (7.28) retaining only $\Delta H_{\rm conf}$ in the bias vector], which we can compare to the statistical error $\Delta\boldsymbol{\theta}_{\rm noise}$ [found from (7.28) with n only]. We show the accumulation of the biases from confusion noise in Fig. 7.1 by plotting the ratio $\mathcal{R}(\Delta\boldsymbol{\theta}_{\rm conf})$. In this plot, calculations with different numbers of sources use different noise realisations, but consistent source catalogues, i.e., the data set with $N+1$ confusion sources includes the same sources as the N confusion sources data set, plus one additional source. The ratio, $\mathcal{R}(\Delta\boldsymbol{\theta}_{\rm noise})$, of the noise-induced shift in the peak of the likelihood to the expected

standard deviation of this quantity, is also shown and can be seen to hover around the value of 1, as expected. Conversely, we find that the formalism predicts significant biases ($\mathcal{R} > 1$) from the accumulation of missed signals drawn from a simple, but realistic distribution of the masses. We plot the theoretical prediction from Eq. (7.9) of Sec. 7.1 on top of the found ratios, showing that they (qualitatively) follow the expected $\sqrt{N}$ behaviour. We note that we do not expect the bias to precisely track the theoretical prediction. As sources are added the bias follows a random walk, and Eq. (7.9) gives an approximate 1-σ boundary to that random walk. We have tried many confusion noise realisations with $N_U \gg 1000$ and in all cases the accumulation of the bias follows a similar pattern. The realisation used in this figure happens to track the theoretical prediction quite well, but is reasonably typical.

To assess whether these predictions are sound, we confirm them with an MCMC analysis for the data set that gives the largest bias ($\mathcal{R} \sim 15$) in chirp mass, indicated by the black data point in Fig. 7.1). The result of the MCMC run and the predictions for the shift in the peak of the likelihood due to the confusion sources and noise, computed with Eq. (7.28), are shown in Fig 7.2. Even in this most extreme case, we can clearly see that the predictions for the bias match the MCMC posterior very well, demonstrating that the formalism works well in estimating source confusion from missed signals. We remark that in this example the SNR of the residuals is lower than the SNR of the signal we are inferring from the data stream. This is a regime in which we would expect that the linear signal approximation is valid. In scenarios in which the SNR of the "missed" signals is larger than that of the target source, the linear signal approximation might cease to be valid, but this formalism should at least provide an indication that systematic biases are "large".

7.3.2 Biases from overlapping signals with coincident coalescence

A particularly interesting class of overlapping signals that has attracted attention in the recent literature are those where the coalescence times t_c are nearly simultaneous. Such a scenario could be relevant to mergers of MBHs observed by LISA or to stellar-origin BBHs observed by ET and CE, but this will depend on the rate of such mergers and, therefore, the probability that mergers happen within the same time period. Quantitative studies of the rate of overlapping mergers have been carried out for advanced LIGO and CE. In [303, 304, 316, 317], the authors conclude that coincident (meaning merger times within 2 seconds) mergers of BBH binaries will occur tens of times per year for CE, and BNS mergers could occur coincidentally with other BNS or BBH mergers hundreds or even thousands of times per year.

The same papers, as well as [318], also present the first Bayesian inference analyses with

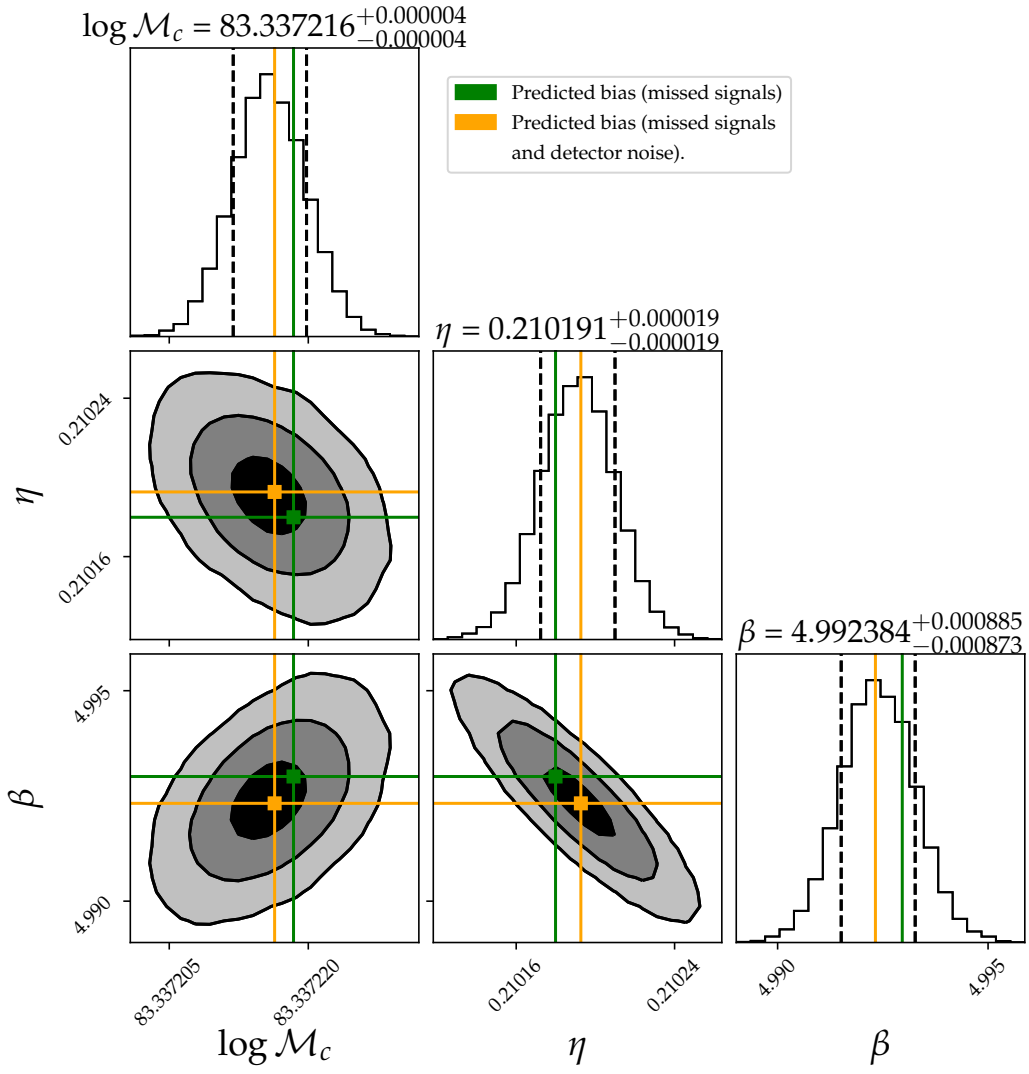

Figure 7.2: *Biases from source confusion and detector noise.* MCMC posteriors and predictions from the Fisher formalism for the largest-bias case in Fig. 7.1. The values in green are predictions considering source confusion only. Those in orange combine biases from source confusion and detector noise (which we cannot access in a realistic situation). The true values are well beyond the range of the plot at $\sim 8\sigma$ for each parameter (see Fig. 7.1).

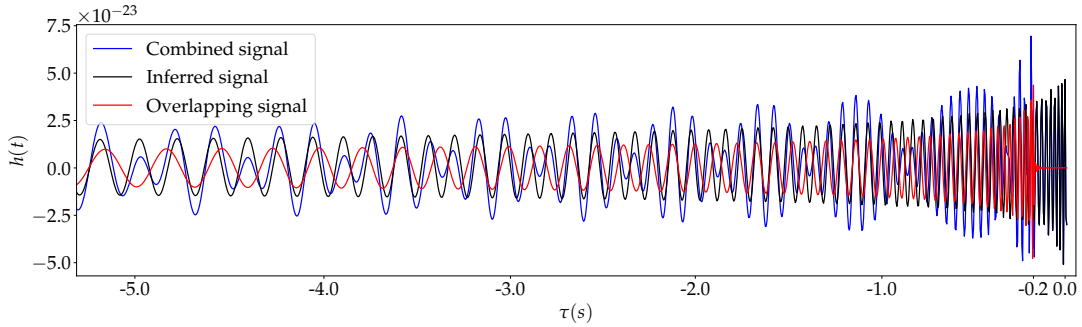

Figure 7.3: *Waveforms for overlapping signals.* We plot the waveforms for signal $h_e^{(1)}(t)$ in black; this represents the "inferred source" for which we are attempting to recover the parameters. We plot the waveform of the overlapping signal $h_e^{(2)}(t)$ in red; the signal has a coalescence time at $\tau = -0.2s$ relative to the one of the inferred source. The sum of the two signals is shown in blue.

overlapping signals, with some critical differences. Reference [318] studies the simultaneous inference of overlapping BNSs, in such a way that no biases on the parameters are expected from confusion noise. The authors in [317] perform a similar analysis for the second-generation LIGO-Voyager detector, [303] for pairs of BBH-BBH, BBH-BNS and BNS-BNS systems using `LAL-inference` [319], and [304] for BBH pairs with `bilby` [320]. However, in these last two papers, inference is performed for one binary only, treating the second as confusion noise. They find that biases occur when the difference between the coalescence times $\tau = t_c^{(2)} - t_c^{(1)}$ of signals "(1)" and "(2)" is sufficiently small, roughly $\tau \lesssim 0.5s$. Here we analyse a similar scenario to that of [304], interpreting the bias as arising from a single confusion source, to see whether the analytic formalism presented here can reproduce that result without the need for expensive Bayesian posterior computation. Notice that a (joint) FM analysis is presented in [316] for a similar scenario, though the similarities end there.

We consider an ET data stream composed of a signal $h^{(1)}$ to be inferred and a missed signal $h^{(2)}$ that creates confusion noise

$$\hat{d}(f) = \hat{h}_e^{(1)}(f; \boldsymbol{\theta}^{(1)}) + \hat{h}_e^{(2)}(f; \boldsymbol{\theta}^{(2)})\,. \tag{7.38}$$

For this example we ignore waveform errors and detector noise. The biases arise solely due to the confusion noise $\hat{h}_e^{(2)}$, and can be predicted from (7.28) setting $n = \delta h = 0$. The parameter space of the FM is $\boldsymbol{\theta}^{(1)} = \{\log \mathcal{M}_c^{(1)}, \eta^{(1)}\}$, with true parameters $\boldsymbol{\theta}_{\rm tr}^{(1)} = \{15.4M_\odot, 0.243\}$ (corresponding to a binary with component masses $m_1 = 21M_\odot$ and $m_2 = 15M_\odot$). We take the signal to be nonspinning ($\beta^{(1)} = 0$) with an effective distance $D_{\rm eff}^{(1)} = 5$Gpc, and phase and times at coalescence $\phi_c^{(1)} = \pi/3$ and $t_c^{(1)} = 0s$. The SNR for this source is $\rho(h^{(1)}) \sim 75$.

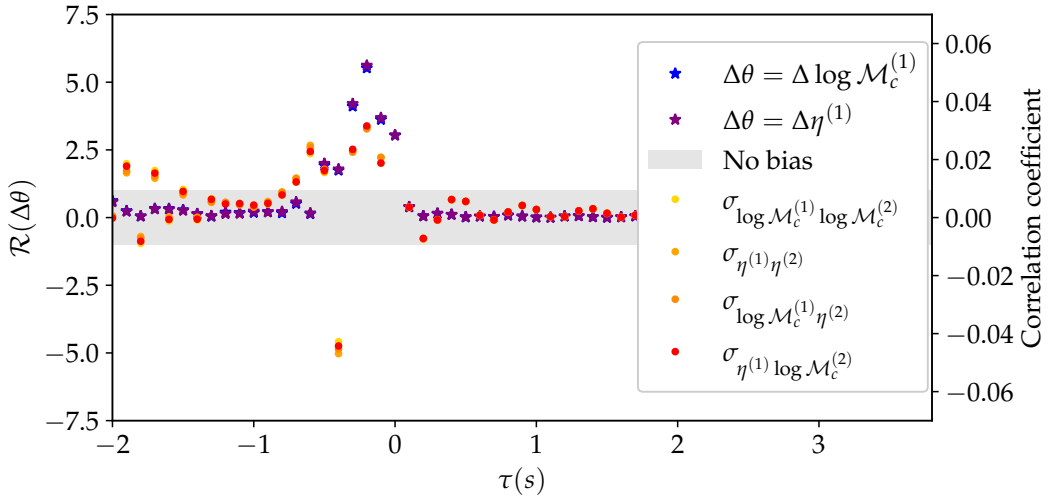

Figure 7.4: *Biases from an overlapping signal as a function of the difference in coalescence time.* In cold (blue, purple) colors, we plot the bias ratios for the parameters of signal "(1)" due to the unaccounted-for presence of signal "(2)", as a function of the coalescence time difference τ between the two signals. The relevant scale is the y-axis on the left, where we see that biases $\mathcal{R} > 1$ can arise. In gray, we indicate the region where we regard biases as not significant ($\mathcal{R} < 1$). In warm colors, we plot the correlation coefficients (with relevant y-axis on the right), defined in Eq. (7.39). We see that the largest correlations $\sigma \gtrsim 0.05$ correspond to the largest biases ($\sim 6\sigma$).

For the overlapping signal, we pick component masses $m_1 = 25M_\odot$ and $m_2 = 20M_\odot$, a non-spinning configuration $\beta^{(2)} = 0$, an effective distance $D_{\rm eff}^{(2)} = 10$Gpc, and phase at coalescence $\phi_c^{(0)} = \pi/3$. We let $t_c^{(2)}$ vary as a free parameter. For a nominal value of $t_c^{(2)} = -0.2s$, the SNR for the overlapping source is $\rho(h^{(2)}) \sim 46$. In Fig. 7.3, we plot time-domain waveforms for this particular configuration.

We now turn to the problem of predicting the biases on $\boldsymbol{\theta}^{(1)}$. From Eqs. (7.28) and (3.77), we compute the bias ratio $\mathcal{R}(\Delta\boldsymbol{\theta}^{(1)}_{\rm conf})$ due to the presence of confusion noise, varying $\tau := t_c^{(2)} - t_c^{(1)}$ between $\tau = -2.0$ and $\tau = 2.0$. The results are shown in Fig. 7.4. In this Figure, we plot both the ratios $\mathcal{R}$ and the Pearson correlation coefficients[3], defined as

$$\sigma_{\theta_1\theta_2} = \frac{(\Gamma^{-1})_{\theta_1\theta_2}}{\sqrt{(\Gamma^{-1})_{\theta_1\theta_1}(\Gamma^{-1})_{\theta_2\theta_2}}}\,. \tag{7.39}$$

We notice that non-trivial biases start appearing when $|\tau| \lesssim 0.5$, which correspond to the largest correlation coefficients ($\sigma_{\theta_1\theta_2} \sim 0.05$). We therefore (qualitatively) confirm the main result of [304] [and of [303, 316, 317] indirectly]. Notice that because of our choice of data

[3]These correlations are calculated using the joint FM, which fundamentally assumes that we have resolved *both* signals. In this case, we would expect no biases from the overlapping signal. In the bias ratios calculation, we treat the second signal as unfitted, which leads us to the shown biases from confusion noise. Regardless of this difference in treating the FM, we conclude that Pearson correlations can be a guide to understand where biases would occur if the overlapping signal were not inferred, as suggested in [304].

Table 7.1: Parameter configurations for the signals in Sec. 7.3.3. We also report the SNR of the source, ρ_h and of the residual $\rho_{\delta h}$. Notice that we do not consider waveform errors for the first (reference) source here, implying its residual is zero. We sample all the sources from $f = 0.5$mHz and stop at 2mHz ($T_{\rm obs} = 0.3$ days), the earliest chirp time for these masses.

i	$M/M_\odot$	η	β	$D_{\rm eff}$	t_c	ϕ_c	ρ_h	$\rho_{\delta h}$
1	$2 \cdot 10^6$	0.20	5.0	10 Gpc	6 h	0	83	-
2	$1 \cdot 10^6$	0.23	1.0	3 Gpc	48 h	π	790	31
3	$4 \cdot 10^6$	0.08	2.4	2 Gpc	6 h	0.9	2216	76

input and parameters, our comparisons with the results of [304] can only be qualitative. They consider noise in Advanced LIGO, while we consider ET with *zero* noise. Furthermore, they model their signals with a different approximant (`IMRPhenomv2`), include detector response functions, sample through masses with different true values and include additional parameters in the analysis, specifically the phase, ϕ_c, and time, t_c, at coalescence, and luminosity distance, d_L.

To check the reliability of our bias predictions, we have also compared them against posteriors from an MCMC run for a configuration with the τ leading to the largest biases ($\sim 6\sigma$, for the $\tau = -0.2s$ configuration shown in Fig. 7.3): we obtain excellent agreement, at the level of the accuracy shown by the (orange) prediction in Fig. 7.2. This example illustrates the advantage of our formalism, namely that the biases can be cheaply and reliably predicted. Our formalism will be a valuable tool for extending previous Bayesian analyses into regions of parameter space that are difficult to sample with fully Bayesian techniques.

7.3.3 Biases from the inaccurate removal of signals

We now consider the situation in which the confusion sources are not "missed", but incorrectly fitted out. To simulate this, we consider a LISA data stream,

$$\hat{d}(f) = \hat{h}_e^{(1)}(f;\boldsymbol{\theta}^{(1)}) + \hat{h}_e^{(2)}(f;\boldsymbol{\theta}^{(2)}) + \hat{h}_e^{(3)}(f;\boldsymbol{\theta}^{(3)}) \tag{7.40}$$

where the signal "(1)" is our reference signal, which we assume is modelled perfectly, and the other sources are incorrectly subtracted using approximate templates $\hat{h}_m(f;\boldsymbol{\theta}^{(2,3)}, \epsilon = 0.3)$. In such a procedure, we expect biases to arise only from the residual that the incorrectly modelled signals leave in the data stream (7.40),

$$\delta h = \sum_{i=2}^{3} \hat{h}_e^{(i)}(f;\boldsymbol{\theta}^{(i)}) - \hat{h}_m^{(i)}(f;\boldsymbol{\theta}^{(i)}, \epsilon = 0.3)\,. \tag{7.41}$$

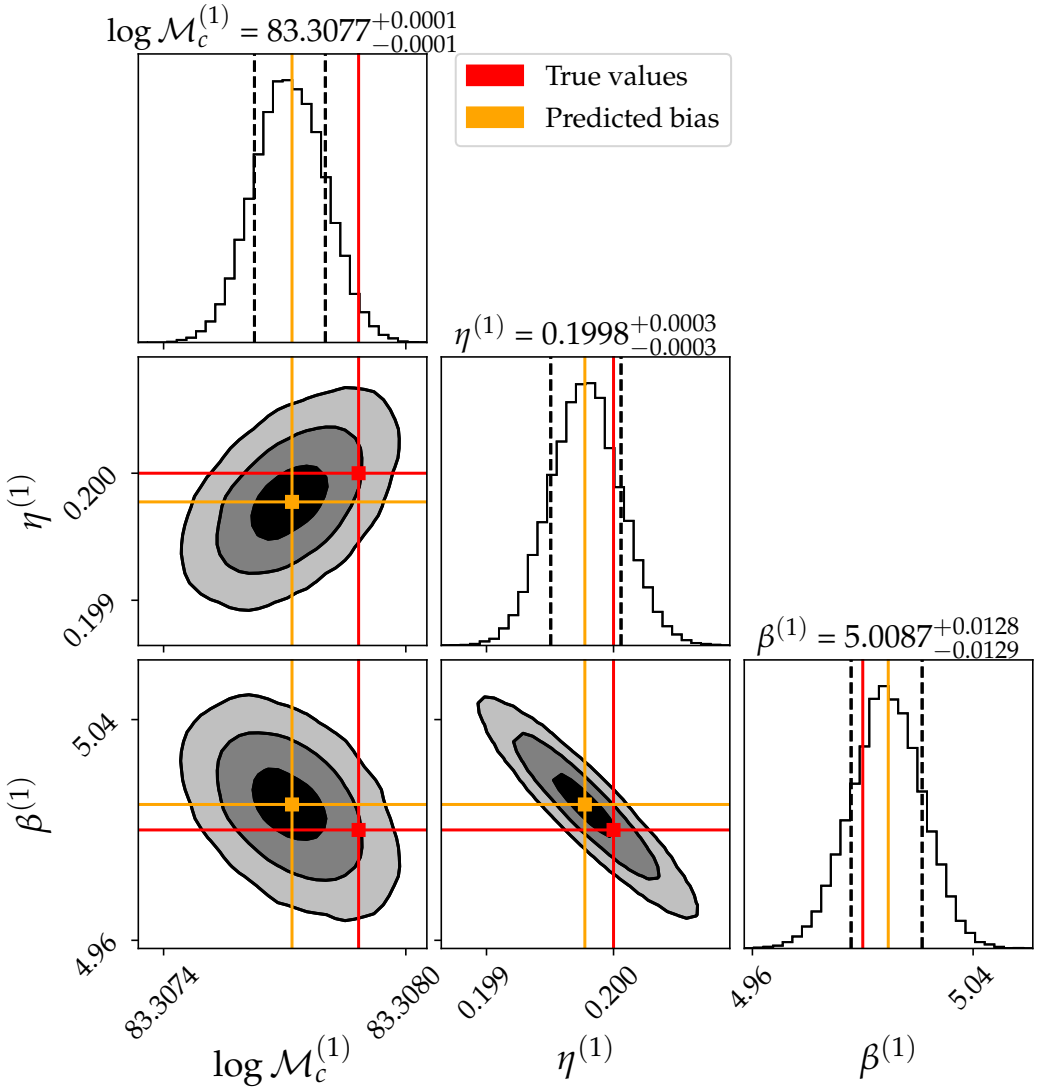

Figure 7.5: *Biases from the inaccurate removal of loud sources.* Posterior distributions for the parameters of a reference signal, computed using MCMC, when 2 mismodelled overlapping signals are removed from the data (with parameters given in Table 7.1). We also show the biases predicted using our formalism.

In this case, the relevant parameter space is $\boldsymbol{\Theta} = \{\boldsymbol{\theta}^{(1)}, \boldsymbol{\theta}^{(2)}, \boldsymbol{\theta}^{(3)}\}$, where we pick each subset to be $\boldsymbol{\theta}^{(i)} = \{\log \mathcal{M}_c^{(i)}, \eta^{(i)}, \beta^{(i)}\}$. The joint FM Γ is therefore a 9×9 matrix (calculated using $\hat{h}_m$). We report the true source parameters in Table 7.1. We calculate the biases $\Delta\boldsymbol{\theta}^{(1)}$ on the reference signal's parameters using (7.26)(or equivalently (7.28)), which leads us to

$$\begin{aligned} \mathcal{R}(\Delta \log \mathcal{M}_c^{(1)}) &= 1.98 > 1 \\ \mathcal{R}(\Delta\eta^{(1)}) &= 0.84 \\ \mathcal{R}(\Delta\beta^{(1)}) &= 0.74\,. \end{aligned} \tag{7.42}$$

Biases are then significant for the chirp mass in this case. These predictions can be checked with an MCMC analysis, see Fig. 7.5. We find that the formalism can accurately predict the biases from the inaccurate removal of signals.

The fact that each contribution to δh in Eqs. (7.26,7.28) affects the parameters of each source equally suggests that residuals effectively behave as missed sources and confusion noise. In fact, we can rewrite the data stream analysed in Fig. 7.5 in the form

$$\hat{d}(f) = \hat{h}_e^{(1)}(f;\boldsymbol{\theta}^{(1)}) + \hat{h}_m^{(2)}(f;\boldsymbol{\theta}^{(2)}, \epsilon = 0.3) + \hat{h}_m^{(3)}(f;\boldsymbol{\theta}^{(3)}, \epsilon = 0.3) + \delta h, \tag{7.43}$$

which explicitly separates out the modelled part using the models employed by the MCMC analysis and the calculation of the joint FM. Doing so leaves an extra term, δh, which plays the role of the confusion noise caused by the residuals. One can check that the biases predicted from the data stream (7.43) (and obtained using the joint FM with $\hat{h}_m$) match the predictions reported in Fig. 7.5. An important implication of this equivalence of results is that significant biases may arise from the incorrect removal of a very large number of signals drawn from the same population, in direct analogy with the findings of the previous section.

7.3.4 Waveform errors & confusion noise

7.3.4.1 LISA

We now bring together the ideas described in sections (7.3.1) and (7.3.3), and show that the formalism developed in Sec. (7.1) can accurately predict biases on parameter estimates when we simultaneously fit $N_{\rm fit}$ sources with inaccurate waveforms, while confusion and detector noise

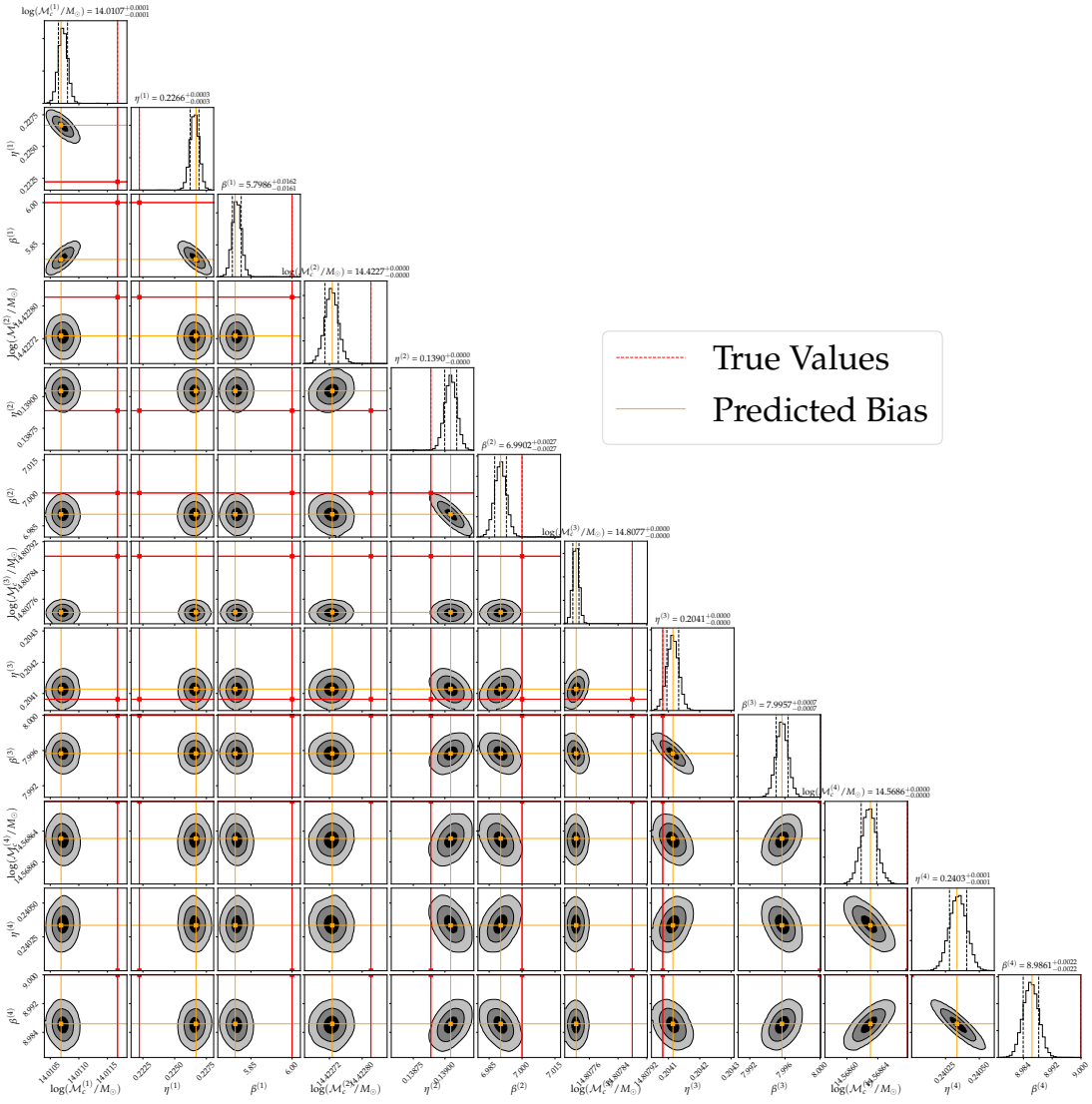

Figure 7.6: Triangle plot of the one-dimensional (on the diagonal) and two-dimensional marginalised posterior distributions for the inferred parameters in the LISA scenario considered in Sec. 4.3. The red lines indicate the true parameters and orange lines indicate the biases predicted from (7.28).

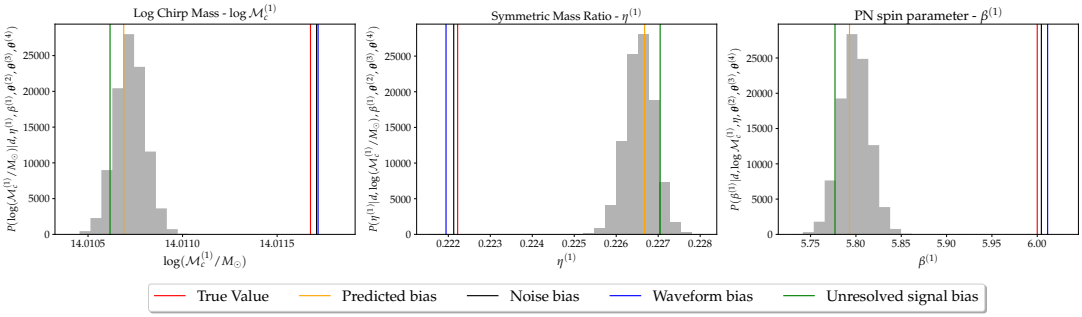

Figure 7.7: (top/bottom left to right) The grey histograms are the posterior samples for $\log M_c^{(1)}, \eta^{(1)}$ and $\beta^{(1)}$ for the LISA scenario considered in Sec. 4.3. The red lines indicate the true parameters, blue lines the biases arising from the use of inaccurate waveforms as templates, the black ones the noise induced shift in the peak of the likelihood, the green lines the biases due to unresolved signals and the orange lines show the approximation to the total bias computed from (7.28).

are also present in the data stream. The data stream in this case is

$$\hat{d}(f) = \sum_{i=1}^{N_{\rm fit}} \hat{h}_e^{(i)}(f; \boldsymbol{\theta}_{\rm tr}^{(i)}) + \Delta H_{\rm conf} + \hat{n}(f). \tag{7.44}$$

We assume $\Delta H_{\rm conf}$ arises from the galactic foreground of white-dwarf binaries (WDB). LISA is guaranteed to detect WDBs in their thousands or even tens of thousands [299, 300] (depending on the imposed SNR threshold), but there will also be millions of unresolved WDBs radiatig in the LISA band. Here we assume that WDBs with $\rho < 8$ have been folded into the PSD [300]. We additionally assume that only WDBs with $\rho > 15$ have been detected by dedicated pipelines, which leaves us with missed WDBs with SNRs in the range $8 < \rho < 15$. To simulate these sources, we construct a superposition of signals, see Eq. (7.2), with frequencies chosen from $f_i \in (10^{-4}, 10^{-3})$Hz. For simplicity, we only retain the leading PN term in the waveform, computed for random masses drawn from $(m_1, m_2) \sim 10^2 \cdot U^2[0.3, 1] M_\odot$. We finally draw effective distances $D_{\rm eff} \sim 10^4 \cdot U[1, 3]$pc. We discard binaries not in the specified range of SNRs, until $N_U = 1000$ are found. To complete the input data stream, we add $N_{\rm fit} = 4$ fitted signals with waveform errors $\epsilon = 0.04$ and source parameters $\boldsymbol{\theta}^{(i)}$ given in Tab.7.2. We choose initial frequencies $f_0 = 10^{-4}$Hz and sample the sources simultaneously with a maximum frequency given by the highest ISCO frequency among the fitted sources. For simplicity, we set $(\phi_c, t_c) = (0, T_{\rm min})$ for all sources, where $T_{\rm min}$ is the minimum chirping time allowed over all parameter configurations. The SNRs are of order $\mathcal{O}(10^3)$ for all fitted sources.

Corner plots displaying *all* parameter biases can be found in Fig. 7.6. We see that the predicted biases from (7.28) are in remarkable agreement with the posteriors from the MCMC algorithm. Additionally, in Fig.7.7 we show how the total shift in the peak of the posterior of the

Table 7.2: Parameters for the simultaneously-fitted LISA signals in Sec. 4.3.

i	$M/M_\odot$	η	β	$D_{\rm eff}$/Gpc
1	3×10^6	0.222	6	2
2	6×10^6	0.139	7	3
3	7×10^6	0.204	8	1
4	5×10^6	0.240	9	1

parameters $\boldsymbol{\theta}^{(1)}$ of the first source, computed from Eq. (7.26), breaks down into its constituent contributions. Firstly, we see that biases from confusion noise, unresolved sources or waveform residuals can deconstructively interfere, i.e., the combined contribution can be smaller than the worst of the individual contributions. Secondly, we notice that there are large biases from confusion noise, which implies that if global-fit analyses miss $\mathcal{O}(1000)$ WDBs, this will lead to a significant bias in parameter estimates for other GW sources. We have further explored how biases change when the threshold is taken to be any value $\rho_{\rm th} \in [8, 15]$. We have tested that, when this threshold is increased towards $\rho_{\rm th} = 15$, biases tend to increase as the SNR of $\Delta H_{\rm conf}$ increases. While the model used here is approximate, it suggests that the completeness of LISA data analysis algorithms needs to be sufficiently high down to sufficiently low threshold SNRs for biases on other parameters to be minimized.

7.3.4.2 ET

We repeat the analysis of Sec. 4.3 for a source in ET. We use the same data stream as (7.44), modelling $N_{\rm fit} = 2$ simultaneously-fitted signals in a similar manner. We pick waveform errors $\epsilon = 0.02$ and a starting frequency $f_0 = 5$Hz. As for confusion noise, we construct it with a series of missed signals which we model without errors. We report the parameters for both fitted and missed sources in Tab. (7.3). The SNRs of the fitted signals are $\mathcal{O}(10^3)$, those of the missed signals $\lesssim 1000$ (with the lowest ~ 200). The SNRs of the missed signals for ET are noticeably high, and would likely be detected in a future analysis. However, for sake of example, treat these signals as missed signals in the parameter estimation scheme. The predictions for the biases of all parameters, Fig. 7.3.4.2, show that the formalism can predict the mean of the posterior as remarkably well as in the case of LISA. The individual bias contributions, Fig. 7.8, confirm that biases can deconstructively interfere.

7.4 Global-fit schemes

So far, we have defined the global-fit as the simultaneous search for and parameter estimation of *all* GW signals in the LISA data stream. In Sec. 7.3.4, this was achieved by assuming the

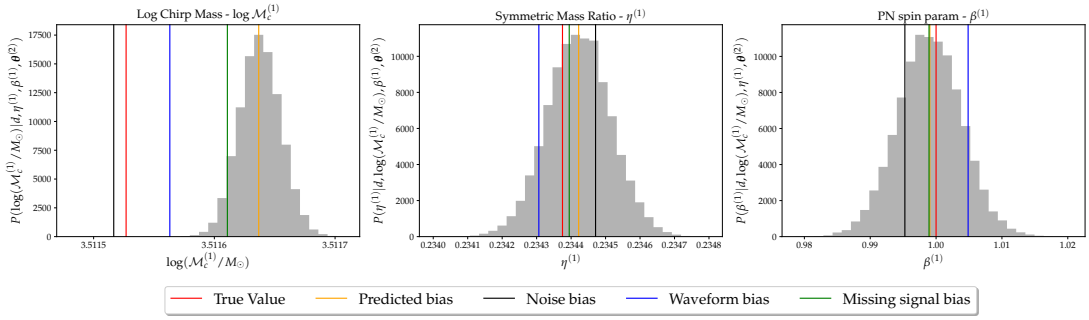

Figure 7.8: Same as Figure 7.7 but for the ET configuration of section 7.3.4.2.

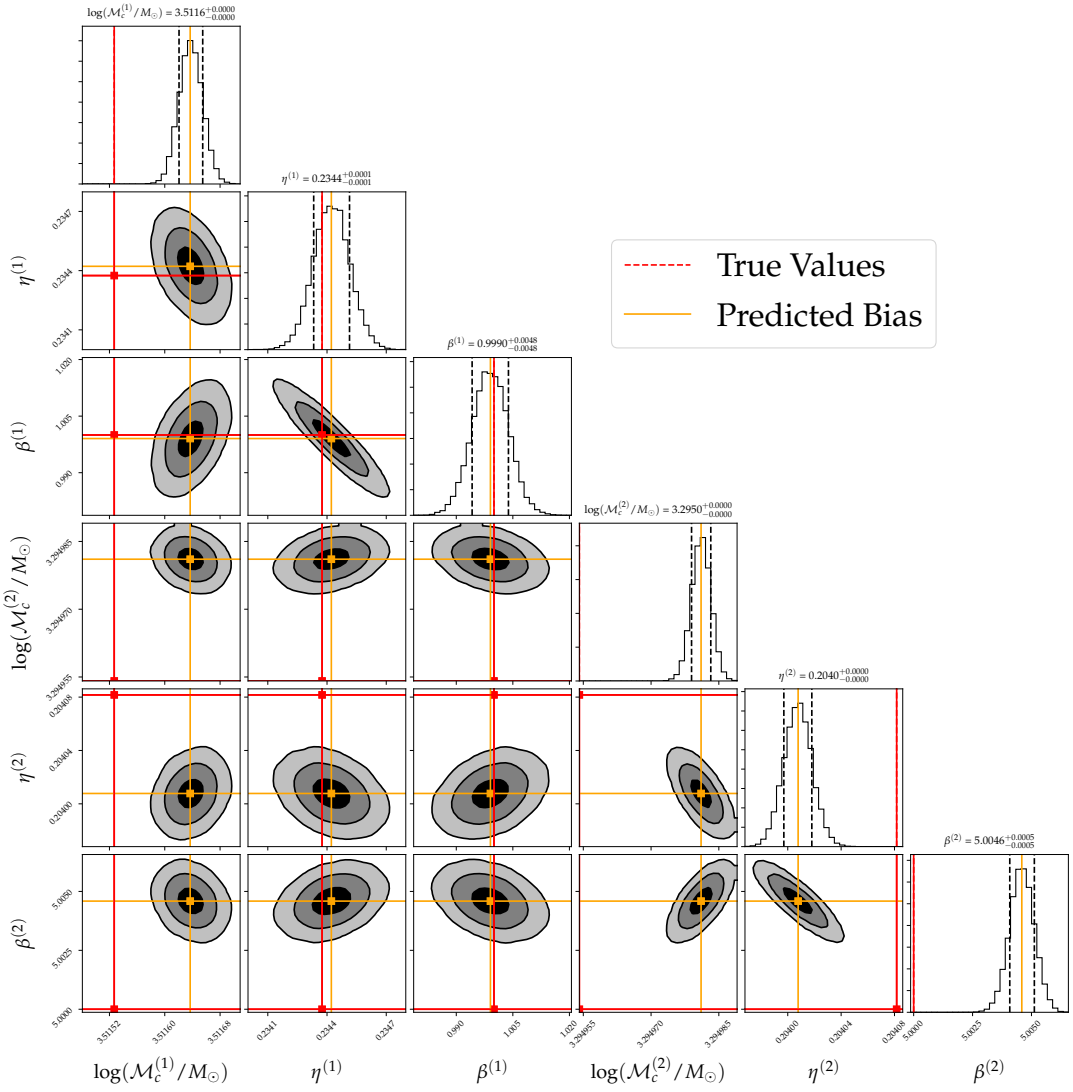

Figure 7.9: Same as Fig. 7.6 but for the ET configuration of section 7.3.4.2.

Table 7.3: Parameter configurations for the ET case.

	Fitted			
i	$M/M_\odot$	η	β	$D_{\rm eff}$/Mpc
1	80	0.234	1	400
2	70	0.204	5	40
	Missed			
i	$M/M_\odot$	η	β	$D_{\rm eff}$/Mpc
1	2.22	2.708	5.04	259.93
2	2.886	0.247	3.882	253.36
3	4.395	0.2264	5.539	324.227
4	6.452	0.1991	4.404	305.828

number of signals (and the associated parameter space) present in the data stream was known precisely. However, in a realistic scenario, we will not know how many signals are present in the data. Furthermore, the number of signals present at any given time may be large, leading to a prohibitively large parameter space. Consider, for example, the simultaneous inference of an EMRI and an massive black hole binary. Both systems will have parameter spaces $\gtrsim$ 14 dimensions, requiring parameter estimation algorithms to sample from a $\gtrsim 28$ dimensional posterior. This could stretch the capabilities of current inference techniques (especially when correlations between parameters of different sources are high). The problem is likely to worsen as more signals are included in the model. One solution is to use state-of-the-art parameter estimation techniques that are able to efficiently sample such complicated, high-dimensional posterior distributions. The overall aim of this section is to provide alternative ideas to tackle the global fit problem. We begin by proposing an (expensive) iterative approach to sample reduce portions of the parameter space. Then, using the formalism developed above, we illustrate how to cheaply correct for the biases arising within the first few parameter estimation simulations. The algorithm described is not intended to fully replace general global-fit analyses. Instead, it could provide a way to aid full-fledged global-fit pipelines (for instance, accelerating their convergence), as well as potentially providing a quick cross-check of the results [4]. Global-fit parameter estimation algorithms, which can account for parameter correlations, will always outperform the algorithm we present. If well designed, global-fit pipelines can also be comparable in computational cost to such an algorithm. However, the algorithm we describe is easier to implement efficiently.

[4]We note here that cross checks are likely to be useful only in the domain in which the FM is a good approximation for all the considered parameters. The range of applicability of the FM, whose extent is to be substantiated with future analyses, may be further restricted with the addition of realistic features such as the detector response functions.

7.4.1 Parameter estimation through local-fits

Let $h^{(\mathcal{A})} \in \mathcal{A}$ and $h^{(\mathcal{B})} \in \mathcal{B}$ denote a set of distinct signals with parameters $\boldsymbol{\theta}^{\mathcal{A}}_{\rm tr}$ and $\boldsymbol{\theta}^{\mathcal{B}}_{\rm tr}$ we wish to infer. The joint data stream is given by

$$d(\mathcal{A},\mathcal{B}) = \sum_{\mathcal{A}} h_e^{(\mathcal{A})}(\boldsymbol{\theta}^{\mathcal{A}}_{\rm tr}) + \sum_{\mathcal{B}} h_e^{(\mathcal{B})}(\boldsymbol{\theta}^{\mathcal{B}}_{\rm tr}) + n(t). \tag{7.45}$$

For simplicity, we ignore effects coming from unresolved signals. Global-fit pipelines are concerned with the data stream (7.45) with the goal to simultaneously infer both signal sets $h^{(\mathcal{A})} \in \mathcal{A}$ and $h^{(\mathcal{B})} \in \mathcal{B}$.

In a local-fit procedure, we consider performing parameter estimation *only* on signal set $\mathcal{A}$ and treat signals from the set $\mathcal{B}$ as missed signals. We write this data stream as

$$d(\mathcal{A}|\mathcal{B}) = \sum_{\mathcal{A}} h_e^{(\mathcal{A})}(\boldsymbol{\theta}^{\mathcal{A}}_{\rm tr}) + \Delta H_{\rm conf} + n(t), \tag{7.46}$$

$$\Delta H_{\rm conf} = \sum_{\mathcal{B}} h_e^{(\mathcal{B})}(\boldsymbol{\theta}^{\mathcal{B}}_{\rm tr}). \tag{7.47}$$

The best fit parameters for $\mathcal{A}$ obtained in this stage can be denoted $\boldsymbol{\theta}^{\mathcal{A}|\mathcal{B}}_{\rm bf}$, the conditioning on $\mathcal{B}$ indicating that the estimate was obtained with $\mathcal{B}$ present in the data. In the second step, we use the recovered parameters $\boldsymbol{\theta}^{\mathcal{A}|\mathcal{B}}_{\rm bf}$ to subtract out an estimate of $h^{\mathcal{A}}$ from the joint data stream using our approximate model

$$d(\mathcal{B}|\mathcal{A}_{\rm res}) = d(\mathcal{A},\mathcal{B}) - \sum_{\mathcal{A}} h_m^{(\mathcal{A})}(\boldsymbol{\theta}^{\mathcal{A}|B}_{\rm bf}). \tag{7.48}$$

Then one estimates the parameters of signal $\mathcal{B}$ using the data stream (7.48) with signal templates representing signals in $\mathcal{B}$. This will yield parameters $\boldsymbol{\theta}^{\mathcal{B}|\mathcal{A}_{\rm res}}_{\rm bf}$, where $\mathcal{A}_{\rm res}$ indicates that this analysis was done on a "residual data set" from which an estimate of $h^{\mathcal{A}}$ had been subtracted. This estimate can be used to *update* the initial data stream $d(\mathcal{A}|\mathcal{B})$, now denoted $d(\mathcal{A}|\mathcal{B}_{\rm res}) = d(\mathcal{A},\mathcal{B}) - \sum_{\mathcal{B}} h^{(\mathcal{B})}(\boldsymbol{\theta}^{\mathcal{B}|\mathcal{A}_{\rm res}}_{\rm bf})$. Again, we can perform parameter estimation on signals $\mathcal{A}$, now with residuals from $\mathcal{B}$ in the data stream, using this updated data array and recovering $\boldsymbol{\theta}^{\mathcal{A}|\mathcal{B}_{\rm res}}_{\rm bf}$. These recovered parameters should be *closer* to the true parameters than $\boldsymbol{\theta}^{\mathcal{A}|\mathcal{B}}_{\rm bf}$. We can continue this scheme by then searching over

$$d(\mathcal{B}|\mathcal{A}_{\rm res}) = d(\mathcal{A},\mathcal{B}) - \sum_{\mathcal{A}} h_m^{(\mathcal{A})}(\boldsymbol{\theta}^{\mathcal{A}|\mathcal{B}_{\rm res}}_{\rm bf}), \tag{7.49}$$

recovering parameters, then searching over $d(\mathcal{A}|\mathcal{B}_{\rm res})$, and so on and so forth. What we would

find is that the recovered parameters for both $\boldsymbol{\theta}^{\mathcal{A}}_{\rm bf}$ and $\boldsymbol{\theta}^{\mathcal{B}}_{\rm bf}$ tend towards the "true" parameters, i.e., the parameters that would have been recovered if a global fit procedure was carried out. An advantage of this procedure is that it sidesteps issues arising from sampling the joint posterior for $\mathcal{A}$ and $\mathcal{B}$, but a clear disadvantage is that it requires a number of repeated parameter inference calculations. Computationally, this is expensive and time consuming. As an alternative, we propose that one can use the algorithm presented in Sec.(7.1) to correct the biases found above. In doing so, one may be able to get a reliable estimate of the true parameters $\boldsymbol{\theta}^{(\mathcal{A})}_{\rm tr}$ and $\boldsymbol{\theta}^{(\mathcal{B})}_{\rm tr}$ without having to iterate, i.e., using just the first two parameter inference calculations.

7.4.2 Correcting biases in the local-fit analysis

Before we talk about the details of our algorithm, it is instructive to discuss the source of the biases in parameters $\boldsymbol{\theta}^{\mathcal{A}|\mathcal{B}}_{\rm bf}$ and $\boldsymbol{\theta}^{\mathcal{B}|\mathcal{A}_{\rm res}}_{\rm bf}$. For the data stream (7.46), the bias in the recovered parameter $\boldsymbol{\theta}^{\mathcal{A}|\mathcal{B}}_{\rm bf}$ is sourced by

$$\delta h^{\mathcal{A}|\mathcal{B}} = \sum_{\mathcal{B}} \hat{h}^{(\mathcal{B})}_e(\boldsymbol{\theta}_{\rm tr}) + \sum_{\mathcal{A}} \left[\hat{h}^{(\mathcal{A})}_e(\boldsymbol{\theta}^{(\mathcal{A})}_{\rm tr}) - \hat{h}^{(\mathcal{A})}_m(\boldsymbol{\theta}^{(\mathcal{A})}_{\rm tr})\right] + \hat{n}(f), \tag{7.50}$$

and similarly the bias in $\boldsymbol{\theta}^{\mathcal{B}}_{\rm tr}$ when performing parameter estimation on the data stream (7.48)

$$\delta h^{\mathcal{B}|\mathcal{A}_{\rm res}} = \sum_{\mathcal{A}} \left[\hat{h}^{(\mathcal{A})}_e(\boldsymbol{\theta}^{(\mathcal{A})}_{\rm tr}) - \hat{h}^{(\mathcal{A})}_m(\boldsymbol{\theta}^{\mathcal{A}|\mathcal{B}}_{\rm bf})\right] + \sum_{\mathcal{B}} \left[\hat{h}^{(\mathcal{B})}_e(\boldsymbol{\theta}^{(\mathcal{B})}_{\rm tr}) - \hat{h}^{(\mathcal{B})}_m(\boldsymbol{\theta}^{(\mathcal{B})}_{\rm tr})\right] + \hat{n}(f). \tag{7.51}$$

In Eq.(7.50), the first term is the bias due to missed signals $\mathcal{B}$, the second term the residuals due to incorrect subtraction of the true signals and finally the noise. The noise related bias should be consistent with the width of the posterior. Also, the errors due to inaccurate waveforms should decrease as more accurate waveforms are developed. Thus, we believe it is reasonable to assume that the dominant contribution to the bias comes from the first term in Eq.(7.50). A similar story can be told for Eq.(7.51) where we expect the first term will dominate and the latter two will be subdominant corrections. Finally, we do not have access to the true parameters $\boldsymbol{\theta}^{\mathcal{A}}_{\rm tr}$ and $\boldsymbol{\theta}^{\mathcal{B}}_{\rm tr}$, nor the exact models for $h^{(\mathcal{A})}_e$ or $h^{(\mathcal{B})}_e$. We make a further approximation for the $\mathcal{B}$ true parameters $\boldsymbol{\theta}^{\mathcal{B}}_{\rm tr} \approx \boldsymbol{\theta}^{\mathcal{B}|\mathcal{A}_{\rm res}}_{\rm bf}$ and assume that $h_e \approx h_m$. We have access to these parameters from our first parameter estimation run on signal set $\mathcal{B}$ using the data stream $d(\mathcal{B}|\mathcal{A}_{\rm res})$. From this

information, we can approximate both Eqs.(7.50) and Eq.(7.51) by

$$\delta h^{\mathcal{A}|\mathcal{B}} \approx \sum_{\mathcal{B}} \hat{h}_m^{(\mathcal{B})}(\boldsymbol{\theta}_{\rm bf}^{\mathcal{B}|\mathcal{A}_{\rm res}}) \tag{7.52}$$

$$\delta h^{\mathcal{B}|\mathcal{A}_{\rm res}} \approx \sum_{\mathcal{A}} \left[\hat{h}_m^{(\mathcal{A})}(\boldsymbol{\theta}_{\rm tr}^{(\mathcal{A})}) - \hat{h}_m^{(\mathcal{A})}(\boldsymbol{\theta}_{\rm bf}^{\mathcal{A}|\mathcal{B}})\right]. \tag{7.53}$$

A similar complication arises from our lack of access to $\boldsymbol{\theta}_{\rm tr}^{\mathcal{A}}$ in Eq.(7.53). However, the true parameter $\boldsymbol{\theta}_{\rm tr}^{\mathcal{A}}$ can be estimated by calculating the CV bias using $\delta h^{\mathcal{A}|\mathcal{B}}$ from Eq.(7.52) with the FM and numerical derivatives calculated at parameter values $\boldsymbol{\theta}_{\rm bf}^{\mathcal{A}|\mathcal{B}}$. This will produce an estimate of the bias, $\Delta\boldsymbol{\theta}^{\mathcal{A}|\mathcal{B}}$, which can be subtracted from $\boldsymbol{\theta}_{\rm bf}^{\mathcal{A}|\mathcal{B}}$, to give an updated estimate of $\boldsymbol{\theta}^{\mathcal{A}}$ that should lie closer to the true parameters, $\boldsymbol{\theta}_{\rm tr}^{\mathcal{A}}$. This new parameter $\widehat{\boldsymbol{\theta}_{\rm bf}^{\mathcal{A}|\mathcal{B}}} = \boldsymbol{\theta}_{\rm bf}^{\mathcal{A}|\mathcal{B}} - \Delta\boldsymbol{\theta}^{\mathcal{A}|\mathcal{B}}$ can be used to approximate $\boldsymbol{\theta}_{\rm tr}^{\mathcal{A}}$ in Eq.(7.53). Finally, using parameter values $\boldsymbol{\theta}_{\rm res}^{\mathcal{B}|\mathcal{A}}$ to evaluate waveform derivatives and FMs, one can compute a new estimate of the bias in the $\mathcal{B}$ set signal parameters, $\Delta\boldsymbol{\theta}^{\mathcal{B}|\mathcal{A}_{\rm res}}$ by using Eq.(7.53) with $\widehat{\boldsymbol{\theta}_{\rm bf}^{\mathcal{A}|\mathcal{B}}} \approx \boldsymbol{\theta}_{\rm tr}^{A}$. This new bias can be used to update our best guess for the true parameters if the set of $\mathcal{B}$ signals, namely $\widehat{\boldsymbol{\theta}_{\rm bf}^{\mathcal{B}|\mathcal{A}_{\rm res}}} = \boldsymbol{\theta}_{\rm bf}^{\mathcal{B}|\mathcal{A}_{\rm res}} - \Delta\boldsymbol{\theta}^{\mathcal{B}|\mathcal{A}_{\rm res}}$. By construction, the parameter values $\widehat{\boldsymbol{\theta}_{\rm bf}^{\mathcal{A}|\mathcal{B}}}$ and $\widehat{\boldsymbol{\theta}_{\rm bf}^{\mathcal{B}|\mathcal{A}_{\rm res}}}$ should lie closer to the true values $\boldsymbol{\theta}_{\rm tr}^{\mathcal{A}}$ and $\boldsymbol{\theta}_{\rm tr}^{\mathcal{B}}$ respectively.

To summarise, the algorithm is as follows:

1. Calculate $\boldsymbol{\theta}_{\rm bf}^{\mathcal{A}|\mathcal{B}}$ and $\boldsymbol{\theta}_{\rm bf}^{\mathcal{B}|\mathcal{A}_{\rm res}}$ by performing parameter estimation on signals $\mathcal{A}$ and $\mathcal{B}$ using data streams $d(\mathcal{A}|\mathcal{B})$ then $d(\mathcal{B}|\mathcal{A}_{\rm res})$.

2. Calculate

$$\delta h_{\rm conf}^{\mathcal{A}|\mathcal{B}} \approx \sum_{\mathcal{B}} \hat{h}_m(\boldsymbol{\theta}_{\rm bf}^{\mathcal{B}|\mathcal{A}_{\rm res}}) \tag{7.54}$$

   and then compute an estimate of the bias on the parameters specific to $\mathcal{A}$, denoted $\Delta\boldsymbol{\theta}_{\rm bf}^{\mathcal{A}|\mathcal{B}}$, evaluating the waveform derivatives at the parameter values $\boldsymbol{\theta}_{\rm bf}^{\mathcal{A}|\mathcal{B}}$. Set new best fit parameters for $\mathcal{A}$ as $\widehat{\boldsymbol{\theta}_{\rm bf}^{\mathcal{A}|\mathcal{B}}} = \boldsymbol{\theta}_{\rm bf}^{\mathcal{A}|\mathcal{B}} - \Delta\boldsymbol{\theta}_{\rm bf}^{\mathcal{A}|\mathcal{B}}$.

3. Then calculate

$$\delta h_{\rm conf}^{\mathcal{B}|\mathcal{A}_{\rm res}} = \hat{h}_m(\widehat{\boldsymbol{\theta}_{\rm bf}^{\mathcal{A}|\mathcal{B}_{\rm res}}}) - \hat{h}_m(\boldsymbol{\theta}_{\rm bf}^{\mathcal{A}|\mathcal{B}_{\rm res}}) \tag{7.55}$$

   and calculate the CV bias $\Delta\boldsymbol{\theta}_{\rm bf}^{\mathcal{B}|\mathcal{A}_{\rm res}}$ on parameters specific to $\mathcal{B}$ using parameter values $\boldsymbol{\theta}_{\rm bf}^{\mathcal{B}|\mathcal{A}_{\rm res}}$. Now set new parameters $\widehat{\boldsymbol{\theta}_{\rm bf}^{\mathcal{B}|\mathcal{A}_{\rm res}}} = \boldsymbol{\theta}_{\rm bf}^{\mathcal{B}|\mathcal{A}_{\rm res}} - \Delta\boldsymbol{\theta}_{\rm bf}^{\mathcal{B}|\mathcal{A}_{\rm res}}$.

We illustrate the algorithm above by considering a noisy data stream containing two signals, each of which have waveform errors $\epsilon \neq 0$. We lose no generality here since the algorithm

Table 7.4: This table presents the true parameter values for source 1 ($\mathcal{A}$) and source 2 ($\mathcal{B}$) for the example of the local-fit procedure presented in section 7.4.3. The SNR of each signal within the data stream $\rho_h^2 = (h_e|h_e)$ is given in the final column.

i	$M/M_\odot$	η	β	$D_{\rm eff}$/Gpc	ρ_h
1 ($\mathcal{A}$)	1.2×10^7	0.222	8	2	~ 1850
2 ($\mathcal{B}$)	5×10^6	0.160	7	4	~ 379

presented above is easily generalised to handle a greater number of signals. Thus we consider

$$\hat{d}(f) = \underbrace{\hat{h}_e^{(1)}(f;\boldsymbol{\theta}^{(1)},\epsilon=10^{-3})}_{\mathcal{A}} + \underbrace{\hat{h}_e^{(2)}(f;\boldsymbol{\theta}^{(2)},\epsilon=10^{-3})}_{\mathcal{B}} + \hat{n}(f). \tag{7.56}$$

With parameters for the $\mathcal{A}$ and $\mathcal{B}$ sources given in table 7.4. The results of applying the local-fit procedure are presented in the next section.

7.4.3 Results

Following the algorithm above, we present results for the marginalised posteriors in Fig. 7.10. In the top row, the blue histogram is the posterior $p(\mathcal{A}|d(\mathcal{A}|\mathcal{B}),\mathcal{B})$ obtained fitting for source $\mathcal{A}$ with source $\mathcal{B}$ in the data, the orange histogram is the posterior for the global-fit solution $p(\mathcal{A},\mathcal{B}|d(\mathcal{A},\mathcal{B}))$, the red lines mark the true parameters and the black line the predicted bias using the formalism. The bottom row of figure 7.10 show corresponding results for the inference of source $\mathcal{B}$, with, for example, the orange histograms representing posterior samples from $p(\mathcal{B}|d(\mathcal{B}|\mathcal{A}_{\rm res}),\mathcal{A}_{\rm res})$. In each case, the algorithm is able to correct the bias from the poorly subtracted other signal in the data. In all cases, after subtracting the predicted bias, the true parameters lie within the 1σ width of the posteriors.

In fig.(7.10), the local fit posterior for source $\mathcal{B}$ appears to provide a more conservative estimate on how well we can constrain each parameter in comparison to the global fit analysis. Shifting the posterior by the amount predicted by the preceding algorithm will therefore yield a posterior that is broader, and hence more conservative than that which would be obtained from a full analysis. We are yet to develop a strategy to correct parameter uncertainties from the prior local fit analysis. This implies that one must retain precision measurement statements on parameters from the first two parameter estimation runs on $d(\mathcal{A}|\mathcal{B})$ and $d(\mathcal{B}|\mathcal{A}_{\rm res})$. Correcting the widths of the local fit posteriors are beyond the scope of this paper and we leave this for future work.

To conclude this section, we make a few important remarks about the algorithm given above. First of all, the algorithm is likely to be less effective if the recovered best fit parameters are far from the true value. This would cause a breakdown of the linear-signal approximation,

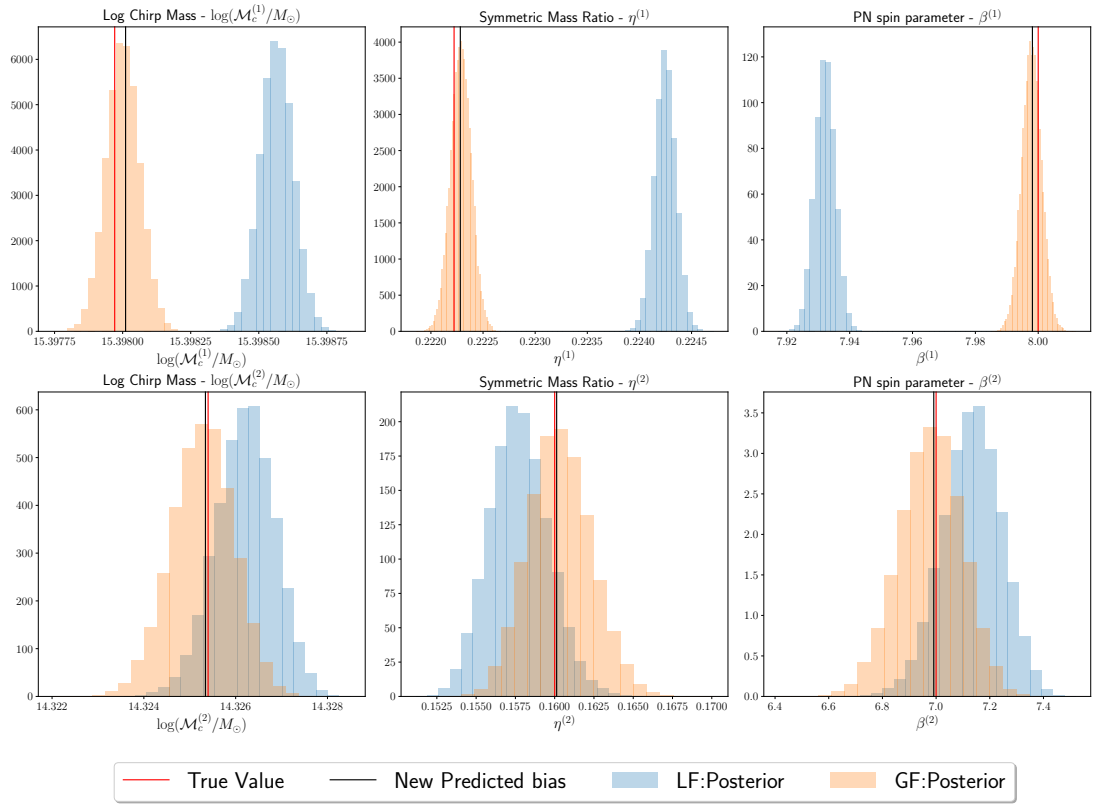

Figure 7.10: The orange histograms are the global-fit (GF) posteriors from searching the joint data stream $d(\mathcal{A}, \mathcal{B})$ for both $\mathcal{A}$ and $\mathcal{B}$ simultaneously. The red lines are true values and black lines the (corrected) new predicted bias using the generalised CV formalism in section 7.1. The blue histograms in the top row are posterior samples from the local-fit (LF) $p(\mathcal{A}|d(\mathcal{A}|\mathcal{B}), \mathcal{B})$ for missed signals $\mathcal{B}$. Similarly, the blue histograms in the bottom row are samples from $p(\mathcal{B}|d(\mathcal{B}|\mathcal{A}_{\rm res}), \mathcal{A}_{\rm res})$ for signal $\mathcal{B}$.

which is a key assumption in the generalised CV algorithm presented in 7.1. We also assume that, through many local-fits, we have found all the signals present in the data stream we are studying. Further, the two signals present here are near orthogonal with relatively little correlation between the two signals. If there were significant overlap, then the posteriors for the global-fit procedure would be wider since extra uncertainty would be introduced into the parameters in question. This would mean that the procedure presented here, in which we shift a posterior computed with a single source model into the correct location, but do not modify the posterior width, would yield overly optimistic estimates of the source parameters. There are two approaches to address this shortcoming. Firstly, the correlation between sources identified in the data can be evaluated, and any pairs of source with sufficiently high correlation can be reanalysed jointly. Alternatively, it is possible to generate an updated posterior for the parameters of each source by marginalising over the biases due to the other source. The procedure is similar to the algorithm described here, but rather than shift each sample in the $\mathcal{A}$ source posterior by the same amount, given by the best-fit parameters of source $\mathcal{B}$, we instead shift them by an amount given by Eq. (7.21) evaluated for the $\mathbf{h}^{(2)}$ waveform computed as a random sample drawn from the $\mathcal{B}$ source distribution. This approach is beyond the scope of the analysis presented here, but we leave it for future work.

7.5 Conclusions

In this paper, we have generalized the approach in [308] to provide metrics for the parameter estimation biases on individually resolved sources from the presence of confusion noise from missed signals or incorrectly fitted waveforms. We have illustrated these generalisations with simple (yet realistic) scenarios relevant to the LISA and ET detectors, and we can collect several generic findings. We found that the presence of altogether missed signals drawn from the same population could lead to significant biases on the parameter estimation of other signals which are instead fitted out of the data. We then confirmed one of the main results of [303, 304, 316, 317]. The coincident arrival of two signals in a ground-based detector, with nearly overlapping mergers, may lead to biases when the difference between coalescence times of the signals is less than a fraction of a second. We argued that residuals in the data arising from the incorrect removal of sources effectively behave like missed signals, and may lead to significant biases. Our results suggest that galactic binaries which are missed by dedicated searches [89], and not accounted for in confusion noise estimates, may lead to significant biases on the parameter estimation of other typical LISA sources. Finally, we proposed a proof-of-concept global-fit

scheme in which, starting from local-fits of LISA sources, guesses for the true parameters are obtained through bias predictions from previous parameter estimation simulations. We found the corrected recovered parameters lie within the 1σ interval of global-fit posteriors across all sources. This has potential applications to confirm global-fit search algorithms, and as a standalone novel local-fit parameter estimation algorithm.

In all the cases outlined above, the formalism we have developed plays an important role in providing a theoretical ground for the described biases and a solid tool to address them. We believe this formalism could be useful in exploratory studies of future GW detectors, to assess under what circumstances we expect the biases described above to appear. We also believe this formalism is an early but significant step towards an understanding of how to simultaneously infer parameters from multiple signals of different nature with future detectors, as we highlight with our global-fit algorithm scheme.

There are several ways in which the application of this formalism could be extended. One could perform systematics studies for realistic populations of missed signals using realistically modelled waveforms. One could check whether inaccurately modelled signals could lead to significant biases when several of them are incorrectly subtracted from the data, which our understanding of residuals as missed signals and the biases they lead to strongly suggests. This is a possibility that we have not explored due to the technical challenge in dealing with very large FMs and MCMC sampling algorithms to sample over such a large parameter space. Given more complex waveform models and response functions for either detectors, one could use this algorithm to understand the impact on parameter estimation studies of non-stationarities in the data stream. Finally, one could explore further the applications of this formalism for global-fit algorithms, which could be extended to take into account significant overlaps between the signals in the data stream, and to explore correcting the width as well as the peak location of the parameter posteriors.

As a final note, the formalism itself can be extended to take into account brighter confusion sources and more pronounced waveform errors (as would happen with different families of waveform models or models within the same family containing different physics). To do so, one could derive higher order terms in the equations present in Sec.7.1 to describe biases that are farther from the true parameters than those considered in this work.

Modelling noise in GW astronomy is complicated. We gave two interpretations of the noise arising from confusion between un-modelled sources. The first that it is simply an extra term in (7.10), unmodelled and a source of parameter biases. Second that it is *included* in the overall noise model and introduced as an extra contribution to the PSD (see (3.36) and (C.7)). In

this second model, we assumed that the confusion noise was *stationary* and modelled by a PSD $S_c(f)$ measuring the power of the background across the frequency spectrum. This will not always be the case. The assumption that the background confusion, or even the instrumental noise is globally stationary is *very* strong. The definition of a stationary time series is that probabilistic statements do not vary over time. For example, the mean or variance does not cause a trend. Given the fact that LISA will be subjected to noise transients (glitches) or gaps in the data stream, the noise properties *will* change. This change introduce *non-stationary* noise which must be handled very carefully. In the next chapter, the focus will be on the impact of non-stationary noise sources in parameter estimation studies.

Chapter 8

Impact of mis-modelling non-stationary noise on parameter estimation

8.1 Introduction

In the previous chapters, we assumed that the instrumental noise was a zero-mean Gaussian stationary random process. In subsection 3.2.2, we described stationary noise processes and the construction of the Whittle-likelihood (3.31). Unfortunately, given the complexity of the LISA mission, it would be crude to assume that the detector noise properties will be stationary over the full mission lifetime.

As discussed in section 1.3.3.2, potential noise transients from hardware malfunctions or even the presence of data gaps can hamper the statistical properties of the noise. Recall that a stationary time series has constant mean and variance in the time domain. Having a series of glitches or data gaps will change the noise properties over particular time segments, thus inducing non-stationarities. The technical term for this *assumed-to-be* periodic type of non-stationary noise is *cyclostationary*. In the grand scheme of things, glitches and data gaps (such as excess charging of the test masses or scheduled gaps due to repointing) are out of our control, so either non-stationarities must be taken into account *or* techniques to enforce stationarity must be used.

Non-stationarities present in the time series are manifest in the covariance matrix describing the noise process [321]. In the case of stationary noise, the noise-covariance matrix in the

frequency domain is diagonal – offering rapid calculation of the likelihood (as in Eq.(3.20)). However, for non-stationary noise, correlations between noise components appear at different frequencies and the noise-covariance matrix is *non-diagonal*. For this reason, the Whittle-likelihood is no longer a suitable approximation to the likelihood in the time domain. As we will see later, the consequence of mismodelling the likelihood by using the Whittle-likelihood when the signal is buried in non-stationary noise, is to increase the chance of recovering parameters that are far from the true parameters in parameter space. For this reason, these non-stationarities must be taken into account. Below we summarise previous work on this topic.

One of the first studies of the impact on gaps on parameter estimation and precision studies was performed by Carré and Porter in [322]. Using ultra-compact GB, they simulated the effect of a gap by smoothly windowing the data set to zero before and after the gap segment. Their results showed that gaps in the data stream can lead to biases in the parameter estimates, which we now know is a consequence of introducing correlations between different frequencies. They used the Whittle-likelihood, which is an *incorrect* likelihood for such a situation. The analysis we describe below improves and generalises their windowing approach. Another technique that has gained popularity is *data augmentation* [323, 130]. This technique uses Bayesian techniques to *fill in* the data in the gaps, usually learning the behaviour of the noise through training data sets. The parameters of the signal are then recovered assuming a complete data set was observed. In the author's opinion, this algorithm, although impressive, is unnecessarily computationally expensive, since the imputed data can not provide any extra information on the source parameters. In this chapter, we provide an alternative methods to not just handle data gaps, but inference involving specific forms of non-stationary noise.

In the construction of LISA, instrumentalists will try to build an instrument such that its noise properties remain as close to stationary as possible. However, there will inevitably be some drift in the PSD (in the time domain), which is a type of non-stationary feature. Environmental noise caused by solar winds will change, the effect of antennae re-pointing could change the noise properties between gap segments and there will be short transient noise bursts in the form of glitches in the instrument. These will all break the stationary behavior of the noise. We believe that it may be mildly non-stationary over long time-scales, so treating the noise as stationary could, perhaps, be a good approximation, but not be affirmed until LISA is launched.

For simplicity, we assume that the underlying noise process is stationary but modified by a *known* time dependent function. In section 8.2, we derive the full form of the likelihood,

taking into account correlations between frequencies present in the noise-covariance matrix as a result of non-stationary noise. We discuss how to draw non-stationary noise in the frequency domain in section 8.2.3. We generalise the notion of SNR and the FM in sections (8.3.1) and (8.3.2). We then argue that mis-modelling the data stream will change the variance of the estimated parameters, so they are inconsistent with the recovered posterior. This variance is given by equation (8.28). Finally, in section 8.4, we test the ideas above by performing a simple parameter estimation study on a waveform buried in non-stationary noise. The conclusions and scope for future work are presented in section 8.5.

8.2 Non-stationary noise

Gravitational wave data analysis usually assumes that the underlying noise $n(t)$ is a stationary random process. In subsection 3.2.2, we gave a review on how to model stationary noise. In particular, we showed how the noise could be characterised using a PSD using equations (3.21) and (3.20). We then gave an alternate derivation of the Whittle-likelihood using complex normal distributions (3.18). In this section, we will perform the same procedure assuming the noise process can be modelled by $N(t) = w(t)n(t)$. Here $w(t)$ is some *known* time dependent function and $n(t)$ is the underlying stationary Gaussian noise with zero mean. Such a model could represent data gaps in the data stream. It could also be used to represent a transient noise burst by taking $w(t)$ to be an exponential function representing a sudden rise and fall of the amplitude of the noise process. The function $w(t)$, in essence, alters the covariance of the random process in both time *and* frequency, thus introduces non-stationary features.

In this chapter we treat $w(t)$ as a window function in order to to mimic gaps in the data stream. The observed data stream $D(t) = w(t)d(t)$ is given by

$$D(t) = w(t)h(t;\boldsymbol{\theta}) + w(t)n(t) \tag{8.1}$$

$$= H(t;\boldsymbol{\theta}) + N(t)\,. \tag{8.2}$$

We will refer to $N(t)$ and $H(t)$ as the *gated* noise and signal in the time domain. When the noise is stationary, the frequencies amongst noise components are uncorrelated. This provides a simple diagonal covariance structure that, in turn, facilitates rapid calculation of the likelihood (3.31). When windows are introduced, the tampered noise in the frequency domain exhibits correlations that violate the validity of the Whittle-likelihood. In the next section, we derive the full form of the noise-covariance matrix.

8.2.1 The noise covariance matrix

Observe that

$$
\begin{aligned}
.\langle \hat{N}^\star(f)\hat{N}(f')\rangle &= \left\langle \int_{-\infty}^{\infty}\int_{-\infty}^{\infty} \hat{w}^\star(f-u)\hat{n}^\star(u)\hat{w}(f'-v)\hat{n}(v)\mathrm{d}u\mathrm{d}v \right\rangle \\
&= \int_{-\infty}^{\infty}\int_{-\infty}^{\infty} \hat{w}^\star(f-u)\hat{w}(f'-v)\langle\hat{n}^\star(u)\hat{n}(v)\rangle\mathrm{d}u\mathrm{d}v \\
&= \frac{1}{2}\int_{0}^{\infty} [\hat{w}^\star(f-u)\hat{w}(f'-u) + \hat{w}^\star(f+u)\hat{w}(f'+u)]S_n(u)\mathrm{d}u \\
&= \frac{1}{2}\int_{-\infty}^{\infty} \hat{w}^\star(f-u)\hat{w}(f'-u)S_n(u)\mathrm{d}u\,. \qquad (8.3)
\end{aligned}
$$

Where we have used Eq.(3.20) and the convolution theorem

$$
\begin{aligned}
\hat{N}(f) = \mathcal{F}(w(t)n(t)) &= \int_{-\infty}^{\infty} \hat{w}(f-f')\hat{n}(f')\mathrm{d}f' \\
&= \int_{0}^{\infty} [\hat{w}(f-f')\hat{n}(f') + \hat{w}(f+f')\hat{n}^\star(f')]\mathrm{d}f'.
\end{aligned}
$$

If $w(t)$ is not constant, individual frequency components are now correlated and the assumptions leading to the Whittle-likelihood are violated and so the latter cannot be used.

The discrete analogue of (8.3) is

$$
\langle \tilde{N}^\star(f_i)\tilde{N}(f_j)\rangle = \frac{1}{2N\Delta t}\sum_{p=-\lfloor N/2+1\rfloor}^{\lfloor N/2+1\rfloor} \tilde{w}^\star(f_i-v_p)\tilde{w}(f_j-v_p)S_n(v_p). \qquad (8.4)
$$

The expression (8.4) agrees with (3.24) if and only if $w(t) = 1$. Consider the case of a constant function $w(t) \approx w[t_n] = 1$ for all time bins. It can be shown that

$$
\tilde{w}(f_i - v_p) = \frac{1}{\Delta t}\hat{w}(f_i - v_p) = \frac{1}{\Delta t}\delta(f_i - v_p) \approx \frac{1}{\Delta t \Delta f}\delta_{ip}, \qquad (8.5)
$$

where in the last approximation we used (3.23). Assuming that $w(t_i) = 1$ for all time bins, $\tilde{w}(f_i + v_p) = \delta(f_i + v_p) = 0$ for $f_i, v_p > 0$. Inserting these results into (8.4) one obtains (3.24).

8.2.2 Modifying the likelihood function

To derive the modified likelihood, we note that since $n(t)$ is Gaussian, $\hat{n}(f)$ is also Gaussian implying that $\hat{N}(f)$ is a complex zero-mean normal distribution, which takes a form similar to (3.18). Such a distribution is completely characterised by its covariance and relation matrices. It is easily shown that the relation matrix $R_N(f,f') = \langle\hat{N}(f)\hat{N}(f')\rangle = 0$ since $\langle\hat{n}(f)\hat{n}(f')\rangle = 0$, from Eq.(3.22) for $f, f' > 0$. The noise covariance matrix takes the form $\Sigma_N(f,f') =$

$\langle \hat{N}(f)\hat{N}^{\star}(f')\rangle$ with (discrete) components given by (8.4). Substituting into (3.18), we find that the log-likelihood takes the form up to a constant of proportionality

$$\log p(\boldsymbol{D}|\boldsymbol{\theta}) \propto -(\hat{\boldsymbol{D}} - \hat{\boldsymbol{H}})^{\dagger}\Sigma_N^{-1}(\hat{\boldsymbol{D}} - \hat{\boldsymbol{H}})\,. \tag{8.6}$$

Notice now that the likelihood has lost its simplistic form due to the non-diagonal structure of Σ_N due to (8.4). In this prescription, $\hat{\Sigma}_N = \mathbb{E}[\hat{\boldsymbol{N}}\hat{\boldsymbol{N}}^{\dagger}]$ is a hermitian matrix satisfying $\hat{\Sigma}_N^{\dagger} = \hat{\Sigma}_N$.

There are a few practical issues we must address when calculating the likelihood (8.6). Due to the presence of gaps, the matrix Σ_N is degenerate with multiple zero eigenvalues. To understand this, let $\mathcal{M} = \{t_1, t_1, \ldots, t_M\}$ denote the set of M time bins such that the gated noise $N(t_i) = 0$. Using the discrete form of the IFT (3.3)

$$N(t_i) = \sum_k \hat{N}(f_k)\exp(2\pi i f_k t_i) = \hat{\boldsymbol{N}}^T\boldsymbol{a}_i. \tag{8.7}$$

where $\boldsymbol{N} = \{\hat{N}(f_k)\}_{k=0}^{\lfloor N/2+1\rfloor}$ and $\boldsymbol{a}_i = \{\exp(2\pi i f_k t_i)\}_{k=0}^{\lfloor N/2+1\rfloor}$ at a time bin t_i. We can compute the covariance $\forall t_i, t_j \in \mathcal{M}$,

$$\begin{aligned}\langle N(t_i)N(t_j)^{\star}\rangle &= \langle \hat{\boldsymbol{N}}^T\boldsymbol{a}_i(\hat{\boldsymbol{N}}^T\boldsymbol{a}_j)^{\star}\rangle = \boldsymbol{a}_i^T\langle\hat{\boldsymbol{N}}\hat{\boldsymbol{N}}^{\dagger}\rangle\boldsymbol{a}_j^{\star} \\ &= \boldsymbol{a}_i^T\Sigma_N\boldsymbol{a}_j^{\star}\,.\end{aligned} \tag{8.8}$$

Notice that $\forall t_i, t_j \in \mathcal{M}$, we have that $N(t_i) = N(t_j) = 0$ and so the covariance between different time components must be zero within the gated segment. We deduce that $\Sigma_N\boldsymbol{a}_j^{\star} = 0 \iff \boldsymbol{a}_j^{\star} \in \text{Null}(\Sigma_N)$ for all $t_j \in \mathcal{M}$. Since no component of $\boldsymbol{a}_j^{\star}$ is zero, we deduce from $\Sigma_N\boldsymbol{a}_j^{\star} = \lambda\boldsymbol{a}_j^{\star} = 0$ that there must be an M dimensional subspace where the eigenvalues $\lambda = 0$.

In practice then, we compute the singular value decomposition (SVD) of the matrix $\Sigma_N = U\Lambda V^{\dagger}$ and *remove* each zero eigenvalue from Λ with corresponding rows and columns of U and V. We can then construct a non-singular noise-covariance matrix $\mathring{\Sigma}_N$, an approximation to Σ_N, where $\mathring{\Sigma}_N$ is the *truncated* SVD of the matrix Σ_N. To evaluate expressions like (8.6), we solve the system of equations $\mathring{\Sigma}_N\boldsymbol{x} = (\hat{\boldsymbol{D}} - \hat{\boldsymbol{H}})$ and then compute the inner product $(\hat{\boldsymbol{D}} - \hat{\boldsymbol{H}})^{\dagger}\boldsymbol{x}$. We remark that we remove elements of $(\hat{\boldsymbol{D}} - \hat{\boldsymbol{H}})$ corresponding to the zero eigenvalues of Σ_N.

From hereon and without loss of generality, we will continue to use the matrix Σ_N in theoretical sections 8.2.3, 8.3.1, 8.3.2. In the practical implementation, we will use the *truncated* SVD decomposition of Σ_N, denoted $\mathring{\Sigma}_N$.

In section 3.2.2, we showed how to simulate stationary noise given a known PSD $S_n(f)$. From equations (3.32) and (3.33), we derived expressions for the variances of the real and

imaginary parts of the noise $\hat{n}(f)$ and their joint covariance. Since the joint covariance was zero, stationary noise can be simulated by drawing the real and imaginary parts *separately* from a Gaussian distribution with equal variance given by (3.32). In the case of non-stationary noise, this is no longer the case, and instead we must account for the joint covariance between real and imaginary parts.

8.2.3 Simulating non-stationary noise

We now discuss how to generate noise realisations for gated data $N(t) = w(t)n(t)$ using (8.3). Consider $\hat{N}(f) = \hat{N}_1(f) + i\hat{N}_2(f)$ and consider the real and imaginary parts

$$\begin{aligned}\mathrm{Re}(\langle \hat{N}^\star(f)\hat{N}(f')\rangle) &= \langle \hat{N}_1(f)\hat{N}_1(f')\rangle + \langle \hat{N}_2(f))\hat{N}_2(f')\rangle \\ \mathrm{Im}(\langle \hat{N}^\star(f)\hat{N}(f')\rangle) &= \langle \hat{N}_2(f)\hat{N}_1(f')\rangle - \langle \hat{N}_1(f))\hat{N}_2(f')\rangle\end{aligned}$$

Given the result from (3.22), the ensemble average $\langle \hat{N}(f)\hat{N}(f')\rangle = 0$ gives

$$\langle \hat{N}_1(f)\hat{N}_1(f')\rangle = \langle \hat{N}_2(f))\hat{N}_2(f')\rangle, \quad \langle \hat{N}_1(f)\hat{N}_2(f')\rangle = -\langle \hat{N}_2(f)\hat{N}_1(f')\rangle. \tag{8.9}$$

Giving the result

$$\begin{aligned}\langle \hat{N}_1(f)\hat{N}_1(f')\rangle &= \langle \hat{N}_2(f))\hat{N}_2(f')\rangle = \Sigma_{\parallel}(f, f') \\ \langle \hat{N}_1(f)\hat{N}_2(f')\rangle &= -\langle \hat{N}_2(f)\hat{N}_1(f')\rangle = \Sigma_{\perp}(f, f')\end{aligned}$$

with $\Sigma_{\parallel}(f, f') = \frac{1}{2}\mathrm{Re}(\Sigma)$ and $\Sigma_{\perp}(f, f') = -\frac{1}{2}\mathrm{Im}(\Sigma)$. Explicitly,

$$\hat{\Sigma}_{\parallel}(f, f') = \frac{1}{4}\int_{-\infty}^{\infty} [\hat{w}_1(f - v)\hat{w}_1(f' - v) + \hat{w}_2(f - v)\hat{w}_2(f' - v)]S_n(v)\mathrm{d}v \tag{8.10}$$

$$\hat{\Sigma}_{\perp}(f, f') = \frac{1}{4}\int_{-\infty}^{\infty} [\hat{w}_1(f' - v)\hat{w}_2(f - v) - \hat{w}_2(f' - v)\hat{w}_1(f - v)]S_n(v)\mathrm{d}v. \tag{8.11}$$

where we have made the split $\hat{w}(f) = \hat{w}_1(f) + i\hat{w}_2(f)$. The first equation gives the covariance for both the real and imaginary parts of $\hat{N}(f)$. The second equation gives the covariance *between* the real and imaginary parts of the complex fourier noise $\hat{N}(f)$. By writing the vector of frequency domain gated noise components $\hat{\boldsymbol{N}} = \boldsymbol{N}_1 + i\boldsymbol{N}_2$ where each vector is of length K_f, we can write down the *joint* normal distribution in a block matrix form [223]

$$\begin{pmatrix} \boldsymbol{N}_1 \\ \boldsymbol{N}_2 \end{pmatrix} \sim N\left[\begin{pmatrix} \boldsymbol{0} \\ \boldsymbol{0} \end{pmatrix}, \begin{pmatrix} \Sigma_{\parallel} & \Sigma_{\perp} \\ -\Sigma_{\perp} & \Sigma_{\parallel} \end{pmatrix}\right]. \tag{8.12}$$

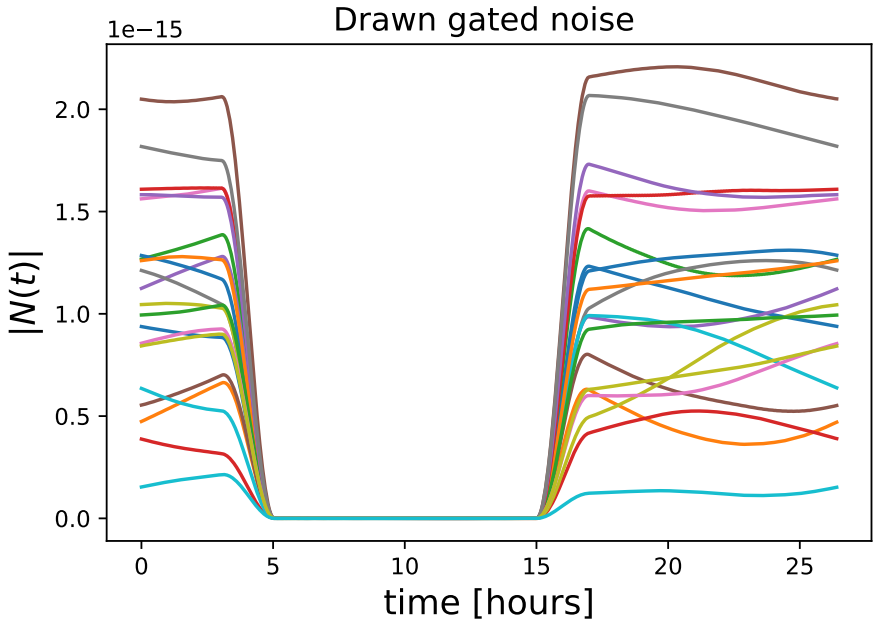

Figure 8.1: Here we draw 20 random samples from the multivariate distribution using equation (8.12). Notice that the gap is placed between the fifth and fifteenth hour as expected.

since $\mathbb{E}[\boldsymbol{N}_1] = \mathbb{E}[\boldsymbol{N}_2] = 0$. Here the covariance matrix between real and imaginary parts have dimension $2K_f$. To draw non-stationary realisations, we draw a sample from the *joint* normal distribution (8.12), which contains information about how $\hat{N}_1(f)$ and $\hat{N}_2(f)$ depend on each other.

Consider a stationary zero-mean Gaussian time series $n(t)$, generated from (3.34), that lasts for 20 hours. We construct $N(t) = w(t)n(t)$ from this noise series with $w(t)$ given by a Tukey window (3.6) where a gap is placed between the fifth and fifteenth hour. To minimise leakage effects, we choose the lobe parameter $\alpha = 0.5$. By calculating equation (8.4), we can build the matrices (8.10) and (8.11). Through constructing (8.12), we can now draw real and associated imaginary components of the gated noise, which we denote $\boldsymbol{V} = [\boldsymbol{N}_1^T, \boldsymbol{N}_2^T]$. We then make the split

$$\boldsymbol{N} = \{V_k\}_{k=1}^{K_f} + i\{V_k\}_{k=K_f+1}^{2K_f}\,, \tag{8.13}$$

and use the inverse CTFT (3.3) to compute $N(t)$. We plot the time domain variates of $N(t)$ in figure 8.1. We see that the gap appears between the fifth and fifteenth hour as expected. This gives us confidence that the calculation of (8.4) is correct and that the derived covariance matrix is properly representing the gated noise.

These drawn samples can be used to generate non-stationary noise realisations directly in the frequency domain. In the next section, we discuss how the usual expressions for the SNR and FM must be modified in order to properly account for non-stationary noise of the form

$N(t) = w(t)n(t)$.

8.3 Non-stationary analogues of stationary quantities

Gating stationary noise realisations using a time dependent function introduces correlations amongst frequencies in the frequency domain. Similar to the likelihood, expressions for the optimal matched filtering SNR and the FM will change. We will begin by deriving the general expression for the SNR given any noise covariance matrix $\Sigma_N(f, f') = \langle \hat{N}(f)\hat{N}^\star(f')\rangle$.

For practical reasons, we will work in the discrete domain rather than the continuous domain. In appendix D, we generalise the following results to the continuous domain.

8.3.1 Signal-to-noise ratio

As we did in section 3.2.3, we consider the cross correlation between some filter function $K(t)$ and the *gated* signal $H(t)$. We will compare this cross correlation with the root-mean-square amplitude of the correlated gated noise and $K(t)$. Discretising equation (D.2) we obtain

$$\left(\frac{S}{N}\right)(t) = \frac{|\boldsymbol{K}^\dagger \boldsymbol{H}|}{\sqrt{\boldsymbol{K}^\dagger \Sigma_N \boldsymbol{K}}}. \tag{8.14}$$

Where $\Sigma_N = \mathbb{E}[\boldsymbol{N}\boldsymbol{N}^\dagger]$ is the hermitian symmetric noise covariance matrix with components (8.4). Equation (8.14) is valid over both positive and negative frequencies. Restricting only to the positive frequencies results in an extra factor of two in both the numerator and denominator. Since our time-series are real, we will only consider the positive frequencies for the rest of this discussion. Hence, each of the vectors above are of the form $\boldsymbol{X} = \{X(f_i)\}_{i=0}^{\lfloor N/2+1 \rfloor}$ for N the number of time bins. By using a form of the Cauchy-Schwarz inequality $|\boldsymbol{a}^\dagger \boldsymbol{b}| \leq \sqrt{(\boldsymbol{a}^\dagger \boldsymbol{a})(\boldsymbol{b}^\dagger \boldsymbol{b})}$ we can rewrite the numerator as

$$|\boldsymbol{K}^\dagger \boldsymbol{H}| = |(\Sigma_N^{1/2}\boldsymbol{K})^\dagger (\Sigma_N^{-1/2}\boldsymbol{H})| \leq \sqrt{\boldsymbol{K}^\dagger \Sigma_N \boldsymbol{K}}\sqrt{\boldsymbol{H}^\dagger \Sigma_N^{-1} \boldsymbol{H}}.. \tag{8.15}$$

We remark here that since Σ_N is hermitian, there exists exactly one positive semi-definite matrix $\Sigma^{1/2}$ such that $\Sigma_N = (\Sigma_N)^{1/2}\Sigma_N^{1/2}$ [324]. Thus we are justified in rewriting the identity matrix $I = (\Sigma_N^\dagger)^{1/2}\Sigma_N^{-1/2}$ as we did above. Using (8.15), we see that the maximum attainable bound for the SNR is

$$\left(\frac{S}{N}\right)(t) = \frac{|2\boldsymbol{K}^\dagger \boldsymbol{H}|}{\sqrt{2\boldsymbol{K}^\dagger \Sigma_N \boldsymbol{K}}} \leq \sqrt{2\boldsymbol{H}^\dagger \Sigma_N^{-1} \boldsymbol{H}}\,. \tag{8.16}$$

The bound in equation (8.16) is achieved by choosing the vector $\boldsymbol{K}$ such that $\boldsymbol{K} \propto \Sigma_N^{-1} H$. For this choice of $\boldsymbol{K}$, the optimal matched filtering SNR in the case of gated noise takes the form

$$\rho^2_{\text{gate}} = 2\boldsymbol{H}^\dagger \Sigma_N^{-1} \boldsymbol{H}. \tag{8.17}$$

We now define a general inner product of the form

$$(a|b) = (\boldsymbol{a}^\dagger \Sigma_N^{-1} \boldsymbol{b} + \boldsymbol{b}^\dagger \Sigma_N^{-1} \boldsymbol{a}) = 2\text{Re}\left(\boldsymbol{a}^\dagger \Sigma_N^{-1} \boldsymbol{b}\right), \tag{8.18}$$

implying that the (squared) SNR takes the form $\rho^2_{\text{gate}} = (H|H)$. Similarly, using (8.18), the log-likelihood is given by

$$\log p(D|\boldsymbol{\theta}) = -\frac{1}{2}(D - H(t;\boldsymbol{\theta})|D - H(t;\boldsymbol{\theta})). \tag{8.19}$$

Precisely the same form as (3.31), except that we now use a *general* noise covariance matrix and the data stream and signal template must be gated by a time dependent function $w(t)$.

As discussed in 3.3.2, the FM is an excellent tool for understanding precision measurements of parameters in gravitational wave astronomy. In the next section, we compute the form of the FM in the case of non-stationary noise. Using this FM formalism, we are able to predict the statistical spread of the recovered parameters (due to gated noise) when the true noise covariance matrix is inconsistent with the likelihood. Some of the following results may be found in [321], which appeared while this work was in preparation. We extend their results to arbitrary windowing functions $w(t)$ and provide a clearer interpretation of their calculations.

8.3.2 Fisher matrix

In this section, we take the likelihood of the form (8.19) with inner product given by (8.18)

$$\log p(D|\boldsymbol{\theta}) = -\frac{1}{2}(D - H(t;\boldsymbol{\theta})|D - H(t;\boldsymbol{\theta})). \tag{8.20}$$

$$(a|b) = (\hat{\boldsymbol{a}}^\dagger \Sigma^{-1} \hat{\boldsymbol{b}} + \hat{\boldsymbol{b}}^\dagger \Sigma^{-1} \hat{\boldsymbol{a}}) \tag{8.21}$$

but with Σ the covariance matrix *assumed* to be consistent with the underlying noise. In other words, we relax the assumption that $\Sigma \equiv \Sigma_N = \langle \boldsymbol{N}\boldsymbol{N}^\dagger \rangle$.

Consider the linear-signal approximation (3.57) for the gated signal function

$$H(t;\boldsymbol{\theta}) \approx H(t;\boldsymbol{\theta}_0) + \partial_i H(t;\boldsymbol{\theta}) \Delta\theta^i, \tag{8.22}$$

Substituting into (8.19) and following a near identical calculation to the FM in the case of stationary noise (see (3.58b)), we find that

$$\log p(d|\boldsymbol{\theta}) \propto -\frac{1}{2}(\Delta\theta^i - (\Gamma^{-1})^{ik}(\partial_k H|N))\Gamma_{ij}(\Delta\theta^j - (\Gamma^{-1})^{jl}(\partial_l H|N)) \tag{8.23}$$

with FM

$$\Gamma_{ij} = (\partial_i H|\partial_j H) \approx 2\ \mathrm{Re}\left(\partial_i \hat{\boldsymbol{H}}^\dagger \Sigma^{-1} \partial_j \hat{\boldsymbol{H}}\right). \tag{8.24}$$

Identifying the maximum likelihood estimator as $\widehat{\Delta\theta}^i_{\mathrm{bf}} = (\Gamma^{-1})^{ik}(\partial_k H|N)$, it can verified that $\langle\widehat{\Delta\boldsymbol{\theta}}\rangle = 0$, since $\mathbb{E}[\hat{\boldsymbol{N}}] = 0$. Hence, this statistic is an unbiased estimator of the true parameter $\boldsymbol{\theta}_0$, which is to be expected. However, the covariance of $\widehat{\Delta\theta}^i_{\mathrm{bf}}$ and $\widehat{\Delta\theta}^j_{\mathrm{bf}}$ is of significant interest. First, it can be shown that

$$\begin{aligned}\langle(a|N)(b|N)\rangle = \mathbb{E}[(\hat{\boldsymbol{a}}^\dagger\Sigma^{-1}\hat{\boldsymbol{N}})(\hat{\boldsymbol{b}}^\dagger\Sigma^{-1}\hat{\boldsymbol{N}}) + (\hat{\boldsymbol{b}}^\dagger\Sigma^{-1}\hat{\boldsymbol{N}}\hat{\boldsymbol{N}}^\dagger\Sigma^{-1}\hat{\boldsymbol{a}}) + & \qquad (8.25)\\ (\hat{\boldsymbol{a}}^\dagger\Sigma^{-1}\hat{\boldsymbol{N}}\hat{\boldsymbol{N}}^\dagger\Sigma^{-1}b) + (\hat{\boldsymbol{N}}^\dagger\Sigma^{-1}\hat{\boldsymbol{a}})(\hat{N}^\dagger\Sigma^{-1}\hat{\boldsymbol{b}}) & \qquad (8.26)\\ = 2\ \mathrm{Re}\left(\hat{\boldsymbol{b}}^\dagger\Sigma^{-1}\Sigma_N\Sigma^{-1}\hat{\boldsymbol{a}}\right). & \qquad (8.27)\end{aligned}$$

Where we used the inner product (8.21) alongside $\mathbb{E}[\boldsymbol{N}]\rangle = 0$ and $\mathbb{E}[\boldsymbol{N}\boldsymbol{N}^\dagger] = \Sigma_N$. It can then be shown that

$$\mathbb{E}[\widehat{\Delta\theta}^i_{\mathrm{bf}}\widehat{\Delta\theta}^j_{\mathrm{bf}}] = 2(\Gamma^{-1})^{ik}\mathrm{Re}\left(\partial_k\boldsymbol{H}\Sigma^{-1}\Sigma_N\Sigma^{-1}\partial_p\boldsymbol{H}\right)(\Gamma^{-1})^{pj}. \tag{8.28}$$

Notice that in the case when the covariance matrix derived from the noise properties matches the noise covariance present in the likelihood (8.20), $\Sigma_N = \hat{\Sigma}$, the above simplifies to

$$\mathbb{E}[\widehat{\Delta\theta}^i_{\mathrm{bf}}\widehat{\Delta\theta}^j_{\mathrm{bf}}]_{\Sigma=\Sigma_N} = (\Gamma^{-1})^{ij}, \tag{8.29}$$

which is identical to the FM (3.59) for $w(t) = 1$. Assuming that the true noise covariance is consistent with the likelihood, then equation (8.29) gives the correct result to determine parameter precision. However, if the analysis is performed incorrectly by assuming the wrong form of the likelihood, then (8.28) shows the covariance is different and so the posterior will be inconsistent with the data.

Equation (8.28) can be used to quantify the spread in recovered parameters in the case that the noise-covariance matrix in the likelihood *is not* consistent with the true noise-covariance matrix for the data. In the next section, we test the formalism developed above on a simple toy model embedded in non-stationary noise.

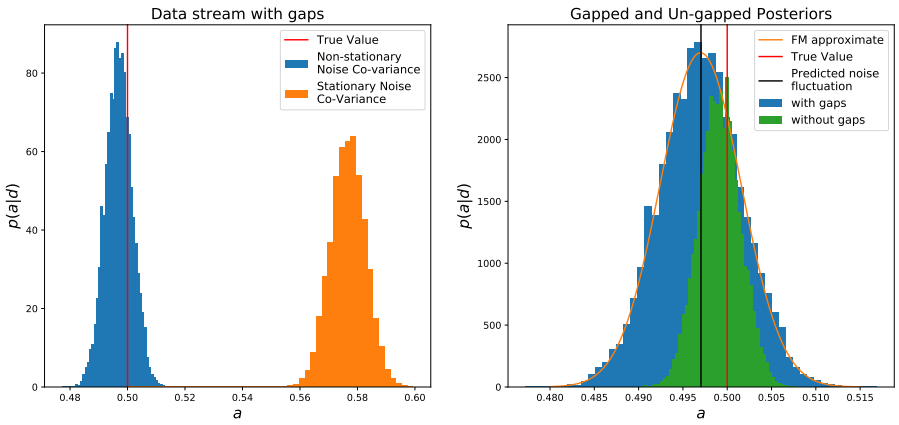

Figure 8.2: (left plot) The orange and blue histograms represent posterior samples obtained by analysing the gapped data stream using the stationary covariance matrix (3.24) and non-stationary (gapped) covariance matrix (8.4) respectively. The red lines on both plots indicate the true value, and black line on the right plot the predicted statistical fluctuation calculated using $\widehat{\Delta\boldsymbol{\theta}} = (\Gamma^{-1})^{ik}(\partial_k H|N)$. driven by the noise realisation. The green histogram was obtained by analysing a non-gapped data stream using non-gapped signal templates. The yellow curve on the right plot is the FM prediction (8.29) fisher eq on the width of the posterior using the non-stationary covariance matrix.

8.4 Parameter estimation: a case study

We choose to use a simple chirping waveform of the form

$$h(t;a) = a \cdot \mathcal{A}\sin(2\pi f(t)t), \quad f(t) = 10^{-5}\sqrt{t}\,, \tag{8.30}$$

with $\mathcal{A} = 3 \cdot 10^{-20}$. Our goal here is to estimate the parameter $a = 0.5$ in (8.30) when the signal is embedded in non-stationary noise.

We set the length of the signal to be 30 hours long with sampling interval $\Delta t \sim 152$ seconds. To place the gap, we use a modified Tukey function $w(t) = 1 - \omega(t)$ where $\omega(t)$ is a Tukey window defined by (3.6). We consider a 15-hour-long gap in the data stream, starting at the tenth hour and ending on the 25th hour with 2.5 hour lobe lengths. We use the one-sided analytical fit to the PSD from Eq.(3.36). Stationary noise is generated using (3.34), transformed to the time domain and added to the true signal, windowed, and then converted into the frequency domain to construct $\hat{D}(f)$.

From the analytical fit to the PSD and the window function $w(t)$, one is able to construct the non-stationary covariance matrix (8.4). To calculate the likelihood (8.6), we use the truncated SVD matrix $\overset{\circ}{\Sigma}_N$. This is for reasons discussed below equation (8.8).

The injected signal excluding gaps has an optimal matched filtering SNR $\rho = (h|h)^{1/2} \sim 214$. Calculating the optimal matched filtering SNR for the gapped injected signal using (8.17) one

obtains $\rho_{\rm gate} = (H|H)^{1/2} \sim 109$. Since precision measurements on the amplitude scale inversely with the optimal matched filtering SNR, we would expect a weaker constraint on the amplitude parameter by roughly a factor of two.

Figure (8.2) shows parameter recoveries in the case of performing parameter estimation on a gapped data stream when using the correct noise covariance matrix (blue posterior) and performing PE on a gapped data stream when using the Whittle-likelihood (orange posterior). Using Σ_N to perform the parameter estimation on the gapped data set, we are able to recover the parameter a with a small statistical fluctuation due to the gated noise. More so, this fluctuation is consistent with the width of the inferred posterior distribution, as expected. However, when one uses the Whittle-likelihood to perform PE (yellow posterior) we see that the recovered parameter is $\sim 12\sigma$ away from the true parameter. This is because the underlying data generating process is inconsistent with the likelihood model assumed for parameter estimation.

In the right plot of figure 8.2, the green histogram represents posterior samples when searching for an injected signal when *no* gaps are induced. In this situation, the Whittle-likelihood applies as the underlying noise is stationary. One can see that the constraint on the parameter a is tighter in the stationary case than in the non-stationary gapped case. This is not a consequence of whether the noise is stationary or non-stationary, but is driven by the loss of SNR due to the presence of gaps in the data stream. The yellow curve is a Gaussian, centered on the mean of the posterior samples and variance equal to the FM prediction (8.29). The ratio between the blue and green posterior widths is approximately ~ 2. This implies that we lose a factor ~ 2 in our ability to constrain the parameter a, consistent with the change on SNR.

The statistical fluctuation of the recovered parameter when assuming the Whittle-likelihood to analyse the gated data is quite large this fluctuation can be understood using (8.28). Computing Eq.(8.28) with the likelihood covariance $\Sigma = \Sigma_n$ whilst the noise process is non-stationary gives $\mathbb{E}[\widehat{\Delta a}^2] \sim 0.0415$ giving a 1σ deviation of statistical fluctuations $\sim \sqrt{0.0415} \approx 0.2037$. This is approximately ~ 44 times the width of the true gapped posterior found in 8.2. This highlights the importance of using a noise-covariance matrix in the likelihood that is consistent with the data generating process.

One can test the validity of equation (8.28) by performing PE multiple times when using the incorrect noise covariance matrix in the likelihood. Figure 8.3 shows the distribution of recovered parameters, i.e., posterior means, from 4000 MCMC simulations. The yellow curve is a Gaussian, centered on the mean of the recovered parameters, with variance equivalent to (8.28). Figure 8.3 shows that (8.28) accurately predicts the variance of the statistical fluctuations in the case when the likelihood is inconsistent with the true data generating procedure. Furthermore,

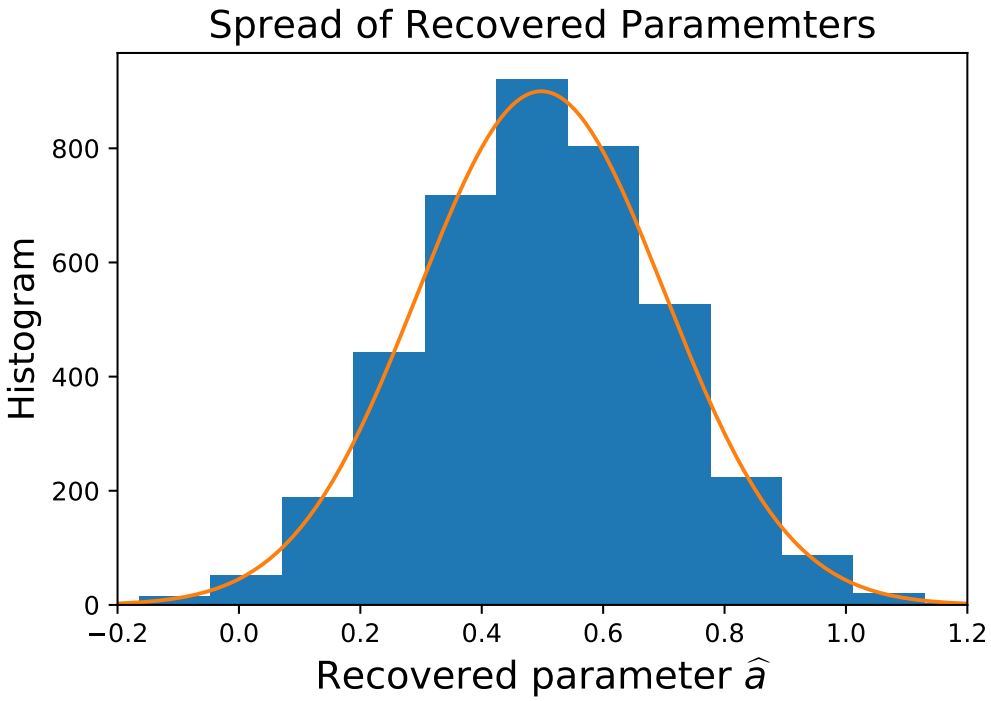

Figure 8.3: Blue histogram quantifies the spread of the recovered $\hat{a}$ parameter when using the Whittle-likelihood to analyse the gated data stream. The orange curve is a Gaussian, centred on the mean recovered parameter with variance equivalent to the FM prediction (8.28).

we have verified that, on average, the statistical fluctuations averages to zero as over many gated noise realisations.

What we take away from this example is that it is of utmost importance to use the correct noise covariance matrix in the likelihood. Otherwise, it is possible to systematically underestimate the uncertainty in the recovered parameters.

8.5 Conclusions and future work

This chapter has described some preliminary work in the impact of parameter estimation/precision of non-stationary noise. For a model $N(t) = w(t)n(t)$, with $n(t)$ a zero-mean Gaussian stationary process and $w(t)$ some known time dependent function, we were able to derive corresponding form of the noise covariance matrix (8.3) in the frequency domain. For functions $w(t)$ where the Fourier transform is not a delta function, i.e., for $w(t)$ non-constant, the covariance matrix for $\hat{N}(f)$ is *non-diagonal*. This non-diagonal covariance matrix make the Whittle-likelihood of Eq.(3.31) invalid. From the theory of complex normal distributions, we wrote down the most general likelihood (8.6) that describes the probability distribution of the non-stationary gated noise process $\hat{N}(f)$. We argued that the form of the joint probability

distribution between real and imaginary parts of $\hat{N}(f)$ is given by (8.12). This joint covariance matrix can be used to draw random samples of non-stationary noise. In section 8.3.1 and 8.3.2, we argued that the form of the optimal matched filtering SNR and FM must change when the underlying noise properties are not stationary. We derived a formula (8.28) that represents the spread of the statistical fluctuations from the true parameters when the noise covariance matrix present in the likelihood is inconsistent with the true noise properties of the data. This formula is very powerful and, in conjunction with equation (8.3), can be used to test parameter estimation schemes for analysing non-stationary data. Finally, we illustrated the ideas above using a simple chirping sinusoid model and verified the main results of this chapter.

The research presented in this chapter is the first stage of a longer research program. There are a large number of open questions. We have only considered the case of a single (long duration) gap whereas, in reality, the LISA data stream will contain multiple gaps that will be shorter. The end goal of this project would be to consider a data stream with an EMRI signal embedded in Gaussian noise with scheduled gaps occurring every 3.5 hours for 1 week or 7 hours for 2 weeks mimicking the re-pointing of the LISA antennae. We would assess which scenario leads to the greatest degradation of the measurement precision. Further, we would try to understand whether the addition of frequent (but very short duration) gaps could be suitably approximated using the diagonal noise-covariance matrix arising from stationary noise. One of the major pitfalls of the above formalism is the dimension of the non-stationary noise covariance matrix as the time series becomes larger. This can introduce numerical instabilities and make parameter estimation algorithms prohibitively expensive. To overcome the problem, we believe that Σ_N could be approximated by $\sim D$ diagonals and then be treated as a sparse matrix. This will rapidly increase the computational efficiency but introduce variability in the recovered parameters through (8.28). This is a topic we are still investigating.

We have considered one model for non-stationary noise, but this might not always apply. Another model would be to treat the noise in each data chunk as *independent*. Such a situation might apply in LISA when there is a major disturbance in the satellite that causes the gap. When the noise in each between-gap data segment is independent, one can treat the noise as a stationary process and the Whittle-likelihood is valid. The log-likelihood for the whole data stream is then the sum of the log-likelihoods over the data segments. Parameter estimation will benefit from using the diagonal Whittle-likelihood in each data segment.

A question of key importance is to understand the noise model mis-specification. Neither the first model, where the gaps are treated as missing data, nor the second, where each between gap segment is treated as independent of the others, is likely to fully represent the entire LISA

data stream. It is important to understand what impact this has and whether our assumptions or the other is less likely to lead to under or overestimating the covariance of the recovered parameters. Using the formalism introduced in this chapter, in particular Eq.(8.28), we can address the question of what would happen if we used the "unobserved data" covariance when the noise between data segments are independent or vice versa. We plan to address these questions when we finalise this project for publication.

Chapter 9

Concluding remarks

The focus of this thesis was to address questions related to data analysis and waveform modelling for the LISA mission. In chapter 4, we provided an analytic treatment on the transition from inspiral to plunge for a CO in a circular equatorial orbit around a MBH, for all spin parameters $a \in [0, 1]$. From the resultant radial trajectory, we were able to build a waveform model that may be suitable for parameter estimation purposes. This body of work is not only useful for data analysis, but can also be used to compare GSF results with NR data in order to gain insight on the magnitude of the second-order GSF. For a discussion of this work, see [182] and more recently [181].

In chapter 5 we showed that precision measurements on the spin parameter from EMRI observations with near-extremal primaries are much tighter when compared to moderately spinning sources with $a \sim 0.9$. This work not only focused on near-extremal BHs but also provided a rigorous analytical formalism to investigate *why* one can measure EMRI parameters with such excellent precision. In this work we focused on the spin parameter, but the same formalism can be applied to other intrinsic parameters such as the component masses, or the initial radius. In future work we plan to combine the work of chapters 4 and 5 to calculate constraints on parameters using complete radial trajectories of particles spiraling into MBHs. This study would be a first of its kind, providing a valuable addition to the literature on both waveform modelling and GW data analysis. The end goal of this work is to build a toolkit that is able to generate full inspirals of small CO, for generic orbits, into a massive near-extremal BHs. Incorporating work from [287] one could include the spin of the secondary as a further parameter into the waveform model. Observing near-extremal black holes using LISA would be very exciting and could pose a plethora of questions: How can they attain that rotation rate? How did they form? Are they primordial? Could one test theories of quantum gravity?

For these reasons, building a data analysis pipeline that is able to accurately search for and perform parameter estimation on near-extremal BHs is, in the author's opinion, essential. The goal would be to construct a toolkit, suitably named Parameter Inference for Near-extremal Kerr Toolkit for Accessing Cosmological Observations (PINK-TACO). The author is keen to continue working towards the construction of PINK-TACO in the hope that near-extremal BHs, if they exist, can be discovered by the LISA mission.

The results presented in chapter 6 focused on the impact on parameter estimation when using imperfect EMRI waveform models. We investigated the numerical precision required in both the adiabatic and 1PA components of low eccentricity Schwarzschild based EMRI waveforms. We were able to conclude that, for such orbits, the adiabatic and 1PA components of the self-force must be computed to roughly six and two decimal digits of precision at signal-to-noise ratios of ~ 100 respectively. The answer to this question is highly sought for and details contained in chapter 6 are, in essence, a first study of its kind. At the moment 1PA information is known for generic Kerr orbits across the parameter space, but there exists no method to efficiently generate waveforms. The goal would be to come up with a suitable criterion that determines how accurately the 1PA components must be computed for *generic* orbits in the Kerr space-time. Rather than using the usual rule of thumb that we require tracking the orbital phase to within ~ 0.1 radians, the CV algorithm could be used to place more rigorous bounds on accuracy requirements of EMRI signals. The field of EMRI systematics is undeniably extremely important and requires both blood (waveform model), sweat (FMs) and tears (MCMC) in order to suitably determine accuracy requirements.

In chapter 7 we performed a systematic study when imperfect waveforms were used to perform parameter estimation of a data stream containing multiple signals, detector noise and an astrophysical foreground. The equation used to predict biases in parameters in such a circumstance (7.25) is *general* with no theoretical reliance on the dimensions of the parameter space, source-types, numbers and what type of astrophysical foreground is present. The author's hope is that the GW community consider using this formalism, rather than spending hundreds of thousands of CPU hours on expensive parameter estimation schemes. In section 7.4, we showed that one could perform ~ 2 miniature global fits (which we called local fits) and use the formalism outlined in 7.1 to *correct* the recovered biased parameters where they hone in closer to the true parameter. This result is powerful and could be used to aid global-fit pipelines where the sources under consideration have a valid linear signal approximation. In the author's opinion, perhaps because this was one of the sections he took the main lead, this is the most interesting section. Constructing a global-fit search pipeline is a brutal task and one of the

author's major goals in future is work on global-fit strategies. The gold standard, yet unsolved, problem is the inference of a data set containing a number of MBHs, resolvable/unresolvable GBs and, the real devil in the data, EMRIs. This problem of huge interest to the author and he hopes to continue contributing to the field with the goal of solving this problem as part of a team.

Finally, chapter 8 described a method to handle the presence of non-stationary noise sources when performing parameter estimation. This analysis improves upon [321] in a number of ways. Firstly, our work is valid for any such time dependent function $w(t)$ tampering Gaussian stationary noise whereas they had to estimate the noise-covariance matrix over ~ 1000 noise realisations. This may not be feasible for LISA since there will be stretches of data that may contain traces of GW signals. We need to know *when in time* the non-stationaries occur and an *approximation* of their shape. Unlike the earlier chapters, this chapter is far from complete and there is a huge amount the author wants to continue working on. No one thus far has studied the effect of data gaps on EMRI waveforms, likely because of the common belief that data gaps will not impede parameter constraints for these sources. The author shares this belief, however, analysing non-stationary data streams using the Whittle-likelihood could drastically underestimate the covariance on the EMRI parameters. The power of the formalism introduced in chapter 8 is huge, and the author plans to use it to solve the latest (and most complex) *Sangria* LISA data challenge.

The first observation of GWs, GW150914, spectacularly opened the field of GW astronomy. Approximately six years have passed, and our understanding of the universe has changed drastically. From the sheer number of discoveries, it is staggering to say that the field of observable GW astronomy is still in its early stages. With the addition of third generation ground-based detectors extending the current aLIGO's sensitivity range and the space-based LISA mission opening the mHz frequency band, the scope for science from GWs will be tremendous. The author can say, with remarkable ease, that it has been his pleasure to be part of such an astounding journey and contribute not only to the present, but to the future of gravitational wave astronomy.

Bibliography

[1] Ollie Burke, Jonathan Gair, and Joan Simón. "Transition from inspiral to plunge: A complete near-extremal trajectory and associated waveform". In: *Physical Review D* 101.6 (2020), p. 064026.

[2] Ollie Burke et al. "Constraining the spin parameter of near-extremal black holes using LISA". In: *Physical Review D* 102.12 (2020), p. 124054.

[3] Andrea Antonelli, Ollie Burke, and Jonathan R Gair. "Noisy neighbours: inference biases from overlapping gravitational-wave signals". In: *arXiv preprint arXiv:2104.01897* (2021).

[4] C. W. Misner, K. S. Thorne, and J. A. Wheeler. *Gravitation*. 1973.

[5] Albert Einstein. "The field equations of gravitation". In: *Sitzungsber. Preuss. Akad. Wiss. Berlin (Math. Phys.)* 1915 (1915), pp. 844–847.

[6] Albert Einstein. "Zur Allgemeinen Relativitätstheorie". In: *Sitzungsber. Preuss. Akad. Wiss. Berlin (Math. Phys.)* 1915 (1915). [Addendum: Sitzungsber.Preuss.Akad.Wiss.Berlin (Math.Phys.) 1915, 799–801 (1915)], pp. 778–786.

[7] Albert Einstein. "Über gravitationswellen". In: *Sitzungsberichte der Königlich Preußischen Akademie der Wissenschaften (Berlin* (1918), pp. 154–167.

[8] Andrzej Trautman. "Editorial note to: JL Synge, On the deviation of geodesics and null geodesics, particularly in relation to the properties of spaces of constant curvature and indefinite line-element and to: FAE Pirani, On the physical significance of the Riemann tensor". In: *General Relativity and Gravitation* 41.5 (2009), pp. 1195–1203.

[9] Felix AE Pirani. "On the physical significance of the Riemann tensor". In: *Acta Physica Polonica* 15 (1956), pp. 389–405.

[10] Cécile M. DeWitt and Dean Rickles. *The role of gravitation in physics: report from the 1957 Chapel Hill Conference*. Vol. 5. epubli, 2011.

[11] Joseph Weber. “Detection and generation of gravitational waves”. In: *Physical Review* 117.1 (1960), p. 306.

[12] Joseph Weber. “Observation of the thermal fluctuations of a gravitational-wave detector”. In: *Physical Review Letters* 17.24 (1966), p. 1228.

[13] Joseph Weber. “Evidence for discovery of gravitational radiation”. In: *Physical Review Letters* 22.24 (1969), p. 1320.

[14] Russell A Hulse and Joseph H Taylor. “Discovery of a pulsar in a binary system”. In: *The Astrophysical Journal* 195 (1975), pp. L51–L53.

[15] Joseph H Taylor and Joel M Weisberg. “A new test of general relativity-Gravitational radiation and the binary pulsar PSR 1913+ 16”. In: *The Astrophysical Journal* 253 (1982), pp. 908–920.

[16] Joseph H Taylor and Joel M Weisberg. “Further experimental tests of relativistic gravity using the binary pulsar PSR 1913+ 16”. In: *The Astrophysical Journal* 345 (1989), pp. 434–450.

[17] Joel M Weisberg and Joseph H Taylor. “Gravitational radiation from an orbiting pulsar”. In: *General Relativity and Gravitation* 13.1 (1981), pp. 1–6.

[18] Joseph H Taylor, LA Fowler, and PM McCulloch. “Measurements of general relativistic effects in the binary pulsar PSR1913+ 16”. In: *Nature* 277.5696 (1979), pp. 437–440.

[19] Albert A Michelson and Edward W Morley. “On the Relative Motion of the Earth and of the Luminiferous Ether”. In: *Sidereal Messenger, vol. 6, pp. 306-310* 6 (1887), pp. 306–310.

[20] RWP Drever et al. “Laser phase and frequency stabilization using an optical resonator”. In: *Applied Physics B* 31.2 (1983), pp. 97–105.

[21] A Perot and Charles Fabry. “On the application of interference phenomena to the solution of various problems of spectroscopy and metrology”. In: *The Astrophysical Journal* 9 (1899), p. 87.

[22] Denis V Martynov et al. “Sensitivity of the Advanced LIGO detectors at the beginning of gravitational wave astronomy”. In: *Physical Review D* 93.11 (2016), p. 112004.

[23] Alex Abramovici et al. “LIGO: The laser interferometer gravitational-wave observatory”. In: *science* 256.5055 (1992), pp. 325–333.

[24] B. P. et al Abbott. "Observation of Gravitational Waves from a Binary Black Hole Merger". In: *Phys. Rev. Lett.* 116 (6 Feb. 2016), p. 061102. DOI: 10.1103/PhysRevLett.116.061102. URL: https://link.aps.org/doi/10.1103/PhysRevLett.116.061102.

[25] Benjamin P Abbott et al. "Properties of the binary black hole merger GW150914". In: *Physical review letters* 116.24 (2016), p. 241102.

[26] Benjamin P Abbott et al. "Tests of general relativity with GW150914". In: *arXiv preprint arXiv:1602.03841* (2016).

[27] Benjamin P Abbott et al. "The rate of binary black hole mergers inferred from Advanced LIGO observations surrounding GW150914". In: *The Astrophysical journal letters* 833.1 (2016), p. L1.

[28] Benjamin P Abbott et al. "Observing gravitational-wave transient GW150914 with minimal assumptions". In: *Physical Review D* 93.12 (2016), p. 122004.

[29] Benjamin P Abbott et al. "Astrophysical implications of the binary black hole merger GW150914". In: *The Astrophysical Journal Letters* 818.2 (2016), p. L22.

[30] Benjamin P Abbott et al. "GW150914: Implications for the stochastic gravitational-wave background from binary black holes". In: *Physical review letters* 116.13 (2016), p. 131102.

[31] Silvia Adrín-Martínez et al. "High-energy neutrino follow-up search of gravitational wave event GW150914 with ANTARES and IceCube". In: *Physical Review D* 93.12 (2016), p. 122010.

[32] Benjamin P Abbott et al. "GW151226: observation of gravitational waves from a 22-solar-mass binary black hole coalescence". In: *Physical review letters* 116.24 (2016), p. 241103.

[33] LIGO Scientific. "GWTC-1: A gravitational-wave transient catalog of compact binary mergers observed by LIGO and Virgo during the first and second observing runs". In: *arXiv preprint arXiv:1811.12907* 2 (1811).

[34] Benjamin P Abbott et al. "GW170817: observation of gravitational waves from a binary neutron star inspiral". In: *Physical Review Letters* 119.16 (2017), p. 161101.

[35] Daniel Kasen et al. "Origin of the heavy elements in binary neutron-star mergers from a gravitational-wave event". In: *Nature* 551.7678 (Oct. 2017), pp. 80–84. ISSN: 1476-4687. DOI: 10.1038/nature24453. URL: http://dx.doi.org/10.1038/nature24453.

[36] Irwin I Shapiro. "Fourth test of general relativity". In: *Physical Review Letters* 13.26 (1964), p. 789.

[37] "A gravitational-wave standard siren measurement of the Hubble constant". In: *Nature* 551.7678 (Oct. 2017), pp. 85–88. ISSN: 1476-4687. DOI: 10.1038/nature24471. URL: http://dx.doi.org/10.1038/nature24471.

[38] B. F. Schutz. "Determining the Hubble constant from gravitational wave observations". In: *Nature* 323.6086 (Sept. 1986), pp. 310–311. DOI: 10.1038/323310a0.

[39] Stephen M Feeney et al. "Prospects for resolving the Hubble constant tension with standard sirens". In: *Physical review letters* 122.6 (2019), p. 061105.

[40] Koutarou Kyutoku and Naoki Seto. "Gravitational-wave cosmography with LISA and the Hubble tension". In: *Physical Review D* 95.8 (2017), p. 083525.

[41] Martin G Haehnelt. "Low-frequency gravitational waves from supermassive black holes". In: *Monthly Notices of the Royal Astronomical Society* 269.1 (1994), pp. 199–208.

[42] Tessa Baker et al. "Strong constraints on cosmological gravity from GW170817 and GRB 170817A". In: *Physical review letters* 119.25 (2017), p. 251301.

[43] David Langlois et al. "Scalar-tensor theories and modified gravity in the wake of GW170817". In: *Phys. Rev. D* 97.6 (2018), p. 061501.

[44] Jose María Ezquiaga and Miguel Zumalacárregui. "Dark energy after GW170817: dead ends and the road ahead". In: *Physical review letters* 119.25 (2017), p. 251304.

[45] Jeremy Sakstein and Bhuvnesh Jain. "Implications of the neutron star merger GW170817 for cosmological scalar-tensor theories". In: *Physical review letters* 119.25 (2017), p. 251303.

[46] Sibel Boran et al. "GW170817 falsifies dark matter emulators". In: *Phys. Rev. D* 97.4 (2018), p. 041501.

[47] R Abbott et al. "GWTC-2: Compact Binary Coalescences Observed by LIGO and Virgo During the First Half of the Third Observing Run". In: *arXiv preprint arXiv:2010.14527* (2020).

[48] BP Abbott et al. "GW190425: observation of a compact binary coalescence with total mass, roughly 3.4 solar masses". In: *The Astrophysical Journal Letters* 892.1 (2020), p. L3.

[49] R. Abbott et al. "GW190412: Observation of a binary-black-hole coalescence with asymmetric masses". In: *Physical Review D* 102.4 (Aug. 2020). ISSN: 2470-0029. DOI: 10.1103/physrevd.102.043015. URL: http://dx.doi.org/10.1103/PhysRevD.102.043015.

[50] Charles D Bailyn et al. “The mass distribution of stellar black holes”. In: *The Astrophysical Journal* 499.1 (1998), p. 367.

[51] Will M Farr et al. “The mass distribution of stellar-mass black holes”. In: *The Astrophysical Journal* 741.2 (2011), p. 103.

[52] Feryal Özel et al. “The black hole mass distribution in the galaxy”. In: *The Astrophysical Journal* 725.2 (2010), p. 1918.

[53] R Abbott et al. “GW190521: A binary black hole merger with a total mass of 150 solar masses”. In: *Physical review letters* 125.10 (2020), p. 101102.

[54] R Abbott et al. “Properties and astrophysical implications of the 150 solar mass binary black hole merger GW190521”. In: *The Astrophysical Journal Letters* 900.1 (2020), p. L13.

[55] Jocelyn S Read et al. “Measuring the neutron star equation of state with gravitational wave observations”. In: *Physical Review D* 79.12 (2009), p. 124033.

[56] Eemeli Annala et al. “Gravitational-wave constraints on the neutron-star-matter Equation of State”. In: *Physical review letters* 120.17 (2018), p. 172703.

[57] Andreas Bauswein et al. “Equation-of-state dependence of the gravitational-wave signal from the ring-down phase of neutron-star mergers”. In: *Physical Review D* 86.6 (2012), p. 063001.

[58] M Punturo et al. “The Einstein Telescope: a third-generation gravitational wave observatory”. In: *Classical and Quantum Gravity* 27.19 (2010), p. 194002.

[59] Bangalore Sathyaprakash et al. “Scientific objectives of Einstein telescope”. In: *Classical and Quantum Gravity* 29.12 (2012), p. 124013.

[60] Michele Maggiore et al. “Science case for the Einstein telescope”. In: *Journal of Cosmology and Astroparticle Physics* 2020.03 (2020), p. 050.

[61] Benjamin P Abbott et al. “Exploring the sensitivity of next generation gravitational wave detectors”. In: *Classical and Quantum Gravity* 34.4 (2017), p. 044001.

[62] David Reitze et al. “Cosmic explorer: the US contribution to gravitational-wave astronomy beyond LIGO”. In: *arXiv preprint arXiv:1907.04833* (2019).

[63] Salvatore Vitale and Matthew Evans. “Parameter estimation for binary black holes with networks of third-generation gravitational-wave detectors”. In: *Physical Review D* 95.6 (2017), p. 064052.

[64] Darren J Croton et al. “The many lives of active galactic nuclei: cooling flows, black holes and the luminosities and colours of galaxies”. In: *Monthly Notices of the Royal Astronomical Society* 365.1 (2006), pp. 11–28.

[65] P. Amaro-Seoane et al. “Laser Interferometer Space Antenna”. In: *ArXiv e-prints* (Feb. 2017). arXiv: 1702.00786 [astro-ph.IM].

[66] Waldemar Martens and Eric Joffre. *Trajectory Design for the ESA LISA Mission*. 2021. arXiv: 2101.03040 [gr-qc].

[67] Michele Armano et al. “Sub-femto-g free fall for space-based gravitational wave observatories: LISA pathfinder results”. In: *Physical review letters* 116.23 (2016), p. 231101.

[68] O Jennrich. “LISA technology and instrumentation”. In: *Classical and Quantum Gravity* 26.15 (July 2009), p. 153001. ISSN: 1361-6382. DOI: 10.1088/0264-9381/26/15/153001. URL: http://dx.doi.org/10.1088/0264-9381/26/15/153001.

[69] Enrico Barausse et al. “Massive Black Hole Science with eLISA”. In: *Journal of Physics: Conference Series*. Vol. 610. 1. IOP Publishing. 2015, p. 012001.

[70] Antoine Klein et al. “Science with the space-based interferometer eLISA: Supermassive black hole binaries”. In: *Physical Review D* 93.2 (2016), p. 024003.

[71] Pau Amaro-Seoane et al. “Low-frequency gravitational-wave science with eLISA/NGO”. In: *Classical and Quantum Gravity* 29.12 (2012), p. 124016.

[72] Volker Bromm, Paolo S Coppi, and Richard B Larson. “Forming the first stars in the universe: the fragmentation of primordial gas”. In: *The Astrophysical Journal Letters* 527.1 (1999), p. L5.

[73] Volker Bromm and Abraham Loeb. “Formation of the first supermassive black holes”. In: *The Astrophysical Journal* 596.1 (2003), p. 34.

[74] Nicola Tamanini et al. “Science with the space-based interferometer eLISA. III: Probing the expansion of the Universe using gravitational wave standard sirens”. In: *Journal of Cosmology and Astroparticle Physics* 2016.04 (2016), p. 002.

[75] Alberto Sesana, Marta Volonteri, and Francesco Haardt. “The imprint of massive black hole formation models on the LISA data stream”. In: *Monthly Notices of the Royal Astronomical Society* 377.4 (2007), pp. 1711–1716.

[76] JE Pringle, MJ Rees, and AG Pacholczyk. “Accretion onto massive black holes”. In: *Accretion: A Collection Of Influential Papers* 5 (1989), p. 179.

[77] AC Fabian. "The obscured growth of massive black holes". In: *Monthly Notices of the Royal Astronomical Society* 308.4 (1999), pp. L39–L43.

[78] Timothy M Heckman et al. "Present-day growth of black holes and bulges: The Sloan Digital Sky Survey perspective". In: *The Astrophysical Journal* 613.1 (2004), p. 109.

[79] M. Volonteri. "The Formation and Evolution of Massive Black Holes". In: *Science* 337.6094 (Aug. 2012), pp. 544–547. ISSN: 1095-9203. DOI: 10.1126/science.1220843. URL: http://dx.doi.org/10.1126/science.1220843.

[80] Christopher S Reynolds. "The spin of supermassive black holes". In: *Classical and Quantum Gravity* 30.24 (2013), p. 244004.

[81] Massimo Dotti et al. "On the search of electromagnetic cosmological counterparts to coalescences of massive black hole binaries". In: *Monthly Notices of the Royal Astronomical Society* 372.2 (2006), pp. 869–875.

[82] Emanuele Berti, Alessandra Buonanno, and Clifford M Will. "Testing general relativity and probing the merger history of massive black holes with LISA". In: *Classical and Quantum Gravity* 22.18 (2005), S943.

[83] Emanuele Berti, Vitor Cardoso, and Clifford M Will. "Gravitational-wave spectroscopy of massive black holes with the space interferometer LISA". In: *Physical Review D* 73.6 (2006), p. 064030.

[84] Vitor Cardoso and Paolo Pani. "Tests for the existence of black holes through gravitational wave echoes". In: *Nature Astronomy* 1.9 (2017), pp. 586–591.

[85] Emanuele Berti and Vitor Cardoso. "Supermassive black holes or boson stars? Hair counting with gravitational wave detectors". In: *International Journal of Modern Physics D* 15.12 (2006), pp. 2209–2216.

[86] Tyson B. Littenberg et al. *Astro2020 Decadal Science White Paper: Gravitational Wave Survey of Galactic Ultra Compact Binaries*. 2019. arXiv: 1903.05583 [astro-ph.HE].

[87] Neil Cornish and Travis Robson. "Galactic binary science with the new LISA design". In: *Journal of Physics: Conference Series*. Vol. 840. 1. IOP Publishing. 2017, p. 012024.

[88] Travis Robson and Neil Cornish. "Impact of galactic foreground characterization on a global analysis for the LISA gravitational wave observatory". In: *Class. Quant. Grav.* 34.24 (2017), p. 244002. DOI: 10.1088/1361-6382/aa9601. arXiv: 1705.09421 [gr-qc].

[89] Tyson Littenberg et al. "Global Analysis of the Gravitational Wave Signal from Galactic Binaries". In: *Phys. Rev. D* 101.12 (2020), p. 123021. DOI: 10.1103/PhysRevD.101.123021. arXiv: 2004.08464 [gr-qc].

[90] Neil J Cornish and Edward K Porter. "Detecting galactic binaries with LISA". In: *Classical and Quantum Gravity* 22.18 (2005), S927.

[91] A Stroeer and A Vecchio. "The LISA verification binaries". In: *Classical and Quantum Gravity* 23.19 (2006), S809.

[92] Samaya Nissanke et al. "Gravitational-wave emission from compact Galactic binaries". In: *The Astrophysical Journal* 758.2 (2012), p. 131.

[93] Curt Cutler, William A Hiscock, and Shane L Larson. "LISA, binary stars, and the mass of the graviton". In: *Physical Review D* 67.2 (2003), p. 024015.

[94] Nicolás Yunes, Frans Pretorius, and David Spergel. "Constraining the evolutionary history of Newton's constant with gravitational wave observations". In: *Phys. Rev. D* 81 (6 Mar. 2010), p. 064018. DOI: 10.1103/PhysRevD.81.064018. URL: https://link.aps.org/doi/10.1103/PhysRevD.81.064018.

[95] Scott E. Perkins, Nicolás Yunes, and Emanuele Berti. "Probing fundamental physics with gravitational waves: The next generation". In: *Phys. Rev. D* 103 (4 Feb. 2021), p. 044024. DOI: 10.1103/PhysRevD.103.044024. URL: https://link.aps.org/doi/10.1103/PhysRevD.103.044024.

[96] Karsten Danzmann, LISA Study Team, et al. "LISA: Laser interferometer space antenna for gravitational wave measurements". In: *Classical and Quantum Gravity* 13.11A (1996), A247.

[97] Stanislav Babak et al. "Science with the space-based interferometer LISA. V. Extreme mass-ratio inspirals". In: *Physical Review D* 95.10 (2017), p. 103012.

[98] Christopher P. L. Berry et al. *The unique potential of extreme mass-ratio inspirals for gravitational-wave astronomy*. 2019. arXiv: 1903.03686 [astro-ph.HE].

[99] David Merritt. *Dynamics and evolution of galactic nuclei*. Vol. 23. Princeton University Press, 2013.

[100] Leor Barack and Adam Pound. "Self-force and radiation reaction in general relativity". In: *Reports on Progress in Physics* 82.1 (2018), p. 016904.

[101] Leor Barack and Curt Cutler. "LISA capture sources: Approximate waveforms, signal-to-noise ratios, and parameter estimation accuracy". In: *Physical Review D* 69.8 (2004), p. 082005.

[102] Alvin JK Chua, Christopher J Moore, and Jonathan R Gair. "Augmented kludge waveforms for detecting extreme-mass-ratio inspirals". In: *Physical Review D* 96.4 (2017), p. 044005.

[103] Stanislav Babak et al. ""Kludge" gravitational waveforms for a test-body orbiting a Kerr black hole". In: *Physical Review D* 75.2 (2007), p. 024005.

[104] Steve Drasco and Scott A. Hughes. "Gravitational wave snapshots of generic extreme mass ratio inspirals". In: *Phys. Rev. D* 73.2 (2006). [Erratum: Phys.Rev.D 88, 109905 (2013), Erratum: Phys.Rev.D 90, 109905 (2014)], p. 024027. DOI: 10.1103/PhysRevD.73.024027. arXiv: gr-qc/0509101.

[105] Pau Amaro-Seoane et al. "Research update on extreme-mass-ratio inspirals". In: *Journal of Physics: Conference Series*. Vol. 610. 1. IOP Publishing. 2015, p. 012002.

[106] Stanislav Babak, Jonathan R Gair, and Edward K Porter. "An algorithm for the detection of extreme mass ratio inspirals in LISA data". In: *Classical and quantum gravity* 26.13 (2009), p. 135004.

[107] Stanislav Babak et al. "The mock lisa data challenges: from challenge 1b to challenge 3". In: *Classical and Quantum Gravity* 25.18 (2008), p. 184026.

[108] Curt Cutler et al. "The last three minutes: Issues in gravitational-wave measurements of coalescing compact binaries". In: *Phys. Rev. Lett.* 70 (20 May 1993), pp. 2984–2987. DOI: 10.1103/PhysRevLett.70.2984. URL: https://link.aps.org/doi/10.1103/PhysRevLett.70.2984.

[109] L. S. Finn and K. S. Thorne. "Gravitational waves from a compact star in a circular, inspiral orbit, in the equatorial plane of a massive, spinning black hole, as observed by LISA". In: *prd* 62.12, 124021 (Dec. 2000), p. 124021. DOI: 10.1103/PhysRevD.62.124021. eprint: gr-qc/0007074.

[110] S. Babak et al. "Science with the space-based interferometer LISA. V. Extreme mass-ratio inspirals". In: 95.10, 103012 (May 2017), p. 103012. DOI: 10.1103/PhysRevD.95.103012. arXiv: 1703.09722 [gr-qc].

[111] Pau Amaro-Seoane et al. "Intermediate and extreme mass-ratio inspirals—astrophysics, science applications and detection using LISA". In: *Classical and Quantum Gravity* 24.17 (2007), R113.

[112] Jonathan R Gair. "The black hole symphony: probing new physics using gravitational waves". In: *Philosophical Transactions of the Royal Society of London A: Mathematical, Physical and Engineering Sciences* 366.1884 (2008), pp. 4365–4379.

[113] Scott A Hughes. "(Sort of) Testing relativity with extreme mass ratio inspirals". In: *AIP Conference Proceedings*. Vol. 873. 1. AIP. 2006, pp. 233–240.

[114] Jonathan R Gair et al. "Testing general relativity with low-frequency, space-based gravitational-wave detectors". In: *Living Reviews in Relativity* 16.1 (2013), p. 7.

[115] Kostas Glampedakis and Stanislav Babak. "Mapping spacetimes with LISA: inspiral of a test body in a 'quasi-Kerr'field". In: *Classical and Quantum Gravity* 23.12 (2006), p. 4167.

[116] Leor Barack and Curt Cutler. "Using LISA extreme-mass-ratio inspiral sources to test off-Kerr deviations in the geometry of massive black holes". In: *Physical Review D* 75.4 (2007), p. 042003.

[117] Nicolás Yunes, Paolo Pani, and Vitor Cardoso. "Gravitational waves from quasicircular extreme mass-ratio inspirals as probes of scalar-tensor theories". In: *Physical Review D* 85.10 (2012), p. 102003.

[118] Chelsea L MacLeod and Craig J Hogan. "Precision of Hubble constant derived using black hole binary absolute distances and statistical redshift information". In: *Physical Review D* 77.4 (2008), p. 043512.

[119] Danny Laghi et al. "Gravitational wave cosmology with extreme mass-ratio inspirals". In: *arXiv preprint arXiv:2102.01708* (2021).

[120] Jonathan R Gair et al. "Event rate estimates for LISA extreme mass ratio capture sources". In: *Classical and Quantum Gravity* 21.20 (2004), S1595.

[121] Charles R Evans, Icko Iben Jr, and Larry Smarr. "Degenerate dwarf binaries as promising, detectable sources of gravitational radiation". In: *The Astrophysical Journal* 323 (1987), pp. 129–139.

[122] Tyson B. Littenberg et al. "Global analysis of the gravitational wave signal from Galactic binaries". In: *Physical Review D* 101.12 (June 2020). ISSN: 2470-0029. DOI: 10.1103/physrevd.101.123021. URL: http://dx.doi.org/10.1103/PhysRevD.101.123021.

[123] Neil J Cornish and Jeff Crowder. "LISA data analysis using Markov chain Monte Carlo methods". In: *Physical Review D* 72.4 (2005), p. 043005.

[124] Kallol Dey et al. “The effect of data gaps on the detectability and parameter estimation of massive black hole binaries with LISA”. In: *arXiv preprint arXiv:2104.12646* (2021).

[125] Adam Smetana. “Background for gravitational wave signal at LISA from refractive index of solar wind plasma”. In: *Monthly Notices of the Royal Astronomical Society: Letters* 499.1 (Sept. 2020), pp. L77–L81. ISSN: 1745-3933. DOI: 10.1093/mnrasl/slaa155. URL: http://dx.doi.org/10.1093/mnrasl/slaa155.

[126] Barrett M Frank et al. “Spurious Acceleration Noise on the LISA Spacecraft due to Solar Activity”. In: *arXiv preprint arXiv:1912.07715* (2019).

[127] Quentin Baghi et al. “Gravitational-wave parameter estimation with gaps in LISA: a Bayesian data augmentation method”. In: *Physical Review D* 100.2 (2019), p. 022003.

[128] Sandrine Pires et al. “Dealing with missing data in the MICROSCOPE space mission: An adaptation of inpainting to handle colored-noise data”. In: *Physical Review D* 94.12 (2016), p. 123015.

[129] Quentin Baghi et al. “Gaussian regression and power spectral density estimation with missing data: The MICROSCOPE space mission as a case study”. In: *Physical Review D* 93.12 (2016), p. 122007.

[130] Aurore Blelly, Jérôme Bobin, and Hervé Moutarde. *Sparse data inpainting for the recovery of Galactic-binary gravitational wave signals from gapped data*. 2021. arXiv: 2104.05250 [gr-qc].

[131] Richard Arnowitt, Stanley Deser, and Charles W Misner. “Republication of: The dynamics of general relativity”. In: *General Relativity and Gravitation* 40.9 (2008), pp. 1997–2027.

[132] Manuela Campanelli et al. “Accurate evolutions of orbiting black-hole binaries without excision”. In: *Physical Review Letters* 96.11 (2006), p. 111101.

[133] John G Baker et al. “Gravitational-wave extraction from an inspiraling configuration of merging black holes”. In: *Physical review letters* 96.11 (2006), p. 111102.

[134] Carlos O Lousto and James Healy. “Exploring the Small Mass Ratio Binary Black Hole Merger via Zeno’s Dichotomy Approach”. In: *Physical Review Letters* 125.19 (2020), p. 191102.

[135] Carlos O Lousto and Yosef Zlochower. “Orbital evolution of extreme-mass-ratio black-hole binaries with numerical relativity”. In: *Physical review letters* 106.4 (2011), p. 041101.

[136] Clifford M Will. "On the unreasonable effectiveness of the post-Newtonian approximation in gravitational physics". In: *Proceedings of the National Academy of Sciences* 108.15 (2011), pp. 5938–5945.

[137] Michael Boyle et al. "High-accuracy comparison of numerical relativity simulations with post-Newtonian expansions". In: *Physical Review D* 76.12 (2007), p. 124038.

[138] Roy P Kerr. "Gravitational field of a spinning mass as an example of algebraically special metrics". In: *Physical review letters* 11.5 (1963), p. 237.

[139] Robert H Boyer and Richard W Lindquist. "Maximal analytic extension of the Kerr metric". In: *Journal of mathematical physics* 8.2 (1967), pp. 265–281.

[140] Charles W Misner, Kip S Thorne, John Archibald Wheeler, et al. *Gravitation*. Macmillan, 1973.

[141] Stephen W Hawking and George Francis Rayner Ellis. *The large scale structure of space-time*. Vol. 1. Cambridge university press, 1973.

[142] Subrahmanyan Chandrasekhar and Subrahmanyan Chandrasekhar. *The mathematical theory of black holes*. Vol. 69. Oxford university press, 1998.

[143] Robert M Wald. *General relativity*. University of Chicago press, 2010.

[144] Sean M Carroll. *Spacetime and geometry*. Cambridge University Press, 2019.

[145] Karl Schwarzschild. "Über das gravitationsfeld eines massenpunktes nach der einsteinschen theorie". In: *Sitzungsberichte der Königlich Preußischen Akademie der Wissenschaften (Berlin* (1916), pp. 189–196.

[146] Roger Penrose. "Gravitational collapse: The role of general relativity". In: *Nuovo Cimento Rivista Serie* 1 (1969), p. 252.

[147] James M. Bardeen and Gary T. Horowitz. "The Extreme Kerr throat geometry: A Vacuum analog of AdS(2) x S**2". In: *Phys. Rev. D* 60 (1999), p. 104030. DOI: 10.1103/PhysRevD.60.104030. arXiv: hep-th/9905099.

[148] Hari K. Kunduri, James Lucietti, and Harvey S. Reall. "Near-horizon symmetries of extremal black holes". In: *Class. Quant. Grav.* 24 (2007), pp. 4169–4190. DOI: 10.1088/0264-9381/24/16/012. arXiv: 0705.4214 [hep-th].

[149] Monica Guica et al. "The Kerr/CFT correspondence". In: *Physical Review D* 80.12 (Dec. 2009). ISSN: 1550-2368. DOI: 10.1103/physrevd.80.124008. URL: http://dx.doi.org/10.1103/PhysRevD.80.124008.

[150] Geoffrey Compère. "The Kerr/CFT correspondence and its extensions". In: *Living reviews in relativity* 20.1 (2017), pp. 1–101.

[151] Andrew Strominger and Cumrun Vafa. "Microscopic origin of the Bekenstein-Hawking entropy". In: *Physics Letters B* 379.1-4 (1996), pp. 99–104.

[152] S. E. Gralla, A. P. Porfyriadis, and N. Warburton. "Particle on the innermost stable circular orbit of a rapidly spinning black hole". In: *prd* 92.6, 064029 (Sept. 2015), p. 064029. DOI: 10.1103/PhysRevD.92.064029. arXiv: 1506.08496 [gr-qc].

[153] James Bardeen and Gary T Horowitz. "Extreme Kerr throat geometry: A vacuum analog of AdS 2× S 2". In: *Physical Review D* 60.10 (1999), p. 104030.

[154] Achilleas P Porfyriadis. "Near-

*AdS*_2

AdS2 perturbations and the connection with near-extreme Reissner–Nordstrom". In: *The European Physical Journal C* 79.10 (2019), pp. 1–7.

[155] Samuel E Gralla, Achilleas P Porfyriadis, and Niels Warburton. "Particle on the innermost stable circular orbit of a rapidly spinning black hole". In: *Physical Review D* 92.6 (2015), p. 064029.

[156] Achilleas P Porfyriadis and Andrew Strominger. "Gravity waves from the Kerr/CFT correspondence". In: *Physical Review D* 90.4 (2014), p. 044038.

[157] Alejandra Castro and Victor Godet. "Breaking away from the near horizon of extreme Kerr". In: *arXiv preprint arXiv:1906.09083* (2020).

[158] Oscar JC Dias, Harvey S Reall, and Jorge E Santos. "Kerr-CFT and gravitational perturbations". In: *Journal of High Energy Physics* 2009.08 (2009), p. 101.

[159] Alejandra Castro and Finn Larsen. "Near extremal Kerr entropy from AdS2 quantum gravity". In: *Journal of High Energy Physics* 2009.12 (2009), p. 037.

[160] E. Noether. "Invariante Variationsprobleme". ger. In: *Nachrichten von der Gesellschaft der Wissenschaften zu Göttingen, Mathematisch-Physikalische Klasse* 1918 (1918), pp. 235–257. URL: http://eudml.org/doc/59024.

[161] Brandon Carter. "Global structure of the Kerr family of gravitational fields". In: *Physical Review* 174.5 (1968), p. 1559.

[162] James M Bardeen, William H Press, and Saul A Teukolsky. "Rotating black holes: locally nonrotating frames, energy extraction, and scalar synchrotron radiation". In: *The Astrophysical Journal* 178 (1972), pp. 347–370.

[163] Amos Ori and Kip S Thorne. "Transition from inspiral to plunge for a compact body in a circular equatorial orbit around a massive, spinning black hole". In: *Physical Review D* 62.12 (2000), p. 124022.

[164] J. M. Bardeen, W. H. Press, and S. A. Teukolsky. "Rotating Black Holes: Locally Non-rotating Frames, Energy Extraction, and Scalar Synchrotron Radiation". In: *apj* 178 (Dec. 1972), pp. 347–370. DOI: 10.1086/151796.

[165] F Rohrlich. "The self-force and radiation reaction". In: *American Journal of Physics* 68.12 (2000), pp. 1109–1112.

[166] David J Griffiths. *Introduction to electrodynamics*. 2005.

[167] John David Jackson. *Classical electrodynamics*. 1999.

[168] Bence Kocsis, Nicolás Yunes, and Abraham Loeb. "Observable signatures of extreme mass-ratio inspiral black hole binaries embedded in thin accretion disks". In: *Physical Review D* 84.2 (July 2011). ISSN: 1550-2368. DOI: 10.1103/physrevd.84.024032. URL: http://dx.doi.org/10.1103/PhysRevD.84.024032.

[169] Enrico Barausse, Vitor Cardoso, and Paolo Pani. "Can environmental effects spoil precision gravitational-wave astrophysics?" In: *Physical Review D* 89.10 (May 2014). ISSN: 1550-2368. DOI: 10.1103/physrevd.89.104059. URL: http://dx.doi.org/10.1103/PhysRevD.89.104059.

[170] Yasushi Mino. "Perturbative approach to an orbital evolution around a supermassive black hole". In: *Physical Review D* 67.8 (2003), p. 084027.

[171] Tanja Hinderer and Eanna E Flanagan. "Two-timescale analysis of extreme mass ratio inspirals in Kerr spacetime: Orbital motion". In: *Physical Review D* 78.6 (2008), p. 064028.

[172] Wolfram Schmidt. "Celestial mechanics in Kerr spacetime". In: *Classical and Quantum Gravity* 19.10 (2002), p. 2743.

[173] Soichiro Isoyama et al. "Gravitational self-force correction to the innermost stable circular equatorial orbit of a Kerr black hole". In: *Physical review letters* 113.16 (2014), p. 161101.

[174] Ryuichi Fujita, Wataru Hikida, and Hideyuki Tagoshi. "An Efficient Numerical Method for Computing Gravitational Waves Induced by a Particle Moving on Eccentric Inclined Orbits around a Kerr Black Hole". In: *Prog. Theor. Phys.* 121 (2009), pp. 843–874. DOI: 10.1143/PTP.121.843. arXiv: 0904.3810 [gr-qc].

[175] Maarten Van De Meent. "Gravitational self-force on generic bound geodesics in Kerr spacetime". In: *Physical Review D* 97.10 (2018), p. 104033.

[176] Eran Rosenthal. "Second-order gravitational self-force". In: *Physical Review D* 74.8 (2006), p. 084018.

[177] Adam Pound. "Second-order gravitational self-force". In: *Physical review letters* 109.5 (2012), p. 051101.

[178] Adam Pound. "Nonlinear gravitational self-force: Field outside a small body". In: *Physical Review D* 86.8 (2012), p. 084019.

[179] Samuel D Upton and Adam Pound. "Second-order gravitational self-force in a highly regular gauge". In: *Physical Review D* 103.12 (2021), p. 124016.

[180] Adam Pound et al. "Second-Order Self-Force Calculation of Gravitational Binding Energy in Compact Binaries". In: *Physical review letters* 124.2 (2020), p. 021101.

[181] Niels Warburton et al. *Gravitational-wave energy flux for compact binaries through second order in the mass ratio*. 2021. arXiv: 2107.01298 [gr-qc].

[182] Maarten van de Meent and Harald P Pfeiffer. "Intermediate mass-ratio black hole binaries: Applicability of small mass-ratio perturbation theory". In: *Physical Review Letters* 125.18 (2020), p. 181101.

[183] Maarten van de Meent. "Conditions for sustained orbital resonances in extreme mass ratio inspirals". In: *Physical Review D* 89.8 (2014), p. 084033.

[184] Béatrice Bonga, Huan Yang, and Scott A Hughes. "Tidal resonance in extreme mass-ratio inspirals". In: *Physical review letters* 123.10 (2019), p. 101103.

[185] Eanna E Flanagan, Scott A Hughes, and Uchupol Ruangsri. "Resonantly enhanced and diminished strong-field gravitational-wave fluxes". In: *Physical Review D* 89.8 (2014), p. 084028.

[186] Rebecca Grossman, Janna Levin, and Gabe Perez-Giz. "Faster computation of adiabatic extreme mass-ratio inspirals using resonances". In: *Physical Review D* 88.2 (2013), p. 023002.

[187] Christopher PL Berry et al. "Importance of transient resonances in extreme-mass-ratio inspirals". In: *Physical Review D* 94.12 (2016), p. 124042.

[188] Lorenzo Speri and Jonathan R Gair. "Assessing the impact of transient orbital resonances". In: *arXiv preprint arXiv:2103.06306* (2021).

[189] Saul A. Teukolsky. "Perturbations of a Rotating Black Hole. I. Fundamental Equations for Gravitational, Electromagnetic, and Neutrino-Field Perturbations". In: 185 (Oct. 1973), pp. 635–648. DOI: 10.1086/152444.

[190] Hermann Weyl. "Reine infinitesimalgeometrie". In: *Mathematische Zeitschrift* 2.3-4 (1918), pp. 384–411.

[191] William Kinnersley. "Type D vacuum metrics". In: *Journal of Mathematical Physics* 10.7 (1969), pp. 1195–1203.

[192] Ezra Newman and Roger Penrose. "An approach to gravitational radiation by a method of spin coefficients". In: *Journal of Mathematical Physics* 3.3 (1962), pp. 566–578.

[193] Emanuele Berti, Vitor Cardoso, and Marc Casals. "Eigenvalues and eigenfunctions of spin-weighted spheroidal harmonics in four and higher dimensions". In: *Physical Review D* 73.2 (2006), p. 024013.

[194] Scott A Hughes. "Evolution of circular, nonequatorial orbits of Kerr black holes due to gravitational-wave emission". In: *Physical Review D* 61.8 (2000), p. 084004.

[195] Reinhard A Breuer, Michael P Ryan, and Sergio Waller. "Some properties of spin-weighted spheroidal harmonics". In: *Proceedings of the Royal Society of London. A. Mathematical and Physical Sciences* 358.1692 (1977), pp. 71–86.

[196] Saul A Teukolsky and WH Press. "Perturbations of a rotating black hole. III-Interaction of the hole with gravitational and electromagnetic radiation". In: *The Astrophysical Journal* 193 (1974), pp. 443–461.

[197] Daniel Kennefick. "Stability under radiation reaction of circular equatorial orbits around Kerr black holes". In: *Physical Review D* 58.6 (1998), p. 064012.

[198] P Szekeres. "The gravitational compass". In: *Journal of Mathematical Physics* 6.9 (1965), pp. 1387–1391.

[199] Richard A Isaacson. "Gravitational radiation in the limit of high frequency. II. Nonlinear terms and the effective stress tensor". In: *Physical Review* 166.5 (1968), p. 1272.

[200] Michele Maggiore. *Gravitational waves: Volume 1: Theory and experiments*. Vol. 1. Oxford university press, 2008.

[201] Stephen W Hawking and JB Hartle. "Energy and angular momentum flow into a black hole". In: *Communications in mathematical physics* 27.4 (1972), pp. 283–290.

[202] Theocharis Apostolatos et al. “Gravitational radiation from a particle in circular orbit around a black hole. III. Stability of circular orbits under radiation reaction”. In: *Phys. Rev. D* 47.12 (1993), p. 5376.

[203] Daniel Kennefick. “Stability under radiation reaction of circular equatorial orbits around Kerr black holes”. In: *prd* 58.6, 064012 (Sept. 1998), p. 064012. DOI: 10.1103/PhysRevD.58.064012. arXiv: gr-qc/9805102 [gr-qc].

[204] *Black Hole Perturbation Toolkit*. bhptoolkit.org.

[205] G. Compère et al. “Gravitational waves from plunges into Gargantua”. In: *Classical and Quantum Gravity* 35.10, 104002 (May 2018), p. 104002. DOI: 10.1088/1361-6382/aab99e. arXiv: 1712.07130 [gr-qc].

[206] Achilleas P. Porfyriadis and Andrew Strominger. “Gravity waves from the Kerr/CFT correspondence”. In: *Phys. Rev.* D90.4 (2014), p. 044038. DOI: 10.1103/PhysRevD.90.044038. arXiv: 1401.3746 [hep-th].

[207] Shahar Hadar, Achilleas P. Porfyriadis, and Andrew Strominger. “Gravity Waves from Extreme-Mass-Ratio Plunges into Kerr Black Holes”. In: *Phys. Rev.* D90.6 (2014), p. 064045. DOI: 10.1103/PhysRevD.90.064045. arXiv: 1403.2797 [hep-th].

[208] Shahar Hadar, Achilleas P. Porfyriadis, and Andrew Strominger. “Fast plunges into Kerr black holes”. In: *JHEP* 07 (2015), p. 078. DOI: 10.1007/JHEP07(2015)078. arXiv: 1504.07650 [hep-th].

[209] Maurice HPM Van Putten. “Near-extremal Black Holes as Initial Conditions of Long GRB Supernovae and Probes of Their Gravitational Wave Emission”. In: *The Astrophysical Journal* 810.1 (2015), p. 7.

[210] Shahar Hadar and Achilleas P. Porfyriadis. “Whirling orbits around twirling black holes from conformal symmetry”. In: *JHEP* 03 (2017), p. 014. DOI: 10.1007/JHEP03(2017)014. arXiv: 1611.09834 [hep-th].

[211] S. E. Gralla, S. A. Hughes, and N. Warburton. “Inspiral into Gargantua”. In: *Classical and Quantum Gravity* 33.15, 155002 (Aug. 2016), p. 155002. DOI: 10.1088/0264-9381/33/15/155002. arXiv: 1603.01221 [gr-qc].

[212] K. Chatziioannou et al. “Measuring the properties of nearly extremal black holes with gravitational waves”. In: *ArXiv e-prints* (Apr. 2018). arXiv: 1804.03704 [gr-qc].

[213] Geoffrey Compère et al. “Gravitational waves from plunges into Gargantua”. In: *Classical and Quantum Gravity* 35.10 (2018), p. 104002.

[214] Maarten van de Meent and Niels Warburton. "Fast self-forced inspirals". In: *Classical and Quantum Gravity* 35.14 (2018), p. 144003.

[215] Charles Delaunay. *Théorie du Mouvement de la Lune*. Vol. 2. Mallet-Bachelier, 1867.

[216] H von Zeipel. *Recherches sur le mouvement des petites planètes*. Almqvist & Wiksells Boklvyekevi-AB, 1921.

[217] Claude Elwood Shannon. "Communication in the presence of noise". In: *Proceedings of the IRE* 37.1 (1949), pp. 10–21.

[218] James W Cooley and John W Tukey. "An algorithm for the machine calculation of complex Fourier series". In: *Mathematics of computation* 19.90 (1965), pp. 297–301.

[219] Fredric J Harris. "On the use of windows for harmonic analysis with the discrete Fourier transform". In: *Proceedings of the IEEE* 66.1 (1978), pp. 51–83.

[220] William H Press et al. *Numerical recipes 3rd edition: The art of scientific computing*. Cambridge university press, 2007.

[221] Norbert Wiener et al. "Generalized harmonic analysis". In: *Acta mathematica* 55 (1930), pp. 117–258.

[222] Alexander Khintchine. "Korrelationstheorie der stationären stochastischen Prozesse". In: *Mathematische Annalen* 109.1 (1934), pp. 604–615.

[223] Bernard Picinbono. "Second-order complex random vectors and normal distributions". In: *IEEE Transactions on Signal Processing* 44.10 (1996), pp. 2637–2640.

[224] Curt Cutler and Eanna E Flanagan. "Gravitational waves from merging compact binaries: How accurately can one extract the binary's parameters from the inspiral waveform?" In: *Physical Review D* 49.6 (1994), p. 2658.

[225] P. Whittle. "Curve and periodogram smoothing". In: *Journal of the Royal Statistical Society: Series B (Statistical Methodology)* 19 (1957), pp. 38–63.

[226] N. Cornish and T. Robson. "The construction and use of LISA sensitivity curves". In: *ArXiv e-prints* (Mar. 2018). arXiv: 1803.01944 [astro-ph.HE].

[227] Philip M Woodward. *Probability and information theory, with applications to radar: international series of monographs on electronics and instrumentation*. Vol. 3. Elsevier, 2014.

[228] George Turin. "An introduction to matched filters". In: *IRE transactions on Information theory* 6.3 (1960), pp. 311–329.

[229] Linqing Wen and Jonathan R Gair. "Detecting extreme mass ratio inspirals with LISA using time–frequency methods". In: *Classical and Quantum Gravity* 22.10 (2005), S445.

[230] Jonathan R Gair, Ilya Mandel, and Linqing Wen. "Improved time–frequency analysis of extreme-mass-ratio inspiral signals in mock LISA data". In: *Classical and Quantum Gravity* 25.18 (2008), p. 184031.

[231] Jonathan R Gair et al. "A constrained Metropolis–Hastings search for EMRIs in the mock LISA data challenge 1b". In: *Classical and Quantum Gravity* 25.18 (2008), p. 184030.

[232] Yadolah Dodge. *The Oxford dictionary of statistical terms*. Oxford University Press on Demand, 2006.

[233] Harald Cramér. *Mathematical Methods of Statistics (PMS-9), Volume 9*. Princeton university press, 2016.

[234] C Radhakrishna Rao. "Information and the accuracy attainable in the estimation of statistical parameters". In: *Breakthroughs in statistics*. Springer, 1992, pp. 235–247.

[235] Bengt Fornberg. "Generation of finite difference formulas on arbitrarily spaced grids". In: *Mathematics of computation* 51.184 (1988), pp. 699–706.

[236] Edward K Porter and Neil J Cornish. "Fisher versus Bayes: A comparison of parameter estimation techniques for massive black hole binaries to high redshifts with eLISA". In: *Physical Review D* 91.10 (2015), p. 104001.

[237] Edward K Porter. "An Overview of LISA Data Analysis Algorithms". In: *arXiv preprint arXiv:0910.0373* (2009).

[238] Michele Vallisneri. "Use and abuse of the Fisher information matrix in the assessment of gravitational-wave parameter-estimation prospects". In: *Physical Review D* 77.4 (2008), p. 042001.

[239] Pau Amaro-Seoane. "Relativistic dynamics and extreme mass ratio inspirals". In: *Living reviews in relativity* 21.1 (2018), p. 4.

[240] Carl L Rodriguez, Ilya Mandel, and Jonathan R Gair. "Verifying the no-hair property of massive compact objects with intermediate-mass-ratio inspirals in advanced gravitational-wave detectors". In: *Physical Review D* 85.6 (2012), p. 062002.

[241] Fredrik Johansson et al. *mpmath: a Python library for arbitrary-precision floating-point arithmetic (version 0.18)*. `http://mpmath.org/`. Dec. 2013.

[242] Lee Lindblom, Benjamin J Owen, and Duncan A Brown. "Model waveform accuracy standards for gravitational wave data analysis". In: *Physical Review D* 78.12 (2008), p. 124020.

[243] Eanna E. Flanagan and Scott A. Hughes. "Measuring gravitational waves from binary black hole coalescences: 2. The Waves' information and its extraction, with and without templates". In: *Phys. Rev. D* 57 (1998), pp. 4566–4587. DOI: 10.1103/PhysRevD.57.4566. arXiv: gr-qc/9710129.

[244] Mark Miller. "Accuracy requirements for the calculation of gravitational waveforms from coalescing compact binaries in numerical relativity". In: *Phys. Rev. D* 71 (10 May 2005), p. 104016. DOI: 10.1103/PhysRevD.71.104016. URL: https://link.aps.org/doi/10.1103/PhysRevD.71.104016.

[245] Michael Pürrer and Carl-Johan Haster. "Gravitational waveform accuracy requirements for future ground-based detectors". In: *Physical Review Research* 2.2 (2020), p. 023151.

[246] Curt Cutler and Michele Vallisneri. "LISA detections of massive black hole inspirals: Parameter extraction errors due to inaccurate template waveforms". In: *Physical Review D* 76.10 (2007), p. 104018.

[247] Andrew Gelman et al. *Bayesian data analysis*. CRC press, 2013.

[248] Walter R Gilks. "M arkov Chain M onte C arlo". In: *Encyclopedia of biostatistics* 4 (2005).

[249] Edwin T Jaynes. *Probability theory: The logic of science*. Cambridge university press, 2003.

[250] John G Kemeny and J Laurie Snell. *Markov chains*. Vol. 6. Springer-Verlag, New York, 1976.

[251] Nicholas Metropolis et al. "Equation of state calculations by fast computing machines". In: *The journal of chemical physics* 21.6 (1953), pp. 1087–1092.

[252] W Keith Hastings. "Monte Carlo sampling methods using Markov chains and their applications". In: (1970).

[253] Andrew Gelman, Walter R Gilks, and Gareth O Roberts. "Weak convergence and optimal scaling of random walk Metropolis algorithms". In: *The annals of applied probability* 7.1 (1997), pp. 110–120.

[254] A. Ori and K. S. Thorne. "Transition from inspiral to plunge for a compact body in a circular equatorial orbit around a massive, spinning black hole". In: *prd* 62.12, 124022 (Dec. 2000), p. 124022. DOI: 10.1103/PhysRevD.62.124022. eprint: gr-qc/0003032.

[255] Alessandra Buonanno and Thibault Damour. "Transition from inspiral to plunge in binary black hole coalescences". In: *Physical Review D* 62.6 (2000), p. 064015.

[256] Michael Kesden. "Transition from adiabatic inspiral to plunge into a spinning black hole". In: *Phys. Rev. D* 83.10 (2011), p. 104011.

[257] Yasushi Mino. "Perturbative approach to an orbital evolution around a supermassive black hole". In: *Phys. Rev.* D67 (2003), p. 084027. DOI: 10.1103/PhysRevD.67.084027. arXiv: gr-qc/0302075 [gr-qc].

[258] Leor Barack. "Gravitational self-force in extreme mass-ratio inspirals". In: *Classical and Quantum Gravity* 26.21 (2009), p. 213001.

[259] Maarten Van De Meent. "Self-force corrections to the periapsis advance around a spinning black hole". In: *Physical review letters* 118.1 (2017), p. 011101.

[260] E. Poisson, A. Pound, and I. Vega. "The motion of point particles in curved spacetime". In: *ArXiv e-prints* (Feb. 2011). arXiv: 1102.0529 [gr-qc].

[261] Kostas Glampedakis and Daniel Kennefick. "Zoom and whirl: Eccentric equatorial orbits around spinning black holes and their evolution under gravitational radiation reaction". In: *prd* 66.4, 044002 (Aug. 2002), p. 044002. DOI: 10.1103/PhysRevD.66.044002. arXiv: gr-qc/0203086 [gr-qc].

[262] Ted Jacobson. "Where is the extremal Kerr ISCO?" In: *Class. Quant. Grav.* 28 (2011), p. 187001. DOI: 10.1088/0264-9381/28/18/187001. arXiv: 1107.5081 [gr-qc].

[263] Samuel E. Gralla, Achilleas P. Porfyriadis, and Niels Warburton. "Particle on the Innermost Stable Circular Orbit of a Rapidly Spinning Black Hole". In: *Phys. Rev.* D92.6 (2015), p. 064029. DOI: 10.1103/PhysRevD.92.064029. arXiv: 1506.08496 [gr-qc].

[264] Anuj Apte and Scott A Hughes. "Exciting black hole modes via misaligned coalescences: I. Inspiral, transition, and plunge trajectories using a generalized Ori-Thorne procedure". In: *arXiv preprint arXiv:1901.05901* (2019).

[265] Pranesh A Sundararajan. "Transition from adiabatic inspiral to geodesic plunge for a compact object around a massive Kerr black hole: Generic orbits". In: *Physical Review D* 77.12 (2008), p. 124050.

[266] Geoffrey Compère, Kwinten Fransen, and Caroline Jonas. "Transition from inspiral to plunge into a highly spinning black hole". In: *arXiv e-prints*, arXiv:1909.12848 (Sept. 2019), arXiv:1909.12848. arXiv: 1909.12848 [gr-qc].

[267] Andrea Taracchini et al. "Small mass plunging into a Kerr black hole: Anatomy of the inspiral-merger-ringdown waveforms". In: *prd* 90.8, 084025 (Oct. 2014), p. 084025. DOI: 10.1103/PhysRevD.90.084025. arXiv: 1404.1819 [gr-qc].

[268] Huan Yang et al. "Quasinormal modes of nearly extremal Kerr spacetimes: spectrum bifurcation and power-law ringdown". In: *Phys. Rev.* D88.4 (2013). [Phys. Rev.D88,044047(2013)], p. 044047. DOI: 10.1103/PhysRevD.88.044047. arXiv: 1307.8086 [gr-qc].

[269] G Risaliti et al. "A rapidly spinning supermassive black hole at the centre of NGC 1365". In: *Nature* 494.7438 (2013), p. 449.

[270] Benny Trakhtenbrot. "The Most Massive Active Black Holes at z 1.5-3.5 Have High Spins and Radiative Efficiencies". In: *The Astrophysical Journal Letters* 789.1 (2014), p. L9.

[271] Jeffrey E McClintock et al. "The spin of the near-extreme Kerr black hole GRS 1915+ 105". In: *The Astrophysical Journal* 652.1 (2006), p. 518.

[272] Lijun Gou et al. "The extreme spin of the black hole in Cygnus X-1". In: *The Astrophysical Journal* 742.2 (2011), p. 85.

[273] K. S. Thorne. "Disk-Accretion onto a Black Hole. II. Evolution of the Hole". In: *apj* 191 (July 1974), pp. 507–520. DOI: 10.1086/152991.

[274] Alexandre Arbey, Jérémy Auffinger, and Joseph Silk. "Evolution of primordial black hole spin due to Hawking radiation". In: *Monthly Notices of the Royal Astronomical Society* 494.1 (2020), pp. 1257–1262.

[275] Yuri Levin. "Starbursts near supermassive black holes: young stars in the Galactic Center, and gravitational waves in LISA band". In: *Mon. Not. Roy. Astron. Soc.* 374 (2007), pp. 515–524. DOI: 10.1111/j.1365-2966.2006.11155.x. arXiv: astro-ph/0603583.

[276] Aleksander Skadowski et al. "Spinning up black holes with super-critical accretion flows". In: *Astronomy & Astrophysics* 532 (2011), A41.

[277] Philip C Peters and Jon Mathews. "Gravitational radiation from point masses in a Keplerian orbit". In: *Physical Review* 131.1 (1963), p. 435.

[278] Kostas Glampedakis and Daniel Kennefick. “Zoom and whirl: Eccentric equatorial orbits around spinning black holes and their evolution under gravitational radiation reaction”. In: *Physical Review D* 66.4 (2002), p. 044002.

[279] Gerardo F Torres del Castillo. *3-D spinors, spin-weighted functions and their applications*. Vol. 32. Springer Science & Business Media, 2003.

[280] Curt Cutler. “Angular resolution of the LISA gravitational wave detector”. In: *Physical Review D* 57.12 (1998), p. 7089.

[281] Neil J Cornish and Louis J Rubbo. “LISA response function”. In: *Physical Review D* 67.2 (2003), p. 022001.

[282] Ollie Burke, Jonathan R. Gair, and Joan Simón. “Transition from Inspiral to Plunge: A Complete Near-Extremal Trajectory and Associated Waveform”. In: *Phys. Rev. D* 101.6 (2020), p. 064026. DOI: 10.1103/PhysRevD.101.064026. arXiv: 1909.12846 [gr-qc].

[283] Geoffrey Compère, Kwinten Fransen, and Caroline Jonas. *Transition from inspiral to plunge into a highly spinning black hole*. 2019. arXiv: 1909.12848 [gr-qc].

[284] Geoffrey Compère, Kwinten Fransen, and Caroline Jonas. “Transition from inspiral to plunge into a highly spinning black hole”. In: *arXiv preprint arXiv:1909.12848* (2019).

[285] Gabriel Andres Piovano et al. “Assessing the detectability of the secondary spin in extreme mass-ratio inspirals with fully-relativistic numerical waveforms”. In: *arXiv preprint arXiv:2105.07083* (2021).

[286] Gabriel Andres Piovano, Andrea Maselli, and Paolo Pani. “Model independent tests of the Kerr bound with extreme mass ratio inspirals”. In: *Physics Letters B* 811 (2020), p. 135860.

[287] Gabriel Andres Piovano, Andrea Maselli, and Paolo Pani. “Extreme mass ratio inspirals with spinning secondary: a detailed study of equatorial circular motion”. In: *Physical Review D* 102.2 (2020), p. 024041.

[288] EA Huerta, Jonathan R Gair, and Duncan A Brown. “Importance of including small body spin effects in the modelling of intermediate mass-ratio inspirals. II. Accurate parameter extraction of strong sources using higher-order spin effects”. In: *Physical Review D* 85.6 (2012), p. 064023.

[289] EA Huerta and Jonathan R Gair. “Importance of including small body spin effects in the modelling of extreme and intermediate mass-ratio inspirals”. In: *Physical Review D* 84.6 (2011), p. 064023.

[290] Niels Warburton et al. “Evolution of inspiral orbits around a Schwarzschild black hole”. In: *Physical Review D* 85.6 (2012), p. 061501.

[291] Niels Warburton, Thomas Osburn, and Charles R Evans. “Evolution of small-mass-ratio binaries with a spinning secondary”. In: *Physical Review D* 96.8 (2017), p. 084057.

[292] Thomas Osburn, Niels Warburton, and Charles R Evans. “Highly eccentric inspirals into a black hole”. In: *Physical Review D* 93.6 (2016), p. 064024.

[293] Tanja Hinderer and Eanna E. Flanagan. “Two timescale analysis of extreme mass ratio inspirals in Kerr. I. Orbital Motion”. In: *Phys. Rev. D* 78 (2008), p. 064028. DOI: 10.1103/PhysRevD.78.064028. arXiv: 0805.3337 [gr-qc].

[294] Charles Galton Darwin. “The gravity field of a particle”. In: *Proceedings of the Royal Society of London. Series A. Mathematical and Physical Sciences* 249.1257 (1959), pp. 180–194.

[295] Charles Galton Darwin. “The gravity field of a particle. II”. In: *Proceedings of the Royal Society of London. Series A. Mathematical and Physical Sciences* 263.1312 (1961), pp. 39–50.

[296] Adam Pound and Eric Poisson. “Osculating orbits in Schwarzschild spacetime, with an application to extreme mass-ratio inspirals”. In: *Phys. Rev. D* 77.4 (2008), p. 044013.

[297] Jonathan R Gair, Daniel J Kennefick, and Shane L Larson. “Semirelativistic approximation to gravitational radiation from encounters with nonspinning black holes”. In: *Physical Review D* 72.8 (2005), p. 084009.

[298] Seth Hopper, Chris Kavanagh, and Adrian C Ottewill. “Analytic self-force calculations in the post-Newtonian regime: eccentric orbits on a Schwarzschild background”. In: *Physical Review D* 93.4 (2016), p. 044010.

[299] Jeff Crowder and Neil J. Cornish. “Solution to the galactic foreground problem for LISA”. In: *Physical Review D* 75.4 (Feb. 2007). ISSN: 1550-2368. DOI: 10.1103/physrevd.75.043008. URL: http://dx.doi.org/10.1103/PhysRevD.75.043008.

[300] Arkadiusz Błaut, Stanislav Babak, and Andrzej Królak. “Mock LISA data challenge for the Galactic white dwarf binaries”. In: *Physical Review D* 81.6 (Mar. 2010). ISSN: 1550-2368. DOI: 10.1103/physrevd.81.063008. URL: http://dx.doi.org/10.1103/PhysRevD.81.063008.

[301] Elinore Roebber et al. “Milky Way Satellites Shining Bright in Gravitational Waves”. In: *Astrophys. J. Lett.* 894.2 (2020), p. L15. DOI: 10.3847/2041-8213/ab8ac9. arXiv: 2002.10465 [astro-ph.GA].

[302] Valeriya Korol et al. “Weighing Milky Way Satellites with LISA”. In: (Oct. 2020). DOI: 10.1093/mnrasl/slab003. arXiv: 2010.05918 [astro-ph.GA].

[303] Anuradha Samajdar et al. “Biases in parameter estimation from overlapping gravitational-wave signals in the third generation detector era”. In: (Feb. 2021). arXiv: 2102.07544 [gr-qc].

[304] Elia Pizzati et al. “Bayesian inference of overlapping gravitational wave signals”. In: (Feb. 2021). arXiv: 2102.07692 [gr-qc].

[305] Nikolaos Karnesis et al. “Characterization of the stochastic signal originating from compact binaries populations as measured by LISA”. In: (Mar. 2021). arXiv: 2103.14598 [astro-ph.IM].

[306] David Coward and Tania Regimbau. “Detection regimes of the cosmological gravitational wave background from astrophysical sources”. In: *New Astronomy Reviews* 50.6 (2006), pp. 461–467.

[307] Bruce Allen et al. “FINDCHIRP: An Algorithm for detection of gravitational waves from inspiraling compact binaries”. In: *Phys. Rev. D* 85 (2012), p. 122006. DOI: 10.1103/PhysRevD.85.122006. arXiv: gr-qc/0509116.

[308] Curt Cutler and Michele Vallisneri. “LISA detections of massive black hole inspirals: Parameter extraction errors due to inaccurate template waveforms”. In: *Phys. Rev. D* 76 (2007), p. 104018. DOI: 10.1103/PhysRevD.76.104018. arXiv: 0707.2982 [gr-qc].

[309] Emanuele Berti, Alessandra Buonanno, and Clifford M. Will. “Estimating spinning binary parameters and testing alternative theories of gravity with LISA”. In: *Phys. Rev. D* 71 (2005), p. 084025. DOI: 10.1103/PhysRevD.71.084025. arXiv: gr-qc/0411129.

[310] Tania Regimbau et al. “Mock data challenge for the einstein gravitational-wave telescope”. In: *Physical Review D* 86.12 (2012), p. 122001.

[311] Jonathan R. Gair et al. “Constraining properties of the black hole population using LISA”. In: *Class. Quant. Grav.* 28 (2011). Ed. by William Trischuk, p. 094018. DOI: 10.1088/0264-9381/28/9/094018. arXiv: 1009.6172 [gr-qc].

[312] Jonathan R. Gair, Christopher Tang, and Marta Volonteri. "LISA extreme-mass-ratio inspiral events as probes of the black hole mass function". In: *Phys. Rev. D* 81 (2010), p. 104014. DOI: 10.1103/PhysRevD.81.104014. arXiv: 1004.1921 [astro-ph.GA].

[313] Alberto Sesana et al. "Reconstructing the massive black hole cosmic history through gravitational waves". In: *Phys. Rev. D* 83 (2011), p. 044036. DOI: 10.1103/PhysRevD.83.044036. arXiv: 1011.5893 [astro-ph.CO].

[314] Jenny E. Greene and Luis C. Ho. "The Mass Function of Active Black Holes in the Local Universe". In: *Astrophys. J.* 667 (2007). [Erratum: Astrophys.J. 704, 1743–1747 (2009)], pp. 131–148. DOI: 10.1088/0004-637X/704/2/1743. arXiv: 0705.0020 [astro-ph].

[315] B.S. Sathyaprakash and B.F. Schutz. "Physics, Astrophysics and Cosmology with Gravitational Waves". In: *Living Rev. Rel.* 12 (2009), p. 2. DOI: 10.12942/lrr-2009-2. arXiv: 0903.0338 [gr-qc].

[316] Yoshiaki Himemoto, Atsushi Nishizawa, and Atsushi Taruya. "Impacts of overlapping gravitational-wave signals on the parameter estimation: Toward the search for cosmological backgrounds". In: (Mar. 2021). arXiv: 2103.14816 [gr-qc].

[317] Philip Relton and Vivien Raymond. "Parameter Estimation Bias From Overlapping Binary Black Hole Events In Second Generation Interferometers". In: (Mar. 2021). arXiv: 2103.16225 [gr-qc].

[318] Rory Smith et al. "Bayesian inference for gravitational waves from binary neutron star mergers in third-generation observatories". In: (Mar. 2021). arXiv: 2103.12274 [gr-qc].

[319] J. Veitch et al. "Parameter estimation for compact binaries with ground-based gravitational-wave observations using the LALInference software library". In: *Phys. Rev. D* 91.4 (2015), p. 042003. DOI: 10.1103/PhysRevD.91.042003. arXiv: 1409.7215 [gr-qc].

[320] Gregory Ashton et al. "BILBY: A user-friendly Bayesian inference library for gravitational-wave astronomy". In: *Astrophys. J. Suppl.* 241.2 (2019), p. 27. DOI: 10.3847/1538-4365/ab06fc. arXiv: 1811.02042 [astro-ph.IM].

[321] O Edy, A. Lundgren, and L. K. Nuttall. *The Issues of Mismodelling Gravitational-Wave Data for Parameter Estimation*. 2021. arXiv: 2101.07743 [astro-ph.IM].

[322] Jérôme Carré and Edward K Porter. "The effect of data gaps on LISA galactic binary parameter estimation". In: *arXiv preprint arXiv:1010.1641* (2010).

[323] Quentin Baghi et al. "Gravitational-wave parameter estimation with gaps in LISA: A Bayesian data augmentation method". In: *Physical Review D* 100.2 (July 2019). ISSN: 2470-0029. DOI: 10.1103/physrevd.100.022003. URL: http://dx.doi.org/10.1103/PhysRevD.100.022003.

[324] Roger A Horn and Charles R Johnson. *Matrix analysis*. Cambridge university press, 2012.

Appendix A

Transition from Inspiral to Plunge

A.1 The innermost stable circular orbit

In this appendix we review the main properties of the function $G(\tilde{r}, \tilde{E}, \tilde{L})$ determining the radial geodesic (2.5a)

$$G(\tilde{r}, \tilde{E}, \tilde{L}) = \tilde{E}^2 - 1 + \frac{a^2(\tilde{E}^2 - 1) - \tilde{L}^2}{\tilde{r}^2} + \frac{2(a\tilde{E} - \tilde{L})^2}{\tilde{r}^3} + \frac{2}{\tilde{r}}, \tag{A.1}$$

together with its derivatives when evaluated at the ISCO orbit $\tilde{r}_{\rm isco}$. The spin dependence of these quantities will play a critical role in the identification of the different transition regimes discussed in section 4.2.

Remember the ISCO radial coordinate $\tilde{r}_{\rm isco}$ is characterised by marginal stability

$$G(\tilde{r}, \tilde{E}_{\rm isco}, \tilde{L}_{\rm isco}) = \left.\frac{\partial G}{\partial \tilde{r}}\right|_{\rm isco} = \left.\frac{\partial^2 G}{\partial \tilde{r}^2}\right|_{\rm isco} = 0\,. \tag{A.2}$$

Labelling the energy and angular momentum of the ISCO orbit by $\tilde{E}_{\rm isco}$ and $\tilde{L}_{\rm isco}$, we can solve the second and third constraint equations by

$$\begin{aligned} \tilde{L}_{\rm isco} &= \frac{\tilde{r}_{\rm isco}^2 - 3a^2 + 6\tilde{r}_{\rm isco}}{2\sqrt{3}\,\tilde{r}_{\rm isco}}\,, \\ \tilde{E}_{\rm isco} &= \frac{6\tilde{r}_{\rm isco} - 3a^2 - \tilde{r}_{\rm isco}^2}{2\sqrt{3}\,a\,\tilde{r}_{\rm isco}}\,. \end{aligned} \tag{A.3}$$

Plugging these into $G(\tilde{r}_{\rm isco},\tilde{E}_{\rm isco},\tilde{L}_{\rm isco})=0$, one derives the relation

$$\frac{2}{3\tilde{r}_{\rm isco}}=1-\tilde{E}^2_{\rm isco}\,, \tag{A.4}$$

which combined with (A.3) yields

$$\tilde{r}^2_{\rm isco}-6\tilde{r}_{\rm isco}+8a\sqrt{\tilde{r}_{\rm isco}}-3a^2=0\,, \tag{A.5}$$

whose solution $r_0(a)$ reproduces (2.18) [164]. This equality allows to simplify the energy (2.8a) and angular momentum (2.8b) of equatorial circular orbits when evaluated at ISCO to

$$\tilde{E}_{\rm isco}=\frac{1-2/\tilde{r}_{\rm isco}+a/\tilde{r}^{3/2}_{\rm isco}}{\sqrt{1-3/\tilde{r}_{\rm isco}+2a/\tilde{r}^{3/2}_{\rm isco}}}=\frac{4\sqrt{\tilde{r}_{\rm isco}}-3a}{\sqrt{3\tilde{r}_{\rm isco}}} \tag{A.6}$$

$$\tilde{L}_{\rm isco}=\tilde{r}^{1/2}\frac{1-2a/\tilde{r}^{3/2}+a^2/\tilde{r}^2}{\sqrt{1-3/\tilde{r}+2a/r^{3/2}}}=2\sqrt{3}-\frac{4a}{\sqrt{3\tilde{r}_{\rm isco}}}\,. \tag{A.7}$$

Armed with these identities, we move towards the evaluation of the derivatives controlling the expansions (4.16) relevant to the transition regime. First, we introduce some notation

$$\begin{aligned}
A_n&=\frac{\partial^n G}{\partial\tilde{r}^n}\Big|_{\rm isco}\,,\\
B_n&=\left(\frac{\partial^{n+1}G}{\partial\tilde{r}^n\partial\tilde{E}}\tilde{\Omega}+\frac{\partial^{n+1}G}{\partial\tilde{r}^n\partial\tilde{L}}\right)_{\rm isco}\,,\\
C_n&=\left(\frac{\partial^{n+2}G}{\partial\tilde{r}^n\partial\tilde{E}^2}\tilde{\Omega}^2+2\frac{\partial^{n+2}G}{\partial\tilde{r}^n\partial\tilde{L}\partial\tilde{E}}\tilde{\Omega}+\frac{\partial^{n+2}G}{\partial\tilde{r}^n\partial\tilde{L}^2}\right)_{\rm isco}
\end{aligned} \tag{A.8}$$

with $\tilde{\Omega}$ as in(2.10). Either by explicit calculation or by induction, one can prove for any integer $n\geq 0$

$$\begin{aligned}
\frac{\partial^n G}{\partial\tilde{r}^n}&=(-1)^n\left(\frac{(n+2)!(a\tilde{E}-\tilde{L})^2}{\tilde{r}^{n+3}}+\frac{(n+1)!(a^2(\tilde{E}^2-1)-\tilde{L}^2)}{\tilde{r}^{n+2}}+\frac{2n!}{\tilde{r}^{n+1}}\right)-\delta_{n0}(1-\tilde{E}^2)\,,\\
\frac{\partial^{n+1}G}{\partial\tilde{r}^n\partial\tilde{E}}&=(-1)^n\left(\frac{2(n+2)!(a^2\tilde{E}-a\tilde{L})}{\tilde{r}^{n+3}}+\frac{2(n+1)!a^2\tilde{E}}{\tilde{r}^{n+2}}\right)+2\delta_{n0}\tilde{E}\,,\\
\frac{\partial^{n+1}G}{\partial\tilde{r}^n\partial\tilde{L}}&=-(-1)^n\left(\frac{2(n+2)!(a\tilde{E}-\tilde{L})}{\tilde{r}^{n+3}}+\frac{2(n+1)!\tilde{L}}{\tilde{r}^{n+2}}\right)\,,\\
\frac{\partial^{n+2}G}{\partial\tilde{r}^n\partial\tilde{L}^2}&=(-1)^n\left(\frac{2(n+2)!}{\tilde{r}^{n+3}}-\frac{2(n+1)!}{\tilde{r}^{n+2}}\right)\,,\\
\frac{\partial^{n+2}G}{\partial\tilde{r}^n\partial\tilde{L}\partial\tilde{E}}&=-(-1)^n\left(\frac{2a(n+2)!}{\tilde{r}^{n+3}}\right)\,,\\
\frac{\partial^{n+2}G}{\partial\tilde{r}^n\partial\tilde{E}^2}&=(-1)^n\left(\frac{2a^2(n+2)!}{\tilde{r}^{n+3}}-\frac{2a^2(n+1)!}{\tilde{r}^{n+2}}\right)+2\delta_{n0}\,,
\end{aligned}$$

where $\delta_{n0} = 1$ for $n = 0$ and zero otherwise. Finally, evaluating these derivatives at $(\tilde{r}_{\rm isco}, \tilde{E}_{\rm isco}, \tilde{L}_{\rm isco})$ and using the properties (A.2)-(A.7), we can derive the exact results

$$A_n = (1-\delta_{n0})\frac{(-1)^n(n-1)(n-2)n!}{3\tilde{r}_{\rm isco}^{1+n}}\,, \tag{A.9}$$

$$B_n = 2(1-\delta_{n0})(-1)^n(n+1)!\,\frac{n(a-\sqrt{\tilde{r}_{\rm isco}})+a-2\sqrt{\tilde{r}_{\rm isco}}+\tilde{r}_{\rm isco}^{3/2}}{\tilde{r}_{\rm isco}^n\sqrt{3\tilde{r}_{\rm isco}}\left(a-\sqrt{\tilde{r}_{\rm isco}}\right)\left(a+\tilde{r}_{\rm isco}^{3/2}\right)}\,, \tag{A.10}$$

$$C_n = 2\cdot\frac{\delta_{0n}-(-1)^n(2a+\sqrt{\tilde{r}_{\rm isco}}[\tilde{r}_{\rm isco}-2-n])(n+1)!}{\tilde{r}_{\rm isco}^{(2n+1)/2}(a+\tilde{r}_{\rm isco}^{3/2})^2}\,, \tag{A.11}$$

Notice equations (A.9)-(A.10) recover the familiar identities for circular orbits

$$\left(\frac{\partial G}{\partial\tilde{E}}\tilde{\Omega}+\frac{\partial G}{\partial\tilde{L}}\right)_{\rm isco}=0,$$
$$G_{\rm isco}=\left.\frac{\partial G}{\partial\tilde{r}}\right|_{\rm isco}=\left.\frac{\partial^2 G}{\partial\tilde{r}^2}\right|_{\rm isco}=0.$$

Let us study the behaviour of these derivatives for near extremal black holes, i.e. in the limit $\epsilon \to 0$ as introduced in section 2.2.3. Recall the ISCO location for rapidly rotating black holes is given by equation (2.20). The next order correction $\epsilon^{4/3}$ is given by

$$\tilde{r}_{\rm isco} \to 1 + 2^{1/3}\epsilon^{2/3} + \frac{7}{4\cdot 2^{1/3}}\epsilon^{4/3} + \mathcal{O}(\epsilon^2)\,. \tag{A.12}$$

Using this expansion together with $a = \sqrt{1-\epsilon^2}$, we can evaluate the leading terms of all previous derivatives to be

$$A_n \to (1-\delta_{n0})(n-2)(n-1)\left(\frac{1}{3}(-1)^n\Gamma(n+1)+\mathcal{O}(\epsilon^{2/3})\right)\,, \tag{A.13}$$

$$B_n \to (1-\delta_{n0})\frac{(-1)^n\Gamma(n+2)}{\sqrt{3}}\left(n-1-\frac{4n^2+n+1}{2^{5/3}}\epsilon^{2/3}\right)+\mathcal{O}(\epsilon^{4/3})\,, \tag{A.14}$$

$$C_n \to -\frac{1}{4}(-1)^n(n-1)\left(-2+2^{1/3}\epsilon^{2/3}[2n+3]\right)(n+1)! + \frac{(-1)^n(4n^2-3n-3)(n+2)!}{2^{10/3}}\epsilon^{4/3}+p_{n0} \tag{A.15}$$

and

$$\left.\frac{\partial^{n+1}G}{\partial\tilde{r}^n\partial\tilde{E}}\right|_{\rm isco} \to \frac{2}{\sqrt{3}}(-1)^{n+1}(n+1)![(n+1)-2^{1/3}(n^2+3n+3)\epsilon^{2/3}]+ \frac{2}{\sqrt{3}}(1+2^{1/3}\epsilon^{2/3})\delta_{n0}+\mathcal{O}(\epsilon^{4/3}) \tag{A.16}$$

$$\left(\frac{\partial^{n+2}G}{\partial\tilde{r}^n\partial\tilde{E}}+\tilde{\Omega}\frac{\partial^{n+2}G}{\partial\tilde{r}^n\partial\tilde{E}^2}\right)_{\rm isco} \to (\delta_{0n}-(-1)^n(n+1)^2n!)+ \frac{(-1)^n(7+13n+4n^2)(n+1)!-3\delta_{0n}}{2^{5/3}}\epsilon^{2/3}+\mathcal{O}(\epsilon^{4/3}) \tag{A.17}$$

$$\left.\frac{\partial^{n+2}G}{\partial\tilde{r}^n\partial\tilde{E}^2}\right|_{\rm isco} \to 2((-1)^n(3+n)(n+1)!+\delta_{0,n}) -2^{4/3}(-1)^n(4+n)(n+2)!\epsilon^{2/3}+\mathcal{O}(\epsilon^{4/3}) \tag{A.18}$$

where we defined

$$p_{n0}=\frac{2-3\cdot 2^{1/3}\epsilon^{2/3}}{4}\delta_{0n}+\mathcal{O}(\epsilon^2). \tag{A.19}$$

What we learn is that $A_n \sim \mathcal{O}(1)$ for all $n \geq 3$, $B_1 \sim \epsilon^{2/3}$, $B_n \sim \mathcal{O}(1)$ for $n \geq 2$, $C_0 \sim C_1 \sim \epsilon^{4/3}$ and $C_n \sim \mathcal{O}(1)$ for $n \geq 2$. Furthermore, (A.16) and (A.17) are $\mathcal{O}(\epsilon^{2/3})$ for $n = 0$ and $\mathcal{O}(1)$ for $n \geq 1$, whereas (A.18) is always $\mathcal{O}(1)$.

A.2 Retrograde orbits

In this section, we will restrict our attention to retrograde orbits. That is, orbits opposing the direction with the primary's angular momenta. These orbits are of interest because the ISCO is much further away from the horizon, which implies that the radial distance travelled during plunge time is much longer. We plot the location of the ISCO as a function of spin a in figure (A.1). Due to frame-dragging, we expect the ISCO to be farther from the hole since the space is dragged in the opposite direction to the compact objects orbital direction. In our conventions, retrograde orbits correspond to $a < 0$ and $\tilde{L} > 0$. Hence, near-extremal ones are characterised by $a \to -1$, or equivalently, by

$$a \to -\sqrt{1-\epsilon^2}, \text{ where } \epsilon \ll 1. \tag{A.20}$$

Notice that the horizon takes the same form as in the case of prograde orbits

$$\tilde{r}_+ = 1+\sqrt{1-a^2} = 1+\epsilon\,,$$

as to be expected. Using a spin parameter of negative parity, the expressions for $\tilde{E}, \tilde{L}, \tilde{\Omega}$ and

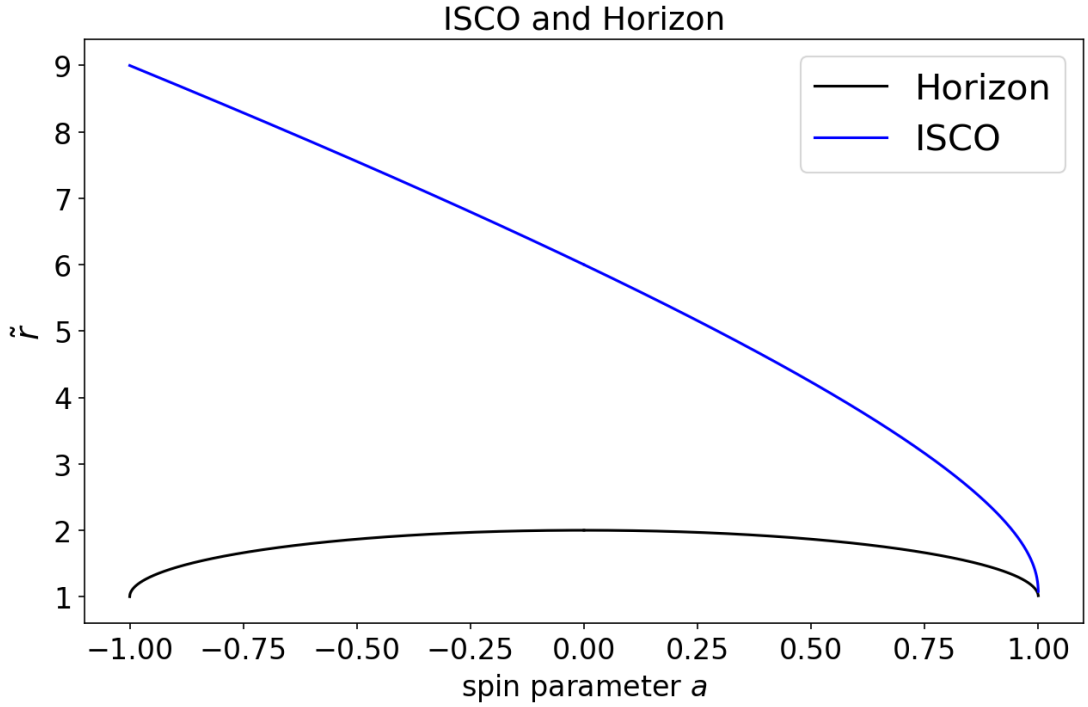

Figure A.1: This plot shows the relationship between $\tilde{r}_{\rm isco}$ and $\tilde{r}_+$ with the spin parameter $a \in [-1, 1]$. Notice that for $a > 0$ (prograde orbits), the ISCO and horizon locations coincide in B-L coordinates, whereas for $a < 0$ (retrograde orbits), these remain at a finite B-L coordinate distance.

$\tilde{r}_{\rm isco}$ remain the same. However, each quantity will be different at the ISCO of a retrograde orbit. By substituting Eq. (A.20) into Eqs.(2.18), (2.8a), (2.8b) and (2.10) for small $\epsilon \ll 1$, one finds

$$\tilde{r}_{\rm isco} = 9 - \frac{45}{32}\epsilon^2 + \mathcal{O}(\epsilon^4) \tag{A.21}$$

$$\tilde{E}_{\rm isco} = \frac{5}{3\sqrt{3}} - \frac{1}{96\sqrt{3}}\epsilon^2 + \mathcal{O}(\epsilon^4) \tag{A.22}$$

$$\tilde{L}_{\rm isco} = \frac{22}{3\sqrt{3}} - \frac{3\sqrt{3}}{16}\epsilon^2 + \mathcal{O}(\epsilon^4) \tag{A.23}$$

$$\tilde{\Omega}_{\rm isco} = \frac{1}{26} + \frac{373}{43264}\epsilon^2 + \mathcal{O}(\epsilon^4). \tag{A.24}$$

Notice here that the expansion in ϵ is no longer increasing in powers of $\epsilon^{2/3}$ and now in ϵ^2. Also notice that $|\tilde{r}_{\rm isco} - \tilde{r}_+| \sim \mathcal{O}(1)$ rather than of order $\epsilon^{2/3}$ like in the case of near-extremal prograde orbits. Like we have done previously, we consider the Kerr radial velocity expanded around the ISCO

$$\left(\frac{dR}{d\tilde{\tau}}\right)^2 \simeq -\frac{2}{3}\alpha R^3 + 2\beta\delta LR + \gamma\delta LR^2 + \Gamma_\odot + \dots, \tag{A.25}$$

with small variables

$$\tilde{E} - \tilde{E}_{\rm isco} = \tilde{\Omega}_{\rm isco}\delta E \tag{A.26}$$

$$\tilde{L} - \tilde{L}_{\rm isco} = \delta L \tag{A.27}$$

$$\tilde{r} - \tilde{r}_{\rm isco} = R. \tag{A.28}$$

The coeffcients in (A.25) can be approximated for $\epsilon \to 0$ under the retrograde condition Eq.(A.20)

$$\begin{aligned}
\alpha &= -\frac{1}{4}\frac{\partial^3 G}{\partial \tilde{r}^3}\bigg|_{\rm isco} \to \frac{1}{6561} \\
\beta &= \frac{1}{2}\left(\frac{\partial^2 G}{\partial \tilde{r}\partial \tilde{L}} + \tilde{\Omega}\frac{\partial^2 G}{\partial \tilde{r}\partial \tilde{E}}\right)_{\rm isco} \to \frac{4}{351\sqrt{3}} \\
\gamma &= \frac{1}{2}\left(\frac{\partial^3 G}{\partial \tilde{r}^2\partial \tilde{L}} + \tilde{\Omega}\frac{\partial^3 G}{\partial \tilde{r}^2\partial \tilde{E}}\right)_{\rm isco} \to -\frac{1}{351\sqrt{3}}\,,
\end{aligned}$$

and $\Gamma_\odot$ in (A.25) defined through equation (4.19). Notice that none of the coefficients in our transition equation of motion depend on the extremality parameter ϵ. This gives us no reason to introduce any scalings on $\tilde{r}, \tilde{\tau}$ and δL with respect to ϵ like we did for prograde orbits around rapidly rotating black holes. As such, let us introduce similar scalings to OT

$$R = \eta^{2/5}\alpha^{-3/5}(\beta\kappa)^{2/5}X \tag{A.29}$$

$$\tilde{\tau} - \tilde{\tau}_{\rm isco} = \eta^{-1/5}(\alpha\beta\kappa)^{-1/5}T \tag{A.30}$$

$$\delta E - \delta L = \eta^{6/5}Y \tag{A.31}$$

$$\delta L = -\eta^{4/5}(\alpha\beta)^{-1/5}\kappa^{4/5}T\,. \tag{A.32}$$

Substituting these results into Eq.(A.25) we find that

$$\left(\frac{dX}{dT}\right)^2 = -\frac{2}{3}X^3 - 2XT + \alpha^{4/5}(\eta\beta\kappa)^{-6/5}\Gamma_\odot. \tag{A.33}$$

Since $R \sim \eta^{2/5}$, we only need the first term of $\Gamma_\odot$

$$\Gamma_\odot = \eta^{6/5}\left(\tilde{\Omega}\frac{\partial G}{\partial \tilde{E}}\right)_{\rm isco} Y\,. \tag{A.34}$$

Taking derivatives of Eq.(A.33) and following an identical procedure to subsection (4.2.4), we obtain

$$\frac{d^2X}{dT^2} = -X^2 - T\,, \tag{A.35}$$

with evolution equation for Y

$$\frac{dY}{dT} = -\frac{\partial \log \tilde{\Omega}}{\partial \tilde{r}}\bigg|_{\rm isco} (C_1 K_0)^{-1} X \,, \tag{A.36}$$

for $K_0 = \alpha^{4/5}(\beta\kappa)^{-6/5}$. Which is precisely the equation of motion for the transition regime derived by OT in [254]. Although the quantities α, β and κ present in the change of coordinates are different, the physics and ultimate end goal are the same. As a result, we stop our analysis of retrograde orbits here since we feel that this problem has already been solved by the community for smaller spin values $a \geq -0.999$. We conclude that, for near-extremal retrograde orbits, there is nothing new to learn about the transition regime. It can be solved in the matter of OT in [254]. We do remark that the quantity κ can no longer be computed using the near-extremal formula defined by $\dot{\tilde{E}}_{GW} = (\tilde{C}_H + \tilde{C}_\infty)(\tilde{r} - \tilde{r}_+)/\tilde{r}_+$. This is because the transition region is far in Boyer-Lindquist radial coordinate from the horizon of the primary hole. Instead we have to use the numerical quantity

$$\begin{aligned}\kappa &= \left(\tilde{\Omega}^{-1}\frac{d\tilde{t}}{d\tilde{\tau}}\frac{d\tilde{E}}{d\tilde{t}}\right)_{\rm isco} \\ &= \left(-\frac{32}{5}\tilde{\Omega}^{7/3}\frac{1 + a/\tilde{r}^{3/2}}{\sqrt{1 - 3/\tilde{r} + 2a/\tilde{r}^{3/2}}}\dot{\mathcal{E}}(\tilde{r})\right)_{\rm isco} .\end{aligned}$$

Various results are tabulated (including retrograde orbits) in [109]. The downside of this equation is that it can only be evaluated numerically.

A.3 Osculating elements equations

The proper time derivative of the radial geodesic equation (2.5a) yields (4.4)

$$\frac{d^2\tilde{\tilde{r}}}{d\tilde{\tau}^2} - \frac{1}{2}\frac{\partial G}{\partial \tilde{r}} = \frac{1}{2}\left(\frac{d\tilde{E}}{d\tilde{\tau}}\frac{\partial G}{\partial \tilde{E}} + \frac{d\tilde{L}}{d\tilde{\tau}}\frac{\partial G}{\partial \tilde{L}}\right)\left(\frac{d\tilde{r}}{d\tilde{\tau}}\right)^{-1} . \tag{A.37}$$

The purpose of this appendix is to review how this equation is equivalent to the radial component of a forced geodesic equation

$$u^\nu \nabla_\nu u^{\tilde{r}} = \frac{d^2\tilde{x}^{\tilde{r}}}{d\tilde{\tau}^2} + \Gamma^{\tilde{r}}_{\rho\sigma}\frac{d\tilde{x}^\rho}{d\tilde{\tau}}\frac{d\tilde{x}^\sigma}{d\tilde{\tau}} = \tilde{f}^{\tilde{r}} \,, \tag{A.38}$$

where $\tilde{x}^\mu = (\tilde{r}, \tilde{t}, \theta, \phi)$, $\nabla_\nu = \nabla_{\tilde{x}^\nu}$, $u^\mu = d\tilde{x}^\mu/d\tilde{\tau}$ is the four-velocity of the particle and $\tilde{f}^\mu$ a forcing term driving deviations from geodesic motion.

To show the equivalence between (A.37) and (A.38), we use the osculating elements formu-

lation [296]. Since this method does not take into account conservative effects arising from the self-force [100], the component $\tilde{f}^{\tilde{r}}$ in this appendix will only account for the dissipative piece in (4.6). Its conservative piece is treated in more detail in the main text (See section 4.2.1).

Since the four velocity u^α is normalised, it follows $\tilde{f}^\alpha$ is normal to it by proper time differentiation

$$u^\alpha u_\alpha = -1 \implies \tilde{f}^\alpha u_\alpha = 0\,. \tag{A.39}$$

Solving (A.39) for $\tilde{f}^{\tilde{r}}$ and plugging it into (A.38) yields

$$\frac{d^2\tilde{r}}{d\tilde{\tau}^2} + \Gamma^r_{\rho\sigma}\frac{d\tilde{x}^\rho}{d\tilde{\tau}}\frac{d\tilde{x}^\sigma}{d\tilde{\tau}} = -\frac{\tilde{f}^\phi \tilde{u}_\phi + \tilde{f}^{\tilde{t}}\tilde{u}_{\tilde{t}}}{\tilde{u}_{\tilde{r}}}\,. \tag{A.40}$$

The left-hand side

$$\Gamma^{\tilde{r}}_{\rho\sigma}\frac{d\tilde{x}^\rho}{d\tilde{\tau}}\frac{d\tilde{x}^\sigma}{d\tilde{\tau}} = \Gamma^{\tilde{r}}{}_{\tilde{r}\tilde{r}}\left(\frac{d\tilde{r}}{d\tilde{\tau}}\right)^2 + \Gamma^{\tilde{r}}{}_{\phi\phi}\left(\frac{d\phi}{d\tilde{\tau}}\right)^2 + \Gamma^{\tilde{r}}{}_{\tilde{t}\tilde{t}}\left(\frac{d\tilde{t}}{d\tilde{\tau}}\right)^2 + 2\Gamma^{\tilde{r}}{}_{\tilde{t}\phi}\frac{d\tilde{t}}{d\tilde{\tau}}\frac{d\phi}{d\tilde{\tau}} \tag{A.41}$$

is computed using the Kerr Christoffel symbols and the geodesic equations (2.5a)-(2.5d)

$$\Gamma^{\tilde{r}}_{\rho\sigma}\frac{dx^\rho}{d\tilde{\tau}}\frac{d\tilde{x}^\sigma}{d\tilde{\tau}} = \frac{3(a\tilde{E}-\tilde{L})^2}{\tilde{r}^4} - \frac{a^2(\tilde{E}^2-1)-\tilde{L}^2}{\tilde{r}^3} + \frac{1}{r^2} = -\frac{1}{2}\frac{\partial G}{\partial \tilde{r}}$$

To evaluate the right-hand side, $\tilde{f}^{\tilde{r}}$, we know that the Kerr space-time has two Killing vectors : $\xi^\mu = \partial/\partial\tilde{t}$ and $\psi^\mu = \partial/\partial\phi$, associated with time translation and axialsymmetry, respectively. There exists a conserved charge associated with each :

$$\tilde{E} = -\xi^\mu u_\mu, \quad \tilde{L} = \psi^\mu u_\mu. \tag{A.42}$$

It follows from Eq.(A.42) that $u_\phi = \tilde{L}$ and $u_{\tilde{t}} = -\tilde{E}$. Finally, we relate the proper time derivatives of these charges with the forcing terms in (A.38). For example, consider the proper time derivative of $\tilde{E}$

$$\begin{aligned} -\frac{d\tilde{E}}{d\tilde{\tau}} &= u^\beta \nabla_\beta(\xi^\alpha u_\alpha) \\ &= \xi^\alpha(u^\beta\nabla_\beta u_\alpha) + u^\alpha u^\beta(\nabla_\beta \xi_\alpha) \\ &= \tilde{f}_{\tilde{t}}\,, \end{aligned} \tag{A.43}$$

where Killing's equation was used in the last step. A similar calculation leads to $d\tilde{L}/d\tilde{\tau} = \tilde{f}_\phi$.

Solving the two equations $d\tilde{L}/d\tilde{\tau}$ and $d\tilde{E}/d\tilde{\tau}$ for $\tilde{f}^{\phi}$ and $\tilde{f}^{\tilde{t}}$ gives

$$\tilde{f}^{\phi} = -\frac{1}{\Delta}\left(g_{\tilde{t}\tilde{t}}\frac{d\tilde{L}}{d\tilde{\tau}} + g_{\phi\tilde{t}}\frac{d\tilde{E}}{d\tilde{\tau}}\right),$$
$$\tilde{f}^{\tilde{t}} = \frac{1}{\Delta}\left(g_{\tilde{t}\phi}\frac{d\tilde{L}}{d\tilde{\tau}} + g_{\phi\phi}\frac{d\tilde{E}}{d\tilde{\tau}}\right).$$

Here we used the identity $(g_{\phi\tilde{t}})^2 - g_{\phi\phi}g_{\tilde{t}\tilde{t}} = \Delta$ for $\Delta = \tilde{r}^2 - 2\tilde{r} + a^2$. Since $u_{\tilde{r}} = g_{\tilde{r}\tilde{r}}(d\tilde{r}/d\tilde{\tau})$, it follows the right hand side of (A.40) is

$$\tilde{f}^{\tilde{r}} = \frac{1}{\Delta g_{\tilde{r}\tilde{r}}}\left(\frac{d\tilde{E}}{d\tilde{\tau}}[g_{\phi\tilde{t}}\tilde{L} + g_{\phi\phi}\tilde{E}] + \frac{d\tilde{L}}{d\tilde{\tau}}[g_{\tilde{t}\tilde{t}}\tilde{L} + g_{\tilde{t}\phi}\tilde{E}]\right)\left(\frac{d\tilde{r}}{d\tilde{\tau}}\right)^{-1}$$

Noticing that

$$\frac{1}{\Delta g_{\tilde{r}\tilde{r}}}(g_{\phi\tilde{t}}\tilde{L} + g_{\phi\phi}\tilde{E}) = \frac{1}{2}\frac{\partial G}{\partial \tilde{E}} \tag{A.44}$$
$$\frac{1}{\Delta g_{\tilde{r}\tilde{r}}}(g_{\tilde{t}\tilde{t}}\tilde{L} + g_{\tilde{t}\phi}\tilde{E}) = \frac{1}{2}\frac{\partial G}{\partial \tilde{L}} \tag{A.45}$$

we reach the desired conclusion

$$\tilde{f}^{\tilde{r}} = \frac{1}{2}\left(\frac{d\tilde{E}}{d\tilde{\tau}}\frac{\partial G}{\partial \tilde{E}} + \frac{d\tilde{L}}{d\tilde{\tau}}\frac{\partial G}{\partial \tilde{L}}\right)\left(\frac{d\tilde{r}}{d\tilde{\tau}}\right)^{-1}. \tag{A.46}$$

Appendix B

Constraining the spin parameter of near-extreme black holes using LISA

B.1 Analytic estimation of the Fisher matrix

The derivation of the Fisher matrix estimate (5.19) is provided below.

Consider the gravitational wave amplitude

$$h(t) = \sum_m h_m(t) \approx \sum_m \frac{2\sqrt{\dot{E}_m^\infty}}{m\tilde{\Omega}\tilde{D}} \sin(m\tilde{\Omega}\tilde{t}) \,, \tag{B.1}$$

where we chose $\phi = 0$ for simplicity. The spin dependence of each individual amplitude equals

$$\partial_a h_m(t) = |h_m(t)| \left\{ \sin(m\tilde{\Omega}\tilde{t})\, \mathcal{B}_m + (m\tilde{t}\partial_a\tilde{\Omega})\, \cos(m\tilde{\Omega}\tilde{t}) \right\} \tag{B.2}$$

where $|h_m(t)|$ stands for the amplitude without oscillatory factor and we defined

$$\mathcal{B}_m \equiv \frac{\partial_a \dot{E}_m^\infty}{2\dot{E}_m^\infty} - \frac{\partial_a\tilde{\Omega}}{\tilde{\Omega}} \,. \tag{B.3}$$

Using Parseval's identity, the integrand in the Fisher matrix can be decomposed

$$|\partial_a h(t)|^2 = \sum_m (\partial_a h_m)^2 + 2 \sum_{n<m} \partial_a h_n\, \partial_a h_m \,, \tag{B.4}$$

into *diagonal* and *off-diagonal* contributions. Consider the diagonal ones, first. Using $\sin^2 x = (1-\cos 2x)/2$ and $\cos^2 x = (1+\cos 2x)/2$, any such contribution equals

$$(\partial_a h_m)^2 = \frac{|h_m|^2}{2}\Big\{(m\tilde{t}\,\partial_a\tilde{\Omega})^2 + (\mathcal{B}_m)^2 + \cos(2m\tilde{\Omega}\tilde{t})\left[(m\tilde{t}\,\partial_a\tilde{\Omega})^2 - (\mathcal{B}_m)^2\right] \\ +2\sin(2m\tilde{\Omega}\tilde{t})\,\mathcal{B}_m\,(m\tilde{t}\,\partial_a\tilde{\Omega})\Big\}\,. \quad \text{(B.5)}$$

The crucial observation is $\tilde{t}\sim\mathcal{O}(\eta^{-1})$. This follows from integrating (5.20) and is an inherent consequence of adiabatic inspirals evolving on the orbital timescale. Hence, we expect the dominant term to be the one of order $\mathcal{O}(\tilde{t}^2)$. Furthermore, the second and third lines above have oscillatory behaviour, which when integrated in (5.18) will give rise to subleading contributions. Despite the robustness of these arguments, let us state the precise condition under which the order $\mathcal{O}(\tilde{t}^2)$ term is dominant

$$\left|\frac{\partial_a \dot{E}^{\infty}_m}{\tilde{t}\,\dot{E}^{\infty}_m}\right| \ll \partial_a\tilde{\Omega}\,. \quad \text{(B.6)}$$

Notice that both partial derivatives should be understood as in the left hand side of our equations (5.21). Since $\dot{E}^{\infty}_m$ typically requires numerical evaluation, we have indeed numerically checked this assumption holds for both, moderately and near-extremal primary holes. Thus, the contribution from the diagonal terms can be approximated by

$$\sum_m (\partial_a h_m)^2 \approx \frac{|h_m|^2}{2}\,(m\tilde{t}\,\partial_a\tilde{\Omega})^2\,. \quad \text{(B.7)}$$

It is worth stressing that for sources lying entirely in the close to ISCO region of a near extremal primary, this condition is under more analytical control using the NHEK flux (5.2). Whenever $\partial_a \log\tilde{C}_{\infty m} \ll \tilde{t}\,\partial_a\tilde{r}$ holds (which we checked numerically), the full condition reduces to $x\,\tilde{t}\gg 1$, which is satisfied for all secondary locations x before entering the transition regime.

The discussion of the off-diagonal terms is very similar. Any such term can be written as

$$\partial_a h_m\,\partial_a h_n = \frac{|h_m||h_n|}{2}\Big\{\cos((m-n)\tilde{\Omega}\tilde{t})\,\left[\mathcal{B}_m\,\mathcal{B}_n + mn(\tilde{t}\,\partial_a\tilde{\Omega})^2\right] + \\ \cos((m+n)\tilde{\Omega}\tilde{t})\,\left[-\mathcal{B}_m\,\mathcal{B}_n + mn(\tilde{t}\,\partial_a\tilde{\Omega})^2\right] + \sin((m+n)\tilde{\Omega}\tilde{t})\left[n\tilde{t}\,\partial_a\tilde{\Omega}\,\mathcal{B}_m + m\tilde{t}\,\partial_a\tilde{\Omega}\,\mathcal{B}_n\right] + \\ \sin((m-n)\tilde{\Omega}\tilde{t})\left[n\tilde{t}\,\partial_a\tilde{\Omega}\,\mathcal{B}_m - m\tilde{t}\,\partial_a\tilde{\Omega}\,\mathcal{B}_n\right]\Big\}\,. \quad \text{(B.8)}$$

The key point is that *all* such terms involve oscillatory functions, even the ones having $\mathcal{O}(\tilde{t}^2)$ dependence. Hence, when compared to the contribution from the diagonal ones, they are subleading. This justifies our claim in (5.19).

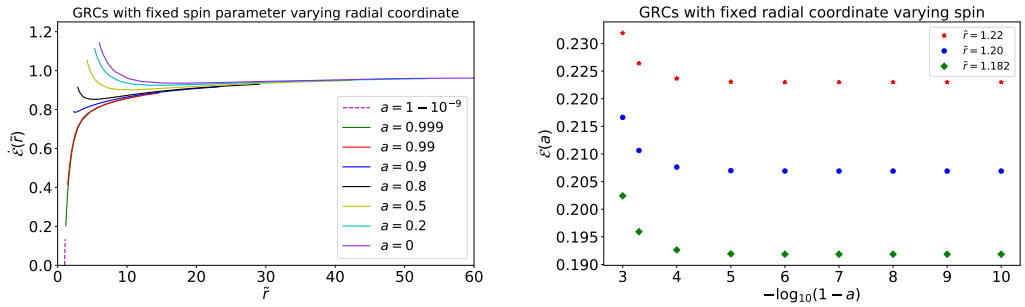

Figure B.1: The figure on the left shows the values of the GRCs $\dot{\mathcal{E}}(\tilde{r})$ evaluated at a fixed spin parameter. The purple dashed line (bottom left of leftmost plot) uses the near-extremal approximation to the flux (2.59). The other colours are the tabulated values GRCs presented in Table IV in Ref.[109]. The figure on the right shows the GRCs evaluated at a fixed radial coordinate $\tilde{r}$ whilst varying the spin parameter a. The GRCs for $a > 0.999$ were computed using the BHPT [204].

B.2 General relativistic corrections

We begin by focusing on the total energy flux $\dot{\tilde{E}}_{\rm GW}$. The left most panel of figure B.1 shows $\dot{\mathcal{E}}(\tilde{r})$ at fixed a and the right most panel $\dot{\mathcal{E}}(a)$ at fixed $\tilde{r}$. The left plot of Fig.(B.1), shows that for moderately rotating holes with $a \lesssim 0.99$, the corrections $\dot{\mathcal{E}}$ are not strongly dependent on the radial coordinate $\tilde{r}$. However, approaching an extremal spin parameter a indicates that $\dot{\mathcal{E}}$ rapidly goes to zero as the ISCO is approached. This matches the description given by both NHEK fluxes (5.2) and (2.59).

Using a Teukolsky solver from the BHPT, we generated our own energy flux values for spin parameters $a \geq 0.999$. The corresponding corrections are shown in the right panel of figure B.1 for fixed coordinate radii. This shows that at a fixed coordinate radius $\tilde{r}$, the corrections approach a constant as $a \to 1$. What we learn from this is that the behaviour of the relativistic corrections becomes somewhat universal as $a \to 1$. In other words, as the near extremal parameter approaches unity, the corrections approach a constant value. This means that the correction values at some $\tilde{r}$ will not differ much as the spin parameter is changed providing the spin parameter is close to one. That is, spin dependence on $\dot{\mathcal{E}}$ is weak "far" from ISCO.

We emphasise that this does *not* mean that $\partial_a \dot{\mathcal{E}} \approx 0$ throughout the entire inspiral. Here we have shown three radial coordinates which are considerably far away from the ISCO in the near-extreme spin parameter case. The closer in radial coordinate to the ISCO, the larger the spin dependence in the relativistic corrections. This can be observed in Fig.(B.2). For a weak gravitational field, the spin dependence on the flux corrections for near-extreme inspirals is small, approaching $\dot{\tilde{E}}_{\rm GW} \to 0$ for $a \to 1$ as the ISCO is approached. Much smaller than when compared to moderately spinning holes, where the total energy flux is approximately

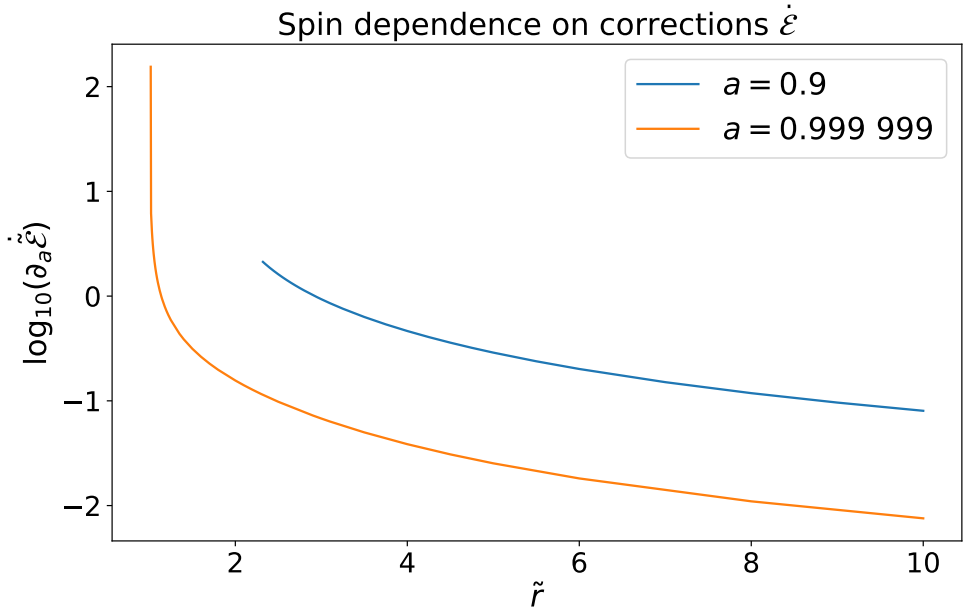

Figure B.2: Here we compute $\partial_a \dot{\mathcal{E}}$ for the two spin parameters $a = 0.999999$ (orange) and $a = 0.9$ (blue). The growth in $\partial_a \dot{\mathcal{E}}$ for rapidly rotating holes is larger closer to ISCO than for moderately spinning holes.

constant. Only when very close to the ISCO does the spin dependence on $\dot{\mathcal{E}}$ grow significantly for near-extremal holes.

A comparison of our interpolant, $\dot{\mathcal{E}}$ for $a = 1 - 10^{-9}$ with high spinning fluxes computed from the BHPT are given in Fig.(B.3). A useful approximant for the relativistic corrections

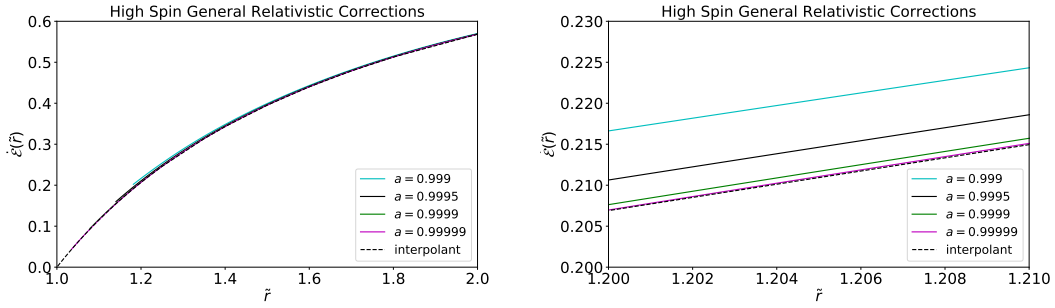

Figure B.3: On the left panel, we have used the BHPT to compute the total energy flux for near-extremal spin parameters with our interpolant (black dashed line) overlaid. The right panel is a zoom in of the left plot giving visual aid as to why our interpolant can be used to approximate a larger regime of spin parameters.

$\dot{\mathcal{E}}(r)$ is given by

$$\dot{\mathcal{E}}(x) = ax \arctan(bx^c), \quad x = \tilde{r} - 1 \tag{B.9}$$

with constants $(a, b, c) = (0.6897912, 1.084803, -0.936685)$. This approximates the high spin corrections $\dot{\mathcal{E}}(r, 1 - 10^{-9})$ for $\tilde{r} \lesssim 6$ with largest fractional error $\sim 1\%$ at the ISCO.

B.3 Verification of Fisher matrix calculations

For a single parameter analysis, we used three different methods to verify the Fisher matrix calculations without performing a Bayesian analysis:

1. Verification of the linear signal approximation

$$h(a+\Delta a) \approx h(a) + \Delta a \frac{\partial h}{\partial a}.$$

2. Overlaps defined through (3.67) — perturbing the spin parameter by Δa given by the Fisher matrix should return overlaps close to one.

3. Likelihood — The log-likelihood is maximised at the true parameters $\boldsymbol{\theta}_0$. If a parameter is perturbed by the Fisher matrix estimate then it should be a measure of the 1σ width of this log-likelihood.

As a proof of principle of these methods, we will compute the precision on the spin parameter for a heavy source $\boldsymbol{\theta}_{\rm heavy}$ (see (5.58)), viewed face-on with $\rho \sim 20$. For a source with this configuration of parameters, we found $\Delta a_{\rm NHEK} \sim 2 \times 10^{-10}$ numerically.

B.3.1 Linear-signal-approximation

In the derivation of the Fisher matrix (3.59), we used the linear-signal approximation (3.57) so a first test would be to test whether it is valid in our analysis. To test whether the expansion is valid in the regime of SNR we are considering, we compute the overlap

$$\mathcal{O}\left(h(a+\Delta a)|h(a)+\Delta a\frac{\partial h}{\partial a}\right)\Big|_{a=a_{\rm true}} \approx 1-10^{-5} \tag{B.10}$$

Hence we conclude that our waveform model at $\rho \sim 20$ does not violate the linear-signal approximation.

B.3.2 Overlaps

In the limit of high SNR, the inner product (3.29) can be expanded in ρ. Observe for small Δa

$$(h(a+\Delta a)|h(a)) \approx \rho^2 + \Delta a\left(\frac{\partial h}{\partial a}\middle|h\right) + \frac{\Delta a^2}{2}\left(h\middle|\frac{\partial^2 h}{\partial a^2}\right),$$

where $(h|h) = \rho^2$ as in (3.47). Since the SNR is fixed, it's easy to show that $(\partial_a h|h) = 0$ and $\Gamma_{aa} = -(\partial_a^2 h|h)$. We thus obtain for $\rho \gg 1$

$$\mathcal{O}(h(a+\Delta a), h(a)) \approx 1 - \frac{1}{\rho^2} + O\left(\rho^{-4}\right). \tag{B.11}$$

Substituting $\Delta a = \Delta a_{\rm NHEK}$ into the left hand side of (B.11), we numerically find an agreement of $\sim 0.01\%$.

B.3.3 Likelihood

In the high SNR limit, the precision pridicted by the fisher matrix should approximate the 1σ width of the likelihood function. Using Eq.(3.31), we can rewrite the log-likelihood as

$$\log p(d|a) \propto (d|h) - \frac{1}{2}(h|h).$$

In the following analysis, we consider $n(t) = 0$ since the inclusion of noise induces a statistical fluctuation from the true parameters and does not have a direct influence on the width of the likelihood. As such, we will consider a zero noise approximation and use $d = h(a)$ with signal templates $h := h(a + \Delta a; t)$. Substituting this into the likelihood above we find that

$$\log p(d|a) \approx \frac{1}{2}(\rho^2 - 1). \tag{B.12}$$

Here we have *assumed* that $\Gamma^{-1}_{aa} = \Delta a^2$. Calculating $\log p(d|a)$ for $d = h(a + \Delta a)$ with Δa our Fisher matrix estimate we found that $\log p(d|a) \approx 199.46$ which agrees with the above formula, to a precision of 0.05%.

Since we are interested in only one parameter, it is easy to evaluate the likelihood function

$$p(d|a) \propto \exp[-(d-h|d-h)/2] \tag{B.13}$$

on a grid of spin parameter values. In doing so, we find Fig.(B.4). The area between the yellow line and red line is approximately 31.51%, which is a reasonable approximation to the true $1 - \sigma \approx 34\%$ width of likelihood.

To conclude these subsections, we are confident that our Fisher matrix approximations in the single parameter study give a good guide to the spin parameter uncertainty.

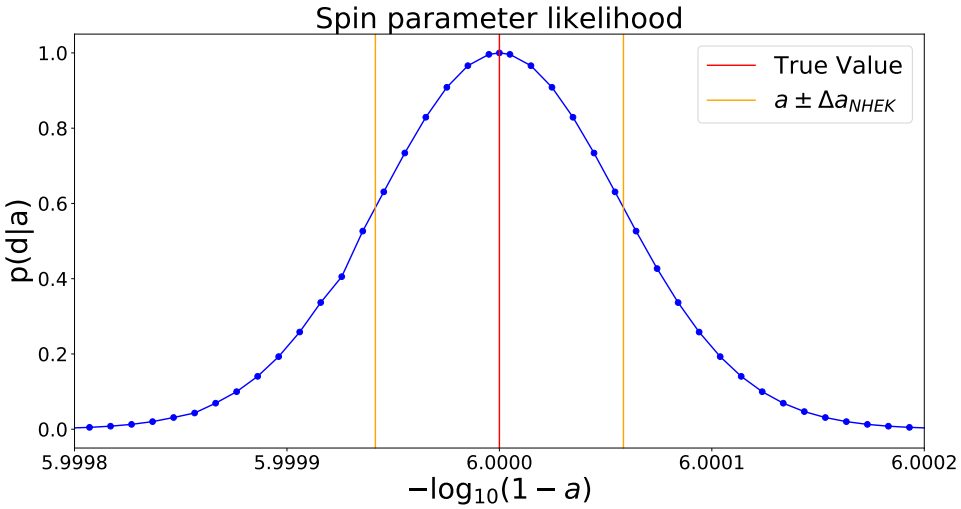

Figure B.4: The blue curve is the likelihood (B.13) evaluated on a grid of points. The red the true value $a = 1 - 10^{-6}$ and orange the precision measurement predicted by the 1 parameter Fisher matrix Δa_{NHEK}.

Appendix C

Noisy neighbours: quantifying bias due to overlapping gravitational-wave signals

C.1 Stationary treatment of foreground noise

When the confusion noise is generated by a very large population of sources, it is common to treat it analogously to the instrumental noise with $f, f' > 0$,

$$\langle \widehat{\Delta H_{\rm conf}}(f) \rangle = 0, \tag{C.1a}$$

$$\langle \widehat{\Delta H_{\rm conf}}(f) \widehat{\Delta H^{\star}_{\rm conf}}(f') \rangle = \frac{1}{2} \delta(f - f') S_{\rm conf}(f'), \tag{C.1b}$$

$$\langle \widehat{\Delta H_{\rm conf}}(f) \widehat{\Delta H_{\rm conf}}(f') \rangle = 0\,. \tag{C.1c}$$

For $S_{\rm conf}(f)$ the PSD representing the power of the confusion noise at a particular bin of frequency. In this current discussion we are assuming that the confusion noise acts as a *stationary* time-series that is then fully described by an auto-correlation function.

Under these assumptions, the mean bias is zero and the covariance from the confusion background (7.7) takes the alternative form [1]

[1] Note that $S_{\rm conf}$ describes the contribution from the whole astrophysical population, while $\Sigma_{\rm conf}$ defined in Eq. (7.7) was the contribution from a single source in the population. For consistency, we therefore denote the total covariance by $N\Sigma_{\rm conf}$ in Eq. (C.2).

$$N\Sigma^{ij}_{\rm conf} = (\Gamma^{-1})^{ik}(\Gamma^{-1})^{jl}$$
$$\left\langle \int_{-\infty}^{\infty} \frac{(\partial_k^* h_m(f)\widehat{\Delta H}(f) + \partial_k h_m(f)\widehat{\Delta H}^*(f))}{S_n(f)}\,{\rm d}f \int_{-\infty}^{\infty} \frac{(\partial_l^* h_m(f')\widehat{\Delta H}(f') + \partial_l h_m(f')\widehat{\Delta H}^*(f'))}{S_n(f')}\,{\rm d}f' \right\rangle$$
$$= 2(\Gamma^{-1})^{ik}(\Gamma^{-1})^{jl} \int_0^{\infty} \frac{(\partial_k h^\star_m(f)\partial_l h_m(f) + \partial_l h^\star_m(f)\partial_k h_m(f))S_{\rm conf}(f)}{S_n^2(f)}\,{\rm d}f\,. \tag{C.2}$$

Where we have used (C.1b)-(C.1c) to reach the final equality. If we use this prescription within the formalism we have here described, we can calculate the total covariance in the parameter estimates arising from instrumental noise and source confusion, which is $\langle(\Delta\theta^i_{\rm noise} + \Delta\theta^i_{\rm conf})(\Delta\theta^j_{\rm noise} + \Delta\theta^j_{\rm conf})\rangle = \Gamma^{-1} + N\Sigma_{\rm conf}$, with $\Sigma_{\rm conf}$ defined by Eq. (7.7). This results follows because $\langle\Delta\theta^i_{\rm noise}\Delta\theta^i_{\rm conf}\rangle = 0$, since the instrumental and astrophysical noises should not depend on one another. To calculate the total variance $[\Gamma^{-1} + \Sigma_{\rm conf}]^{ij}$, we first quote the general result

$$\langle(\partial_i h_m|\widehat{\Delta H_{\rm conf}})(\partial_j h_m|\widehat{\Delta H_{\rm conf}})\rangle = \Gamma_{ij}\,, \tag{C.3}$$

that is easily proved using (C.1b)-(C.1c). We can then re-write $(\Gamma^{-1})^{ij}$ as

$$(\Gamma^{-1})^{ij} = \int (\Gamma^{-1})^{ip}\Gamma_{pm}(\Gamma^{-1})^{mj} p_{\rm pop}(\boldsymbol{\theta}_{\rm conf})d\boldsymbol{\theta}_{\rm conf} \tag{C.4}$$

since the Fisher matrix is independent of the confusion population and thus population parameters. Integrating over this ensemble of sources is equivalent to taking an ensemble average. Using (C.3), (C.4) and (7.7), we find

$$\left[\Gamma^{-1} + \Sigma_{\rm conf}\right]^{ij} = (\Gamma^{-1})^{ik}\Sigma^{kl}_{\rm mix}(\Gamma^{-1})^{jl},\,, \tag{C.5}$$

where

$$\Sigma^{ij}_{\rm mix} = 4{\rm Re}\int_0^{\infty} \frac{(\partial_k \hat{h}_m(f)\partial_l \hat{h}^\star_m(f))(S_{\rm conf}(f) + S_{\rm n}(f))}{S^2_{\rm n}(f)}\,. \tag{C.6}$$

In contrast to this, the standard approach when modelling the confusion background is to combine the instrumental and confusion noises into a single noise term, $N = n + \Delta H_{\rm conf}$. Then the standard parameter estimation formalism can be used, with the substitution $S_{\rm n}(f) \to S_{\rm n}(f) + S_{\rm conf}(f)$ in the inner product (3.29). In this case the inference uncertainties are given

by the inverse of the Fisher matrix, $\Gamma^{-1}_{\rm n+conf}$, where

$$\Gamma^{ij}_{\rm n+conf} = 4{\rm Re}\int_0^\infty \frac{(\partial_k \hat{h}_m(f)\partial_l \hat{h}^\star_m(f))}{S_{\rm n}(f)+S_{\rm conf}(f)}. \tag{C.7}$$

The variance given by Eq. (C.5) is, in general, larger than that predicted by Eq. (C.7). This is because it has been derived by maximizing the standard likelihood as an estimator of the parameters, which is no longer the correct likelihood when random confusion noise is included in the model. Expression (C.7) gives the variance of the true maximum likelihood estimator, which is known to be the minimum variance unbiased estimator and must therefore be smaller than (C.5). Incorporating the confusion noise uncertainty into the PSD is the correct thing to do when Eq. (C.1b) is known to be a good approximation, but the formalism described here can be used when that equation is not valid, and to assess when confusion noise is likely to be problematic for parameter estimation. As a final remark, we note that in the limit that there are a large number of sources contributing to the confusion background, the central limit theorem allows us to approximate the probability distribution of the parameter bias correction, $p(\Delta\boldsymbol{\theta}_{\rm conf})$, as a Gaussian with mean $\boldsymbol{\mu}_{\rm conf}$, given by Eq. (7.6), and covariance $\Sigma_{\rm conf}$. The correct statistical procedure of marginalising the likelihood for $d(t) - \Delta H(t)$ over the confusion noise distribution thus amounts, in the linear signal approximation, to shifting the mean by $\boldsymbol{\mu}_{\rm conf}$ and adding $\Sigma_{\rm conf}$ to the covariance. The results described here can therefore be used not only to assess when confusion is important but also to compute leading order corrections to posterior parameter estimates arising from the presence of confusion.

Appendix D

Impact of mismodelling non-stationary noise on parameter estimation studies

D.1 Generalisations from discrete to continuous

The details discussed in section 3.2.3 remain unchanged up to equation (3.41)

$$\left(\frac{S}{N}\right)(t) = \frac{\left|\int_{-\infty}^{\infty} K^{\star}(t+t')H(t')\mathrm{d}t'\right|}{\sqrt{\left\langle\left|\int_{-\infty}^{\infty} K^{\star}(t+t')N(t')\mathrm{d}t'\right|^2\right\rangle}}, \tag{D.1}$$

where now $H(t) = w(t)h(t)$ and $N(t) = w(t)n(t)$ are gapped variates of $h(t)$ and $n(t)$ respectively. We remind the reader that t stands for the lag and $K(t)$ is an arbitrary function acting as a filter. We seek the *optimal* filter which maximizes (D.1). At zero lag and Working in the Fourier domain, it can be shown that

$$\left(\frac{S}{N}\right)(0) = \frac{\left|\int_{-\infty}^{\infty} \hat{K}^{\star}(f)\hat{H}(f)\mathrm{d}f\right|}{\sqrt{\int_{-\infty}^{\infty}\int_{-\infty}^{\infty} \hat{K}(f)\Sigma_N(f,f')\hat{K}(f')\mathrm{d}f\mathrm{d}f'}} \tag{D.2}$$

The presence of the double integral on the denominator is a mild inconvenience. To make progress, we define the inverse $\Sigma_N^{-1}(f,f')$ to satisfy the equality

$$\int_{-\infty}^{\infty} \Sigma_N^{-1}(f,f'')\Sigma_N(f'',f')\mathrm{d}f'' = \delta(f-f') \tag{D.3}$$

From the Hölder inequality, we can rewrite the numerator of (D.2) as

$$\left|\int_{-\infty}^{\infty}\hat{K}^{\star}(f)\hat{H}(f)\mathrm{d}f\right| = \int_{-\infty}^{\infty}\int_{-\infty}^{\infty}|\hat{H}(f)\Sigma_N(f,f')^{-1/2}||\Sigma_N(f,f')^{1/2}\hat{K}^{\star}(f')|\mathrm{d}f\mathrm{d}f' \tag{D.4}$$

$$\leq \sqrt{\int_{-\infty}^{\infty}\int_{-\infty}^{\infty}|\hat{H}(f)\Sigma_N(f,f')^{-1/2}|^2\mathrm{d}f\mathrm{d}f'}\times \tag{D.5}$$

$$\sqrt{\int_{-\infty}^{\infty}\int_{-\infty}^{\infty}|\hat{K}^{\star}(f')\Sigma_N(f,f')^{1/2}|^2\mathrm{d}f\mathrm{d}f'}. \tag{D.6}$$

Notice for an arbitrary complex function $\hat{G}(f)$

$$|\hat{G}^{\star}(f)\Sigma_N(f,f')^{-1/2}|^2 = \hat{G}(f)(\Sigma_N^{\dagger})(f,f')^{-1/2}\Sigma_N(f,f')^{-1/2}\hat{G}^{\star}(f) = \hat{G}^{\star}(f)\Sigma_N^{-1}(f,f')\hat{G}(f). \tag{D.7}$$

Where $\Sigma_N^{\dagger}$ is the hermitian adjoint of the matrix Σ_N. These are equal from equation (8.3). Using (D.7) alongside the latter inequality (D.4) we can place an upper bound the SNR (D.2)

$$\left(\frac{S}{N}\right)(t) = \frac{\left|\int_{-\infty}^{\infty}\hat{K}^{\star}(f)\hat{H}(f)\mathrm{d}f\right|}{\sqrt{\int_{-\infty}^{\infty}\int_{-\infty}^{\infty}\hat{K}^{\star}(f)\Sigma_N(f,f')\hat{K}(f')\mathrm{d}f\mathrm{d}f'}} \leq \sqrt{\int_{-\infty}^{\infty}\int_{-\infty}^{\infty}\hat{H}^{\star}(f)\Sigma_N(f,f')\hat{H}(f')\mathrm{d}f\mathrm{d}f'}.$$

This bound is attained by choosing the filter

$$\hat{K}(f) = \int_{-\infty}^{\infty}\Sigma_N(f,f')^{-1}\hat{H}^{\star}(f')\mathrm{d}f'. \tag{D.8}$$

This can be checked by substituting (D.8) into (D.1) and using (D.3). From these results, we can define the optimal matched filtering SNR in the case of gated data

$$\rho^2_{\mathrm{gap}} = \int_{-\infty}^{\infty}\int_{-\infty}^{\infty}\hat{H}(f)\Sigma_N(f,f')^{-1}\hat{H}(f')\mathrm{d}f\mathrm{d}f' = (H|H), \tag{D.9}$$

with *general* inner product

$$(a|b) = \frac{1}{2}\int_{-\infty}^{\infty}\int_{-\infty}^{\infty}(\hat{a}^{\star}(f)\Sigma_N(f,f')^{-1}\hat{b}(f') + \hat{b}^{\star}(f)\Sigma_N(f,f')^{-1}\hat{a}(f'))\mathrm{d}f\mathrm{d}f'. \tag{D.10}$$

By splitting the integral $f \in (-\infty,0)\cup(0,\infty)$, we can rewrite the inner product above (D.10) over only the positive frequencies

$$(a|b) = \int_{0}^{\infty}\int_{0}^{\infty}(\hat{a}^{\star}(f)\Sigma_N(f,f')^{-1}\hat{b}(f') + \hat{b}^{\star}(f)\Sigma_N(f,f')^{-1}\hat{a}(f'))\mathrm{d}f\mathrm{d}f', \tag{D.11}$$

where we have used the fact that $\Sigma_N(-f,-f') = \langle\hat{N}(-f)\hat{N}^{\star}(-f')\rangle = \langle\hat{N}(f')\hat{N}^{\star}(f)\rangle = \Sigma_N(f',f)$.

In the stationary noise case, we can define the inverse to $\Sigma_n(f, f') = \frac{1}{2}\delta(f - f')S_n(f')$ as $\Sigma_n^{-1}(f, f') = 2\delta(f - f')/S_n(f')$. This is easily validated using (D.3). It is easy to check that for stationary noise defined by (3.20) and no window applied to $h(t)$, equation (D.9) does reduce to (3.46). From the results above, the likelihood will take the form

$$\log p(D|\boldsymbol{\theta}) = -\frac{1}{2}(D - H(t;\boldsymbol{\theta})|D - H(t;\boldsymbol{\theta})) \tag{D.12}$$

with inner product given by (D.11).

Equation (D.12) is the continuous analogue to the discrete form of the likelihood given in equation (8.6). Given that there exists a closed form expression for the inverse function for stationary noise, $\Sigma_n^{-1}(f, f') = 2\delta(f - f')S_n(f)^{-1}$, one can verify that (D.12) does reduce to the discrete form of the Whittle-likelihood (3.27). In the non-stationary noise case, the author has not found an explicit expression for the inverse function $\Sigma_N^{-1}(f, f')$. Thus, for practical reasons, in the remainder of chapter 8 we will work with discretised expressions.